

Ana Laura Domingues Costa

# PLANNING FOR ROBUST HIGH-SPEED RAIL SYSTEMS: THE EFFECTS OF NATURAL HAZARDS

Thesis for the Doctoral Program in Transport Systems, supervised by  
Professor Doctor Paulo Alexandre Lopes de Figueiredo Coelho and  
Professor Doctor Maria da Conceição Morais de Oliveira Cunha  
and submitted to the Faculty of Sciences and Technology  
of the University of Coimbra

September, 2013



UNIVERSIDADE DE COIMBRA



## Financial support

This research work was conducted under the MIT-Portugal Program and financed by “Fundação para a Ciência e a Tecnologia” (FCT, Portugal) through the Ph.D. grant with reference SFRH / BD / 43012 / 2008, and was co-financed by the European Social Fund (ESF) within the “Programa Operacional Potencial Humano” (POPH). The POPH research program is integrated in the “National Strategic Reference Framework 2007-2013 - Tipologia 4.1 – Formação Avançada” (QREN 2007-2013).

# MIT Portugal

**FCT** Fundação para a Ciência e a Tecnologia  
MINISTÉRIO DA EDUCAÇÃO E CIÊNCIA





# Acknowledgements

I would like to firstly express my sincere gratitude to Professor Einstein. Thank you for receiving and treating me as one of your students, although I was not officially one, and for the many and valuable insights on all the transatlantic e-mails. You have truly inspired me to be a better researcher but especially a better person. Thank you for all your guidance.

I would like to express my sincere appreciation to my supervisors Professors Paulo Coelho and Maria da Conceição Cunha for their guidance and encouragement. Thank you for your unconditional support and motivation. The last five years have been a smoother journey made possible by your vast knowledge and immense patience. Thank you for challenging me into writing this thesis Professor Paulo Coelho!

My deepest appreciation goes to the Fundação para a Ciência e Tecnologia (FCT) and the MIT|Portugal Program for the financial support. Without it this thesis would not be possible. To Professor Pais Antunes, thank you for inviting me to the many discussions and for your ever-important insights. To Professor Sussman, at MIT, thank you for allowing me to participate in your HSR group's weekly discussion meetings.

Thank you to all my friends and colleagues at the University of Coimbra for sharing these five years. Thank you António Pedro, Rui, Andreia, Ricardo, Luís and Cristina for keeping the spirits high in the office. Thank you Diana, João, Hugo, Miguel and Bruno for your companionship all this time. Thank you for the support from all within the Geotechnical Lab, namely Sr. Zé António and Professors Lemos, Paulo da Venda, Grazina, António Alberto, Paulo Pinto and Almeida e Sousa.

I have made dear friends during my stays at MIT. To my colleagues, Aiden, Despina, Brendan and Eva, thank you for making the office a better place. To Mehdi, Muhannad, Amer, Bruno, Jana, Stephen, Yvonne, Vikrant, Sevara thank you for your companionship at the CEE. To Rita, many thanks for the all the Portuguese chatting. A big thank you to my roommates João,

Sérgio and particularly Ivo and Sofia for their loving patience. A big thank you to the Wednesdays weekly group Ana, Maria, Eunice, David, Rita, Enrico and Gyorgy for all the relaxed laughs. To Cami and Alda, thank you for your friendship and all the event planning!

To Élsio, whose geek help, always with a smile, I truly appreciate! Mark, thank you for always being there for me! Thank you my dear friend Zita for the jogging and chatting after work, to André, Inês and Pedro for the laughs and for always keeping me up-to-date technology-wise, to Virgínia, Nádia and Joana for allowing me to have a Lisbon home.

I could not have done this without my family's support. To my mother and father, who have unconditionally supported my studies since 1<sup>st</sup> grade, who encouraged me to be open-minded and to have a free spirit, working hard and appreciate the good things in life, my deepest gratitude. To Zé Manel, a big thank you for constantly stimulating my reasoning and for showing me how to take chances and go off the beaten path. To Teresinha, thank you for always remembering me of those important dates but mostly for your companionship in crossing deserts, discovering cities or just looking at the horizon. To my grandfather, Tita and Zézinha thank you for all the love and encouragement.

Last but not least I want to thank Ricardo, for his loving support, overwhelming patience and extraordinary willingness to take on new challenges.

# Abstract

Planning for a High-Speed Rail (HSR) system involves decisions concerning the macro-location of the infrastructure, defining boundaries for the detailed project design. Within the planning stage, opportunities exist for the consideration of significantly different alignments, each having a particular performance considering construction and operation characteristics.

The large investments required to build a HSR network are generally supported by public funding, which require a conscious allocation of resources and increase the demand for a high-level of performance. The safety and quality of service offered by high-speed trains are influenced by the HSR configuration and by its interrelations with the deployment site characteristics. And, while standard planning conditions (SPC) are those prevailing within the infrastructure's lifetime, uncertain and extreme events can severely damage and disrupt transportation infrastructure as clearly shown by recent history (e.g. 2011 Japan Earthquake, 2012 Hurricane Sandy).

Decisions, however, can be made at the HSR planning stage that reduce the exposure, such as the corridors to cross, and that reduce the vulnerability, such as the cross-sections to adopt. The HSR is commonly exposed and vulnerable to multiple and uncertain natural hazards but planning for the worst-case is economically unfeasible. On the other hand, weighting the importance attributed to the effects of natural hazards according to their probability of occurrence can result in HSR configurations essentially neglecting low probability but potentially destructive events.

Addressing these issues, the thesis proposes a robust optimization model for the consideration of the effects of natural hazards in HSR planning. The model aims at finding optimal or near-optimal HSR configurations that are not overly sensitive to any specific natural hazard, while capturing the risk aversion context of decision-making generally observed for public and expensive infrastructure. The performance for each of the scenarios, representing a particular

natural hazard, is assessed by the direct market losses pertaining to the physical damage of the HSR. In many cases, the HSR scenario performance can be improved at larger construction costs but the latter are often budget constrained. The approach trades-off the HSR performance for natural hazards and the performance for SPC, the regular conditions under which to perform.

The robust approach builds on the SPC model, considering the construction costs, the demanding geometry design of the alignment, the connection of intermediate locations and land-use concerns, which is extended to incorporate scenario-descriptions of the uncertain natural hazards. Different geotechnical structures and design solutions can be chosen for the layout (cuts, embankments, tunnels and bridges) each having a particular performance depending on the deployment site characteristics. In the planning context, covering large areas and considering significantly different HSR, it is extremely complex to ascertain the HSR configuration yielding the most value.

To assist the decision-making process, a user-friendly computational tool is developed. It is programmed in Microsoft Visual Studio C# linked to a Microsoft SQL Server 2008 database. The tool applies both the SPC and robust models and implements a local search technique, the Simulated Annealing Algorithm, to solve the problem. The tool is able to cope with the interrelation of factors affecting the HSR performance and the capabilities of both the SPC and robust models are shown for a large and complex real-world problem. Applications to a Portuguese case, the Lisbon-Oporto HSR planning problem are presented. The results obtained for the SPC show the ability of the SAA to find sound configurations within the cost bounds of existing HSR. The robust model is solved considering two seismic scenarios and one rainfall scenario inducing floods. The robust HSR solutions consistently improve the natural hazards performance of the SPC optimization solutions at moderately larger construction costs. Moreover, increasing the importance attributed to the natural hazards performance results in solutions less affected by such extreme events but also more expensive.



# Resumo

O planeamento de Redes Ferroviárias de Alta Velocidade (AV) envolve decisões para a macro localização da infraestrutura, definindo delimitações para o projecto final. Na fase de planeamento é possível considerar alinhamentos significativamente diferentes, cada um dos quais associado a uma performance específica de características de construção e operação.

Os grandes investimentos necessários à construção de AV são em geral suportados por financiamento público, requerendo uma conscienciosa alocação dos recursos e exigindo elevados níveis de performance. A segurança e a qualidade do serviço oferecido são influenciadas pela configuração das AV e pela sua inter-relação com as características do local de implementação. E, enquanto as condições de planeamento *standard* (SPC) serão predominantes durante o tempo de vida útil, eventos extremos e incertos podem degradar e interromper as AV como claramente demonstrado pela história recente (p. ex. o Grande Terramoto do Leste do Japão em 2011 e o Furação Sandy em 2012).

No entanto, decisões podem ser tomadas na fase de planeamento das AV para a redução da exposição, como a escolha dos corredores, e para a redução da vulnerabilidade, como a escolha das secções transversais a adoptar. As AV estão em geral expostas e vulneráveis a múltiplos perigos naturais de ocorrência incerta e o planeamento para as condições mais desfavoráveis é economicamente inviável. Por outro lado, atribuir uma importância para os efeitos dos perigos naturais proporcional à probabilidade de ocorrência pode resultar na negligência de perigos de baixa probabilidade mas potencialmente destrutivos.

Abordando estas questões, a tese propõe um modelo de optimização robusta para a consideração dos efeitos dos perigos naturais no planeamento de AV. O modelo robusto tem como objectivo encontrar configurações de AV óptimas ou próximas do óptimo que não sejam excessivamente sensíveis a nenhum perigo natural específico e que consigam capturar o contexto de aversão ao risco geralmente observado em infraestruturas públicas e dispendiosas.

A performance para cada cenário, individualmente representando um perigo natural específico, é avaliada pelos custos directos correspondentes aos danos físicos das AV. Em muitas circunstâncias, a performance das AV para os cenários pode ser melhorada através de custos de construção mais elevados mas estes estão frequentemente sujeitos a restrições orçamentais. A abordagem estabelece uma relação de compromisso entre a performance para perigos naturais e a performance para SPC, as condições normais de performance.

A abordagem robusta fundamenta-se no modelo de optimização SPC, que considera os custos de construção, os exigentes parâmetros geométricos do alinhamento, a ligação de localizações intermédias e questões do uso do solo, que é estendido para incorporar os perigos naturais incertos representados por cenários. Diferentes estruturas geotécnicas e soluções de projecto podem ser decididas para a configuração (escavações, aterros, túneis e pontes) cada um dos quais tendo uma performance específica dependendo das características do local de implementação. No contexto do planeamento, que considera uma área extensa e configurações de AV significativamente diferentes, é extremamente complexo determinar a configuração para as AV com mais valor.

Uma ferramenta computacional amigável do utilizador é desenvolvida para apoiar o processo de decisão. Esta é programada em Microsoft Visual Studio C# conectada a uma base de dados Microsoft SQL Server 2008. A ferramenta tem a capacidade de aplicar ambos os modelos SPC e robusto e implementa uma técnica de procura local, o *Simulated Annealing Algorithm* (SAA), para a resolução do problema. A ferramenta é capaz de lidar com a inter-relação de factores que afectam a performance de AV e as capacidades de ambos os modelos SPC e robusto são demonstradas com a aplicação a um problema complexo do mundo real. Aplicações para um caso português, o planeamento da ligação Lisboa-Porto por AV, são apresentadas. Os resultados obtidos para o modelo SPC demonstram a capacidade do SAA em encontrar configurações fundamentadas com custos enquadrados nos custos de AV existentes. O modelo robusto é resolvido considerando dois cenários sísmicos e um cenário de chuvas intensas com geração de inundações. As soluções robustas melhoram consistentemente, com custos de construção moderadamente mais elevados, a performance para os perigos naturais das soluções obtidas para as SPC. Ainda, o aumento da importância atribuída à performance para os perigos naturais resulta em soluções menos afectadas por este tipo de eventos extremos mas sendo também mais dispendiosas.

# Table of Contents

- Acknowledgements ..... i
- Abstract ..... iii
- Resumo ..... v
- Table of Contents ..... vii
- Notation ..... xiii
- List of Figures ..... xxi
- List of Tables ..... xxxiii
- Chapter 1. Introduction ..... 1
  - 1.1 Problem Statement and Motivation ..... 1
  - 1.2 Current Needs of High-Speed Rail Planning Models ..... 2
  - 1.3 Research Objectives, Scope and Contributions ..... 3
    - 1.3.1 Objectives ..... 3
    - 1.3.2 Scope of the Research ..... 4
    - 1.3.3 Research Contributions ..... 5
  - 1.4 Thesis Layout ..... 6
- Chapter 2. High-Speed-Rail: State-of-the-Practice and State-of-the-Art ..... 9
  - 2.1 Geometric Design ..... 10
    - 2.1.1 Track Gauge ..... 10
    - 2.1.2 Horizontal Curve Radius ..... 11
    - 2.1.3 Gradients ..... 14
    - 2.1.4 Vertical Curves ..... 15
  - 2.2 General Design Principles for Earthworks ..... 16
    - 2.2.1 Displacement Limits and Seismic Design ..... 16
    - 2.2.2 Earthworks Geotechnical Design: Platform Requirements ..... 18
      - 2.2.2.1 Ballast ..... 19
      - 2.2.2.2 Blanket Layer ..... 19
      - 2.2.2.3 Subgrade or Platform ..... 20
      - 2.2.2.4 Design of the Platform Layers ..... 20
    - 2.2.3 Earthworks Geotechnical Design: Geometry and Ground Improvement ..... 23
    - 2.2.4 Hydraulics Design ..... 24
  - 2.3 High-Speed Rail Costs ..... 25
    - 2.3.1 Variability of HSR Construction Costs ..... 26
  - 2.4 Rail Disruptions due to Natural Hazards ..... 28

|            |  |     |
|------------|--|-----|
| 2.4.1      | Destructive and Disruptive Capabilities of Natural Hazards.....                                    | 28  |
| 2.4.2      | Terminology and Concepts .....   | 34  |
| 2.4.3      | Transportation Performance and the Impacts of Disruption.....                                      | 38  |
| 2.4.4      | Remarks on the Natural Hazards HSR Performance Assessment in the Context of the Research..         | 43  |
| Chapter 3. | Optimization of Linear Transportation Infrastructures: State-of-the-Art .....                      | 45  |
| 3.1        | Modelling the Optimization Problem .....   | 45  |
| 3.1.1      | The Consideration of Uncertainty .....   | 55  |
| 3.1.2      | Robust Optimization .....  | 57  |
| 3.1.3      | Remarks for the HSR Planning Optimization Considering Natural Hazards .....                        | 62  |
| 3.2        | Solving Techniques .....   | 64  |
| 3.2.1      | Solving Techniques for models of Linear Transportation Infrastructures .....                       | 65  |
| 3.2.2      | Remarks on Solving the HSR Planning Problem .....  | 68  |
| 3.2.2.1    | The Simulated Annealing Algorithm.....   | 69  |
| Chapter 4. | Modeling and Solving the HSR Planning Optimization Problem Considering Natural Hazards ....        | 73  |
| 4.1        | Optimization Model for Standard Planning Conditions .....  | 74  |
| 4.1.1      | Objective Function .....   | 75  |
| 4.1.1.1    | Construction cost.....   | 81  |
| 4.1.1.2    | Geometry Penalties: Horizontal Angle and Gradient .....  | 88  |
| 4.1.1.3    | Land Use Penalty.....  | 91  |
| 4.1.1.4    | Location Benefits .....  | 91  |
| 4.1.2      | Constraints .....  | 92  |
| 4.1.2.1    | Location Constraint .....  | 92  |
| 4.1.2.2    | Geometry Constraints.....  | 92  |
| 4.1.2.3    | Land-Use Constraint.....   | 92  |
| 4.2        | Implementation of the Simulated Annealing Algorithm .....  | 93  |
| 4.2.1      | Generation of HSR Candidate Configurations .....   | 95  |
| 4.2.2      | Cooling Schedule .....   | 98  |
| 4.3        | Software Testing: Application to a Synthetic Case-Study for Standard Planning Conditions.....      | 100 |
| 4.3.1      | Characteristics of the Base Case .....   | 101 |
| 4.3.2      | Results of the Base Case .....   | 102 |
| 4.3.3      | Sensitivity Analysis.....  | 107 |
| 4.3.3.1    | Penalty Coefficients.....  | 107 |
| 4.3.3.2    | Location Benefit Term .....  | 108 |
| 4.3.3.3    | Normal and Limit Horizontal Angles .....   | 109 |
| 4.3.4      | Remarks on the Synthetic Case-Study Application.....   | 109 |
| 4.4        | Extending the Software Capabilities .....  | 110 |
| 4.4.1      | Influence of the Forbidden Land-Use Areas on the Generation of HSR Candidate Configurations<br>111 |     |
| 4.4.2      | Minimum Length of Linear Sections .....  | 118 |
| 4.5        | The HSR Planning Robust Optimization Model .....   | 119 |
| 4.5.1      | Objective Function .....   | 121 |
| 4.5.2      | Constraints .....  | 125 |

|  |     |
|--|-----|
| Chapter 5. The Lisbon-Oporto HSR Planning Problem.....   | 127 |
| 5.1 Input Spatial Data .....   | 129 |
| 5.1.1 Lithology .....  | 132 |
| 5.1.2 Land-use.....  | 135 |
| 5.1.3 Ground Use Classes: Expropriation Costs .....  | 138 |
| 5.1.4 Digital Elevation Model.....   | 143 |
| 5.1.5 Portuguese Main Rivers .....   | 145 |
| 5.2 HSR Configuration Geometry Layout.....   | 148 |
| 5.2.1 Horizontal Angle Limit and Normal Values .....   | 148 |
| 5.2.2 Minimum Length of the HSR Linear Sections.....   | 151 |
| 5.3 Cross-Sections and Construction Costs .....  | 151 |
| 5.3.1 Expropriation Costs.....   | 151 |
| 5.3.2 Earthworks .....   | 151 |
| 5.3.3 Bridges .....  | 161 |
| 5.3.3.1 The Influence of the Bridge Maximum Height Cost Factor .....                               | 162 |
| 5.3.4 Tunnels.....   | 168 |
| 5.3.5 Length-Dependent Costs.....  | 168 |
| 5.4 Seismic Scenarios.....   | 168 |
| 5.4.1 Earthquake Characteristics .....   | 170 |
| 5.4.1.1 Seismic Scenario 1 .....   | 171 |
| 5.4.1.2 Seismic Scenario 2 .....   | 172 |
| 5.4.2 Earthquake Triggered Landslides.....   | 172 |
| 5.4.2.1 Susceptibility Assessment .....  | 176 |
| 5.4.2.2 Triggering Conditions .....  | 184 |
| 5.4.2.3 Damages Cost Evaluation.....   | 187 |
| 5.4.3 Liquefaction .....   | 188 |
| 5.4.3.1 Susceptibility Assessment .....  | 190 |
| 5.4.3.2 Triggering Conditions .....  | 197 |
| 5.4.3.3 Damages Cost Evaluation.....   | 202 |
| 5.5 Intense Rainfall Scenario.....   | 204 |
| 5.5.1 Rainfall Characteristics .....   | 205 |
| 5.5.2 Rainfall-Triggered Landslides.....   | 207 |
| 5.5.2.1 Susceptibility Assessment .....  | 209 |
| 5.5.2.2 Triggering Conditions .....  | 216 |
| 5.5.2.3 Damages Cost Evaluation.....   | 219 |
| 5.5.3 Flood .....  | 220 |
| 5.5.3.1 Damages Cost Evaluation.....   | 222 |
| 5.6 Summary Remarks on the Formulation of Scenarios .....  | 223 |
| Chapter 6. Solving the Lisbon-Oporto HSR Planning Problem: Standard Planning Conditions (SPC)..... | 227 |
| 6.1 Application of the SPC Model to the Lisbon-Oporto HSR .....                                    | 228 |
| 6.1.1 Geometry Penalties: Horizontal Angle and Gradient .....                                      | 228 |

|            |  |     |
|------------|--|-----|
| 6.1.2      | Land-Use Penalty .....   | 229 |
| 6.1.3      | Location Benefit.....  | 229 |
| 6.1.4      | Location Constraints .....   | 230 |
| 6.1.5      | Geometry Constraints.....  | 230 |
| 6.1.6      | Land-Use Constraint .....  | 230 |
| 6.2        | Implementation of the Simulated Annealing Algorithm .....            | 231 |
| 6.2.1      | Initial HSR Configuration .....                                      | 231 |
| 6.2.2      | Generation of Candidate HSR Configurations .....                     | 234 |
| 6.2.3      | Cooling Schedule .....   | 234 |
| 6.3        | SPC Application Results .....  | 245 |
| 6.3.1      | Characterization of the Solution.....                                | 245 |
| 6.3.2      | Construction Costs of the Solution.....                              | 265 |
| 6.3.3      | Comparison with the Portuguese Conventional Rail Line .....          | 268 |
| 6.4        | The Effect of Reducing the Location Benefit Coefficients.....        | 270 |
| 6.4.1      | Characterization of the Solution.....                                | 270 |
| 6.5        | Remarks on the SPC Application .....                                 | 282 |
| Chapter 7. | Solving the Lisbon-Oporto HSR Planning Problem: Robust Approach..... | 285 |
| 7.1        | Application of the Robust Model to the Lisbon-Oporto HSR .....       | 286 |
| 7.1.1      | Geometry Penalties: Horizontal Angle and Gradient .....              | 287 |
| 7.1.2      | Land-Use Penalty .....   | 288 |
| 7.1.3      | Location Benefit.....  | 288 |
| 7.1.4      | Location Constraints .....   | 289 |
| 7.1.5      | Geometry Constraints.....  | 289 |
| 7.1.6      | Land-Use Constraint .....  | 290 |
| 7.1.7      | Scenario-Weight ( $\Psi_c$ ) Combinations.....                       | 290 |
| 7.1.8      | The Robust Applications Performed for Comparative Analyses .....     | 291 |
| 7.2        | Implementation of the Simulated Annealing Algorithm .....            | 292 |
| 7.3        | Scenario-Weight Combination #1 .....                                 | 295 |
| 7.3.1      | Location Benefit Coefficient $\gamma$ ( $\omega=1$ ) .....           | 295 |
| 7.3.1.1    | Detailed Analysis of the Aveiro-Leiria Section.....                  | 310 |
| 7.3.1.2    | Detailed Analysis of the Leiria-Lisbon Section.....                  | 317 |
| 7.3.2      | Location Benefit Coefficient $\gamma/3$ ( $\omega=1$ ).....          | 321 |
| 7.3.3      | Location Benefit Coefficient $\gamma/3$ ( $\omega=30$ ) .....        | 337 |
| 7.4        | Scenario-Weight Combination #2 .....                                 | 355 |
| 7.4.1      | Location Benefit Coefficient $\gamma/3$ ( $\omega=1$ ).....          | 355 |
| 7.5        | Remarks on the Robust Approach Applications .....                    | 369 |
| Chapter 8. | Conclusions and Future Research .....                                | 373 |
| 8.1        | Conclusions .....  | 374 |
| 8.1.1      | Modelling the HSR Planning Problem.....                              | 374 |
| 8.1.2      | Computational Tool and Solving Technique.....                        | 376 |
| 8.1.3      | The Lisbon-Oporto HSR Planning Problem.....                          | 378 |

Table of Contents

---

|                              |     |
|------------------------------|-----|
| 8.2 Future Developments..... | 380 |
| Literature References .....  | 383 |





# Notation

## Acronyms

|       |  |
|-------|--|
| AFP   | Agence France-Presse   |
| APA   | The Portuguese Agency of the Environment ( <i>Agência Portuguesa do Ambiente</i> ) |
| CEN   | European Committee for Standardization ( <i>Comité Européen de Normalisation</i> ) |
| CGE   | Computable General Equilibrium   |
| CRED  | Center for Research on the Epidemiology of Disasters                               |
| CSIRO | Commonwealth Scientific and Industrial Research Organization                       |
| DB    | <i>Deutsche Bahn</i>   |
| DEM   | Digital Elevation Model  |
| EC    | European Commission  |
| FEMA  | Federal Emergency Management Agency  |
| FHWA  | Federal Highway Administration   |
| GIS   | Geographic Information Systems   |
| HAZUS | HAZards United States  |
| HSR   | High-Speed Rail  |

|          |   |
|----------|---|
| IGeoE    | Portuguese Geographical Institute of the Army ( <i>Instituto Geográfico do Exército</i> )                                       |
| IPCC     | Intergovernmental Panel on Climate Change   |
| ISSMGE   | International Society for Soil Mechanics and Geotechnical Engineering   |
| I-O      | Input-Output  |
| JR       | Japan Railways Group  |
| JRC      | Joint Research Centre   |
| LTV      | Lower Tagus Valley  |
| OFDA     | Office of U.S. Foreign Disaster Assistance  |
| RAVE     | Portuguese High Speed Rail Network company ( <i>Rede Ferroviária de Alta Velocidade, S.A.</i> )                                 |
| RTRI     | Railway Technical Research Institute  |
| SNCF     | French National Railways ( <i>Société Nationale des Chemins de Fer</i> )  |
| SNIRH    | Portuguese National Information System on Hydrological Resources ( <i>Sistema Nacional de Informação de Recursos Hídricos</i> ) |
| SAA      | Simulated Annealing Algorithm   |
| SLP      | Stochastic Linear Programming   |
| SPC      | Standard Planning Conditions  |
| TEN-T EA | Trans-European Transport Network Executive Agency   |
| TSI      | Technical Specification for Interoperability  |
| UIC      | International Union of Railways ( <i>Union Internationale des Chemins de Fer</i> )  |
| UK       | United Kingdom  |
| UNISDR   | The United Nations International Strategy for Disaster Reduction  |

|          |  |
|----------|--|
| USA      | United States of America                   |
| U.S.     | United States                              |
| USGS     | United States Geological Survey            |
| U.S. DOT | United States Department of Transportation |
| WB       | World Bank                                 |

## Symbols

### *Roman*

|                       |  |
|-----------------------|--|
| $a_c$                 | Centrifugal acceleration   |
| $a$                   | SAA elasticity of acceptance   |
| $B_{(i,j)}$           | Bridges cost of a HSR linear section linking nodes $i$ and $j$               |
| $C_{ij}$              | Total construction cost of a HSR linear section linking nodes $i$ and $j$    |
| $cm_b$                | Construction method of bridge $b$  |
| $C_{unit}^{ballast}$  | Unit construction cost (€/m) of ballast                                      |
| $C_{unit}^{catenary}$ | Unit construction cost (€/m) of catenary                                     |
| $C_{unit}^{cutB}$     | Unit construction cost (€/m <sup>3</sup> ) of excavation by blasting         |
| $C_{unit}^{cutMM}$    | Unit construction cost (€/m <sup>3</sup> ) of excavation by mechanical means |

|                    |  |
|--------------------|--|
| $C_{unit}^{emb}$   | Unit construction cost (€/m <sup>3</sup> ) of embankment                       |
| $C_{unit}^{FL}$    | Unit construction cost (€/m <sup>3</sup> ) of form layer                       |
| $C_{unit}^{GI}$    | Unit construction cost (€/m <sup>3</sup> ) of ground improvement               |
| $C_{unit}^{SB}$    | Unit construction cost (€/m <sup>3</sup> ) of sub-ballast                      |
| $C_{unit}^{track}$ | Unit construction cost (€/m) of track  |
| $Ex_{(i,j)}$       | Expropriation cost of a HSR linear section linking nodes $i$ and $j$           |
| $EW_{(i,j)}$       | Earthworks cost of a HSR linear section linking nodes $i$ and $j$              |
| $f_b$              | Bridge global cost function (€)  |
| $f_t$              | Tunnel global cost function (€)  |
| $Gb(t)$            | Ground behavior in tunnel $t$  |
| $h_b^{\max}$       | Maximum height of bridge $b$   |
| $k_{CM}$           | Bridge cost construction method coefficient                                    |
| $k_h$              | Bridge cost height coefficient   |
| $LD_{(i,j)}$       | Linear-dependent cost of a HSR linear section linking nodes $i$ and $j$        |
| $l_b$              | Length of bridge $b$   |
| $l_{(i,j)}$        | Length of a HSR linear section linking nodes $i$ and $j$                       |
| $l_s$              | Length of space property element $s$ overlaid by a HSR linear section          |
| $l_t$              | Length of tunnel $t$   |
| $n_1$              | SAA minimum number of algorithm iterations to be performed at each temperature |
| $n_2$              | SAA number of temperature decreases to be performed without                    |

|                     |  |
|---------------------|--|
|                     | improvement of the optimum or the average cost   |
| $M_L$               | Local magnitude of an earthquake   |
| $M_S$               | Surface-wave magnitude of an earthquake  |
| $M_W$               | Moment magnitude of an earthquake  |
| $P_{\beta(i,j,k)}$  | Horizontal angle penalty value of a HSR linear section linking nodes $i$ , $j$ and $k$         |
| $P_{\lambda_s}$     | Land-use penalty value of space property element $s$   |
| $P_{\eta(i,j)}$     | Gradient penalty value of a HSR linear section linking nodes $i$ and $j$                       |
| $P_{v_i}$           | Location benefit value of a nodes $i$  |
| $r$                 | SAA temperature decrease rate  |
| $R$                 | Radius of a curve  |
| $RC_{ij}^c$         | Reconstruction/repair costs a HSR linear section linking nodes $i$ and $j$ for scenario $c$    |
| $T_{(i,j)}$         | Tunnels cost of a HSR linear section linking nodes $i$ and $j$                                 |
| $v$                 | Design speed of a railway  |
| $V_{(i,j)}^{cutB}$  | Volume ( $m^3$ ) of cuts by blasting of a HSR linear section linking nodes $i$ and $j$         |
| $V_{(i,j)}^{cutMM}$ | Volume ( $m^3$ ) of cuts by mechanical means of a HSR linear section linking nodes $i$ and $j$ |
| $V_{(i,j)}^{emb}$   | Volume ( $m^3$ ) of embankments of a HSR linear section linking nodes $i$ and $j$              |
| $V_{(i,j)}^{FL}$    | Volume ( $m^3$ ) of form layer of a HSR linear section linking nodes $i$ and $j$               |
| $V_{(i,j)}^{GI}$    | Volume ( $m^3$ ) of ground improvement of a HSR linear section linking nodes $i$ and $j$       |

$V_{(i,j)}^{SB}$  Volume ( $m^3$ ) of sub-ballast of a HSR linear section linking nodes  $i$  and  $j$

### ***Greek***

$\beta_{(i,j,k)}$  Angle measured in the horizontal projection of the HSR at node  $j$  formed by two linear sections linking nodes  $i$ ,  $j$  and  $k$

$\beta_{\text{limit}}$  Horizontal angle limit value

$\beta_{\text{normal}}$  Horizontal angle normal value

$\gamma_{\beta}$  Horizontal angle penalty coefficient

$\gamma_{\eta}$  Gradient penalty coefficient

$\gamma_{\lambda_s}$  Land use penalty coefficient of space property element  $s$

$\gamma_{v_i}$  location benefit coefficient of node  $i$

$\eta_{(i,j)}$  Gradient of linear section linking nodes  $i$  and  $j$

$\eta_{\text{limit}}$  Gradient limit value

$\eta_{\text{normal}}$  Gradient normal value

$\Psi_c$  Weight of scenario  $c$

$\Omega_E$  Set of all space property elements

$\Omega_E^{ij}$  subset of  $\Omega_E$ , representing the space property elements overlaid in the plan view by a linear section linking nodes  $i$  and  $j$

$\Omega_{FE}$  Subset of  $\Omega_E$  containing all space property elements of forbidden land-use.

$\Omega_{MN}$  Subset of  $\Omega_N$  containing all mandatory nodes.

|               |   |
|---------------|---|
| $\Omega_N$    | Set of all three-dimensional nodes of the discretization mesh                       |
| $\Omega_{SC}$ | Set of all scenarios  |
| $\omega$      | Weight multiplying the natural hazards performance in the robust objective function |





# List of Figures

|                    |   |    |
|--------------------|---|----|
| <b>Figure 2-1</b>  | General rail track cross-section in a straight line. ....   | 10 |
| <b>Figure 2-2</b>  | General rail track cross-section for a horizontal curve.....  | 12 |
| <b>Figure 2-3</b>  | Example of two clothoid curves of 300 m length between linear sections (radius $R=\infty$ ) and a circular curve (radius $R = 5350$ m) from km1+000m to km 2+200m of a HSR line.....  | 14 |
| <b>Figure 2-4</b>  | General Cross-section for embankments and cuts adapted from (UIC 1994).....   | 19 |
| <b>Figure 2-5</b>  | Range of average construction cost per kilometer of new HSR lines around the world in 2005 million euros (planning and land costs excluded) (Mendoza et al. 2009). ....   | 28 |
| <b>Figure 2-6</b>  | Number of people reported killed by natural disasters in the period 1975-2011. Source: EM-DAT: The OFDA/CRED International Disaster Database <a href="http://www.emdat.be">www.emdat.be</a> , Université Catholique de Louvain, Brussels (Belgium).....                 | 29 |
| <b>Figure 2-7</b>  | Estimated damage in US\$ billion caused by reported natural disasters in the period 1975-2011. Source: EM-DAT: The OFDA/CRED International Disaster Database <a href="http://www.emdat.be">www.emdat.be</a> , Université Catholique de Louvain, Brussels (Belgium)..... | 30 |
| <b>Figure 2-8</b>  | Submerged rail track used for coal transport in Queensland, Australia, January 2, 2011 (Munoz 2011).....  | 31 |
| <b>Figure 2-9</b>  | Damage to the rail infrastructure in Cumbria, UK, in August 30, 2012 caused by rainfall-triggered landslides. (Network Rail in BBC News (2012)). ....   | 32 |
| <b>Figure 2-10</b> | Train derailment in Dongxiang county, Jiangxi Province, China, May 23, 2010 caused by a rainfall-triggered landslide. (AFP in BBC News (2010)). ....  | 32 |
| <b>Figure 2-11</b> | Support column failure and collapsed upper deck on the Cypress viaduct, Oakland (USGS 1998f). ....  | 33 |
| <b>Figure 2-12</b> | Liquefaction damages to the rail infrastructure from the 2004 Niigata Ken Chuetsu earthquake: a) the derailed Shinkanzen train and b)   |    |

|                    |  |     |
|--------------------|--|-----|
|                    | damages to the viaduct columns where the derailment occurred. (Ogura 2006).....  | 34  |
| <b>Figure 3-1</b>  | Plan view of highway alignments: a) non-backtracking and b) backtracking. (Jong 1998). .....   | 48  |
| <b>Figure 3-2</b>  | The optimal alignment for the case-study application by Jong et al. (2000).....  | 50  |
| <b>Figure 3-3</b>  | The optimal alignment plan view and longitudinal profile for a synthetic case-study application of highway alignment optimization considering bridges and tunnels ( Kim et al. 2007). Dimensions in the plan view and for elevation in ft (1 ft = 30.48 cm). ..... | 52  |
| <b>Figure 3-4</b>  | Simulated Annealing Algorithm flow chart (Cohanin et al. 2004). .....  | 70  |
| <b>Figure 3-5</b>  | Local and global optima for a unidimensional minimization problem. ....  | 72  |
| <b>Figure 4-1</b>  | Ground elevation of a synthetic case-study and the 3D mesh defining the permissible node positions for each HSR configuration. ....  | 79  |
| <b>Figure 4-2</b>  | Plan view detail of the permissible node positions mesh defining $\Omega_N$ overlaying the space property elements forming $\Omega_E$ and representing the discretization of elevation data. ....  | 80  |
| <b>Figure 4-3</b>  | Determination of $\Omega_E^{ij}$ .....   | 81  |
| <b>Figure 4-4</b>  | HSR configuration and the respective overlay on the expropriation cost map. ....   | 82  |
| <b>Figure 4-5</b>  | Diagram of HSR and ground elevations and volume calculation with the average end-area method. ....   | 84  |
| <b>Figure 4-6</b>  | HSR overlaying the ground behavior layer. ....   | 85  |
| <b>Figure 4-7</b>  | Gradient penalty formulation.....  | 90  |
| <b>Figure 4-8</b>  | Horizontal angle penalty formulation.....  | 90  |
| <b>Figure 4-9</b>  | Identification of forbidden land-use space property elements $\Omega_{FE}$ . ....  | 93  |
| <b>Figure 4-10</b> | SAA flowchart.....   | 94  |
| <b>Figure 4-11</b> | 3D neighborhood definition for a current gray (center) node. ....  | 96  |
| <b>Figure 4-12</b> | Perturbing a current configuration into a neighboring candidate configuration.....   | 97  |
| <b>Figure 4-13</b> | Case study specifics: a) Nodes overlaying the elevation-, ground behavior-, expropriation cost - and land-use layers; b) Ground elevation and 3D mesh defining the permissible node positions in each configuration.....   | 102 |
| <b>Figure 4-14</b> | Influence of temperature decrease rate $r$ on the average cost of the configurations. ....   | 103 |

|                    |  |     |
|--------------------|--|-----|
| <b>Figure 4-15</b> | Convergence history for $a = 0.9$ , $r = 0.9$ , $n_1 = 5,000$ and $n_2 = 10$ : evolution of the last accepted configuration before a temperature decrease and of the current optimum at the time of each temperature decrease. ....  | 105 |
| <b>Figure 4-16</b> | Plan view of the best configurations: a) and b) for the base case, c) and d) for $\gamma_{vB} = 0$ and e) and f) for sensitivity analysis of $\beta_{normal}/\beta_{limit}$ ; configurations overlay the ground elevation layer in a), c) and e) and the land-use layer in b), d) and f). .... | 107 |
| <b>Figure 4-17</b> | HSR configurations overlaying the protected land-use layer map (scale 1:2 000 000): a) initial configuration and b) best configuration found by the SAA. ....  | 112 |
| <b>Figure 4-18</b> | Leaping over “islands” of forbidden land-use by moving only one node of the current HSR configuration: a) successfully and b) unsuccessfully. ....   | 113 |
| <b>Figure 4-19</b> | Leaping over the forbidden land-use area of Figure 4-18 (b) with the repositioning of node N, the anterior node (N-1) and the posterior node (N+1). ....   | 114 |
| <b>Figure 4-20</b> | Leaping over “islands” of forbidden land-use: a) displacement of 2 anterior and 2 posterior nodes and b) displacement of 3 anterior and 3 posterior nodes. ....  | 116 |
| <b>Figure 4-21</b> | Leaping over “islands” of forbidden land-use with displacement of 4 anterior and 4 posterior nodes. ....   | 117 |
| <b>Figure 4-22</b> | Plan view a HSR configuration showing evidence of node clustering, overlaying a land-use layer. ....   | 118 |
| <b>Figure 5-1</b>  | Location of the cities of interest to the Lisbon-Porto HSR case study, the existing conventional railway network and identification of the study area (APA 2012). ....   | 128 |
| <b>Figure 5-2</b>  | Zoom of a $1,200 * 800 \text{ m}^2$ rectangle of the search area: grid elevation data and the corresponding discretization space property elements. Elevation data in meters. ....   | 130 |
| <b>Figure 5-3</b>  | Location of the nodes representing each city: a) by the (x;y;z) coordinates in (km;km;m) overlaying the search area map with the Portuguese border and b) overlaying the discretization mesh plan view. ....   | 131 |
| <b>Figure 5-4</b>  | Lithological map of the study area (APA 2012). Scale: 1/1,500,000. ....  | 133 |
| <b>Figure 5-5</b>  | Map of the protected land-use areas (APA 2012). Scale: 1/1,500,000. ....   | 137 |
| <b>Figure 5-6</b>  | Ground use classes map (APA 2012). Scale: 1/1,500,000. ....  | 139 |
| <b>Figure 5-7</b>  | Expropriation cost map. Scale: 1/1,500,000. ....   | 142 |
| <b>Figure 5-8</b>  | Elevation map. Scale: 1/1,500,000. ....  | 144 |
| <b>Figure 5-9</b>  | Main rivers map. Scale: 1/1,500,000 (APA 2012). ....   | 145 |

|                    |   |     |
|--------------------|---|-----|
| <b>Figure 5-10</b> | Main rivers' map, location of the cross-section line defining the upstream limits of the 70 m bridge height feasibility requirement and location of the cities to connect with the HSR.....   | 147 |
| <b>Figure 5-11</b> | Variations of the external secant ( $\Delta$ ), the curve radius (R) and the tangent (T) for three horizontal angles: $\beta= 100^\circ$ , $\beta= 120^\circ$ and $\beta= 140^\circ$ .....  | 149 |
| <b>Figure 5-12</b> | Maximum distance from a space property element center for which boundary is within an adjacent space property element, in any given direction. ....   | 150 |
| <b>Figure 5-13</b> | General cross-sections for embankments. ....  | 156 |
| <b>Figure 5-14</b> | General cut cross-section with different slopes and maximum depth of 8 m. ....  | 157 |
| <b>Figure 5-15</b> | General cut cross-section for different slopes and depths between 8 m to 18 m. ....   | 157 |
| <b>Figure 5-16</b> | General cut cross-section for different slopes and depths between 18 m to 26 m. ....  | 158 |
| <b>Figure 5-17</b> | General cut cross-section for different slopes and depths between 26 m to 34 m. ....  | 159 |
| <b>Figure 5-18</b> | Plan view overlay of the best HSR configuration found for the Lisbon-Oporto case-study considering $k_h=1$ for all bridges: a) lithological map, b) land-use map, c) expropriation cost map, d) elevation map and e) main rivers map. ....  | 163 |
| <b>Figure 5-19</b> | Longitudinal profile of the best HSR configuration found by the SAA, considering $k_h=1$ for all bridges.....   | 166 |
| <b>Figure 5-20</b> | Seismic zoning for interplate (left) and intraplate (right) earthquakes affecting mainland Portugal proposed by the Eurocode 8 working group for the Portuguese National Annexes of Eurocode 8 (NP EN 1998-1) (Campos Costa and Sousa 2008). ....   | 169 |
| <b>Figure 5-21</b> | Identification of earthquake-triggered landslides susceptible deposits. ....  | 178 |
| <b>Figure 5-22</b> | Slope angle obtained from the DEM. ....   | 179 |
| <b>Figure 5-23</b> | Slope angle obtained from the DEM, grouped into 2 intervals: $< 20^\circ$ and $20^\circ - 36.51^\circ$ . ....   | 180 |
| <b>Figure 5-24</b> | Overlay of earthquake-triggered landslides susceptible lithology units and the slope angle intervals: non-susceptible deposits in white; susceptible deposits where slope angle is $<20^\circ$ in green (lighter gray shade) and susceptible areas in red (darker gray shade) pictured within the zoom frames Z1_EQ_LS, Z2_EQ_LS, Z3_EQ_LS and Z4_EQ_LS. .... | 182 |
| <b>Figure 5-25</b> | Zoom-in of zone Z1_EQ_LS: susceptible earthquake-triggered landslide areas in red (darker shade). ....  | 183 |

|                    |   |     |
|--------------------|---|-----|
| <b>Figure 5-26</b> | Zoom-in of zone Z2_EQ_LS susceptible earthquake-triggered landslide areas in red (darker shade).....  | 183 |
| <b>Figure 5-27</b> | Zoom-in of zone Z3_EQ_LS: susceptible earthquake-triggered landslide areas in red (darker shade).....   | 183 |
| <b>Figure 5-28</b> | Zoom-in of zone Z4_EQ_LS: susceptible earthquake-triggered landslide areas in red (darker shade).....   | 184 |
| <b>Figure 5-29</b> | Maximum epicentral distance to disrupted landslides as a function of magnitude ( $M_w$ ) (Rodríguez et al. 1999). Solid line shows upper bound determined by Keefer (1984) and circles represent events by Rodríguez et al. (1999).....   | 185 |
| <b>Figure 5-30</b> | Maximum epicentral distance within which the earthquakes are capable of triggering landslides of susceptible deposits. ....   | 186 |
| <b>Figure 5-31</b> | Flowchart of the evaluation of the repair costs due to earthquake-triggered landslides.....   | 188 |
| <b>Figure 5-32</b> | Historical liquefaction events in Portugal (Jorge 1993). ....   | 190 |
| <b>Figure 5-33</b> | Identification of earthquake-induced liquefaction susceptible deposits.....   | 192 |
| <b>Figure 5-34</b> | Identification of lithology units (7) Sands, pebbles, lightly consolidated sandstone and (8) Sandstones, argillaceous limestones, sands, gravels and clays. ....  | 193 |
| <b>Figure 5-35</b> | Major rivers (Figure 5-9) overlaying the earthquake-induced liquefaction susceptible deposits (Figure 5-33). ....   | 195 |
| <b>Figure 5-36</b> | Liquefaction susceptibility zoning proposed by Jorge (1993): high to very high susceptibility in red (horizontal stripes); moderate susceptibility in yellow (oblique stripes) and low to very low susceptibility in green (vertical stripes). ....   | 196 |
| <b>Figure 5-37</b> | Maximum epicentral distance to liquefaction occurrence as a function of moment magnitude $M_w$ (Rodríguez et al. 1999). Solid line shows upper bound determined by Keefer (1984), circles represent events by Rodríguez et al. (1999) and dashed line shows the bound proposed by Ambraseys (1988)..... | 198 |
| <b>Figure 5-38</b> | Maximum epicentral distance within which the earthquakes are capable of inducing liquefaction of susceptible deposits.....  | 199 |
| <b>Figure 5-39</b> | Comparison of the research approach and past liquefaction: a) liquefaction susceptible deposits within the 45 km epicentral distance (in red) for the intraplate earthquake of $M_w=6.3$ (seismic scenario 1) and b) past liquefaction occurrences extracted from Figure 5-32. ....                     | 200 |
| <b>Figure 5-40</b> | Comparison of the research approach and past liquefaction: a) liquefaction susceptible deposits within 600 km epicentral distance (in   |     |

|                    |  |     |
|--------------------|--|-----|
|                    | red) for the interplate earthquake of $M_w = 8.7$ (seismic scenario 2) and b) past liquefaction occurrences extracted from Figure 5-32. ....   | 202 |
| <b>Figure 5-41</b> | Flowchart of the evaluation of repair costs due to earthquake-induced liquefaction. ....   | 204 |
| <b>Figure 5-42</b> | Isohyetal maps of mainland Portugal for a return period of 100 years and different rainfall durations by Brandão et al. (2004): a) 30 minutes; b) 60 minutes; c) 6 hour; d) 24 hour and e) 48 hour. ....   | 206 |
| <b>Figure 5-43</b> | Identification of rainfall-triggered landslides susceptible deposits. ....   | 211 |
| <b>Figure 5-44</b> | Slope angle obtained from DEM, grouped into 2 intervals: $< 17^\circ$ and $20^\circ - 36.51^\circ$ . ....  | 212 |
| <b>Figure 5-45</b> | Overlay of rainfall-triggered landslide susceptible lithology units and the slope angle intervals: non-susceptible deposits in white; susceptible deposits where slope angle is $< 17^\circ$ in green (lighter shade) and susceptible areas in red (darker shade) pictured within zoom frames Z1_RF_LS, Z2_RF_LS, Z3_RF_LS, Z4_RF_LS, Z5_RF_LS. .... | 214 |
| <b>Figure 5-46</b> | Zoom-in of zone Z1_RF_LS: susceptible rainfall-triggered landslide areas in red (darker shade). ....   | 215 |
| <b>Figure 5-47</b> | Zoom-in of zone Z2_RF_LS: susceptible rainfall-triggered landslide areas in red (darker shade). ....   | 215 |
| <b>Figure 5-48</b> | Zoom-in of zone Z3_RF_LS: susceptible rainfall-triggered landslide areas in red (darker shade). ....   | 215 |
| <b>Figure 5-49</b> | Zoom-in of zone Z4_RF_LS: susceptible rainfall-triggered landslide areas in red (darker shade). ....   | 216 |
| <b>Figure 5-50</b> | Zoom-in of zone Z5_RF_LS: susceptible rainfall-triggered landslide areas in red (darker shade). ....   | 216 |
| <b>Figure 5-51</b> | Rainfall distribution in a 24 hour period and considering 100 years return period. Adapted from Brandão et al. (2004). ....  | 218 |
| <b>Figure 5-52</b> | Flowchart of the evaluation of repair costs due to rainfall-triggered landslides. ....   | 219 |
| <b>Figure 5-53</b> | Flood map for 100 years return period: main rivers in blue (darker shade) and flooding areas in gray (lighter shade). ....   | 221 |
| <b>Figure 5-54</b> | Flowchart of the evaluation of repair costs due to floods. ....  | 223 |
| <b>Figure 6-1</b>  | Plan view of the initial HSR configuration overlaying the forbidden land-use layer. Aveiro and Leiria represented by yellow nodes and Oporto, Coimbra and Lisbon represented by red nodes. Numbers 1 through 16 correspond to the node numbering of Table 6-4. ....  | 233 |

|                    |   |     |
|--------------------|---|-----|
| <b>Figure 6-2</b>  | Plan view of the best HSR configurations found with ( $a = 0.9$ ; $r = 0.7$ ; $n_1 = 10,000$ ; $n_2 = 10$ ) in white and with ( $a = 0.9$ ; $r = 0.8$ ; $n_1 = 5,000$ ; $n_2 = 10$ ) in black, overlaying the land-use layer.....   | 238 |
| <b>Figure 6-3</b>  | Comparison of the longitudinal profiles of the best HSR configurations: C1 found for ( $a = 0.9$ ; $r = 0.8$ ; $n_1 = 5,000$ ; $n_2 = 10$ ) in black and C2 found for ( $a = 0.9$ ; $r = 0.7$ ; $n_1 = 10,000$ ; $n_2 = 10$ ) in red.....   | 239 |
| <b>Figure 6-4</b>  | Convergence history for $a = 0.9$ , $r = 0.8$ , $n_1 = 5,000$ and $n_2 = 10$ : evolution of the last accepted configuration before a temperature decrease and of the current optimum at the time of each temperature decrease. ....   | 240 |
| <b>Figure 6-5</b>  | Current HSR configuration at the end of the temperature step $k$ , overlaying the land-use layer.....   | 241 |
| <b>Figure 6-6</b>  | Plan view overlay of the best HSR configuration found for the Lisbon-Oporto SPC case-study: a) lithological map, b) land-use map, c) expropriation cost map, d) elevation map and e) main rivers map.....   | 247 |
| <b>Figure 6-7</b>  | Longitudinal profile of the best HSR configuration found for the Lisbon-Oporto SPC case-study. Vertical scale 1/10,000 and longitudinal scale 1/1,500,000. ....   | 253 |
| <b>Figure 6-8</b>  | Longitudinal profile of the HSR solution found for the Lisbon-Oporto SPC case-study from km 0 (Oporto) to km 150. Vertical scale 1/2,000 and longitudinal scale 1/750,000. ....   | 254 |
| <b>Figure 6-9</b>  | Longitudinal profile of the HSR solution found for the Lisbon-Oporto SPC case-study from km 150 to km 296.332 (Lisbon). Vertical scale 1/2,000 and longitudinal scale 1/750,000. ....   | 255 |
| <b>Figure 6-10</b> | Detail of the HSR plan view overlaying the expropriation cost map in Coimbra. ....  | 257 |
| <b>Figure 6-11</b> | Detail of the HSR plan view overlaying the land-use map between Aveiro and Leiria.....  | 258 |
| <b>Figure 6-12</b> | Detail of the HSR plan view overlaying the ground elevation map between Aveiro and Leiria. ....   | 259 |
| <b>Figure 6-13</b> | Detail of the HSR plan view overlaying the main rivers map between Aveiro and Leiria.....   | 260 |
| <b>Figure 6-14</b> | Detail of the HSR plan view overlaying the main rivers map between Coimbra and Node 8: zoom-in of the dashed box of Figure 6-13. Cross-sections are represented by different colors: cuts in blue, embankments in green, bridge with fixed scaffolding in red, bridges requiring launching systems in yellow and tunnels in light gray..... | 261 |
| <b>Figure 6-15</b> | Detail of the HSR plan view overlaying the lithological map between Aveiro and Leiria.....  | 262 |

|                    |   |     |
|--------------------|---|-----|
| <b>Figure 6-16</b> | Detail of the HSR plan view overlaying the land-use map between Coimbra and Lisbon. ....  | 263 |
| <b>Figure 6-17</b> | Accumulated costs along the longitudinal profile. ....  | 267 |
| <b>Figure 6-18</b> | Plan view of the best found HSR configuration and the existing conventional rail line overlaying the land-use layer.....  | 269 |
| <b>Figure 6-19</b> | Plan view overlay of HSR_SPC (in black) and HSR_SPC_1/2 (in white): a) lithological map, b) land-use map, c) expropriation cost map, d) elevation map and e) main rivers map.....   | 271 |
| <b>Figure 6-20</b> | Comparison of the longitudinal profiles of HSR_SPC (in black) and HSR_SPC_1/2 (in red). ....  | 274 |
| <b>Figure 6-21</b> | Accumulated costs along the longitudinal profile: total construction costs, earthworks, linear- dependent and expropriation. Costs for HSR_SPC represented in a thick line and for HSR_SPC_1/2 in a thin line. ....   | 279 |
| <b>Figure 6-22</b> | Accumulated costs along the longitudinal profile: total construction costs, bridges and tunnels. Costs for HSR_SPC represented in a thick line and for HSR_SPC_1/2 in a thin line. ....   | 280 |
| <b>Figure 7-1</b>  | Plan view overlay of configurations HSR_Comb#1_γ and HSR_SPC: a) lithological map, b) land-use map, c) expropriation cost map, d) elevation map, e) main rivers map, f) intraplate landslide map, g) intraplate liquefaction map, h) interplate landslide map, i) interplate liquefaction map, j) rainfall landslide map and k) flood pap. HSR_SPC white and HSR_Comb#1_γ in black in a), b), c), d) and e). HSR_SPC in gray and HSR_Comb#1_γ in blue in f), g), h), i), j) and k). Aveiro and Leiria in yellow circles and Lisbon, Oporto and Coimbra in red circles. .... | 298 |
| <b>Figure 7-2</b>  | Comparison of the longitudinal profiles of HSR_Comb#1_γ (in red) and HSR_SPC (in black). ....   | 305 |
| <b>Figure 7-3</b>  | Accumulated costs along the longitudinal profile: total construction costs, earthworks, linear- dependent and expropriation. Costs for HSR_Comb#1_γ represented in a thick line and for HSR_SPC in a thin line. ....  | 308 |
| <b>Figure 7-4</b>  | Accumulated costs along the longitudinal profile: total construction costs, bridges and tunnels. Costs for HSR_Comb#1_γ represented in a thick line and for HSR_SPC in a thin line.....   | 309 |
| <b>Figure 7-5</b>  | Detail of HSR_Comb#1_γ (in black) and HSR_SPC (in white) plan view overlaying the land-use layer between Aveiro and Leiria. ....  | 310 |
| <b>Figure 7-6</b>  | Detail of the HSR configurations plan view between Aveiro and Leiria overlaying: a) the main rivers map with HSR_Comb#1_γ in blue and HSR_SPC in gray and b) the elevation map with HSR_Comb#1_γ in black and HSR_SPC in white.....   | 311 |



- Figure 7-7** Detail of HSR\_Comb#1\_γ (blue) and HSR\_SPC (gray) plan view between Aveiro and Leiria overlaying: a) the interplate liquefaction hazard map and b) the flood map. .... 313
- Figure 7-8** Detail of HSR\_Comb#1\_γ and HSR\_SPC plan views between Aveiro and Coimbra overlaying: a) the interplate liquefaction hazard map and b) the flood map. Cross-sections are represented by different colors: cuts in blue, embankments in green, bridges in yellow and tunnels in light white. .... 314
- Figure 7-9** Detail of HSR\_Comb#1\_γ and HSR\_SPC plan views between Coimbra and Leiria overlaying the interplate liquefaction hazard map. Cross-sections are represented by different colors: cuts in blue, embankments in green, bridges in yellow and tunnels in white. .... 315
- Figure 7-10** Detail of HSR\_Comb#1\_γ and HSR\_SPC plan views between Coimbra and Leiria overlaying the flood map. Cross-sections are represented by different colors: cuts in blue, embankments in green, bridges in yellow and tunnels in white. .... 316
- Figure 7-11** Detail of HSR\_Comb#1\_γ (in black) and HSR\_SPC (in white) plan view overlaying the land-use layer between Leiria and Lisbon. .... 317
- Figure 7-12** Detail of the HSR configurations plan view between Leiria and Lisbon overlaying: a) the main rivers map with HSR\_Comb#1\_γ in dark blue and HSR\_SPC in gray and b) the elevation map with HSR\_Comb#1\_γ in black and HSR\_SPC in white. .... 318
- Figure 7-13** Detail of HSR\_Comb#1\_γ (blue) and HSR\_SPC (green) plan view for the dashed rectangles of Figure 7-12 overlaying: a) the flood map and b) the rainfall triggered landslides hazard map. .... 319
- Figure 7-14** Detail of HSR\_Comb#1\_γ (blue) and HSR\_SPC (green) plan view for the dashed rectangles of Figure 7-12 overlaying: a) the intraplate liquefaction map and b) the interplate liquefaction map. .... 320
- Figure 7-15** Detail of HSR\_Comb#1\_γ and HSR\_SPC plan views for the dashed rectangles of Figure 7-12 overlaying the interplate liquefaction hazard map. Cross-sections are represented by different colors: cuts in blue, embankments in green, bridges in yellow and tunnels in white. .... 321
- Figure 7-16** Plan view overlay of configurations HSR\_Comb#1\_γ/3 and HSR\_Comb#1\_γ (section 7.3.1): a) lithological map, b) land-use map, c) expropriation cost map, d) elevation map, e) main rivers map, f) intraplate landslide map, g) intraplate liquefaction map, h) interplate landslide map, i) interplate liquefaction map, j) rainfall landslide map and k) flood map. HSR\_Comb#1\_γ in white and HSR\_Comb#1\_γ/3 in black in a), b), c), d) and e). HSR\_Comb#1\_γ in gray and HSR\_Comb#1\_γ/3 in blue in f), g), h), i), j) and k). Node numbers of HSR\_Comb#1\_γ/3 are

|                    |   |     |
|--------------------|---|-----|
|                    | identified in b). Zoom-ins of the dashed boxes of g), i) and k) are presented in Figures 20, 21 and 22. ....  | 323 |
| <b>Figure 7-17</b> | Comparison of the longitudinal profiles of HSR_Comb#1_γ/3 (in red) and HSR_Comb#1_γ (in black). ....  | 330 |
| <b>Figure 7-18</b> | Accumulated costs along the longitudinal profile: total construction costs, earthworks, linear- dependent and expropriation. Costs for HSR_Comb#1_γ/3 represented in a thick line and for HSR_Comb#1_γ in a thin line. ....   | 333 |
| <b>Figure 7-19</b> | Accumulated costs along the longitudinal profile: total construction costs, bridges and tunnels. Costs for HSR_Comb#1_γ/3 represented in a thick line and for HSR_Comb#1_γ in a thin line. ....   | 334 |
| <b>Figure 7-20</b> | Detail of HSR_Comb#1_γ (blue) and HSR_Comb#1_γ/3 (green) plan views for the dashed rectangles of Figure 7-16 overlaying: a) intraplate earthquake-induced liquefaction map b) interplate earthquake-induced liquefaction map. ....  | 336 |
| <b>Figure 7-21</b> | Detail of HSR_Comb#1_γ and HSR_Comb#1_γ/3 plan view for the dashed rectangle of Figure 7-16 overlaying the interplate earthquake-induced liquefaction hazard map. Cross-sections identified by different colors. ....   | 336 |
| <b>Figure 7-22</b> | Detail of HSR_Comb#1_γ and HSR_Comb#1_γ/3 plan views for the dashed rectangle of Figure 7-16 overlaying the flood hazard map: a) HSR_Comb#1_γ in blue and HSR_Comb#1_γ/3 in green and b) cross-sections of both configurations represented by different colors. ....  | 337 |
| <b>Figure 7-23</b> | Plan view overlay of configurations HSR_Comb#1_γ/3_ω30 and HSR_Comb#1_γ/3: a) lithological map, b) land-use map, c) expropriation cost map, d) elevation map, e) main rivers map, f) intraplate landslide map, g) intraplate liquefaction map, h) interplate landslide map, i) interplate liquefaction map, j) rainfall landslide map and k) flood map. HSR_Comb#1_γ/3_ω30 in black and HSR_Comb#1_γ/3 in white in a), b), c), d) and e). HSR_Comb#1_γ/3_ω30 in blue and HSR_Comb#1_γ/3 in gray in f), g), h), i), j) and k). Node numbers of HSR_Comb#1_γ/3_ω30 are identified in b). .... | 340 |
| <b>Figure 7-24</b> | Comparison of the longitudinal profiles of HSR_Comb#1_γ/3_ω30 (in red) and HSR_Comb#1_γ/3 (in black). ....  | 347 |
| <b>Figure 7-25</b> | Accumulated costs along the longitudinal profile: total construction costs, earthworks, linear- dependent and expropriation. Costs for HSR_Comb#1_γ/3_ω30 represented in a thick line and for HSR_Comb#1_γ/3 in a thin line. ....   | 350 |

- Figure 7-26** Accumulated costs along the longitudinal profile: total construction costs, bridges and tunnels. Costs for HSR\_Comb#1\_γ/3\_ω30 represented in a thick line and for HSR\_Comb#1\_γ/3 in a thin line. .... 351
- Figure 7-27** Detail of HSR\_Comb#1\_γ/3\_ω30 (blue) and HSR\_Comb#1\_γ/3 (gray) plan view between Oporto and Coimbra overlaying: a) the interplate liquefaction map, b) the flood hazard map and c) elevation map..... 352
- Figure 7-28** Detail of HSR\_Comb#1\_γ/3\_ω30 and HSR\_Comb#1\_γ/3 plan view between Oporto and Coimbra overlaying the elevation map. The cross-sections of both configurations are represented by different colors..... 353
- Figure 7-29** Detail of HSR\_Comb#1\_γ/3\_ω30 (blue nodes) and HSR\_Comb#1\_γ/3 (grey nodes) plan view between Leiria and Lisbon overlaying: a) the interplate liquefaction map and b) the flood hazard map. The cross-sections of both configurations are represented by different colors..... 354
- Figure 7-30** Plan view overlay of configurations HSR\_Comb#2\_γ/3 and HSR\_Comb#1\_γ/3: a) lithological map, b) land-use map, c) expropriation cost map, d) elevation map, e) main rivers map, f) Intraplate landslide map, g) Intraplate liquefaction map, h) Interplate landslide map, i) Interplate liquefaction map, j) Rainfall landslide map and k) Flood map. HSR\_Comb#2\_γ/3 in black and HSR\_Comb#1\_γ/3 in white in a), b), c), d) and HSR\_Comb#2\_γ/3 in blue and HSR\_Comb#1\_γ/3 in gray e). in f), g), h), i), j) and k). Aveiro and Leiria are represented by yellow circles and Lisbon, Oporto and Coimbra by red circles..... 357
- Figure 7-31** Comparison of the longitudinal profiles of HSR\_Comb#2\_γ/3 (in red) and HSR\_Comb#1\_γ/3 (in black). Identification of HSR\_Comb#2\_γ/3 node numbers..... 363
- Figure 7-32** Accumulated costs along the longitudinal profile: total construction costs, earthworks, linear- dependent and expropriation. Costs for HSR\_Comb#2\_γ/3 represented in a thick line and for HSR\_Comb#1\_γ/3 in a thin line. .... 367
- Figure 7-33** Accumulated costs along the longitudinal profile: total construction costs, bridges and tunnels. Costs for HSR\_Comb#2\_γ/3 represented in a thick line and for HSR\_Comb#1\_γ/3 in a thin line. .... 368



# List of Tables

|                  |  |     |
|------------------|--|-----|
| <b>Table 2-1</b> | Variation of cant, cant deficiency, cant excess and minimum radius with different speeds and within different countries. ....                          | 13  |
| <b>Table 2-2</b> | Limit values for vertical curves' radius (CEN 2002). ....  | 16  |
| <b>Table 2-3</b> | Design Limit Values for Running Safety in Ordinary Conditions for Shinkansen (RTRI 2007a) .....  | 17  |
| <b>Table 2-4</b> | Limit Values for Running Safety in a Seismic Condition for Shinkansen (RTRI 2007a).....  | 18  |
| <b>Table 2-5</b> | Degree of Damage and Standard Settlement Amounts for Embankments (RTRI 2007b) .....  | 18  |
| <b>Table 2-6</b> | Soil Quality Classes (UIC 1994). ....  | 22  |
| <b>Table 2-7</b> | Design thicknesses of platform layers (UIC 1994). ....   | 23  |
| <b>Table 3-1</b> | Assumptions by Jha et al. (2007) in the assessing the cost of a railway line. ....   | 47  |
| <b>Table 3-2</b> | Advantages and disadvantages of existing approaches for optimizing road alignments (Kang et al. 2007). ....  | 66  |
| <b>Table 3-3</b> | Highway alignment optimization approaches ( Kang et al. 2012). References for applications are listed in the original table by Kang et al. (2012)..... | 67  |
| <b>Table 4-1</b> | Cost breakdown of HSR configurations. ....   | 106 |
| <b>Table 4-2</b> | Geometry of HSR configurations. ....   | 106 |
| <b>Table 5-1</b> | Identification of each of the lithological units in Figure 5-4 (APA 2012). ....  | 134 |
| <b>Table 5-2</b> | Identification of each of the preservation areas in Figure 5-5 (APA 2012). ...   | 138 |
| <b>Table 5-3</b> | Identification of each of ground-use classes in Figure 5-6 (APA 2012). ....  | 140 |
| <b>Table 5-4</b> | Expropriation types and respective unit costs. ....  | 141 |
| <b>Table 5-5</b> | Expropriation type for each ground use category provided by APA (2012).....  | 141 |
| <b>Table 5-6</b> | Cross-section specifics dependent on the lithological unit.....  | 153 |
| <b>Table 5-7</b> | Earthworks unit costs.....   | 161 |

|                   |   |     |
|-------------------|---|-----|
| <b>Table 5-8</b>  | Cost of bridges composing the HSR configuration for the initial bridge cost formulation without the consideration of the height factor $k_h$ . ....                               | 167 |
| <b>Table 5-9</b>  | Magnitudes and origins of the earthquakes affecting mainland Portugal. ....   | 189 |
| <b>Table 5-10</b> | Susceptibility and triggering conditions for earthquake- and rainfall-triggered landslides and earthquake- triggered liquefaction.....  | 224 |
| <b>Table 6-1</b>  | Geometry parameters for the SPC application. ....   | 229 |
| <b>Table 6-2</b>  | Location and location benefit coefficients for Aveiro and Leiria. ....  | 230 |
| <b>Table 6-3</b>  | Definition of the location constraints for the SPC application.....   | 230 |
| <b>Table 6-4</b>  | Geometry of the initial HSR configuration for the SPC application.....  | 232 |
| <b>Table 6-5</b>  | Cost breakdown of the initial HSR configuration. ....   | 233 |
| <b>Table 6-6</b>  | SPC objective function value of the solutions for 3 sets of SAA cooling schedule parameters.....  | 237 |
| <b>Table 6-7</b>  | Best found HSR configuration geometry for SPC.....  | 246 |
| <b>Table 6-8</b>  | Cost breakdown of the best HSR configuration found for the Lisbon-Oporto SPC case-study.....  | 250 |
| <b>Table 6-9</b>  | Cost breakdown of HSR_SPC and HSR_SPC_1/2 and comparison of the partial costs and the objective function value of both HSR solutions. ....  | 277 |
| <b>Table 6-10</b> | Geometry of the configuration HSR_SPC_1/2. ....   | 278 |
| <b>Table 7-1</b>  | Geometry parameters for the robust approach application.....  | 288 |
| <b>Table 7-2</b>  | Location and location benefit coefficients for Aveiro and Leiria. ....  | 288 |
| <b>Table 7-3</b>  | Definition of the location constraints for the robust approach application. ....  | 289 |
| <b>Table 7-4</b>  | Return period and the scenario-weight $\Psi_c$ combinations.....  | 290 |
| <b>Table 7-5</b>  | The robust applications performed for comparative analyses. ....  | 292 |
| <b>Table 7-6</b>  | Geometry of the configuration HSR_Comb#1_ $\gamma$ . ....   | 297 |
| <b>Table 7-7</b>  | Value of both HSR_Comb#1_ $\gamma$ and HSR_SPC considering the Combination#1, the location benefit coefficient of $\gamma$ and $\omega=1$ .....                                   | 306 |
| <b>Table 7-8</b>  | Geometry of the configuration HSR_Comb#1_ $\gamma/3$ . ....   | 322 |
| <b>Table 7-9</b>  | Value of both HSR_Comb#1_ $\gamma/3$ and HSR_Comb#1_ $\gamma$ considering the Combination#1, the location benefit coefficient of $\gamma/3$ and $\omega=1$ . ....                 | 331 |
| <b>Table 7-10</b> | Geometry of the configuration HSR_Comb#1_ $\gamma/3$ _ $\omega 30$ .....  | 339 |
| <b>Table 7-11</b> | Value of both HSR_Comb#1_ $\gamma/3$ _ $\omega 30$ and HSR_Comb#1_ $\gamma/3$ considering the Combination#1, the location benefit coefficient of $\gamma/3$ and $\omega=30$ ..... | 348 |
| <b>Table 7-12</b> | Geometry of the configuration HSR_Comb#2_ $\gamma/3$ . ....   | 356 |
| <b>Table 7-13</b> | Value of both HSR_Comb#2_ $\gamma/3$ and HSR_Comb#1_ $\gamma/3$ considering the Combination#2, the location benefit coefficient of $\gamma/3$ and $\omega=1$ . ....               | 364 |

# Chapter 1.

## Introduction

### 1.1 PROBLEM STATEMENT AND MOTIVATION

High-Speed Rail (HSR) infrastructure projects evolve in sequential stages of increasing detail. When planning for a HSR, initial decisions are made concerning the infrastructure macro-location, defining boundaries for the detailed project design. The interrelation of factors affecting the HSR performance, however, makes the HSR planning a very complex problem. The high operating speeds require that the infrastructure complies with demanding design specifics, such as large horizontal radii in the plan view, small gradients in the longitudinal profile and large displacement restrictions for the track geometry. To comply with these, different geotechnical structures and design solutions can be chosen (cuts, embankments, tunnels and bridges) each having a particular performance depending on the deployment site specifics such as elevation, geology, geotechnical behavior, population density or weather conditions. These features can vary significantly along the HSR given its characteristic linear development. In addition, the HSR must cope with land-use protected areas, crossing bodies of water and the intersection with existing infrastructure. In this context, it is extremely complex to ascertain the HSR configuration yielding the most value, especially in the planning stage in which large areas and significantly different configurations can be up for consideration.

In addition to the complexity of the problem, large investments are required for building HSR lines. The capital costs of building a HSR, however, are not fixed and depend on the project specifics and the characteristics of the deployment site. Project specifics such as the type of traffic (passenger-only, freight or mixed) and the design speed imply different geometry requirements and track displacement limits, which influence the HSR configuration. These

specifics coupled with the deployment site's characteristics are conditional for the cross-sections to adopt along the HSR, for which construction costs vary. Mendoza et al. (2009) compiled data from HSR projects in Europe, South Korea and Taiwan observing that the construction cost per km (without planning and land expropriation costs) varied between €4.7 million and €65.8 million (2005).

The large HSR investments are generally supported by public funds, as is the case in Japan, Europe and South Korea (UIC 2010). This requires a conscious allocation of resources and increases the demand for a high-level of performance. The performance is affected by ordinary operating conditions, those prevailing within the infrastructure's lifetime, but also by uncertain and extreme events, such as natural hazards, that can severely damage and disrupt transportation infrastructure. The damages to transportation systems by events such as the 1994 Northridge earthquake (Gordon et al. 1998), Hurricane Katrina (Link 2010) or the 2010-2011 Australian floods (Munoz 2011) attest the destructive and disruptive capabilities of natural hazards. Furthermore, the HSR infrastructure is often subject to the effects of multiple hazards, given the relatively long distances between the cities to link. Planning for the worst-case scenario is economically unrealistic. However, prevention may contain the damages inflicted to the built environment and may be cost effective (World Bank and United Nations 2010). The consequences of natural hazards depend not only on the hazard itself but also on the corridors crossed and the technical solution of the cross-section.

Considering the complexity of the HSR planning problem and its vulnerability to the effects of natural hazards, coupled with the large, commonly public, investments and a society which grows less willing to pay for expensive and lengthy recoveries, with minimal tolerance to disruptions, make a strong case for an integrated decision-making considering natural hazards at the HSR planning stage. This can hardly be achieved without the support of comprehensive tools capable of dealing with large datasets and establishing data relations for systematically addressing the complexities involved in decision-making.

## **1.2 CURRENT NEEDS OF HIGH-SPEED RAIL PLANNING MODELS**

An optimization model, considering problem costs and constraints, has been applied by Jha et al. (2007) to the optimization of transit rail lines between stations distancing 3.43 km. This work is based on previous works for highway alignment optimization. Similarities exist



between the railway- and highway alignment optimization problems and comprehensive research exists for highways (Kang et al. 2012), mostly for project design detail level. Given the large datasets required to characterize the problem and the complex relations between the project specifics, the HSR configuration details and the deployment site characteristics, these approaches are valuable tools in assisting decision-making. However, two limitations in applying such models to the HSR planning are identified.

Firstly, HSR planning optimization is conducted at a scale that allows one to consider large areas for the infrastructure deployment and considerably different HSR configurations. It is within the planning stage that configurations establishing trade-offs between the project costs, the cities to connect and the layout performance of the infrastructure can be comprehensively captured, given the boundaries set for subsequent stages. In addition, it considers the analysis of larger areas than that of highways or conventional railways given the larger intercity distances of HSR, increasing the complexity of the problem to solve.

Secondly, such models do not consider the uncertainties associated with the effects of natural hazards. For varying loading conditions, such as those imposed by natural hazards, some configurations may yield better performance but incur in larger capital costs and trade-offs can be made. The need to consider uncertain and incomplete information when planning for large-scale systems is recognized by World Bank and United Nations (2010), particularly for critical infrastructure. This includes electricity, water and gas supply and telecommunications and transportation networks, which are becoming ever more important to the economy and to society. In fact, robust approaches have been applied to consider uncertainty in planning and in the design of critical infrastructure such as water distribution networks (Cunha and Sousa 2010a), telecommunications networks (Laguna 1998) and power systems (Malcolm and Zenios 1994).

## **1.3 RESEARCH OBJECTIVES, SCOPE AND CONTRIBUTIONS**

### **1.3.1 OBJECTIVES**

The objectives of this research are:

- To develop a Standard Planning Conditions (SPC) optimization model representing, from a HSR planning perspective, the infrastructure construction costs, the geometry, land-use and location constraints and to consider trade-offs in adopting recommended geometry values over the feasibility limits, in connecting intermediate cities and in avoiding restricted land-use areas;
- To extend the SPC model to include the effects of natural hazards in HSR decision-making through an integrated and robust approach with scenario descriptions of uncertainty;
- To implement both the SPC model and the robust approach in a computational tool capable of dealing with the sheer-size of real-world problem data from Geographic Information Systems (GIS) and capable of implementing the Simulated Annealing Algorithm to solve the models;
- To apply the SPC model and robust approach (considering rainfall-, flood- and earthquake-hazard scenarios) to a real world case-study in order to show the capabilities in assisting the HSR decision-making process.

### 1.3.2 SCOPE OF THE RESEARCH

This research intends to develop decision-aid tools for the consideration of natural hazards in HSR decision-making at a planning stage. It aims at capturing the main characteristics of the infrastructure that influence the construction cost and the HSR performance while exploring a large number of deployment options and covering a significant area.

In the research, SPC and robust optimization models are formulated and solved with the Simulated Annealing Algorithm (SAA). The sheer-size of the problem dictated the use of a heuristic technique, within which the SAA was chosen given the good results obtained in solving deterministic route optimization models and in solving robust optimization models for other problems, and the fact that the SAA is the only local search algorithm with theoretical convergence proof to the global optimum. It is not a purpose of this research to prove that the SAA works best for the HSR planning problem than other heuristic methods.

The time factor is not considered. Although time influences operation costs and the performance in disruption recovery, difficulties in its inclusion in the planning optimization context of the research are acknowledged. An identical consideration is made for the HSR interference with existing infrastructure such as roads, gas, water or power supply. Infrastructure construction costs and direct market losses pertaining to the physical damage repair and/or replacement of sections damaged by natural hazards are considered. The scenarios describing the natural hazards are case-study specific and the number and types of scenarios are dependent on the hazard potential of the problem.

### 1.3.3 RESEARCH CONTRIBUTIONS

The main original contributions of the research are: the consideration of natural hazards for HSR planning in an integrated and robust approach and the development of innovative decision aid-tools.

The infrastructure performance for natural hazards is considered in the HSR planning through a robust optimization model. The performance of the HSR is jointly analyzed for SPC and for a set of scenarios describing the expected potential natural hazards. This allows for the three-dimensional optimization of the HSR configuration considering cost trade-offs between initial construction costs, geometry layout, land-use, cities to connect and the costs derived from repairing the damages inflicted by natural hazards. Acknowledging that other factors beyond the scope of this research, such as time-dependent factors and existing infrastructure, affect the decision-making, the approach is formulated so that, in future developments, the model can be expanded to include additional complexities.

To apply and solve the proposed SPC and robust models a computational tool is developed. The tool accommodates real-world project data, implements the models and the solving technique and delivers output which can be analyzed for decision-making. The HSR planning problem is data-intensive, requiring the spatial characterization of the deployment area for several features and covering large areas. Nowadays, Geographical Information Systems (GIS) techniques are commonly used to store and manage such type of data across institutions. The tool developed supports GIS input, which is essential for real applications. Given the case-specificity of the problem parameters and the scenarios representing the

natural hazards, the tool can be expanded to implement additional complexities derived from a model expansion or from the case-study properties.

Both the feasibility and the capabilities of the approach and the tool are demonstrated with a practical application to a new HSR infrastructure in Portugal, linking Lisbon and Oporto. Sound results are obtained for the SPC model and for the robust approach considering scenarios defining earthquake, rainfall and flood hazards. It is shown that the HSR solutions of the robust approach improve the performance for natural hazards, when comparing to the results of solving the SPC model (without the scenario descriptions of uncertainty). The approach can also accommodate different decision-maker preferences towards the performance requirements for different natural hazards.

## **1.4 THESIS LAYOUT**

This thesis is structured in 8 chapters.

The current Chapter introduces the subject of the research.

Chapter 2 reviews the HSR state-of-the-practice regarding the geometric design, the earthworks design and the project costs. The state-of-the-art in assessing transportation performance for natural hazards and the impacts of disruption is discussed.

Chapter 3 reviews existing models for the optimization of linear transport infrastructures and presents the need to consider uncertain natural hazards through robust models. Available techniques for solving the models are discussed.

Chapter 4 presents the SPC and robust optimization models proposed for the HSR planning problem. A software test is presented for the SPC model applied to a simple synthetic case-study and solved with the implementation of the SAA. Software capabilities are extended to accommodate further complexities of real world problems.

Chapter 5 presents the specifics of the Lisbon-Oporto case-study: input spatial data, geometry layout specifics, cross-sections and construction costs and the scenarios representing natural hazards. The hazards' susceptibility, triggering conditions and the vulnerability of the infrastructure are discussed.

Chapter 6 discusses the SPC model applied to the Lisbon-Oporto case-study. The model is solved with the implementation of the SAA and a study for estimating the algorithm parameters is presented. Problem complexities including “islands” of forbidden land-use are addressed and trade-offs between construction costs and geometry layout are observed. Different values for connecting intermediate locations are considered.

Chapter 7 discusses the robust model applied to the Lisbon-Oporto case-study and solved with the implementation of the SAA. All problem requisites of Chapter 6 are considered, in addition to the impacts of natural hazards. Different attitudes of the decision-maker towards such impacts are considered. The influence of the merits of connecting intermediate locations is discussed. The robust solutions are compared with the results from solving the SPC model in Chapter 6. The comparison highlights the opportunities arising from the consideration of natural hazards at the planning stage.

Lastly, Chapter 8 summarizes the findings of this research and proposes suggestions for future research.



## Chapter 2.

# High-Speed-Rail: State-of-the-Practice and State-of-the-Art

HSR trains circulate, as the designation suggests, at significantly higher speeds than those operated in conventional railways. Based on the design speed and the rail line specifics, three categories of HSR lines are defined by the European Commission (EC 2008):

- Category I: specially built high-speed lines equipped for speeds generally equal to or greater than 250 km/h;
- Category II: specially upgraded high-speed lines equipped for speeds of the order of 200 km/h;
- Category III: specially upgraded high-speed lines which have special features as a result of topographical, relief or town-planning constraints, on which the speed must be adapted to each case.

These high operating speeds require that the infrastructure complies with demanding design specifics. In general, the highest the operating speed is the stricter the design requirements are, resulting in large investment costs for the infrastructure. In addition, such linear transportation infrastructures are commonly exposed and vulnerable to the effects of natural hazards. The following sub-sections overview the HSR state-of-the-practice geometric design and earthworks design and the state-of-the-art in assessing the costs involved in a HSR network and the impacts of rail disruptions due to natural hazards.

## 2.1 GEOMETRIC DESIGN

The geometric design of HSR, which sets limitations for the operating speed, is herein discussed including existing standards and recommendations for the track layout parameters. This overview does not intend to present all the geometric parameters involved in the HSR track design but rather discuss the main features to account for in the planning context of the present research.

The main parameters discussed are the track gauge, the horizontal curve radius (defined in the plan view) and the gradient of linear sections and the vertical curves (both defined in the longitudinal profile). General provisions are defined by standards and, in particular cases, exceptions are allowed, revealing important correlations with the implementation site.

### 2.1.1 TRACK GAUGE

Track gauge is the distance that separates the head inner side of the two rails of the track and according to Profillidis (2006) and Lindahl (2001) is measured 14 mm below the rolling surface (Figure 2-1). Besides the obvious issues of compatibility between trains and tracks, the track gauge is related with the track cant if measured in mm, which in turn influences the horizontal curve radii.

The nominal track gauge defined by the Technical Specification for Interoperability (TSI) in EC (2008) is 1435 mm.

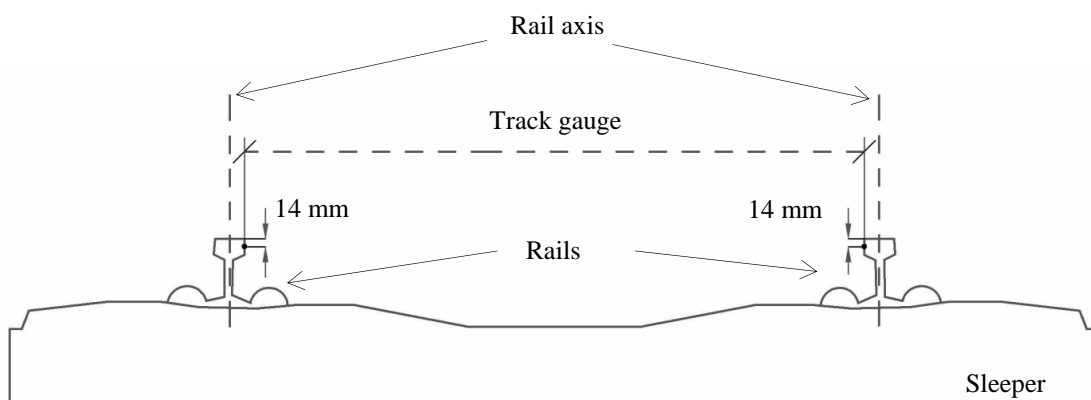


**Figure 2-1** General rail track cross-section in a straight line.



### 2.1.2 HORIZONTAL CURVE RADIUS

Circular horizontal curves are designed between two linear sections of the HSR layout to allow for a smooth change of direction. The constant radius  $R$  of a circular curve determines, for a given circulating speed  $v$ , the centrifugal acceleration  $a_c$  imposed on the train as shown in equation (2.1).

$$a_c = v^2 / R \quad (2.1)$$

Large centrifugal acceleration values compromise the quality of the service and, in extreme cases, safety. They can also increase the degradation of the track, reducing the lifetime of its components. Lindahl (2001) specifies that negative effects of large centrifugal accelerations may include passenger discomfort, displacement of wagon loads, train overturn if combined with strong winds, train derailment and large lateral forces on the track. According to the standard by the European Committee for Standardization (CEN 2002), the radius of circular curves is, in general, defined as large as feasible, complying with other existing geometric constraints for a given design speed: applied cant, cant excess and cant deficiency.

Cant (Figure 2-2), also known as superelevation, is the height difference measured at the head mid-points of the rails. In linear sections of the track, the two rails are placed at the same height and the cant is null. In a circular curve, however, the cant is applied to balance the centrifugal force derived from the centrifugal acceleration. The theoretical cant that fully balances the force derived from the lateral acceleration, meaning the resulting force of the vehicle weight and the centrifugal force is perpendicular to the plane formed by the rails, is named equilibrium cant. The applied cant, however, is defined as a function of the design speed and the curve radius but a maximum value is imposed, to account for the fact that a train may need to stop or circulate at low speeds, in extraordinary situations. This results in a cant deficiency, which cannot fully compensate the lateral acceleration when trains are circulating at the high design speeds, and a cant excess if a train stops or circulates at a lower speed than the one corresponding to the equilibrium cant.

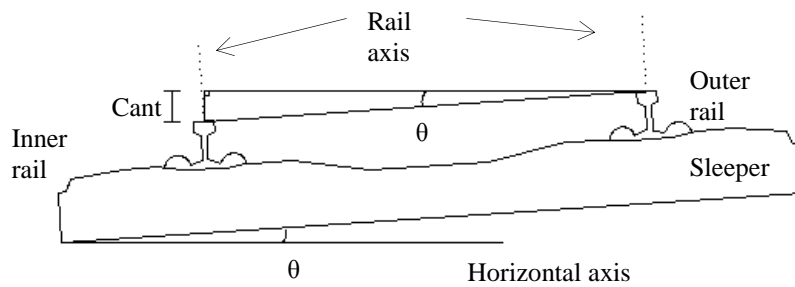


**Figure 2-2** General rail track cross-section for a horizontal curve.

Table 2-1 shows variations of maximum cant, maximum cant deficiency, maximum cant excess and minimum radius for different design speeds. One observes that values differ with standards and line specifics. Recommended, normal and limit values exist for the parameters, reflecting the fact that recommended values are difficult to implement in all situations, thus the allowance of less restrictive values when necessary, up to an absolute limit. This is expressly stated in the TSI by EC (2008).

**Table 2-1** Variation of cant, cant deficiency, cant excess and minimum radius with different speeds and within different countries.

| Organization                        | TSI <sup>(a)</sup> / CEN <sup>(b)</sup> |                                      | JR <sup>(c)</sup>  | JR <sup>(c)</sup> | JR <sup>(c)</sup>       | DB <sup>(c)</sup>   | DB <sup>(c)</sup> | SNCF <sup>(d)</sup> |                    |      |
|-------------------------------------|---|--------------------------------------|--------------------|-------------------|-------------------------|---------------------|-------------------|---------------------|--------------------|------|
|                                     | Line                                    | category I, HSR lines <sup>(1)</sup> | Tokaido Shinkansen | Sanyo Shinkansen  | Tokyo-Joetsu Shinkansen | Hannover - Würzburg | Köln-Rhein/Mann   |                     |                    |      |
| Maximum design speed                |   |                                      |                    |                   |                         | 280                 | 300               | 270                 | 300                | 350  |
| Maximum service speed               | 300                                     | >300                                 | 270                | 300               | 275                     | 250                 |                   |                     |                    |      |
| Maximum cant (mm)                   |   |                                      |                    |                   |                         |                     |                   |                     |                    |      |
| - Normal                            | 180                                     | 180                                  | 200                | 180               | 180                     | 65                  | 160               | 180                 | 180                | 180  |
| - Exceptional                       | 200 <sup>(3)</sup>                      | 200 <sup>(3)</sup>                   |                    |                   |                         |                     |                   | 180                 | 180                | 180  |
| Maximum cant deficiency (mm)        |   |                                      |                    |                   |                         |                     |                   |                     |                    |      |
| - Normal                            | 100                                     | 80                                   | 100                | 100               | 100                     | 80                  | 150               | 100                 | 85                 | 65   |
| - Exceptional                       | 130 <sup>(2)</sup>                      | 80                                   |                    |                   |                         |                     |                   | 130                 | 100                | 85   |
| Maximum cant excess (mm)            |   |                                      |                    |                   |                         |                     |                   |                     |                    |      |
| - Normal                            | 110                                     | 110                                  |                    |                   |                         | 50                  |                   | 100 <sup>(4)</sup>  | 100 <sup>(4)</sup> |      |
| - Exceptional                       | 110                                     | 110                                  |                    |                   |                         |                     |                   | 110 <sup>(4)</sup>  | 110 <sup>(4)</sup> |      |
| Minimum horizontal curve radius (m) |   |                                      |                    |                   |                         |                     |                   |                     |                    |      |
| - Recommended                       |   |                                      |                    |                   |                         |                     |                   | 3846                | 4545               | 7143 |
| - Normal                            |   |                                      | 2500               | 4000              | 4000                    | 5100                | 3425              | 3226                | 4000               | 6250 |
| - Exceptional                       |   |                                      |                    |                   |                         |                     |                   | 3125                | 4000               | 5556 |
| Maximum gradient (‰)                | 35                                      | 35                                   | 20                 | 15                | 15                      | 12.5                | 40                |                     |                    |      |

<sup>(1)</sup> According to TSI<sup>(a)</sup>, The infrastructure manager will declare in the Infrastructure Register the line sections where it considers that there are constraints which prevent compliance with the normal values. In these cases exceptional values may be adopted.

<sup>(2)</sup> The maximum value of 130 mm may be raised to 150 mm for non-ballasted track

<sup>(3)</sup> allowed on tracks with passenger traffic only

<sup>(4)</sup> Excess of cant in normal conditions experienced by freight trains

<sup>(a)</sup> (EC 2008); <sup>(b)</sup>(CEN 2002); <sup>(c)</sup> (Lindhahl 2001); <sup>(d)</sup> (UIC 2001);

Transitions curves of varying radius and cant are used to make a smooth transition from the linear sections to the circular curves or between 2 circular curves of different radii. These curves are designed to avoid sudden changes in the lateral acceleration, being tangent to the linear segment and/or circular curves at each respective end (Figure 2-3). According to CEN (2002), clothoids, in which the curvature varies linearly with its length, applied with linear

cant variation are commonly used, although curves with nonlinear variations of cant and curvature such as the Bloss curve, the cosine curve, the Schramm curve and the Klein curve (sine curve) may also be used. Furthermore, the standard indicates that the minimum length of clothoid transition curves is such that maximum rates of cant and cant deficiency variation with time are complied with. The maximum cant variation rate is required to comply with safety and comfort requisites, varying for passenger and freight traffic. The maximum rate of cant deficiency variation with time is 75 mm/s for passenger dedicated HSR lines with design speeds between 250 km/h and 300 km/h (CEN 2002); however, a more restrictive value of 50 mm/s is recommended by the standard.

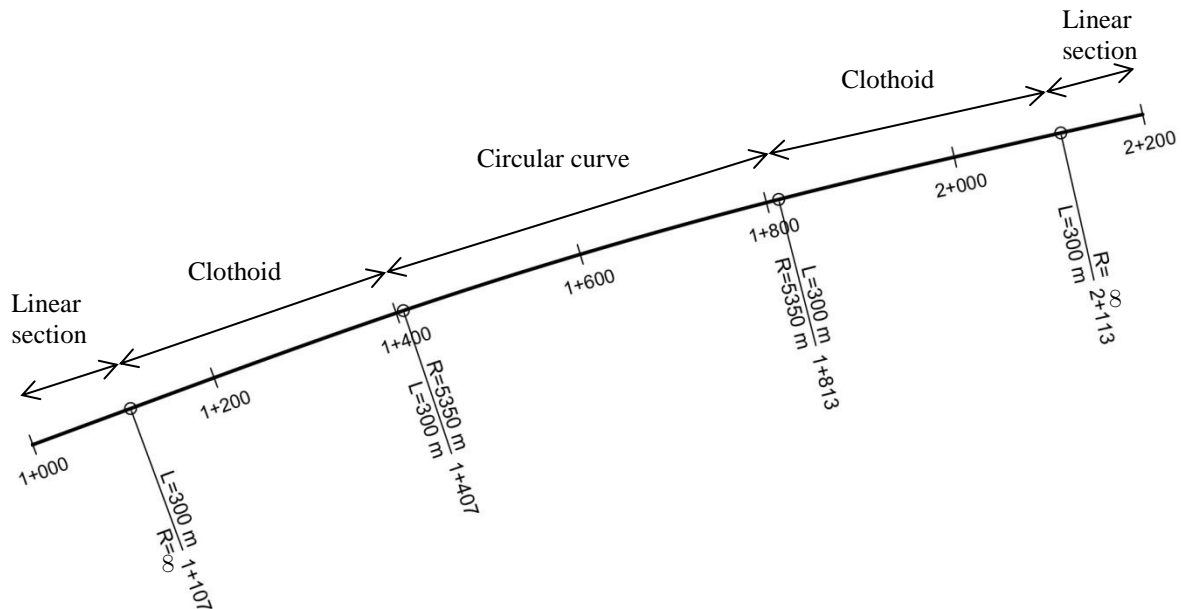


**Figure 2-3** Example of two clothoid curves of 300 m length between linear sections (radius  $R=\infty$ ) and a circular curve (radius  $R = 5350$  m) from km1+000m to km 2+200m of a HSR line.

### 2.1.3 GRADIENTS

The HSR longitudinal profile should minimize the costs due to the construction of bridges and tunnels and the earthwork volumes, following the ground profile whenever possible. However, gradient values are limited for a number of reasons. Lindahl (2001) discusses the effects associated with large gradients, namely, the increase of power supply and energy consumption, difficulties in climbing steep slopes especially by freight trains and the increase of braking distances when moving downwards. These effects can result in, amongst others,

loss of line capacity. Profillidis (2006) discusses this issue, stating that usual maximum values, for principal lines with mixed traffic (passenger and freight) and speeds up to 200km/h, range between 12‰ and 15‰. But, as one observes in Table 2-1, variations exist, depending on characteristics such as the type of traffic, operating speed or topographical conditions.

A maximum rising or falling gradient value for category I high-speed lines of 35‰ is established by the TSI (EC 2008), provided the following requirements are complied with:

- the slope of the moving average profile over 10 km is less than or equal to 25 ‰;
- the maximum length of continuous 35‰ gradient does not exceed 6000 meters.

#### 2.1.4 VERTICAL CURVES

Vertical curves are designed between two linear sections of different gradient, in the longitudinal plan. The CEN (2002) defines that in gradient changing sections, curves should be adopted with a minimum length of 20 m if the gradient change is within the following:

- superior to 2‰ (2mm/m) for speeds equal or inferior to 230 km/h;
- superior to 1‰ (1mm/m) for speeds above 230km/h.

Table 2-2 presents the limit values for vertical curve radii defined by the CEN (2002). For a passenger-dedicated line with a design speed of 250 km/h, the standard indicates that the vertical recommended radius is 21,875 m with a minimum of 10,937.5 m. Compared with the recommended/normal and limit horizontal radii in Table 2-1, one observes that the vertical radii are around three times larger than the horizontal ones. Profillidis (2006) further states that simultaneous vertical curves and horizontal transition curves should be avoided. Whenever this is not possible, the maximum feasible radius should be used.

**Table 2-2** Limit values for vertical curves' radius (CEN 2002).

| Traffic categories<br><br>$v$ (speed in<br>km/h) | Mixed lines conceived<br>for passenger trains of<br>speed | Mixed lines with<br>passenger trains of<br>speed                              | High-speed lines<br>exclusively dedicated<br>to passenger trains |
|--|---|---|--|
| <b>Vertical<br/>Curve Radius</b>                 | $200 < v \leq 300$  | $v \leq 230$ (or 250)<br>(for vehicles with<br>special technical<br>features) | $250 \leq v \leq 300$  |
| Recommended limit value<br>(m)                   | $0.35v_{\max}^2$  | $0.35v_{\max}^2$  | $0.35v_{\max}^2$   |
| Minimum limit value (m)                          | $0.175v_{\max}^2$   | $0.25v_{\max}^2 \geq 2000$  | $0.175v_{\max}^2$  |

## 2.2 GENERAL DESIGN PRINCIPLES FOR EARTHWORKS

### 2.2.1 DISPLACEMENT LIMITS AND SEISMIC DESIGN

HSR construction and operation, given its characteristic linear development, must cope with a variety of local ground behavior. Nonetheless, the design constraints must be met at all locations. For the strict horizontal and vertical design parameters of the alignments presented in the previous section, different geotechnical structures and design solutions can be chosen, each having a particular performance. Allowances in the track geometry are also very tight, translating into high displacement restrictions for geotechnical structures. Indeed, in Japan where HSR has been in service for a long time, standards concerning both displacement limits and seismic design were elaborated by the Railway Technical Research Institute (RTRI). The performance is required to be evaluated for three categories (RTRI 2007a):

- safety, with items “running safety in ordinary conditions” and “displacement associated with running safety in a seismic condition”;
- serviceability, with item “riding comfort”;
- restorability, with items “restorability of track damage in ordinary conditions” and “displacement of track damage in a seismic condition”. These performance items require that track maintains a sound or usable condition without any repairs, except

usual maintenance and if an earthquake occurs, where some quick repairs are acceptable.

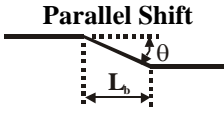


The seismic design standard, RTRI (2007b), comprehends provisions for bridges, viaducts, foundation structures, retaining structures such as retaining walls and abutments, cut and cover tunnels and embankments. For the latter, seismic design is applicable when necessary, concluding important embankments at locations where severe damage in an earthquake is anticipated (judging from the embankment shape, the geographical features, the geological conditions and the history of past disasters) and at locations where high seismic performance is required. According to past experience, the standard considers particularly high embankments as likely to be damaged, as well as embankments built on any of the following conditions: soft ground, slopes, at boundaries between cutting and embankments and on ground with sloped bedrock.

Tables 2-3, 2-4 and 2-5 present values for the verification items. Although such displacement limits specifications are defined for structures, the high demanding level to geotechnical structures in HSR can be devised. Also, linear infrastructures such as HSR cannot perform properly unless all continuous structures are operational.

**Table 2-3** Design Limit Values for Running Safety in Ordinary Conditions for Shinkansen (RTRI 2007a)

| Design Limit Values                                       | Maximum Speed<br>(km/h) | Span Length ( $L_b$ ) (m) |                          |
|---|-------------------------|---------------------------|--------------------------|
|   |                         | 0-60                      | 60-100 or more           |
| Maximum Girder Deflection                                 | 300<br>360              | $L_b/1500$<br>$L_b/1900$  | $L_b/1700$<br>$L_b/2000$ |
| Vertical Alignment Irregularity                           | 300<br>360              |                           | 2.5 (mm)<br>2.0 (mm)     |
| Angular Rotation on Track Surfaces (Vertical Direction)   | 300<br>360              |                           | 2.5/1000<br>2.0/1000     |
| Angular Rotation on Track Surfaces (Horizontal Direction) | 300<br>360              |                           | 1.0/1000<br>1.0/1000     |

**Table 2-4** Limit Values for Running Safety in a Seismic Condition for Shinkansen (RTRI 2007a)

| Maximum Speed (km/h) | Angular Rotation ( $\theta$ )   |   | Folding   | Alignment Irregularity (mm) |
|----------------------|---|---|---|-----------------------------|
|                      | Parallel Shift  |   |   |                             |
|                      |  |  |  |                             |
|                      | $L_b = 10 \text{ m}$  | $L_b = 30 \text{ m}$  |   |                             |
| 300                  | 4.5/<br>1000  | 2.5/<br>1000  | 3.0/<br>1000  | 7.0                         |
| 360                  | 4.0/<br>1000  | 2.0/<br>1000  | 2.0/<br>1000  | 6.0                         |

**Table 2-5** Degree of Damage and Standard Settlement Amounts for Embankments (RTRI 2007b)

| Degree of Damage                        | Extent of Settlement Amount            |
|---|--|
| No damage                               | No damage                              |
| Slight damage                           | Settlement amount less than 20 cm      |
| Recovery possible by temporary measures | Settlement amount between 20 and 50 cm |
| Long time required for recovery         | Settlement amount more than 50 cm      |

### 2.2.2 EARTHWORKS GEOTECHNICAL DESIGN: PLATFORM REQUIREMENTS

The compliance with the restrictive displacement limits (Tables 2-3 and 2-4) for HSR embankments and cuts depends on the geotechnical strength and deformation behavior of the substructure, on which the ballast is placed, and the static and dynamic loads imposed on the tracks. The performance of bridges/viaducts and tunnels is, not only related to the site geotechnical characteristics, but also conditioned on the structural design and the relationship and interaction between the two. Given the multitude of bridge/tunnel solutions that can be implemented and the varying geotechnical conditions that may exist for a general case, the design of these types of structures and the analysis of the displacement limits is deferred to subsequent detailed stages of the HSR project.

The International Union of Railways (UIC) defines provisions for railway cross-sections in embankments and cuts in the UIC (1994) standard, from which the general cross-section in Figure 2-4 is adapted. A multi-layered substructure, varying with the loads that propagate from the superstructure, is proposed. The following subsections describe the general



characteristics and functions of each substructure layer and the design of the respective thicknesses in relation to the traffic requirements.

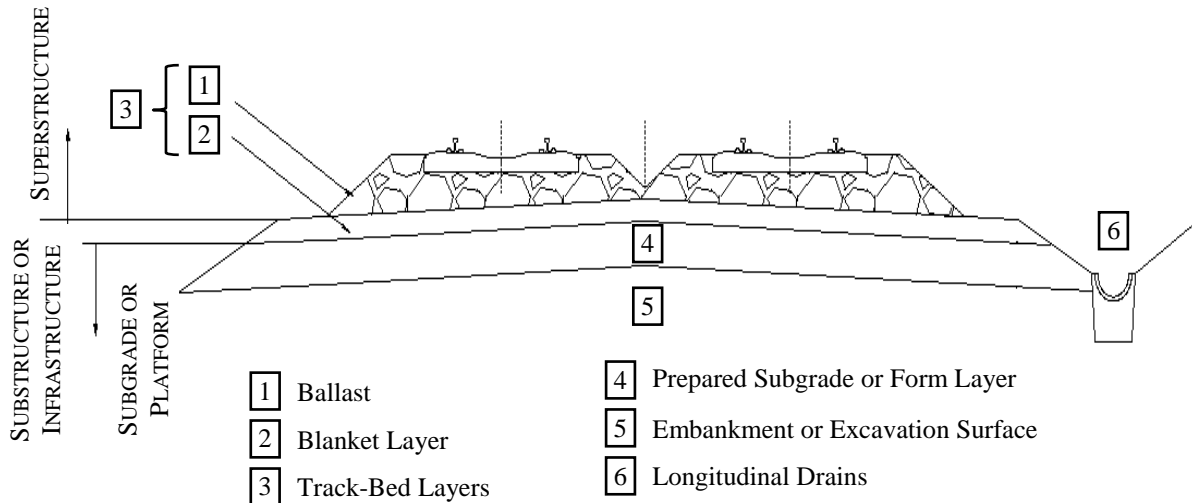


**Figure 2-4** General Cross-section for embankments and cuts adapted from (UIC 1994).

#### 2.2.2.1 BALLAST

The ballast is formed by crushed rock, coarse and uniformly graded. Ballast is required to comply with hardness and abrasion requirements, allowing the adequate transmission of loads to the infrastructure and keeping the sleepers and rails in the correct alignment, but also permeability requirements, allowing a fast drainage of the surficial water. While its quality and performance influence the quality of the HSR service, the ballast is, however, considered part of the superstructure and its design is not dependent on the infrastructure characteristics. Ballastless concrete slab tracks can also be implemented.

#### 2.2.2.2 BLANKET LAYER

The blanket layer supports the ballast and transmits the loads downwards to the platform. The UIC (1994) standard indicates that the blanket layer may be formed by a single or a multilayered structure including sub-ballast, frost protection and/or filtering layers. The blanket layer main functions are (Fortunato 2005; UIC 1994):

- To improve the bearing capacity by changing the stiffness and to achieve a better distribution of transmitted loads;

- To improve the dynamic properties of the platform;
- To act as a filter between the platform and the ballast, preventing the ballast contamination with fines;
- To protect the platform against erosion and frost;
- To shed the surface water.

The blanket single or multiple layer constituents and thicknesses thus depend on the climatic conditions of the site, the design traffic specifics and the materials available for the construction, amongst others. However, the sub-ballast layer thickness is usually defined *a priori* and constant along the railway, facilitating the systematic use of machinery during repairs and maintenance (Fortunato 2005). In Europe, sub-ballast thicknesses ranging from 20 cm to 30 cm are commonly used in conventional all-granular ballasted HSR tracks (Teixeira et al. 2010). Other design solutions exist, such as the slab track or the inclusion of a bituminous sub-ballast layer, with larger capital costs and reduced maintenance requirements

#### 2.2.2.3 SUBGRADE OR PLATFORM

The performance of the embankments and cuts, in respect to the displacements of the rail alignment, is related to the geotechnical and hydrological properties of the platform, especially within a depth of 1-2 meters from the base of the sleepers supporting the rails (Fortunato 2005). If the characteristics of the materials composing the embankment or at the excavation surface do not fulfill the requirements, a top layer of prepared subgrade, also known as form layer, is considered.

#### 2.2.2.4 DESIGN OF THE PLATFORM LAYERS

The design traffic specifics define the characteristics of the loads to be supported by the substructure, thus defining the platform requirements. Three bearing capacity classes for the platform are defined by UIC (1994):

- P1: Poor subgrade
- P2: Average subgrade

- P3: Good Subgrade

The technical memorandum by Parsons Brinckerhoff (2009) further defines limits of deformation modulus for each of the classes. The platform classification is a consequence of the characteristics of its constituting soils, for which quality classes are also defined, according to the specifications in Table 2-6. The relation proposed by UIC (1994) between the bearing capacity of the platform and the soil quality, both at the embankment or excavation surface and of the prepared subgrade, is presented in Table 2-7.

**Table 2-6** Soil Quality Classes (UIC 1994).

| Soil Type (Geotechnical Classification)  | Soil Quality Class |
|--|--------------------|
| 0.1 Organic Soils  |                    |
| 0.2 Soft soils containing more than 15% of fines <sup>(1)</sup> , with a high moisture content therefore unsuitable for compaction |                    |
| 0.3 Thixotropic soils <sup>(2)</sup> (e.g. quick-clay)   | QS0                |
| 0.4 Soils containing soluble material (.g. rock salt or gypsum)  |                    |
| 0.5 Contaminated ground (e.g. industrial waste)  |                    |
| 0.6 Mixed material / organic soils <sup>(2)</sup>  |                    |
| 1.1 Soils containing more than 40% of fines <sup>(1)</sup> (except for soils classified under 0.2)                                 |                    |
| 1.2 Rocks which are very susceptible to weathering, e.g.:<br>- Marl<br>- Weathered shale   | QS1                |
| 1.3 Soils containing more than 15% to 40% of fines <sup>(1)</sup> (except for soils classified under 0.2)                          |                    |
| 1.4 Rocks which are moderately susceptible to weathering (unweathered shale)   | QS1 <sup>(3)</sup> |
| 1.5 Soft Rocks   |                    |
| 2.1 Soils containing from 5 to 15% of fines <sup>(1)</sup>   |                    |
| 2.2 Uniformly graded soils containing less than 5% of fines  | QS2 <sup>(4)</sup> |
| 2.3 Moderately hard rocks  |                    |
| 3.1 Well graded soils containing less than 5% of fines <sup>(1)</sup>  | QS3                |
| 3.2 Hard rock  |                    |

<sup>(1)</sup> These percentages are calculated from particle size distribution analysis undertaken on material passing through a 60 mm sieve. The percentage indicated here have been rounded down (practices vary slightly from one Railway to another); they may be increased by up to 5% if a sufficiently representative number of samples is taken.

<sup>(2)</sup> Certain Railways include these soils in quality QS1

<sup>(3)</sup> These soils are classified under quality QS2 if the hydrogeological and hydrological conditions are good.

<sup>(4)</sup> These soils are classified under quality QS3 if the hydrogeological and hydrological conditions are good.

**Table 2-7** Design thicknesses of platform layers (UIC 1994).

| Quality Class of the Soil | Class of bearing required for the subgrade | Requirements of prepared subgrade |                       |
|---------------------------|--|-----------------------------------|-----------------------|
|                           |  | Soil Quality Class                | Minimum thickness (m) |
| QS1                       | P1   | QS1                               | -                     |
|                           | P2   | QS2                               | 0.50                  |
|                           | P2   | QS3                               | 0.35                  |
|                           | P3   | QS3                               | 0.50                  |
| QS2                       | P2   | QS2                               |                       |
|                           | P3   | QS3                               | 0.35                  |
| QS3                       | P3   | QS3                               | -                     |

The soil quality classification requires that *in situ* and laboratory tests are performed and geotechnical strength and deformation parameters are further discussed in the existing standards. This is unfeasible at a planning stage but needs to be assessed during the detailed stages of the HSR project. However, large scale analyses allow one to anticipate the general requirements of the platform and are thus included in the present research.

### 2.2.3 EARTHWORKS GEOTECHNICAL DESIGN: GEOMETRY AND GROUND IMPROVEMENT

The geotechnical design of earthworks, besides complying with the platform requirements, is constrained by slope stability analyses and by construction methods. The slope stability is influenced by the ground geotechnical and hydrological characteristics, the imposed loads, the geometry of the cuts and the embankments, the seismic design, amongst others. While detailed data are required for accurate slope stability analyses, it is important to assess the influence of varying HSR cross-section slopes, affecting expropriation areas and earthworks volumes, for the cost estimates at the planning stage. In this regard and based on the available data, slopes are usually defined by expert engineering judgment (Parsons Brinckerhoff 2009). Smoother slopes may relate to larger safety factors but result in wider footprints of the earthworks and thus larger areas to expropriate and volumes of excavations and embankments. In specific cases, retaining walls and other support structures may allow one to overcome space constraints that hinder smooth lateral slopes.

In addition to the slope stability analysis, involving the natural ground for cuts and the project specified materials for embankments, the strength and deformation behavior of the natural ground at the base of the embankments and cuts has to be assessed. This is particularly relevant for soft and/or organic soils in which creep, strain at constant stress, is expected. To overcome the settlements associated with the long term deformations of these materials, several techniques of ground improvement may be used, including geotextile-encased columns, the mass stabilization technique (the soft soil is mixed with cement, fly ash or blast furnace slag, applicable only for upper 3-5 m depth), deep mixing (lime-cement) columns, amongst others, as discussed by the Federal Highway Administration (FHWA) (Dumas et al. 2003).

#### 2.2.4 HYDRAULICS DESIGN

The linear characteristic of the HSR system often implies crossing rivers and other bodies of water. To overcome these, bridges and other structures such as culverts are used. Culverts are used to cross water bodies of smaller extents than bridges, thus requiring detailed data on the catchment basins of the territory to identify where the culverts are needed. Furthermore, the design depends on factors such as the hydrogeological characteristics of the site, land-use or the precipitation characteristics such as the intensity, duration and return period.

Besides cross-sectional drainage systems, longitudinal drains are also necessary to prevent the water from interfering with the HSR performance. Longitudinal drains should be included along the top of excavations and the bottom of embankments, as well as on the platform, on both sides of the track. Other structures, such as deep drains may be required. Parsons Brinckerhoff (2010) presents guidelines for the design of culverts, bridges and drains, amongst other hydraulic facilities, complying with the applicable laws and standards for the California High-Speed Rail Project. The report indicates that the return periods to adopt for culverts in rural and urban areas are, respectively, 50 years and 100 years, and for drains adjacent to the tracks in rural and urban areas are, respectively, 25years and 50 years. Additionally, Parsons Brinckerhoff (2010) state that when crossing a floodplain, the changes to the existing environment shall not increase the flood hazard to the adjacent properties, raise the flood level of the drainage way or reduce the flood storage capacity.

The hydrology can vary considerably from one region to another and, while the same hydrologic design principles may apply, the design specifics of the HSR hydraulic systems are case-specific.

### **2.3 HIGH-SPEED RAIL COSTS**

The design specifics discussed in sections 2.1 and 2.2 have a major influence on the construction and maintenance costs of a HSR network. Additionally, other important cost components exist that depend on the network characteristics and determine the overall cost value of the HSR.

Levinson et al. (1997) propose a comprehensive model to estimate the overall costs of intercity transportation systems, independently of the transportation mode, and apply it to a HSR link between Los Angeles and San Francisco, California, USA. The authors define the full link cost as the sum of the private and social costs, considering the following components:

- Infrastructure costs (capital construction cost, debt service, costs of maintenance and operation);
- Carrier costs (capital and operating costs);
- User money costs (fees, fares and tariffs);
- User travel time costs (for regular uncongested conditions);
- User delay costs;
- Social costs (net external costs derived from emissions, accidents and noise).

Levinson et al. (1997) estimate these costs, except for the infrastructure costs, based on data such as demand forecasts, number of operating trains and schedules, which vary with the HSR configuration. The authors compare the costs obtained for HSR, air travel and highways for the same Californian corridor concluding that the HSR is the costliest mode, mainly due to the large infrastructure capital costs.

Mendoza et al. (2009) discuss the costs of building and operating new HSR lines in the European context. The report does not address the external costs of HSR and considers the following two main categories: costs related to the infrastructure and costs related to the rolling stock. The costs of the infrastructure are further subdivided into construction costs and maintenance costs. Infrastructure construction costs of new HSR lines are incurred prior to operation start while infrastructure maintenance occurs periodically during operation and according to planned schedules. The rolling stock costs (acquisition, operation and maintenance) depend on the number of trains that in turn indirectly depends on demand. The report further discusses the HSR project timeline and the influence of time for the different cost components.

The research in this thesis acknowledges the importance of all of the above cost components and finds their assessment vital for a sound comparison of alternative intercity transportation modes. However, the consideration of operation and maintenance costs require that the time dimension and demand estimates (which also influence external costs) are included in the analysis. Recognizing the importance, but also the difficulties, in incorporating time and demand within the HSR optimization scope of this research, only the infrastructure construction cost is considered. It is important to note that construction costs also spread in time, though in a smaller interval than operation and maintenance costs. For detailed modeling of time and cost variations in HSR construction, please refer to Moret (2011).

### **2.3.1 VARIABILITY OF HSR CONSTRUCTION COSTS**

The construction costs of new HSR infrastructures can vary significantly, depending on the project specifics and the need to build bridges or tunnels that are considerably more expensive than earthworks.

Mendoza et al. (2009) identify 3 major categories of HSR construction costs: planning and land costs, infrastructure building costs and superstructure building costs. According to the study, planning and land costs represent 5% to 10% of the total construction costs and include sunk costs such as the expenditures for feasibility studies and for expropriation, amongst others. The infrastructure building costs may vary from 10%-25% up to 40%-50% of the total, depending on the deployment site characteristics, such as the ground geotechnical behavior or elevation, including the construction cost of earthworks, bridges and tunnels. The



superstructure cost includes the construction cost of HSR components, such as tracks, sidings along the line, signaling systems, catenary and electrification, that can be considered proportional to the length of the line, varying marginally with the site characteristics, and represent, individually, 5-10% of the total HSR construction cost.

Based on data from 45 HSR projects, Mendoza et al. (2009) observe that the construction cost per km (without planning and land expropriation costs) can vary between €4.7 million and €65.8 million (2005), as depicted in Figure 2-5. These large variations relate to intrinsic characteristics of the project such as the fact that France and Spain have lower building costs due to less populated areas outside the major urban centers or the fact that in France HSR passenger dedicated lines allow steeper slopes than those in mixed traffic lines (Mendoza et al. 2009).

Given the evidence of the influence of the project specifics and the deployment site on the HSR construction costs, the data presented are valuable indicators for cost bounds but comparative analysis of HSR average construction costs per kilometer should take into consideration each case particulars.

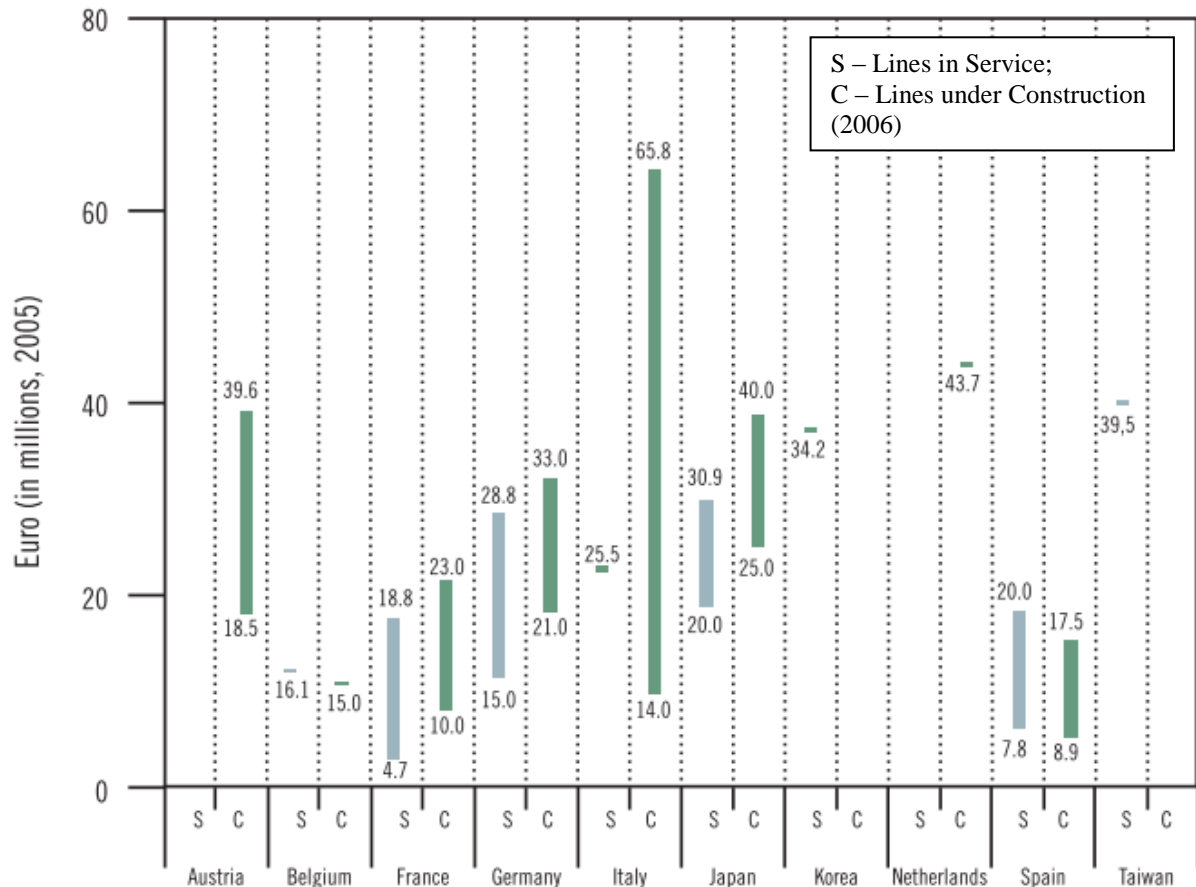


**Figure 2-5** Range of average construction cost per kilometer of new HSR lines around the world in 2005 million euros (planning and land costs excluded) (Mendoza et al. 2009).

## 2.4 RAIL DISRUPTIONS DUE TO NATURAL HAZARDS

### 2.4.1 DESTRUCTIVE AND DISRUPTIVE CAPABILITIES OF NATURAL HAZARDS

Natural hazards happen across the globe causing life, social and economic losses. These include earthquakes, extreme droughts and rainfall, floods, wildfires among others and their consequences depend not only on the severity of the hazards but also on the exposure and vulnerability of the elements at risk (IPCC 2012). Analyzing trend data compiled by the Center for Research on the Epidemiology of Disasters (CRED) for the period 1970-2010, the World Bank and United Nations (2010) observed that mortality does not have a clear rising trend (Figure 2-6), even with the increase in population and exposure. The absolute value of damages from natural hazards, however, is rising (Figure 2-7), markedly in rich countries. While reporting on the natural hazards and losses may have improved over time, the exposure

of valuable assets, profuse in rich countries, due to the construction in sites prone to natural hazards, definitely did increase. Also, critical infrastructure, including electricity, water and gas supply and telecommunications and transportation networks, are becoming ever more important to the economy and to society, which is less willing to pay for lengthy and expensive recoveries and shows minimal tolerance to disruptions.

Floods and storms are the most common hazards in the world (World Bank and United Nations 2010). Perry (2000) reviews different origins of floods: regional floods occurring seasonally due to rainfall and or snow; flash floods depending on rainfall intensity, duration, topography and slope; ice jam floods; storm-surge floods when onshore winds push water into otherwise dry land and levee or dam failure originated floods. According to Perry (2000), floods accounted for the highest number of life losses and property damages in the United States during the 20<sup>th</sup> century.

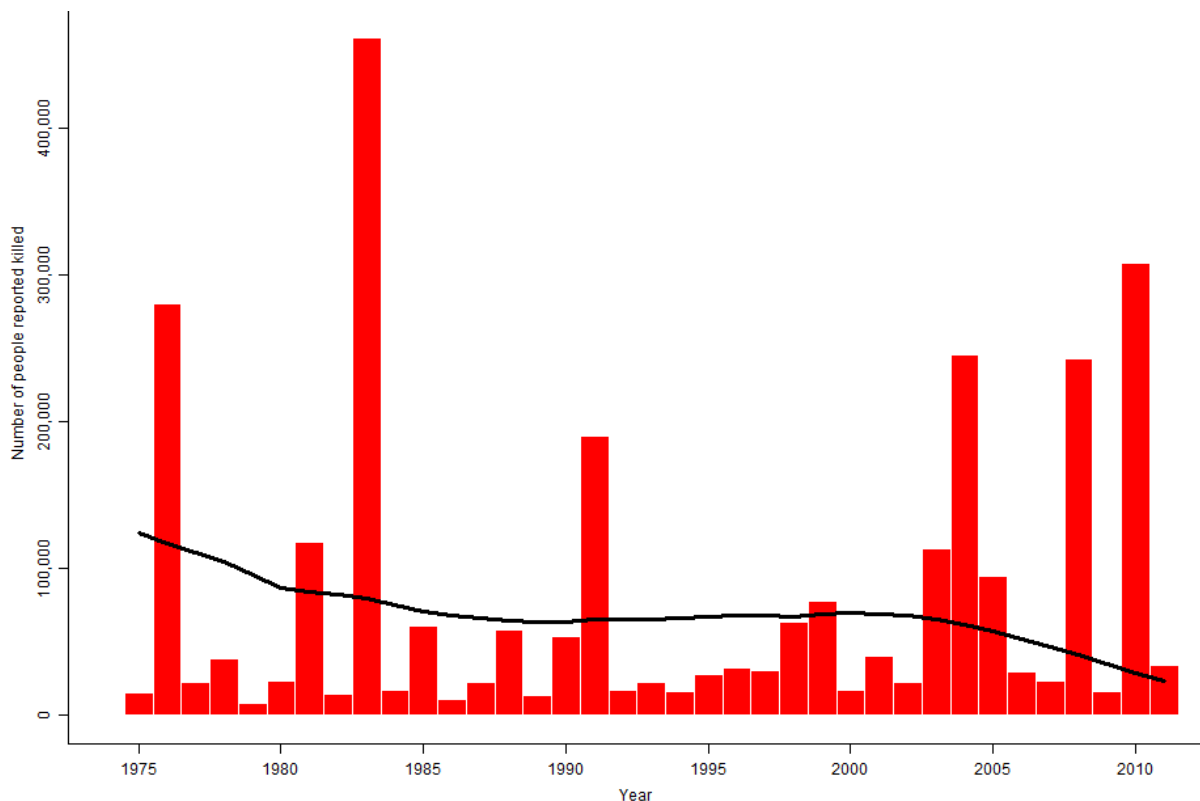


**Figure 2-6** Number of people reported killed by natural disasters in the period 1975-2011. Source: EM-DAT: The OFDA/CRED International Disaster Database [www.emdat.be](http://www.emdat.be), Université Catholique de Louvain, Brussels (Belgium).

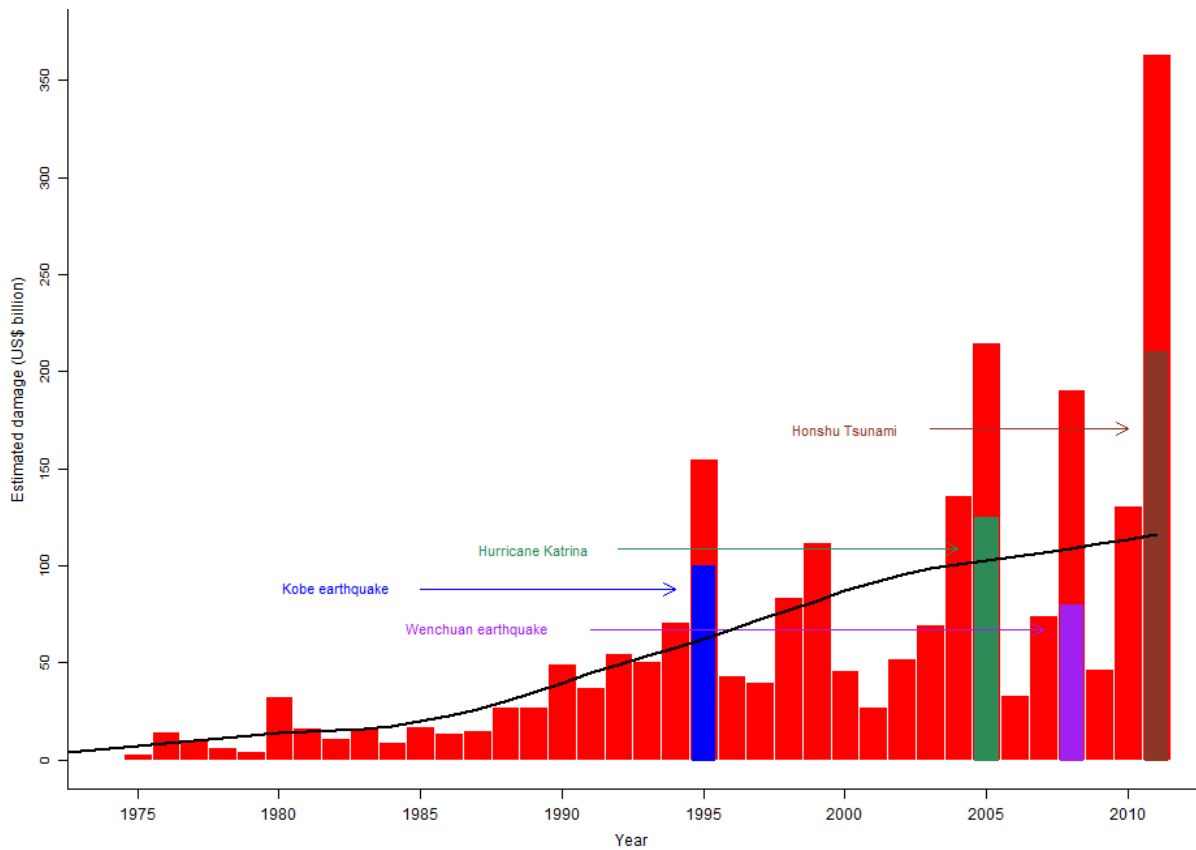


**Figure 2-7** Estimated damage in US\$ billion caused by reported natural disasters in the period 1975-2011. Source: EM-DAT: The OFDA/CRED International Disaster Database [www.emdat.be](http://www.emdat.be), Université Catholique de Louvain, Brussels (Belgium).

Transportation systems are among the infrastructures vulnerable and exposed to floods. Hurricane Katrina affecting the U.S. in 2005 is reported by Link (2010) to have caused over 1600 fatalities and \$30 billion in direct losses in southern Louisiana. Of the total direct losses, \$1 billion dollars was required to repair and replace damaged bridges (Link 2010). In Australia, the 2010-2011 floods resulted in direct losses of around \$5 billion (Munoz 2011). The rail and road disruptions of coal mine links in Queensland, Australia (Figure 2-8), prevented the export of coking coal, used in steel production, resulting in both national and international large economic consequences. In Europe, transportation systems have also been disrupted by flood events such as the 2002 floods affecting Germany, Czech Republic, Austria, Italy and Slovakia with reported overall losses ranging from €15 billion to €20 billion (EQECAT 2002). Moran et al. (2010) analyze the specific railway physical damage caused by the 2006 floods in Austria along a 10 km stretch leading to passenger and freight service interruption for months and in damages of several million euros.



**Figure 2-8** Submerged rail track used for coal transport in Queensland, Australia, January 2, 2011 (Munoz 2011).

Besides flooding, the capability of severe rainfall to trigger landslides in susceptible areas is a major concern for transportation systems (Figure 2-9). The Joint Research Centre (JRC 2003) discusses landslide hazards that occurred in Europe including the November 2000 Stoze, Slovenia, landslide and the October 1997 landslides in San Miguel Island, Azores, Portugal, that destroyed important road connections. Additionally, the JRC (2003) states that the impact of landslides is often underestimated due to difficulties in assessing the direct and indirect costs of major hazards and also smaller landslides occurring more frequently and affecting mostly the transportation systems. The European Environmental Agency (EEA 2010) reviews more recent landslide hazards, covering the 2003-2009 period, including two major events: the 2003 Italian (Alpine region) and the 2005 Austrian landslides that have disrupted roads, highways and railways, including the complete destruction of 3 bridges. Also Chinese railways have been disrupted by rainfall-triggered landslides, including the train derailment in 2010 (BBC News 2010) depicted in Figure 2-10 and 5000 people stranded in four trains in 2011 as the result of a buried section of a railway line in Southwest China (China Daily 2011).



**Figure 2-9** Damage to the rail infrastructure in Cumbria, UK, in August 30, 2012 caused by rainfall-triggered landslides. (Network Rail in BBC News (2012)).



**Figure 2-10** Train derailment in Dongxiang county, Jiangxi Province, China, May 23, 2010 caused by a rainfall-triggered landslide. (AFP in BBC News (2010)).

Transportation disruptions as a consequence of strong earthquakes can also result in great economic losses, injuries and even life loss. The U.S. Geological Survey (USGS 1998a; 1998b) finds that the failure of the highway systems in San Francisco and Monterey Bay areas in the October 17, 1989 Loma Prieta earthquake was the largest single cause of deaths, mainly due to the collapse of the Cypress Viaduct in Oakland (Figure 2-11). According to USGS (1998c) 80% of the regional economic losses were recovered in the 1<sup>st</sup> semester of 1990. However, the economic disruption in two months amounted to \$2.9 billion (USGS 1994). The effects of the earthquake on the surface included ground failure by liquefaction of floodplains and artificial fills and landslides. The USGS (1998d) identifies the occurrence of liquefaction at 134 sites, causing \$99.2 million in losses. The USGS (1998e) describes that landslides

occurred in the earthquake affected area with direct losses amounting to \$30 million and serious indirect costs by disruption of two major freeways. According to the reports, liquefaction and landslides due to the 1989 Loma Prieta earthquake were observed to have similarities with the past occurrences due to the 1906 San Francisco earthquake, leading to regulatory hazard zonation requirements for California in 1990.



**Figure 2-11** Support column failure and collapsed upper deck on the Cypress viaduct, Oakland (USGS 1998f).

In 1994 the Northridge earthquake hit the highly populated area of Southern California and it was at the time reported by the Federal Emergency Management Agency (FEMA) as one of the most costly federal disasters with a \$25 billion worth of damages, according to the U.S. Department of Transportation (U.S. DOT 2002). The major damages to engineered structures were caused by the earthquake-induced ground motion of the  $M_w$  6.7 main shock (EQE 1994). The report observes that liquefaction and lateral spreading did not account for as much damages as the ground motion but were responsible for settlements and pavement cracking, occurring in locations where they had occurred previously in the past, during the 1971 San Fernando earthquake. The other cause of damage cited by EQE (1994) was earthquake-triggered landslides, damaging homes and temporarily blocking the Pacific Coast Highway. Gordon et al. (1998) discuss the indirect economic transport related impacts of the 1994 Northridge earthquake and estimate that the road network disruptions were responsible for losses of \$1.5 billion, representing 27.3% of the overall business interruptions.

Affecting an also heavily populated area, the  $M_w$  6.9 1995 Kobe, Japan, earthquake had far worse consequences than the 1994 Northridge earthquake (EQE 1995). According to the summary report by EQE (1995) ground motion and extensive liquefaction account for most of the damages that in total amounted to \$147 billion in direct costs. Extensive damages to transportation are reported, including the failure of a 3 km long viaduct disrupting the critical Japanese HSR – Shinkansen. However, an earthquake-triggered derailment of the Shinkansen did not occur until the 2004 Niigata Ken Chuetsu earthquake hit Japan (Ogura 2006), as shown in Figure 2-12. A train of the Joetsu Shinkansen Line, in operation since 1982, derailed on a viaduct crossing a rice field (Ashford and Kawamata 2006). The report proposes the large amplitude of the viaduct displacement induced by the softening of the liquefied soil as one of the possible causes of the derailment. According to Ashford and Kawamata (2006), other HSR infrastructures, conventional railways and roads were also affected by the earthquake and landslides accounted for an important part of the disruption.



**Figure 2-12** Liquefaction damages to the rail infrastructure from the 2004 Niigata Ken Chuetsu earthquake: a) the derailed Shinkansen train and b) damages to the viaduct columns where the derailment occurred. (Ogura 2006).

#### 2.4.2 TERMINOLOGY AND CONCEPTS

The European Commission (EC 2010) defined guidelines for risk assessment and mapping for disaster management considering a multi-hazard approach. These guidelines aim at improving consistency of risk assessments across the European Members States, for which varying disaster risk and impact assessment criteria exist, impairing comparability of the results and



conclusions. Challenges to coherence and consistency pointed out by the EC (2010) include the lack of a single common terminology for disasters, of natural or man-made origins, and related concepts, due to linguistic diversity and different approaches by research communities studying different types of hazards. To overcome this, the guidelines propose a definition of terms, in which some are adopted from the United Nations International Strategies For Disaster Reduction (UNISDR 2009) and others are originally proposed by EC (2010). The terminology defined by the UNISDR (2009) is the result of an update of previous documents and was commissioned by the Hyogo Framework for Action 2005-2015: “Building the Resilience of Nations and Communities to Disasters” (UNISDR 2005). The UNISDR (2009) states that the terms are not mutually exclusive and overlapping concepts may exist.

The research in this PhD dissertation adopts the following concepts and terminology from both UNISDR (2009) and EC (2010), but also from the Technical Committee on Risk Assessment and Management of the International Society for Soil Mechanics and Geotechnical Engineering (ISSMGE 2004):

- Danger (Threat): “The natural phenomena that could lead to damage, described in terms of its geometry, mechanical and other characteristics. The danger can be an existing one (such as a creeping slope) or a potential one (such as a rockfall). The characterization of a danger or threat does not include any forecasting.” (ISSMGE 2004);
- Disaster: “A serious disruption of the functioning of a community or a society involving widespread human, material, economic or environmental losses and impacts, which exceeds the ability of the affected community or society to cope using its own resources” (ISSMGE 2004; UNISDR 2009);
- Critical Facilities: “The primary physical structures, technical facilities and systems which are socially, economically or operationally essential to the functioning of a society or community, both in routine circumstances and in the extreme circumstances of an emergency. *Comment: Critical facilities are elements of the infrastructure that support essential services in a society. They include such things as transport systems, (...)*” (UNISDR 2009);

- Hazard: “Probability that a particular danger (threat) occurs within a given period of time” (ISSMGE 2004);
- Land-use Planning: “The process undertaken by public authorities to identify, evaluate and decide on different options for the use of land, including consideration of long term economic, social and environmental objectives and the implications for different communities and interest groups, and the subsequent formulation and promulgation of plans that describe the permitted or acceptable uses. *Comment: Land-use planning is an important contributor to sustainable development (...) Land-use planning can help to mitigate disasters and reduce risks by discouraging settlements and construction of key installations in hazard-prone areas, including consideration of service routes for transport, power, water, sewage and other critical facilities.*” (UNISDR 2009);
- Exposure: “People, property, systems, or other elements present in hazard zones that are thereby subject to potential losses.” (UNISDR 2009);
- Vulnerability: “The degree of loss to a given element or set of elements within the area affected by a hazard. It is expressed on a scale of 0 (no loss) to 1 (total loss). Also, a set of conditions and processes resulting from physical, social, economic, and environmental factors, which increase the susceptibility of a community to the impact of hazards.” (ISSMGE 2004);
- Human Impacts: “The quantitative measure of the following factors: number of deaths, number of severely injured or ill people, and number of permanently displaced people.” (EC 2010);
- Economic and Environmental Impacts: “The sum of the costs of cure or healthcare, cost of immediate or longer-term emergency measures, costs of restoration of buildings, public transport systems and infrastructure, property, cultural heritage, etc., costs of environmental restoration and other environmental costs (or environmental damage), costs of disruption of economic activity, value of insurance pay-outs, indirect costs on the economy, indirect social costs, and other direct and indirect costs, as relevant.” (EC 2010);

- Political/Social Impacts: “Usually rated on semi-quantitative scale and may include categories as public outrage and anxiety, encroachment of the territory, infringement of the international position, violation of the democratic system, and social psychological impact, impact on public order and safety, political implications, psychological implications, and damage to cultural assets, and other factors considered important which cannot be measured in single units, such as certain environmental damage.” (EC 2010).

In the previous section, which presents examples of the destruction and disruption caused by natural hazards, terms such as “economic losses”, “direct losses”, “indirect costs” or “indirect economic losses” are used by different authors/institutions for describing the impacts caused. However, it is unclear what these assessments exactly account for. A World Bank (WB) working paper on the economics of disasters (Hallegatte and Przulski 2010) indicates the existing different methodologies, the multi-dimensionality of disaster impacts, the redistributive effects and the different cost assessment purposes, corresponding to different issues included and definitions of what a cost includes, as the causes of discrepancies often observed in results from different impact assessments of the same hazard. A joint report from the World Bank and the United Nations (World Bank and United Nations 2010) also discusses the bias in measuring the effects of natural hazards, in a comprehensive and systematic analysis of the disasters caused by natural hazards, with focus on prevention. The report states that loss estimates often mix several concepts and that both double-counting and underestimation may influence the results. Addressing these issues, Hallegatte and Przulski (2010) propose a definition that includes the assessment of disaster impacts by two categories: direct and indirect losses, each further sub-divided into market and non-market losses.

Hallegatte and Przulski (2010) define direct losses as the immediate consequences of the physical phenomenon such as an earthquake’s ground motion. Mileti (1999) details that any losses derived from the destruction of buildings, machinery or public infrastructure are categorized as direct, citing as an example the employment losses due to the physical damage of an office building, in addition to the building physical damage itself. Rose (2004) discusses that direct losses may occur even if no physical damage is observed, mentioning the case of a factory that may be forced to shut down because of transportation-related damages preventing employees and suppliers from reaching it. Hallegatte and Przulski (2010) further identify direct market losses as the direct consequences of the hazards that have a market value, losses

of assets such as damage to the building environment or manufactured goods, for which a cost may be easily obtained from observed prices or inventories. Non-market direct losses are direct consequences of the hazards that cannot be repaired or replaced, losses such as damage to historical, cultural or natural assets, health impacts or loss of life, for which a value is difficult to estimate.

Indirect losses are harder to identify. Mileti (1999) states that while the concept of indirect losses has evolved over time, it still remains a rather amorphous one. Hallegatte and Przulski (2010) identify losses as indirect if caused by secondary effects of the hazard, such as the losses imposed on a factory that cannot obtain its input materials because the suppliers had their own business closed due to the hazard physical destruction of the building, as in a chain reaction (Rose 2004). Additionally, Hallegatte and Przulski (2010) state that one may identify the losses as indirect if they are beyond the time period, space or economic sector of the hazard. Indirect market losses are those for which a market value exists, analogously to the direct market losses. The indirect non-market losses include issues such as the impact on poverty and the creation or escalation of inequalities (Hallegatte and Przulski 2010; Rose 2004; World Bank and United Nations 2010).

The detailed categorization of the losses into direct, indirect, market and non-market losses is a complex subject beyond the overview scope of this thesis. Besides terminology and concepts, other factors influencing the hazard loss assessment results exist, such as the methodology used or the purpose of the analysis (insurers and governmental institutions may have different views of which are the pertinent impacts). These are discussed comprehensively in literature (Hallegatte and Przulski 2010; Mileti 1999; Rose 2004; World Bank and United Nations 2010). The following section overviews existing literature addressing the specific case of transportation performance during natural hazards and the impacts of disruption. The applicability and required data for a HSR rail network are discussed.

### **2.4.3 TRANSPORTATION PERFORMANCE AND THE IMPACTS OF DISRUPTION**

The capabilities of natural hazards to seriously affect the physical transportation infrastructure have been demonstrated in section 2.4.1. In the case of railways and roads, the performance of the network is seldom uniform: while specific sections may be damaged, others may still

perform in post-hazard as they did in the pre-hazard conditions. The repair requirements in the damaged sections have to be assessed and repair operations planned for, incurring in a physical damage repair cost. Depending on the damages, repairs may be conducted with traffic circulating at reduced speeds or may require the closure of the section and completely cut off the traffic in the respective link. Ogura (2006) and Ashford and Kawamata (2006) report the performance of the transportation systems in Japan during the 2004 Niigata Chuetsu earthquakes, discussing the effects of the physical damage to the HSR infrastructure on traffic. Ogura (2006) presents the timeline of railway response and reconstruction, including the Shinkansen derailment. The author states that a temporary substitution bus service was in operation in one of the links until passenger service could be resumed. Ashford and Kawamata (2006) discuss the damages to HSR, conventional rail and roads reporting the absence of collapses and the fact that all but two bridges were open to limited traffic.

The service disruptions, ranging from short delays to the complete lack of service, produce additional impacts and losses, adding to the physical damage costs. Acknowledging the implications of transportation disruption, existing literature addresses the assessment of the resulting impacts. Different unplanned events, including natural hazards, have been studied as causes of transportation disruption, ranging from short delays to service interruption, and several methodologies have been applied to assess the complex impacts at the personal, societal and economical levels.

Törnquist and Persson (2007) propose a model for railway traffic re-scheduling during disturbances and apply it to a Swedish case-study that includes high-speed passenger trains. Delay costs of a given HSR passenger train are modeled by Törnquist and Persson (2007) by two cost components: a delay cost per minute based on literature and a fictive fixed penalty value representing accumulated costs of passengers, delayed over one hour, exiting at each station and the potential for missed connections; the fixed cost penalty, for exceeding the also fictively defined one-hour delay, is given by a coefficient times the number of segments to that train has to transverse, without a direct correlation to the potential missed connections. Wardman (2004) also discusses the value of time related to public transport use, based on British data sets, including in-vehicle time and out-of-vehicle time.

Evans and Morrison (1997) incorporate accident risk and disruption in economic models of public transportation considering three equations: a demand function, the user cost and the

cost to the operator providing the service. The approach considers risks to both passengers and non-passengers with a financial value to accident casualties per statistical life (fatal, serious and slight casualties are weighted to produce “equivalent casualties”) and the value of delays derived from disruptions are included in the user costs. Considering a hypothetical rail system, Evans and Morrison (1997) state that basic data required includes detailed information, such as passenger-journeys per year, average fare per passenger-journey, train-kilometers per year, train operating cost per year, operator fixed costs per year or operator’s revenue and surplus per year.

Rose (2004) discusses comprehensive methodologies, including input-output (I-O) models and computable general equilibrium (CGE) models, for the assessment of economic losses from natural hazards. These models are used in literature to estimate the specific transport-related losses in case of disruption (Cho et al. 2001; Gordon et al. 1998; Tatano and Tsuchiya 2008; Ueda and Koike 2000).

Gordon et al. (1998) estimate the transport-related impacts of the 1994 Northridge earthquake considering business interruptions and their effects on the regional economy and disruption of commuting and leisure trips. An I-O model was applied and data on how business and individuals travelling were affected were collected by surveys. Gordon et al. (1998) assess that the transport-related impacts represent circa one quarter (27.3%) of the overall business interruptions, though moderate (\$1.5 billion) when compared to the estimated \$27 billion total cost of the earthquake impacts. The authors also highlight the importance of the highway system redundancy, allowing for travel flexibility (markedly larger for highways than for HSR), in limiting the potential impacts of the disrupted links in the network. Also considering earthquake impacts, Cho et al. (2001) propose an I-O model to estimate disruption in transportation and industrial capacity and their regional economic implications. The authors state that the implementation requires the damage to infrastructure to be first identified by location, followed by the identification of loss in industrial production, such as operation hiatus, that in turn allows the estimation of the loss costs.

Tatano and Tsuchiya (2008) propose a framework for the estimation of economic loss due to seismic transportation disruption for both highways and railroads and consider spillover effects through a spatial CGE model. The input includes transit time or cost varying with the damage extent and requires interregional input-output data in a benchmark year, for which

economic equilibrium is considered. Tatano and Tsuchiya (2008) apply the model to estimate the transportation-related economic losses due to the 2004 Niigata-Chuetsu earthquake observing that losses spread across several regions and that negative spillovers disturbed supposedly unaffected regions. Ueda and Koike (2000) also applied a spatial CGE model to estimate the economic damage of earthquake-disrupted HSR in Japan observing the interregional propagation of the impacts.

The use of methodologies including I-O models and CGE models to estimate the economic losses from transportation disruption due to natural hazards require that comprehensive data are available for pre-disaster and post-disaster conditions. Especially for the post-disaster situation, these data are difficult to obtain. Moreover, planning for transportation infrastructure, such as the HSR research in this thesis, requires the estimation of the expected possible impacts of the hazards, bearing additional difficulties from the already challenging post-disaster data gathering. Chang and Nojima (1997) address the need for highway infrastructure performance measures in a post-earthquake condition that may be readily available and that allow the estimation of the economic losses due to the highway system disruption. The authors propose two summary performance measures to estimate the damage to the infrastructure and then relate the performance measures to the economic loss: a measure  $L$  estimating the total length of undisrupted highway and a measure  $C$  estimating the remaining degree of connectedness within the network. These measures require pre-earthquake network configuration and traffic volumes and post-earthquake damage and recovery patterns. Chang and Nojima (1997) applied the proposed measures to the 1994 Northridge and the 1995 Kobe earthquakes, obtaining good correlations to the actual traffic volumes, and suggested an approach to estimate the economic loss considering the traffic volume as an economic activity indicator. In subsequent work, Chang and Nojima (2001) propose two additional post-earthquake transportation performance measures for the overall system based on the network coverage and accessibility. The performance measures were also developed to conduct rapid post-disaster conditions assessment and were applied to the urban rail and the highway systems considering the damages caused by the 1995 Kobe earthquake. Chang (2003) further developed an accessibility (Hansen 1959; Koenig 1980) approach to address the performance of transportation systems in post-disaster conditions. The approach was applied to the 1995 Kobe earthquake focusing on passenger rail disruption, assessing

service disruption and the spatial disparities, and to a hypothetical Seattle, WA, earthquake focusing on the possible loss of road and highway service and its spatial implications.

Also with emphasis on accessibility, Sohn (2006) discusses the performance of highways subject to flood damages with an application to a 100-year flood in Maryland, US. Sohn (2006) indicates that the consideration of different degrees of physical vulnerability of the network infrastructure influences the modeling of the disruption level and the recovery process. Lu and Peng (2011) propose a methodology for transportation network vulnerability analysis based on accessibility considering different sea-level scenarios. An application to the south Miami area for the target year of 2060 is presented and the results indicate 100% decrease in accessibility with the entire network inundated and a 30% decrease in accessibility for zones partly disrupted or undisrupted. Jenelius and Mattsson (2012) also discuss road network vulnerability considering area-covering disruptive events, such as floods or earthquakes, as opposed to events concentrated in single network links, such as a car crash or road works. The methodology considers the spatial discretization of the study area through cells of uniform shape and size. The vulnerability assessment, defined as susceptibility to events capable of producing service disruption, translates unsatisfied travel demand and delays for users.

Transportation network reliability is related to the vulnerability concept and addresses the probability of the network remaining unaffected and capable of normal functioning (Lu and Peng 2011). Günneç and Salman (2011) propose a methodology for assessing the reliability and the expected performance of a network under disaster risk and present an application to the Istanbul, Turkey, highway system under earthquake risk. Cimellaro et al. (2010) argue that while a vulnerability approach emphasizes the ability to resist to hazard damages, a resilience approach focuses on the improvement of the quality of life and the capacity of recovery and propose a framework for the analytical quantification of disaster resilience. Ip and Wang (2011) propose an approach to quantify the resilience of transportation networks and apply it to the mainland Chinese railway network.



#### 2.4.4 REMARKS ON THE NATURAL HAZARDS HSR PERFORMANCE ASSESSMENT IN THE CONTEXT OF THE RESEARCH

An insight on the existing research for the performance and disruption assessment of transportation systems for natural hazards is provided. While some studies are complementary, others partially overlap and others address different dimensions of the problem. Furthermore, the complexity in defining measures of HSR performance and the impacts of disruption are acknowledged.

In particular for the planning and optimization context of the present research, several difficulties exist. Detailed data is not generally available at the early stages of the project. Decision making at the planning stage relates to small scale data, usually covering substantially different options and, once a solution is chosen, the project advances for increasingly detailed stages. Additionally, the optimization context implies that the deployment location and characteristics of the HSR are yet to be defined.

Most of the approaches of disruption assessment overviewed require detailed input data in pre-hazard conditions, such as timetables, demand, trip fares or operator costs and revenues. These input data, along with the performance in the post-hazard conditions, are then used to estimate the transportation-related impacts. The type of detailed data required for the pre-hazard conditions is not available at the planning stage. Furthermore, given that the HSR location and layout is to be defined, the analysis of transportation-related impacts of disruption, in a post-hazard condition, would have to be projected.

Several methods to estimate the transportation-related impacts have been discussed. These require that the alternative paths to the damaged sections and the redundancy of the network along with the accessibility and the potential for business interruptions due to physical damage of the infrastructure are assessed. For the HSR optimization process, as opposed to an established HSR network, the former vary and have to be assessed for every particular configuration of the HSR network studied.

Moreover, if substitution bus services are used to detour damaged links, the impact assessment relates, for instance, to the detour route, frequency of the substitution service and the number of passengers. If the damage repairs allow traffic, but at reduced speeds, impacts relate to delays and the potential missed connections. In both cases, the time it takes to resume

full operation influences the extent of the impacts, requiring that the time dimension is taken into account. This is also true when considering the evaluation of the resiliency of the network. However, the time dimension is not included in the present research. If time was to be included, a comprehensive survey had to be accomplished on how long the repair of any type of damage would take. This would mean to assess the time and precedence of each repair activity to achieve the full operation, requiring detailed data and depending on the location of the physical damage of the HSR.

This research acknowledges the importance in determining the HSR disruption impacts due to natural hazards. However, the difficulties derived from the planning and optimization contexts of the analysis, as well as the omission of the time dimension, are documented. The HSR network performance for natural hazards is thus assessed only by the direct market losses pertaining to the physical damage repair and/or replacement of damaged sections.

## Chapter 3.

# Optimization of Linear Transportation Infrastructures: State-of-the-Art

Planning for a new HSR network requires large investments to build the infrastructure, which represent an important part of the overall cost of the project. The large expenditures require a conscious use of the resources, particularly when large public investments are made. Difficulties however exist in determining which network configuration yields the most value.

A complex relation exists between the constraints of the HSR design and the multiple HSR configurations, both in terms of 3D layout and the cross-sections that may be used. Particularly given that the quality of the HSR performance concurrently depends on the 3D layout, the deployment site and the cross-sections used (sections 2.1, 2.2 and 2.3). Furthermore, considering the effects of natural hazards, some cross-sections will have lower capital construction costs but may be more vulnerable to the effects of natural hazards. Hence, larger capital construction investments may prevent or minimize future damages of a HSR hit by natural hazards, though not necessarily for all circumstances. In addition to the complex and interrelated factors influencing the value of a HSR network, the analysis at a planning scale is required to cover large areas, which involve dealing with large input data. While trained engineers produce good estimates, data can be extensive. An integrated approach capable of dealing with large datasets and systematically establishing the relationship between the influencing factors is thus a valuable tool for decision-making.

### 3.1 MODELLING THE OPTIMIZATION PROBLEM

Mathematical optimization models are commonly used to solve large and complex problems, such as planning a HSR network. An objective function expresses the features to be optimized

(either for minimization or maximization problems) by changing the design variables and subject to constraints that define the feasibility of the solutions, such as generally stated in the standard linear programming problem of (3.1) to (3.3) (Bai et al. 1997).

$$\text{Maximize} \quad c^T x \quad (3.1)$$

$$\text{subject to} \quad Ax = b, \quad (3.2)$$

$$x \geq 0. \quad (3.3)$$

Expression (3.1) defines a measure of wealth which one aims at maximizing, equation (3.2) defines the constraints of the problem, such as resource limitations or corporate policies and  $x$  represents the design variables of the problem. It is noted that models are always a representation of reality and, as such, their ability to express the real problems depends on the simplifications assumed.

Deterministic approaches are the most common and widely used in engineering. These assume that all of the problem input is 100% known. Extensive literature on the application of such models to the optimization of highway and railway infrastructure exists. Jha et al. (2007) propose an approach for optimizing transit rail lines when station locations are known and present an application to a case study with a 3.43 km distance between two stations. The authors consider the minimization of an objective function representing the sum of alignment costs. Two types, operator costs ( $OC_1, OC_2, OC_3, OC_4$  and  $OC_5$ ) and user costs ( $UC_1, UC_2$  and  $UC_3$ ), are considered according to the assumptions in Table 3-1. Samanta and Jha (2011) further determine the optimal location of rail stations to be connected by optimal alignments.

**Table 3-1** Assumptions by Jha et al. (2007) in the assessing the cost of a railway line.

| Cost type  | Assumptions   |
|--|---|
| 1) Track related construction cost ( $OC_1$ ) (\$)   | Unit track related construction cost (\$/ft) is given   |
| 2) Station construction cost ( $OC_2$ ) (\$)         | Location specific estimated station construction cost is available exogenously  |
| 3) Right-of-way cost ( $OC_3$ ) (\$)                 | Average land value is known from a geographic database  |
| 4) Earthwork cost ( $OC_4$ ) (\$)                    | Topography and terrain elevations are known   |
| 5) Operating Cost ( $OC_5$ ) (expressed as \$/day)   | Relevant input parameters (such as the hourly wage rate of the train operators) needed to calculate the operating cost is known |
| 6) Access-time cost ( $UC_1$ ) (expressed as \$/day) | The travel time to access the stations is known as well as unit access-time cost is given                                       |
| 7) Riding-time cost ( $UC_2$ ) (expressed as \$/day) | The average train speed is known as well as the unit ride-time cost is known  |
| 8) Wait-time cost ( $UC_3$ ) (expressed as \$/day)   | The unit wait-time cost (\$/min) is given   |

The research by Jha et al. (2007) is based on previous works for highway alignment optimization. Similarities exist between the railway- and highway- alignment optimization problems and comprehensive research exists for highways. Jong (1998) addresses the optimization of three-dimensional highway alignments, research which is later extended with the incorporation of Geographic Information Systems (GIS) by Jha and Schonfeld (2000) for the optimization of highway horizontal alignments.

Jong (1998) formulates 4 highway alignment optimization models, considering: (i) non-backtracking horizontal alignments; (ii) backtracking horizontal alignments; (iii) non-backtracking 3D alignments and (iv) backtracking 3D alignments. Considering backtracking (versus non-backtracking) alignments has implications for the representation of the alignments proposed by Jong (1998) since cutting planes ( $N$ ) orthogonal to a linear section linking two nodes will intersect more than one point of the highway alignment (Figure 3-1). Horizontal versus 3D alignment optimization has implications for the cost assessments as some cost components of the highway alignment optimization problem depend on the difference between the ground and highway elevation.

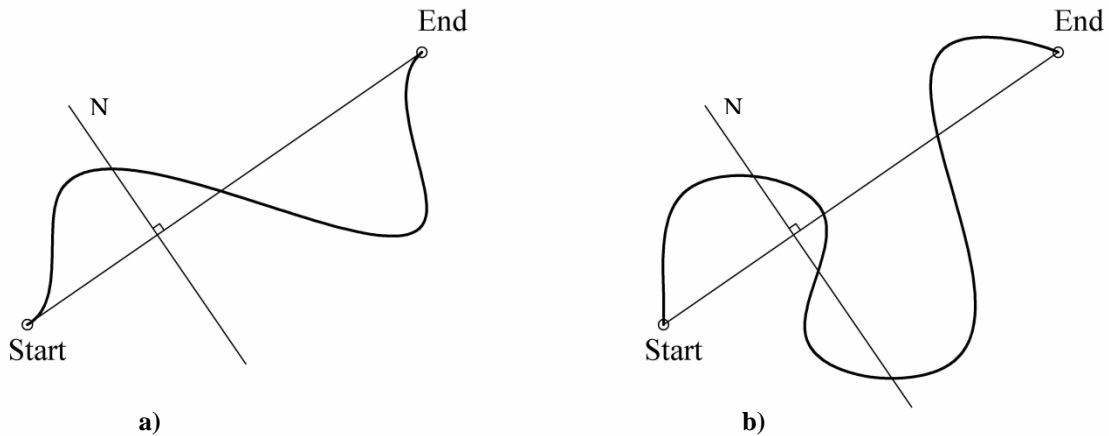


**Figure 3-1** Plan view of highway alignments: a) non-backtracking and b) backtracking. (Jong 1998).

The alignment representation proposed by Jong (1998) considers the decision variables defined as coordinates in relation to a coordinate system in which the origin depends on the cutting planes. Other representations may be used which avoid the difficulties posed by backtracking alignments and, as such, let us consider the decision variables represented by a position vector  $x$  representing the 3D configuration of the alignments. A general formulation for the model is defined by Jong (1998) as the minimization of the total highway costs (equation 3.4) subject to a set of constraints.

$$\text{Minimize} \quad C_T(x) = C_N(x) + C_L(x) + C_A(x) + C_V(x) + C_U(x) \quad (3.4)$$

subject to

- Boundary conditions. These ensure the alignment starts and ends at the locations the highway aims at connecting.
- Alignment necessary conditions. These ensure that the plan view of the alignment is solely formed by a combination of tangent sections, circular curves and spirals (transition curves) and that the longitudinal profile is solely formed by a combination of tangent sections and parabolic curves.

- Horizontal curvature constraint. This ensures that the curvature of the alignment curves on the plan view is equal or smaller than the project-specified maximum curvature.
- Gradient constraint. This ensures that the gradient of the alignment is equal or smaller than the project-specified maximum gradient.
- Vertical curvature constraint. This ensures that the curvature of the alignment curves on the longitudinal profile is equal or smaller than the project-specified maximum curvature.
- Inaccessible region. This constraint ensures problem-specified inaccessible regions are not crossed by the highway.

$C_N(x)$  are location dependent costs such as right-of-way and environmental costs,  $C_L(x)$  are length dependent costs such as construction of track or ballast and maintenance that vary only with the alignment length,  $C_A(x)$  are area dependent costs including construction which varies only with the area,  $C_V(x)$  are volume dependent costs including cuts and embankments and  $C_U(x)$  are user costs including fuel consumption cost, travel time costs and accident costs on curves.

Given that GIS integration is not included in the models proposed by Jong (1998), difficulties exist in representing location cost items and in storing and managing data characterizing the search space of the problem. This is overcome by Jong et al. (2000) who propose a method for horizontal alignment optimization of highways between two given points (Figure 3-2), based on the previous work by Jong (1998) and incorporating GIS. The minimization of an objective function including location-dependent costs, length-dependent costs and user costs is considered, while satisfying the applicable standard minimum radius for horizontal curves. In optimizing the horizontal alignment only, the costs for earthworks cannot be accurately formulated, as these costs depend on the difference between the ground and infrastructure elevation. Also, bridges and tunnels are not included. Kim et al. (2004) further introduce a method for estimating intersection construction costs of earthworks, pavement and right-of-way.

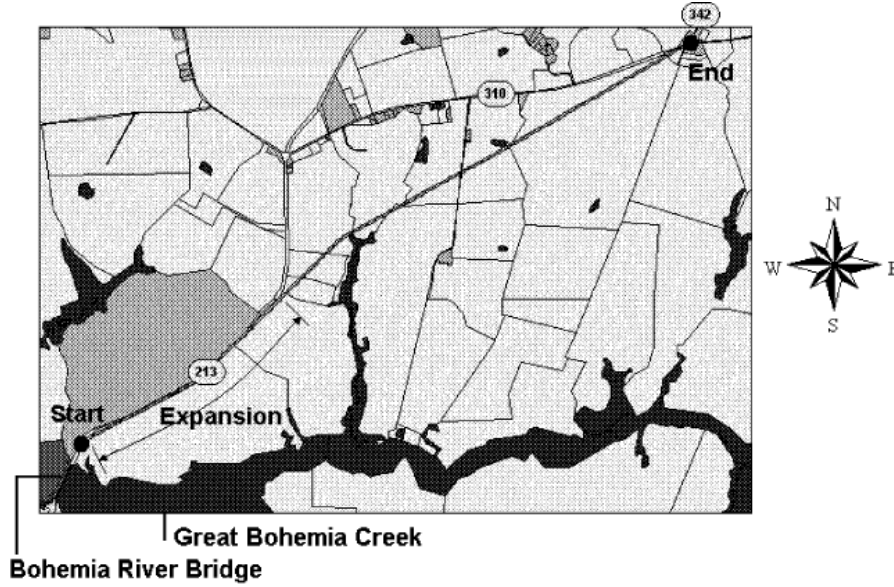


Figure 3-2 The optimal alignment for the case-study application by Jong et al. (2000).

Jha and Schonfeld (2004) extend the work of Jong (1998) and incorporate penalties to limit the environmental impacts on floodplains and wetlands and to avoid geometry design violations such as exceeding the maximum gradient. The penalty costs of crossing individual floodplains and wetlands are formulated by, respectively, expressions (3.5) and (3.6). Gradient penalties are formulated by (3.7).

$$C_{pf_j} = \gamma_0 + \gamma_2 \left( \frac{A_{l_j}}{A_{p_j}} \right)^{\gamma_3} \quad (3.5)$$

where  $C_{pf_j}$  is the individual penalty associated with the intersection of the  $j^{\text{th}}$  floodplain;  $\gamma_0, \gamma_2, \gamma_3$  are user-specified coefficients;  $A_{l_j}$  is the intersected area of the  $j^{\text{th}}$  floodplain and  $A_{p_j}$  is the total area of the  $j^{\text{th}}$  floodplain.

$$C_{pw_k} = \eta_0 + \eta_1 \left( \frac{A_{l_k}}{A_{w_k}} \right)^{\eta_2} \quad (3.6)$$

where  $C_{pw_k}$  is the individual penalty associated with the intersection of the  $k^{\text{th}}$  wetland;  $\eta_0, \eta_1, \eta_2$  are user-specified coefficients;  $A_{l_k}$  is the intersected area of the  $k^{\text{th}}$  wetland and  $A_{w_k}$  is the total area of the  $k^{\text{th}}$  wetland.



$$C_{pg_i} = \begin{cases} \alpha_0 + \alpha_2 (|g_i| - G_{\max})^{\alpha_3} & \text{if } |g_i| > G_{\max} \\ 0 & \text{otherwise} \end{cases} \quad \forall i = 0, \dots, n \quad (3.7)$$

where  $C_{pg_i}$  is the individual penalty cost of violating the gradient maximum value,  $G_{\max}$ , at the  $i^{\text{th}}$  linear section;  $\alpha_0, \alpha_2, \alpha_3$  ( $\alpha_3 > 1$ ) are user-specified coefficients and  $g_i$  is the actual gradient of the  $i^{\text{th}}$  linear section.

A total penalty cost,  $C_p(x)$ , is computed by summing all the individual penalties, which is added to the objective function as shown by (3.8). This increase of the objective value in such a minimization problem penalizes the configurations that cross the undesirable areas and that do not comply with the limits established for the geometry parameters.

$$\text{Minimize} \quad C_T(x) = C_O(x) + C_U(x) + C_P(x) \quad (3.8)$$

$C_O(x)$  are operator costs including linear-dependent costs, right-of-way and earthwork,  $C_U(x)$  are user costs considering travel-time costs, vehicle-operating costs and accident costs and  $C_P(x)$  are penalty costs including the floodplain and wetland crossing penalties.

Fwa et al. (2002) address the optimization of the highway vertical alignment by minimizing the total construction cost due to earthworks and pavement construction costs. This is an important component of highway costs but requires a horizontal highway alignment to be previously established.

Kim et al. (2007) extend the model formulation by Jong (1998) with the incorporation of bridges and tunnels in the highway alignment optimization. The authors consider a 4.5 m threshold between the alignment and ground elevation of height and depth for building, respectively, bridges and tunnels. Linear bridge cost functions are considered, varying with the bridge span length. Tunnel costs are based on the tunnel excavation costs of a circular cross-section of radius equal to a two-lane typical cross-section defined by the applicable standard. Applications of the approach are presented by Kim et al. (2007) for alignments linking 2 points distancing circa 1.5 km, as shown in Figure 3-3.

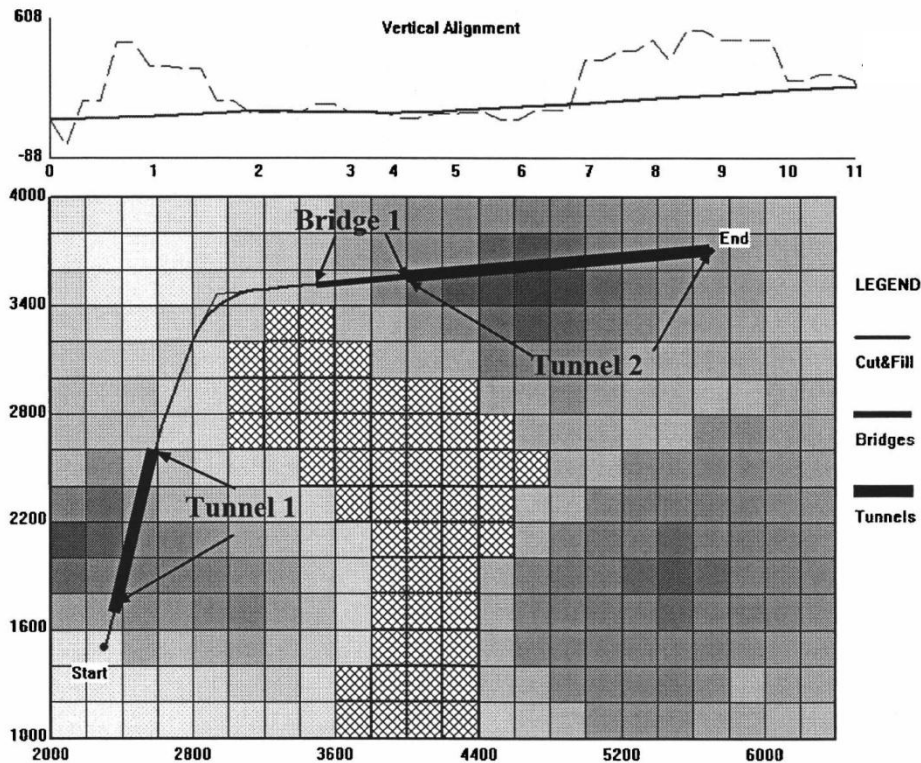


**Figure 3-3** The optimal alignment plan view and longitudinal profile for a synthetic case-study application of highway alignment optimization considering bridges and tunnels ( Kim et al. 2007). Dimensions in the plan view and for elevation in ft (1 ft = 30.48 cm).

Other specifics common to railway- and highway- projects have been studied. Jha (2003) discusses environmental impacts and the selection of alignments along different corridors with an objective function minimizing operator, user and penalty costs (3.8) based on the cost formulations by Jong (1998) and Jong and Schonfeld (1999). After solving the model and obtaining the near-optimal configuration, the authors employ a method for sampling intermediate configurations of the optimization process which cross significantly different corridors. Cheng and Lee (2006) propose a 3D highway alignment optimization considering heavy vehicle speeds, restricted areas and control points. A restricted area is an area where highway use is discouraged or prohibited and a control point represents a location the highway is preferred to cross. Penalties are used for the consideration of these locations. For control points, a maximum threshold distance may define the maximum desirable distance between the control and the highway and penalties for the exceeding distance, if that is the case, are computed penalizing the configuration. Penalties for restricted areas are analogously computed. Lee et al. (2009) address the horizontal alignment optimization problem also considering areas where crossing is restricted and controlled, minimizing the weighted sum of

the total length of a piecewise linear line and penalty terms associated with control areas as well as restricted areas. This improves the work by Cheng and Lee (2006) in the model-solving technique but not the model formulation itself. Kang et al. (2012) propose a highway alignment model that incorporates transition curves in the horizontal alignment considering the minimization of the total costs given by the sum of operator costs, user costs, penalty costs and environmental costs.

The aforementioned research deals mainly with the alignment optimization for detailed stages of the project. With a different perspective, Gipps et al. (2001) propose a transport route optimization planning tool: Quantm. According to Gipps et al. (2001) planning aims at determining where the route should go and at attaining preliminary cost estimates whereas design aims at detailing the route configuration and at producing more accurate cost estimates. In this context, the author states that it is within the global perspective of planning that the greatest opportunities to reduce overall costs arise. A cost-based alignment optimization is performed by the tool considering the following possible cross-sections:

- Cuts and embankments. Costs are computed based on the volume and the type of material to be excavated/placed. Retaining walls are included for steep cross-slopes and the cost varies linearly with the height and longitudinal extension.
- Culverts. The cost varies with the number and type of channels, and the channeling length (measured at the base of the embankment).
- Viaducts. The costs are formulated as a linear combination of length and the profile area. This represents a fixed cost component for foundations plus a variable component proportional to the height.
- Tunnels. The costs are defined proportionally to the length.

Developed at the Commonwealth Scientific and Industrial Research Organization (CSIRO), Quantm has been acquired by Trimble Navigation and applied to several real-world problems, including HSR projects (Trimble 2013). To create realistic alignments, Gipps et al. (2001) refer the need to consider, at least, the following information: (i) geometry standard parameters such as minimum radii and maximum gradient; (ii) a digital elevation model (DEM); (iii) Geotechnical information defining embankments and cuts slopes and excavation

costs; (iv) existing linear infrastructure, such as roads, railroads and pipelines, and the required clearances and (v) the identification of zones requiring special treatment, for social or environmental reasons. Additionally, Gipps et al. (2001) discuss the need to include subjective factors such as preserving environmental amenity. Two strategies for dealing with subjectivity are suggested: (i) quantify the subjective aspects and incorporate their value in the optimization or (ii) produce a set of alternative solutions and posteriorly perform a selection on subjective grounds. However, the mathematical formulation of the optimization model used by Gipps et al. (2001) is not disclosed. Greager et al. (2005) perform a study to evaluate the usefulness of the Quantm system for planning transportation improvements in Colorado, USA. Neither Gipps et al. (2001) nor Greager et al. (2005) discuss capabilities for allowing the consideration of connecting intermediate cities and adopting the more restrictive and desirable radii or gradient, instead of the feasibility limits, and the respective trade-offs with the capital construction costs of the HSR configurations.

Also for the planning stage, Angulo et al. (2012) present a demand-based model for determining potential highway corridors. The authors consider the maximization of the served flow subject to budget constraints. An initial interpolation function is used to estimate the mean construction cost of each linear unit between 2 given points of the search space.

The literature reviewed discusses different model formulations for the optimization of linear transport routes, mostly applied to roads and highways. Most consider the minimization of the total costs subject to constraints defining limitations to the geometric design of the infrastructure. Other features are included by several authors such as the consideration of environmental issues, demand and speed of heavy vehicle speeds (one may draw an analogy with rail freight service).

Some of the discussed models address, separately, the optimization of horizontal alignments and vertical alignments while other models address the integrated 3D alignment optimization. Important construction cost components such as earthworks, bridges and tunnels cannot be properly captured with models optimizing the horizontal alignment separately. On the other hand, optimizing the vertical alignment requires a horizontal alignment to be previously defined. An integrated 3D optimization is more complex but allows one to overcome these shortcomings of separate analyses. In this context, however, a 3D approach was not found in literature for dealing with large data sets, such as required for HSR planning, and concurrently

establishing trade-offs between construction costs, geometry layout, connection of intermediate cities and protected land-use areas. Also an important factor in realistically assessing the costs of linear transportation routes is the consideration of the geological geotechnical characteristics of the deployment site (Cheng and Lee 2006; Gipps et al. 2001). These characteristics influence the construction costs, maintenance costs and the future performance of the infrastructure (sections 2.2.2 and 2.2.3).

In addition, the research overviewed, while extensive, does not consider uncertainty. Moret (2011) discusses how variability of geologic input affects the construction cost and time of a HSR. Furthermore, uncertainty is inherent to the effects of natural hazards, such as geotechnical and hydrologic risks, which are not addressed by the reviewed models.

The following section discusses the need to consider uncertainty for optimization models representing real-world problems such as planning for a HSR network.

### 3.1.1 THE CONSIDERATION OF UNCERTAINTY

While the use of deterministic models in engineering applications is common, most real-world problems are, in fact, affected by uncertainty. Two types, according to the origin and affecting civil engineering projects, are identified by Faber and Stewart (2003): random uncertainty from variability of phenomena and epistemological uncertainty, according to Betâmio de Almeida (2011) derived from the lack of complete knowledge of a process or its enclosing system behavior. Epistemological uncertainty may be reduced with the collection and analysis of additional data but random uncertainty, however, cannot. The need to consider uncertainty, in particular for geotechnical engineering, is also recognized by Christian (2004). Mulvey et al. (1995) discuss different approaches used to tackle uncertainty in the optimization of large-scale systems.

One is to ascertain the solution for the “worst-case” problem. This approach is conservative and, in many cases, economically unfeasible.

The second approach discussed is to solve the deterministic optimization problem, obtain an optimal or near-optimal solution and then perform studies of sensitivity analysis. These will assess the solution’s susceptibility to the realization of uncertain but plausible events. If the solution remains relatively immune to the tested perturbations, the goal is achieved and the

solution stands. However, if perturbations prove to have unacceptable consequences, changes are required. The adoption of mitigation measures, creation of restrictions of use or even changing the solution at its core may be necessary. The new solution should be again tested and reformulated, if needed, until satisfactory results are obtained.

Opposed to the reactive post-optimality studies of sensitivity analysis, Mulvey et al. (1995) suggest the need for a proactive approach introducing probabilistic information. Stochastic Linear Programming (SLP) is considered such an approach, providing mechanisms with which the model solution may be adjusted to the uncertainty realization.

Mulvey et al. (1995) discuss the consideration of uncertainty in mathematical optimization models which have two distinct components: (i) a structural component that is not conditioned by the realization of uncertain parameters and which cannot be adjusted and (ii) a control component that is subject to noisy input data and which can be adjusted for realizations of uncertainty. Let  $x \in R^{n_1}$  be a vector of structural decision variables and let  $y \in R^{n_2}$  be a vector of control decision variables, consider the following linear optimization model of expressions (3.9) to (3.12) generically formulated by the authors.

$$\text{Minimize} \quad c^T x + d^T y \quad (3.9)$$

$$\text{subject to} \quad Ax = b, \quad (3.10)$$

$$Bx + Cy = e, \quad (3.11)$$

$$x, y \geq 0. \quad (3.12)$$

where  $Ax = b$  defines the structural constraints with coefficients fixed and free of noise and  $Bx + Cy = e$  defines the control constraints in which the coefficients are affected by uncertainty.

To define an SLP model, a set of scenarios  $\Omega = \{1, 2, \dots, S\}$  is introduced. Each scenario  $s \in \Omega$  corresponds to one possible realization of uncertainty and provides a conceivable course of events (Bai et al. 1997), in which a set  $\{d_s, B_s, C_s, e_s\}$  represents the realizations of the coefficients of the control constraints and  $p_s$  represents the probability that scenario  $s$  occurs with  $\sum_{s=1}^S p_s = 1$ . The set  $\{y_1, y_2, \dots, y_S\}$  defines the control variables (termed recourse

variables in SLP parlance (Mulvey et al. 1995)) of each scenario  $s \in \Omega$ . An SLP model can be defined by (3.13) to (3.16).

$$\text{Minimize} \quad \sigma(x, y_1, y_2, \dots, y_S) \quad (3.13)$$

$$\text{subject to} \quad Ax = b, \quad (3.14)$$

$$B_s x + C_s y_s = e_s, \quad \text{for all } s \in \Omega \quad (3.15)$$

$$x \geq 0, y_s \geq 0, \quad \text{for all } s \in \Omega \quad (3.16)$$

For multiple scenarios, the objective function  $\xi = c^T x + d^T y$  becomes a random variable taking the value  $\xi_s = c^T x + d_s^T y_s$  with probability  $p_s$ . SLP optimizes the first moment of the distribution of the objective function, the expected value, and tradeoffs among the scenarios are weighted according to (3.17).

$$\sigma(x, y_1, y_2, \dots, y_S) = \sum_{s \in \Omega} p_s \xi_s \quad (3.17)$$

This assumes an active management style for which variables are adjusted as scenarios unfold. Mulvey et al. (1995) and Bai et al. (1997), however, discuss that by minimizing only expected costs or maximizing only expected profits, SLP fails to reduce variability. While flexibility is provided by SLP, the decision-maker's preferences towards risk are not taken into account, particularly important for asymmetric distributions and in a risk aversion context. One additional shortcoming of SLP discussed by Mulvey et al. (1995) concerns solution unfeasibility. The authors state that if no feasible pair  $(x, y_s)$  exists for every scenario the SLP model is declared unfeasible, despite the fact that such situations inevitably occur, particularly in engineering applications due to measurement errors. Mulvey et al. (1995) and Bai et al. (1997) thus propose the use of robust optimization, which explicitly addresses unfeasibility and considers higher moments of the objective value.

### 3.1.2 ROBUST OPTIMIZATION

Two notions of robustness are introduced by Mulvey et al. (1995): solution robustness and model robustness. If the optimal solution of formulation (3.9) to (3.12) is robust with respect

to optimality, remaining “close” to the optimal for any scenario realization, it is termed solution robust while if the optimal solution is robust with respect to feasibility, remaining “almost” feasible for any scenario realization, it is termed model robust.

Consider the introduction of the set  $\{z_1, z_2, \dots, z_S\}$  of error vectors measuring the unfeasibility allowed in the control constraints of scenario  $s$ . Mulvey et al. (1995) propose the robust optimization model of (3.18) to (3.21).

$$\text{Minimize} \quad \sigma(x, y_1, y_2, \dots, y_S) + \omega \rho(z_1, z_2, \dots, z_S) \quad (3.18)$$

$$\text{subject to} \quad Ax = b, \quad (3.19)$$

$$B_s x + C_s y_s + z_s = e_s, \quad \text{for all } s \in \Omega \quad (3.20)$$

$$x \geq 0, y_s \geq 0, \quad \text{for all } s \in \Omega \quad (3.21)$$

The first term of the objective function (3.18),  $\sigma(x, y_1, y_2, \dots, y_S)$ , measures the solution robustness while the second term  $\rho(z_1, z_2, \dots, z_S)$ , a feasibility penalty function, measures the model robustness. The weight  $\omega$  can be used to establish a variety of configurations that tradeoff solution robustness and model robustness. Two formulations are proposed by Mulvey et al. (1995) for the feasibility penalty formulation: the quadratic penalty function of (3.22) for cases in which both positive and negative violations are equally undesirable and the exact penalty function of (3.23) for cases when only positive violations are undesirable.

$$\rho(z_1, z_2, \dots, z_S) = \sum_{s \in \Omega} p_s z_s^T z_s \quad (3.22)$$

$$\rho(z_1, z_2, \dots, z_S) = \sum_{s \in \Omega} p_s \max\{0, z_s\} \quad (3.23)$$

One observes that the stochastic linear programming of expressions (3.13) to (3.16) is a particular case of the robust optimization if uncertainty does not affect feasibility and in which solution robustness is measured by (3.17) and the worst-case scenario analysis is also a particular case if the objective function is given by (3.24) (Mulvey et al. 1995, Bai et al. 1997).

$$\sigma(x, y_1, y_2, \dots, y_S) = \max \xi_s \quad (3.24)$$



Mulvey et al. (1995) discuss that while the expected value of SLP can be used for low risk decisions, this is inappropriate in moderate- to high-risk decisions since most decision-makers are risk averse and expected value does not capture either the decision-maker's preferences towards risk or the distribution of the objective value  $\xi_s$ . Mulvey et al. (1995) suggest the use of other aggregate functions  $\sigma(x, y_1, y_2, \dots, y_s)$  for measuring solution robustness, including (i) the mean/variance approach (Markowitz 1991) of (3.25) considering the expected value plus a constant ( $\lambda$ ) times the variance and (ii) the von Neumann-Morgenstern utility curves (Von Neumann and Morgenstern 1953) according to (3.26).

$$\sigma(x, y_1, y_2, \dots, y_s) = E(\xi_s) + \lambda \text{Var}(\xi_s) \quad (3.25)$$

$$\sigma(x, y_1, y_2, \dots, y_s) = \sum_{s \in \Omega} p_s U(\xi_s) \quad (3.26)$$

Mulvey et al. (1995), Bai et al. (1997) and Watkins and McKinney (1997) discuss that, while being a more general approach than the mean/variance, the utility curves pose an additional burden on the user by having to specify his or her level of aversion in the form of the utility function.

With the consideration of higher moments than the expected value, robust optimization assumes a more passive management style than SLP since the objective function value will not vary significantly across the scenarios and little or no adjustments of the control variables will be required. Accordingly, the fundamental goal of robust optimization is to find an optimal or near-optimal solution that is not overly sensitive to any specific realization of uncertainty (Bai et al. 1997). Lempert et al. (2006) also consider robustness as a key criterion for evaluating strategies under conditions of deep uncertainty, the state in which analysts do not know or decision makers cannot agree upon. The authors discuss the difficulties of considering a multitude of future states, claiming robust decision-making as a prescriptive, systematic and quantitative approach to it.

Robust optimization models have been successfully applied to fields as diverse as supply chain management and logistics, economics, water management, transportation systems, amongst others. Bertsimas et al. (2011) review robust optimization theory and discuss applications in portfolio optimization, supply chain management and engineering, the latter

including applications for structural design, circuit design, power control in wireless channels and antenna design.

Malcolm and Zenios (1994) propose a robust model for planning power systems capacity expansion considering uncertain future demand. The approach follows the robust optimization framework of expressions (3.18) to (3.21) considering a mean/variance measure of solution robustness and is discussed by Mulvey et al. (1995) as an example of robust optimization applications to real-world problem domains. Also for planning capacity expansion considering uncertain demand, but for telecommunications, Laguna (1998) propose a robust optimization model within the framework by Mulvey et al. (1995). In fact, this robust optimization framework has been applied to several engineering problems including applications for water systems such as: (i) the design of water distribution networks considering the uncertainty of the network's working conditions (Cunha and Sousa 2010a), (ii) urban water supply planning considering uncertainties in future demand and supply (Watkins and McKinney 1997), (iii) for ground-water contaminant plume containment with unknown aquifer parameters (Watkins and McKinney 1997) and (iv) regional wastewater system planning for capital and operational costs of the infrastructure and the water quality of the river in which the treated wastewater is discharged, considering an uncertain river flow (Zeferino et al. 2012). In the field of transportation systems, Ukkusuri et al. (2007) propose a robust model for the network design problem considering origin-destination demand uncertainty.

In some applications, however, solution robustness measures differ from the mean/variance approach and the von Neumann-Morgenstern utility curves. Watkins and McKinney (1997) use a mean/upper-partial-mean formulation in the ground-water contaminant plume containment problem to avoid penalizing costs lower than the expected cost. Ukkusuri et al. (2007), while using the mean/variance approach, state that another possibility for measuring solution robustness could be the use of the maximum regret of not following the optimal scenario. Regret is stated by the authors as the difference between the objective function value when scenario  $s$  occurs and the optimal objective function value had it been known that the respective scenario  $s$  was going to materialize. Mudchanatongsuk et al. (2008) also formulate a robust approach to the network design problem considering demand and transportation cost uncertainty aiming at finding the solution with the best objective function value for the worst-case scenario. Computational experiments are used to compare the robust and deterministic

solutions. While the robust solution behaves efficiently for all uncertain parameter scenarios, which is not the case of the deterministic one, the authors conclude the results suggest a conservative robust solution which does not adapt to the uncertainty level.

Daskin et al. (1997) propose a different measure of robustness for facility location modeling considering scenario descriptions of uncertainty: the  $\alpha$ -reliable p-minmax regret. The authors argue that systems affected by uncertainty are, in general, neither designed for the expected nor the worst-case performance, giving as an example an airport capacity design. Regret is also defined as the difference between the objective function value when scenario  $s$  occurs and the optimal system configuration for the same scenario  $s$ . However, Daskin et al. (1997) discuss that minimizing the maximum regret may be overly sensitive to extreme scenarios, which, even if very unlikely to occur, can govern the solution configuration. The  $\alpha$ -reliable p-minmax regret proposed by the authors considers: (i) a set of conceivable scenarios with the respective probabilities of occurrence, (ii) the definition of a subset of scenarios with a collective probability of scenarios of, at least, the specified reliability level  $\alpha$  and (iii) minimizes the maximum regret within the scenario subset. The authors state that this prevents a single and very-low probability scenario from conditioning the entire solution, unless  $\alpha$  is close to 1 (standard minmax problem).

In the transportation systems field, List et al. (2003) propose the robust optimization of vehicle fleet sizing considering uncertainties in the future demand to be served by the vehicle fleet and the productivity of individual vehicles, reflecting uncertainties in operating conditions. The robust model by List et al. (2003) considers the tradeoff between the expected cost of a solution (across all scenarios of uncertainty in demand and vehicle productivity) and a measure of the risk of the cost exceeding some threshold (i.e., highest acceptable) value. List et al. (2003) show, for a simple network example, that the mean/variance approach leads to an optimized solution in which empty vehicles operate for low demand scenarios in order to increase the costs in these scenarios and thus reduce variability. To overcome this type of effect, an upper-partial-moment approach, the partial expectation of costs above the threshold, is used.

### 3.1.3 REMARKS FOR THE HSR PLANNING OPTIMIZATION CONSIDERING NATURAL HAZARDS

The existing deterministic models discussed for alignment optimization are valuable approaches. For realistic formulations an integrated 3D optimization should be considered and difficulties exist in representing location cost items and in storing and managing data characterizing the search space of the problem unless GIS are incorporated. The intersection of the HSR with existing infrastructure, such as roads and railroads, should not be built at grade and additional costs of the construction of overpasses or underpasses and/or relocation of the existing infrastructure or detour the HSR may arise. Furthermore, geotechnical/geological behavior influences the construction costs of the HSR cross-sections and the performance of the infrastructure. As such, information characterizing the ground behavior should be incorporated in the model.

The deterministic models overviewed consider, in general, the minimization of reference total costs subject to geometric constraints such as minimum radii and maximum gradient. Operator costs, which may include construction and maintenance costs, and user costs, considering travel-time vehicle operating and accident costs, are generally included. In some cases, environmental restrictions are formulated as penalty costs and added in the objective function.

The discussed deterministic models, however, do not consider uncertainty. The need to consider uncertain and incomplete information when planning for large-scale systems has been recognized. Several sources of uncertainty affect a HSR network project. Incomplete and uncertain geologic and geotechnical input may lead to cost and time overruns (Moret 2011). In addition, the occurrence of natural hazards disrupting the HSR is dependent on the infrastructure characteristics and on the deployment site but uncertain. Only one reference was found in literature considering natural hazards in the alignment optimization of linear transport infrastructures. Pantha et al. (2009) propose the preliminary optimization of a new road alignment considering slope failure susceptibility. An application to the Himalayan Region is presented for a preliminary optimal alignment around 45 km long. The research, however, does not consider an integrated 3D approach and costs are not realistically expressed in terms of the alignment configuration. A map defining an expected overall cost, including land acquisition cost, land-use, slope, unit cost of earthwork excavation and

landslide susceptibility is established with GIS and the goal of the optimization is to define the horizontal alignment minimizing the overall averaged cost. Furthermore, several different natural hazards may affect the HSR, especially given its characteristic linear development.

As planning the HSR infrastructure for the worst-case scenario is economically unfeasible, a robust approach should be considered. Scenarios describing the possible natural hazards affecting the HSR network should be defined, aiming at finding optimal or near-optimal HSR network configurations that are not overly sensitive to any of the natural hazards represented by the scenarios.

It is important to note two aspects. Firstly, each natural hazard is associated with a return period which allows the definition of the probability of occurrence within the HSR lifetime. Secondly, if the scenarios were to be weighted with the respective probability of occurrence, the effects of earthquakes with large return periods, low probabilities, would essentially be neglected. However, the effects of large earthquakes may be catastrophic and decision-making for public and expensive infrastructure such as HSR is generally made in a risk aversion context. To address these two aspects, the research in this thesis should reflect the decision-maker's risk aversion when weighting the effects of natural hazards, which are assessed by the direct market losses pertaining to the physical damage repair and/or replacement of the HSR damaged sections, as discussed in section 2.2.4. Model robustness measures, such as evaluating a measure of regret, could be implemented. This, however, would require the optimal or near-optimal HSR configuration for each scenario to be firstly devised and solving the HSR planning optimization problem is significantly consuming time-consuming, in the order of days as discussed in sections 6 and 7.

The literature overviewed, both for deterministic alignment optimization models and robust models applied to problems in other fields, frameworks the approach for the consideration of natural hazards in planning for a HSR network. However, intersection of the HSR with existing infrastructure is not included. While HSR bridges and tunnels are included in the research, structures which may be required for overpasses and underpasses, the intersection of the existing infrastructure requires detailed input data characterizing plan view and elevation of the infrastructure. User costs are also not accounted for. Also, uncertainty in the geologic and geotechnical input data maps is not included in the proposed model. Recognizing their importance, these costs factors and uncertainty sources are proposed to be incorporated in

future developments. The research presented in this thesis considers the infrastructure construction costs, geometric specifications from HSR applicable standards, control and restricted areas and the performance assessment for natural hazards.

### **3.2 SOLVING TECHNIQUES**

Models are mathematical representations of problems and to attain the respective solution, the models need to be solved. Different techniques, which may be categorized into exact and approximation methods, exist for solving the models.

Exact methods are guaranteed to find the optimal solution. Such methods include branch-and-bound and other linear integer programming based methods (such as branch-and-cut and branch-and-price), dynamic programming and Lagrangian relaxation based methods (Puchinger and Raidl 2005). However, there are problems, termed NP-hard problems, for which an exact optimal solution cannot be obtained within a polynomially-bounded computation time and many such problems are found in combinatorial optimization (Aarts and Lenstra 1997). According to Aarts and Lenstra (1997), combinatorial optimization deals with making discrete choices for solving a problem which aims at finding an optimal solution among a finite or countably infinite number of alternatives. The HSR planning optimization problem considered in this research thesis is formulated in this manner. Kirkpatrick et al. (1983) discuss solving the famous travelling salesman problem, for which given a  $N$  number of cities and the ability to calculate the costs of travelling between any two cities of  $N$ , one aims at defining the salesman route so he passes in every city, ending the route at the start point, with the minimum cost. Kirkpatrick et al. (1983) state that, in practice, exact solutions can only be attempted for  $N$  in the range of a few hundred cities, given computation effort requirements.

Similarly to the traveling salesman problem, many real-world problems are unreasonable, time-wise, to be solved by exact methods. In this context, approximation methods are of great interest by aiming at optimal or near-optimal solutions within reasonable computation times. (Aarts and Lenstra 1997; Johnson 2012). Local search methods are such approximate methods representing a trade-off between optimality and computation effort. To obtain a local search heuristic, a neighborhood structure is superimposed on each system configuration, meaning that a set of neighboring configurations is specified for each system configuration (Aarts and

Lenstra 1997). The heuristic starts from an initial configuration of the system, generated either randomly or by an algorithm, that is modified until a termination point for which no better neighboring configurations are found. Multiple local search methods exist, including the simulated annealing, tabu search, genetic algorithms and artificial neural networks (Aarts and Lenstra 1997), and have been applied to a wide range of problem. Osman and Laporte (1996) present extensive bibliography for applications of local search methods.

Kirkpatrick et al. (1983) discuss the iterative improvement of an initial known configuration of the system, which is iteratively rearranged into neighboring configurations to be accepted if yielding better objective function value. The process is repeated and accepted system configurations are rearranged into neighboring ones until no further improvements are found. Kirkpatrick et al. (1983), however, state that the iterative approach, as described, usually gets stuck in local optimum. Tackling this, several local search algorithms incorporate mechanisms to avoid getting trapped in local optima (Blum and Roli 2003).

### **3.2.1 SOLVING TECHNIQUES FOR MODELS OF LINEAR TRANSPORTATION INFRASTRUCTURES**

Deterministic models for the optimization of linear transport infrastructures are discussed in section 3.1. In this section 3.2.1 several techniques proposed by the authors to solve the models are discussed.

Kang et al. (2007) discuss advantages and disadvantages of existing approaches, other than local search methods, for optimizing road alignments (Table 3-2), based on the research reviewed by Jong (1998). In the original work (Jong 1998) a clear distinction between models and model solving techniques is absent. The author's context of each of the approaches is presented in the table's notes.

Kang et al. (2012) breakdown the approaches for solving highway alignment optimization models according to the alignment type, as shown in Table 3-3.

**Table 3-2** Advantages and disadvantages of existing approaches for optimizing road alignments (Kang et al. 2007).

| Method                                | Advantages   | Disadvantages   |
|---------------------------------------|--|---|
| Calculus of variations <sup>(1)</sup> | <ul style="list-style-type: none"> <li>- Yields smooth alignment</li> <li>- Possibly finds the global optimum</li> <li>- Has continuous search space</li> </ul>  | <ul style="list-style-type: none"> <li>- Cannot deal with discontinuous cost items (requires well developed objective function)</li> <li>- Complex modeling and computation efforts</li> </ul>  |
| Network optimization <sup>(2)</sup>   | <ul style="list-style-type: none"> <li>- Is simple and easy to use</li> <li>- Well-developed algorithms for solving the problem exist</li> <li>- Possibly finds the global optimum</li> </ul>  | <ul style="list-style-type: none"> <li>- Cannot yield smooth alignment</li> <li>- Uses discrete solution set rather than the continuous search space</li> <li>- Requires large memory</li> </ul>  |
| Dynamic programming <sup>(3)</sup>    | <ul style="list-style-type: none"> <li>- Simple and easy to use</li> <li>- Well-developed algorithms for solving the problem exist</li> <li>- Possibly finds the global optimum</li> </ul>   | <ul style="list-style-type: none"> <li>- Cannot yield smooth alignment</li> <li>- Uses discrete solution set rather than the continuous search space</li> <li>- Requires large memory</li> <li>- Has difficulty in handling backward bends</li> </ul> |
| Enumeration <sup>(4)</sup>            | <ul style="list-style-type: none"> <li>- Can yield a realistic alignment</li> <li>- Possibly finds the global optimum</li> <li>- Can consider most important constraints</li> </ul>  | <ul style="list-style-type: none"> <li>- Is inefficient</li> <li>- Uses discrete solution set rather than continuous search space</li> </ul>  |
| Linear programming <sup>(5)</sup>     | <ul style="list-style-type: none"> <li>- Is simple and easy to use</li> <li>- Can use well-developed algorithms</li> <li>- Possibly finds the global optimum</li> <li>- Can yield smooth alignment</li> <li>- Has a continuous search space</li> </ul> | <ul style="list-style-type: none"> <li>- Uses formulation only for limited cost items and constraints (must be linear)</li> <li>- Gradient and curvature constraint are formulated for a limited number of points</li> </ul>                          |
| Numerical search <sup>(6)</sup>       | <ul style="list-style-type: none"> <li>- Can yield a realistic alignment</li> <li>- Can consider most of the important constraints and various costs</li> <li>- Has continuous search space</li> </ul>   | <ul style="list-style-type: none"> <li>- Produces multiple local optima</li> <li>- Complex modeling and computation efforts</li> <li>- Has difficulty in modeling discontinuous cost items</li> </ul>   |

Notes (according to Jong 1998):

<sup>(1)</sup> The basic problem of Calculus of Variations is to seek a curve connecting two end points in space which minimizes the integral of a function, concept which has been applied for horizontal highway alignment optimization.

<sup>(2)</sup> Formulation of the horizontal alignment as a network problem (using arcs to represent the alignment) and use solving techniques such as shortest path algorithms.

<sup>(3)</sup> Assumes the problem can be subdivided into sub-problems whose contributions to the objective function are both independent and additive. The optimization of highway alignments is usually performed for a coarse discretization and the solution can be refined by subsequent searches with a confined and more detailed discretization.

<sup>(4)</sup> Discussed for earthwork costs minimization for a given horizontal alignment. Consists in evaluating all possible feasible vertical alignments within a given geometric boundary and choose the least costly.

<sup>(5)</sup> Discussed for optimizing the coefficients of a polynomial function defining a highway vertical alignment, using the simplex algorithms.

<sup>(6)</sup> The search space is defined continuously, the objective function is differentiable and solving techniques such as Quasi-Newton methods and line-search methods are used.



**Table 3-3** Highway alignment optimization approaches ( Kang et al. 2012). References for applications are listed in the original table by Kang et al. (2012).

| <b>Alignment</b>          | <b>Optimization approach</b>   |
|---------------------------|--|
| Horizontal alignment only | Calculus of variations<br>Network optimization<br>Dynamic programming<br>Mixed integer programming<br>Neighborhood search heuristic with mixed integer programming<br>Genetic algorithms |
| Vertical alignment only   | Enumeration<br>Dynamic programming<br>Linear programming<br>Numerical search<br>Genetic algorithms   |
| 3D alignment              | Numerical search<br>Distance transform <sup>(1)</sup><br>Neighborhood search heuristic with mixed integer programming<br>Genetic algorithms  |

<sup>(1)</sup> A sequence of grid points connecting two endpoints is searched

Kang et al. (2012) discuss that the solving techniques listed, other than the use of the genetic algorithms (local search method), presented flaws in solving the highway alignment optimization problem such as: (i) not being able to address discontinuous cost items including expropriation costs; (ii) not being able to yield realistic alignments; (iii) using discrete solution sets rather than continuous search space; (iv) addressing only a limited number of cost components of the problem and (v) possibly producing multiple local optima.

The need to consider realistic formulations in an integrated 3D optimization, including discontinuous cost items, for modeling the HSR planning problem has been discussed in section 3.1. The lack of a comprehensive cost formulation leads to suboptimal solutions but in considering a comprehensive formulation the cost function becomes an implicit function of the decision variable set, which implies the total cost function is non-differentiable and noisy (Jong and Schonfeld 1999). Given these properties, Jong and Schonfeld (1999) discuss that only search methods without gradient information can be used to optimize such comprehensive cost formulations, proposing the use of genetic algorithms.

Besides the use of genetic algorithms to solve the highway alignment optimization problem (Fwa et al. 2002; Jha and Schonfeld 2000, 2004; Jha 2003; Jong and Schonfeld 1999; Jong 1998; Jong et al. 2000; Kang et al. 2012; Kang et al. 2007; Kim et al. 2004, 2007), other local search techniques have been successfully used. Gipps et al. (2001) employ a stochastic optimization technique in which a current configuration of the system is modified in a neighborhood and the cost of the modified configuration is compared with the cost of a current configuration. Worsening configurations can be accepted within a given threshold. The solving technique used by Gipps et al. (2001) can be categorized as a threshold algorithm within local search methods. However, this approach by Gipps et al. (2001) seems to correspond to a second stage optimization in which an initial configuration (termed seed) is refined. Merlot and Gipps (2008) state the seeds are generated by constructing a network over the ground surface and the problem is solved using shortest path algorithms. Then, seeded runs are performed focusing on particular routes for optimization (Greager et al. 2005).

The simulated annealing algorithm is also a threshold algorithm, within local search methods, in which the threshold of accepting worsening system configurations has a specific formulation. Simulated annealing has been successfully used by Angulo et al. (2012) for solving a deterministic model for determining potential highway corridors and for other problems in the context of robust optimization (Bertsimas and Nohadani 2010; Cunha and Sousa 2010a; b; Zeferino et al. 2012). Aarts and Lenstra (1997) discuss that simulated annealing has been successfully applied to solve a broad range of problems. In particular, good results have been obtained by implementing simulated annealing to solve large and complex combinatorial optimization problems (de Weck and Willcox 2010). Furthermore, it can be shown that the algorithm asymptotically converges to the global minimum with probability 1, under certain conditions (Aarts et al. 1997). Note, however, that for a finite-time solution an approximation of the asymptotic convergence is required.

### **3.2.2 REMARKS ON SOLVING THE HSR PLANNING PROBLEM**

The research in this thesis implements the Simulated Annealing Algorithm (SAA) to solve the HSR planning robust optimization model considering natural hazards. This choice is based on the good results obtained in solving deterministic route optimization models and in solving

robust optimization models for other problems, and the fact that the SAA is the only local search algorithm with theoretical convergence proof to the global optimum.

### 3.2.2.1 THE SIMULATED ANNEALING ALGORITHM

The Simulated Annealing Algorithm is credited to Kirkpatrick et al. (1983) and traces its origins to the annealing process of materials to low energy states. In this physical process, the material is first heated, providing the energy necessary for particles to move, followed by a controlled cooling. Despite the fact that lower energy states relate to lower temperatures of the system, a low temperature by itself is not sufficient (Jilla and Miller 2001). Slow cooling is necessary in order to allow particles to rearrange into the lowest energy configuration without being trapped in local minima energy states. The Metropolis algorithm (Metropolis et al. 1953) expresses this concept. Consider a current state  $i$  of corresponding energy  $E_i$ . If state  $i$  is perturbed into state  $j$  of corresponding energy  $E_j$ ,  $j$  will be the new current state with a probability  $p$  given by (3.27).

$$p = \min \left\{ 1, e^{\left( \frac{E_i - E_j}{k_B t} \right)} \right\} \quad (3.27)$$

where  $k_B$  is the Boltzman's constant and  $t$  is the temperature.

The Metropolis algorithm principles were applied by Kirkpatrick et al. (1983) and Cerny (1985) to solve the travelling salesman problem. The analogy is drawn between obtaining the lowest energy configuration of a system and achieving the global optimum solution for the problem, considering equivalences between solutions of the optimization problem and the states of a physical system and between the objective function value of a solution and the energy of a state (Aarts et al. 1997). Figure 3-4 presents a general flowchart of the algorithm.

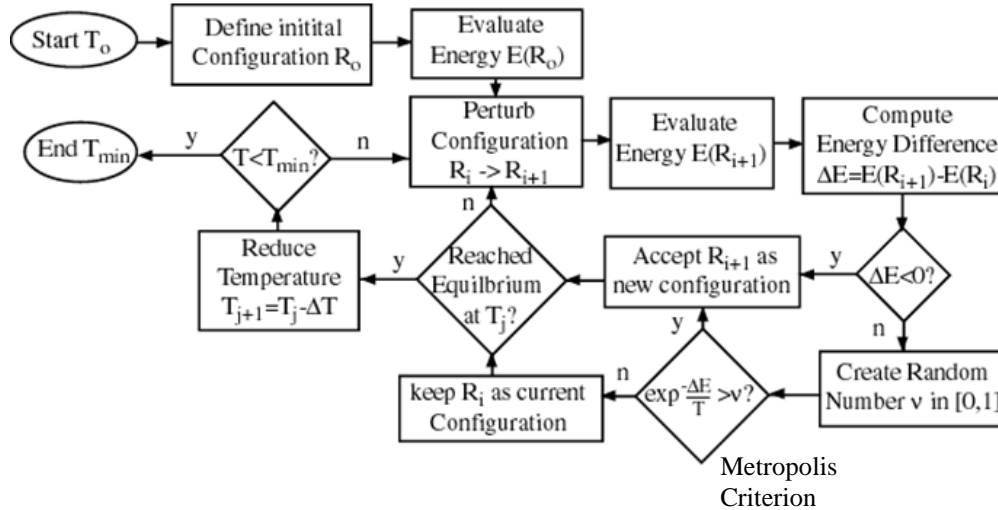


**Figure 3-4** Simulated Annealing Algorithm flow chart (Cohanin et al. 2004).

The flowchart in Figure 3-4 by Cohanin et al. (2004) shows the SAA starts with an initial feasible system configuration  $R_0$  which one has to define, randomly or with an initial best guess, and for which the energy  $E(R_0)$  is assessed. Also an initial temperature  $T_0$  is defined. This initial current configuration is then modified, within its neighborhood structure, into  $R_{i+1}$  with energy  $E(R_{i+1})$  and the energy difference  $\Delta E = E(R_{i+1}) - E(R_i)$  is computed. If  $\Delta E < 0$ ,  $R_{i+1}$  is better than  $R_i$  and  $R_{i+1}$  is accepted as the new current configuration. If  $\Delta E > 0$ ,  $R_{i+1}$  is worse than  $R_i$  and its acceptance is governed by a threshold established with the Metropolis criterion: a uniformly distributed random number  $v \in [0,1]$  is defined and compared with Boltzmann probability  $P(\Delta E) = e^{\left(\frac{-\Delta E}{T}\right)}$ . If  $P(\Delta E) > v$ , the worsening configuration  $R_{i+1}$  is accepted as the new current configuration. If  $P(\Delta E) < v$ , the worsening configuration  $R_{i+1}$  is rejected and  $R_i$  stands as the current configuration. The following step verifies if equilibrium at temperature  $T_j$  has been reached. If equilibrium has not been reached, one continues on creating and perturbing configurations at the same temperature. If equilibrium has been reached, one decreases the temperature by some  $\Delta T$  and continues on creating and perturbing configurations at the new and lower temperature  $T_{j+1}$ . The process is repeated until a termination criterion, in the flowchart defined by temperature  $T_{\min}$ , is reached. Other termination criteria may be defined.

Aarts et al. (1997) show that in mathematically modeling the SAA using Markov chains, for certain conditions, asymptotic convergence to the global optimum can be proven to have

probability 1. A Markov chain can be defined as a sequence of trials from a sampling process in which the probability of a given trial result depends only on the previous trial result and not of the prior sequence of results (3.28).

$$P_{ij}(k) = P\{X(k) = j | X(k-1) = i\} \quad (3.28)$$

where  $P_{ij}(k)$  is the transition probability from result  $i$  to result  $j$  at the  $k^{\text{th}}$  trial and  $X(k)$  is a random variable defining the outcome of the  $k^{\text{th}}$  trial.

It is not intended to present here the convergence proof of the SAA. However, it is important to note that the asymptotic convergence to the global optimum requires cooling schedules reaching an equilibrium distribution of the Markov chains. This is discussed by Johnson et al. (1989) as being of impractical applicability since the convergence to the equilibrium takes a large time and is exponential even for a very simple problem. Thus, the SAA implementation in a finite time requires the generation of a sequence of homogeneous Markov chains (in which the transition probability does not depend on the trial number  $k$ ) of finite length and at descending values of the control parameter (temperature). This implies that the implementation falls short from the true equilibrium distribution of a Markov chain. As such, an implementation of the SAA requires the definition of an initial system configuration, the definition of the neighborhood of any current configuration and the procedures to generate new candidate neighbor configurations and a set of parameters governing the convergence of the algorithm, termed as the cooling schedule.

The cooling schedule defines the finite sequence of values of the temperature (control parameter) and a finite number of transitions at each temperature by specifying (Aarts et al. 1997):

- an initial value of the temperature  $T_0$ ;
- a decrement function for lowering the temperature;
- the finite length of each homogeneous Markov chain, meaning a minimum number of iterations to be performed at each temperature step;
- a termination criterion for the algorithm.

According to Aarts et al. (1997) different cooling schedules may be implemented and two broad classes may be distinguished: static cooling schedules and dynamic cooling schedules. Static cooling schedules implement fixed parameters which are not changed during the algorithm implementation. Dynamic schedules implement parameters which are adapted through the algorithm implementation

The application of the Metropolis criterion allows the SAA to accept worsening solutions. Given that the tested configurations are rearranged within a close neighborhood of the current configuration, if a local optimum is reached, escaping requires that worse solutions are accepted, as illustrated in Figure 3-5. The rate of acceptance of worse solutions is governed by the cooling schedule and decreases as the SAA implementation progresses.

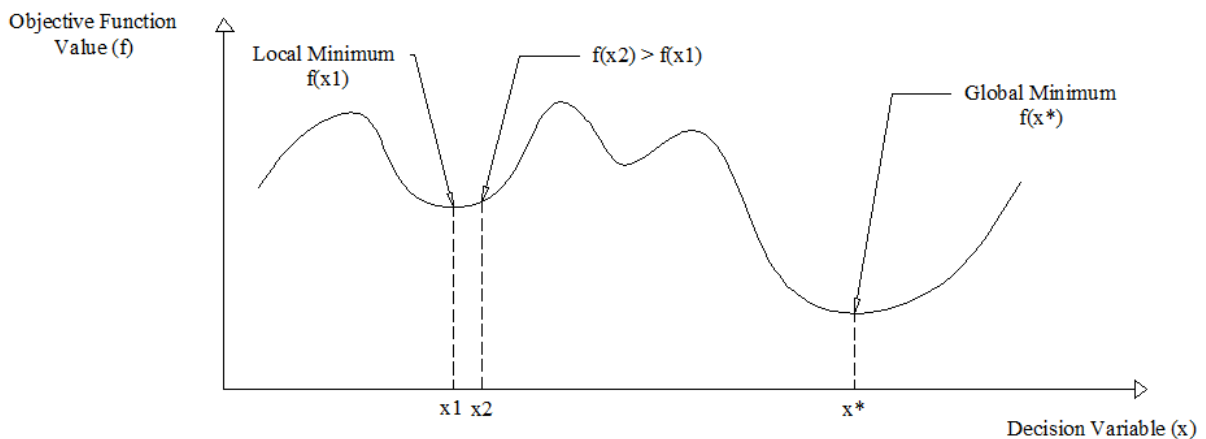


**Figure 3-5** Local and global optima for a unidimensional minimization problem.

## Chapter 4.

# Modeling and Solving the HSR Planning Optimization Problem Considering Natural Hazards

Worldwide, 8,838 km of High-Speed Rail (HSR) lines are under construction and 16,318 km are planned, together with existing lines, adding up to 42,322 km for the year of 2025 (UIC 2011). While different configurations of HSR can fulfill the scope of a project, the chosen corridors and cross sections affect the construction and operation costs of the network, the quality of the service and the broader social, economic and environmental impacts. Especially considering the large public investments required, the HSR network configuration should be optimized during the planning stage, at which the macro location is defined that sets boundaries for the final project design.

Planning for HSR needs to cope with varying local environments and, among these, geotechnical and hydrological factors that affect the construction costs and the quality of the performance. Extreme events, such as storms, floods and earthquakes, have the ability to damage linear transportation systems with important economic and social consequences (section 2.4.1). The geotechnical and hydrological factors are location dependent and thus both the corridors and the cross-sections adopted can avoid or exacerbate an underperformance of the infrastructure. Also, the HSR layout is subject to tight restrictions and safety and riding comfort require that only small tolerances are allowed (section 2.2.1). Standards and guidelines define minimum or maximum design values and consider a tolerance threshold up to a feasibility limit (section 2.1).

This research aims at modeling and solving the HSR planning optimization problem, considering natural hazards and taking into account layout constraints. A robust model with

scenario descriptions of uncertainty and representing natural hazards is ultimately proposed. However, given the sheer size of solving a robust model applied to real world case-study, a progressive development approach was considered. Initially, a deterministic model was developed and applied to an intentionally simple case-study. This deterministic model addresses Standard Planning Conditions (SPC), which are concerned with construction costs and problem constraints. A computational tool was developed to deal with the problem data and used to implement and solve the model with the simulated annealing algorithm (SAA). This application to a simple case-study allowed one to calibrate and test the tool performance. The tool capabilities were sequentially expanded to deal with other real-world complexities. The model was also extended to incorporate the uncertainties related to natural hazards, considering a robust approach.

For the sake of clearness, a sequential introduction of the model, SAA implementation and the tool, following the progressive development stages, is presented. Section 4.1 details the deterministic model for SPC, section 4.2 discusses the implementation of the SAA to solve the model, section 4.3 shows an application to a synthetic case-study for SPC, section 4.4 extends the software capabilities to deal with real-world problem complexities and section 4.5 presents the HSR planning robust optimization model.

#### **4.1 OPTIMIZATION MODEL FOR STANDARD PLANNING CONDITIONS**

The optimization model firstly developed for SPC considers a fully-integrated 3D optimization of the HSR alignment at a planning scale. The goal of the optimization problem is to find the HSR alignment configuration that minimizes an objective function considering construction costs while complying with demanding geometry, land-use and location issues.

The 3D configuration of the HSR is, in reality, defined by a set of tangents and curves, both in the horizontal and vertical planes, as introduced in section 2.1. The proposed model considers a simplified representation of the layout in which the HSR configuration is defined by linear sections that connect a set of sequential 3D points in space. This simplification of reality is able to capture the main plan view and longitudinal profile features without compromising the HSR cost estimation for the planning purposes of an actual HSR network. The simplified HSR representation results in limitations for the horizontal angles, instead of radii of



horizontal curves, of a configuration with effects to both the objective function and the geometry constraints.

The following subsections present the objective function, detailing the cost computation of each term, and the constraints of the model. The implications of representing the HSR by linear sections only are discussed.

#### 4.1.1 OBJECTIVE FUNCTION

The objective function, for standard planning conditions, consists of the minimization of total costs given by the sum of five terms (4.1): construction costs  $\sum_{(i,j) \in \Omega_E^{ij}} C_{ij}$ ; penalty value for gradient noncompliance  $\sum_{(i,j) \in \Omega_N} P_{\eta(i,j)}$ ; penalty value for horizontal angle noncompliance  $\sum_{(i,j,k) \in \Omega_N} P_{\beta(i,j,k)}$ ; penalty value for land use noncompliance  $\sum_{(i,j) \in \Omega_N} \sum_{s \in \Omega_E} P_{\lambda_s}$  and a location benefit term  $\sum_{i \in \Omega_N} P_{v_i}$ . The latter reflects a trade-off between additional construction or operational costs and linking cities or regions identified by the decision-maker as an added value to the network, for economic or equity reasons. Such locations are not fundamental for the scope of the project, otherwise the inclusion would be mandatory.

$$\begin{aligned} \text{Min} \sum_{(i,j) \in \Omega_N} C_{ij} [Ex_{(i,j)}, Ew_{(i,j)}, B_{(i,j)}, T_{(i,j)}, LD_{(i,j)}] + \sum_{(i,j) \in \Omega_N} P_{\eta(i,j)} [\eta_{(i,j)}, \eta_{normal}, \eta_{limit}, \gamma_{\eta}] + \\ \sum_{(i,j,k) \in \Omega_N} P_{\beta(i,j,k)} [\beta_{(i,j,k)}, \beta_{normal}, \beta_{limit}, \gamma_{\beta}] + \sum_{(i,j) \in \Omega_N} \sum_{s \in \Omega_E^{ij}} P_{\lambda_s} [l_s, \gamma_{\lambda_s}] - \sum_{i \in \Omega_N} P_{v_i} [\gamma_{v_i}] \end{aligned} \quad (4.1)$$

Where,

$\Omega_N$  is the set of all 3D nodes of the discretization mesh;

$\Omega_E^{ij}$  is a subset of  $\Omega_E$  (the set of all space property elements in the problem) representing the space property elements overlaid in the plan view by a linear section linking nodes  $i$  and  $j$ ;

$\sum_{(i,j) \in \Omega_N} C_{ij}$  expresses the total construction costs and depends on the expropriation costs  $Ex_{(i,j)}$ , the costs of earthworks  $Ew_{(i,j)}$ , bridges  $B_{(i,j)}$  and tunnels  $T_{(i,j)}$  and linear- dependent costs  $LD_{(i,j)}$  (including cost items such as track and sub-ballast that vary only with the infrastructure length) of a linear section linking nodes  $i$  and  $j$ ;

$\sum_{(i,j) \in \Omega_N} P_{\eta(i,j)}$  expresses the total penalty value for geometry gradient violation of each linear section linking nodes  $i$  and  $j$ ; it depends on the gradient value of the section  $\eta_{(i,j)}$  and three problem parameters defining the normal gradient  $\eta_{normal}$ , the limit gradient  $\eta_{limit}$  and the gradient penalty coefficient  $\gamma_{\eta}$  expressed as a percentage of the configuration construction cost;

$\sum_{(i,j,k) \in \Omega_N} P_{\beta(i,j,k)}$  expresses the total penalty value for geometry horizontal angle violation at each intermediate node  $j$  of the configuration, formed by the two linear sections linking nodes  $i, j$  and  $k$ ; it depends on the angle value at node  $j$ ,  $\beta_{(i,j,k)}$ , and three problem parameters defining the horizontal angle normal value  $\beta_{normal}$ , the horizontal angle limit value  $\beta_{limit}$  and the horizontal angle penalty coefficient  $\gamma_{\beta}$  expressed as a percentage of the configuration construction cost;

$\sum_{(i,j) \in \Omega_N} \sum_{s \in \Omega_E} P_{\lambda_s}$  expresses the total land-use penalty value and depends on the land-use penalty  $P_{\lambda_s}$  of each space property element  $s$  overlaid by each linear section linking nodes  $i$  and  $j$  of the HSR configuration;  $P_{\lambda_s}$  depends on the length  $l_s$  and land use penalty coefficient  $\gamma_{\lambda_s}$  (expressed as a percentage of the configuration construction cost) of the space property element  $s$ ;

$\sum_{i \in \Omega_N} P_{v_i}$  expresses the total location benefit value and depends on the location coefficient  $\gamma_{v_i}$  (expressed as a percentage of the configuration construction cost) of each node  $i$  of  $\Omega_N$ .

While the definition of the construction costs is straightforward, penalties for gradient and horizontal angle noncompliance aim at optimizing the geometry layout. Recommended geometry values exist, as presented in section 2.1, but are difficult to implement in all situations, thus the allowance of less restrictive values when necessary, up to an absolute limit of feasibility. The penalties aim at representing trade-offs between additional construction costs and costs resulting of imposed restrictions to operation by adopting geometry parameters less restrictive than the recommended ones but still within the feasibility limits.

The land-use penalty represents a similar approach for the HSR deployment at locations where construction is not recommended, despite not being forbidden. Ecological, environmental or political issues can lead to the identification of areas where the construction of new infrastructure is interdicted. There may be other areas, however, where construction is

allowed but not desirable due to its impacts on the man-made or natural environment such as induced noise and/or vibration, the creation of artificial barriers, interference with endangered species, amongst others. For example, criticism has been recently directed towards a HSR link between Italy and France, including demonstrations against the projects' deployment site (Urquhart 2011), and towards a new HSR in China, which Beijing protesters claimed to run too close to houses and schools (Blanchard 2012). To minimize such impacts, the decision-maker may identify these as regions to avoid considering a trade-off with the additional costs.

The location benefit term also represents a trade-off between the cities served by the HSR network and the additional costs incurred in. Besides the mandatory cities to link, fundamental for the scope of the HSR project, other cities or regions may be identified by the decision-maker as an added value to the network, for economic or equity reasons. The location benefit term thus reflects a trade-off between linking these non-fundamental cities or regions and the additional construction or operational costs. It is noted that the added-value of connecting these locations influenced by multiple factors and can be counteracted, at least partly, by additional restrictions imposed on the HSR circulating speed.

The success of HSR with regard to operation, is heavily dependent on ridership and demand captured from other transportation modes (Campos and de Rus 2009; Repolho et al. 2013). Amongst others, the accessibility to the rail stations influences the users' decision in traveling by rail (Brons et al. 2009; Givoni and Rietveld 2007). However, if a large number of stations located along a line decrease the access time to the HSR system, these also increase the total journey time. In addition to the stopping time at the HSR intermediate stations, the pre-stop deceleration stage and the post-stop acceleration stage increase the total journey time. Addressing these concerns, Repolho et al. (2013) propose a model for optimizing the number and location of HSR stations taking into account the excess time of intermediate speed reductions. Chang et al. (2000) discuss the optimization of HSR passenger service considering balances in demand and supply. On the demand side, Chang et al. (2000) consider that convenience, related to the service frequency and journey time, is a passenger's major concern when choosing HSR travel.

In addition, political decisions can also influence the location of intermediate HSR stations. Ahlfeldt and Feddersen (2010) argue this has been the case for the German HSR line

connecting Frankfurt (Main) and Cologne, stating that the intermediate stations Montabaur and Limburg resulted from complex political negotiations amongst the German federal states.

Thus, the location benefit considered by the model aims at expressing the overall value in connecting a given city, influenced by the increased accessibility, by the negative impacts that intermediate stops may pose and also by political decisions.

The penalty and benefit coefficients  $\gamma_\eta$ ,  $\gamma_\beta$ ,  $\gamma_{\lambda_s}$  and  $\gamma_{vi}$ , used in the definition of the penalty and benefit objective function terms should be established through expert judgment after consulting stakeholder panels and taking into consideration the problem specifics. Formal procedures exist for the stakeholder consultation. The European Commission Directorate-General Health and Consumers recognizes that policy decisions have an impact on society and has set its consultation commitments and practices in EC (2013). In regard to the consultation activity, the EC (2013) states, amongst others, that: (i) the scope of the consultation should be clearly identified with the definition of where the policy development can be influence, but also where no such influence is possible, and (ii) all relevant background should be provided in the process. As an example, the results of stakeholder analysis for the evaluation of the implementation of Regulation (EC) No 881/2004 establishing the European Railway Agency are disclosed by Steer Davies Gleave (2011). The stakeholder consultation comprised both an online survey and interviews with stakeholders. The overall evaluation by Steer Davies Gleave (2011) was then drawn based on comprehensive information that, apart from the stakeholder consultation, included sources such as expert judgment, published information available from the Agency, the Commission and the Member States and benchmarking of the Agency against selected comparator bodies.

The benefit and penalty coefficients aim at illustrating the influence of such processes and are user-specified coefficients, similarly to the coefficients of geometry penalties and environmental penalties defined by Jha and Schonfeld (2004). Given that the feasible search space of the problem can have configurations with construction costs of different orders of magnitude, establishing a fixed coefficient value that remains unchanged may be conditional to the objective function value of low construction cost configurations and virtually without impact for large construction cost configurations. Thus, for illustrative purposes of the possible effects, the coefficients are formulated indexed to the HSR configuration cost.

The model application requires two levels of discretization. One is related to the definition of the HSR configuration and establishes the 3D nodes that form the set  $\Omega_N$ , containing all possible nodes to be connected by the linear sections forming the network. Figure 4-1 shows such a mesh, equally-spaced in both plan view x- and y-directions and with a different span in the z-direction, orthogonal to the plan view. The other level of discretization is applied to the mapped properties, subdividing the maps that characterize the search space into space property elements that constitute the set  $\Omega_E$ . Figure 4-2 exemplifies, for elevation data, how each of the map layers used to characterize the search space area is discretized. Space property elements are geo-referenced cells or elements for which a given property, elevation in the case of Figure 4-2, assumes a constant value within its boundaries. Graphically, each distinct value within a map is represented by one color (shade of gray), common to all elements with the same value. The size of the space property elements is conditioned by the HSR planning requirements and available data for this type of mapped data representation, also known as raster data type. Figure 4-2 also shows a plan view overlay of the 3D permissible nodes mesh and the space property elements, in which the nodes are positioned at the center of the elements, spanning a dimension equivalent to 5 space property elements in each plan view direction.

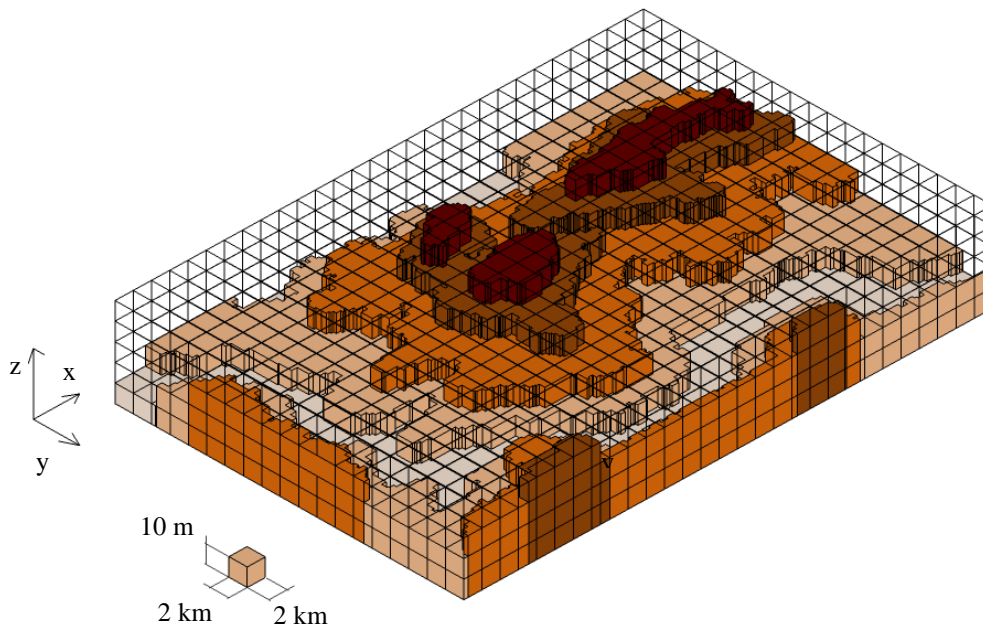


**Figure 4-1** Ground elevation of a synthetic case-study and the 3D mesh defining the permissible node positions for each HSR configuration.

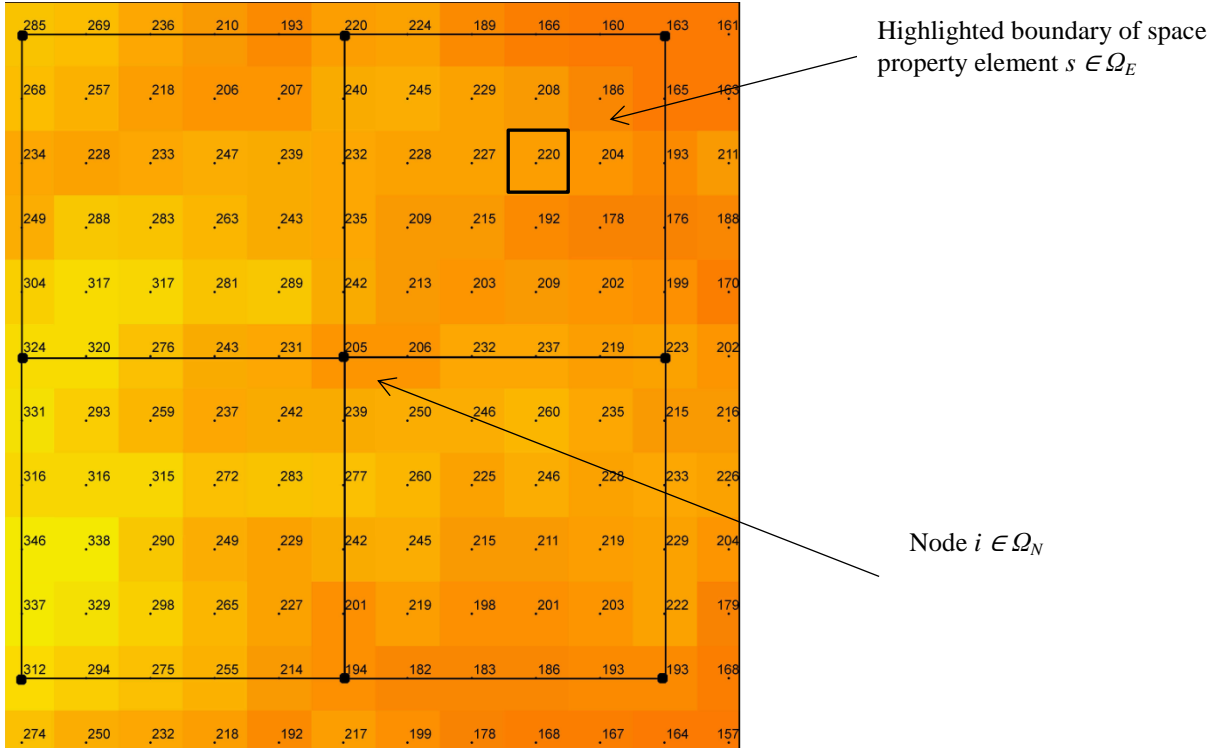


**Figure 4-2** Plan view detail of the permissible node positions mesh defining  $\Omega_N$  overlaying the space property elements forming  $\Omega_E$  and representing the discretization of elevation data.

The node discretization set  $\Omega_N$  and the space property elements set  $\Omega_E$  allow one to define the subset  $\Omega_E^{ij}$  containing the space property elements overlaid in the plan view by a generic linear section linking nodes  $i$  and  $j$ . In the example of Figure 4-3, in which the mapped properties are discretized by 336 space property elements,  $\Omega_E^{ij} = \{s_1, s_{17}, s_{18}, s_{34}, s_{35}, s_{51}, s_{67}, s_{68}, s_{84}, s_{85}, s_{101}, s_{117}, s_{118}, s_{134}, s_{135}, s_{151}, s_{167}, s_{168}, s_{184}, s_{185}, s_{201}, s_{217}, s_{218}, s_{234}, s_{235}, s_{251}\}$  is the subset of  $\Omega_E = \{s_1, s_2, \dots, s_{335}, s_{336}\}$  for the nodes depicted nodes  $i$  and  $j$ . The identification of the space property elements overlaid by the HSR linear sections allows one to compute each of the 5 cost components in the objective function (4.1), as detailed in the following subsections.

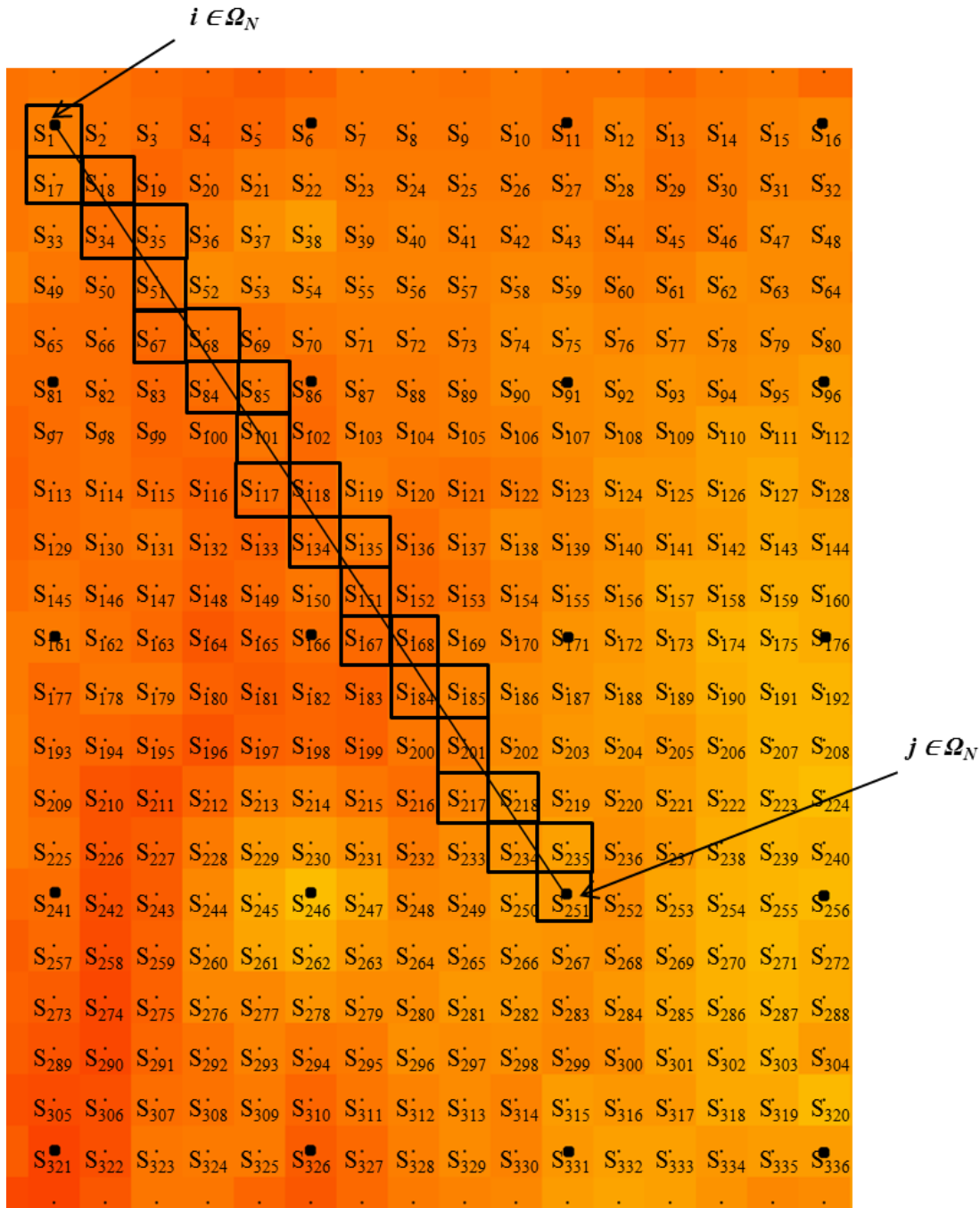


Figure 4-3 Determination of  $\Omega_E^{ij}$ .

#### 4.1.1.1 CONSTRUCTION COST

The construction cost  $\sum_{(i,j) \in \Omega_N} C_{ij}$  of the HSR configuration is obtained by computing the construction cost  $C_{ij}$  of each linear section linking nodes  $i$  and  $j$  composing the configuration given by the sum of (4.2): the expropriation costs  $Ex_{(i,j)}$ , the construction costs of earthworks

$Ew_{(i,j)}$  (for both cuts and embankments), bridges  $B_{(i,j)}$ , tunnels  $T_{(i,j)}$  and other linear- dependent costs  $LD_{(i,j)}$  (such as track and ballast) of that linear section. The methodology used for computing each of these cost items is detailed below.

$$\sum_{(i,j) \in \Omega_N} C_{ij} = \sum_{(i,j) \in \Omega_N} [Ex_{(i,j)} + Ew_{(i,j)} + B_{(i,j)} + T_{(i,j)} + LD_{(i,j)}] \quad (4.2)$$

*EXPROPRIATION COST*

The fact that the land on which the HSR is to be deployed is not owned by the HSR building authority and that compensation is due to the owners results in an expropriation cost  $Ex_{(i,j)}$ . The compensation varies for different ground uses, such as urban or agricultural, and usually a unit value per square meter is established. The cost is thus obtained by overlaying, in the plan view, the HSR configuration with a map of space property elements defining the unit cost per square meter (Figure 4-4).

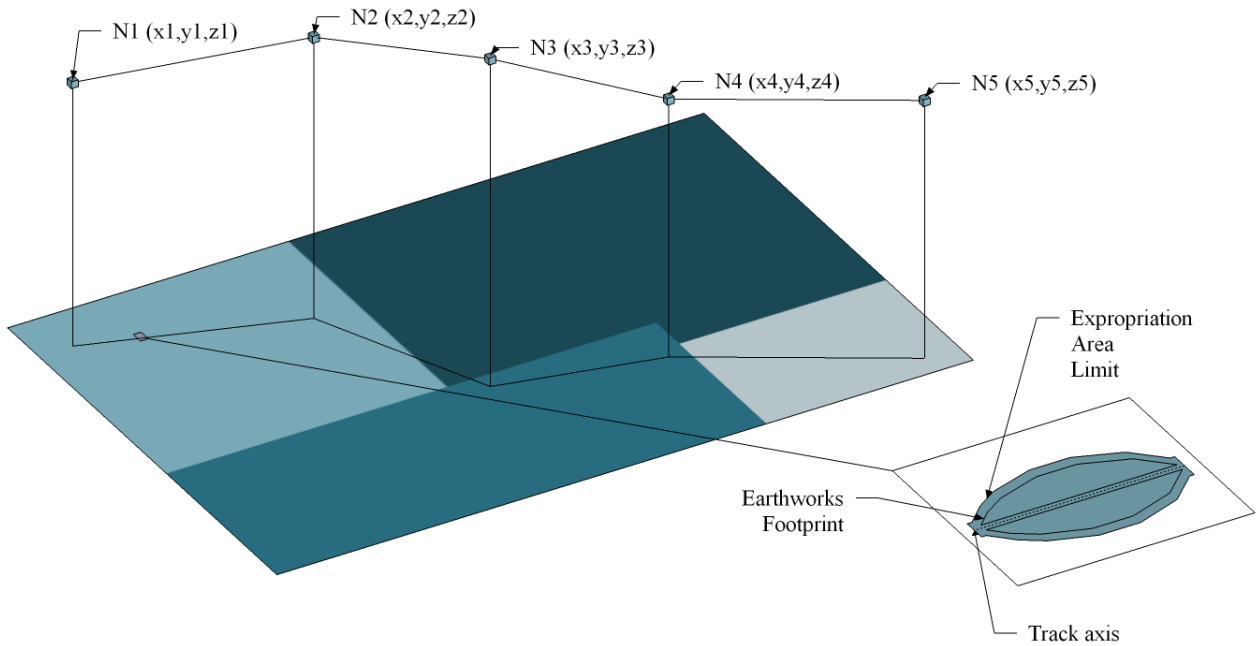


**Figure 4-4** HSR configuration and the respective overlay on the expropriation cost map.

The area to expropriate is established through an offset beyond the footprint of the infrastructure, as shown in the zoom box of Figure 4-4 for a general embankment or cut. Additionally, by overlaying the HSR configuration with the cost map, in which different colors (shades of gray) represent different expropriation costs, one is able to identify the unit



cost corresponding to any given area within the search space. The total expropriation cost is then computed by summing within the area to expropriate, the unit cost times its respective area. The offset and the unit costs are defined by the problem input.

### *EARTHWORKS*

The cross-section to adopt in each case depends on the difference between the ground and the HSR elevation and on the local ground conditions. The construction of bridges and tunnels is defined by thresholds of height and depth of the HSR in relation to the ground elevation. For cross-sections with height and depth below the bridge and tunnel thresholds, embankments and cuts are implemented.

The cost computation of embankments and cuts earthworks,  $Ew_{(i,j)}$ , requires the determination of the total volumes of excavation, embankment, sub-ballast, form layer and of the ground improvement technique along each HSR linear section, defined according to the principles presented in sections 2.2.2 and 2.2.3, and the establishment of a unit cost for each of the items. The average-end area method discussed by Hintz and Vonderohe (2011) is used for the volume calculation of earthworks. The method is illustrated in Figure 4-5 considering ground improvement by removal and replacement of a given soil depth. The computation basically consists in averaging the area measured in two consecutive cross-sections and multiplying it by the distance between the two (4.3).

$$V = \frac{A_c + A_{c+1}}{2} d \quad (4.3)$$

where,

$V$  is the volume,  $A_c$  is the area measured at cross-section  $c$ ,  $A_{c+1}$  is the area measured at cross-section  $c+1$  and  $d$  is the distance between the two cross sections.

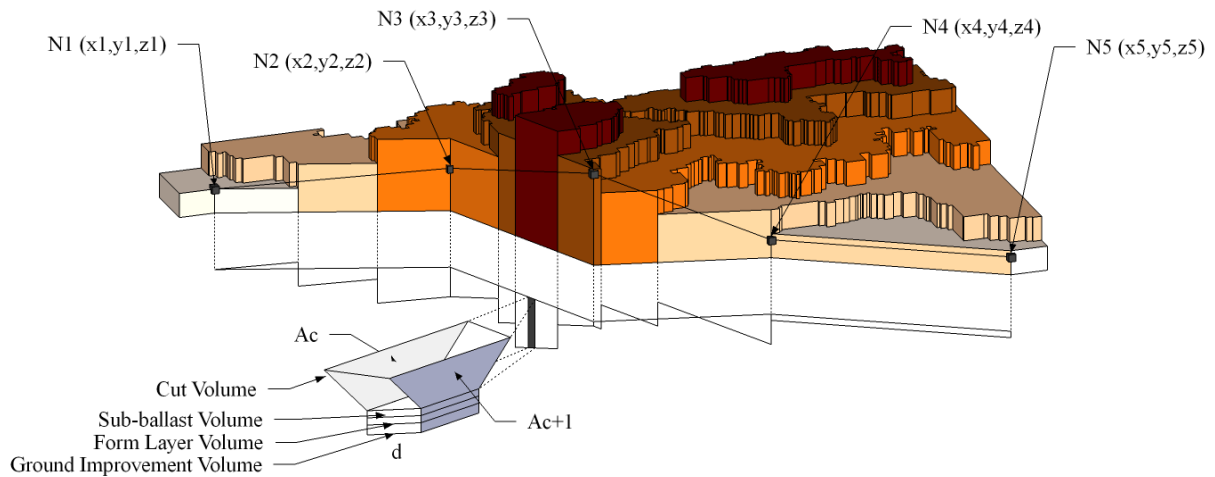


**Figure 4-5** Diagram of HSR and ground elevations and volume calculation with the average end-area method.

At each cross-section, the slopes of cuts and embankments, the thicknesses of the HSR infrastructure layers and the ground improvement requirements depend on the ground behavior, which can be obtained by overlaying the HSR configuration with a ground behavior layer map (Figure 4-6). Different excavation methods (mechanical or blasting) may also be required, depending on the local ground conditions, and affect the excavation unit cost.

Each ground behavior unit may be represented by lithological, geological or geotechnical data or combinations of the above with other site characteristics such as hydrology and slope steepness. Nonetheless, each ground behavior unit specifies a combination of the following cross-section details:

- Slopes of embankments and cuts;
- Excavation method: exclusively with mechanical means, exclusively by blasting or a combination of both expressed by the percentage of the excavated volumes with each method;
- Sub-ballast thickness;
- Form layer thickness;
- Ground improvement technique and requirements.

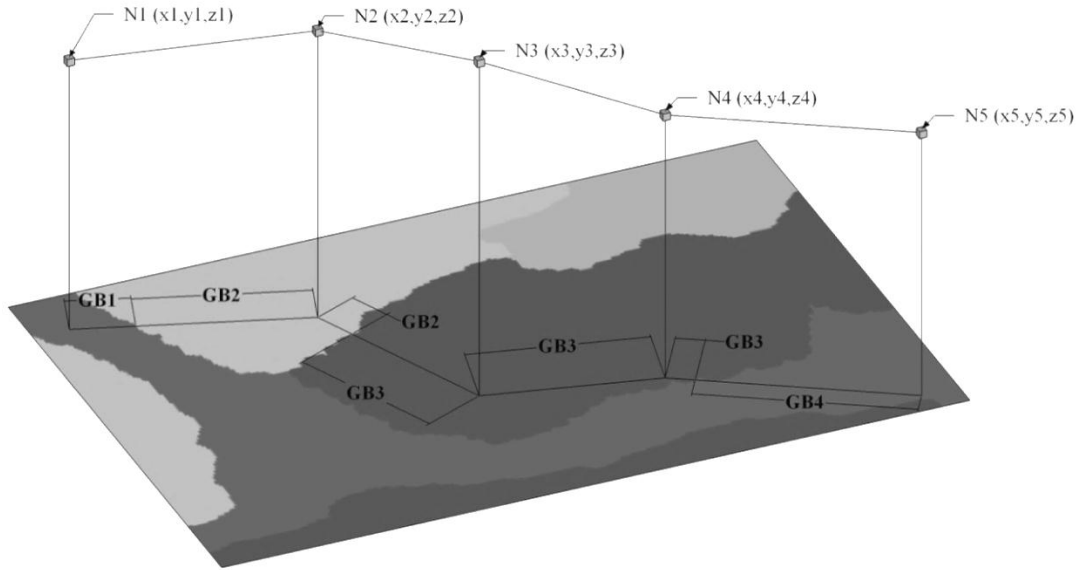


**Figure 4-6** HSR overlaying the ground behavior layer.

The cross-sections are evaluated at the center of each space property element that the HSR linear section overlays,  $\Omega_E^j$ , for which HSR elevation, ground elevation, ground behavior and distance between cross-sections (space property elements are georeferenced) are known. This allows one to compute the quantities of each earthworks item for each linear section linking nodes  $i$  and  $j$ . The linear section total earthwork cost is obtained according to (4.4), by summing each item quantity multiplied by the respective unit cost, given as input. Expression (4.4) considers a ground improvement method for which a unit cost per volume is defined; other methods exist for which a unit cost per area is defined and, accordingly, the respective quantity is defined as an area instead of a volume.

$$EW_{(i,j)} = V_{(i,j)}^{emb} C_{unit}^{emb} + V_{(i,j)}^{cutMM} C_{unit}^{cutMM} + V_{(i,j)}^{cutB} C_{unit}^{cutB} + V_{(i,j)}^{SB} C_{unit}^{SB} + V_{(i,j)}^{FL} C_{unit}^{FL} + V_{(i,j)}^{GI} C_{unit}^{GI} \quad (4.4)$$

Where,

$EW_{(i,j)}$  is the earthworks cost of a linear section of HSR linking nodes  $i$  and  $j$ ;

$V_{(i,j)}^{emb}, V_{(i,j)}^{cutMM}, V_{(i,j)}^{cutB}, V_{(i,j)}^{SB}, V_{(i,j)}^{FL}, V_{(i,j)}^{GI}$  are the volume quantities expressed in  $m^3$  of, respectively, embankment, cut with mechanical means, cut by blasting, sub-ballast, form layer and ground improvement of a linear section of HSR linking nodes  $i$  and  $j$ ;

$C_{unit}^{emb}$ ,  $C_{unit}^{cutMM}$ ,  $C_{unit}^{cutB}$ ,  $C_{unit}^{SB}$ ,  $C_{unit}^{FL}$ ,  $C_{unit}^{GI}$  are the unit costs expressed in €/m<sup>3</sup> of, respectively, embankment, cut with mechanical means, cut by blasting, sub-ballast, form layer and ground improvement given as input independently of the ground behavior.

#### BRIDGES AND VIADUCTS

Bridges are used when the HSR and ground elevation result in a height beyond a pre-set threshold. Additionally, bridges are required when the HSR crosses bodies of water, even if the height is below the threshold.

The model considers the cost of bridges depending on the length, the maximum height and the construction method. A simplified bridge global cost approach is taken by the model and a function establishing the total cost of a general bridge depending on these three parameters, besides the height threshold between embankments and bridges, is case-specific and established by the input. In reality, the construction cost of bridges also varies with factors such as the pier span, the pier height and the foundations. For a detailed formulation of bridge costs please refer to Moret (2011).

Given the global bridge cost approach, the cost  $B_{(i,j)}$  of all bridges of a HSR linear section linking nodes  $i$  and  $j$  is obtained by summing the global cost of each bridge to be constructed in that respective linear section (4.5).

$$B_{(i,j)} = \sum_{b=1}^n f_b(l_b, h_b^{\max}, cm_b), \text{ for all bridges } b=\{1, \dots, n\} \text{ in linear section linking nodes } i \text{ and } j \quad (4.5)$$

Where,

$B_{(i,j)}$  is the bridge cost of a HSR linear section linking nodes  $i$  and  $j$  and  $f_b(l_b, h_b^{\max}, cm_b)$  is the bridge global cost function, varying with the bridge length  $l_b$ , maximum height  $h_b^{\max}$  and the construction method  $cm_b$ .

#### TUNNELS

The model considers a tunnel cost formulation similar to the one used for bridges, with tunnels being built for depths beyond a given threshold and for crossing bodies of water. A global cost per tunnel is defined depending on the length and on the local ground conditions

and a cost function for a general tunnel, depending on these parameters, is established by the problem input. The construction cost  $T_{(i,j)}$  of all tunnels of a HSR linear section linking nodes  $i$  and  $j$  is thus obtained by summing the global cost of each tunnel to be constructed in that respective linear section (4.6).

$$T_{(i,j)} = \sum_{t=1}^n f_t(l_t, Gb(t)), \text{ for all tunnels } t=\{1, \dots, n\} \text{ in linear section linking nodes } (i,j) \quad (4.6)$$

where,

$T_{(i,j)}$  is the tunnels cost of a linear section of HSR linking nodes  $i$  and  $j$  and  $f_t(l_t, Gb(t))$  is the tunnel global cost function, varying with tunnel length  $l_t$  and the ground behavior along the tunnel  $Gb(t)$ .

#### *LINEAR- DEPENDENT COSTS*

The previous HSR construction cost items (expropriation, earthworks, bridges and tunnels) depend on the construction site characteristics. Other HSR components exist, such as track, ballast or catenary, for which the construction cost does not vary significantly with the *in situ* characteristics. The model includes this type of construction cost components labeled as linear- dependent costs. Accordingly, the cost items are considered constant along the HSR and their overall value depends only on the length of the network. The unit value of linear- dependent costs is established by the problem input and the total cost  $LD_{(i,j)}$  of a HSR linear section linking nodes  $i$  and  $j$  is proportional to the linear section length, as shown in (4.7) considering the cost of track, ballast and catenary. While the linear- dependent costs do not add major complexities to the model, their incorporation favors shorter configurations.

$$LD_{(i,j)} = l_{(i,j)} C_{unit}^{track} + l_{(i,j)} C_{unit}^{ballast} + l_{(i,j)} C_{unit}^{catenary} \quad (4.7)$$

Where,

$LD_{(i,j)}$  is the earthworks cost of a linear section of HSR linking nodes  $i$  and  $j$ ;

$l_{(i,j)}$  is the length of linear section linking nodes  $i$  and  $j$  expressed in m;

$C_{unit}^{track}$ ,  $C_{unit}^{ballast}$ ,  $C_{unit}^{catenary}$  are the unit costs expressed in €/m of, respectively, track, ballast and catenary, given as input independently of the ground behavior.

#### 4.1.1.2 GEOMETRY PENALTIES: HORIZONTAL ANGLE AND GRADIENT

In order to maximize the HSR performance for a given speed and traffic type recommended values exist for the geometry design, with allowances that can ascend up to mandatory and less restrictive limits. Examples for such recommended and limit values, for both the radii of horizontal curves and for gradients of linear sections, have been presented in sections 2.1.2 and 2.1.3.

The proposed model includes two geometry penalties in the objective function aiming at encouraging the use of the more restrictive recommended parameters: a penalty value for gradient noncompliance  $\sum_{(i,j) \in \Omega_N} P_{\eta(i,j)}$  and a penalty value for horizontal angle noncompliance  $\sum_{(i,j,k) \in \Omega_N} P_{\beta(i,j,k)}$ . The concept of the gradient penalty derives directly from the HSR configuration allowances while the horizontal angle penalty is a simplified representation of the radii limitations, as a consequence of defining the HSR configuration through linear sections.

The recommended gradient value  $\eta_{normal}$  specifies, for a given HSR speed and traffic type, the maximum desirable gradient to adopt for the linear sections of the configuration. Larger gradients affect the performance and relate, amongst others, with larger energy consumption and breaking distances. On the other hand, the recommended horizontal angle  $\beta_{normal}$  specifies, also for a given speed and traffic type, the minimum desirable angle. Smaller angles in the model representation reflect smaller HSR horizontal radii which may cause passenger discomfort, risk of derailment or extreme overload on the track. Allowances to both parameters, however, permit the use of gradients up to an absolute maximum value  $\eta_{limit}$  and of horizontal angles to an absolute minimum  $\beta_{limit}$ . The consideration of geometry penalties thus implicitly includes operation concerns and aims at trading off operational gains for larger investments.

Gradients and radii (horizontal angles in the model) between the recommended and limit bounds of each parameter are feasible but may impose limitations to the HSR performance. To discourage the use of geometry parameters within such intervals, the geometry penalties

are applied when normal values are not complied with, according to equations (4.8) and (4.9) for, respectively, the gradient (Figure 4-7) and the horizontal angle at intermediate nodes of the configuration (Figure 4-8). For the purpose of illustrating the possible effects of such trade-offs between operational gains and larger investments, the model considers the geometry coefficients defined as a percentage of the HSR construction costs,  $\sum_{(i,j) \in \Omega_N} C_{ij}$ .

$$P_{\eta(i,j)} = \frac{|\eta_{normal} - \eta_{(i,j)}|}{|\eta_{normal} - \eta_{limit}|} \cdot \gamma_{\eta} \quad (4.8)$$

$$P_{\beta(i,j,k)} = \frac{|\beta_{normal} - \beta_{(i,j,k)}|}{|\beta_{normal} - \beta_{limit}|} \gamma_{\beta} \quad (4.9)$$

Where,

$P_{\eta(i,j)}$  is the gradient penalty function of the linear section linking nodes  $i$  and  $j$ ,  $\eta_{(i,j)}$  is the actual gradient of the linear section linking nodes  $i$  and  $j$ ,  $\eta_{normal}$  and  $\eta_{limit}$  are the normal and limit gradient values,  $\gamma_{\eta}$  is the gradient penalty coefficient,  $P_{\beta(i,j,k)}$  is the horizontal angle penalty function at each intermediate node  $j$ , formed by the linear sections linking nodes  $i$ ,  $j$  and  $k$ ,  $\beta_{(i,j,k)}$  is the actual horizontal angle at the intermediate node  $j$ ,  $\beta_{normal}$  and  $\beta_{limit}$  are the normal and limit values of the horizontal angle and  $\gamma_{\beta}$  is the horizontal angle penalty coefficient.

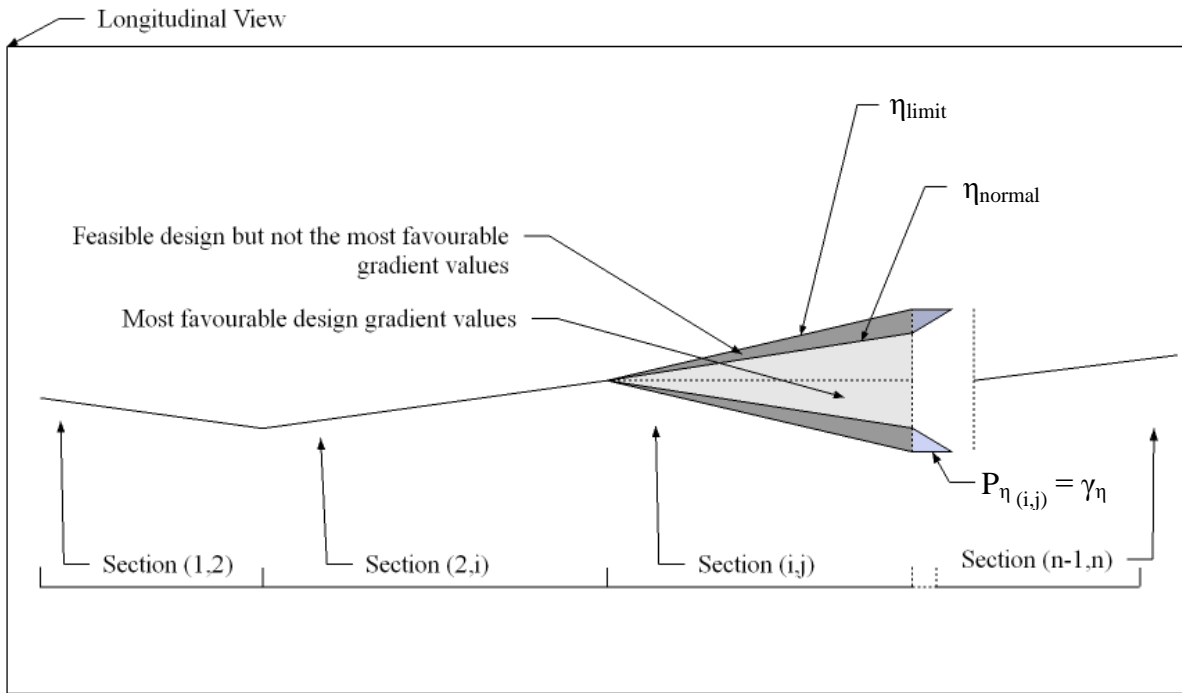


**Figure 4-7** Gradient penalty formulation.

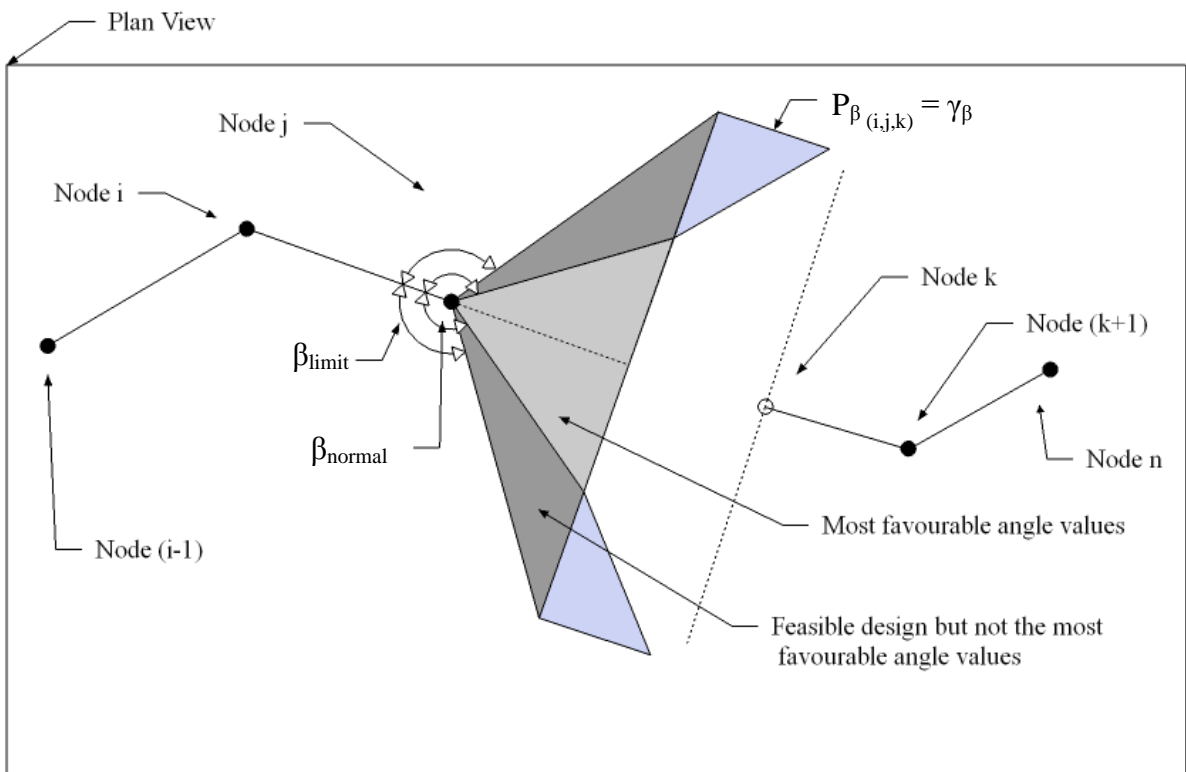


**Figure 4-8** Horizontal angle penalty formulation.



#### 4.1.1.3 LAND USE PENALTY

The model includes in the objective function (4.1) a land use penalty ( $\sum_{(i,j) \in \Omega_N} \sum_{s \in \Omega_E} P_{\lambda_s}^{ij}$ ) to deter HSR configurations that cross land-use restricted areas. A unit land-use cost is attributed to each of the space property elements in  $\Omega_E$ , assuming a null value by default and a non-null cost for restricted land-use elements. The elements of restricted land-use are identified by a land-use map layer and the corresponding unit cost is represented by the land use penalty coefficient  $\gamma_{\lambda_s}$  (defined as a percentage of the construction cost  $\sum_{(i,j) \in \Omega_N} C_{ij}$ ) of each space property element  $s \in \Omega_E$ . Thus, for each linear section linking nodes  $i$  and  $j$  of the HSR, the cost of overlaying the space property elements  $\Omega_E^{ij}$  is computed by summing the land-use penalty coefficient  $\gamma_{\lambda_s}$  times the respective element overlay length  $l_{\lambda_s}$ .

#### 4.1.1.4 LOCATION BENEFITS

The location benefit term in the objective function (4.1) is related with the identification by the decision-maker of cities or regions for which HSR connection is desirable, supported by improved mobility and accessibility or political judgment, in addition to the fundamental locations of the project.

A benefitting cost coefficient  $\gamma_{v_i}$ , defined as a percentage of the construction cost  $\sum_{(i,j) \in \Omega_N} C_{ij}$ , is attributed to each node of the discretization mesh, with a null value by default and a positive non-null value for the nodes representing these additional locations to connect. The overall location benefit term is the sum of the benefit coefficients of each node  $i$  composing the HSR configuration. This term is subtracted to the objective function, reducing its value for networks crossing the desirable but not mandatory locations, which improves the objective function value for minimization problems such as the one represented by the model. The definition of the benefitting coefficients should take into account possible negative impacts resulting from restrictions imposed to the speed of the trains when circulating through these locations.

### 4.1.2 CONSTRAINTS

The model constraints aim at reproducing the existing limitations to a real HSR project from a planning perspective. Namely, limitations exist for the geometry layout of the track and for land-use, as introduced in section 2.1 for geometry and above for the land-use penalty definition, in addition to the locations the HSR is required to link, defined by the scope of the project. The constraints thus define the feasible search space of the optimization problem and, depending on its specifics, can impose difficulties to the search that are to be dealt with by the algorithm used to solve the model.

Three constraint categories are considered: location, geometry and land-use.

#### 4.1.2.1 LOCATION CONSTRAINT

The location constraint ensures that the HSR network links all the fundamental locations established by the decision-maker.  $\Omega_{MN}$ , the set of all mandatory nodes to be connected by the HSR, defined for the project and a sub-set of all 3D nodes of the discretization mesh  $\Omega_N$ , is established by the problem input.

#### 4.1.2.2 GEOMETRY CONSTRAINTS

Geometry constraints are considered in the model based on existing standards (Table 2-1) for both the gradient and the horizontal angle at intermediate nodes of the HSR configuration. The latter represents the radii limitations as the result of the simplified representation of the HSR configurations by linear sections only. The gradient constraint ensures that the gradient of each linear section  $\eta_{(i,j)}$  forming the network, either rising or falling, is smaller than the limit gradient  $\eta_{limit}$  (Figure 4-7). The horizontal angle constraint ensures that all angles at intermediate nodes of the HSR configuration  $\beta_{(i,j,k)}$ , the smaller angle between the linear sections and ranging from  $0^\circ$  to  $180^\circ$ , are larger than the limit value  $\beta_{limit}$  (Figure 4-8).

#### 4.1.2.3 LAND-USE CONSTRAINT

Protected areas may be identified for different reasons, including the preservation of cultural and natural heritage (UNESCO 2013). The land-use constraint ensures that the HSR project

does not conflict with protected areas, where construction is prohibited. This is accomplished by identifying, with map layers, the forbidden land-use areas (Figure 4-9). The discretization of the map into search space elements allows one to define the set of forbidden land-use elements  $\Omega_{FE}$ , a subset of all space property elements discretizing the search space  $\Omega_E$ .

The land-use constraint guarantees, for each linear section linking nodes  $i$  and  $j$  composing the HSR configuration, that all elements in  $\Omega_{FE}$  are excluded from set of space property elements overlaid by that linear section,  $\Omega_E^{ij}$ .

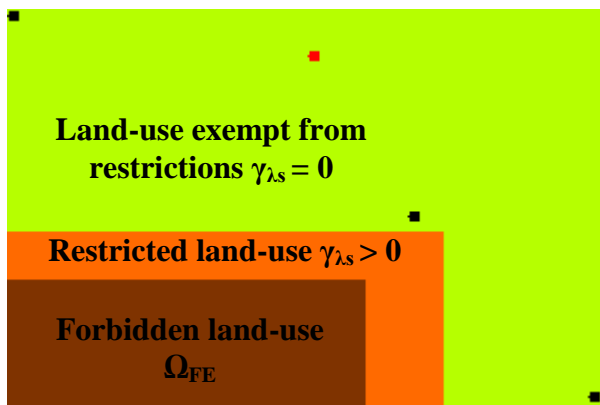


**Figure 4-9** Identification of forbidden land-use space property elements  $\Omega_{FE}$ .

## 4.2 IMPLEMENTATION OF THE SIMULATED ANNEALING ALGORITHM

The implementation of the SAA to solve the HSR planning optimization problem is based on previous applications of the algorithm. Particularly, the implementation follows closely Cunha (1999) and Cunha and Sousa (2001), according to the flowchart in Figure 4-10.

As discussed in section 3.2.2 the implementation of the SAA requires the definition of an initial HSR configuration, the definition of the neighborhood of any current configuration and the procedures to generate new candidate HSR configurations and the cooling schedule of the algorithm.

The procedures for the generation of candidate configurations allow one to define a new HSR candidate configuration by perturbing the current configuration within its neighborhood structure. The cooling schedule defines the initial temperature of the SAA, the stopping

temperature criteria, the rate of temperature decrease and the minimum number of iterations to be assessed before equilibrium is reached at each temperature step. The following sections detail both the procedures for generating candidate HSR configurations and the cooling scheduled implemented for solving the HSR planning optimization problem.

Existing literature discusses different possible methodologies for defining an initial system configuration such as the use of heuristics (Johnson and McGeoch 1997) or an arbitrarily random or best guess configuration (Bertsimas and Nohadani 2010; de Weck and Willcox 2010). Bertsimas and Nohadani (2010) discuss that if the SSA implementation allows the global search of the feasible space, the initial configuration will not interfere with the accessibility of the search space nor interfere with the quality of the final solution. Given that random- and heuristic- generated initial configurations lead to significant overhead computation time and complexity, an arbitrarily user-specified and feasible HSR configuration is considered.

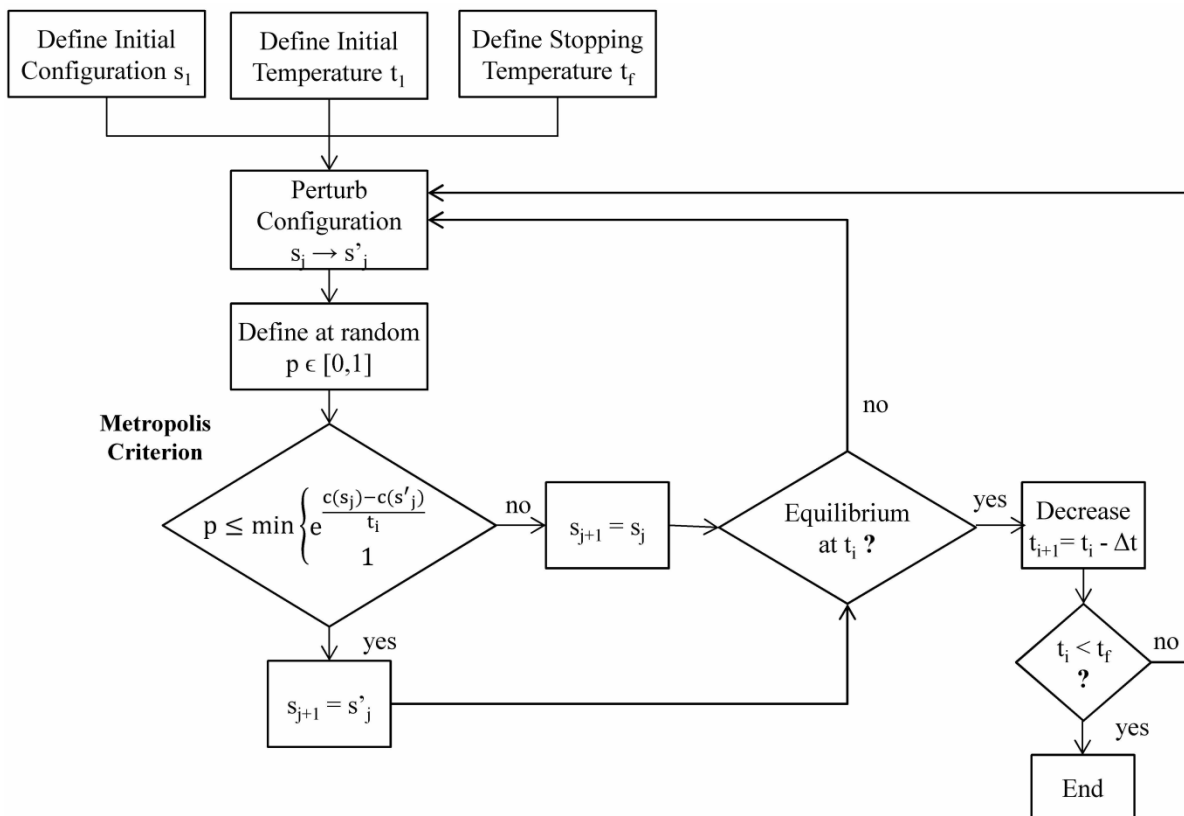


Figure 4-10 SAA flowchart.

#### 4.2.1 GENERATION OF HSR CANDIDATE CONFIGURATIONS

The procedure to generate new candidate HSR configurations starts by establishing the neighborhood of any current configuration and the new candidate configuration is obtained by changing, randomly in the neighborhood, the current one. The procedures adopted allow a fully integrated 3D change of the configurations by a random 3D repositioning of the nodes of the discretization mesh  $\Omega_N$  constituting the HSR configuration, within the neighborhood structure.

Consider the definition of the discretization mesh  $\Omega_N$ . The vertices of the mesh represent the allowed 3D position for the nodes of each solution. Figure 4-1 illustrates such a 3D discretization mesh defining the permissible node positions for the HSR configurations for a synthetic case-study.

Given the representation of the HSR configurations by linear sections, obtaining a new configuration layout consists in defining a new set of nodes and their respective linear sections. The neighborhood structure thus defines the maximum envelope distance at which each node can be repositioned.

Figure 4-11 shows the 3D neighborhood of a general node of  $\Omega_N$  for the discretization mesh in Figure 4-1. Moves are allowed to any of the immediate nodes varying x, y or z, or a combination of the three. As shown in Figure 4-11, the current gray (center) node may be randomly moved to one of the 26 neighboring yellow positions, in addition to be allowed to remain at the current one. Effectively, the new candidate configuration's node position is randomly drawn from the set of the 27 3D positions within the neighborhood envelope.

The neighborhood of a mandatory node differs from the general case. This should be specified for each case-study application and two options are available: randomly move the nodes vertically to the upper or lower positions keeping the current plan view projection (x- and y-coordinates) or disallowing moves of any kind.

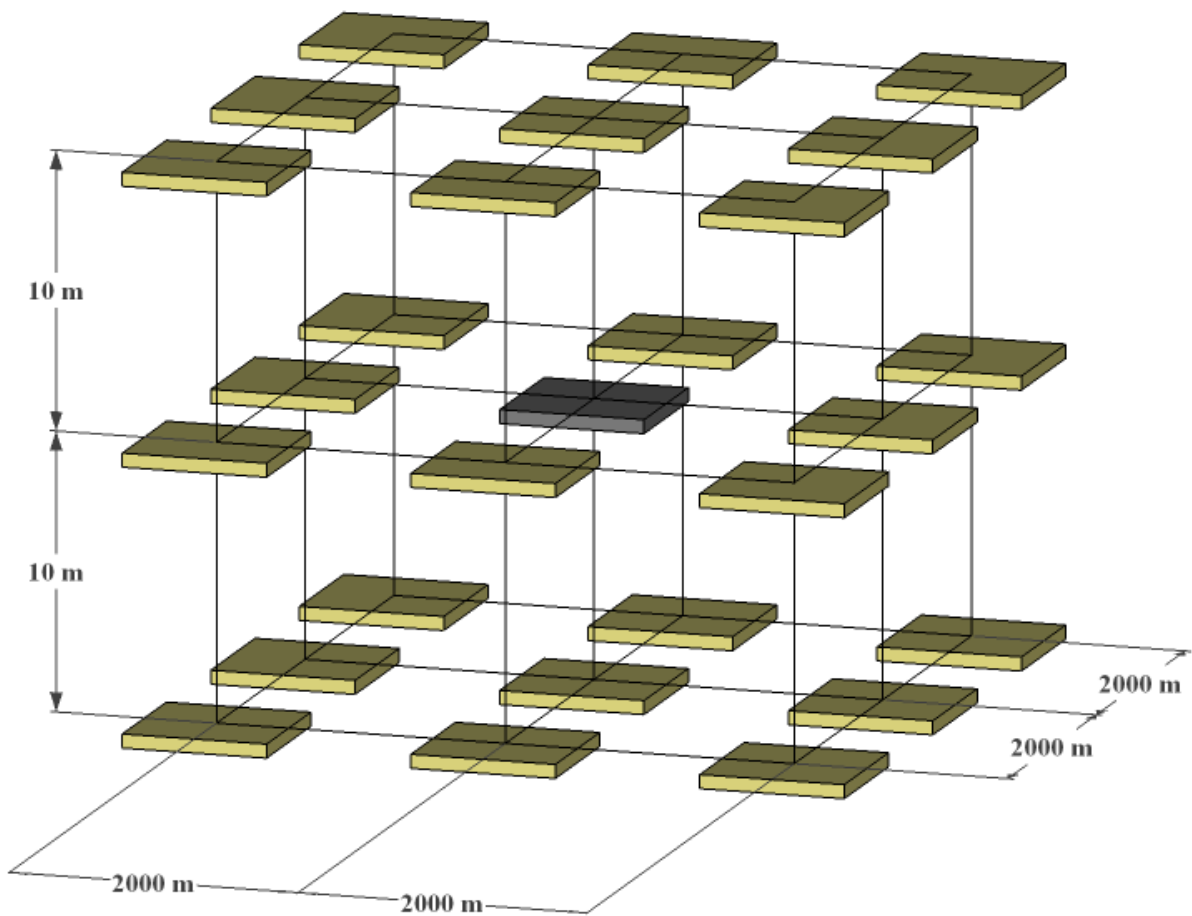


**Figure 4-11** 3D neighborhood definition for a current gray (center) node.

An example of a current configuration perturbed into a neighboring candidate configuration is shown in the plan view of Figure 4-12. For this simple case, a current configuration is formed by linear sections  $c_1$ ,  $c_2$  and  $c_3$ , connecting the start and end mandatory nodes. Analyzing the transformation from the start node towards the end node of the configuration, one observes the end node of section  $c_1$  is randomly moved to the indicated neighbor position, forming the new candidate configuration section  $n_1$ . Since, except for the end of the configuration, the end node of a linear section is the start node of the consecutive linear section, also section  $n_2$  of the new configuration will differ from section  $c_2$ . The alignment of sections  $c_3$  and  $n_3$ , however, coincide. This analysis assumes that variations in the  $z$ -direction are null.

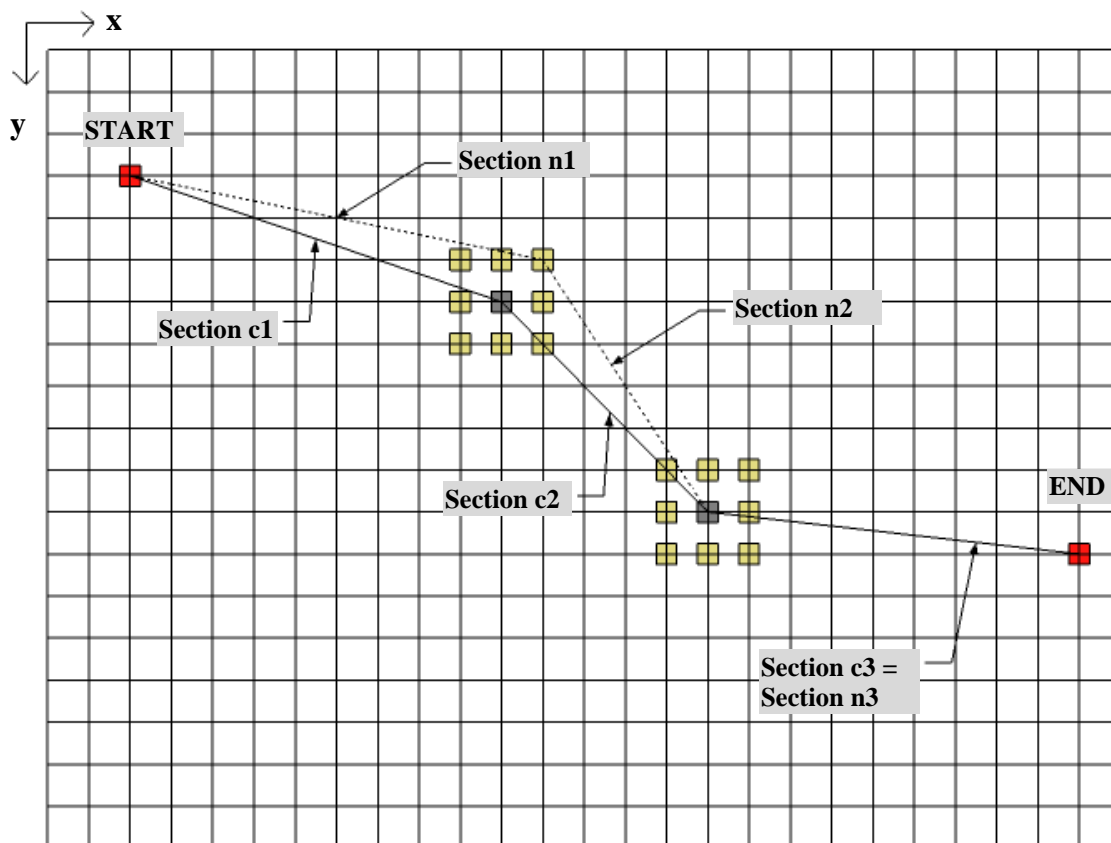


**Figure 4-12** Perturbing a current configuration into a neighboring candidate configuration.

Stating sections c3 and n3 are coincident, even if three-dimensionally coincident, does not mean their cost is the same. Although the cost of a linear section varies with its length, the cross-sections adopted are major factors influencing the cost and these can vary for 2 linear sections with identical 3D configuration.

If a bridge is required in the new section n2, it may be extended into part of section n3, while if section c2 requires only an embankment, section c3 may not include a bridge cross-section. This emphasizes the continuity required in the cross-sections, for which the cross-section at a given point may be influenced by the cross-sections upstream and downstream of that point.

The aim of generating new candidate HSR configurations within a neighborhood is to allow small rearrangements to be tested instead of profound changes. In this context, the degree of freedom with which the current configuration is perturbed is significant. The degree of freedom, in the case of the HSR optimization problem, is related with the number of nodes to

be randomly perturbed in the neighborhood. Jilla and Miller (2001) present a study on the influence of the degree of freedom on the SAA performance for the design of distributed satellite systems. The study observes that if the degree of freedom is too low it is easy for the algorithm to be circumscribed to part of the design space. Conversely, if the degree of freedom is too large the algorithm engages in a random search and no longer takes advantage of the local neighborhood search properties. The implementation of the SAA should thus specify the number of nodes to be randomly perturbed from one configuration to another, adjusted to the case-study specifics.

In summary, the generation of candidate HSR configurations considers the perturbation of a specified number of randomly chosen 3D nodes, to be repositioned according the allowed moves for mandatory and general nodes.

#### 4.2.2 COOLING SCHEDULE

The implementation of the SAA requires that an initially high temperature is considered, which is progressively decreased until an algorithm stopping criterion is reached. Different cooling schedules can be implemented (Aarts et al. 1997; de Weck and Willcox 2010). As discussed by Pardalos et al. (2000) the choice of a cooling schedule is very difficult, as one cannot appreciate, *a priori*, its performance for the problem in question.

The choice relies on an adaptive geometric (Johnson et al. 1989), also termed exponential (Ingber 1993; de Weck and Willcox 2010), cooling schedule based on the implementations for solving water supply infrastructure problems by Cunha (1999) and Cunha and Sousa (2001), and based on the research by Johnson et al. (1989). Four parameters are considered:

- $a$ : the elasticity of acceptance that defines the probability of accepting a transition from the initial configuration to a new candidate configuration that yields higher cost than the initial one. The probability is defined as a percentage and it is used to define the initial temperature of the algorithm by  $t_1 = -0.1c(s_1)/\ln(a)$ , where  $c(s_1)$  is the cost of the initial configuration. This expression defines an initial temperature that allows  $a\%$  of configurations, with a 10% higher cost than the initial configuration, to be accepted.
- $n_j$ : the minimum number of algorithm iterations to be performed at each temperature. A state of equilibrium (although not the equilibrium distribution of Markov chains



which requires an execution time exponentially dependent on the problem size) is to be reached at each temperature before the temperature decrease step. This is measured by decreasing the temperature only when no overall best configuration is attained or the average cost of the evaluated configurations does not improve. If better optimum configurations are found or if the average cost of the configurations improves,  $n_1$  configurations are again evaluated. This defines the adaptability of the cooling schedule.

- $r$ : the rate of temperature decrease, whenever a temperature decrease occurs. A geometric decrease rate is chosen with a constant  $r$  factor. The temperature decrease at each level is governed by  $t_k = r^k t_1$ . The value chosen is of great influence on the quality of the results achieved (Aarts et al. 1997; Johnson et al. 1989): if the rate is too low (large  $r$ ) the algorithm performance can resemble a random search (virtually any neighboring configuration is accepted), whereas small values of  $r$  can relate to performing as an iterative improvement, which terminates at the first local optimum encountered. Typical values can range between 0.7 and 0.99 (Cunha 1999; de Weck and Willcox 2010).
- $n_2$ : the number of temperature decreases to be performed without improvement of the optimum or the average cost. It establishes the stopping criterion of the algorithm.

Johnson et al. (1989) discuss that the amount of time the SAA spends in the intermediate temperature range, between very high and very low temperatures, affects the quality of the solutions. Thus, the adaptive cooling schedule is considered in the implementation presented for the HSR planning problem. When compared with a fixed number of evaluated configurations at each temperature step, the adaptive cooling schedule allows the algorithm to spend more time at these intermediate temperatures.

Finally, some important observations for implementing the SAA to different problems have been introduced in literature. These regard the effectiveness of the cooling schedule and include the following:

- Kirkpatrick (1984) and Van Laarhoven and Aarts (1987) suggest that the initial temperature should be such that at least 80% of the computed configurations are

accepted at that temperature. In these conditions of high initial temperatures, one might expect the final solution to be independent of the initial solution (Cunha 1999).

- Johnson et al. (1989) suggest that obtaining the best results it is necessary to allow for long annealing runs. Increasing the length of an annealing run is more effective if uniformly throughout the schedule rather than at the beginning and at the end of the schedule. This can be done with the increase of the cooling ration  $r$ , the number of iterations  $n_I$ , or by using an adaptive cooling schedule.
- Johnson et al. (1989) observe that even with the implementation of long SAA runs, a large variation in the quality of the solutions can be obtained in different runs.

### **4.3 SOFTWARE TESTING: APPLICATION TO A SYNTHETIC CASE-STUDY FOR STANDARD PLANNING CONDITIONS**

The deterministic model proposed in section 4.1 has been applied to a synthetic case study and solved with the SAA, following the implementation guidelines discussed in section 4.2. Standard planning conditions are considered, meaning that an optimization concerned with construction costs and problem constrains is addressed. Additional applications were run for performing a sensitivity analysis on the coefficients for geometry ( $\gamma_\eta$  and  $\gamma_\beta$ ), land-use ( $\gamma_{\lambda_s}$ ) and location ( $\gamma_{v_i}$ ) and on the normal and limit values of the horizontal angle. The following sub-sections present the characteristics and the results obtained for the base case and the sensitivity analysis.

The SAA may be applied to a wide range of problems (Dekkers and Aarts 1991), although the number of iterations necessary to reach equilibrium at each temperature, for achieving optimal solution, is exponentially dependent on problem-size (Aarts and Vanlaarhoven 1985). Solving a large problem such as the HSR network planning problem becomes unreasonable with an exponential complexity dependent on the problem size and thus the finite-time implementation of the algorithm includes a study for the estimation as to which combination of the SAA parameters works best.

The case-study application herein presented is based on the studies by Costa et al. (2013).

### 4.3.1 CHARACTERISTICS OF THE BASE CASE

The synthetic problem aims at linking three mandatory locations with a HSR network in a rectangular shaped area of 60 km per 40 km (Figure 4-13 a). The search space of the problem is discretized by the 3D mesh in Figure 4-13 b) that spans 2 km in each plan view direction and 10 m vertically and defines the permissible node positions ( $\Omega_N$ ).

The mandatory locations, defined by their (x,y) coordinates, are M1 (0 km,0 km), M2 (40 km, 20km) and M3 (58 km,38 km). An additional desirable location B (30 km,4 km) is considered with a location benefit term to be subtracted to the objective function value when the node is connected by the HSR linear sections, with  $\gamma_{vB}=30\%\sum_{(i,j)\in\Omega_N}C_{ij}$ .

Four input spatial properties are mapped and represented by different raster data type layers: elevation, ground behavior, expropriation cost and land use type. The layers are discretized in 200 m wide square space property elements ( $\Omega_E$ ) that establish a constant value of elevation, ground behavior, expropriation cost and land-use within the boundaries of each element.

Penalties to optimize the geometric and land use design are proportional to the construction cost of the configuration and consider the following coefficients:  $\gamma_\eta=5\%\sum_{(i,j)\in\Omega_N}C_{ij}$  for gradient,  $\gamma_\beta=5\%\sum_{(i,j)\in\Omega_N}C_{ij}$  for horizontal angle and  $\gamma_{\lambda_s}=2\%\sum_{(i,j)\in\Omega_N}C_{ij}$  for land use. The normal and limit gradients and horizontal angles are  $\eta_{normal}=20\%$ ,  $\eta_{limit}=35\%$ ,  $\beta_{limit}=100^\circ$  and  $\beta_{normal}=120^\circ$ .

Figure 4-13 (a) identifies the forbidden land-use elements, the restricted land-use elements that, if crossed by the HSR, incur a land use penalty and the elements exempt from restrictions. The cross-sections, for earthworks and cost calculation, are evaluated at every space search element overlaid by the HSR configuration along the longitudinal profile.

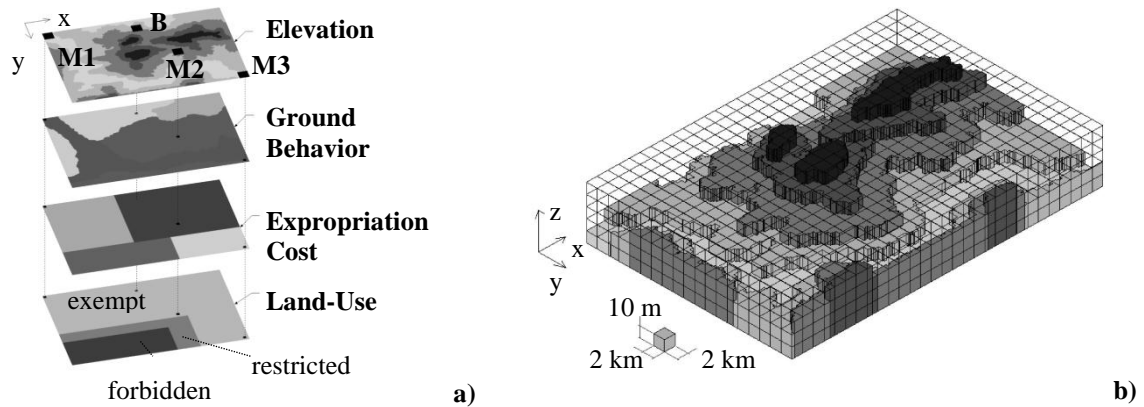


**Figure 4-13** Case study specifics: a) Nodes overlaying the elevation-, ground behavior-, expropriation cost - and land-use layers; b) Ground elevation and 3D mesh defining the permissible node positions in each configuration.

#### 4.3.2 RESULTS OF THE BASE CASE

The SAA was applied to solve the model considering 15 random seed numbers. For each random seed, the SAA was run for the possible combinations of the SAA cooling schedule parameters considering: the elasticity of acceptance  $a$  (0.8; 0.9; 0.93), the temperature decrease rate  $r$  (0.7; 0.8; 0.9; 0.93), the minimum number of computed solutions at each temperature  $n_1$  (1,000; 1,500; 2,000; 5,000; 10,000) and the termination criterion  $n_2$  (5; 10).

A degree of freedom considering the 3D repositioning of two nodes is implemented to perturb the current configuration into a new candidate configuration. Also, vertical moves (along the z-axis) are allowed for mandatory nodes.

The SAA runs performed revealed that increasing values of the elasticity of acceptance  $a$  correspond, as expected, to an increasing percentage of accepted configurations at the initial temperature (Figure 4-14). Kirkpatrick (1984) and Van Laarhoven and Aarts (1987) suggest that the initial temperature should be such that at least 80% of computed configurations are accepted at that temperature, a condition that exists for all tested values of  $a$ .

Additionally, initial SAA runs performed indicate that a minimum number of iterations  $n_1 = 5000$  and a stopping criterion  $n_2 = 10$  from, respectively, (1,000; 1,500; 2,000; 5,000; 10,000) and (5; 10), provide the least costly solutions for the different remaining SAA parameters (elasticity of acceptance  $a$  and temperature decrease rate  $r$ ). Considering the suggestions by Johnson et al. (1989), it is necessary to allow for long annealing runs in order to obtain the

best results. For the SAA runs with  $n_1$  set equal to 1,000, 1,500 and 2,000, the results provided low quality solutions when compared to those obtained with  $n_1 = 5,000$ . On the other hand, the solutions did not improve when the  $n_1$  was set to 10,000, but the computation time increased significantly. Analogously, poor quality configurations were obtained when using  $n_2 = 5$ , as it was observed that the SAA was terminating prematurely. When allowed to consider  $n_2 = 10$ , it was observed that, in some runs, improvements were made after 6 consecutive temperature decreases without improvement of the optimum or the average cost. This meaning the equilibrium had not been reached at  $n_2 = 5$ . Given that no further improvements were obtained past 7 consecutive temperature decreases,  $n_2 = 10$  was considered a suitable value. Had improvements been observed closer to 10 consecutive decreases (say 9), a larger value for the termination criterion would be tested.

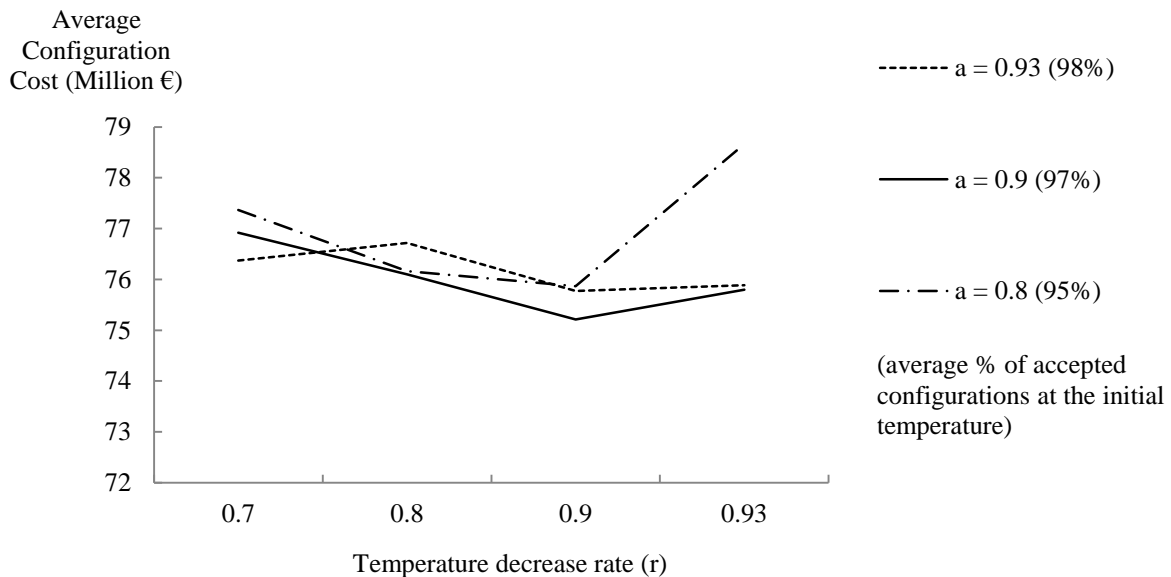


**Figure 4-14** Influence of temperature decrease rate  $r$  on the average cost of the configurations.

Figure 4-14 considers  $n_1 = 5,000$  and  $n_2 = 10$  and shows the variation of the average configuration cost (objective function value) with the temperature decrease rate  $r$ , for different values of elasticity of acceptance  $a$ . Each point in Figure 4-14 represents the average cost of the configurations obtained from solving the model with 15 runs (one for each random seed number) for that same SAA parameter set.

One observes from Figure 4-14 that the average cost tends to decrease with increasing  $r$  up to 0.9. A larger rate ( $r = 0.93$ ) results, on average, in equal or costlier solutions than those

obtained for  $r = 0.9$ . It has been discussed that for low values of  $r$  the SAA behavior resembles that of an iterative improvement which tends to terminate at sub-optimal solutions and long annealing runs are desired to attain the best results. However, if the cooling is too slow (large  $r$ ) the algorithm behavior tends to resemble that of a random walk that fails to take advantage of the SAA principles. In addition, Johnson et al. (1989) discuss that even for long algorithm runs, there can be a large variation in the quality of the solutions. These observations and the fact that Figure 4-14 shows the average cost of the configurations may explain why a perfect clear trend is not observed. In fact, variability in the results pushes the average cost value obtained with  $a = 0.8$ ,  $r = 0.93$ ,  $n_1 = 5,000$  and  $n_2 = 10$  to larger average costs when the optimal solution obtained with this parameter set within the 15 runs is, in reality, equal to the best solutions obtained for  $a = 0.9$ ,  $r = 0.93$ ,  $n_1 = 5,000$  and  $n_2 = 10$  and for  $a = 0.93$ ,  $r = 0.93$ ,  $n_1 = 5000$  and  $n_2 = 10$ .

20 additional SAA runs were performed considering  $a = 0.9$ ,  $r = 0.9$ ,  $n_1 = 5,000$  and  $n_2 = 10$ , the SAA parameter set for which the lowest average cost is obtained (Figure 4-14).

The same overall best configuration was found and only few SAA runs converged for different solutions, with a cost up to 5% larger, as one could expect from a random search algorithm such as the SAA. Figure 4-15 shows the convergence history, evolution of the last accepted configuration before a temperature decrease and of the current optimum, of one SAA run for  $a = 0.9$ ,  $r = 0.9$ ,  $n_1 = 5,000$  and  $n_2 = 10$ . Large objective function value configurations are accepted in the early temperature stages of the implementation, allowing for a comprehensive exploration of the problem search space. As the algorithm progresses the acceptance of worsening solutions decreases and convergence to the best overall configuration occurs.

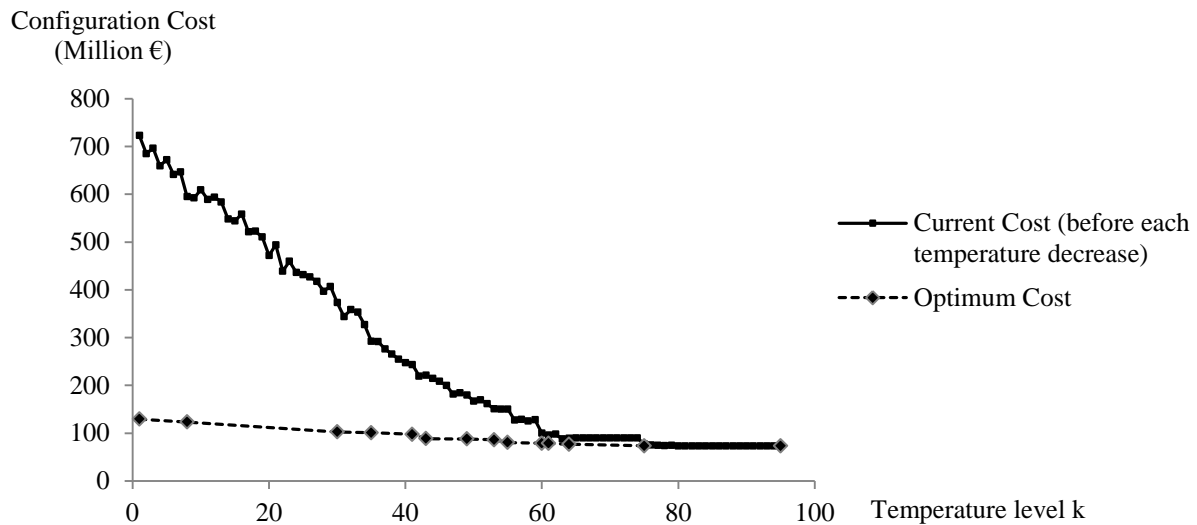


**Figure 4-15** Convergence history for  $a = 0.9$ ,  $r = 0.9$ ,  $n_1 = 5,000$  and  $n_2 = 10$ : evolution of the last accepted configuration before a temperature decrease and of the current optimum at the time of each temperature decrease.

Table 4-1 and Table 4-2 present, respectively, the cost breakdown and the geometry of the best overall configuration found for the base case; Figure 4-16 a) and b) present the configuration plan view overlaying, respectively, the elevation layer and the land-use layer.

The configuration cost (objective function value) is 73,235,813 € and is the result of the construction costs and the location benefit given that both the geometry and the land-use penalties are null. The geometry penalty is null (Table 4-1) since the gradient of each linear section and the angle at each intermediate node are, respectively, smaller and larger than, respectively, the normal values  $\eta_{normal} = 20\%$  and  $\beta_{normal} = 120^\circ$  (Table 4-2). The land-use penalty is also null (Table 4-1) since the configuration does not cross restricted land-use elements (Figure 4-16 b)). The location benefit term, however, is not null as the desirable location B at (30 km;4 km) is linked by the HSR configuration. The configuration also avoids sharp variations of the ground elevation (Figure 4-16 a)) and produces a vertical adjustment of the longitudinal profile that does not require the construction of bridges and tunnels (Table 4-1), costlier than embankments and cuts.

**Table 4-1** Cost breakdown of HSR configurations.

|                              | Base Case   | $\gamma_{vB} = 0$ | $\beta_{normal}/\beta_{limit}$ |
|------------------------------|-------------|-------------------|--------------------------------|
| Objective Function Value (€) | 73,235,813  | 95,673,781        | 78,191,809                     |
| 1. Construction Cost (€)     | 104,622,590 | 95,673,781        | 111,702,584                    |
| 1.1 Expropriation (€)        | 75,261,796  | 71,119,151        | 78,380,116                     |
| 1.2 Earthworks (€)           | 29,360,794  | 24,554,630        | 33,322,468                     |
| 1.3 Bridges (€)              | 0           | 0                 | 0                              |
| 1.4 Tunnels (€)              | 0           | 0                 | 0                              |
| 2. Geometry Penalty (€)      | 0           | 0                 | 0                              |
| 3. Land-Use Penalty (€)      | 0           | 0                 | 0                              |
| 4. Location Benefit (€)      | 31,386,777  | 0                 | 33,510,775                     |

**Table 4-2** Geometry of HSR configurations.

| Node | Base Case            |               |                | $\gamma_{vB} = 0$    |               |                | $\beta_{normal}/\beta_{limit}$ |               |                |
|------|----------------------|---------------|----------------|----------------------|---------------|----------------|--------------------------------|---------------|----------------|
|      | (x;y;z)<br>(km;km;m) | $\eta$<br>(‰) | $\beta$<br>(°) | (x;y;z)<br>(km;km;m) | $\eta$<br>(‰) | $\beta$<br>(°) | (x;y;z)<br>(km;km;m)           | $\eta$<br>(‰) | $\beta$<br>(°) |
| 1    | (0;0;10)             | 1.58          |                | (0;0;10)             | 0.00          |                | (0;0;10)                       | 0.79          |                |
| 2    | (6;2;20)             | 0.00          | 166            | (8;8;10)             | 1.58          | 153            | (12;4;20)                      | 0.00          | 153            |
| 3    | (30;4;20)            | 1.56          | 133            | (26;14;40)           | 0.00          | 177            | (26;2;20)                      | 2.24          | 145            |
| 4    | (38;14;40)           | -1.58         | 160            | (36;18;40)           | 2.24          | 175            | (30;4;30)                      | 0             | 149            |
| 5    | (40;20;30)           | -0.56         | 135            | (40;20;30)           | 0.56          | 180            | (40;20;30)                     | 0             | 144            |
| 6    | (56;28;20)           | 0.00          | 128            | (56;28;20)           | 0.00          | 128            | (50;24;30)                     | -1.24         | 142            |
| 7    | (58;38;20)           |               |                | (58;38;20)           |               |                | 58;38;20)                      |               |                |



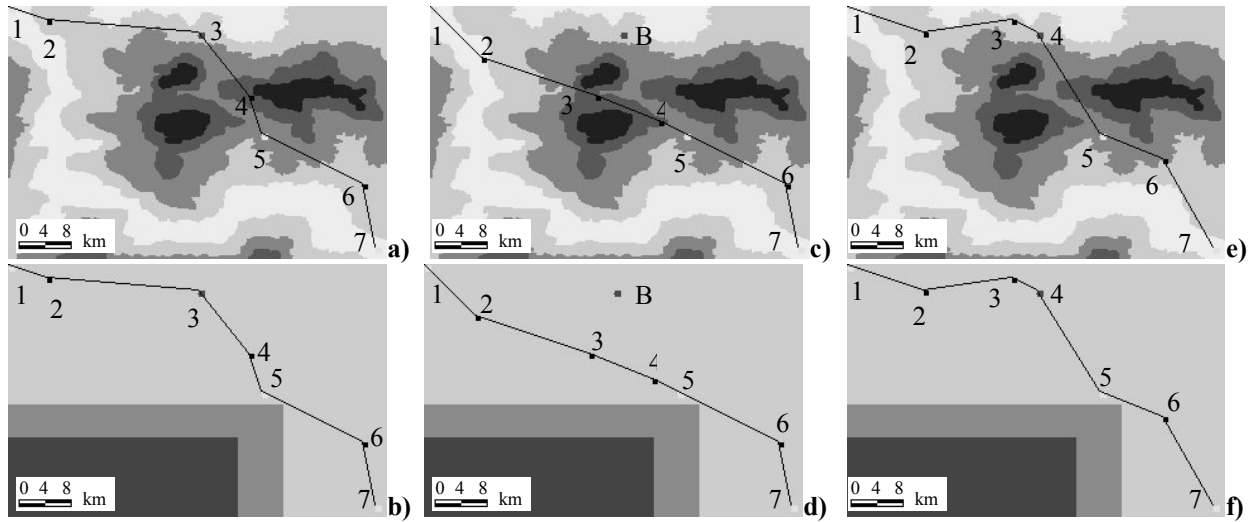


**Figure 4-16** Plan view of the best configurations: a) and b) for the base case, c) and d) for  $\gamma_{vB} = 0$  and e) and f) for sensitivity analysis of  $\beta_{normal}/\beta_{limit}$ ; configurations overlay the ground elevation layer in a), c) and e) and the land-use layer in b), d) and f).

### 4.3.3 SENSITIVITY ANALYSIS

Given that the penalty coefficients for geometry ( $\gamma_{\eta}$  and  $\gamma_{\beta}$ ) and land-use ( $\gamma_{ls}$ ) and the benefit location coefficient ( $\gamma_{vi}$ ) are user-specified and their influence on the problem solution is not known a priori, additional applications were run for performing a sensitivity analysis. In an attempt to isolate the effects of each coefficient, SAA runs were made changing only the respective coefficient value and maintaining all the remaining specifics from the base case. The results are discussed in sections 4.3.3.1 and 4.3.3.2.

In addition to the sensitivity analyses performed on the coefficients values, an additional study was performed for the normal and limit horizontal angle values. While the gradient normal and limit values can be derived directly from existing standards, the consideration of the horizontal angle is a model simplification of the HSR representation. Limit and normal values are defined by standards for the radii of the horizontal circular curves that can be inserted between the linear alignments. The angles are a proxy for the radii. The results on the horizontal angle values are discussed in section 4.3.3.3.

#### 4.3.3.1 PENALTY COEFFICIENTS

The best configuration found for the base case complies with the desirable normal values for geometry (Table 4-2) and does not cross restricted land use elements (Figure 4-16 b)), thus

the penalties were null (Table 4-1). To assess how smaller coefficients could lead to a solution with smaller objective function values, with a trade-off between the construction costs and the violation of the desirable restrictive values, the penalty coefficients were reduced to 1/5 of their base case value. The new coefficient values tested are  $\gamma_\eta = 1\% \sum_{(i,j) \in \Omega_N} C_{ij}$  for gradient,  $\gamma_\beta = 1\% \sum_{(i,j) \in \Omega_N} C_{ij}$  for horizontal angle and  $\gamma_{\lambda_s} = 0.4\% \sum_{(i,j) \in \Omega_N} C_{ij}$  for land use.

The best configuration found for each variation of the penalty coefficients is equal to the best configuration of the base case. This means that even for smaller values of the coefficients, tested separately, the best solution complies with the gradient and horizontal angle normal values and does not cross a restricted land use area. The observation may correspond to the particularity of considering a simple and synthetic case-study in which the effects of these coefficients cannot be properly captured but this may not hold for larger and more complex search areas.

#### 4.3.3.2 LOCATION BENEFIT TERM

The influence of the location benefit coefficient was studied by varying its value with two additional situations:  $\gamma_{vB} = 15\% \sum_{(i,j) \in \Omega_N} C_{ij}$  and  $\gamma_{vB} = 0$ , keeping the penalty coefficients unchanged from the base case.

The solution found considering  $\gamma_{vB} = 15\% \sum_{(i,j) \in \Omega_N} C_{ij}$  has the same geometry as the base case solution (Table 4-2; Figure 4-16 a) and b)) and thus equal construction costs and penalty costs (Table 4-1). The objective function value, however, differs by the smaller location benefit. Instead of benefiting the objective function by 31,386,777 € as in the base case, the new location benefiting term is half of this and the objective function value is  $104,622,590 - 15,693,388 = 88,929,202$  €.

The best HSR configuration found for the null benefit coefficient  $\gamma_{vB} = 0$  is distinct from the previous one, both in terms of cost (Table 4-1) and geometry (Table 4-2; Figure 4-16 c); Figure 4-16 d)). The configuration is shorter, 73,616 m long compared to the base case solution with 77,625 m long, and construction costs are 9% smaller than the base case solution. Similarly to the base case solution, the construction of bridges and tunnels is avoided. The solution for  $\gamma_{vB} = 0$ , however, does not cross the location B and yields a larger objective function value. This is due to the lack of the location benefit since earthworks and

expropriation costs are smaller and penalties are equally null. The configurations neither rely on geometry less restrictive than the recommended values nor overlay restricted land-use space property elements.

From the results of the null benefit coefficient  $\gamma_{vB}=0$ , one can devise that connecting the location B is more expensive in terms of construction costs but the objective function value breaks-even if a benefiting coefficient of  $\gamma_{vB} = 9\% \sum_{(i,j) \in \Omega_N} C_{ij}$  is considered. The solution found when considering  $\gamma_{vB} = 15\% \sum_{(i,j) \in \Omega_N} C_{ij}$  is in accordance with this reasoning.

#### 4.3.3.3 NORMAL AND LIMIT HORIZONTAL ANGLES

Considering that the best configuration found for the base case has 3 angles smaller than  $140^\circ$ , two of which are smaller than  $130^\circ$ , additional computations were performed for  $\beta_{limit} = 130^\circ$  and  $\beta_{normal} = 140^\circ$ . The base case considered  $\beta_{limit} = 100^\circ$  and  $\beta_{normal} = 120^\circ$ , which may be too small angles to represent the large radii required by HSR configurations.

The best configuration found by the algorithm (Table 4-1; Table 4-2 ; Figure 4-16 e); Figure 4-16 f)) is similar to the base case but complying with the new and more restrictive normal and limit values. One observes that bridges and tunnels are also avoided but both expropriation and earthworks costs are larger, resulting in a larger construction cost (Table 4-1). The configuration still crosses the desirable node (Figure 4-16 e); Figure 4-16 f)) and the objective function is improved by the location benefit. No other penalties are applied given that the gradient normal value and the new horizontal angle normal value are both complied with and the solution does not cross restricted land-use elements. In fact, the configuration changes slightly from the base case, producing all intermediate angles larger than  $140^\circ$  at a larger construction cost than the base case.

These results are expected as larger limit and normal horizontal angles restrain the capability of the configurations to adjust to more sinuous paths and lead to smaller construction costs.

#### 4.3.4 REMARKS ON THE SYNTHETIC CASE-STUDY APPLICATION

A model for optimizing the planning stage of high-speed rail networks has been presented in section 4.1. The model represents location dependent properties influencing the configuration,

as well as considering the HSR design requirements and best practice design parameters. It aims at optimizing conflicting design choices that influence the performance of the infrastructure. A heuristic method, the Simulated Annealing Algorithm (SAA), is implemented to solve the model.

A user-friendly tool has been developed that can consider the model input location data, the HSR 3D geometry restrictions and the SAA. The software testing is performed with the application to an intentionally simple and synthetic case study. A scenario of standard planning conditions, considering construction costs and problem constraints, has been used and the combination of SAA parameters that works best is presented. A sensitivity analysis has been performed, varying the model penalty and benefit coefficients and the horizontal angle normal and limit design values.

Sound solutions have been obtained in all cases, suggesting the model and the problem solving methodology are capable of addressing the preliminary design optimization for HSR networks. Indicating this, the problem solution adjusts to include more restrictive horizontal angle values and has a reduced length and smaller construction costs for the null location benefit coefficient. The fact that the solution in this case-study is impervious to variations of the penalty coefficients may relate to the specificity of the synthetic case-study and should not hold in real world applications. In fact, both the model and the tool discussed in this section can be expanded to incorporate additional complexity, establishing the basis for real world applications in which the integration of geotechnical and hydrological risk factors affecting the HSR performance can also be considered.

#### **4.4 EXTENDING THE SOFTWARE CAPABILITIES**

Sound results have been obtained with the application of the deterministic model of the HSR planning optimization problem to the synthetic case-study, solved with the implementation of the SAA. The synthetic case-study is intentionally simple to allow testing the tool performance. However, aiming at solving real-world HSR planning problems requires extended software capabilities.

Besides the fact that real HSR problems involve dealing with larger datasets, other complexities need to be addressed. This research identified two important aspects: dealing

with “islands” of forbidden land-use and establishing a minimum length of the HSR linear sections.

Existing “islands” of forbidden land-use have implications for the generation of new HSR candidate configurations while the lack of a minimum length of linear sections may affect the performance of the SAA. The consideration of these issues is presented in sections 4.4.1 and 4.4.2.

#### **4.4.1 INFLUENCE OF THE FORBIDDEN LAND-USE AREAS ON THE GENERATION OF HSR CANDIDATE CONFIGURATIONS**

As discussed in section 4.1.2 the constraints define the feasible search space and can impose difficulties to the search that should be overcome by the algorithm implementation. An example is the fact that a variety of forbidden land-use areas, differing in size and shape (concave and convex) may exist, which are not represented in the synthetic case-study used for the tool development.

If “islands” of forbidden land-use exist an initial solution is always located on one side of these areas and, depending on the size of the areas and the refinement of the discretization mesh  $\Omega_N$ , so will the new HSR candidate configurations. Such a case is depicted in the land-use layer of Figure 4-17, in which the yellow area covering most of the search space is exempt from restrictions, the black area is outside the feasibility space (ocean) and the remaining colored areas represent forbidden land-use. Starting from the initial HSR configuration of Figure 4-17 a), the SAA is not able to search the entire feasible space unless mechanisms are adopted in the generation of new HSR candidate configurations which allow leaping over these “islands”. Figure 4-17 b) shows an optimized solution, for which the SAA search was able to leap over the smaller forbidden land-use areas but not the larger ones.

To address this issue, mechanisms which allow leaping over forbidden land-use areas of variable sizes and shapes were incorporated in the generation of the HSR candidate configurations. Additionally, these have to take into account the existing constraints to the horizontal angle at intermediate nodes of the HSR configurations.

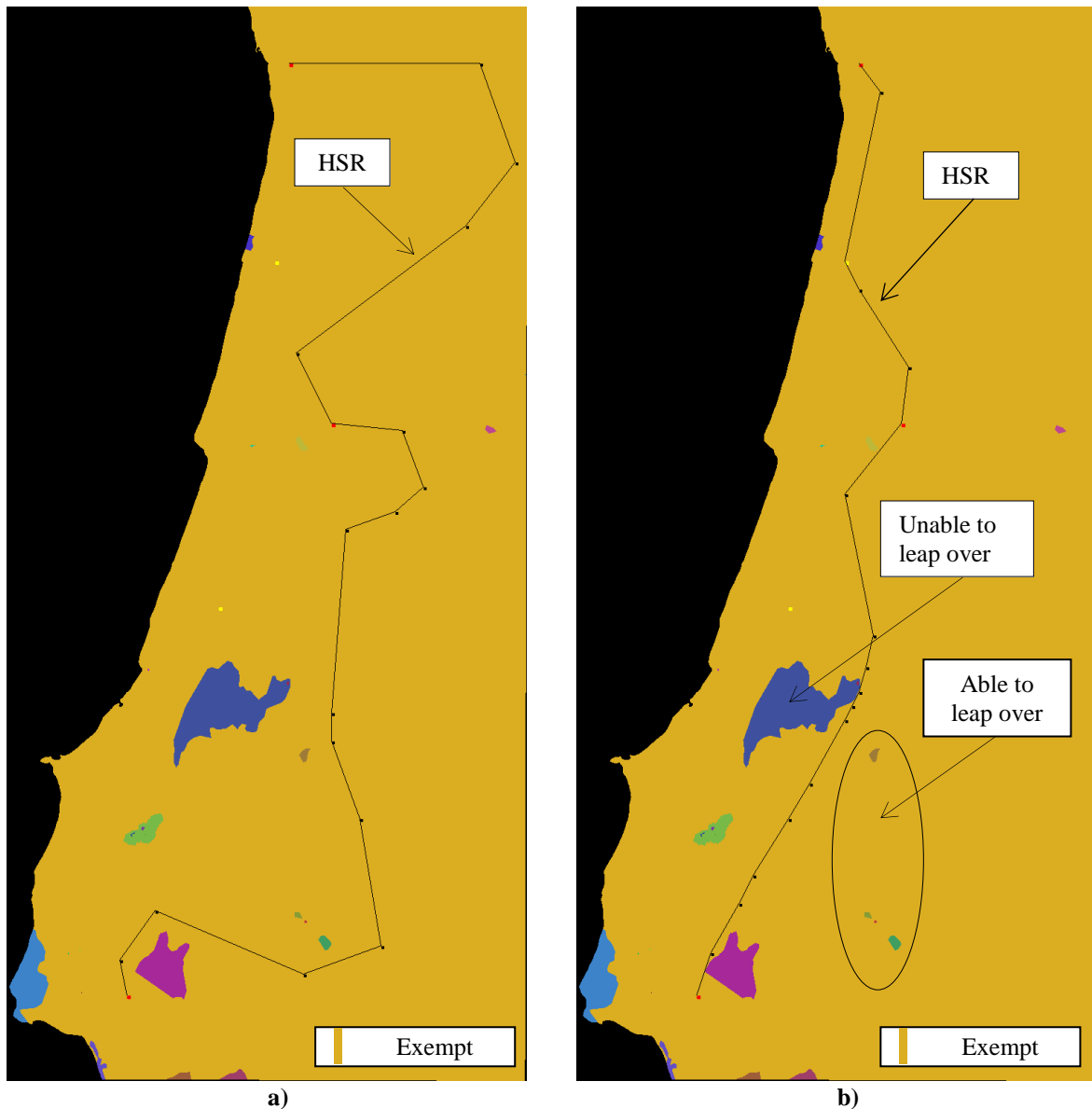


**Figure 4-17** HSR configurations overlaying the protected land-use layer map (scale 1:2 000 000): a) initial configuration and b) best configuration found by the SAA.

Consider the example of Figure 4-18, for which the node  $N$  of the current HSR configuration is randomly chosen to be horizontally repositioned to the right ( $N'$ ). If a small “island” of forbidden land-use exists, such as depicted in Figure 4-18 a), the respective move to  $N'$  can successfully leap over the forbidden land-use area. However, for a larger area such as shown in Figure 4-18 b), this repositioning is not sufficient.

The procedures adopted consist in incrementing the repositioning distance in the original direction by the spacing of the discretization mesh  $\delta$ . One observes in Figure 4-18 b) that

repositioning for both  $\Delta_1 = 1\delta$  and  $\Delta_2 = 2\delta$  still overlays the forbidden land-use but for  $\Delta_3 = 3\delta$  it does not. However, this overstretching effect leads to increasingly smaller horizontal angles at nodes  $N'$ ,  $N-1$  and  $N+1$ .

A new feasible candidate configuration may not be obtained with the incremental displacement of the node, either by not complying with the land-use constraint or the horizontal angle constraint. In this case, a new tentative generation procedure is considered, which also repositions the anterior and posterior nodes. Figure 4-19 shows how the area from Figure 4-18 b) can be successfully dealt with by the repositioning of nodes  $N$ ,  $(N-1)$  and  $(N+1)$ .

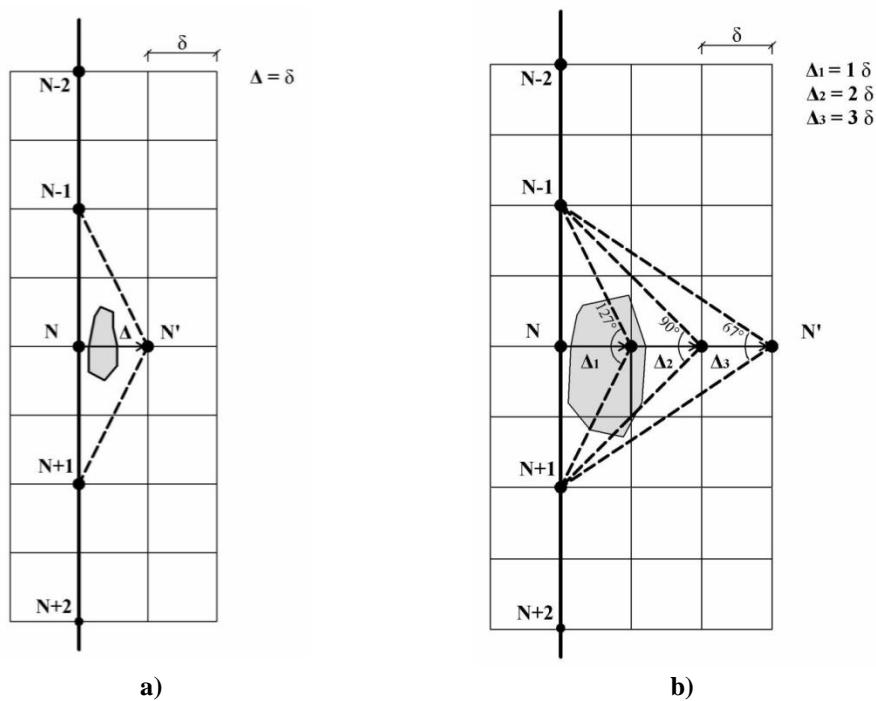


**Figure 4-18** Leaping over “islands” of forbidden land-use by moving only one node of the current HSR configuration: a) successfully and b) unsuccessfully.

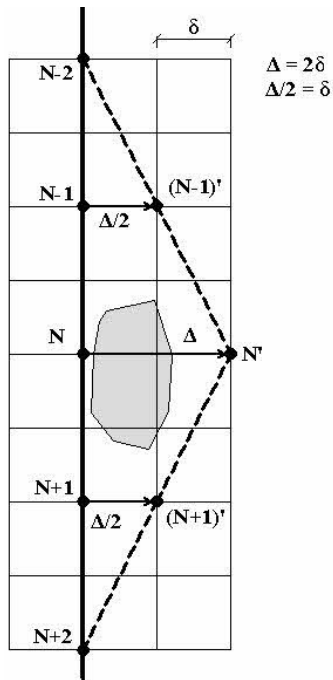


**Figure 4-19** Leaping over the forbidden land-use area of Figure 4-18 (b) with the repositioning of node N, the anterior node (N-1) and the posterior node (N+1).

Given that the procedures to implement may have to deal with various shapes and sizes of forbidden land-use areas, a general procedure was developed and implemented. It consists in the tentative generation of feasible HSR configurations in 5 sequential steps and stopped when a feasible configuration is obtained. Each step relates with a number of anterior and posterior nodes to be displaced, besides the randomly chosen node N. Each step is detailed below.

#### *STEP 0*

This step considers only the displacement of the node N, which is sequentially incremented until a feasible configuration is found. It is illustrated by Figure 4-18. If the displacement causes the non-compliance with the horizontal angle constraint, Step 0 is abandoned and Step 1 is adopted.

#### *STEP 1*

This step considers the displacement of the nodes N, (N-1) and (N+1). It is illustrated by Figure 4-19. (N-1) and (N+1) are repositioned at 1/2 of the N displacement, in the same



direction. The displacement of N is incremented until a feasible configuration is found but if it causes the non-compliance with the horizontal angle constraint, Step 1 is abandoned and Step 2 is adopted.

#### *STEP 2*

This step considers the displacement of the nodes N, (N-1), (N-2), (N+1) and (N+2). It is illustrated by Figure 4-20 (a). (N-1) and (N+1) are repositioned at  $\frac{2}{3}$  of the N displacement and (N-2) and (N+2) are repositioned at  $\frac{1}{3}$ , all in the same direction as N. The displacement of N is incremented until a feasible configuration is found but if it causes the non-compliance with the horizontal angle constraint, Step 2 is abandoned and Step 3 is adopted.

#### *STEP 3*

This step considers the displacement of the nodes N, (N-1), (N-2), (N-3), (N+1), (N+2) and (N+3). It is illustrated by Figure 4-20 (b). (N-1) and (N+1) are repositioned at  $\frac{3}{4}$  of the N displacement, (N-2) and (N+2) are repositioned at  $\frac{1}{2}$  of the N displacement and (N-3) and (N+3) are repositioned at  $\frac{1}{4}$  of the N displacement, all in the same direction as N. The displacement of N is incremented until a feasible configuration is found but if it causes the non-compliance with the horizontal angle constraint, Step 3 is abandoned and Step 4 is adopted.

#### *STEP 4*

This step considers the displacement of the nodes N, (N-1), (N-2), (N-3), (N-4), (N+1), (N+2), (N+3) and (N+4). It is illustrated by Figure 4-21. (N-1) and (N+1) are repositioned at  $\frac{8}{9}$  of the N displacement, (N-2) and (N+2) are repositioned at  $\frac{7}{9}$  of the N displacement, (N-3) and (N+3) are repositioned at  $\frac{2}{9}$  of the N displacement and (N-4) and (N+4) are repositioned at  $\frac{2}{9}$  of the N displacement, all in the same direction as N. The displacement of N is incremented until a feasible configuration is found but if it causes the non-compliance with the horizontal angle constraint, Step 4 is abandoned. At this point, the generation of HSR candidate configurations is restarted and a new node N is randomly chosen to be displaced in the neighborhood.

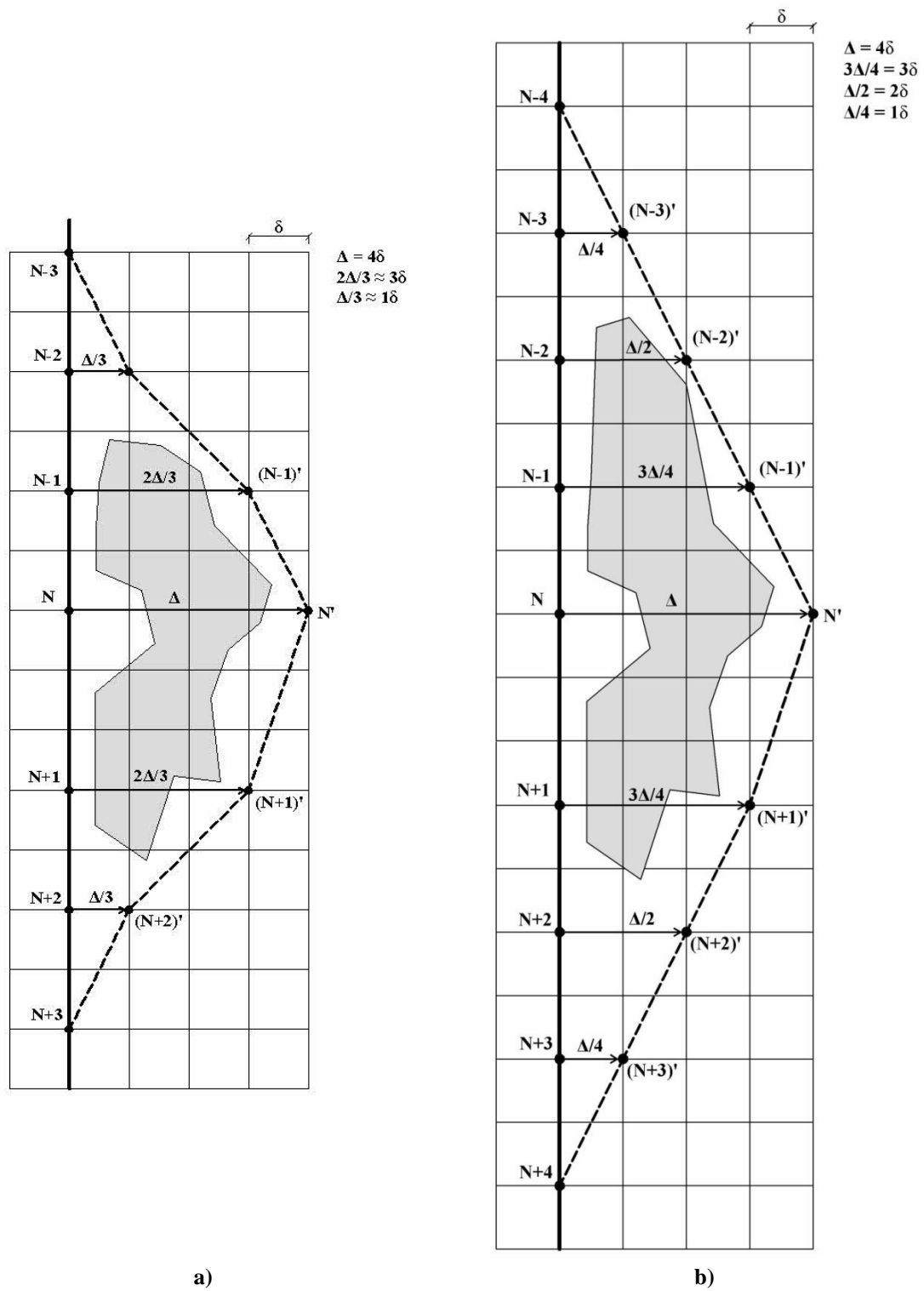


**Figure 4-20** Leaping over “islands” of forbidden land-use: a) displacement of 2 anterior and 2 posterior nodes and b) displacement of 3 anterior and 3 posterior nodes.

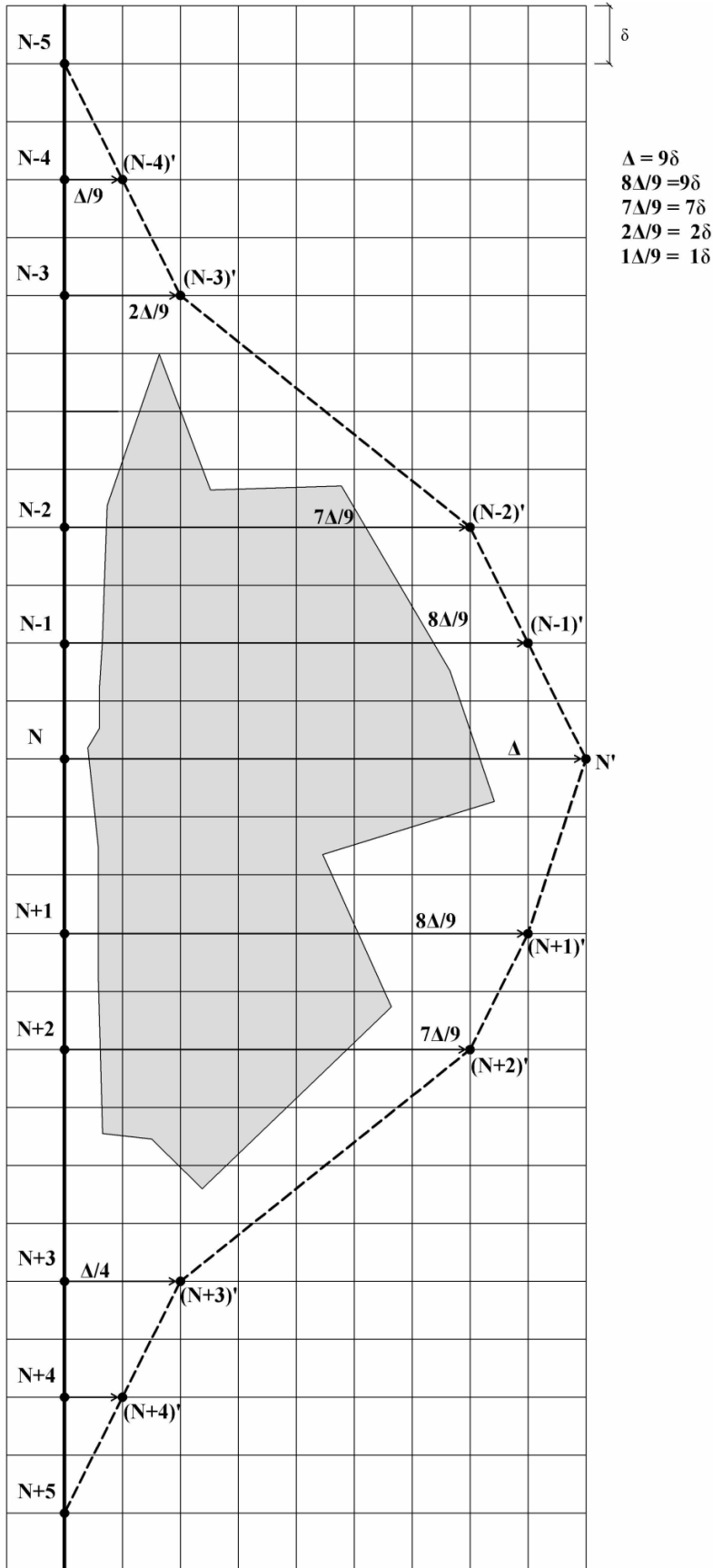


**Figure 4-21** Leaping over “islands” of forbidden land-use with displacement of 4 anterior and 4 posterior nodes.

#### 4.4.2 MINIMUM LENGTH OF LINEAR SECTIONS

Besides the capabilities of the SAA to deal with forbidden land-use areas, one additional requisite was observed when transitioning from an intentionally simple and synthetic case-study (section 4.3) to a real-world case-study: the establishment of a minimum length for the HSR linear sections.

Initial applications to a real world case-study (detailed in section Chapter 5) have shown the formation of node clusters such as shown in Figure 4-22.

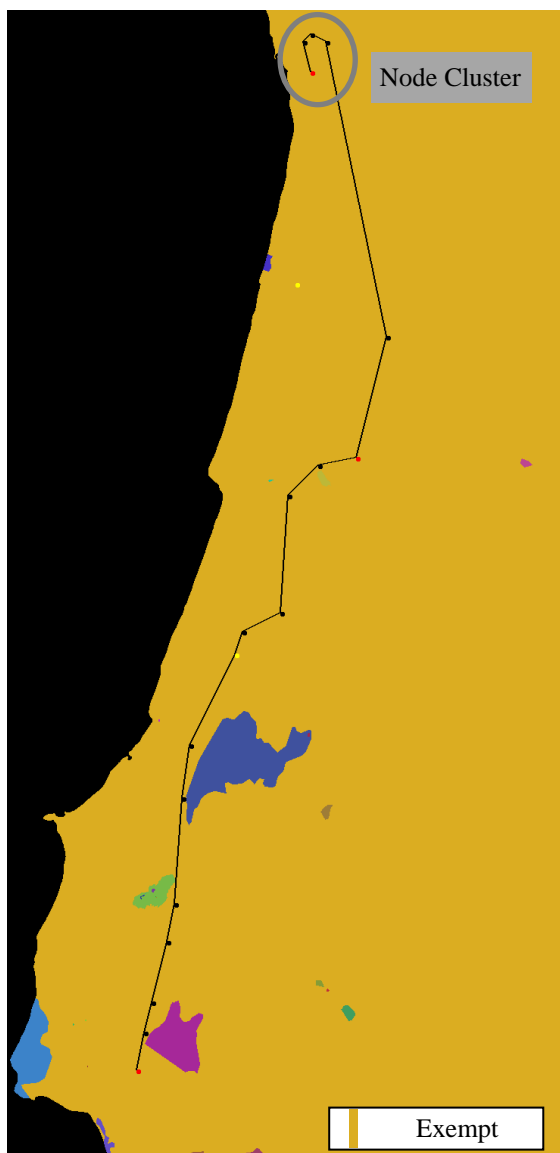


**Figure 4-22** Plan view a HSR configuration showing evidence of node clustering, overlaying a land-use layer.

It is important to note that such a cluster would hardly represent an optimal or near-optimal solution of a real-world high-speed intercity connection such as in the fundamental principles of HSR. However, escaping from node clusters, can be a cumbersome task, mainly due to the fact that for closely positioned nodes, moves in the neighborhood are very conditioned by the horizontal angle feasibility. Furthermore, for SAA low temperature stages, in which the probability of accepting worsening configurations is also low, the HSR configurations required for the escape may yield unaccepted objective function values. In fact, if a cluster forms and propagates to low temperature stages of the SAA implementation most of the moves that would reverse the cluster are either forbidden because of the horizontal angle feasibility requirements or will not be accepted because the probability of accepting worse solutions is very low. It is not impossible for the clusters to be reversed, but it is very unlikely.

A minimum length for the HSR linear sections is to be defined to avoid the formation of the clusters and its propagation to the optimized HSR configurations. This minimum length aims at disallowing candidate configurations in which the nodes are positioned very close to each other and thus avoiding the cluster formation.

However, the value of the linear sections minimum length is conditioned by the case-study and should be defined according to the normal and limit values for the horizontal angles at intermediate nodes. This is discussed for a specific real-world case-study in section 6.1.2.

#### **4.5 THE HSR PLANNING ROBUST OPTIMIZATION MODEL**

A deterministic HSR planning optimization model has been developed (section 4.1) and applied to an intentionally simple and synthetic case-study and solved with the implementation of the SAA (section 4.3). The sound results obtained form the basis for real-world applications, enabled by a computational tool able to deal with large data sets, to apply the model and to implement the SAA. The software capabilities were extended (section 4.4) to deal with complexities existing in real world problems which were not included in the synthetic case-study. This section proposes a HSR planning robust optimization model which builds on the developments achieved by sections 4.1, 4.2, 4.3 and 4.4 and which aims at incorporating the effects of natural hazards into the decision-making process through an integrated approach.

Natural hazards, such as earthquakes, floods, tropical storms, amongst others, happen across the world. However, it is impossible to predict with certainty where and when these hazards will materialize, within the HSR lifetime. Also, natural hazards cannot be prevented. However, prevention may contain the damages inflicted to the built environment and may be cost effective (World Bank and United Nations 2010). Considering the vulnerability of HSR infrastructures to the effects of natural hazards, coupled with the large, commonly public, investments the HSR requires and a society which grows less willing to pay for expensive and lengthy recoveries, with minimal tolerance to disruptions, make a strong case for an integrated decision-making considering natural hazards at the planning stage.

Section 2.4.1 discussed the capabilities of natural hazards in damaging and disrupting the HSR infrastructure. The potential effects of natural hazards such as earthquakes, floods and severe rainfall to the HSR infrastructure were documented. These can cause significant direct and indirect losses, both of which can include market and non-market losses, although, as discussed in section 2.4.4, the natural hazards HSR performance in the planning optimization context of this research is assessed by the direct market losses pertaining to the HSR infrastructure damage.

A HSR planning robust optimization model is proposed to tackle the fact that HSR lines are, in general, required to deal with regions subject to multiple hazards. Different hazards impose different loading conditions to the infrastructure and thus the HSR performance can be subject to a set of different conditions. Planning for the worst case scenario, avoiding the HSR disruption for any of the natural hazards considered, is economically unrealistic. The robust approach thus aims at planning for a HSR that is the most beneficial for an overall set of possible conditions under which to perform, in addition to SPC.

The deterministic model for SPC (section 4.1) is expanded to include the HSR performance under scenarios describing the natural hazards conditions. The robust optimization literature reviewed in section 3.1 did not include such a robust planning approach to rail or road infrastructure, both with similarities to HSR. However, robust approaches have been successfully developed and applied to deal with uncertainty in other design problems, including power and water supply systems.

The robust model proposed herein is drawn from the sound results obtained from the deterministic HSR planning optimization model and from the robust approaches for the consideration of uncertainty in other problems.

#### 4.5.1 OBJECTIVE FUNCTION

The model incorporates a robust approach to the HSR planning optimization through the consideration of scenarios representing natural hazards. HSR networks are, in general, subject to the effects of several natural hazards, especially given the considerable distances between the cities to link. The identification of which scenarios to consider for a given project is related with identification of the natural phenomena that can lead to damages of the HSR, within the boundary of the area established for the HSR deployment (the search space of the HSR optimization problem).

The robust approach to the problem is then required to characterize the natural threats determining, for a given HSR cross-section (cut, embankment, bridge or tunnel), at a given height or depth and at a given plan view location, the damages to the infrastructure. The accuracy in estimating which are the damaged sections of the HSR and the costs of the physical damage repair and/or reconstruction depends on the input data available for the assessment. For instance, the damages to the HSR by a scenario including a flood will depend on the accuracy of the flood map in estimating the flood level that, compared with the elevation of earthworks and bridges at each cross-section, allows one to assess the damages.

Having identified and characterized the set of scenarios to consider for the problem,  $\Omega_{SC}$ , and established the procedures to identify the repair/reconstruction costs for any possible HSR configuration, the robust objective function is computed according to expression (4.10).

$$\begin{aligned}
& \text{Min} \sum_{(i,j) \in \Omega_N} C_{ij} [Ex_{(i,j)}, EW_{(i,j)}, B_{(i,j)}, T_{(i,j)}, LD_{(i,j)}] + \sum_{(i,j) \in \Omega_N} P_{\eta_{(i,j)}} [\eta_{(i,j)}, \eta_{normal}, \eta_{limit}, \gamma_{\eta}] + \\
& \sum_{(i,j,k) \in \Omega_N} P_{\beta_{(i,j,k)}} [\beta_{(i,j,k)}, \beta_{normal}, \beta_{limit}, \gamma_{\beta}] + \sum_{(i,j) \in \Omega_N} \sum_{s \in \Omega_E^j} P_{\lambda_s} [l_s, \gamma_{\lambda_s}] - \sum_{i \in \Omega_N} P_{v_i} [\gamma_{v_i}] + \\
& \omega \cdot \sum_{c \in \Omega_{SC}} \Psi_c \left[ \sum_{(i,j) \in \Omega_N} RC_{ij}^c [EW_{(i,j)}, B_{(i,j)}, T_{(i,j)}, LD_{(i,j)}] \right]
\end{aligned} \tag{4.10}$$

Where,

$\Omega_N$  is the set of all 3D nodes of the discretization mesh;

$\Omega_E^{ij}$  is a subset of  $\Omega_E$  (the set of all space property elements in the problem) representing the space property elements overlaid in the plan view by a linear section linking nodes  $i$  and  $j$ ;

$\Omega_{SC}$  is the set of all scenarios  $c$ , each representing a natural hazard;

$\sum_{(i,j) \in \Omega_N} C_{ij}$  expresses the total construction costs and depends on the expropriation costs  $Ex_{(i,j)}$ , the costs of earthworks  $Ew_{(i,j)}$ , bridges  $B_{(i,j)}$  and tunnels  $T_{(i,j)}$  and linear- dependent costs  $LD_{(i,j)}$  of a linear section linking nodes  $i$  and  $j$ ;

$\sum_{(i,j) \in \Omega_N} P_{\eta_{(i,j)}}$  expresses the total penalty value for geometry gradient violation of each linear section linking nodes  $i$  and  $j$ ; it depends on the gradient value of the section  $\eta_{(i,j)}$  and three problem parameters defining the normal gradient  $\eta_{normal}$ , the limit gradient  $\eta_{limit}$  and the gradient penalty coefficient  $\gamma_\eta$ ;

$\sum_{(i,j,k) \in \Omega_N} P_{\beta_{(i,j,k)}}$  expresses the total penalty value for geometry horizontal angle violation at each intermediate node  $j$  of the configuration, formed by the two linear sections linking nodes  $i, j$  and  $k$ ; it depends on the angle value at node  $j$ ,  $\beta_{(i,j,k)}$ , and three problem parameters defining the horizontal angle normal value  $\beta_{normal}$ , the horizontal angle limit value  $\beta_{limit}$  and the horizontal angle penalty coefficient  $\gamma_\beta$ ;

$\sum_{(i,j) \in \Omega_N} \sum_{s \in \Omega_E^{ij}} P_{\lambda_s}$  expresses the total land-use penalty value and depends on the land-use penalty  $P_{\lambda_s}$  of each space property element  $s$  overlaid by each linear section linking nodes  $i$  and  $j$  of the HSR configuration;  $P_{\lambda_s}$  depends on the length  $l_s$  and land use penalty coefficient  $\gamma_{\lambda_s}$  of the space property element  $s$ ;

$\sum_{i \in \Omega_N} P_{v_i}$  expresses the total location benefit value and depends on the location coefficient  $\gamma_{v_i}$  of each node  $i$  of  $\Omega_N$ .

$\sum_{(i,j) \in \Omega_N} RC_{ij}^c$  expresses the total reconstruction/repair costs deriving from scenario  $c$  in  $\Omega_{SC}$  and depends on the costs of earthworks  $Ew_{(i,j)}$ , bridges  $B_{(i,j)}$  and tunnels  $T_{(i,j)}$  and linear- dependent costs  $LD_{(i,j)}$  of a linear section linking nodes  $i$  and  $j$ ;

$\omega$  is a weight trading off the natural hazards performance and the SPC performance;

$\Psi_c$  expresses the weight given to the reconstruction/repair cost of scenario  $c$  in  $\Omega_{SC}$ .



One observes that the robust objective function in expression (4.10) corresponds to the sum of the HSR construction costs, the penalty terms for horizontal angle, gradient and land-use, the location benefit term and the HSR weighted performance for the scenarios set  $\sum_{c \in \Omega_{sc}} \Psi_c \sum_{(i,j) \in \Omega_N} RC_{ij}^c$ , the latter multiplied by  $\omega$ . This represents the sum of the HSR performance measure in SPC, discussed in section 4.1.1, with the HSR performance measure for natural hazards multiplied by  $\omega$ .

The weight  $\omega$  can be used to establish a spectrum of configurations that trade-off the HSR performance for natural hazards with the HSR performance in SPC, analogously to the robust model of expressions (3.18) to (3.21) by Mulvey et al. (1995). Increasing values of  $\omega$  (larger than 1) allow one to search for optimal or near-optimal HSR configurations that give preference to the natural hazards performance compared to the SPC performance (construction costs and configuration layout). In fact, large values of  $\omega$  increase the importance that the natural hazards performance has in the robust objective function, when compared with the SPC, and can be used to obtain solutions less affected by these extreme events. The larger the value of  $\omega$ , the less affected by the natural hazards the solutions are expected to be, always subject to the compliance with the problem constraints. By optimizing the HSR configurations for different values of  $\omega$ , different perspectives of the decision-maker on how much should the natural hazards performance influence the HSR planning can be studied. In theory, increasing  $\omega$  results in solutions that are less affected by the effects of natural hazards but that may also have a worst SPC performance, including larger construction costs. Studies varying the value of  $\omega$  allow one to assess how increasing the robustness for the extreme events affects the construction costs, the cities connected by the HSR, the geometry of the configuration and the crossing of restricted land-use areas. For the judgment on the HSR level of robustness to adopt for extreme events, the analysis of such possible trade-offs, between the natural hazards and SPC performances, supports an informed decision-making.

The weight  $\omega$  multiplies, in the robust objective function, the weighted performance for the scenario set  $\Omega_{sc}$ ,  $\sum_{c \in \Omega_{sc}} \Psi_c \sum_{(i,j) \in \Omega_N} RC_{ij}^c$ . While  $\omega$  is used to establish trade-offs between the SPC and the natural hazards performance, weights  $\Psi_c$  attributed to each scenario  $c$  are used to define the relative importance attributed to each of the scenarios. Such relative importance given to the performance across the different scenarios considers the sum of the weights of all

scenarios equal to one, according to expression (4.11). In assessing the impacts of a given natural hazard, the model accounts only for the direct market losses pertaining to the physical damage repair and/or replacement of damaged sections. Thus, the weighted scenario performance corresponds to the weighted repair/reconstruction costs of the HSR infrastructure.

$$\sum_{c \in \Omega_{sc}} \Psi_c = 1 \quad (4.11)$$

The attribution of the weights by the decision-maker is based on political decisions that should be supported by expert judgment and the consultation of stakeholder panels, considering the problem specifics. Formal procedures for such task exist (section 4.1.1). The weights  $\Psi_c$  reflect the decision-maker's risk aversion to the effects of a particular natural hazard realization relatively to the other possible natural hazards that may affect the search area. Thus, the weighted performance for the scenarios set  $\sum_{c \in \Omega_{sc}} \Psi_c \sum_{(i,j) \in \Omega_N} RC_{ij}^c$  evaluates the solution robustness (Bai et al. 1997; Mulvey et al. 1995). The term in the objective function representing the weighted reconstruction/repair costs deriving from the HSR performance for the scenarios does not explicitly consider the probability of occurrence. However, this should be included in the scenario definition as an element to support the decision of the weights to attribute.

The approach considers repair and reconstruction costs of structures proportional to the initial construction cost, given the respective damage level classified from 0, no damage, up to 1, complete reconstruction required. Thus, the computation of the reconstruction costs  $RC_{ij}^c$  of scenario  $c$  in the linear section linking nodes  $i$  and  $j$  is given by reproducing the costs of earthworks, tunnels and bridges of that linear section, with a cost proportional to the input construction cost, varying at each cross-section with the expected damage level. Expropriation cost is not considered for the reconstruction cost as it represents the ownership (or right-of-way), which is not subject to physical damages by natural hazards.

The remainder terms of the objective function are identical to the SPC model and have been defined in detail in section 4.1.1. The definition of geometry normal and limit values is independent of a given natural hazard occurrence and the values optimizing the performance for SPC are unchanged for the HSR project definition. The same situation occurs for the land-

use and the cities to be connected by the HSR, which result in the formulation of the land-use penalty and the location benefit terms in the objective function.

#### 4.5.2 CONSTRAINTS

The HSR planning robust optimization model also includes location, geometry and land-use constraints, which are identical to the ones defined for the deterministic model in, respectively, sections 4.1.2.1, 4.1.2.2 and 4.1.2.3.

These constraints represent limitations to the HSR infrastructure that need to be observed independently of the natural hazards materialization.



## Chapter 5.

# The Lisbon-Oporto HSR Planning Problem

In 2004 decisions were made to build a new HSR network in Portugal, which included the connection of Lisbon to Oporto, along with various connections to Spain (REFER 2012). The project is part of the TEN-T program of the European Commission which aims at ensuring the cohesion, interconnection and interoperability of the trans-European transport network, as well as access to it (TEN-T EA 2012). The Portuguese High Speed Rail Network company RAVE (*Rede Ferroviária de Alta Velocidade, S.A.*) was created with the objective of coordinating the studies required for decision making in regard to planning, construction, financing and operation (RAVE 2005). Preliminary design studies were conducted along proposed corridors between Lisbon and Oporto (RAVE 2008).

The Lisbon-Oporto case-study characterized in this chapter is based on real data, from several sources, suitable for a planning scale. Also, data obtained from RAVE (2008) is used, in particular for the definition of the unit construction costs of the infrastructure. However, these studies concerned the assessment of proposed HSR corridors, a different perspective from that of the optimization model proposed by this research. The Lisbon-Oporto HSR case-study is herein presented, with the discussion of the specifics for the model application.

The network aims at linking Lisbon, Coimbra and Porto with a passenger-dedicated double-track HSR line. Both between Coimbra and Lisbon and Coimbra and Porto two other cities exist, Leiria and Aveiro, which the case-study considers to be desirable to be served by the HSR line. However, trade-offs need to be accounted for in order to maintain the infrastructure cost sustainable. Figure 5-1 shows the location of the cities to connect represented by nodes plotted on the existing conventional railway network map.

The cities to consider in the case-study are aligned in a North-South direction, along the Atlantic Ocean coast. This fact allowed one to reduce the Lisbon-Oporto HSR case-study area to the  $147.4 * 304.4 \text{ km}^2$  rectangle depicted in Figure 5-1. The search area comprises a region beyond the almost linear north-south alignment of the cities to connect.

This chapter discusses the problem input, including the characterization of the search area and the formulation of seismic and intense rainfall scenarios. The HSR performance assessment within different scenarios accounts only for the repair/reconstruction costs due to the physical damage of the infrastructure. All costs in this chapter refer to 2008 EUR (€), except if otherwise stated.

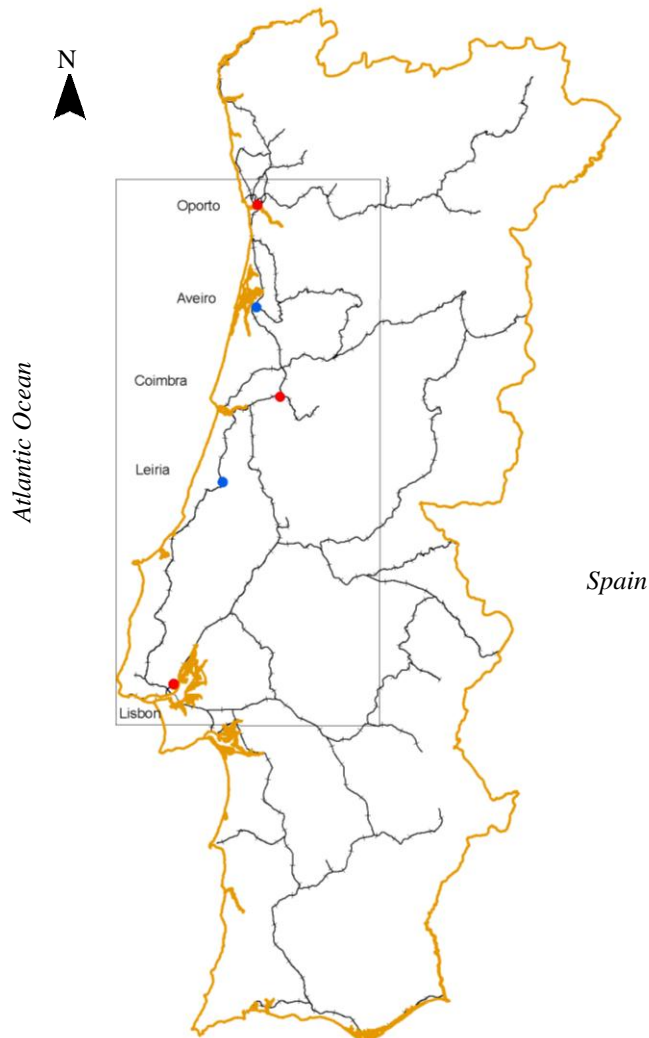


**Figure 5-1** Location of the cities of interest to the Lisbon-Porto HSR case study, the existing conventional railway network and identification of the study area (APA 2012).

## 5.1 INPUT SPATIAL DATA

The input spatial data is formed by digital raster maps. The discretization of each map considers 200 m wide square space property elements ( $\Omega_E$ ). These elements are geo-referenced cells assuming a constant value of the respective map property within its boundaries. The representation is exemplified in Figure 5-2. The original elevation information, formed by 200 m \* 200 m grid points, is considered the center of the elements. Graphically, each distinct value within a map is represented by one color (shade of gray), common to all elements with the same value.

The search area is 147.4 \* 304.4 km<sup>2</sup>, which corresponds to a discretization of 737 by 1,522 space property elements, corresponding to a total of 1,121,714 elements contained in  $\Omega_E$ . Each space property element of the raster map layers is represented by a pixel, not visible to the human eye in the thesis (except for zoom-ins) given the scale limitations of representing the search area in an A4 (21 \* 29.7 cm<sup>2</sup>) paper sheet.

All maps characterizing the search area consider a 3D Cartesian coordinate system. The x- and y- axes presented in Figure 5-3 define the plan view of the problem. The z-coordinate of the system is orthogonal to the plan view and its origin coincides with the origin defined by the Portuguese Geographical Institute of the Army (IGeoE) for mapping Portuguese elevation data.



**Figure 5-2** Zoom of a  $1,200 * 800 \text{ m}^2$  rectangle of the search area: grid elevation data and the corresponding discretization space property elements. Elevation data in meters.

Figure 5-3 a) indicates the 3D Cartesian coordinates of the cities in the format  $(x;y;z)$  with  $x$ - and  $y$ - coordinates in kilometers and the  $z$ -coordinate in meters. Figure 5-3 b) shows a plan view of the discretization mesh of the case-study, considering nodes spaced of 2 km, in both  $x$ - and  $y$ - directions, and 10 m in the  $z$ -direction, starting at the origin of the coordinate system. In addition to these nodes, the problem discretization  $\Omega_N$  includes the 3D points representing Oporto, Coimbra and Lisbon, defined in the plan view by the mesh projection and considering the actual elevation for the nodes, instead of their nearest multiple of 10 m. This prevents the construction of elevated or underground stations for these three cities, which remain a possibility at Aveiro or Leiria.



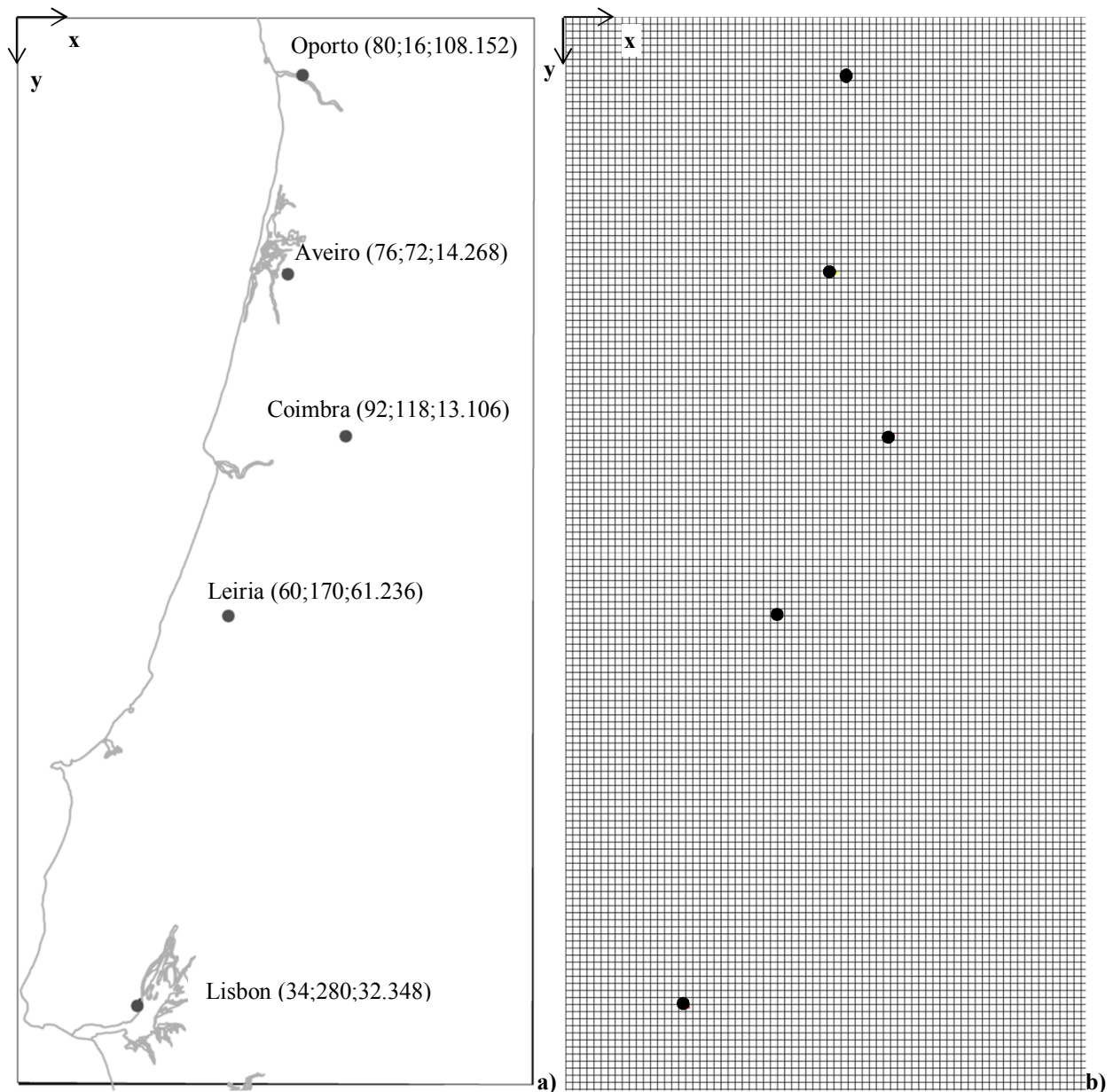


**Figure 5-3** Location of the nodes representing each city: a) by the  $(x;y;z)$  coordinates in  $(\text{km};\text{km};\text{m})$  overlaying the search area map with the Portuguese border and b) overlaying the discretization mesh plan view.

The spatial data characterizing the case-study are presented in sub-sections 5.1.1 through 5.1.5 and are subsequently used for the cross-section definition and construction cost computation described in section 5.3. The spatial data in sub-sections 5.1.1 through 5.1.5 was obtained from two sources: The Portuguese Agency of the Environment (APA) and IGeoE. APA (2012) provides digital nationwide geographic information, for a variety of subjects related to the environment. The information regarding lithology, land-use, ground-use classes and water bodies was obtained from APA data and the elevation data was purchased from

IGeoE. Scenarios representing natural hazards, earthquakes, extreme rainfall and floods, for the study area are defined in sections 5.4 and 5.5. These scenario definitions also use spatial data obtained from APA and IGeoE, amongst other sources.

Independently of the data source, the discretization into space property elements ( $\Omega_E$ ) is identical for any map characterizing the search area of the case-study.

### 5.1.1 LITHOLOGY

A lithological map is provided by APA (2012) in 1/1,000,000 scale, based on the 1972, 1/500,000 Portuguese Geological Map (“Carta Geológica de Portugal”) and a first approximation of the lithological map dated from 1967 (Soares da Silva 1983). The lithological characteristics of the study-area are presented in Figure 5-4 and Table 5-1. Each of the lithological units is described by APA in terms of type (Sedimentary, Metamorphic, Igneous Volcanic and Igneous Plutonic), Era, Period and Epoch of formation and also by a short designation of the soils and/or rocks represented by each unit.

Each color, defined in Table 5-1 by its hexadecimal representation, is unique to each lithological unit and allows one to unequivocally identify the unit in the lithological map in Figure 5-4. APA (2012) also defines unique indices to each of the units mapped in the nationwide map. The indices are not incremented by one in all cases, but it was chosen to maintain the same numbering systems, to avoid errors that could occur during data pretreatment.

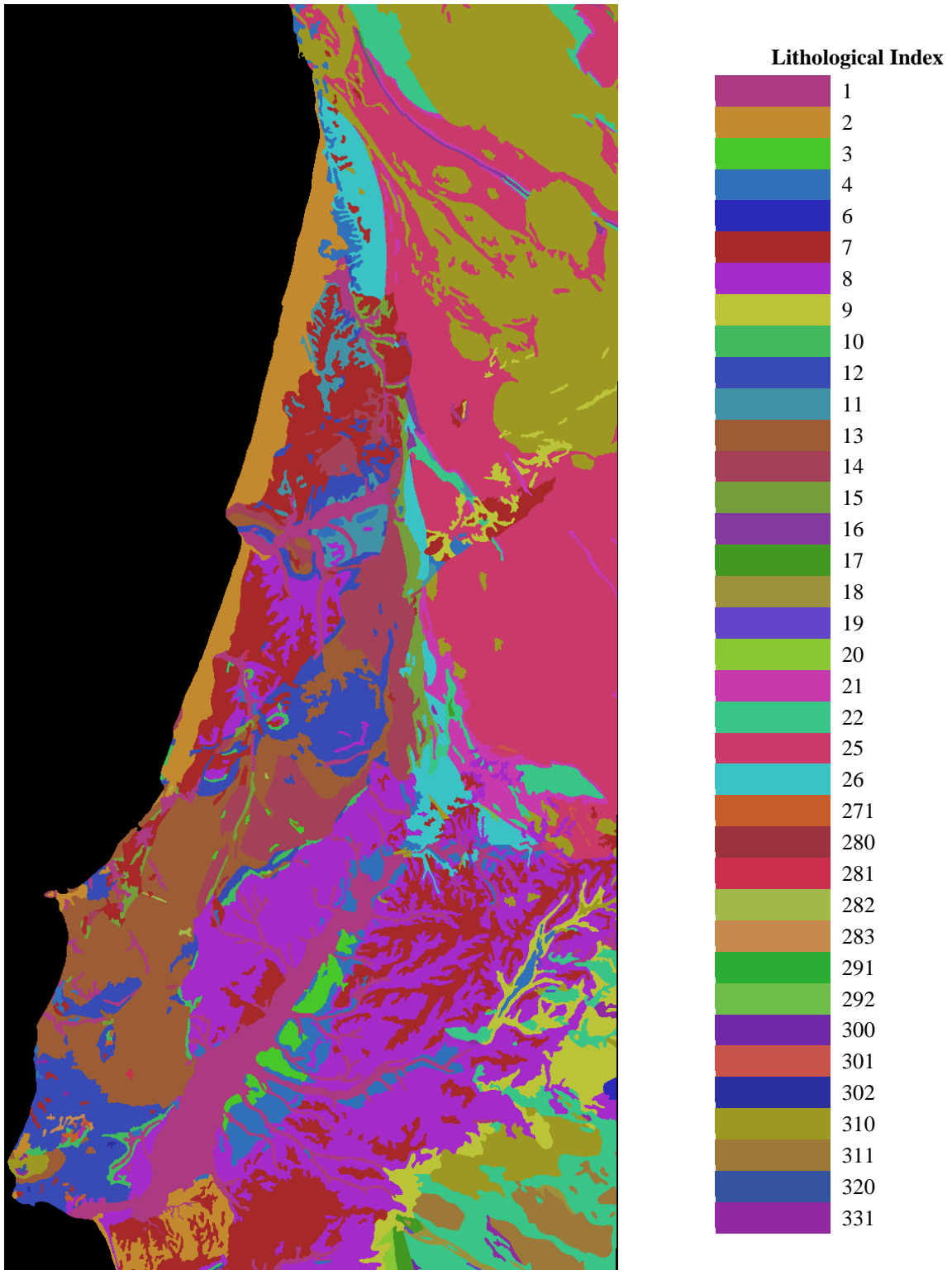


**Figure 5-4** Lithological map of the study area (APA 2012). Scale: 1/1,500,000.

**Table 5-1** Identification of each of the lithological units in Figure 5-4 (APA 2012).

| Unit Index | Hexadecimal Color Code | Type                     | Era       | Period                                    | Epoch             | Lithology Designation  |
|------------|------------------------|--------------------------|-----------|---|-------------------|--|
| 1          | FFAB3A80               | Sedimentary              | Cenozoic  | Quaternary                                | Holocene          | Alluvium   |
| 2          | FFC2892F               | Sedimentary              | Cenozoic  | Quaternary                                | Holocene          | Sand dunes and aeolian sand  |
| 3          | FF47C72A               | Sedimentary              | Cenozoic  | Quaternary                                | Holocene          | Slope deposits (talus), terrace sands  |
| 4          | FF3071BA               | Sedimentary              | Cenozoic  | Quaternary                                | Pleistocene       | Sands and Gravels  |
| 6          | FF2B29BA               | Sedimentary              | Cenozoic  | Quaternary                                | Pleistocene       | Travertine   |
| 7          | FFA62828               | Sedimentary              | Cenozoic  | Plio-Pleistocene                          |                   | Sands, Pebbles, lightly consolidated sandstone, clays  |
| 8          | FFA42AC9               | Sedimentary              | Cenozoic  | Quaternary                                | Mio-Pleistocene   | Sandstones, argillaceous limestones, sands, gravels, clays                                       |
| 9          | FFBBC439               | Sedimentary              | Cenozoic  | Tertiary                                  | Paleogene-Miocene | High plains gravels, Beira-Baixa Arkose, calcareous sandstones                                   |
| 10         | FF41BA5F               | Sedimentary              | Cenozoic  | Tertiary                                  | Paleogene-Miocene | Conglomerates, sandstones, white limestones, red marlstone                                       |
| 12         | FF384BB5               | Sedimentary              | Cenozoic  | Tertiary                                  | Paleogene         | Sandstones, conglomerates, limestones, dolomitic limestones, argillaceous limestones, marlstones |
| 11         | FF4292A6               | Sedimentary              | Mesozoic  | Cretaceous                                | Cretaceous        | Sandstones and Arkose sandstone  |
| 13         | FF9C5D36               | Sedimentary              | Mesozoic  | Jurassic                                  |                   | Conglomerates, sandstones, limestones, dolomitic limestones, argillaceous limestones, marlstones |
| 14         | FFA34158               | Sedimentary              | Mesozoic  | Jurassic                                  |                   | limestones, dolomitic limestones, argillaceous limestones, marlstones                            |
| 15         | FF739E3A               | Sedimentary              | Mesozoic  | Jurassic-Triassic                         |                   | Red sandstones (de Silves), conglomerates, marlstones, limestones (frequently dolomitic)         |
| 16         | FF833A9C               | Sedimentary /Metamorphic | Paleozoic | CPC <sup>(1)</sup>                        |                   | Conglomerates, carbonaceous schists, argillaceous schists  |
| 17         | FF419923               | Sedimentary /Metamorphic | Paleozoic | MC&D <sup>(2)</sup>                       |                   | Argillaceous schists, graywackes, sandstones   |
| 18         | FF9E913C               | Sedimentary /Metamorphic | Paleozoic | since MD <sup>(3)</sup> 'till Precambrian |                   | Metavolcanic Rocks   |
| 19         | FF6444C9               | Sedimentary /Metamorphic | Paleozoic | since MD <sup>(3)</sup> 'till Precambrian |                   | Carbonate rocks  |
| 20         | FF8AC734               | Sedimentary /Metamorphic | Paleozoic | Devonian and Silurian                     |                   | Schists, quartzites, amphibolites  |
| 21         | FFC73AAD               | Sedimentary /Metamorphic | Paleozoic | since Devonian 'till Ordovician           |                   | Quartzites   |
| 22         | FF39C488               | Sedimentary /Metamorphic | Paleozoic | Silurian & Ordovician                     |                   | Schists and graywackes   |
| 25         | FFC93A6A               | Sedimentary /Metamorphic | Paleozoic | since Cambrian 'till Precambrian          |                   | schists, graywackes (complexo xisto-grauvquico)   |
| 26         | FF3BC2C4               | Sedimentary /Metamorphic |           | Precambrian                               |                   | Schists, amphibolites, Mica-schists, graywackes, quartzites, carbonate rocks, gneisses           |
| 271        | FFC75C2A               | Igneous Volcanic         |           |   |                   | pyroclastic rocks (tuffs..)  |

**Table 5-1** Identification of each of the lithological units in Figure 5-4 (APA 2012). (Continued).

| Unit Index | Hexadecimal Color Code | Type                | Era | Period | Epoch | Lithology Designation    |
|------------|------------------------|---------------------|-----|--------|-------|--------------------------|
| 280        | FF9C323B               | Igneous<br>Volcanic |     |        |       | Basalts                  |
| 281        | FFC92E4D               | Igneous<br>Volcanic |     |        |       | Teschenite               |
| 282        | FFA2B849               | Igneous<br>Volcanic |     |        |       | Dolerite                 |
| 283        | FFC78A4E               | Igneous<br>Volcanic |     |        |       | Andesite                 |
| 291        | FF2BAD34               | Igneous<br>Volcanic |     |        |       | Aplites & Pegmatites     |
| 292        | FF6CBD4A               | Igneous<br>Volcanic |     |        |       | Microgranite             |
| 300        | FF7029A6               | Igneous<br>Volcanic |     |        |       | Quartz-porphyry          |
| 301        | FFC9534B               | Igneous<br>Plutonic |     |        |       | Porphyritic granite      |
| 302        | FF2C309E               | Igneous<br>Plutonic |     |        |       | Trachyte                 |
| 310        | FF9C9822               | Igneous<br>Plutonic |     |        |       | Granites and derivations |
| 311        | FF9C7938               | Igneous<br>Plutonic |     |        |       | Quartzdiorite            |
| 320        | FF33539C               | Igneous<br>Plutonic |     |        |       | Syenite                  |
| 331        | FF912AA1               | Igneous<br>Plutonic |     |        |       | Gabbro                   |

Period: <sup>(1)</sup>CPC: Continental Permian Carboniferous ; <sup>(2)</sup>MC&D: Marine Carboniferous and Devonian; <sup>(3)</sup>MD: Marine Devonian

### 5.1.2 LAND-USE

APA (2012) identifies nature preservation areas as presented in the 1/1,500,000 scale map of Figure 5-5. Table 5-2 labels each area by the indices assigned by APA and the hexadecimal color codes that unequivocally identify each area in Figure 5-5.

The protected areas identified by APA (2012) comprise natural reservations, natural parks, protected landscapes, classified sites, dinosaur footprints and fossil sites. The establishment of such protected areas intends the conservation of existing fauna, flora, ecosystems or even historical and archeological sites. Construction within these areas may be forbidden or restricted by law, allowing only infrastructures with minimal impacts or considered as vital at local, regional or national level.

The case-study assumes that the construction of the HSR network is forbidden within all the protected areas, meaning all the space property elements corresponding to indices 9 through

38 of Table 5-2 are contained in the set  $\Omega_{FE}$  of the forbidden land-use elements. Any HSR configuration overlaying these protected areas is unfeasible.

Furthermore, the case-study does not consider land-use restricted areas: the land use penalty coefficient  $\gamma_{\lambda s}$  is null for all space property elements  $s \in \Omega_E$ .

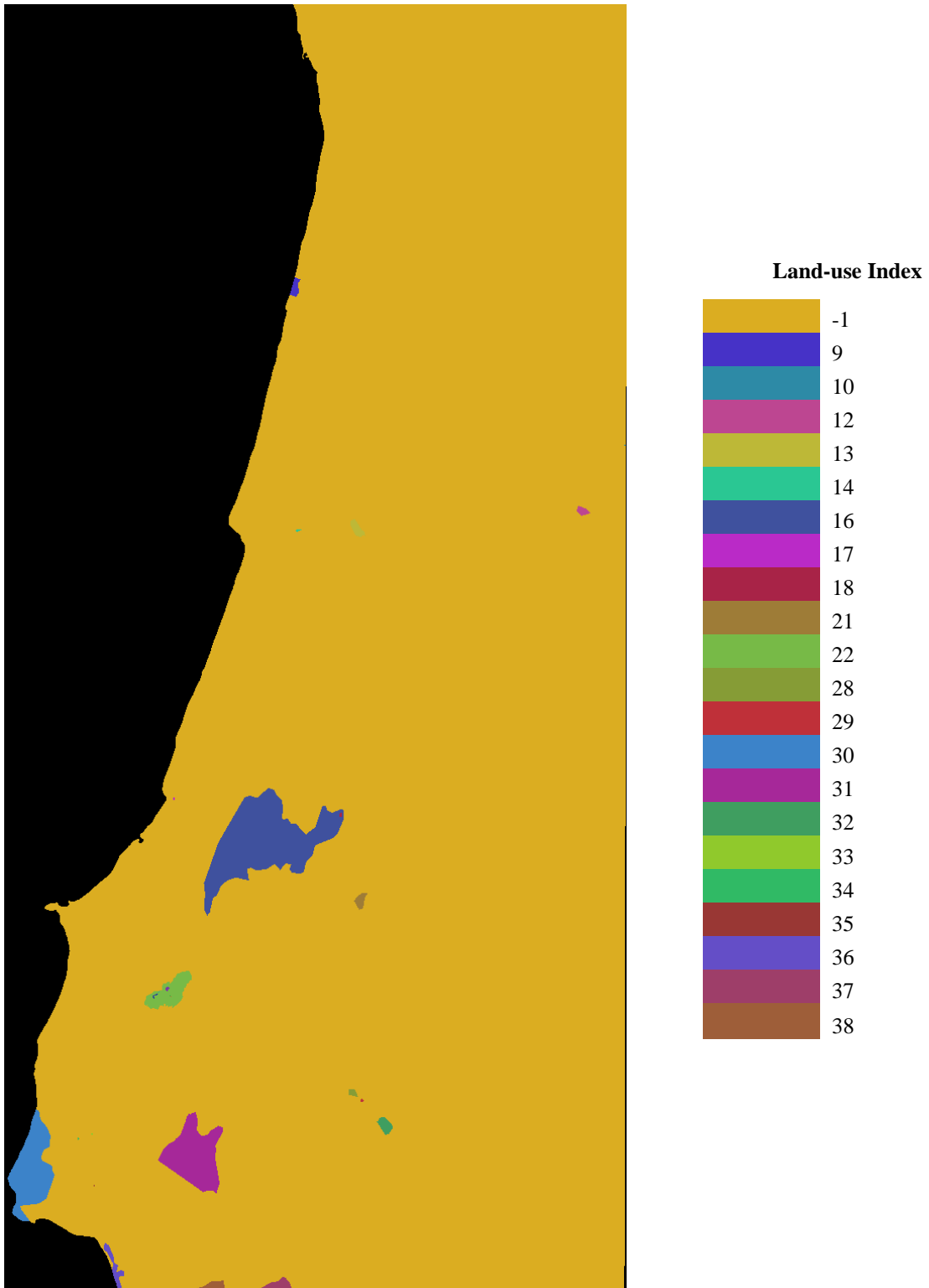


**Figure 5-5** Map of the protected land-use areas(APA 2012). Scale: 1/1,500,000.

**Table 5-2** Identification of each of the preservation areas in Figure 5-5 (APA 2012).

| <b>Index</b> | <b>Hexadecimal Color Code</b> | <b>Designation</b>                                     |
|--------------|-------------------------------|--|
| -1           | FFDBAD21                      | Portuguese territory exempt from land-use restrictions |
| 9            | FF4632C7                      | Dunas de S. Jacinto Natural Reservation                |
| 10           | FF2D8AA6                      | Serra da Estrela Natural Park                          |
| 12           | FFBD4691                      | Serra do Açor Protected Landscape                      |
| 13           | FFBDB837                      | Paúl de Arzila Natural Reservation                     |
| 14           | FF2AC793                      | Montes de Sta Olaia e Ferrestelo Classified Site       |
| 16           | FF3F519E                      | Serras de Aires e Candeeiros Natural Parks             |
| 17           | FFBA2AC7                      | Monte de S. Bartolomeu Classified Site                 |
| 18           | FFA82347                      | Ourém/Torres Novas Dinosaurs Footprints                |
| 21           | FF9E7C37                      | Paúl do Boquilobo Natural Partial Reservation          |
| 22           | FF77BA47                      | Montejunto Mountain                                    |
| 28           | FF869C36                      | Açude da Agolada Classified Site                       |
| 29           | FFBF3039                      | Coruche Historical Center Classified Site              |
| 30           | FF3C83C9                      | Sintra-Cascais Natural Park                            |
| 31           | FFA62899                      | Estuário do Tejo Natural Reservation                   |
| 32           | FF3F9E60                      | Açude do Monte da Barca Classified Site                |
| 33           | FF90C92C                      | Campo de Lapiás dos Serrões Classified Site            |
| 34           | FF30BA65                      | Campo de Lapiás da Granja de Negrals Classified Site   |
| 35           | FF993734                      | Serra de Carenque Fossil Site                          |
| 36           | FF644EC7                      | Costa da Caparica Fossil Cliff Protected Landscape     |
| 37           | FF9E3E69                      | Estuário do Sado Natural Reservation                   |
| 38           | FF9E5E39                      | Arrábida Natural Park                                  |

### 5.1.3 GROUND USE CLASSES: EXPROPRIATION COSTS

Figure 5-6 shows the spatial distribution of ground use (agricultural, forest, social areas, salt evaporation ponds and rivers, ponds and reservoirs) defined by APA (2012) according to Table 5-3. Each class is unequivocally identified by an index and the hexadecimal color code, by which they are represented in the map. Different units with the same ground use are, however, identified in Table 5-3. The reason is that APA (2012) further subdivides the Ground Use Classes beyond the scope of the case study, mapping each subclass separately.



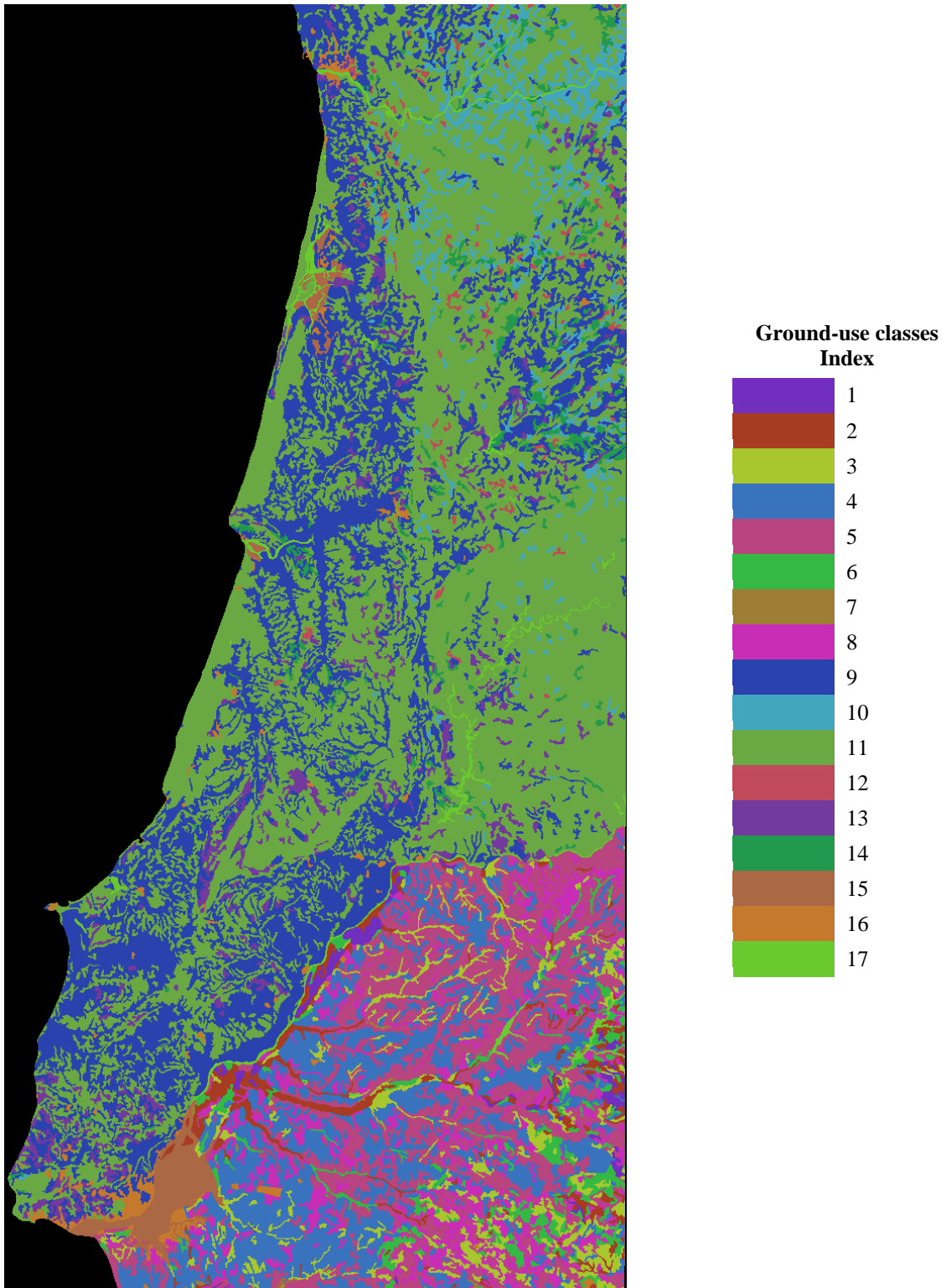


Figure 5-6 Ground use classes map (APA 2012). Scale: 1/1,500,000.

**Table 5-3** Identification of each of ground-use classes in Figure 5-6 (APA 2012).

| <b>Index</b> | <b>Hexadecimal Color Code</b> | <b>Ground Use</b>            |
|--------------|-------------------------------|------------------------------|
| 1            | FF722EBF                      | Agricultural                 |
| 2            | FFA83C23                      | Agricultural                 |
| 3            | FFA8C72E                      | Agricultural                 |
| 4            | FF3972BD                      | Forest                       |
| 5            | FFB84480                      | Forest                       |
| 6            | FF34BA44                      | Agricultural-Multiple        |
| 7            | FF9E7E34                      | Agricultural-Multiple        |
| 8            | FFC72EB5                      | Agricultural-Multiple        |
| 9            | FF2A42AD                      | Agricultural                 |
| 10           | FF42A6BD                      | Agricultural - Conditioned   |
| 11           | FF69A842                      | Forest                       |
| 12           | FFBF4B5A                      | Agricultural-Multiple        |
| 13           | FF713A9C                      | Agricultural-Multiple        |
| 14           | FF23994E                      | Agricultural-Multiple        |
| 15           | FFAB6844                      | Salt Evaporation Ponds       |
| 16           | FFC4792D                      | Social areas                 |
| 17           | FF6BC930                      | Rivers, Ponds and Reservoirs |

The determination of the expropriation costs derives from the ground use planning. Different ground use classes are associated with different land values and hence expropriation costs. The establishment of the unit cost per square meter was based on the principles presented by RAVE (2008). These principles establish the relations between the different ground-use classes and the expropriation values to consider.

Three main expropriation types (Agricultural, Forest and Urban) and respective unit costs are considered (Table 5-4). One of the expropriation types and unit costs was assigned to each of the ground use categories provided by APA (2012) as shown in Table 5-5. As a result, an expropriation cost map is created (Figure 5-7). Unit “17 – Rivers, Ponds and Reservoirs” represents areas that cannot be acquired, thus no expropriation type or costs are assigned.

**Table 5-4** Expropriation types and respective unit costs.

| <b>Expropriation Type</b> | <b>Expropriation unit Cost (€/m<sup>2</sup>)</b> |
|---------------------------|--|
| Agricultural              | 8  |
| Forest                    | 5  |
| Urban                     | 37.5   |

**Table 5-5** Expropriation type for each ground use category provided by APA (2012).

| <b>Index</b> | <b>Ground Use</b>            | <b>Expropriation Type</b> | <b>Expropriation unit Cost (€/m<sup>2</sup>)</b> |
|--------------|------------------------------|---------------------------|--|
| 1            | Agricultural                 | Agricultural              | 8  |
| 2            | Agricultural                 | Agricultural              | 8  |
| 3            | Agricultural                 | Agricultural              | 8  |
| 4            | Forest                       | Forest                    | 5  |
| 5            | Forest                       | Forest                    | 5  |
| 6            | Agricultural-Multiple        | Agricultural              | 8  |
| 7            | Agricultural-Multiple        | Agricultural              | 8  |
| 8            | Agricultural-Multiple        | Agricultural              | 8  |
| 9            | Agricultural                 | Agricultural              | 8  |
| 10           | Agricultural - Conditioned   | Agricultural              | 8  |
| 11           | Forest                       | Forest                    | 5  |
| 12           | Agricultural-Multiple        | Agricultural              | 8  |
| 13           | Agricultural-Multiple        | Agricultural              | 8  |
| 14           | Agricultural-Multiple        | Agricultural              | 8  |
| 15           | Salt Evaporation Ponds       | Agricultural              | 8  |
| 16           | Social areas                 | Urban                     | 37.5   |
| 17           | Rivers, Ponds and Reservoirs | Non applicable            |  |

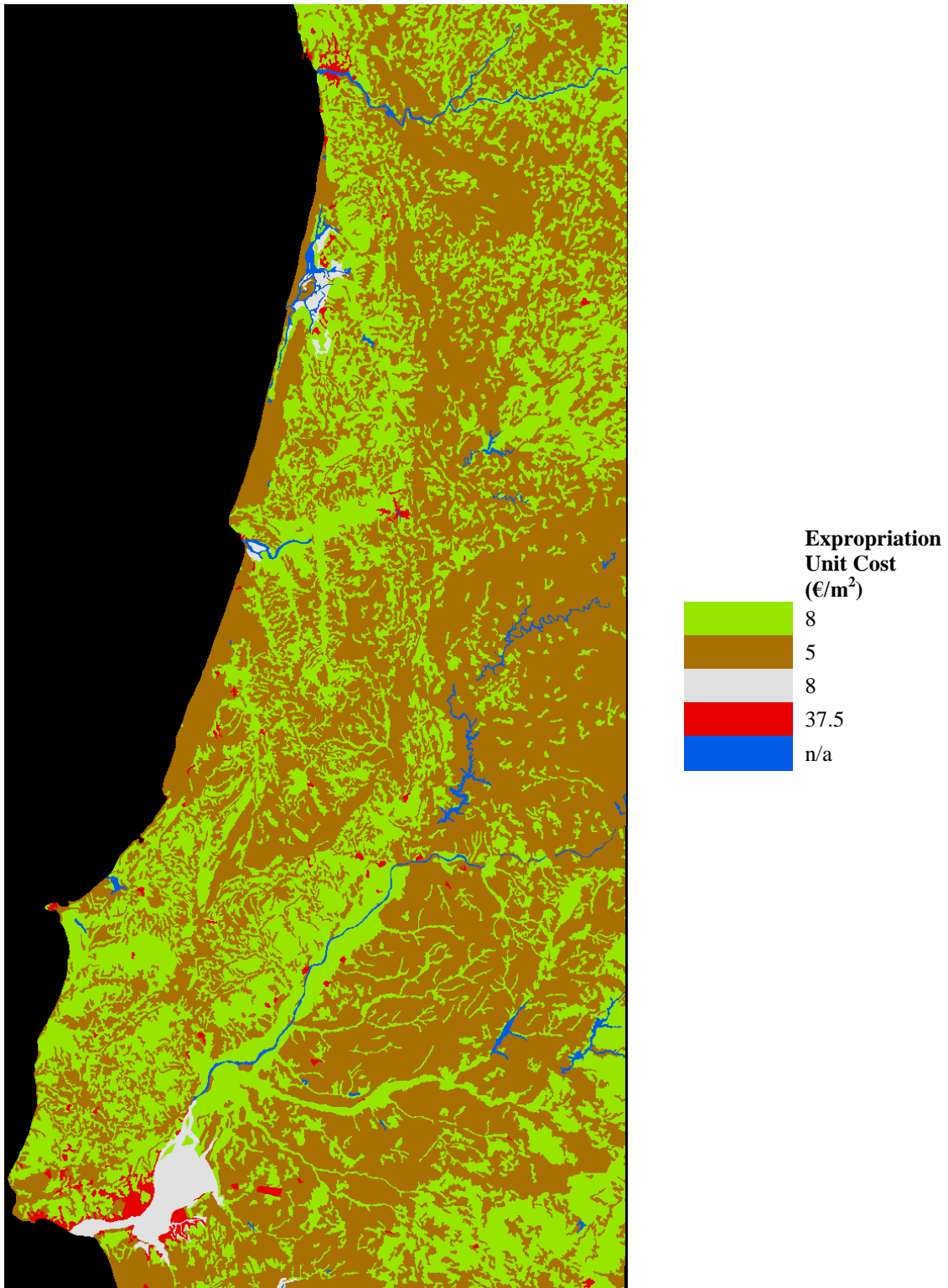
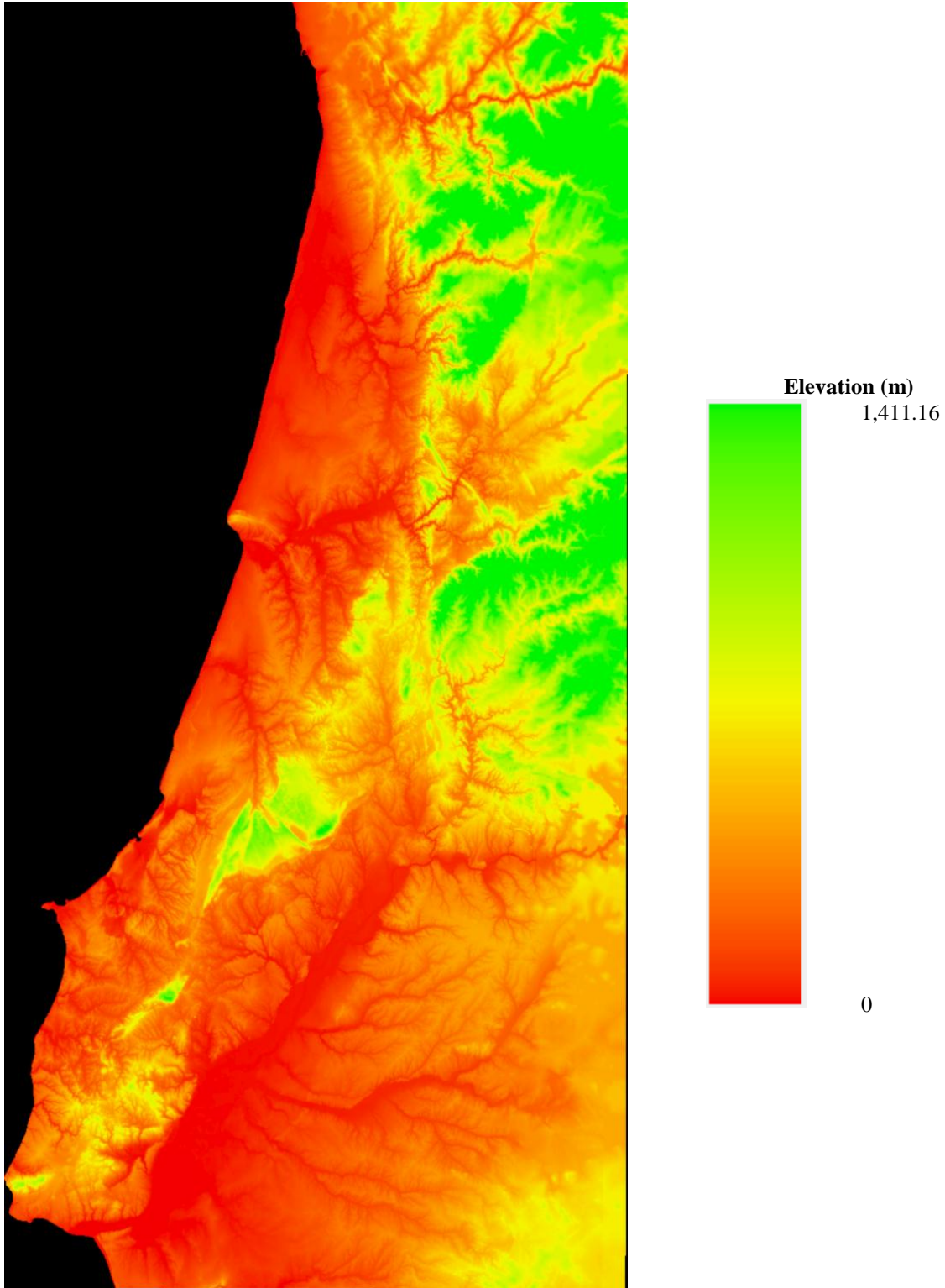


Figure 5-7 Expropriation cost map. Scale: 1/1,500,000.

#### 5.1.4 DIGITAL ELEVATION MODEL

The digital elevation model (DEM) was obtained from the IGeoE. The DEM is formed by the real elevation at points spaced of 200 m in a square grid mesh for the entire search area. The point data is then transformed into the raster data map of Figure 5-8, considering each point positioned at the center of a space property element that represents a uniform elevation equal to the point's elevation. Elevation in the study area ranges from 0 to 1,411.16 m.



**Figure 5-8** Elevation map. Scale: 1/1,500,000.

### 5.1.5 PORTUGUESE MAIN RIVERS

APA (2012) maps the existing rivers in Portugal at a 1/1,000,000 scale. The major rivers are considered in the analysis and represented in Figure 5-9.

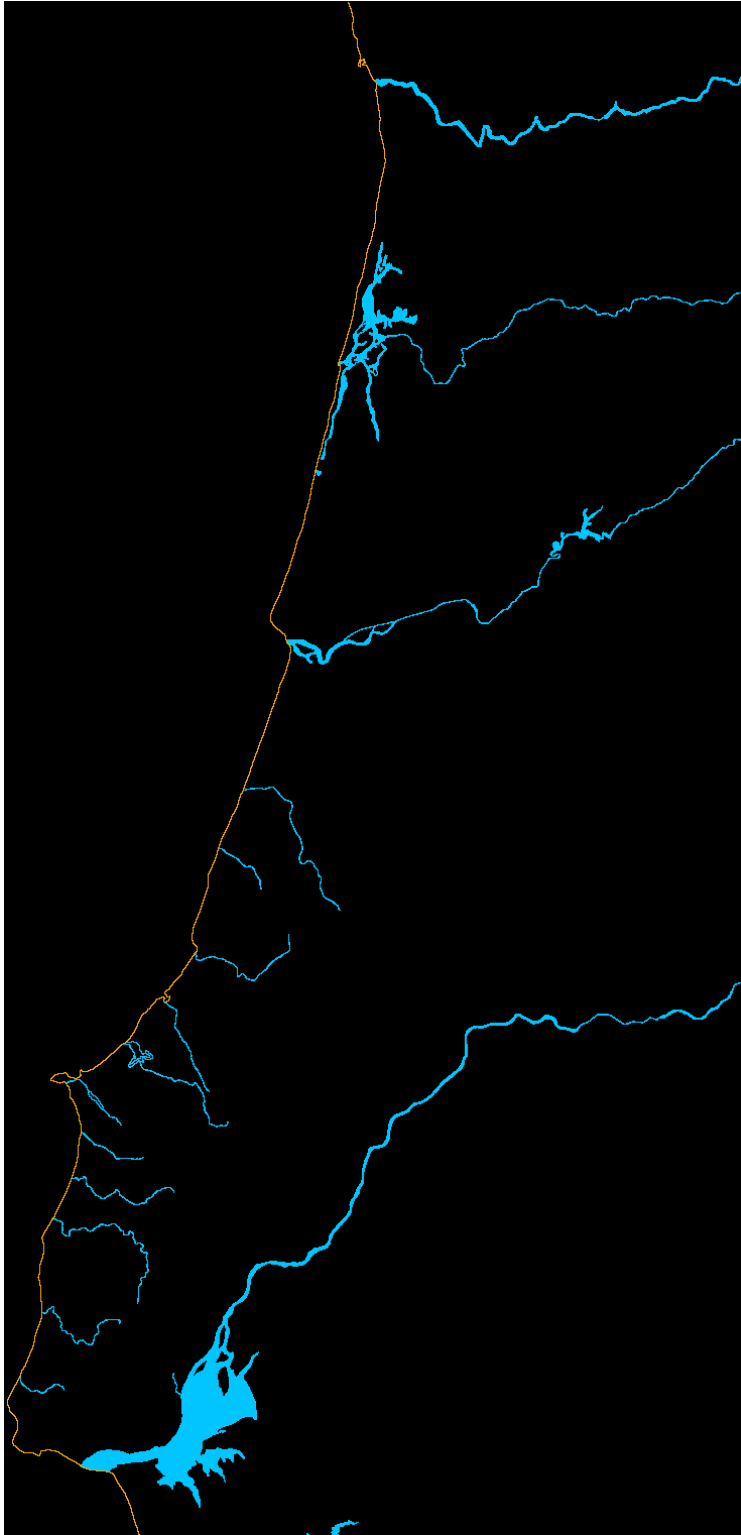


**Figure 5-9** Main rivers map. Scale: 1/1,500,000 (APA 2012).

Feasibility of a given HSR configuration requires that these rivers are crossed by bridges or tunnels. A minimum clearance of 5 m for bridges is required. As an example useful for design practice, additional navigability clearances are considered for the Tagus River. The existing bridges crossing the Tagus River in the Lisbon area, downstream of the depicted cross-sectional line in Figure 5-10, have circa 70 m height above the water level. Given the importance of maintaining navigability in the river, the case study includes a HSR feasibility criterion establishing the minimum height of 70 m for bridges crossing the Tagus, downstream of the cross-section line in Figure 5-10.



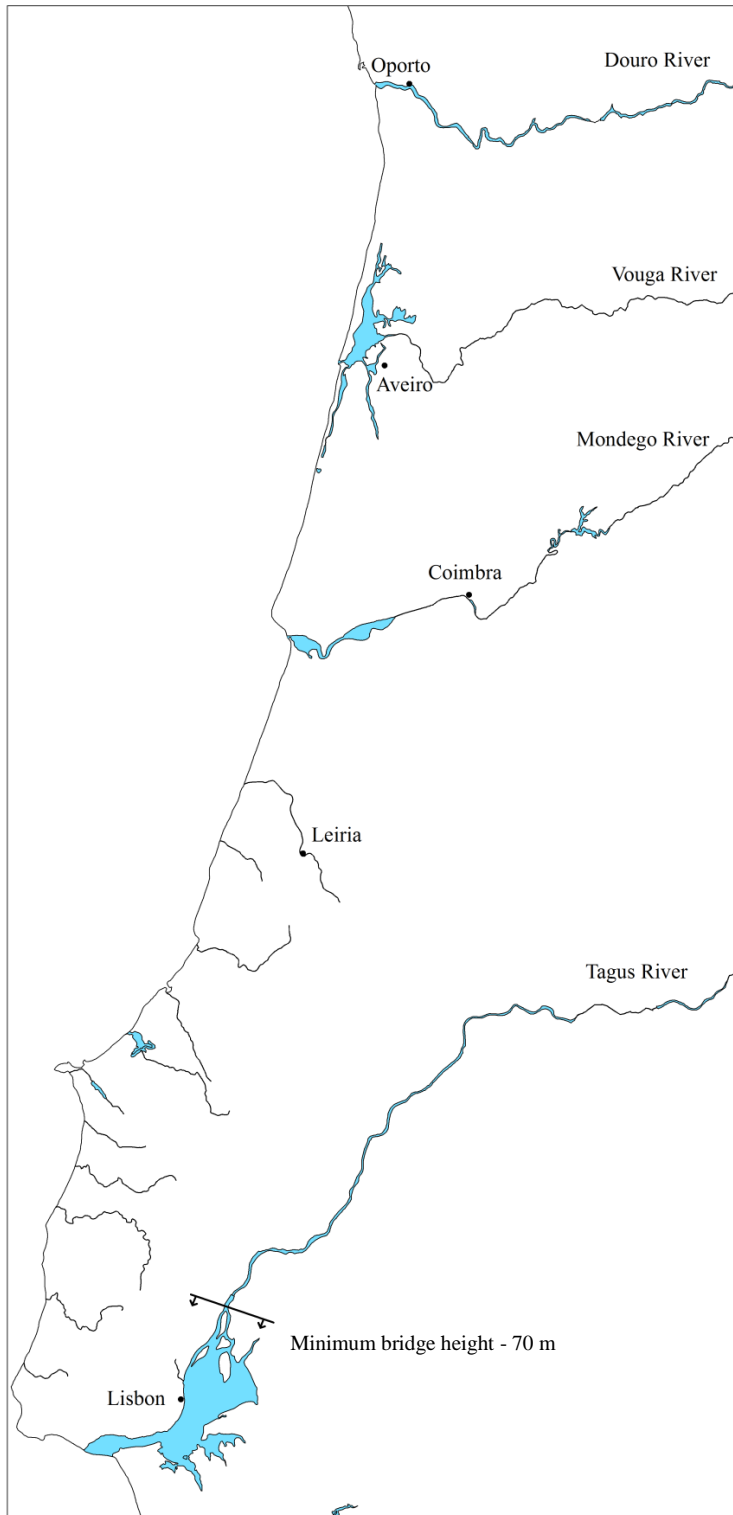


**Figure 5-10** Main rivers' map, location of the cross-section line defining the upstream limits of the 70 m bridge height feasibility requirement and location of the cities to connect with the HSR.

## 5.2 HSR CONFIGURATION GEOMETRY LAYOUT

The HSR normal and limit gradient values, respectively,  $\eta_{normal}$  and  $\eta_{limit}$ , to define for a given type of traffic and design speed can be derived directly from existing standards (section 2.1.3). In fact, considering a passenger-dedicated line and a design speed between 250 km/h and 300 km/h,  $\eta_{limit} = 35\text{‰}$  and  $\eta_{normal} = 20\text{‰}$  are considered. The definition of the horizontal angle limit and normal values, however, requires a study between the correlation of the angles and the curves' radii.

### 5.2.1 HORIZONTAL ANGLE LIMIT AND NORMAL VALUES

The definition of the horizontal angle limit and normal values results from representing the HSR configuration by linear sections only, as a simplification of reality, when in fact circular curves and radii changing (transition) curves are additionally used. Section 2.1.2 introduces the drivers of minimum limit and recommended radii of curves in the plan view design of HSR that, given the simplifications, are represented by the horizontal angle limit and normal values.

While the radii limit and normal values can be derived from existing standards, for the HSR project specifics, the horizontal angles do not have a direct correlation to the standards' provisions. Geometrically, the radii of a given curve to be inserted within 2 concurrent linear sections, in a manner that the curve is tangent at both ends to the linear sections, is dependent on the segments' length and the angle formed by the segments. In this regard, the analysis in Figure 5-11 was performed, varying the curves' parameters for three different horizontal angles. The figure shows:

- for  $\beta=100^\circ$  and  $\beta=120^\circ$  the external secant ( $\Delta$ ) and the tangent (T) values resulting from the insertion of a circular curve of 4000 m radius (R) between two linear sections;
- for  $\beta=100^\circ$ ,  $\beta=120^\circ$  and  $\beta=140^\circ$  the tangent and radius of a circular curve between two linear sections corresponding to an external secant of 300 m.

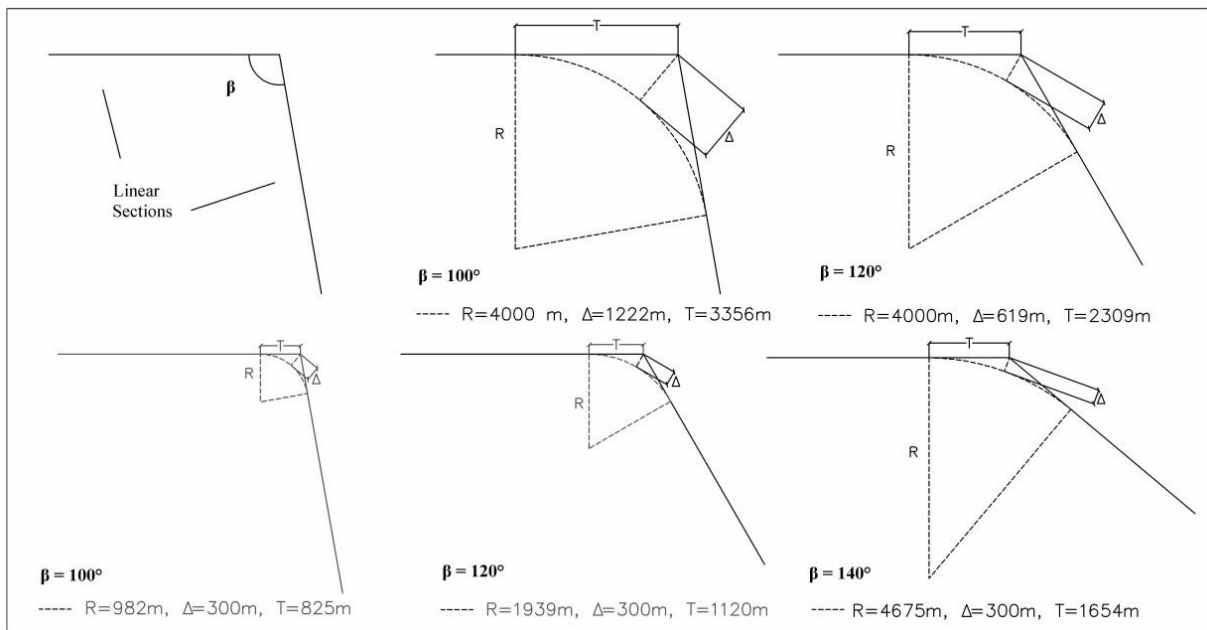


**Figure 5-11** Variations of the external secant ( $\Delta$ ), the curve radius (R) and the tangent (T) for three horizontal angles:  $\beta = 100^\circ$ ,  $\beta = 120^\circ$  and  $\beta = 140^\circ$ .

One observes that for increasing angles between the linear sections ( $\beta$ ), the insertion of a curve with the same radius corresponds to a decreasing tangent (T) defining the minimum length of the linear sections and a decreasing gap (the external secant  $\Delta$ ) between the linear alignments and the arc of the curve. In a different perspective, a constant external secant  $\Delta$  corresponds, for increasing  $\beta$ , to larger radii.

The definition of the normal and limit horizontal angles of the case-study considers a fixed maximum gap (external secant  $\Delta$ ) between the alignments and the curve. The limitation of the external secant is required since the infrastructure costs vary significantly with the plan view location. This limitation ensures that the simplified HSR representation by linear alignments optimized by the model is in fact spatially correlated to the real HSR defined by curves and linear sections, which the model aims at representing. If large gaps were to be allowed, the HSR representation that is optimized by the model could have little correlation to the actual HSR that could be deployed based on those linear sections.

The Lisbon-Oporto case-study considers 200 m wide squares for the space property elements. This implies that from the center of a given space property element, where a node is positioned, 300 m is the maximum radial distance for which any point is located within the

adjacent space property element, in any given direction (Figure 5-12). Considering the gap between the node of the linear alignments (representing the HSR configuration in the model) and a circular curve that may be inserted at that intermediate node limited to one space property element,  $\Delta \leq 300$  m, one observes that the maximum radii are, respectively, for  $\beta=100^\circ$ ,  $\beta=120^\circ$  and  $\beta=140^\circ$ , respectively, 982 m, 1939m and 4675m.

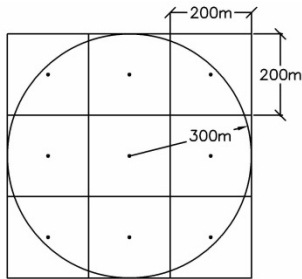


**Figure 5-12** Maximum distance from a space property element center for which boundary is within an adjacent space property element, in any given direction.

Table 2-1, in section 2.1.2., shows that the SNCF indicates the recommended and limit radii for a 300km/h line speed of, respectively, 4545 m and 4000 m. Given the evidence of the maximum radii for a limited external secant varying with the horizontal angle, the normal and limit horizontal angles considered are  $\beta_{\text{normal}} = 140^\circ$  and  $\beta_{\text{limit}} = 120^\circ$ . While a normal angle of  $140^\circ$  allows the inscription of a 4545 m radius circular curve at an external secant of 300 m, a limit angle of  $120^\circ$  does not allow the inscription of the respective 4000 m radius circular curve. However,  $\beta_{\text{limit}} = 120^\circ$  is considered as the limit of feasibility defining the horizontal angle problem constraint. This increases the sinuousness allowed in the generation of new feasible HSR candidate solutions during optimization process. Larger limit horizontal angles, more restrictive, would hamper overcoming the difficulties imposed by the problem constraints such as the forbidden land-use areas, as described in section 4.4.1. This issue is further discussed in chapter 6 with the observations from applying and solving the proposed SPC model to the Lisbon-Oporto case-study. The chosen limit value  $\beta_{\text{limit}} = 120^\circ$  thus aims at facilitating a comprehensive exploration of the search space by algorithm used to solve the models proposed in this research.

### 5.2.2 MINIMUM LENGTH OF THE HSR LINEAR SECTIONS

In addition to the horizontal normal and limit angles, a minimum length for the linear sections composing the HSR configuration is established. From Figure 5-11 one observes that a minimum length equal to the tangent is required for inserting a circular curve between two linear alignments. Initial applications to the Lisbon-Oporto SPC case-study (Figure 4-22) also revealed that node clusters may form without a minimum length imposed to the linear sections (section 4.4.2), and propagate to the algorithm's best found configuration.

The minimum length of the linear sections composing a HSR configuration is set at 4000 m. This length allows the insertion of two consecutive curves of radius larger than 4500 m (recommended by SNCF for 300km/h) at a maximum external secant of 300 m (Figure 5-11). Note that a tangent  $T = 1654$  m corresponds to a radius of  $R = 4675$  m for  $\Delta = 300$  m, which is less than half of the linear section's 4,000 m length.

## 5.3 CROSS-SECTIONS AND CONSTRUCTION COSTS

Construction costs represent the sum of the partial costs for expropriation, earthworks (cuts and embankments), tunnels, bridges and linear- dependent (track, ballast and catenary) costs. These costs, except for the length dependent ones, are determined by the cross-sections that, in turn, depend on the local ground characteristics (elevation, lithological unit, and ground-use type). The cross-section specifics and the unit costs are defined as shown below.

### 5.3.1 EXPROPRIATION COSTS

Expropriation costs are computed by overlaying the HSR configuration in the expropriation cost map of Figure 5-7, as defined in section 4.1.1.1. An offset of 8 m beyond the footprint of the HSR is considered for the computation of the area to expropriate, according to RAVE (2008).

### 5.3.2 EARTHWORKS

Based on the available information from Table 5-1 and RAVE (2008), the cross section specifics for the case study are defined in Table 5-6. Geological and geotechnical studies were

conducted by RAVE (2008) along proposed corridors to establish the Lisbon-Oporto HSR link. These studies comprise *in situ* and laboratory testing to determine the geotechnical behavior of the majority of the units presented in Table 5-1. The definition of cross-section specifics is then based on the geological and geotechnical characterization of the deposits. RAVE (2008) studies are, however, more detailed than the scope of this research but comprise only part of the lithological units identified within the study area. Thus, the definition of the cross-section specifics for the case study is based on the general results from the geological and geotechnical analyses and on engineering judgment, when the lithological units are not covered by the corridors studied by RAVE (2008).

The cross sections of the HSR network (cuts, embankments, tunnels and bridges) to adopt are unequivocally defined by the elevation difference between the natural ground and the planned HSR configuration, except when crossing bodies of water. A more detailed analysis could be used, but this would significantly increase the complexity of the problem. A trade-off between the level of detail and the complexity of the resulting problem is considered. The cross-sections are schematically presented in Figure 5-13, Figure 5-14, Figure 5-15, Figure 5-16 and Figure 5-17 considering a 14 m wide platform for the double track HSR.

**Table 5-6** Cross-section specifics dependent on the lithological unit.

| Information of the lithology layer of the Environmental Atlas (APA 2012) |      |                  |                   |  | Considerations of the analysis |                 |                   |                |               |                          |                   |
|--|------|------------------|-------------------|--|--------------------------------|-----------------|-------------------|----------------|---------------|--------------------------|-------------------|
| Index  | Type | Period           | Epoch             | Designation  | Emb. Slope (V/H)               | Cut Slope (V/H) | Excavation Method |                | GI            | Form Layer Thickness (m) | Tunnel Cost (€/m) |
|  |      |                  |                   |  |                                |                 | MM (V %)          | Blasting (V %) | R&R Depth (m) |                          |                   |
| 1  | Sed. | Quaternary       | Holocene          | Alluvium   | 1/2                            | 1/2             | 100%              | 0%             | 5             | 0.5                      | 35000             |
| 2  | Sed. | Quaternary       | Holocene          | Sand dunes and aeolian sand  | 1/2                            | 1/2             | 100%              | 0%             | 1             | 0.5                      | 35000             |
| 3  | Sed. | Quaternary       | Holocene          | Slope deposits (talus), terrace sands  | 1/2                            | 1/2             | 100%              | 0%             | 2             | 0.5                      | 35000             |
| 4  | Sed. | Quaternary       | Pleistocene       | Sands and Gravels  | 1/2                            | 1/2             | 100%              | 0%             | 1             | 0.5                      | 35000             |
| 6  | Sed. | Quaternary       | Pleistocene       | Travertine   | 1/2                            | 1/2             | 100%              | 0%             | 1             | 0.5                      | 35000             |
| 7  | Sed. | Plio-Pleistocene |                   | Sands, pebbles, lightly consolidated sandstone, clays  | 1/2                            | 1/2             | 100%              | 0%             | 2             | 0.5                      | 35000             |
| 8  | Sed. | Quaternary       | Mio-Pleistocene   | Sandstones, argillaceous limestones, sands, gravels, clays                                       | 1/2                            | 1/2             | 100%              | 0%             | 2             | 0.5                      | 35000             |
| 9  | Sed. | Tertiary         | Paleogene-Miocene | High plains gravels, Beira-Baixa Arkose, calcareous sandstones                                   | 1/2                            | 1/2             | 100%              | 0%             | 1             | 0.5                      | 35000             |
| 10   | Sed. | Tertiary         | Paleogene-Miocene | Conglomerates, sandstones, white limestones, red marlstone                                       | 1/2                            | 1/2             | 100%              | 0%             | 1             | 0.5                      | 35000             |
| 12   | Sed. | Tertiary         | Paleogene         | Sandstones, conglomerates, limestones, dolomitic limestones, argillaceous limestones, marlstones | 1/2                            | 1/2             | 100%              | 0%             | 1             | 0.5                      | 35000             |
| 11   | Sed. | Cretaceous       | Cretaceous        | Sandstones and Arkose sandstone  | 1/2                            | 1/1.5           | 50%               | 50%            | 1             | 0.35                     | 35000             |
| 13   | Sed. | Jurassic         |                   | Conglomerates, sandstones, limestones, dolomitic limestones, argillaceous limestones, marlstones | 1/2                            | 1/1             | 50%               | 50%            | 0             | 0.35                     | 35000             |
| 14   | Sed. | Jurassic         |                   | Limestones, dolomitic limestones, argillaceous limestones, marlstones                            | 1/2                            | 1/1             | 50%               | 50%            | 0             | 0.35                     | 35000             |

**Table 5-6** Cross-section specifics dependent on the lithological unit. (Continued).

| Information of the lithology layer of the Environmental Atlas (APA 2012) |          |                                  |       |  |                  | Considerations of the analysis |                   |                |               |                          |                   |
|--|----------|----------------------------------|-------|--|------------------|--------------------------------|-------------------|----------------|---------------|--------------------------|-------------------|
| Index  | Type     | Period                           | Epoch | Designation  | Emb. Slope (V/H) | Cut Slope (V/H)                | Excavation Method |                | GI            | Form Layer Thickness (m) | Tunnel Cost (€/m) |
|  |          |                                  |       |  |                  |                                | MM (V %)          | Blasting (V %) | R&R Depth (m) |                          |                   |
| 15   | Sed.     | Jurassic-Triassic                |       | Red sandstones (de Silves), conglomerates, marlstones, limestones (frequently dolomitic) | 1/2              | 1/1                            | 50%               | 50%            | 0             | 0.35                     | 35000             |
| 16   | Sed.&Met | CPC                              |       | Conglomerates, carbonaceous schists, argillaceous schists                                | 1/2              | 1/1                            | 50%               | 50%            | 0             | 0.35                     | 35000             |
| 17   | Sed.&Met | MC&D                             |       | Argillaceous schists, graywackes, sandstones   | 1/2              | 1/1                            | 50%               | 50%            | 0             | 0.35                     | 35000             |
| 18   | Sed.&Met | since MD 'till Precambrian       |       | Metavolcanic Rocks   | 1/2              | 1/1                            | 50%               | 50%            | 0             | 0.35                     | 35000             |
| 19   | Sed.&Met | since MD 'till Precambrian       |       | Carbonate rocks  | 1/2              | 1/1                            | 50%               | 50%            | 0             | 0.35                     | 35000             |
| 20   | Sed.&Met | Devonian and Silurian            |       | Schists, quartzites, amphibolites  | 1/2              | 1/1                            | 50%               | 50%            | 0             | 0.35                     | 35000             |
| 21   | Sed.&Met | since Devonian 'till Ordovician  |       | Quartzites   | 1/2              | 1/1                            | 50%               | 50%            | 0             | 0.35                     | 35000             |
| 22   | Sed.&Met | Silurian & Ordovician            |       | Schists and graywackes   | 1/2              | 1/1                            | 50%               | 50%            | 0             | 0.35                     | 35000             |
| 25   | Sed.&Met | since Cambrian 'till Precambrian |       | schists, graywackes (complexo xisto-grauváquico)   | 1/2              | 1/1                            | 50%               | 50%            | 0             | 0.35                     | 35000             |
| 26   | Sed.&Met | Precambrian                      |       | Schists, amphibolites, Mica-schists, graywackes, quartzites, carbonate rocks, gneisses   | 1/2              | 1/1                            | 50%               | 50%            | 0             | 0.35                     | 35000             |
| 271  | Ig. Volc |                                  |       | pyroclastic rocks (tuffs..)  | 1/2              | 2/1                            | 0%                | 100%           | 0             | 0.35                     | 35000             |
| 280  | Ig. Volc |                                  |       | Basalts  | 1/2              | 2/1                            | 0%                | 100%           | 0             | 0.35                     | 35000             |



**Table 5-6** Cross-section specifics dependent on the lithological unit. (Continued).

| Information of the lithology layer of the Environmental Atlas (APA 2012) |           |        |       |                          |                  | Considerations of the analysis |                   |                |               |                          |                   |
|--|-----------|--------|-------|--------------------------|------------------|--------------------------------|-------------------|----------------|---------------|--------------------------|-------------------|
| Index  | Type      | Period | Epoch | Designation              | Emb. Slope (V/H) | Cut Slope (V/H)                | Excavation Method |                | GI            | Form Layer Thickness (m) | Tunnel Cost (€/m) |
|  |           |        |       |                          |                  |                                | MM (V %)          | Blasting (V %) | R&R Depth (m) |                          |                   |
| 281  | Ig. Volc  |        |       | Teschenite               | 1/2              | 2/1                            | 0%                | 100%           | 0             | 0.35                     | 35000             |
| 282  | Ig. Volc  |        |       | Dolerite                 | 1/2              | 2/1                            | 0%                | 100%           | 0             | 0.35                     | 35000             |
| 283  | Ig. Volc  |        |       | Andesite                 | 1/2              | 2/1                            | 0%                | 100%           | 0             | 0.35                     | 35000             |
| 291  | Ig. Volc  |        |       | Aplites & Pegmatites     | 1/2              | 2/1                            | 0%                | 100%           | 0             | 0.35                     | 35000             |
| 292  | Ig. Volc  |        |       | Microgranite             | 1/2              | 2/1                            | 0%                | 100%           | 0             | 0.35                     | 35000             |
| 300  | Ig. Volc  |        |       | Quartz-porphry           | 1/2              | 2/1                            | 0%                | 100%           | 0             | 0.35                     | 35000             |
| 301  | Ig. Plut. |        |       | Porphyritic granite      | 1/2              | 2/1                            | 0%                | 100%           | 0             | 0                        | 35000             |
| 302  | Ig. Plut. |        |       | Trachyte                 | 1/2              | 2/1                            | 0%                | 100%           | 0             | 0                        | 35000             |
| 310  | Ig. Plut. |        |       | Granites and derivations | 1/2              | 2/1                            | 0%                | 100%           | 0             | 0                        | 35000             |
| 311  | Ig. Plut. |        |       | Quartzdiorite            | 1/2              | 2/1                            | 0%                | 100%           | 0             | 0                        | 35000             |
| 320  | Ig. Plut. |        |       | Syenite                  | 1/2              | 2/1                            | 0%                | 100%           | 0             | 0                        | 35000             |
| 331  | Ig. Plut. |        |       | Gabbro                   | 1/2              | 2/1                            | 0%                | 100%           | 0             | 0                        | 35000             |

Notes:

Type: Sed.: Sedimentary Rocks / Sed. & Met.: Sedimentary and Metamorphic Rocks / Ig. Volc.: Igneous Volcanic Rocks; Ig. Plut.: Igneous Plutonic RocksPeriod: CPC: Continental Permian Carboniferous / MC&D: Marine Carboniferous and Devonian / MD: Marine DevonianConsiderations of the analysis: Emb.: Embankment / MM: Mechanical methods / V %: Volume % / GI: Ground Improvement / R&R: Removal and Replacement

Embankments are implemented for sections less than 20 m high (Figure 5-13). When the height difference between the HSR configuration and the natural ground is larger than 10 m, a 3 m wide side bench is placed at a 10 m vertical distance from the top. A viaduct or a bridge is implemented when the height to overcome is greater than 20 m.

Slopes of 1/2 (V/H) inclination are defined for all embankments along the HSR (Figure 5-13; Table 5-6). RAVE (2008) estimates this slope is appropriate to the majority of the geotechnical characteristics of the planned embankments while allowing one to balance the embankment/cut volumes and to implement natural vegetation coatings on the lateral slope areas. Although specific embankments may require different inclinations, it is assumed that slopes of 1/2 (V/H) are representative for budget estimate purposes in a planning scale.

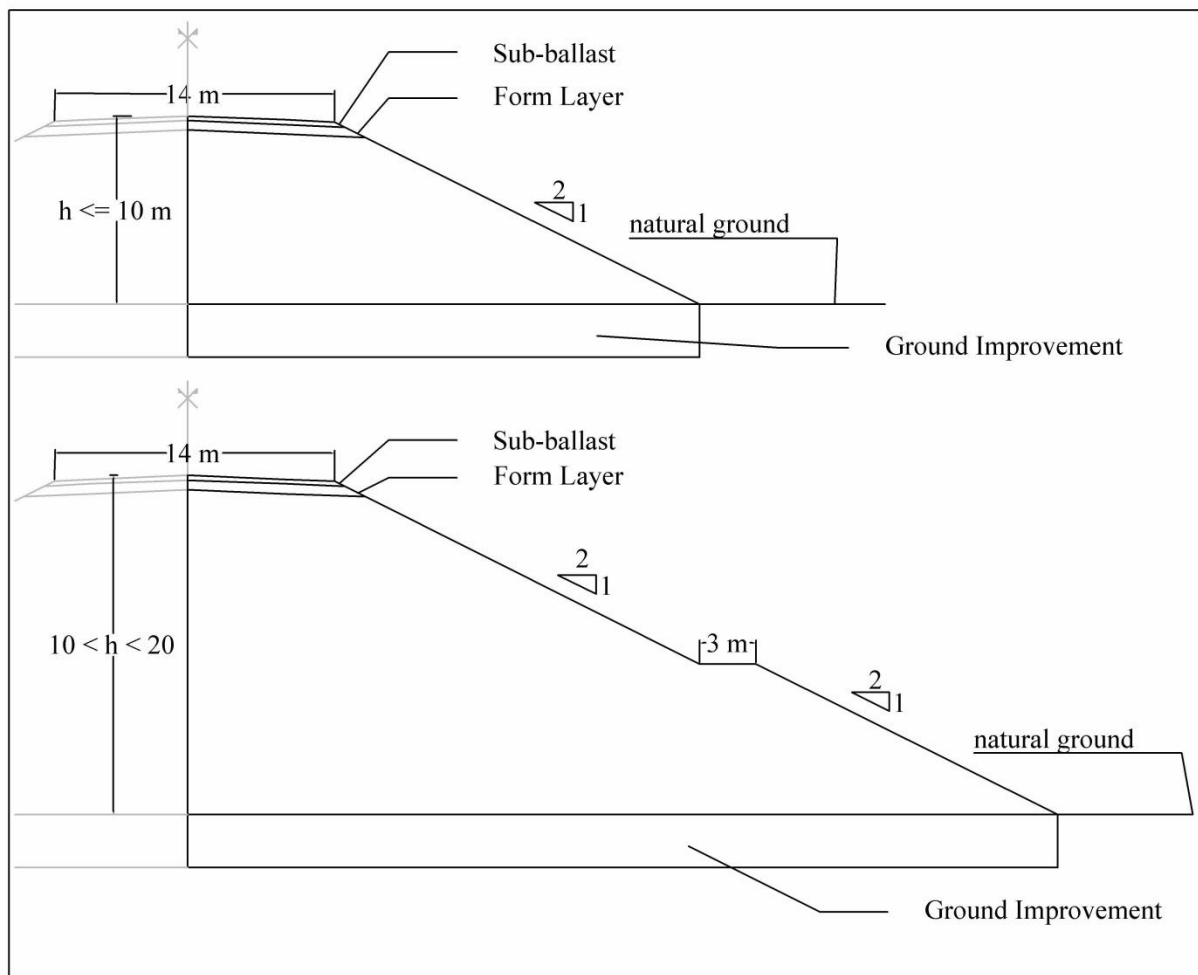


**Figure 5-13** General cross-sections for embankments.

Cuts are implemented for sections less than 34 m deep (Figure 5-14, Figure 5-15, Figure 5-16 and Figure 5-17). When the height difference between the planned alignment and the natural ground is larger than 8 m, 3 m wide side benches are considered, at intervals of 8 m from each other and starting at 8 m vertical distance from the platform. Based on the studies from RAVE (2008), for cuts deeper than 34 m, a tunnel cross-section is implemented.

Cut slopes vary with the lithological unit (Figure 5-14 to Figure 5-17; Table 5-6). The expected slope stability behavior, based on the geological and geotechnical characteristics, determines the slope inclination assigned to each lithological unit. Recent formations with little cohesion (Tertiary period) are considered to require a 1/2 (V/H) slope. The lithological unit of Cretaceous Sandstones and Arkose Sandstones, is cut with a 1/1.5 (V/H) slope. Excavation in all the remaining Sedimentary and Metamorphic Rocks considers a 1/1 (V/H) cut slope. Igneous Plutonic Rocks, Syenite and Gabbro, are excavated with a 2/1 (V/H) cut slope. Analogously to embankments, such lateral cut slopes are considered to be representative for budget estimate purposes but specific cuts may require different slopes.

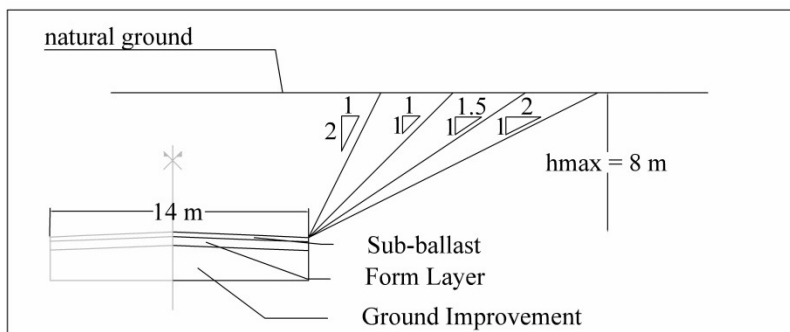


**Figure 5-14** General cut cross-section with different slopes and maximum depth of 8 m.

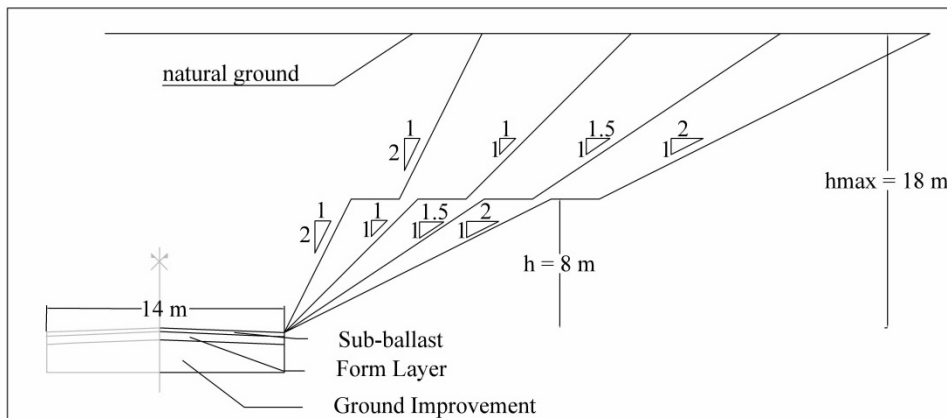


**Figure 5-15** General cut cross-section for different slopes and depths between 8 m to 18 m.

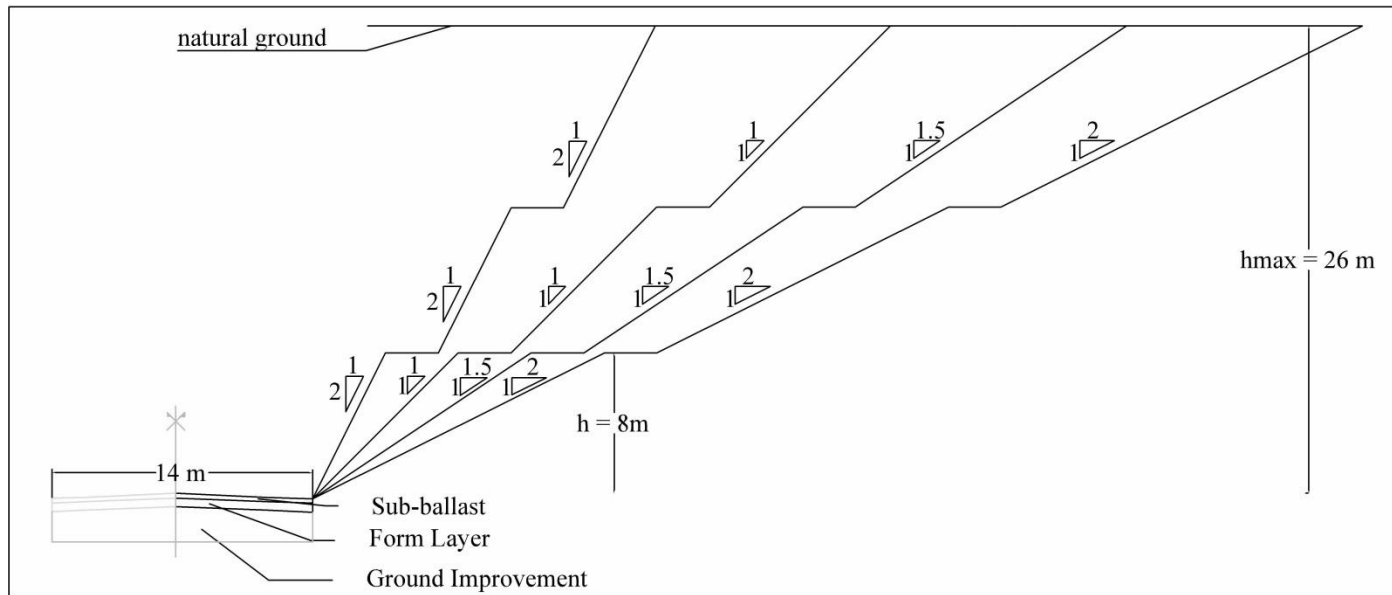


**Figure 5-16** General cut cross-section for different slopes and depths between 18 m to 26 m.

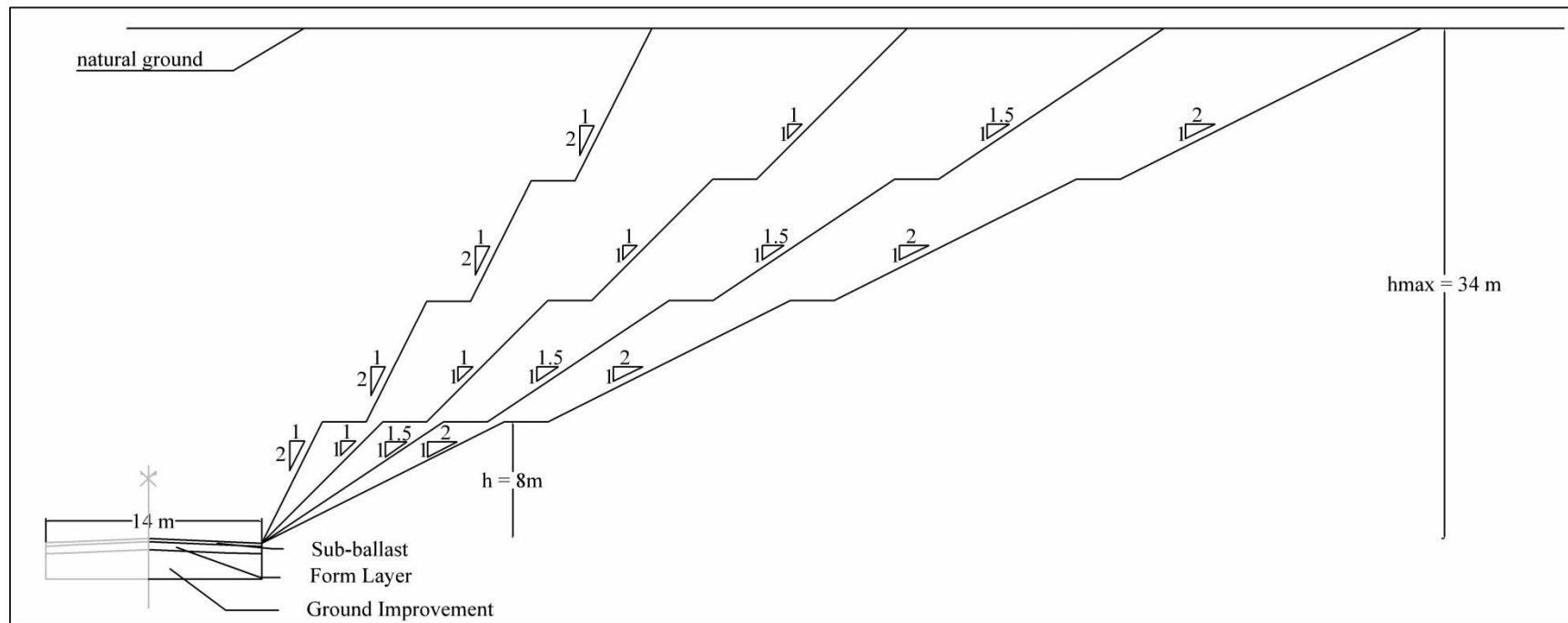


**Figure 5-17** General cut cross-section for different slopes and depths between 26 m to 34 m.

It must be noted that when a bridge or a tunnel are planned, these structures are extended until, respectively, the simple embankment maximum height (10 m) or the simple cut maximum depth (8 m) are observed. Large cuts at tunnel entrances may require additional structures such as retaining walls or safety steel wire netting systems. High embankments at the approaches of bridges are a major factor in the creation differential settlements which rein safety and comfort incompatibilities with the high-speed circulation of trains.

The excavation methods depend on the geological engineering properties of the deposits (Table 5-6). For soils and soft sedimentary rocks, until the inclusive Tertiary period, it is assumed that mechanical means are able to excavate the total volume corresponding to the cross-section. All remaining Sedimentary and Metamorphic rocks are considered to require both mechanical means and blasting in a 50/50 proportion of the total volume to excavate. Igneous Plutonic Rocks are considered to be excavated entirely by blasting.

As discussed in section 2.2.2, HSR platform strength and deformability requisites are defined in order to comply with the demanding track displacement limits. Lithological units in which the strength and deformability characteristics of the materials do not comply with the minimum requisites, ground improvement is necessary to ensure an adequate performance at the base of the embankments and cuts. Various ground improvement techniques exist (section 2.2.3). The case-study considers the removal and replacement of a given depth of the natural ground. Lithological units until the Cretaceous period are identified as having, in general, poor bearing capacity near the surface. A varying depth of removal is considered according to the expected behavior (Table 5-6). Alluvium is particularly expected to perform poorly due to the large clay and organic matter contents.

The form layer thickness is estimated based on the expected characteristics of the foundation soils (Table 5-6) and the requirements for the platform performance, according to the guidelines presented in section 2.2.

The sub-ballast thickness is assumed constant and equal to 0.30 m along the HSR configuration, according to RAVE (2008).

The unit costs for earthworks are listed in Table 5-7. Earthworks total costs are computed by estimating the volumes with the average-end area method, discussed in section 4.1.1.1,

considering cross-sections at the center of each space property element overlaid by the HSR linear sections ( $\Omega_E^{ij}$ ) and the unit cost for each of the earthworks item.

**Table 5-7** Earthworks unit costs.

| Cost Item                                     | Value<br>(€/m <sup>3</sup> ) |
|---|------------------------------|
| Embankment                                    | 2.78                         |
| Excavation with mechanical means              | 3.12                         |
| Excavation by blasting                        | 7.29                         |
| Sub-ballast                                   | 11.46                        |
| Form Layer                                    | 12.75                        |
| Ground Improvement by removal and replacement | 4.37                         |

### 5.3.3 BRIDGES

The real cost of bridges is influenced by specifics such as the number of piers, related to structure length and spans, the foundation type, the height above the surface and the construction method. The design specifying all the elements that compose a given bridge requires detailed studies and data that are not available at a planning stage, hence an approximation of the total cost is considered. For a detailed formulation of bridge and viaduct costs refer to Moret (2011).

The cost formulation considered for the Lisbon-Oporto HSR case-study includes three main factors influencing the total cost of the bridges: the construction method, the total length and the maximum height. A base cost for bridges is defined as a function of the bridge length  $l_b$  (m) in equation (5.1). The influence of different construction methods and maximum height is represented by coefficients that multiply the base cost. These are defined, based on HSR bridge cost estimates proposed by RAVE (2008).

$$\text{Bridge base cost} = 8,886.8 l_b + 124,935 \quad (\text{€}) \quad (5.1)$$

If the bridge construction method requires only fixed scaffolding, the construction method coefficient is  $k_{CM} = 1$ . If construction requires launching systems to be used, the construction method coefficient is  $k_{CM} = 1/0.6$ . This coefficient multiplies the base cost to represent the influence of the construction method on the bridge construction cost. As a simplification of reality, the model considers that the bridge construction method requires the use of launching

systems when crossing a body of water, identified in the rivers layer of the input spatial data in Figure 5-9.

RAVE (2008) proposes coefficients establishing the influence of varying maximum height on a bridge base cost. Based on the proposed coefficients, the height coefficient  $k_h$  of the case study is equal to 1 for a bridge maximum height equal or smaller than 20 m and determined according to (5.3) for maximum heights ( $h_{\max}$ ) larger than 20 m.

$$k_h = 0.7058 e^{0.0182h_{\max}} \quad (5.2)$$

The total cost of a bridge is obtained by multiplying the base cost for the respective bridge length (5.1), by the construction method coefficient  $k_{CM}$  and by the height coefficient  $k_h$ . Accordingly, equation (5.3) presents the global cost function to assess the cost of each bridge  $b$  of length  $l_b$  (m), to be constructed for the Lisbon-Oporto HSR case-study.

$$f_b = [8886.8 \cdot l_b + 124,935] k_{CM} \cdot k_h \quad (\text{€}) \quad (5.3)$$

#### 5.3.3.1 THE INFLUENCE OF THE BRIDGE MAXIMUM HEIGHT COST FACTOR

The importance of considering the cost of bridges varying with their maximum height is shown with an initial application of the SPC model of section 4.1 and solved with the implementation of the SAA. This application corresponds to the initial development stages of the computational tool and is presented for illustrative purposes.  $k_h = 1$  is considered for all bridges.

The best HSR configuration found by the SAA in such conditions is shown overlaying the lithological-, protected land-use-, expropriation cost-, elevation- and river maps in Figure 5-18, with the longitudinal profile presented in Figure 5-19. Observing the graphics in Figure 5-18 one realizes that the HSR configuration connects Aveiro and Leiria, besides the mandatory locations of Oporto, Coimbra and Lisbon. Furthermore, the configuration complies with the forbidden land-use constraint with an alignment that does not significantly deviate from the north-south linear connection of the cities (qualitatively assessed). However, the most relevant characteristic of the HSR configuration is shown in the longitudinal profile of Figure 5-19 and highlights the need for considering the bridge height in the bridge cost formulation.



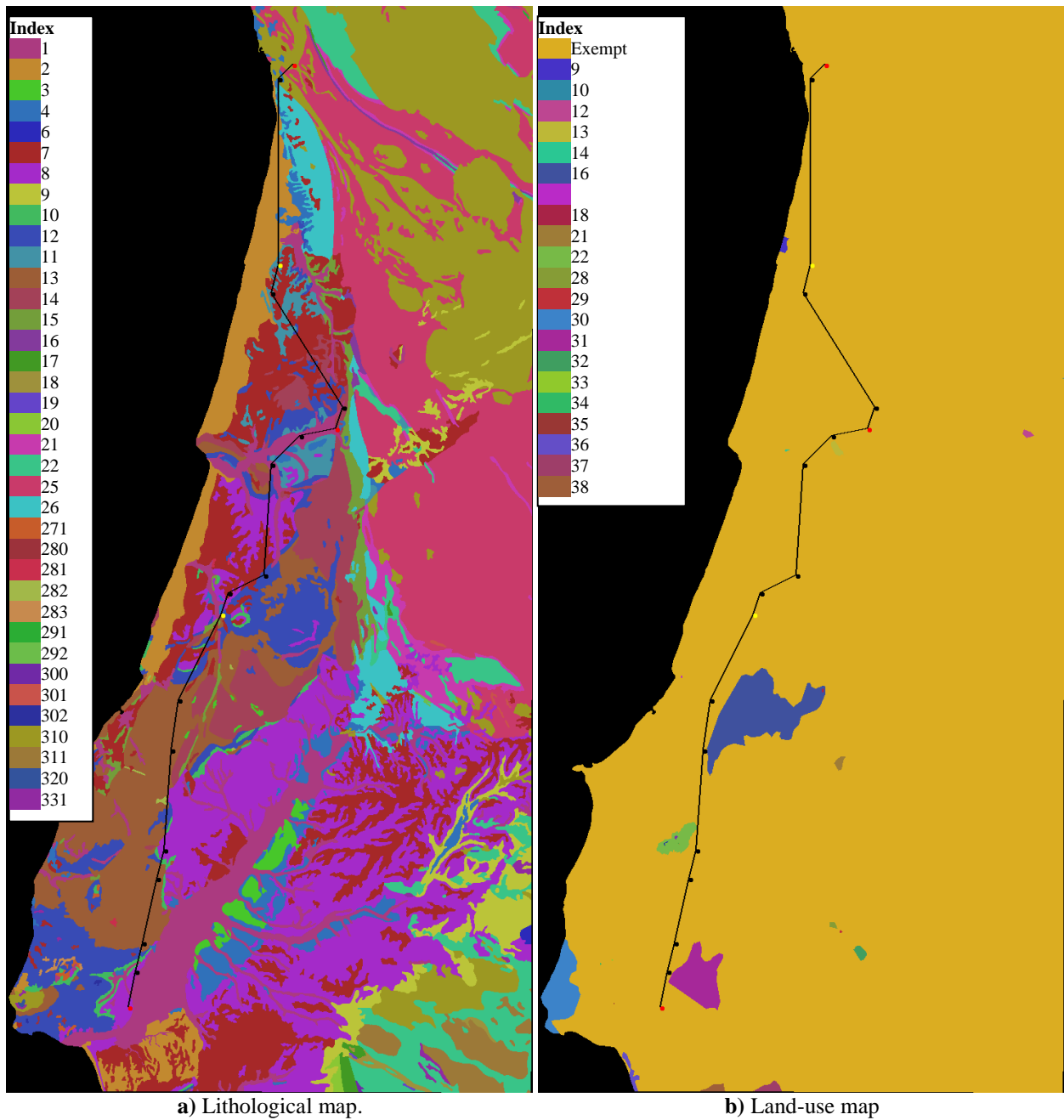
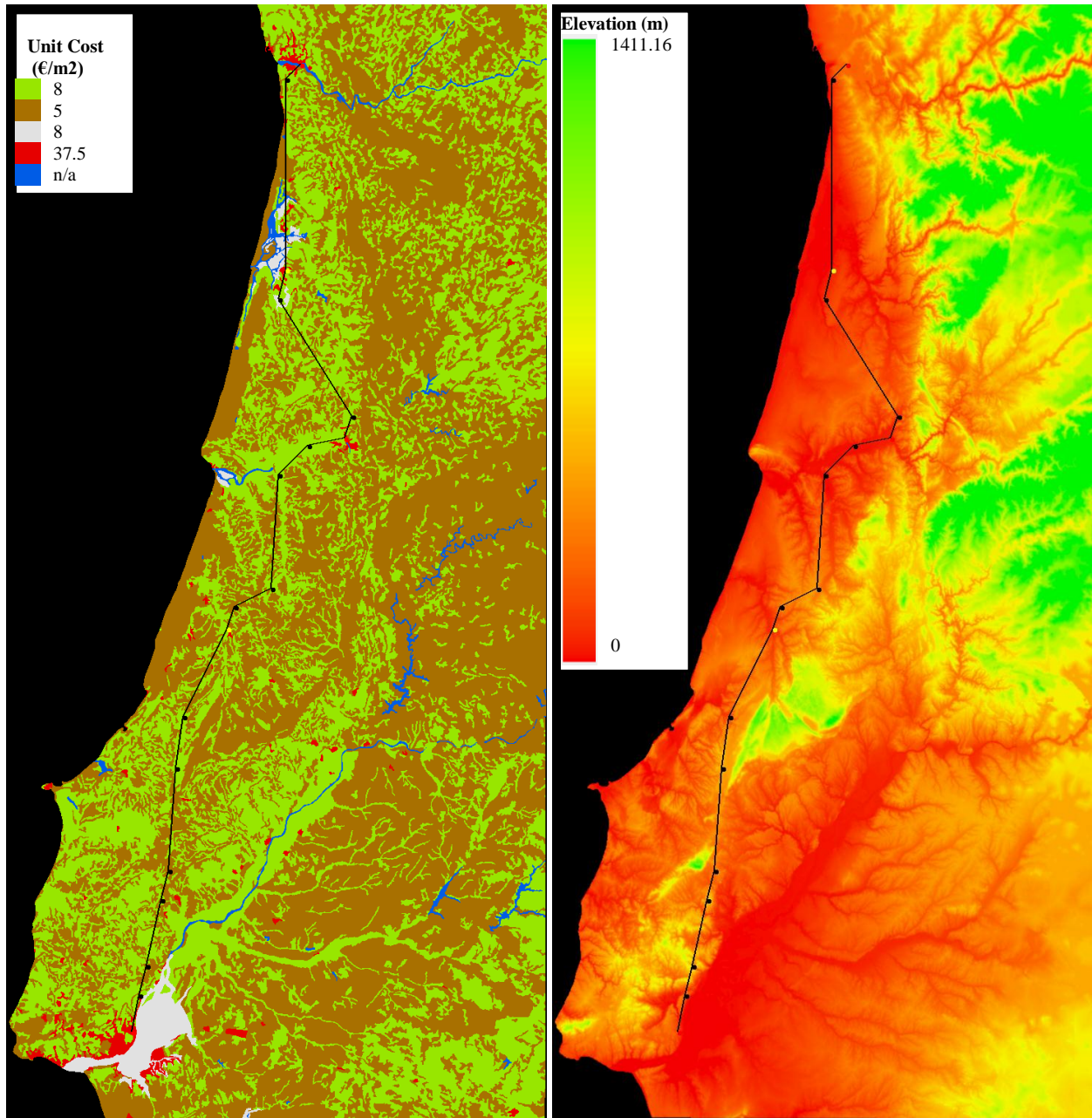


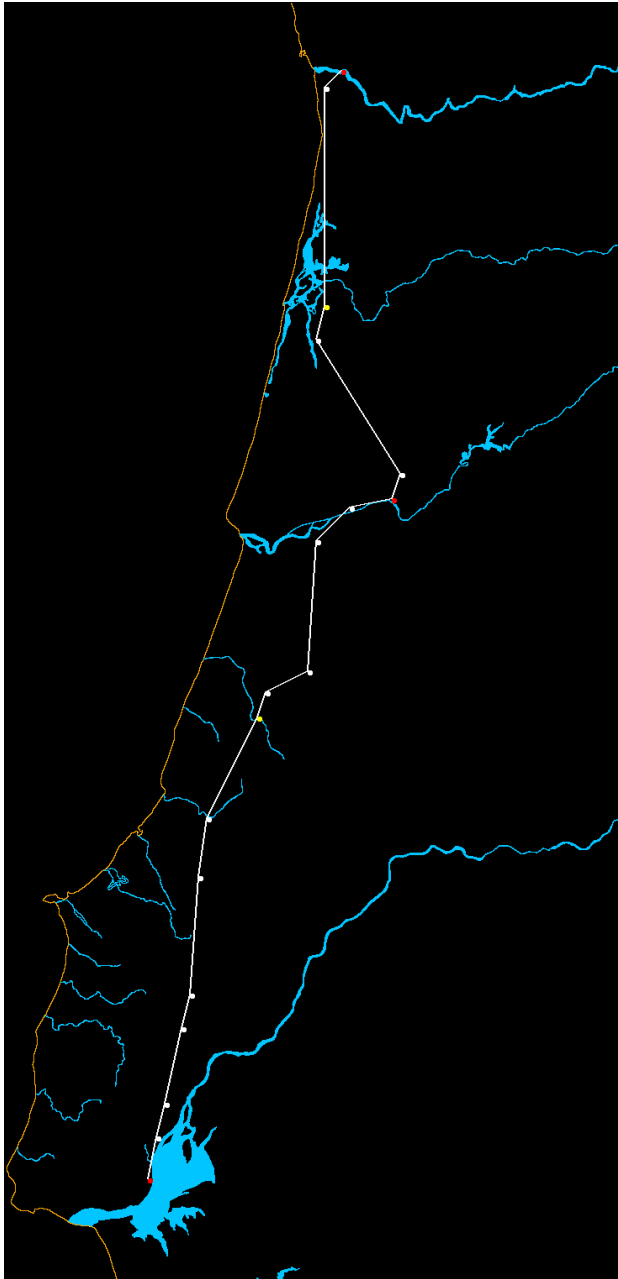
**Figure 5-18** Plan view overlay of the best HSR configuration found for the Lisbon-Oporto case-study considering  $k_{h_i}=1$  for all bridges: a) lithological map, b) land-use map, c) expropriation cost map, d) elevation map and e) main rivers map.



c) Expropriation cost map.

d) Elevation map.

**Figure 5-18** Plan view overlay of the best HSR configuration found for the Lisbon-Oporto case-study considering  $kh=1$  for all bridges: a) lithological map, b) land-use map, c) expropriation cost map, d) elevation map and e) main rivers map. (Continued).



e) Main rivers map.

**Figure 5-18** Plan view overlay of the best HSR configuration found for the Lisbon-Oporto case-study considering  $kh=1$  for all bridges: a) lithological map, b) land-use map, c) expropriation cost map, d) elevation map and e) main rivers map. (Continued).

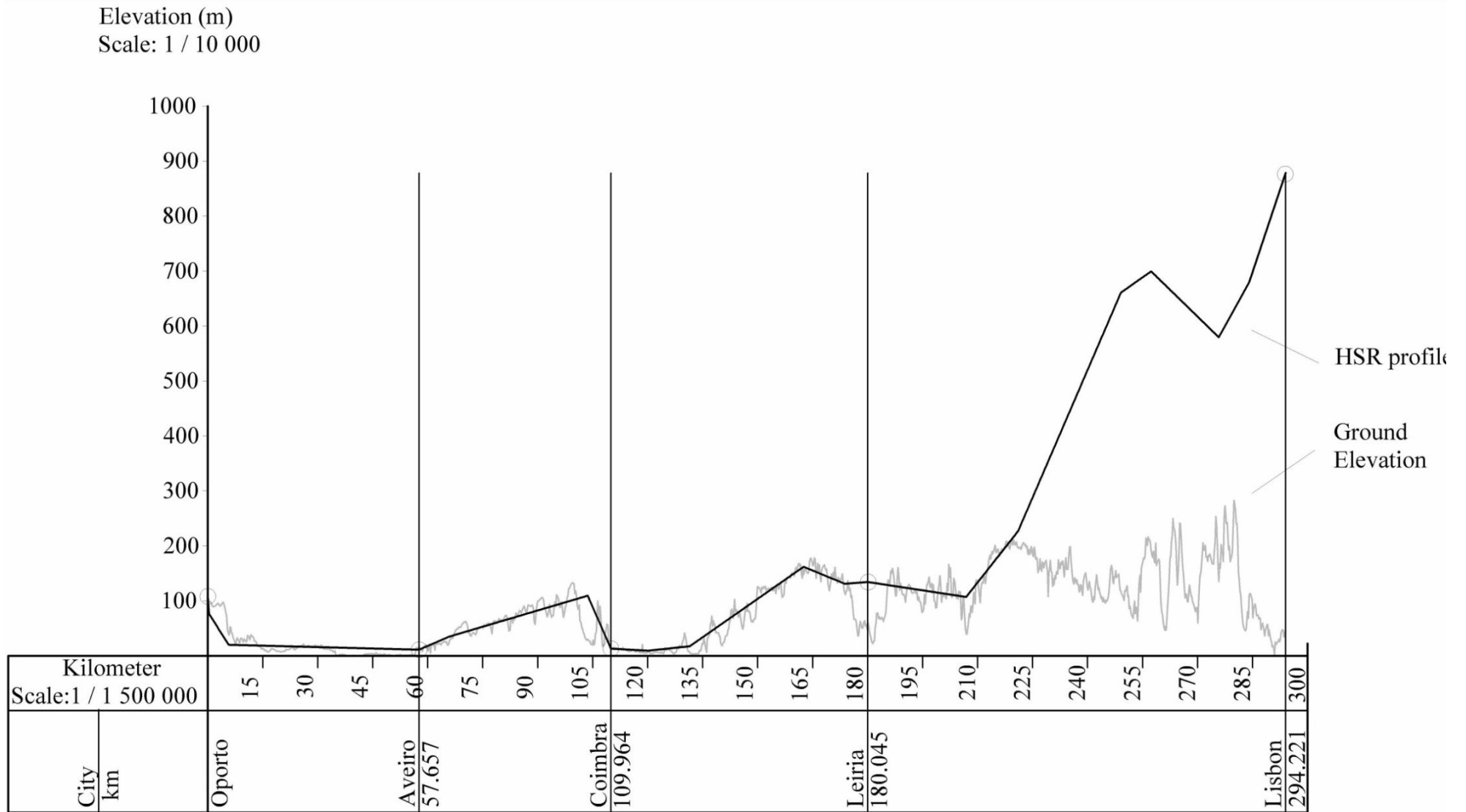


**Figure 5-19** Longitudinal profile of the best HSR configuration found by the SAA, considering  $k_i=1$  for all bridges.

Figure 5-19 shows the HSR configuration with similar elevations as those of the ground, from Oporto to around the 220 km. From this point forward, in the Lisbon direction, the HSR elevation spikes and is almost tenfold the ground elevation, resulting in 3 consecutive bridges (33, 34 and 35 of Table 5-8) of maximum height larger than 700 m and a combined length over 70 km. The results indicating that these very high and long bridges constitute the best HSR configuration are unrealistic.

**Table 5-8** Cost of bridges composing the HSR configuration for the initial bridge cost formulation without the consideration of the height factor  $k_h$ .

| <b>Bridge</b>               | <b>Length<br/>(m)</b> | <b>Maximum height<br/>(m)</b> | <b>Cost<br/>(Million €)</b> |
|-----------------------------|-----------------------|-------------------------------|-----------------------------|
| Bridge Launching Systems_1  | 20.0                  | 12.7                          | 3.17                        |
| Bridge Launching Systems_2  | 1,600.0               | 14.6                          | 23.91                       |
| Bridge Launching Systems_3  | 600.0                 | 12.8                          | 9.10                        |
| Bridge Launching Systems_4  | 600.0                 | 11.7                          | 9.10                        |
| Bridge Fixed Scaffolding_5  | 498.2                 | 22.0                          | 4.55                        |
| Bridge Fixed Scaffolding_6  | 222.6                 | 23.9                          | 2.10                        |
| Bridge Fixed Scaffolding_7  | 222.6                 | 26.1                          | 2.10                        |
| Bridge Fixed Scaffolding_8  | 4,682.5               | 80.5                          | 41.74                       |
| Bridge Fixed Scaffolding_9  | 632.4                 | 30.1                          | 5.75                        |
| Bridge Launching Systems_10 | 565.7                 | 5.9                           | 8.59                        |
| Bridge Fixed Scaffolding_11 | 1,208.0               | 24.0                          | 10.86                       |
| Bridge Fixed Scaffolding_12 | 399.0                 | 22.3                          | 3.67                        |
| Bridge Fixed Scaffolding_13 | 405.8                 | 32.6                          | 3.73                        |
| Bridge Fixed Scaffolding_14 | 1,995.8               | 39.9                          | 17.86                       |
| Bridge Fixed Scaffolding_15 | 1,004.1               | 35.9                          | 9.05                        |
| Bridge Fixed Scaffolding_16 | 1,609.5               | 36.5                          | 14.43                       |
| Bridge Fixed Scaffolding_17 | 798.4                 | 28.7                          | 7.22                        |
| Bridge Fixed Scaffolding_18 | 223.6                 | 24.4                          | 2.11                        |
| Bridge Fixed Scaffolding_19 | 5,282.0               | 96.9                          | 47.06                       |
| Bridge Launching Systems_20 | 669.5                 | 107.7                         | 10.12                       |
| Bridge Fixed Scaffolding_21 | 4,023.5               | 110.4                         | 35.88                       |
| Bridge Fixed Scaffolding_22 | 223.6                 | 26.2                          | 2.11                        |
| Bridge Fixed Scaffolding_23 | 1,341.6               | 40.4                          | 12.05                       |
| Bridge Fixed Scaffolding_24 | 223.6                 | 24.0                          | 2.11                        |
| Bridge Fixed Scaffolding_25 | 447.2                 | 28.4                          | 4.10                        |
| Bridge Fixed Scaffolding_26 | 447.2                 | 42.7                          | 4.10                        |
| Bridge Fixed Scaffolding_27 | 223.6                 | 34.9                          | 2.11                        |
| Bridge Launching Systems_28 | 223.6                 | 56.2                          | 3.52                        |
| Bridge Fixed Scaffolding_29 | 2,044.6               | 69.3                          | 18.30                       |
| Bridge Fixed Scaffolding_30 | 408.8                 | 32.9                          | 3.76                        |
| Bridge Fixed Scaffolding_31 | 409.4                 | 42.9                          | 3.76                        |
| Bridge Fixed Scaffolding_32 | 197.7                 | 20.1                          | 1.88                        |
| Bridge Fixed Scaffolding_33 | 69,320.6              | 768.1                         | 616.16                      |
| Bridge Launching Systems_34 | 392.5                 | 788.0                         | 6.02                        |
| Bridge Fixed Scaffolding_35 | 3,784.7               | 850.0                         | 33.64                       |
| <b>Total Cost</b>           |                       |                               | <b>985.84</b>               |

Putting these results in context, one of the highest transportation bridges built to present, the Si Du River Bridge, China, is 1,222 m long and approximately 500 m high with a reported cost of U.S. \$100 million (Wang et al. 2009). This results in an average cost of U.S. \$81,833 per m, compared with €8,888 per m of bridges 33 and 35 and with €15,357 per m of bridge 34. Even with the exchange rate averaging close but below €1= U.S. \$1.5 for the years of 2008 and 2009 (Eurostat 2013a), the cost formulation considered for very high bridges with  $k_h=1$  is not representative of such a bridge's real cost.

#### 5.3.4 TUNNELS

The model defines a unit cost per linear meter ( $l_t$ ) of constructed tunnel  $t$  dependent on the lithological unit. Considering that the tunnels are not defined in terms of the cross-section, excavation method, support and lining and that geological and geotechnical information at depth is not available, an approximation of 35,000 €/m is used for all lithological units (Table 5-6). This unit cost is based both on RAVE (2008) and expert engineering judgment. The tunnels global cost function is given by (5.4).

$$f_t = 35,000l_t \quad (\text{€}) \quad (5.4)$$

#### 5.3.5 LENGTH-DEPENDENT COSTS

Track and catenary costs do not vary significantly with the *in situ* characteristics. As such, these are considered in the research as length dependent costs. The cost of each component is based on the estimated values by RAVE (2008): track is estimated to cost 785 €/m, including ballast, and catenary is estimated to cost 375 €/m, for the double track HSR. The costs remain unchanged for the different cross-sections (bridges, tunnels cuts and embankments) though in reality small variations of the costs may occur.

### 5.4 SEISMIC SCENARIOS

The capability of earthquakes to damage the HSR infrastructure is acknowledged and has been discussed in section 2.4.1. Causes of damages that have incurred in or are able to produce disruptions in the HSR performance include earthquake-induced ground motion and as a consequence, liquefaction and landslides. This and the fact that Portugal is located on a

seismically active area require that seismic design is taken in consideration when planning the Lisbon-Oporto HSR.

Seismicity in Mainland Portugal is determined by earthquakes of both interplate and intraplate origin. Larger interplate events, such as the catastrophic 1755 Lisbon Earthquake (Betâmio de Almeida 2009) and the 1969 Gorringe Bank earthquake (Fukao 1973), are generated at the contact of the Euro-Asian and African plates. Intraplate events, such as the 1531 or the 1909 Benavente earthquakes, are due to local active faults within the Euro-Asian plate and have in general lower magnitudes, but occur more frequently (Teves-Costa et al. 1999).

The seismicity assessment is based on both historical and instrument data. Based on a comprehensive catalog of seismic events by Sousa and Oliveira (1996), the Eurocode 8 working group (Campos Costa and Sousa 2008) proposes the seismic zoning in Figure 5-20. The seismic zoning 1.1-1.5 and 2.1-2.5 in Figure 5-20 indicates a variable seismicity, larger in the south and southwest of the territory and lower to the north, as a result of the potential location of earthquakes and the related epicentral distances. Each zone is assigned a design reference peak ground acceleration. Zones 2.1 and 2.2 are not assigned to the mainland but they represent the seismicity in the Azores islands.

Considering the area of the Lisbon-Oporto HSR case-study, a larger seismicity is observed in the vicinity of Lisbon and the Lower Tagus River Valley, decreasing towards Oporto.

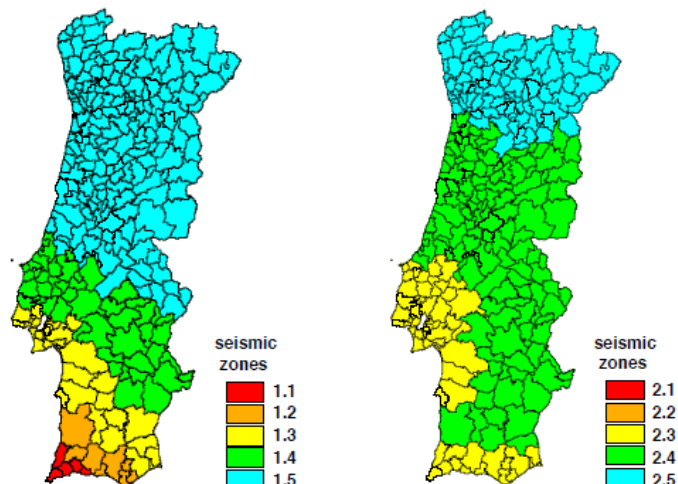


**Figure 5-20** Seismic zoning for interplate (left) and intraplate (right) earthquakes affecting mainland Portugal proposed by the Eurocode 8 working group for the Portuguese National Annexes of Eurocode 8 (NP EN 1998-1) (Campos Costa and Sousa 2008).

Ground motion can cause rails to displace, ground settlements and structural damage to bridges and tunnels. However, a detailed analysis of each of these consequences is outside the scope of the planning scale of this research. Estimating surficial settlements and displacements and their consequences on the HSR infrastructure requires, for instance, a more detailed geotechnical input. The effects of ground motion on tunnels are also difficult to account for. This research does not consider the location of fault planes, prone to differential movement, that primarily affect a crossing HSR tunnel section (Byers 2008). As for bridges, Ranf et al. (2001) suggest that a correlation between epicentral distance and bridge damages is not appropriate as it does not account for the site geotechnical behavior. In fact, Byers (2008) states that damages to railway bridges are mostly due to permanent ground displacement and occur in around half of the cases where earthquakes have damaged railways.

The following section describes the earthquake characteristics considered in the implementation of the seismic scenarios. Two seismic scenarios are considered: the seismic scenario 1 represents the occurrence of a nearby intraplate earthquake and the seismic scenario 2 represents the occurrence of a distant interplate earthquake. HSR disruptions due to earthquake induced liquefaction and landslides are considered. The occurrence of these earthquake effects in a specific location depends on both the earthquake characteristics and the site susceptibility as the result of natural or manmade characteristics such as geology, elevation, slope angle, artificial landfills, etc. The methodology of susceptibility assessment to each of the effects is discussed. The performance of the different HSR cross-sections (embankments, cuts, bridges and tunnels) is then separately assessed for landslides and liquefaction. The estimated costs due to repair of the HSR physical damages are presented. However, derailment occurrence is not included in the analysis.

#### 5.4.1 EARTHQUAKE CHARACTERISTICS

The seismic scenarios considered in the analysis reflect both interplate and intraplate seismicity. In each case the earthquake is defined by a moment magnitude ( $M_w$ ), an epicenter location and a return period.

The magnitude of an earthquake is defined based on the measurements of seismogram data and several scales of magnitude exist, depending on the measurement method (USGS 2012a). USGS (2012a) discusses the different scales of magnitude including local magnitude ( $M_L$ ),



surface-wave magnitude ( $M_S$ ) and moment magnitude ( $M_W$ ). Furthermore, it states that  $M_L$  and  $M_S$  have a limited range of applicability, as a consequence of their measurement methods, and are not suitable for representing very large earthquakes. Conversely,  $M_W$  is uniformly applicable for any earthquake size but its computation is more complex (USGS 2012b). Nonetheless, USGS (2012b) states that, for any given earthquake, all scales within their range of applicability should yield roughly the same value. On the applicability and measurement specifics of  $M_L$ ,  $M_S$  and  $M_W$  USGS (2012a) observes the following:

- $M_L$  – applicable for magnitudes ranging between 2 and 6 and distances in the 0-400 km interval. This magnitude scale is the original developed by Richter and Gutenberg in 1935 and its value derives from the maximum amplitude of a seismogram recorded by a Wood-Anderson torsion seismograph.  $M_L$  may also be calculated using modern instrumentation with appropriate adjustments.
- $M_S$  – applicable for magnitudes ranging between 5 and 8 and distances in the 20°-180° interval.  $M_S$  is used for distant earthquakes and its definition is based on the amplitude of Rayleigh surface waves measured at a period near 20 seconds.
- $M_W$  – applicable for magnitudes larger than 3.5 and within all distances. Its value is based on the moment of the earthquake which is equal to the rigidity of the earth multiplied by the amount of slip on the fault multiplied by the fault area that slipped.

#### 5.4.1.1 SEISMIC SCENARIO 1

An event similar to the 1909 Benavente earthquake represents the nearby intraplate type of seismic scenario 1. Uncertainties still remain regarding the exact location and magnitude of the 1909 earthquake and thus the characterization is based on research by Cabral et al. (2011), Oliveira (2008) and Teves-Costa et al. (1999). Difficulties also exist in estimating the return period for the 1909 earthquake.

Martins and Mendes-Victor (1993) as cited by Teves-Costa et al. (1999) propose a return period of 41+or- 6 years for earthquakes larger than  $M_W > 6.5$  and generated in the seismogenic zone that includes the Lower Tagus Valley (LTV), where the 1909 Benavente earthquake originated. However, this active seismic area (the seismogenic zone) is 10 times larger than the LTV and thus considering a return period of 41+or- 6 years is an

overestimation of the frequency of such earthquake (Teves-Costa et al. 1999). Campos Costa (2008) states a return period of 95 years for a 7.2 magnitude event in the Lisbon area. An intermediate value, 68 years, is considered for the intraplate event scenario.

This research considers the intraplate earthquake scenario defined by a moment magnitude  $M_w = 6.3$  (Vilanova and Fonseca 2004), an epicenter located at latitude  $38.98^\circ\text{N}$  and longitude  $8.86^\circ\text{W}$  (Cabral et al. 2011) and a return period of 68 years.

#### 5.4.1.2 SEISMIC SCENARIO 2

The larger interplate type of events of seismic scenario 2 is represented by an earthquake similar to the 1755 Lisbon earthquake. Uncertainties still exist regarding its magnitude, return period and location.

Literature suggests a  $M_w$  between 8.5 and 9 (Chester (2008); Oliveira (2008); USGS (2012b)) for the 1755 Lisbon earthquake. The return period is estimated as  $614 \pm 105$  years by Chester (2008) and between 1500 to 2000 years by Gutscher (2006). Coelho and Costa (2009) consider an intermediate a return period of 1750 years. Uncertainties also affect the earthquake epicenter location (Zitellini et al. 2009). USGS (2012b) maps the epicenter at  $36^\circ\text{N } 11^\circ\text{W}$ .

Based on the existing literature, the seismic scenario 2 considers the interplate earthquake to be defined by a magnitude of  $M_w=8.7$ , a return period of 1750 years with the epicenter located at  $36^\circ\text{N } 11^\circ\text{W}$ .

#### 5.4.2 EARTHQUAKE TRIGGERED LANDSLIDES

While earthquakes can be devastating, post-hazard inventories present unique opportunities to learn and understand the earthquake induced landslide occurrence. This type of data collection also allows one to formulate models to estimate future landslide events based on the earthquake characteristics and the location susceptibility. Keefer (1984) compiled information regarding 40 worldwide earthquakes in the period 1811-1980 and discussed the characteristics, geological environments and hazards of earthquake-triggered landslides. The author concludes that correlations between landslide affected areas and earthquake magnitude

(M) range from 0 km<sup>2</sup> for  $M_L=4$ , the minimum magnitude capable to induce landslides, and 500,000 km<sup>2</sup> for  $M_W=9.2$  events. The analysis considers 14 different types of landslides according to the terminology and classification, by type of movement firstly and type of material secondly, proposed by Varnes (1978). Keefer (1984) observes from the compiled data that the most frequent earthquake induced landslides are rock falls and disrupted soil slides. The terms broken or disrupted slides are defined by Varnes (1978) as translational slides in which the moving mass consists of many semi-independent units, as opposed to block slides “in which the moving mass consists of a single unit that is not greatly deformed or a few closely related units” (Varnes 1978). Keefer (1984) also established correlations between the lithology of the deposits and the predominant type of landslide. Rodríguez et al. (1999) extended the database of Keefer (1984) considering seismic events in the 1980-1997 period. Rodríguez et al. (1999) generally confirm the previous findings by Keefer (1984) but state that the affected area may be greater for intermediate earthquake magnitudes and indicate the possibility of failure of very susceptible slopes, imminently unstable even in pre-earthquake static conditions, for low earthquake magnitudes.

More recently, the advances in mapping technologies and software development such as Geographic Information Systems assist in the spatial analysis of earthquake-triggered landslides. Wang et al. (2007) analyze the spatial distribution of landslides that occurred during the 2004 Chuetsu earthquakes at Niigata, Japan. The authors perform a statistical analysis considering a DEM of 10 m \* 10 m discretization and based on a landslide inventory including information on location, geometry, type, triggering mechanism and damage to infrastructure. One important factor stated by Wang et al. (2007) that may influence the results is the heavy rainfall three months prior to the earthquake, triggering landslides that were then reactivated by the earthquake event. The correlations between landslide activity and slope steepness, geology and shaking intensity were analyzed. Wang et al. (2007) observe that:

- slopes ranging from 20° to 35° were the most subject to landslides but failure also occurred in slopes steeper than 50°;
- 86.5% of the landslides occurred in tertiary sedimentary rocks, that accounted only for 50% of the study area;

- the correlation between the earthquake magnitude and the area affected by the landslides is similar to the historical databases by Keefer (1984) and Rodríguez et al. (1999).

Considering that the slope stability of the deposits, both in the pre-earthquake static condition and under seismic conditions, depends on the geotechnical strength properties of the materials, the interaction between slope steepness and geology is a major factor for the landslide spatial distribution. Wang et al. (2007) analyze different combinations of slope steepness and geologic units observing, as expected, that unconsolidated sediments fail even for gentle slopes.

Lee et al. (2008) discuss a statistical analysis for earthquake-triggered landslides susceptibility in Taiwan based on landslide inventories before and after the 1999 Chi-Chi earthquake. Two areas of around 700 km<sup>2</sup> each were studied with the goal of developing objective and simple methodologies for susceptibility assessment. The analysis is carried separately for two existing types of terrain (hilly and mountainous) considering 40 m \* 40 m grid DEM, 1/50,000 geologic and earthquake motion maps and images and photos that allowed the interpolation to a 20 m \* 20 m grid used to analyze each landslide instability factor. From an original list of 14 landslide causative factors, six were used in the analysis by Lee et al. (2008):

- lithology;
- slope angle;
- slope aspect defining the horizontal direction a slope faces;
- terrain roughness, defined at each point by the standard deviation in elevation within a given radius;
- slope roughness, defined at each point by the standard deviation in slope angle within a given radius;
- total curvature, as a measure of the terrain curvature (for definition refer to Wilson and Gallant (2000)).

The approach by Lee et al. (2008) computes a landslide susceptibility index for each grid point considering a dry season. The triggering conditions are represented by an intensity factor. Lee et al. (2008) state that the site characteristics found to have the largest correlation with landslide occurrence were slope angle, terrain roughness and lithology. Slope angle, slope aspect and terrain roughness are obtained directly from the DEM and thus Lee et al. (2008) highlight the influence of the input data resolution on the quality of the factors.

A different approach is developed by Wang et al. (2010) for the zonation of earthquake-triggered landslides in Dujiangyan, China, using GIS and an inventory of the 2008 Wenchuan earthquake induced landslides. The authors formulate a different contributing weight model to discuss the influence of the following factors in landslide occurrence:

- slope angle;
- slope aspect;
- geomorphology;
- lithology;
- base level (the difference between the average and the smallest elevation within a point neighborhood range);
- surface roughness (ratio of the topographic surface area and its projected area);
- earthquake intensity;
- fault proximity;
- drainage proximity;
- road proximity.

The analysis is based on a 1/200,000 geologic map and a 25 m \* 25 m grid DEM generated from a 1/50,000 topographic map. Wang et al. (2010) conclude that the factors to be selected for the analysis are dependent on the type of landslide and terrain but also of the data availability and resources. For the Dujiangyan case slope angle, base level and fault, drainage and road proximity were the most influential characteristics. Most of the landslides occurred

for slopes in the 20° to 40° angle range for the Xujiahe unit (fine-grained quartz-sandstones, feldspathic quartz-sandstones, siltstones) and the Mesoproterozoic general granite. No information on weathering or cementation of the different lithological units is provided by Wang et al. (2010). The final zonation is divided into four categories of hazard level: safe, low hazard, moderate hazard and high hazard.

The approach adopted to assess the earthquake-triggered landslide susceptibility for the Lisbon-Oporto HSR case is described in the following section. One important difference to the studies by Wang et al. (2007), Lee et al. (2008) and Wang et al. (2010) is the fact that the analysis is intended for a planning stage of the HSR network. The corridor to use is not defined and a large area needs to be considered in order to evaluate the different network options. Also, at this stage of the project the budget does not allow one to gather detailed information covering the entire area for elevation, geotechnical site properties, current land use, etc. For instance, the elevation data consists of a 200 m \* 200 m grid digital map. Using such a coarse grid mesh does not allow one to represent very steep slopes: the slope angles are interpolated and represent an averaged value and not the actual angle at each site. One other aspect affecting the analysis is the lack of an earthquake-triggered landslide inventory for Portugal. Comparing the landslide locations reported by an inventory with the zoning produced by the chosen methodology would allow one to assess the ability of the methodology to represent past events. This limitation is partially overcome by expertise knowledge but future availability of such data should lead to a verification of capability of the model to capture the earthquake-triggered landslides in Portugal.

Based on the discussed research and the available data, earthquake-triggered landslide susceptibility, triggering conditions and damage cost evaluation are defined for the Lisbon-Oporto HSR case study as presented, respectively, in sections 5.4.2.1, 5.4.2.2 and 5.4.2.3.

#### *5.4.2.1 SUSCEPTIBILITY ASSESSMENT*

The data available for the earthquake-triggered landslide susceptibility analysis is composed by lithology (Figure 5-4) and any characteristic that can be derived from the DEM (Figure 5-8). The quality of the derived maps is influenced by the fact that the DEM is based on a coarse grid of 200 m \* 200 m elevation points. Since the uncertainties in the DEM input propagate to the derived maps and into the susceptibility assessment, only two significant

parameters (Lee et al. 2008; Wang et al. 2007; Wang et al. 2010) are chosen for the susceptibility zoning: lithology and slope angle.

The methodology chosen considers two landslide susceptibility types: susceptible and non-susceptible. In reality landslide susceptibility, as the result of the correlation of several factors, is not generally binary and degrees of susceptibility exist. This is not incorporated in the case-study application but availability of more detailed data would allow one to map additional degrees of landslide susceptibility.

The earthquake-triggered landslides susceptible formations are those where lithology is recent, including materials until the Tertiary period mapped in Figure 5-21 and, simultaneously, where the slope angle is in the range of 20° to 40° (Figure 5-22 and Figure 5-23). The areas where these two criteria are not met simultaneously are classified as non-susceptible.

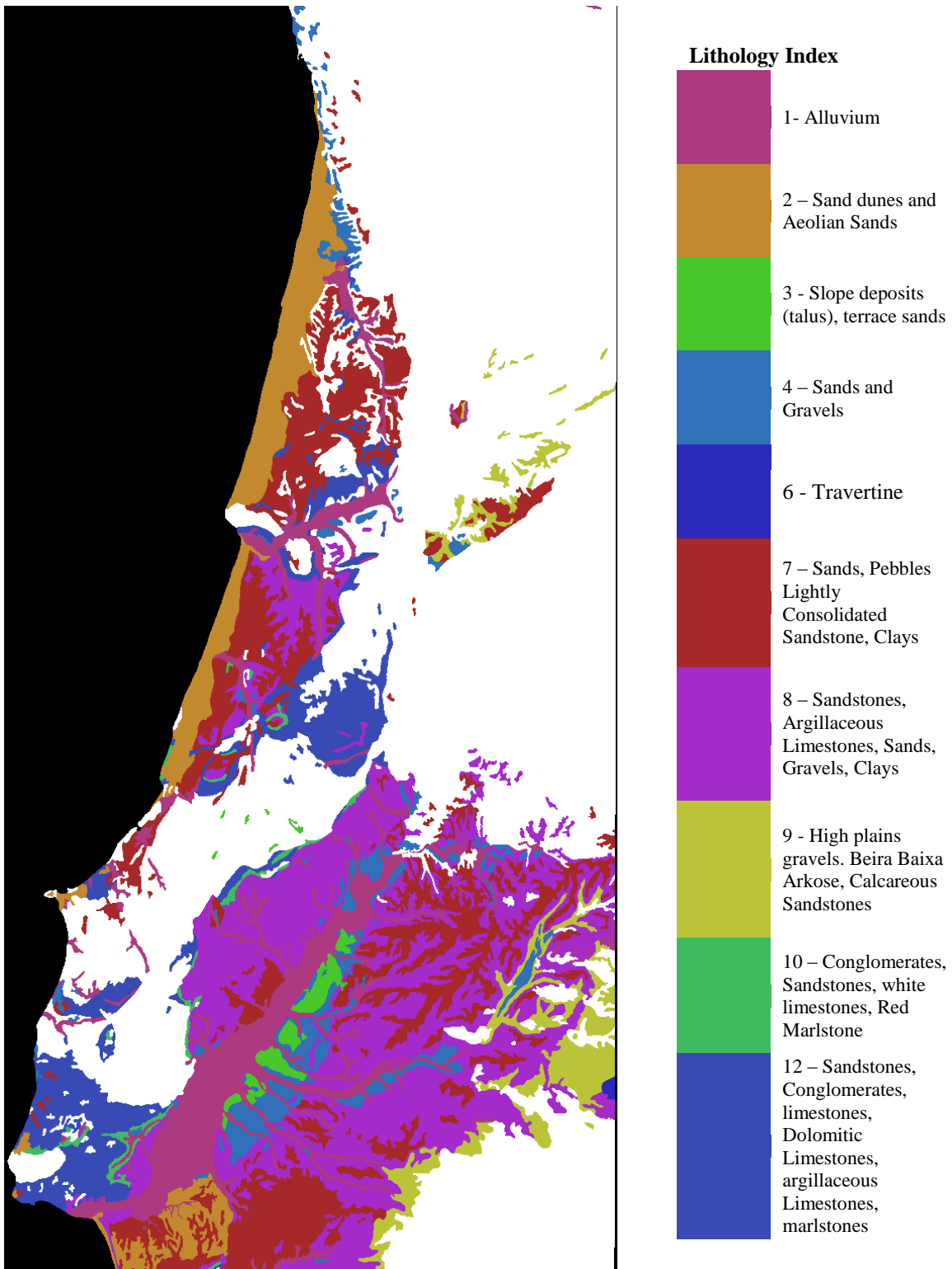


**Figure 5-21** Identification of earthquake-triggered landslides susceptible deposits.



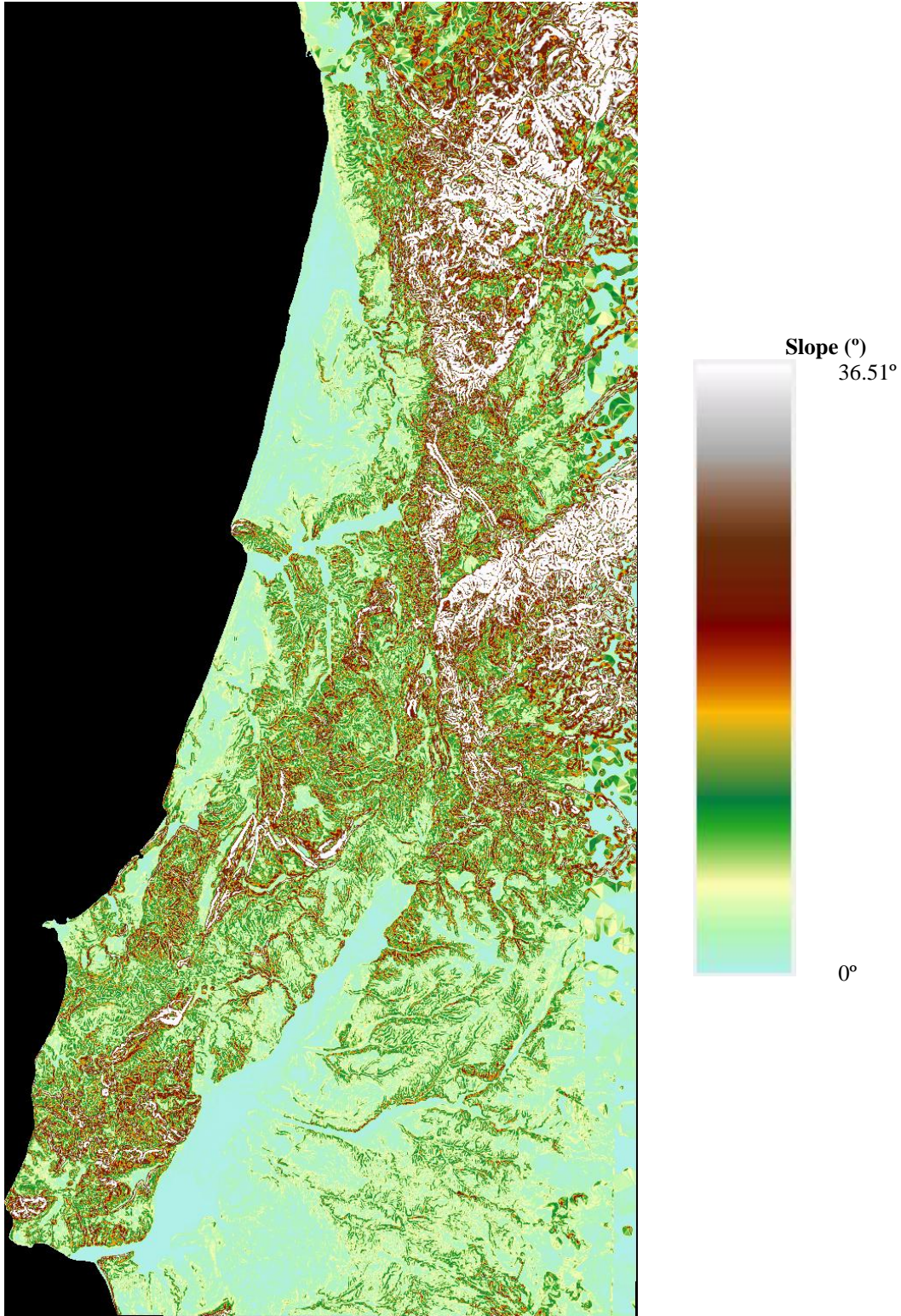
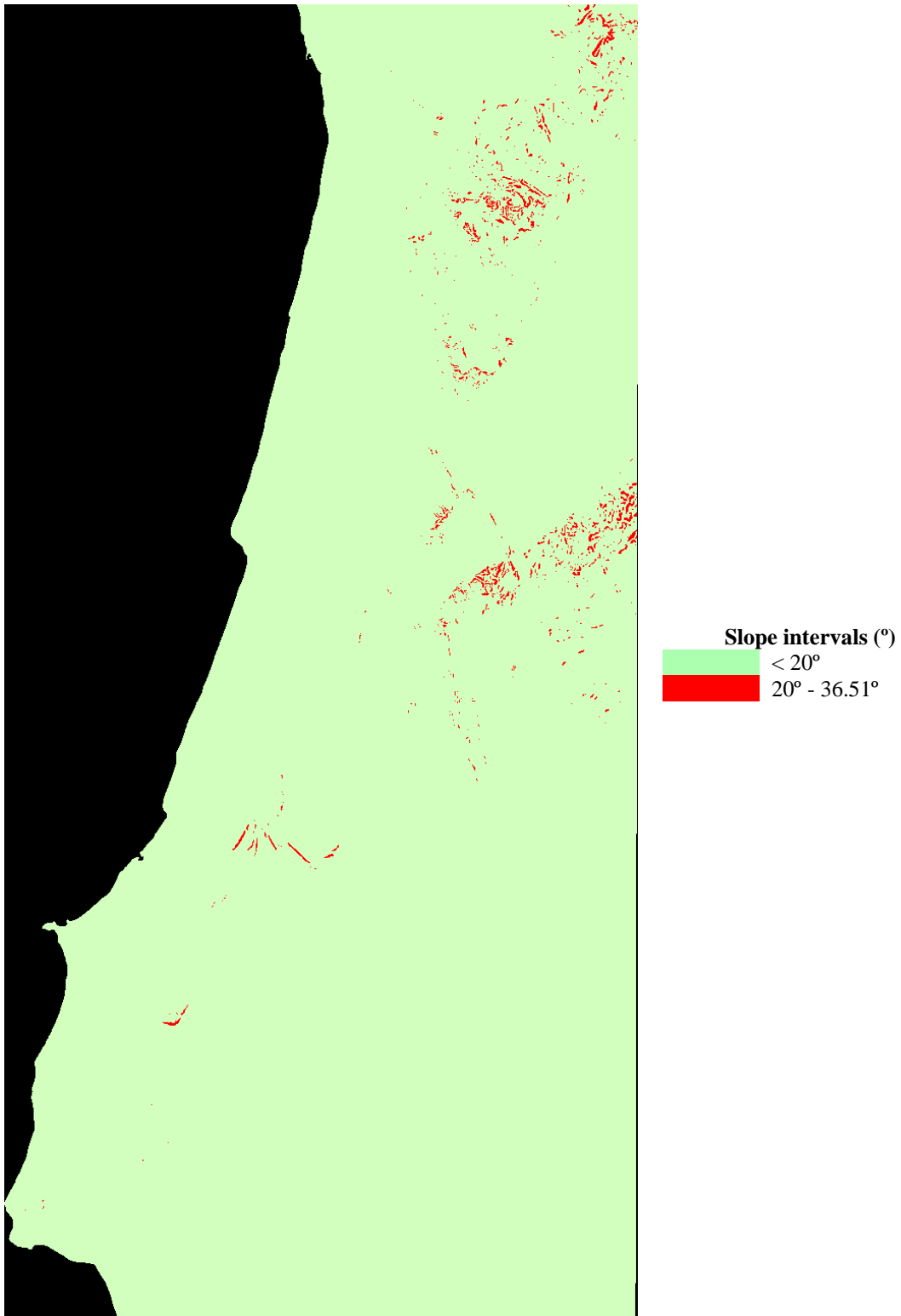


Figure 5-22 Slope angle obtained from the DEM.



**Figure 5-23** Slope angle obtained from the DEM, grouped into 2 intervals: < 20° and 20° - 36.51°.

This simple classification requires that remarks are made regarding the assumptions involved:

- The methodology is not considering the possibility of rock falls. The reasons for this exclusion are the lack of information on the jointing (fractures) and bedding planes of the existing rock masses that make them susceptible to rock falls and the fact that this type of failure typically occurs in steeper slopes (Dorren and Seijmonsbergen 2003; Dorren 2003; Einstein et al. 2010), the latter not being properly captured (Figure 5-22 and Figure 5-23) by the coarse DEM available.
- The fact that the water table level is not taken in consideration is another important issue affecting the analysis. Increase in pore water pressure decreases the shear strength of the soils and thus affects the slope failure susceptibility. The susceptibility zoning for earthquake-triggered landslides is presented for a dry season. The influence of the water contents in landslide susceptibility is not accounted for, due to the scale of the analysis.

Based on the previous assumptions, four earthquake-triggered landslide susceptible zones are identified for the Lisbon-Oporto HSR case-study. Figure 5-24, locates the susceptible areas within the case study by overlaying the lithology and slope maps. Figure 5-25, Figure 5-26, Figure 5-27 and Figure 5-28 are zooms detailing the four susceptible areas.

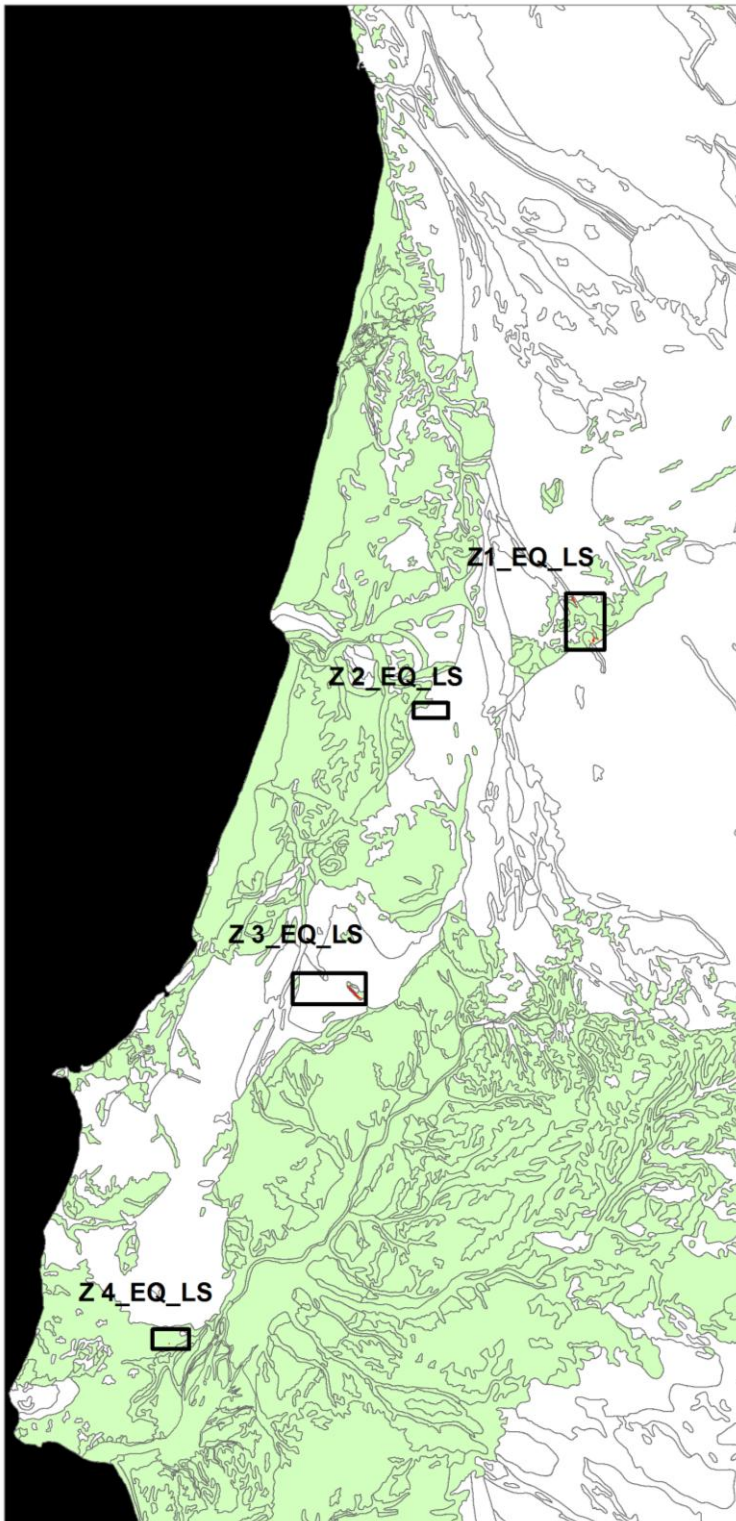


**Figure 5-24** Overlay of earthquake-triggered landslides susceptible lithology units and the slope angle intervals: non-susceptible deposits in white; susceptible deposits where slope angle is  $<20^\circ$  in green (lighter gray shade) and susceptible areas in red (darker gray shade) pictured within the zoom frames Z1\_EQ\_LS, Z2\_EQ\_LS, Z3\_EQ\_LS and Z4\_EQ\_LS.

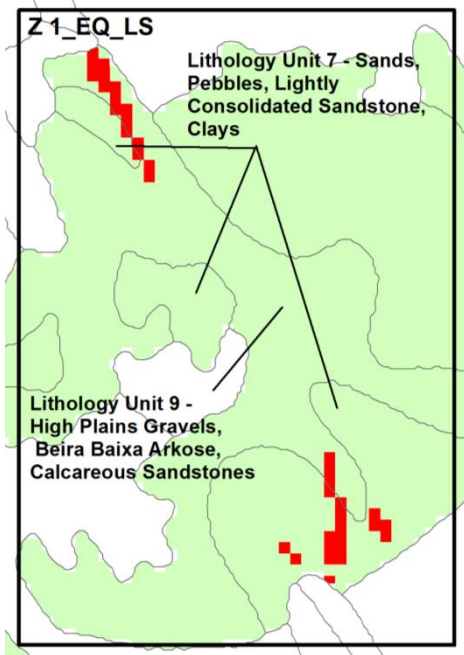


**Figure 5-25** Zoom-in of zone Z1\_EQ\_LS: susceptible earthquake-triggered landslide areas in red (darker shade).

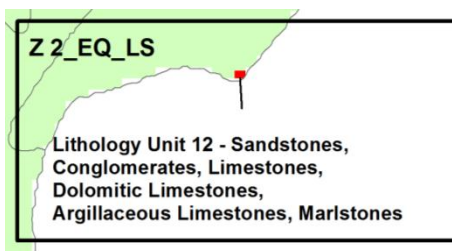


**Figure 5-26** Zoom-in of zone Z2\_EQ\_LS susceptible earthquake-triggered landslide areas in red (darker shade).

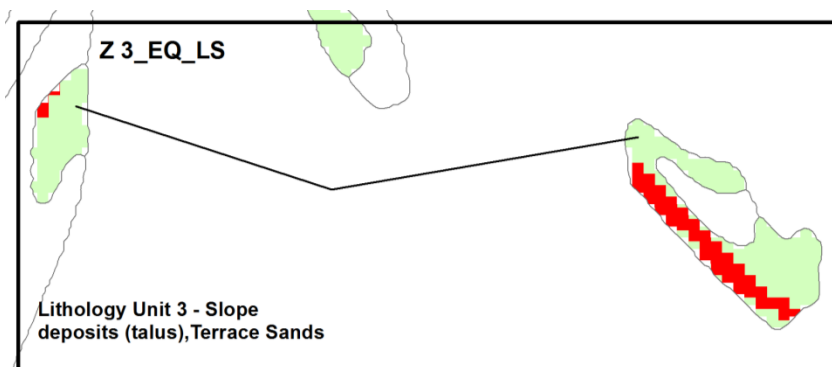


**Figure 5-27** Zoom-in of zone Z3\_EQ\_LS: susceptible earthquake-triggered landslide areas in red (darker shade).

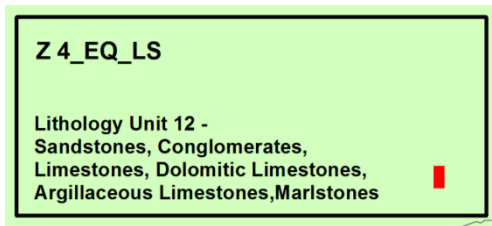


**Figure 5-28** Zoom-in of zone Z4\_EQ\_LS: susceptible earthquake-triggered landslide areas in red (darker shade).

Landslide susceptibility is assessed for the existing natural ground, demonstrating the tool capability to deal with earthquake-triggered landslides. However, the construction of cuts and embankments for the HSR line may also be susceptible to landslides and can be included in a more comprehensive application. In the case of cuts, the same methodology as for the natural ground susceptibility applies. Lithology is the same for both HSR cuts and natural ground and, if no mitigation measures are applied, only the slope angle varies. The water table level and hydraulic effects also change, but are not included in the analysis. When constructing embankments both lithology and slope angle change and are based on the project design specifics including appropriate seismic analyses. The assessment of earthquake-triggered landslide susceptibility for HSR cuts and embankments is not addressed in the current planning stage but it should be taken into account in detail in the project design stage.

#### 5.4.2.2 TRIGGERING CONDITIONS

Having the susceptibility zoning established for the study area, the actual landslide occurrence depends on the correlation of susceptibility and the triggering earthquake characteristics. Since only two susceptibility categories are considered (susceptible and non-susceptible) the identification of the earthquake characteristics capable of causing landslides in susceptible zones determines the occurrence of earthquake-triggered landslides. If degrees of susceptibility were considered, intermediate relations would be established.

The capability of an earthquake to trigger landslides in susceptible areas, for similar problem scales as the Lisbon-Oporto HSR planning scale, has been established by different approaches. Wang et al. (2010) consider earthquake intensity, Lee et al. (2008) also consider a measure of earthquake intensity, the Arias Intensity as defined by Arias (1970), and Keefer (1984), Rodríguez et al. (1999) and Wang et al. (2007) discuss the maximum epicentral

distance within which an earthquake, of a given magnitude, is able to trigger landslides. Intensity relates to the strength of shaking felt during the earthquake, taking into consideration the local conditions. However, mapping intensity for the search area requires that records are available. This research defines the capability of an earthquake to trigger landslides by a threshold of epicentral distance and magnitude, a measure of the energy released, that does not depend on the local characteristics where the shaking is felt. If other mapped measures are available, such as earthquake intensity or Arias intensity, similar approaches can be established and applied by the tool.

Keefer (1984) and Rodríguez et al. (1999) discuss the magnitude and maximum epicentral distance observed to cause earthquake-triggered landslides, covering the period of 1811-1997 and 76 earthquakes, throughout the world, as shown in Figure 5-29.

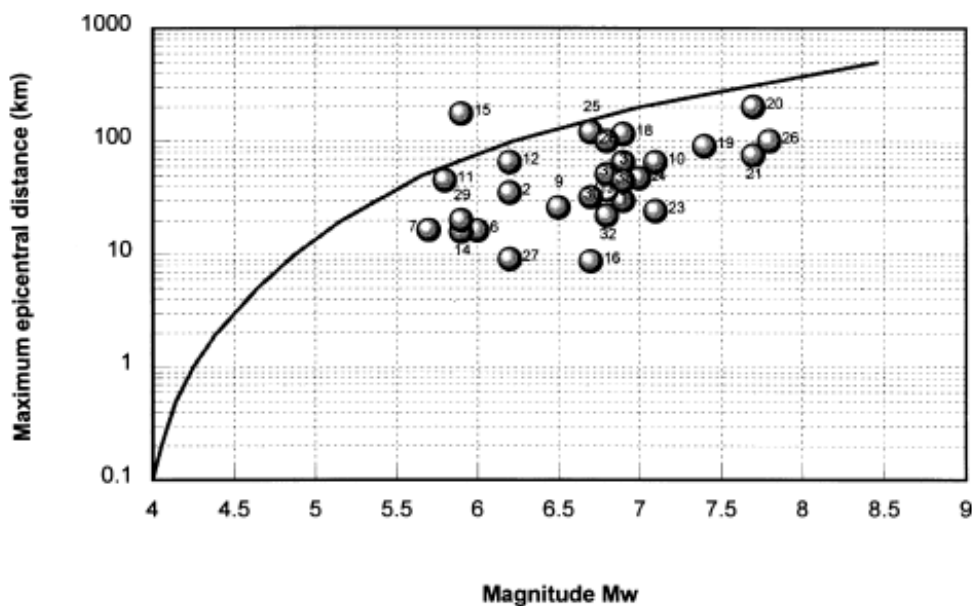


**Figure 5-29** Maximum epicentral distance to disrupted landslides as a function of magnitude ( $M_w$ ) (Rodríguez et al. 1999). Solid line shows upper bound determined by Keefer (1984) and circles represent events by Rodríguez et al. (1999).

Following the conservative approach, the upper bound determined by Keefer (1984) is used and, based on Figure 5-29, for each earthquake of seismic scenarios 1 and 2 defined in 5.4.1, a maximum epicentral distance capable of triggering landslides is established:

- a threshold epicentral distance of 100 km for the  $M_w=6.3$  intraplate earthquake of scenario 1;
- a threshold epicentral distance of 600 km for the  $M_w=8.7$  interplate earthquake of scenario 2 (extrapolated).

Figure 5-30 identifies the threshold epicentral distance for both seismic events.

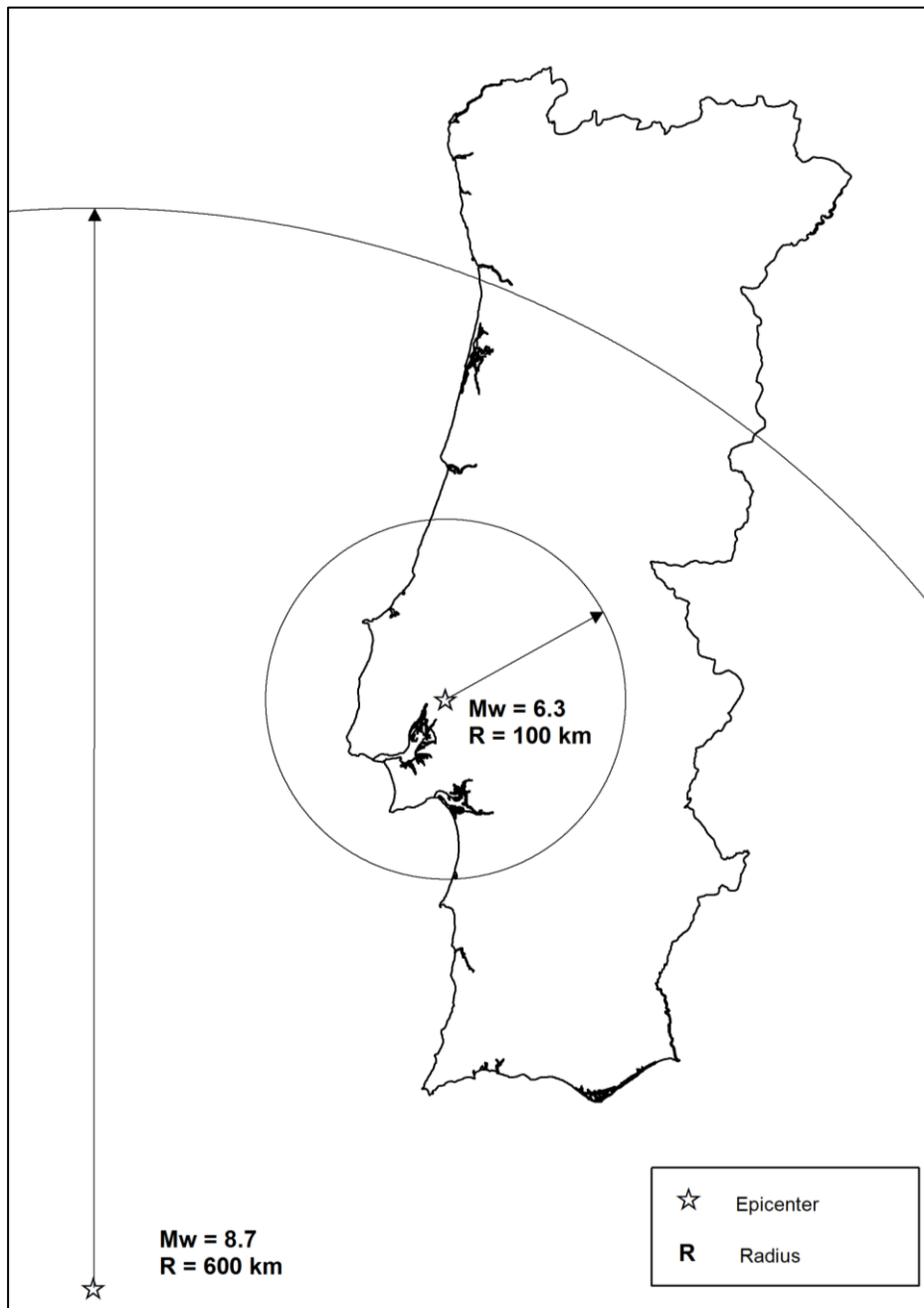


**Figure 5-30** Maximum epicentral distance within which the earthquakes are capable of triggering landslides of susceptible deposits.

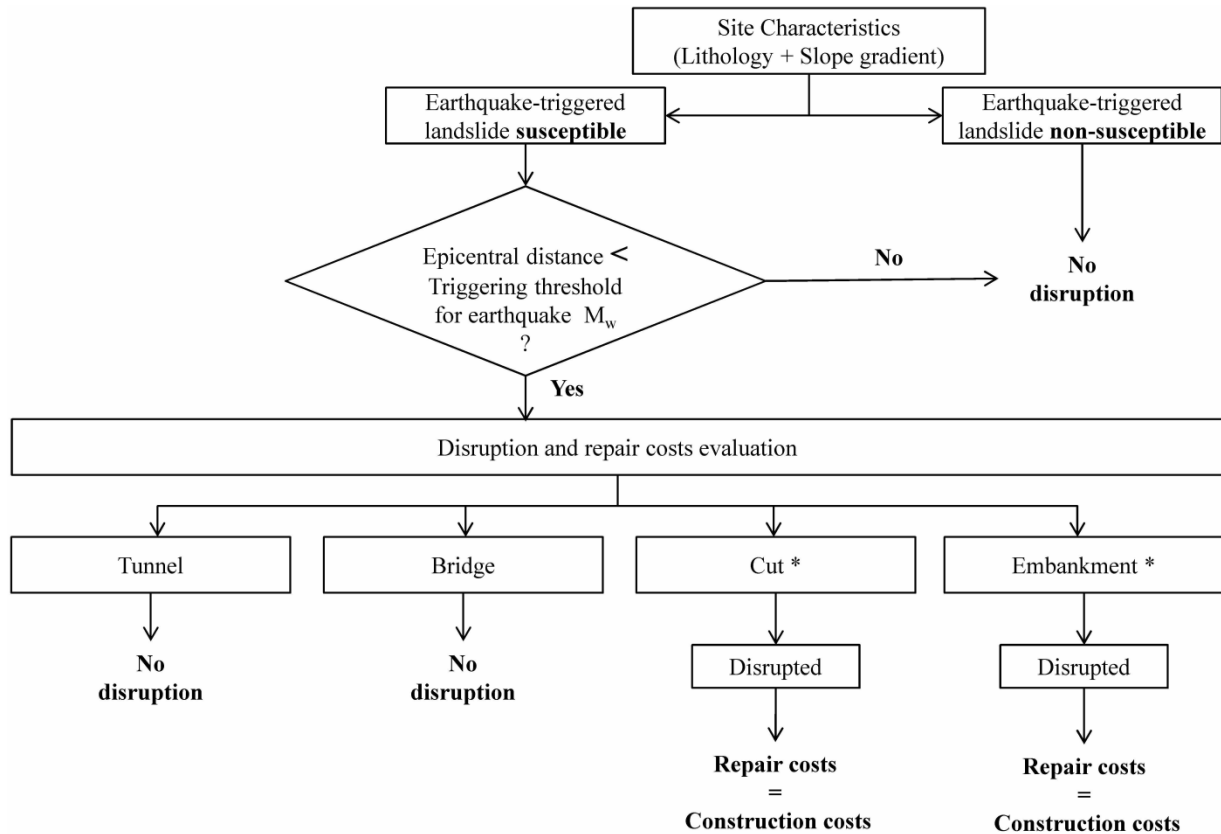


5.4.2.3 *DAMAGES COST EVALUATION*

The definition of the susceptibility zoning and the threshold earthquake magnitude and distance capable of causing landslide failure allows one to evaluate the performance of the HSR infrastructure. The landslide effects on the HSR depend on the location of the correlation of susceptibility and earthquake characteristics and the cross-section at each site.

In this research, as a simplification of reality, tunnel performance is assumed not to be disrupted by the landslides triggered at the surface. Bridges are also assumed not to be affected, considering that the decks are high enough above the ground and the design of the piers is able to withstand, without damage, the horizontal load that is imposed by the moving soil mass. On the other hand, cuts and embankments will be disrupted by landslides. The damage to these structures will require that repairs are made to restore HSR operation. Repairs in general relate to an assessment of a degree of damage, ranging from null to complete destruction. With the same reasoning as for the susceptibility assessment, two categories of repair requirements are established, namely “no repairs” or “reconstruction required”. The direct costs of reconstruction are assumed to be equal to the construction costs.

Figure 5-31 summarizes the methodology adopted for the earthquake-triggered landslides HSR repair costs assessment.



\*Refers to disruptions on the HSR cross-section by landslide failure of the existing natural ground. Landslides on slopes of cuts and embankments designed for the HSR are not included in the analysis.

**Figure 5-31** Flowchart of the evaluation of the repair costs due to earthquake-triggered landslides.

### 5.4.3 LIQUEFACTION

Seismically-induced liquefaction has proven to be responsible for severe damages to transportation infrastructure in the past, as described in section 2.4, including HSR infrastructure. Ishihara (1993) extensively discusses the triggering conditions and the consequences of liquefaction induced by earthquakes. The author states that while in static loading conditions cohesionless soils have been considered as less prone to failure and to major settlements than cohesive soils such as clays, in dynamic loading conditions the soil strength behavior differs. Under dynamic cyclic loading, as caused by an earthquake, cohesionless soils in a loose and saturated condition may suffer from a temporary and large loss of strength that is usually termed liquefaction.

Coelho and Costa (2009) discuss the identification and characterization of liquefaction risks for HSR in Portugal. The authors discuss the susceptibility of a significant area between

Lisbon and Oporto where recent cohesionless soil deposits in a loose state and saturated conditions exist. These geological and hydrological characteristics, along with the seismicity, explain the need of considering liquefaction risks. In fact, seismically-induced liquefaction has occurred in the past, within the Lisbon-Oporto HSR case-study area, as mapped by Jorge (1993) in Figure 5-32 for the earthquakes presented in Table 5-9. Assuming the historical criterion, stating that liquefaction tends to recur in sites where it has occurred for past earthquakes, as observed in the field (Youd 1984) and in centrifuge models (Coelho et al. 2006), Coelho and Costa (2009) state that the minimum annual probability of earthquake-triggered liquefaction is given by the inverse of the return period of an earthquake having induced local liquefaction in the past.

Jorge (1993) proposes a liquefaction potential zoning for mainland Portugal which identifies the areas that are simultaneously liquefaction susceptible and located where expected earthquakes are capable of inducing liquefaction.

In light of the literature discussed and based on previous work by Coelho and Costa (2009), the susceptibility to seismically-induced liquefaction is mapped for the case study area.

**Table 5-9** Magnitudes and origins of the earthquakes affecting mainland Portugal.

| Earthquake characteristics |                                     |                          |
|----------------------------|-------------------------------------|--------------------------|
| Year                       | Origin                              | Magnitude                |
| 1531                       | Lower Tagus Valley region           | $\approx 7$              |
| 1755                       | Interplate (exact location unknown) | 8.5-9 <sup>(1,2)</sup>   |
| 1761                       | Interplate (Gorringe zone)          | $\approx 8$              |
| 1856                       | Loulé Fault                         | -                        |
| 1858                       | Sado Submarine Valley region        | $\approx 7$              |
| 1909                       | Lower Tagus Valley region           | 5.8-6.3 <sup>(3,4)</sup> |

<sup>(1)</sup>(Gutscher 2006); <sup>(2)</sup>(Chester 2008), <sup>(3)</sup>(Teves-Costa et al. 1999); <sup>(4)</sup>(Oliveira 2008)

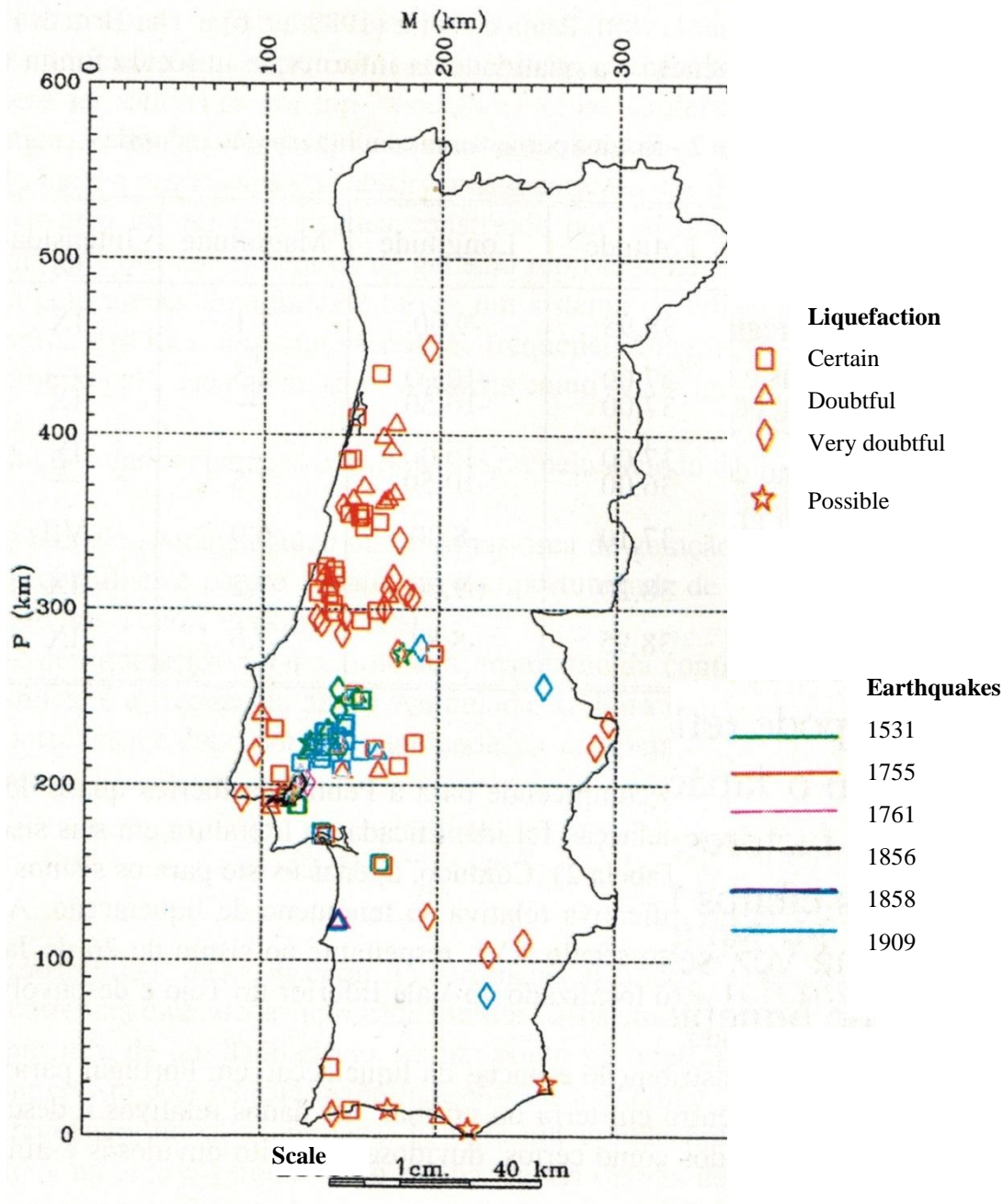


**Figure 5-32** Historical liquefaction events in Portugal (Jorge 1993).

#### 5.4.3.1 SUSCEPTIBILITY ASSESSMENT

The data available for seismically-induced liquefaction susceptibility zoning consists of the lithological surface description, the main rivers' map and the broad location of past liquefaction occurrence due to earthquakes (Figure 5-32) and the liquefaction potential zoning research by Jorge (1993).

Jorge (1993) maps the liquefaction susceptibility based on geological, geomorphologic and historical liquefaction data. The identification is based on 1/500,000 maps of altitude and geology and additional geological detail, covering particular areas with 1/200,000 and 1/50,000 maps. The zoning proposed by Jorge (1993) considers four degrees of liquefaction susceptibility, namely “high to very high”, “moderate”, “low to very low” and “not susceptible”.

Given that the mapped data available for the Lisbon-Oporto HSR planning case study is less detailed, the approach consists in defining the liquefaction susceptibility, in two degrees (“susceptible” and “non-susceptible”). This categorization is based on the lithological surface description in section 5.1.1 and the main rivers’ map (Figure 5-9). The approach then compares the susceptibility proposed by this research with the susceptibility zoning and the location of the past earthquake-triggered liquefaction by Jorge (1993).

The first step identifies the cohesionless soil units within the study area. Four lithological units are identified, as mapped in Figure 5-33, representing (1) Alluvium, (2) Sand dunes and aeolian sand, (3) Slope deposits (talus), terrace sands and (4) Sands and gravels. Lithological units representing (7) Sands, pebbles, lightly consolidated sandstone, clays and (8) Sandstones, argillaceous limestones, sands, gravels, clays in Figure 5-34 are not considered susceptible since, although having cohesionless soils, they are mixed with sedimentary rocks and clays and therefore considered not susceptible to liquefaction, or at least much less susceptible.

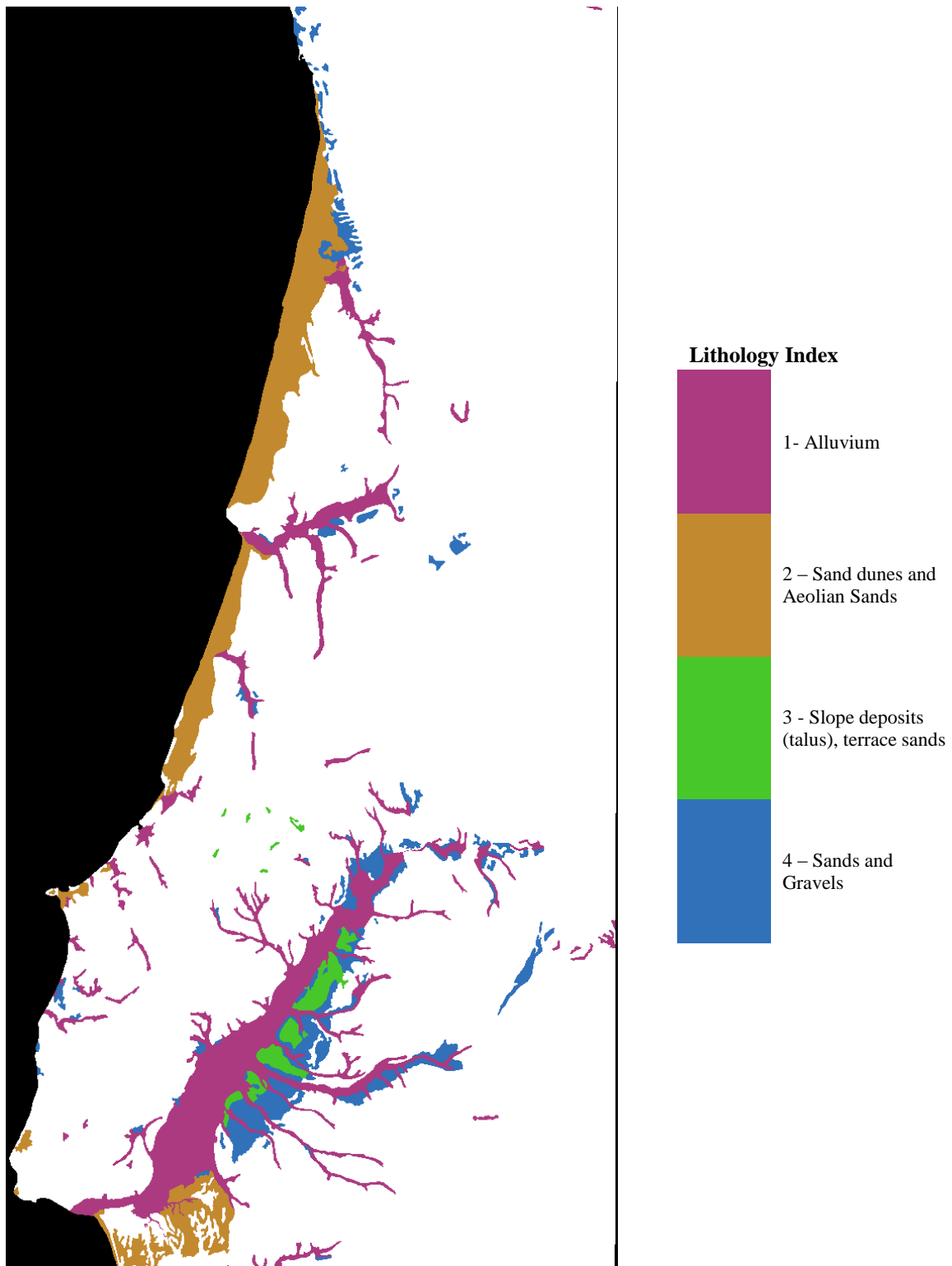


**Figure 5-33** Identification of earthquake-induced liquefaction susceptible deposits.

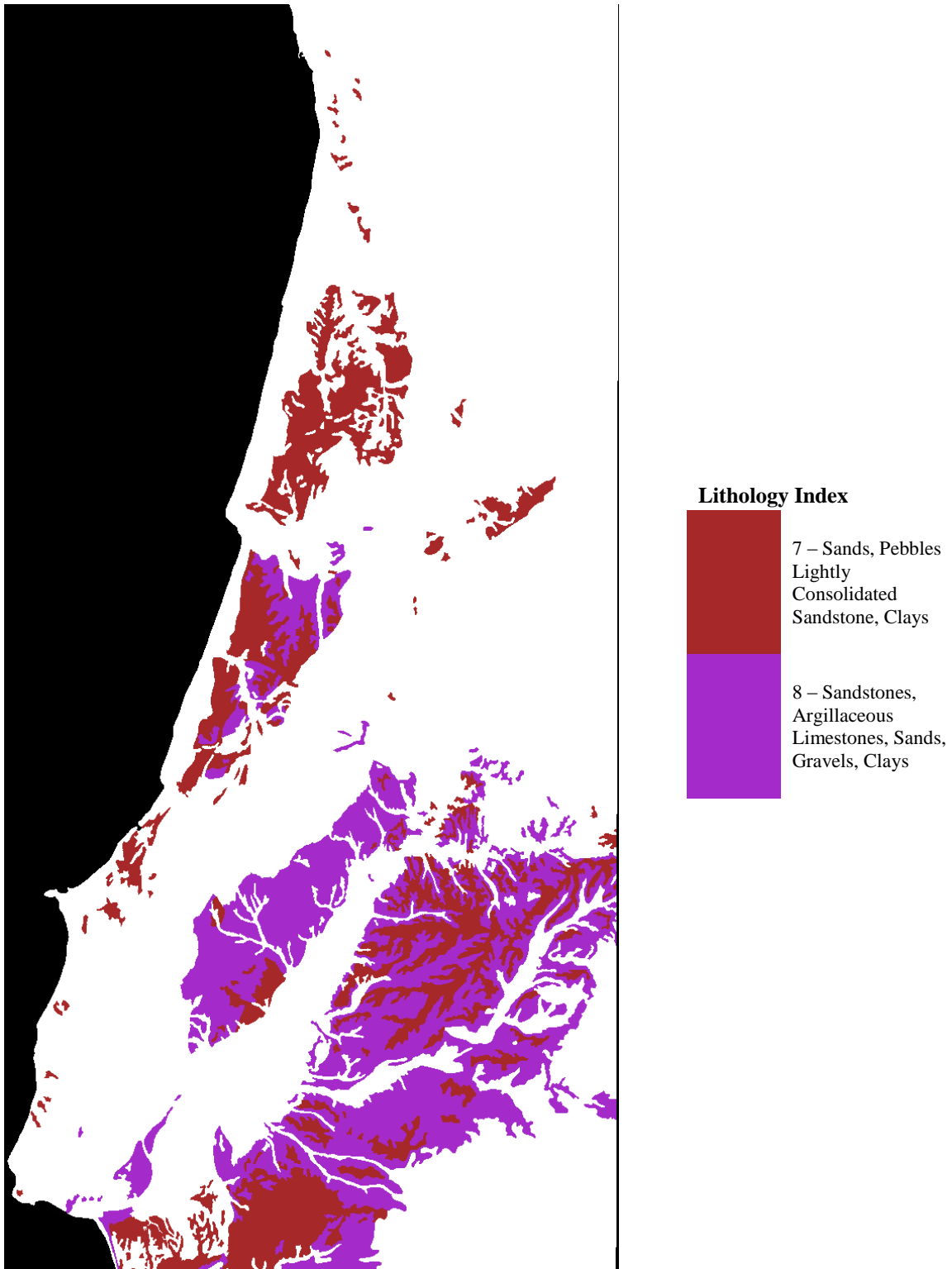


**Figure 5-34** Identification of lithology units (7) Sands, pebbles, lightly consolidated sandstone and (8) Sandstones, argillaceous limestones, sands, gravels and clays.

The lithological units representing cohesionless soil in Figure 5-33 are then mapped and overlaid with the rivers location as shown in Figure 5-35. This allows one to observe that these lithological units are located near major rivers, tributaries and along the Atlantic shoreline. Although it is not conclusive, this fact supports the susceptibility of the units considering that the identified deposits are likely to be in a saturated condition. The same areas were then subject to visual inspection and comparison with the past earthquake-induced liquefaction events mapped in Figure 5-32 and the susceptibility zoning by Jorge (1993) in Figure 5-36. One may observe that the sites of the past liquefaction occurrences (Figure 5-32) are mapped as susceptible in Figure 5-35. Additionally, a good fit exists between the susceptible deposits and the zoning proposed by Jorge (1993), depicted in Figure 5-36: “high to very high” and “moderate” degrees of susceptibility are considered in the Lisbon-Oporto HSR case study as susceptible and some areas of “low to very low” susceptibility degree are also mapped as susceptible while others are not.



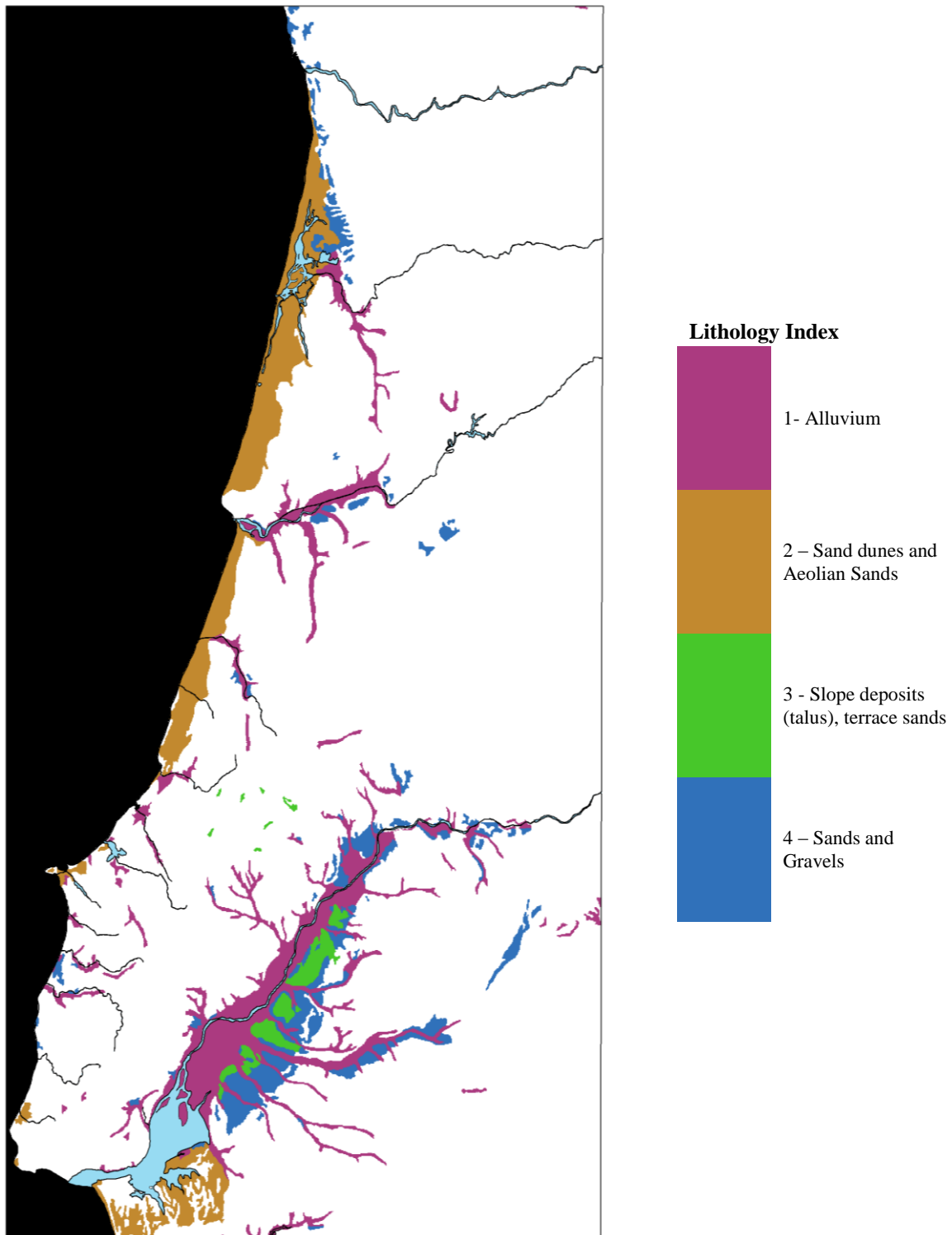


**Figure 5-35** Major rivers (Figure 5-9) overlaying the earthquake-induced liquefaction susceptible deposits (Figure 5-33).

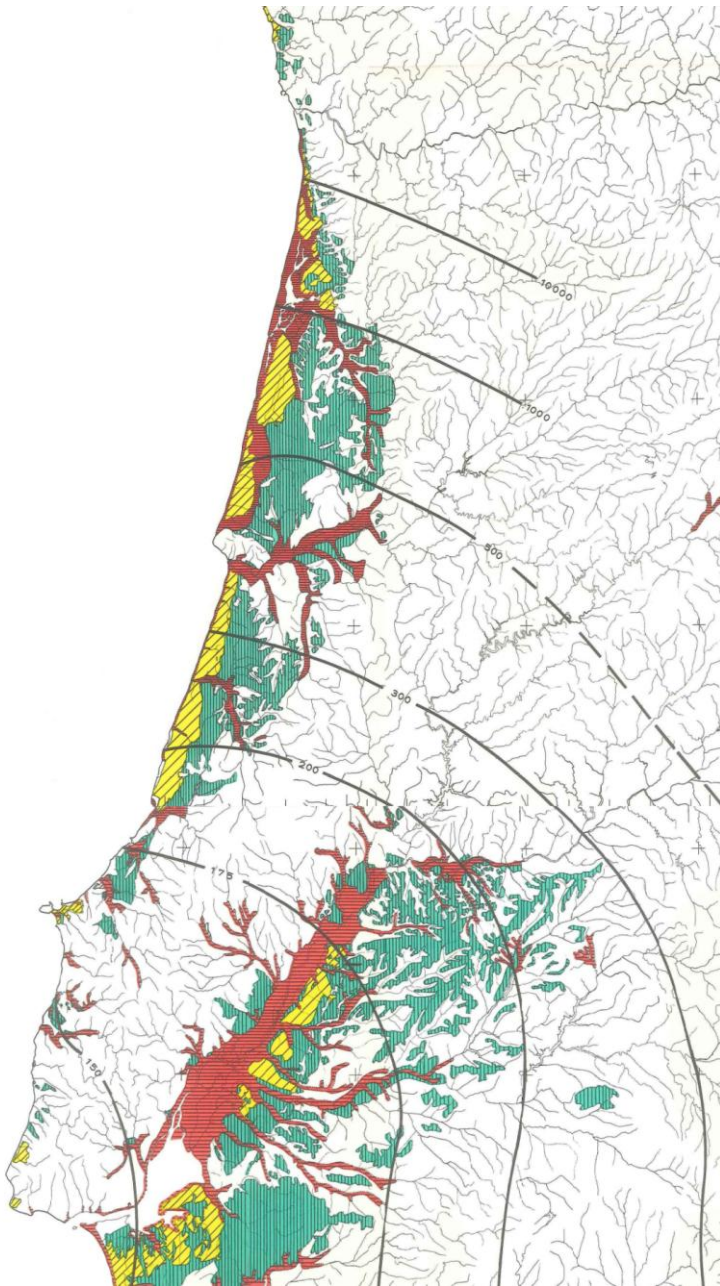


**Figure 5-36** Liquefaction susceptibility zoning proposed by Jorge (1993): high to very high susceptibility in red (horizontal stripes); moderate susceptibility in yellow (oblique stripes) and low to very low susceptibility in green (vertical stripes).

Given the similarities between the susceptibility zoning proposed in this in this research (Figure 5-33 and Figure 5-35) and the one proposed by Jorge (1993) in Figure 5-36 and the fact that the methodology in this research is able to represent, for the specifics of a planning scale, the susceptibility of the locations where liquefaction has occurred in the past (Figure 5-32), the susceptibility map in Figure 5-33 is considered for the case-study.

In summary, the liquefaction susceptibility zoning considers that lithology units of (1) Alluvium, (2) Sand dunes and aeolian sand, (3) Slope deposits (talus), terrace sands and (4) Sands and gravels are susceptible, since they are identified as mostly constituted by cohesionless materials, are reasoned to be in saturated conditions (by proximity to water bodies and the Atlantic Ocean) and include the historical occurrence of the phenomenon. All the remaining lithological units are categorized as non-susceptible to earthquake-induced liquefaction.

#### 5.4.3.2 *TRIGGERING CONDITIONS*

The evaluation of the damages caused to the HSR infrastructure by seismically-induced liquefaction requires one to establish the earthquake capability to cause liquefaction in the susceptible deposits. Jorge (1993) discusses several criteria used by different authors to correlate earthquake characteristics and the potential for triggering liquefaction in susceptible deposits. Similarly to the study of the triggering conditions for earthquake-triggered landslides in section 5.4.2.2., the scope and the scale of the planning analysis lead to the consideration of thresholds of maximum epicentral distance, for a given earthquake magnitude. Figure 5-37 identifies bounds for maximum epicentral distance and magnitude proposed by Ambraseys (1988) and Keefer (1984).

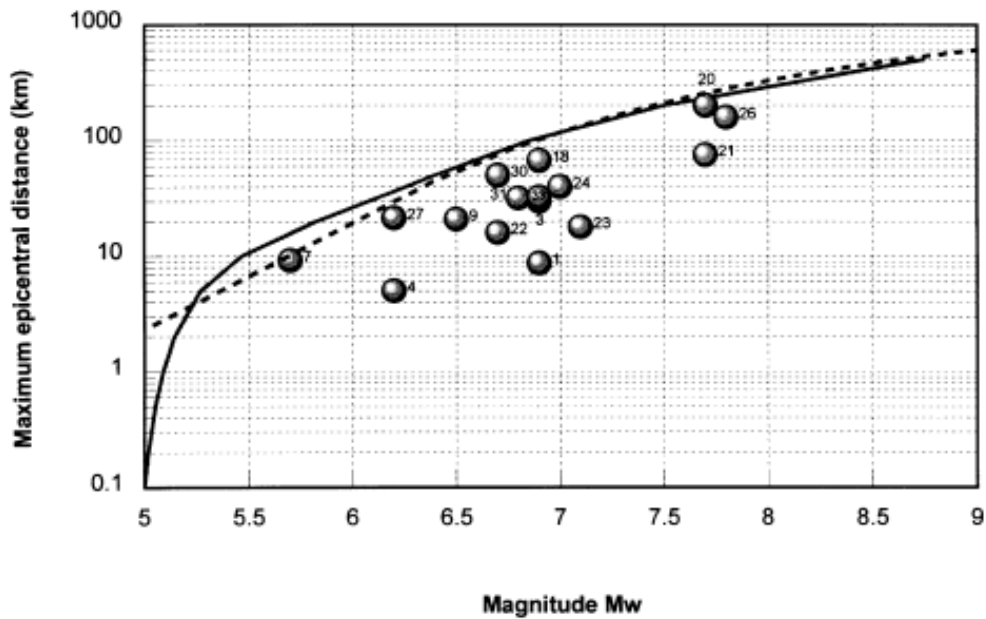


**Figure 5-37** Maximum epicentral distance to liquefaction occurrence as a function of moment magnitude  $M_w$  (Rodríguez et al. 1999). Solid line shows upper bound determined by Keefer (1984), circles represent events by Rodríguez et al. (1999) and dashed line shows the bound proposed by Ambraseys (1988).

Based on Figure 5-37 an initial maximum distance threshold of 45 km is considered for  $M_w = 6.3$  (seismic scenario 1) and 550 km for  $M_w = 8.7$  (seismic scenario 2). Earthquake-triggered liquefaction is predicted to occur in susceptible deposits located within the maximum epicentral distance of the respective earthquake (Figure 5-38) and not to occur otherwise. Conservative values are considered: the first corresponds to the bound proposed by Keefer (1984) and the latter to the bound set by Ambraseys (1988).

Given the existing information on certain liquefaction locations for the 1909 Benavente and the 1755 Lisbon earthquakes (Figure 5-32) a validation of the thresholds is performed. Sites that liquefied for each earthquake should be both mapped as susceptible (Figure 5-33) and comprised within the respective triggering threshold distance.

Comparing the susceptibility classification (Figure 5-33), the location of the liquefied deposits in Figure 5-32 and the maximum epicentral distance thresholds in Figure 5-38, one observes that 1909 liquefaction records are mostly classified as susceptible and are within the 45 km threshold. This comparison is also presented in Figure 5-39, in which one observes that only one “very doubtful” past liquefaction occurrence is not included by the research approach which is thus considered appropriate.

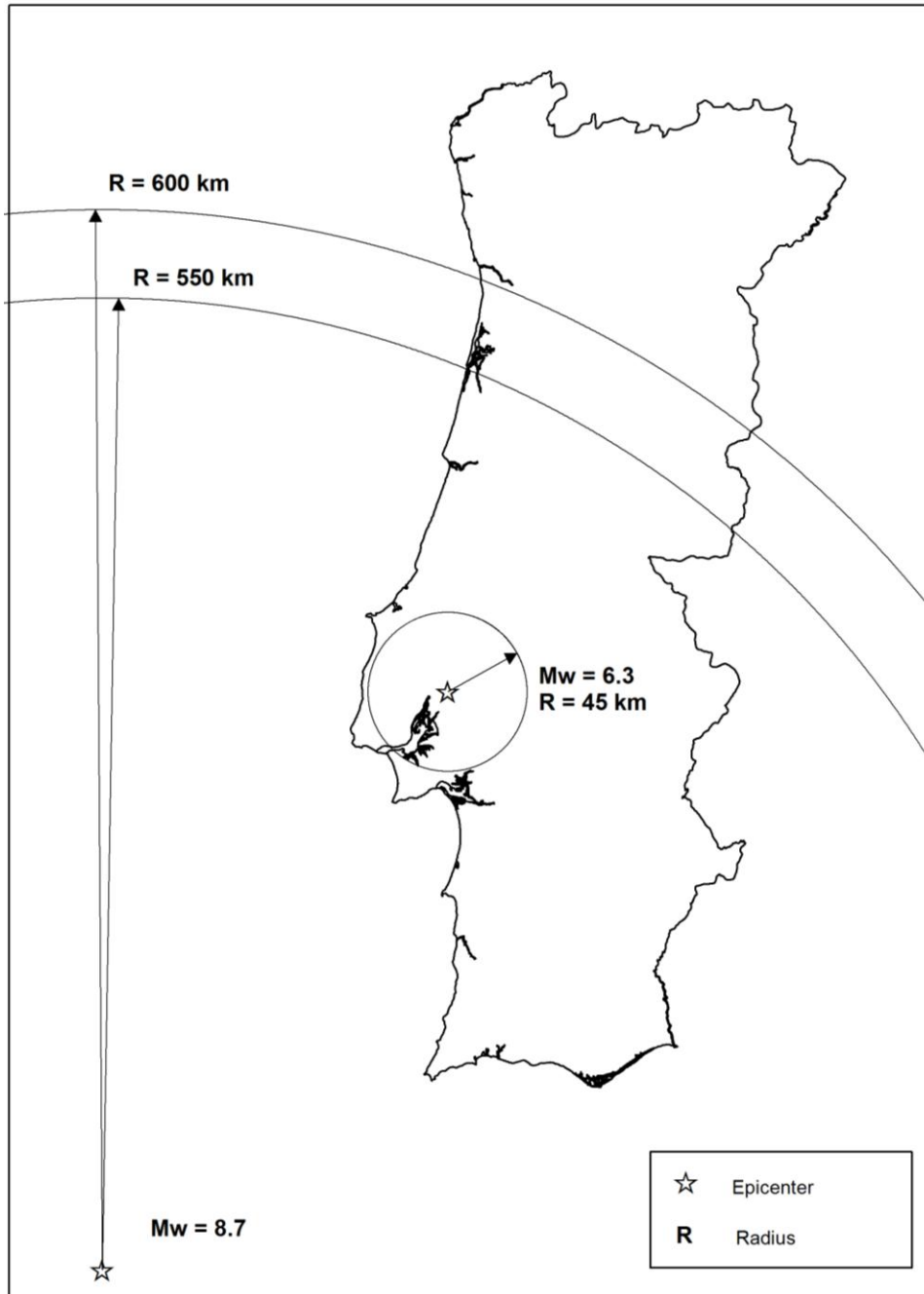


**Figure 5-38** Maximum epicentral distance within which the earthquakes are capable of inducing liquefaction of susceptible deposits.

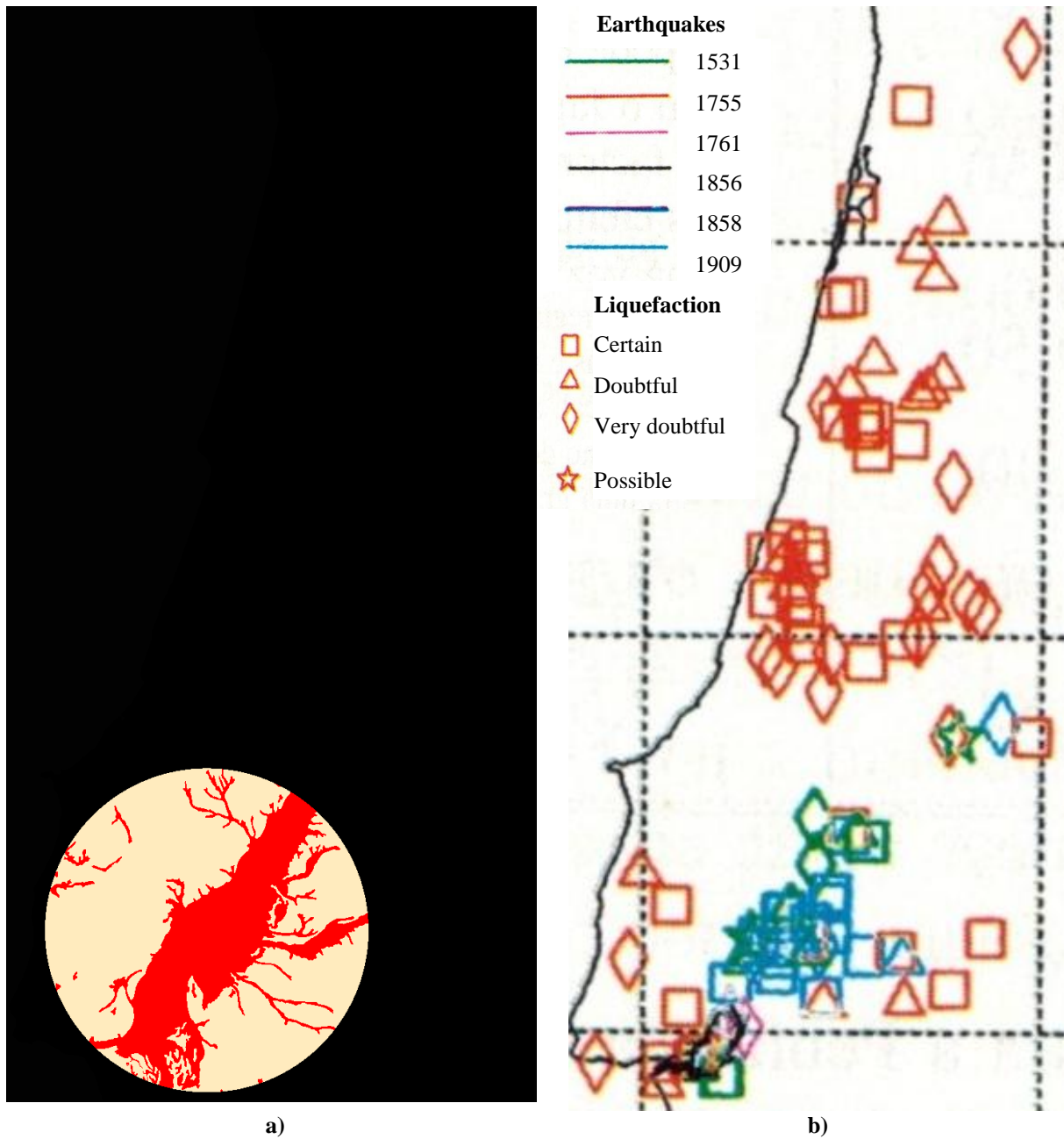


**Figure 5-39** Comparison of the research approach and past liquefaction: a) liquefaction susceptible deposits within the 45 km epicentral distance (in red) for the intraplate earthquake of  $M_w=6.3$  (seismic scenario 1) and b) past liquefaction occurrences extracted from Figure 5-32.

However, for the 1755 Lisbon earthquake, the two most northern and certain liquefaction sites (Figure 5-32, next to Aveiro) are also classified as susceptible but are just outside the 550 km boundary (Figure 5-38). Since uncertainties exist regarding the exact location of the earthquake, its magnitude and also the fact that the threshold definition is not based in an

exact method, an adjustment to the initial threshold is made in order to better represent the past liquefaction records.

Figure 5-40 shows how the susceptible deposits within the 600 km epicentral distance threshold inducing liquefaction (Figure 5-40 a) is able to represent the discussed northernmost certain liquefaction records (Figure 5-40 b). Although the representation in Figure 5-40 b) is not precise, the comparison shows the research approach is capable of representing most certain liquefaction records.

The final thresholds are 45 km for the  $M_w = 6.3$  earthquake of seismic scenario 1 and 600 km for the  $M_w = 8.7$  earthquake of seismic scenario 2 (Figure 5-38).

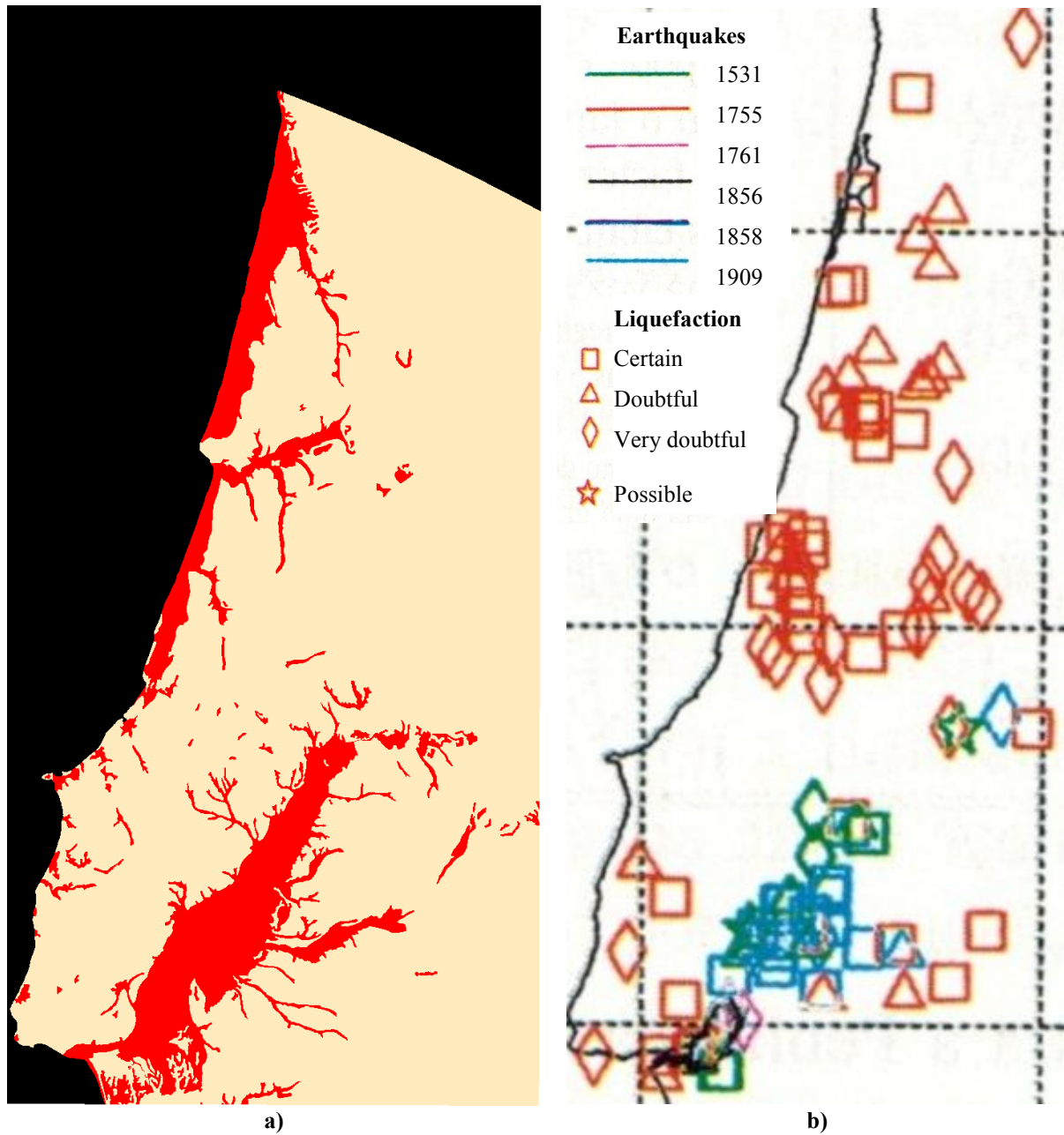


**Figure 5-40** Comparison of the research approach and past liquefaction: a) liquefaction susceptible deposits within 600 km epicentral distance (in red) for the interplate earthquake of  $M_w = 8.7$  (seismic scenario 2) and b) past liquefaction occurrences extracted from Figure 5-32.

#### 5.4.3.3 DAMAGES COST EVALUATION

The previously described susceptibility zoning and triggering conditions allow one to assess the damages to tunnels, bridges, cuts and embankments that compose the HSR infrastructure.

Although liquefaction susceptible soil layers may exist at depth, between non-liquefiable layers, information on such layers is not available. Therefore, underground structures such as



the tunnels built for the HSR are not considered to be disrupted by earthquake-induced liquefaction. However, surficial cuts and embankments built on liquefiable soils are damaged by liquefaction occurrence. Since susceptibility is categorized as either susceptible or non-susceptible, a degree of damages resulting from liquefaction is not assessed. For both cuts and embankments at sites where liquefaction is predicted to occur, total reconstruction is assumed, with a cost equal to the initial construction cost.

Bridges are also vulnerable to liquefaction (Dickenson et al. 2002). Liquefaction of soils under bridge piers has proven to provoke damages to viaducts and bridges, along with the ground motion effects resulting from earthquakes. Kircher et al. (2006) review the loss estimation method HAZUS Earthquake and discuss improvements to building damage assessment. According to the authors, HAZUS Earthquake defines 4 damage states (slight, moderate, extensive and complete) and sets the costs of structural and non-structural damages as a percentage of the replacement cost. Applications of HAZUS Earthquake to transportation systems and analyses of bridge performance are presented both by FEMA (2001) and Luna et al. (2008). An application to lifelines within the Lisbon area by Azevedo et al. (2009) also implements HAZUS99, in which the lack of Portuguese seismic damage inventories requires that an adaptation is made from the seismic behavior of the different classes of bridges in California, USA.

Analyzing the earthquake effects on bridges (Wilson 2003; Yamazaki 2004; Wang and Lee 2009; EQE 1995; Ashford and Kawamata 2006; Dickenson et al. 2002) the main causes of damage observed are strong ground motion and liquefaction. Considering that most of the bridges seismically designed did not collapse, even with the simultaneous effects of ground motion and liquefaction, the repair cost for bridges due to liquefaction occurrence is estimated at 40% of its initial construction costs. Considering the bridge direct losses equal to the total initial construction costs would constitute an overestimation of the costs with unrealistic impacts on the seismic scenario performance of the HSR infrastructure. More detailed analyses and loss predictions can be performed for bridge damages under seismic scenarios (Mackie et al. 2010). These, however, require information that is not available for this analysis such as details of the bridge type and its components' individual performance under seismic conditions.

Figure 5-41 summarizes the methodology adopted for the earthquake-triggered liquefaction HSR repair costs assessment.

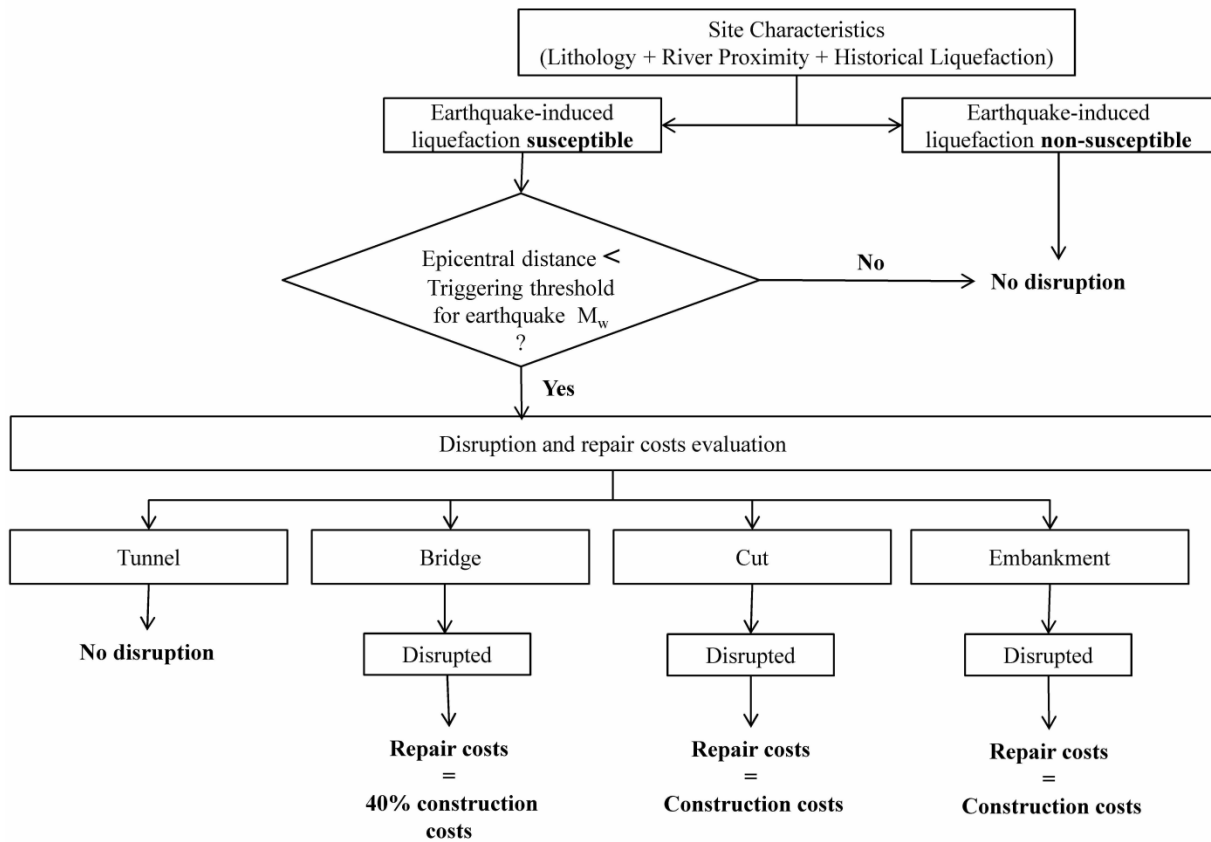


**Figure 5-41** Flowchart of the evaluation of repair costs due to earthquake-induced liquefaction.

## 5.5 INTENSE RAINFALL SCENARIO

The ability of severe rainfall, causing floods and rainfall-triggered landslides, to damage and disrupt transportation systems worldwide has been introduced in section 2.4. This and the fact that rainfall-triggered landslides and floods have occurred in Portugal and particularly in the case-study area lead to the consideration of an intense rainfall scenario when planning the HSR network linking Lisbon and Oporto.

The information on the precipitation intensity and duration and respective return period is used in the analysis to define the rainfall scenario. HSR disruptions due to rainfall-triggered landslides and floods are considered. Similarly to the earthquake-triggered landslides in section 5.4.2, rainfall-triggered landslides depend on both the rainfall characteristics and the

site susceptibility. Flooded areas related with intense rainfall events depend, besides the rainfall and site characteristics, on the configuration of catchment areas.

The next sections describe in detail the methodology used for the HSR performance assessment, in terms of the resulting HSR damage repair costs, considering rainfall-triggered landslides and floods. The methodology used for floods differs from that of the rainfall-triggered landslides. Despite considering only rainfall initiated floods, other origins exist, the hazard level is not derived directly from the precipitation's duration and intensity characteristics. Instead, existing maps of flooding areas are used, considering the same return period as for the isohyetal maps. The performance of the different HSR cross-sections (embankments, cuts, bridges and tunnels) is then separately assessed for landslides and floods. The estimated costs due to repair of the HSR physical damages are presented. However, derailment occurrence is not included in the analysis.

#### 5.5.1 RAINFALL CHARACTERISTICS

The definition of the rainfall characteristics is a result of the available data and the requirements of the Lisbon-Oporto HSR planning. The definition of a flood map at a regional scale requires that extensive data is collected and processed and its elaboration from the measured data is outside the scope of this research. However, the flood map for the Portuguese mainland territory for a return period of 100 years is available. Rainfall intensity-duration maps are also available for different return periods including 100 and 1000 years. Brandão et al. (2001) analyze and characterize intense rainfall for mainland Portugal. As a result of the study, Brandão et al. (2001) present isohyetal maps for different rainfall durations, pertaining to different return periods, later updated with new data by Brandão et al. (2004). Figure 5-42 shows the updated isohyetal maps for the return period of 100 years and rainfall durations of 30 minutes, 1 hour, 6 hours, 24 hours and 48 hours proposed by Brandão et al. (2004).

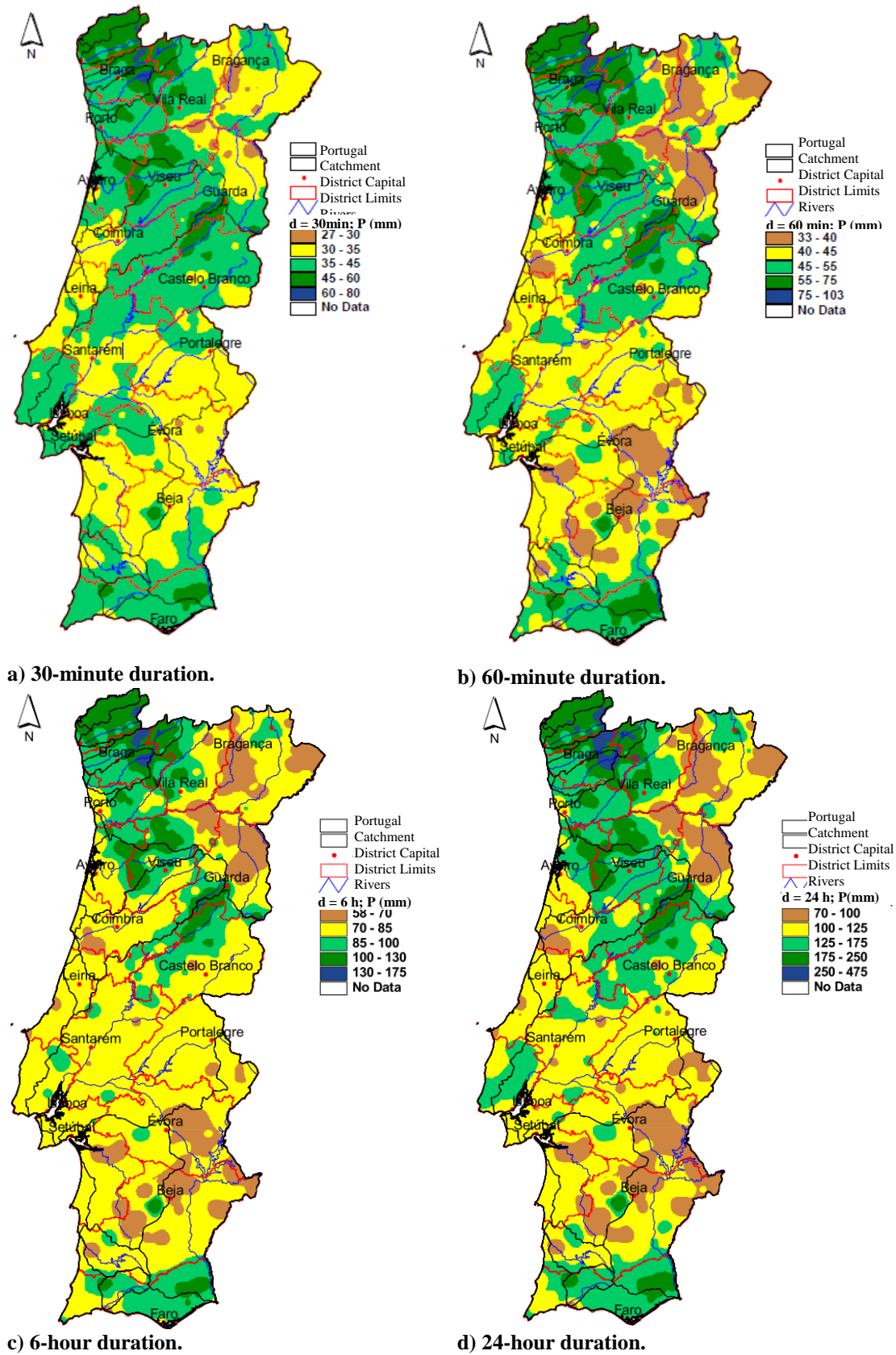
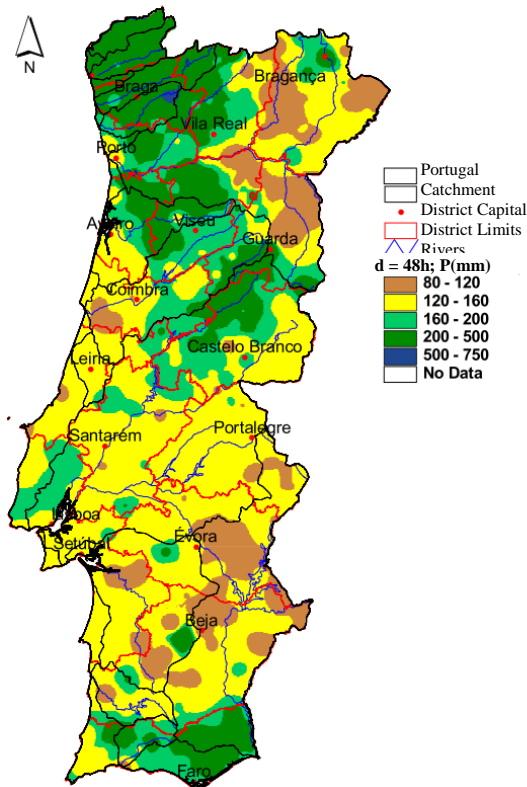


**Figure 5-42** Isohyetal maps of mainland Portugal for a return period of 100 years and different rainfall durations by Brandão et al. (2004): a) 30 minutes; b) 60 minutes; c) 6 hour; d) 24 hour and e) 48 hour.



e) 48-hour duration.

**Figure 5-42** Isohyetal maps of mainland Portugal for a return period of 100 years and different rainfall durations by Brandão et al. (2004): a) 30 minutes; b) 60 minutes; c) 6 hour; d) 24 hour and e) 48 hour. (Continued).

Considering the available data, the rainfall characteristics in the scenario are defined for a 100 year return period. Different return periods can be used provided that the information exists and is relevant for the study, as would be in the case of a tropical area where more frequent events relate to larger rainfall severity and capability to damage HSR infrastructure.

The maps available for the scenario definition, considering different rainfall durations (Figure 5-42) show small variations in the expected rainfall between Lisbon and Oporto. Considering the case study area, one can observe slightly larger rainfall in the region north of Lisbon and between the cities of Aveiro and Oporto.

### 5.5.2 RAINFALL-TRIGGERED LANDSLIDES

The occurrence of rainfall-triggered landslides is the result of the site susceptibility and the type and severity of the precipitation occurring at the same location. Zêzere et al. (1999)

discuss the occurrence of landslides in Portugal, in the North of Lisbon Region, identifying the occurrence of landslides, since 1967, for three distinct rainfall types:

- moderate intensity and 15-day duration, with a return period ranging from 2 to 4.5 years;
- high intensity and short duration (from 6 to 24 hours), with a return period ranging from 55 to 160 years;
- extended rainfall duration events, in which landslide occurrence requires the analysis of antecedent rainfall from 30 days up to 75 days and return periods vary between 6.5 to 25 years.

Zêzere et al. (1999) study 5 sample areas of a total region of 61.7 km<sup>2</sup>, part of the Lisbon-Oporto HSR study-area, and a total of 597 landslides. The study analyzes the relationship between the types of landslide, the site characteristics prompting the susceptibility and the triggering factors. Landslides are grouped into 7 type categories: rockfalls, shallow translational slides, translational slides, rotational slides, slides and falls due to bank erosion and complex and composite slope movements. Site characteristics inducing rainfall-triggered landslide susceptibility include lithology, slope angle, human activity and land-use.

Zêzere et al. (1999) observed that, of the total 597 landslides, nearly 40% are slope movements (including fall, topple and slide movements limited to river banks) due to bank erosion, with mean and standard deviation slope angles of, respectively, 17° and 10°. Around 35% of the 597 landslides are shallow translational slides, with mean and standard deviation slope angles of, respectively, 23° and 8°. The slope movements due to bank erosion occur mainly in the lithological unit composed of the upper Cretaceous basalts and volcanic tuffs and the shallow translational slides occur in deposits lying on an impermeable substratum including clays and marls.

Furthermore, Zêzere et al. (1999) analyze the precipitation characteristics leading to the landslide occurrence and identify critical rainfall thresholds of intensity-duration triggering the landslides. The authors conclude that the susceptibility factors and critical thresholds vary with the type of landslide, observing that:

- Shallow transitional slides have occurred in moderate intensity and 15-day duration events;
- Slides and falls due to bank erosion were associated with flash floods as a result of high intensity and short duration events;
- Deeper translational and rotational landslides were due to extended rainfall events.

The research by Zêzere et al. (1999) was later extended by Zêzere and Rodrigues (2002) and Zêzere et al. (2008) to include antecedent rainfall in the determination of intensity-duration thresholds for the long-lasting landslide-triggering rainfall.

Mapped data for the Lisbon-Oporto HSR planning study area is available for rainfall durations up to 48 hours (Figure 5-42). This restricts the definition of intensity-duration thresholds to intense and short rainfall episodes, only one of the three types of rainfall identified to have triggered landslides in the past in the North of Lisbon area. However, once available, further information on longer periods (15 days and 30-70 days) could be incorporated in the analysis in a similar methodology as herein described for short intense rainfall events.

#### *5.5.2.1 SUSCEPTIBILITY ASSESSMENT*

The data available for the rainfall-triggered landslide susceptibility analysis is composed of lithology (Figure 5-4 and Table 5-1), slope angle (Figure 5-22) and any other characteristic that can be obtained from the DEM, similarly to the earthquake-triggered landslide susceptibility definition in section 5.4.2.1. Due to the coarse nature of the DEM, as explained previously for the earthquake scenario, the quality of the derived maps is poor and to avoid the propagation of uncertainties into the susceptibility assessment, only two parameters were chosen for the susceptibility zoning: lithology and slope angle. Mapped data on land-use, vegetation and the presence of old landslides, as analyzed by Zêzere et al. (1999), are also not included.

The methodology chosen considers two landslide susceptibility types: susceptible and non-susceptible. This is a simple and rough analysis intended to anticipate and consider major landslide hazards at a regional scale and covering a significantly large area. In subsequent

stages of the design, when the area to characterize is reduced and detailed geotechnical and hydrological data are available, intermediate susceptibility categories can be established as done by Castellanos Abella and Van Westen (2008), Ermini et al. (2005), Saldivar-Sali and Einstein (2007) and Van Westen et al. (2003). If more detailed information was available for planning, one could incorporate it in the analysis, bearing in mind that the planning scope and requirements differ from those in a design stage of a project and that increasing refinement of the analysis implies additional computational burden.

The mapped rainfall data defines intense and short duration episodes and thus the susceptibility analysis relates with the landslide mechanism described by Zêzere et al. (1999) as slides and fall due to bank erosion. The analysis considers that the rainfall-triggered landslides susceptible formations are those where lithology is cohesionless and, simultaneously, where the slope angle is equal or larger than  $17^\circ$ . Cohesionless lithological units are mapped in Figure 5-43 and include: (1) alluvium, (2) sand dunes and aeolian sands, (3) slope deposits (talus) and terrace sands, (4) sands and gravels, (7) sands, pebbles, lightly consolidated sandstones, clays, (8) sandstones, argillaceous limestones, sands, gravels, clays, (271) pyroclastic rocks (tuffs...) and (280) basalts. The first four lithological units are assumed to be formed solely by cohesionless materials. Unit (7) sands, pebbles, lightly consolidated sandstones, clays and unit (8) sandstones, argillaceous limestones, sands, gravels, clays, are formed by cohesionless materials and some cohesive materials, the latter assumed to be weathered and with little cementation that makes them prone to intense rainfall triggered landslide. Unit (217) tuffs and unit (280) basalts, have suffered landslides in the northern Lisbon area triggered by short and intense rainfall episodes and are thus assumed as susceptible to intense rainfall triggered-landslides. Slope angles are mapped in Figure 5-22 and are grouped into 2 intervals in Figure 5-44.  $17^\circ$  is the mean angle observed for the landslides in the northern Lisbon area and one can reason that considering the shear resistant of cohesionless soils, smaller slopes correspond to a static equilibrium state having already been eroded and deposited.



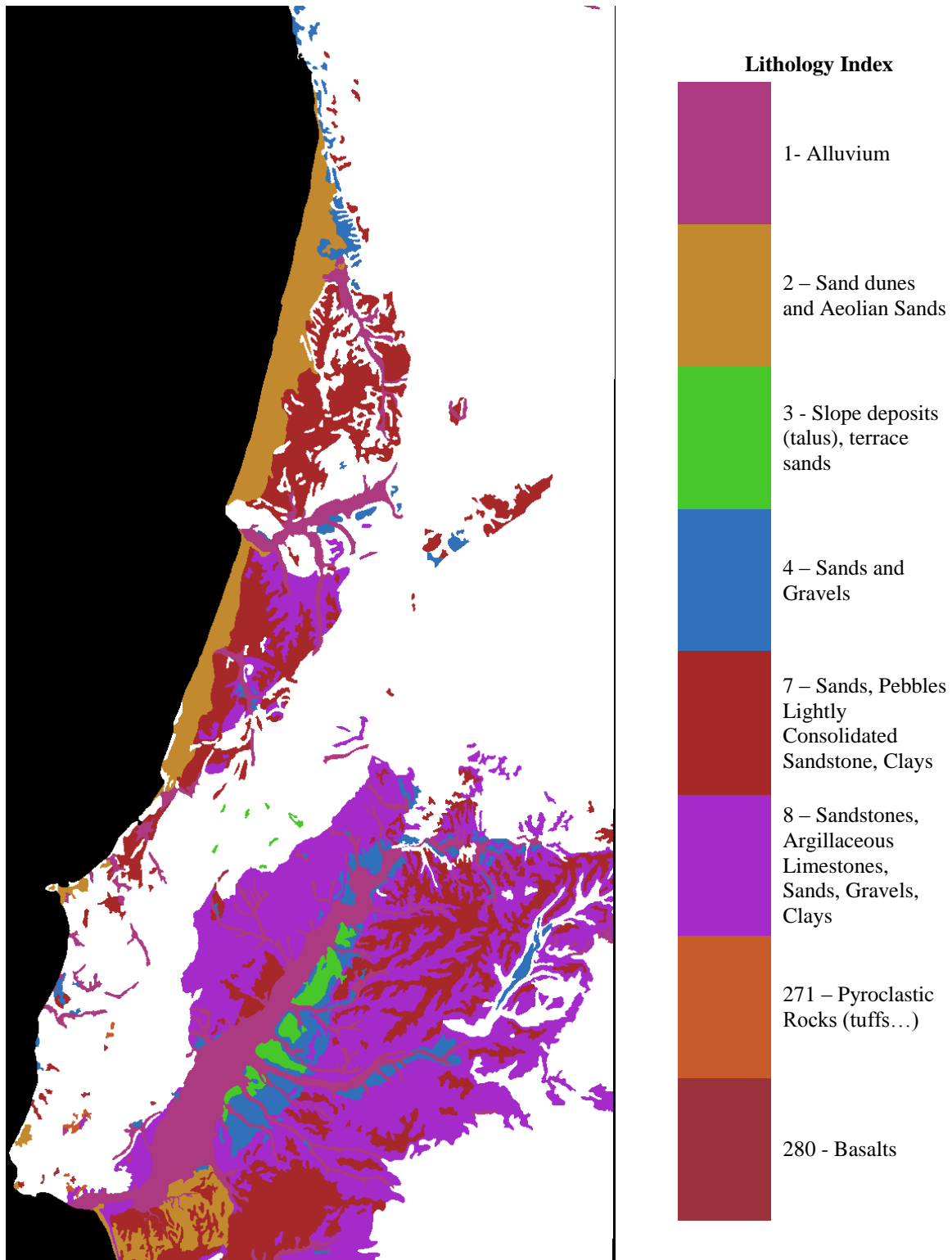


**Figure 5-43** Identification of rainfall-triggered landslides susceptible deposits.

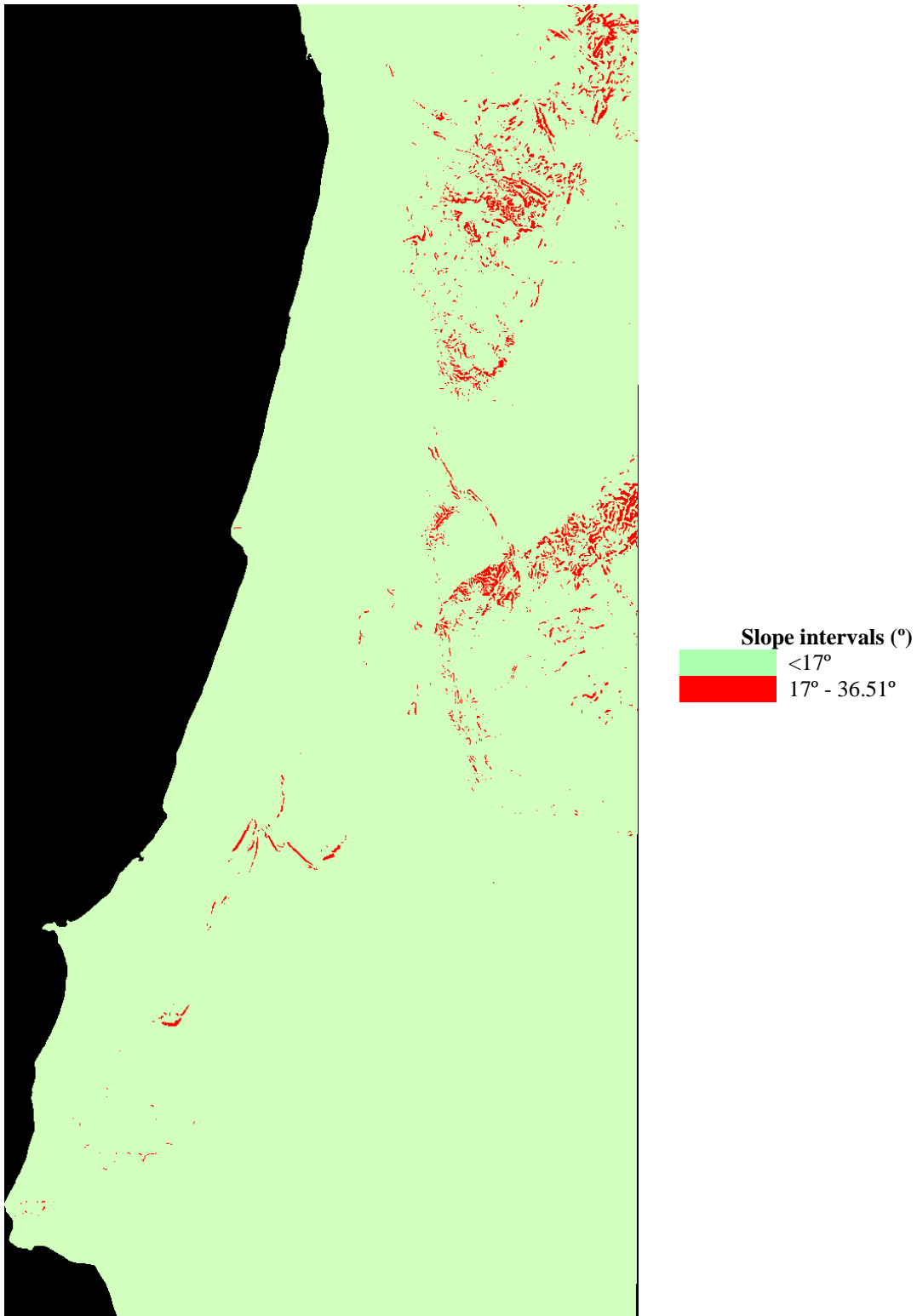


**Figure 5-44** Slope angle obtained from DEM, grouped into 2 intervals: < 17° and 20° - 36.51°.

The areas where the slope angle and the lithology criteria are met simultaneously are classified as susceptible and classified as non-susceptible if otherwise. Five rainfall-triggered landslide susceptible zones are identified for the HSR Lisbon Oporto case study in Figure 5-45 which are zoomed in in Figure 5-46, Figure 5-47, Figure 5-48, Figure 5-49 and Figure 5-50.

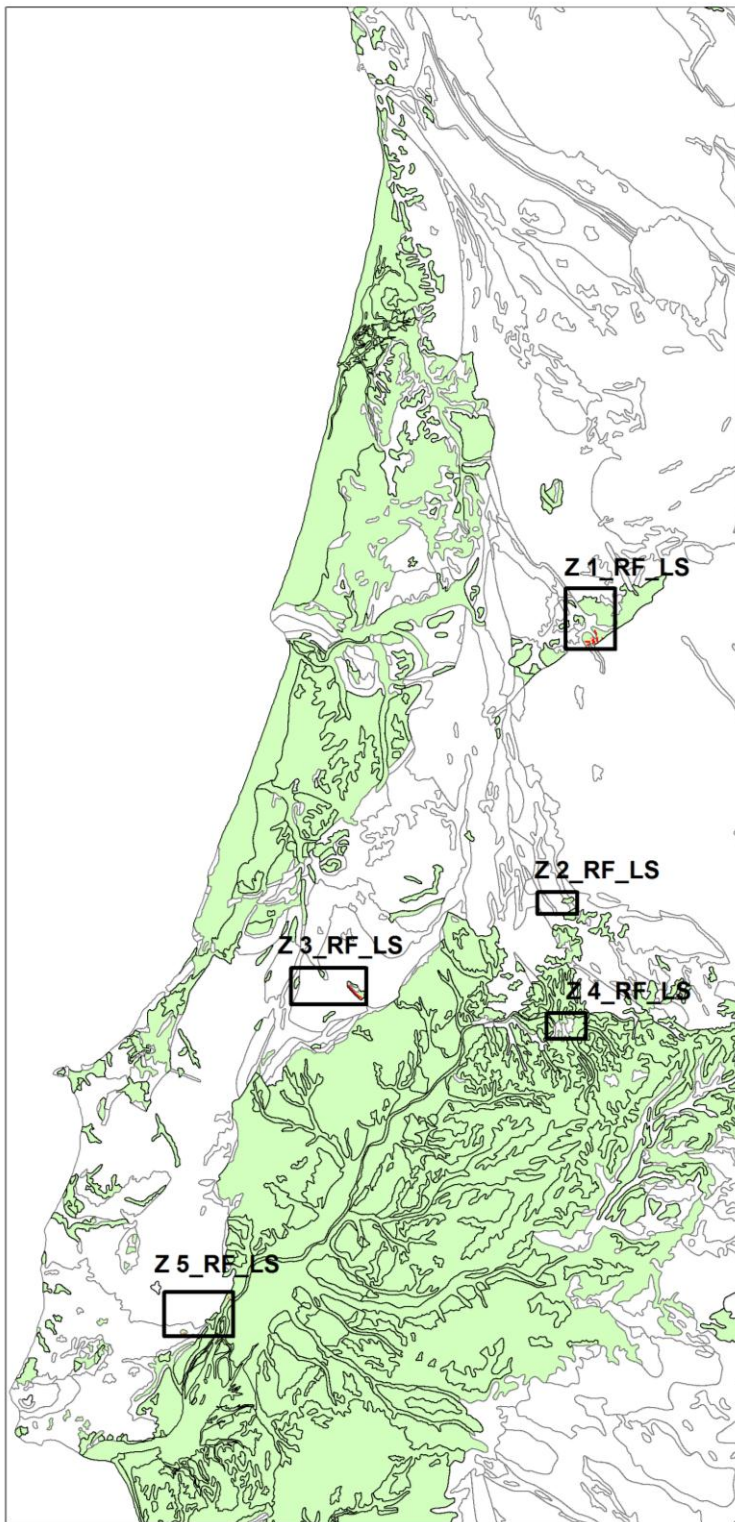


**Figure 5-45** Overlay of rainfall-triggered landslide susceptible lithology units and the slope angle intervals: non-susceptible deposits in white; susceptible deposits where slope angle is  $<17^\circ$  in green (lighter shade) and susceptible areas in red (darker shade) pictured within zoom frames Z1\_RF\_LS, Z2\_RF\_LS, Z3\_RF\_LS, Z4\_RF\_LS, Z5\_RF\_LS.

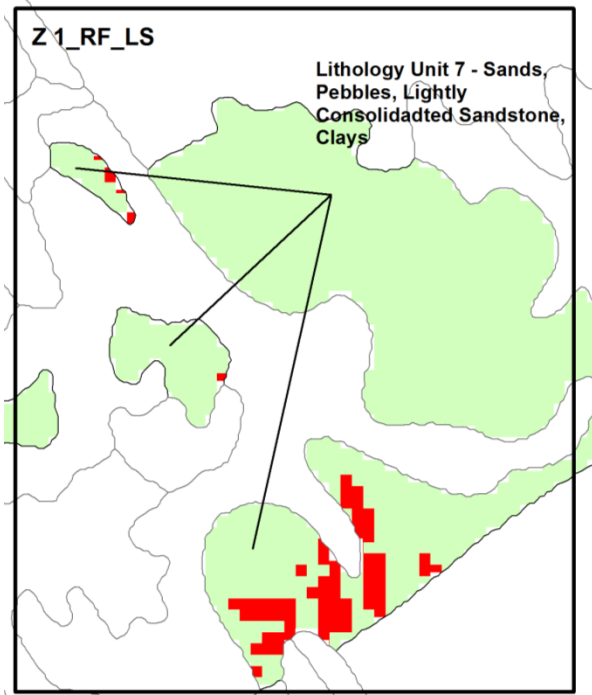


**Figure 5-46** Zoom-in of zone Z1\_RF\_LS: susceptible rainfall-triggered landslide areas in red (darker shade).

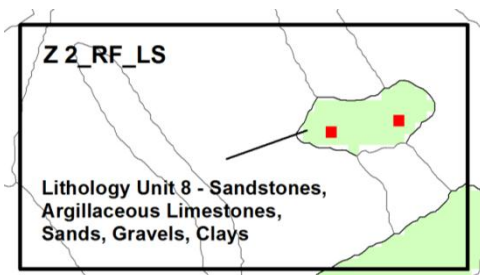


**Figure 5-47** Zoom-in of zone Z2\_RF\_LS: susceptible rainfall-triggered landslide areas in red (darker shade)

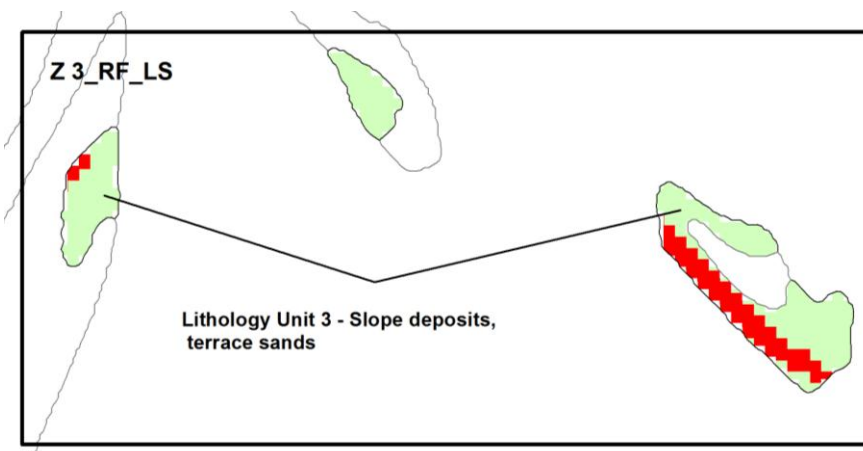


**Figure 5-48** Zoom-in of zone Z3\_RF\_LS: susceptible rainfall-triggered landslide areas in red (darker shade)

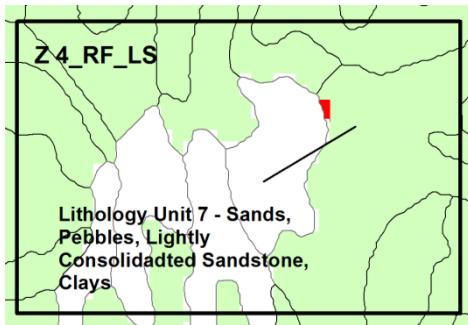


**Figure 5-49** Zoom-in of zone Z4\_RF\_LS: susceptible rainfall-triggered landslide areas in red (darker shade)

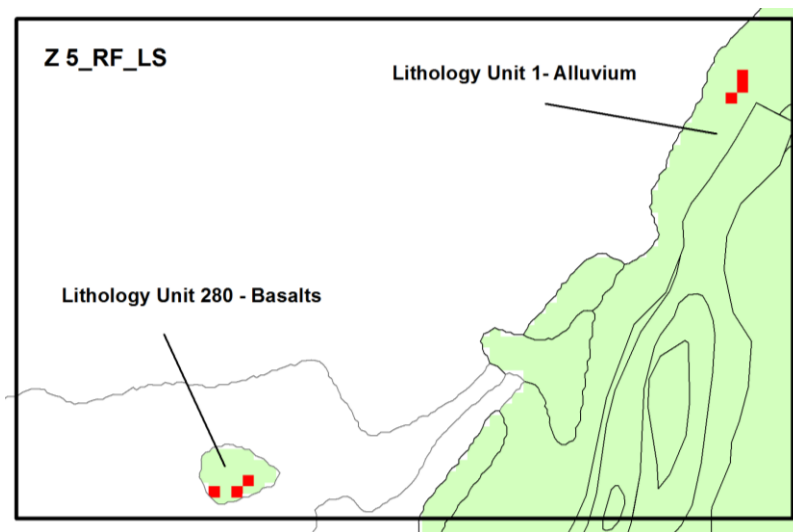


**Figure 5-50** Zoom-in of zone Z5\_RF\_LS: susceptible rainfall-triggered landslide areas in red (darker shade)

The rainfall-triggered landslide susceptibility classification as “susceptible” and “non-susceptible” involves the same assumptions, as previously explained for the earthquake-triggered landslide susceptibility, regarding rock falls (lack of consideration thereof) and the landslide susceptibility assessment solely for the existing natural ground.

#### 5.5.2.2 TRIGGERING CONDITIONS

Having the susceptibility zoning established for the study area, the actual landslide occurrence depends on the triggering rainfall thresholds. Similarly to the earthquake scenario, since only the landslide susceptibility categories “susceptible” and “non-susceptible” are considered, the identification of the rainfall threshold intensity-duration capable of causing landslides on susceptible zones determines the occurrence of rainfall-triggered landslides.

As previously discussed, the lack of data restricts the definition of intensity-duration thresholds to intense and short rainfall episodes. As a generalization of the past landslide occurrence studied by Zêzere et al. (1999), the threshold of precipitation duration-intensity able to trigger landslides is defined as 137 mm for a 24 hour period. Since the precipitation data in Figure 5-42 d) is defined by 5 intervals, a conservative threshold of 125 mm per 24 hours is chosen (the lower bound of the interval containing 137 mm of rainfall for 24 hour duration a return period of 100 years). Figure 5-51 identifies the case-study areas where rainfall larger than the threshold is observed, based on Figure 5-42 d).

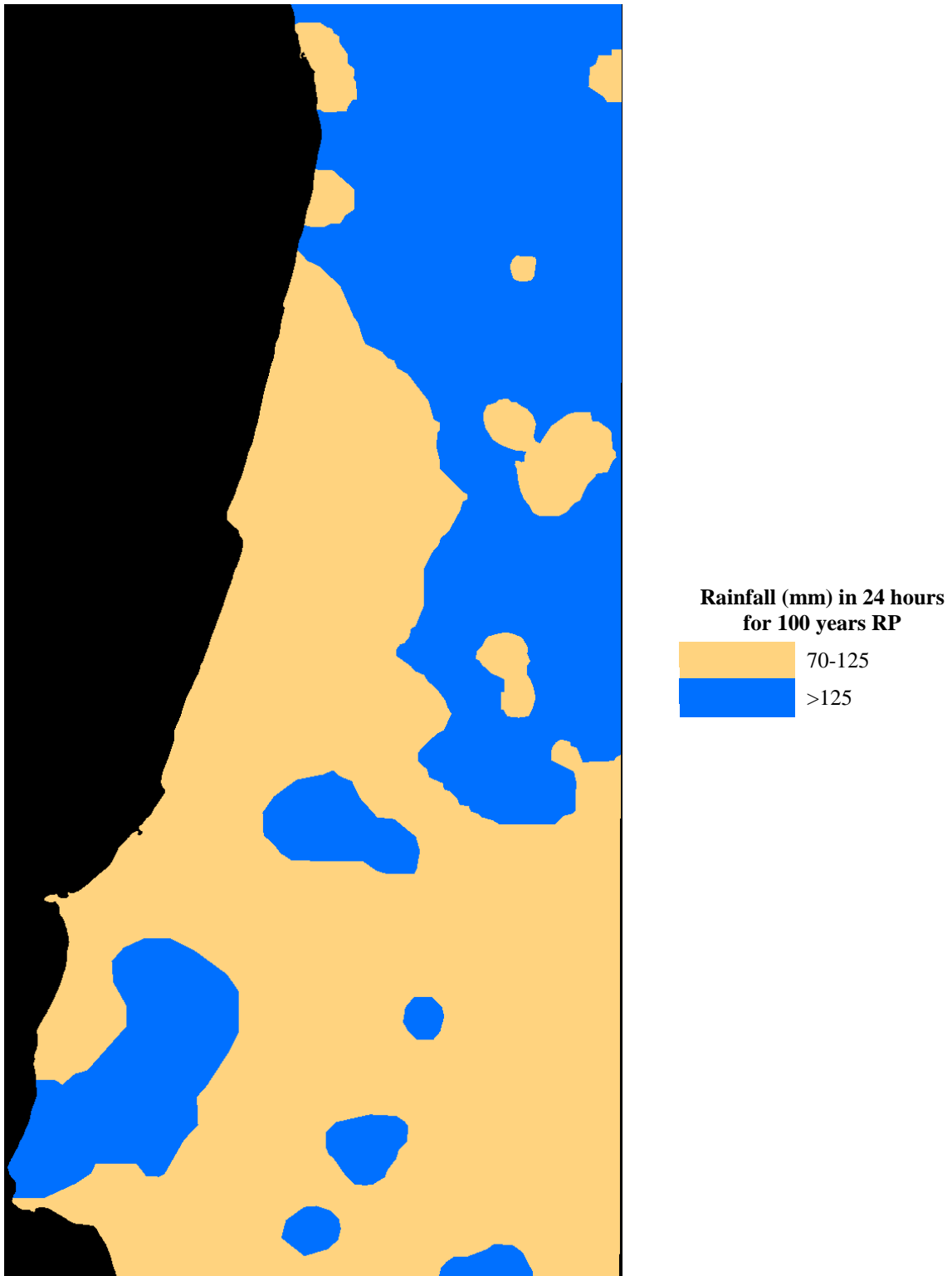


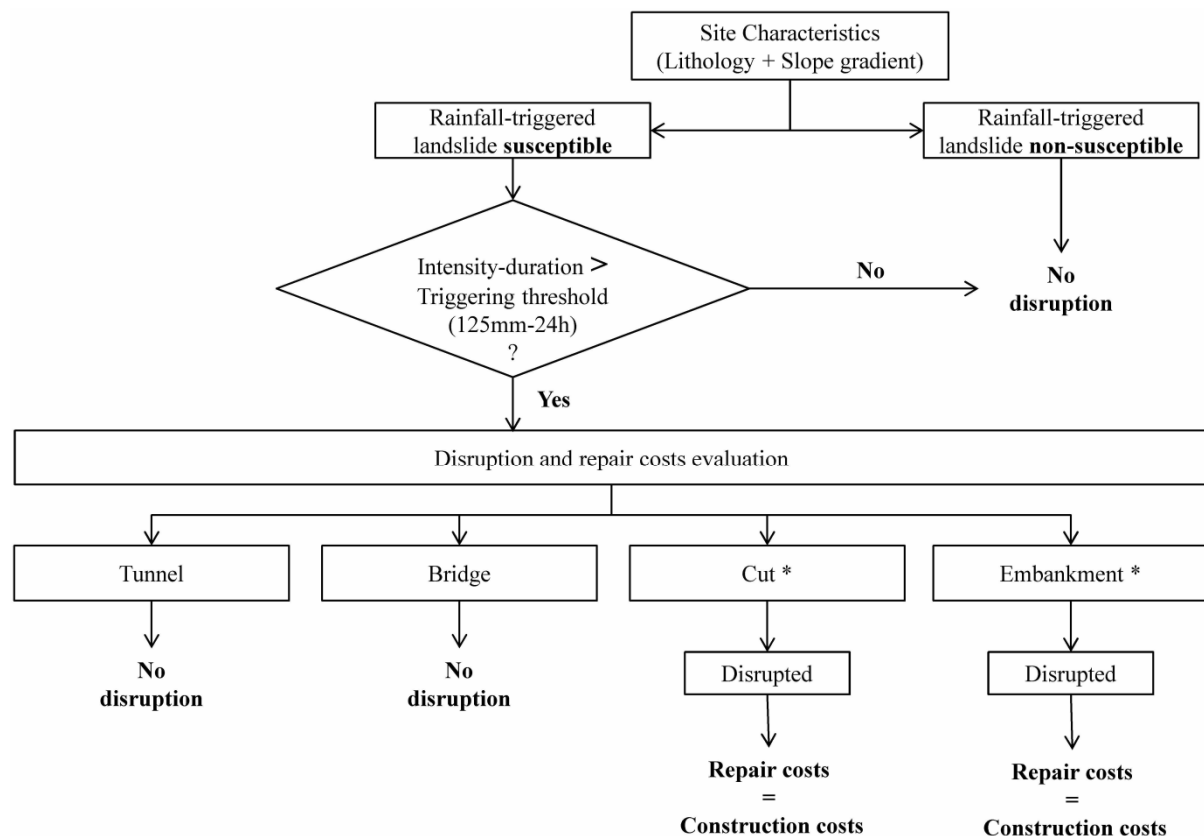
**Figure 5-51** Rainfall distribution in a 24 hour period and considering 100 years return period. Adapted from Brandão et al. (2004).



## 5.5.2.3 DAMAGES COST EVALUATION

The definition of the susceptibility zoning and the rainfall threshold capable of causing landslide failure allows one to evaluate the performance of the HSR infrastructure. The landslide effects to the HSR depend on the location of the correlation of susceptibility zoning and rainfall characteristics and the HSR location and cross-section (tunnel, bridge, cut or embankment) at each site.

It is assumed that, despite having different triggering mechanisms, the effects of both earthquake-triggered and rainfall-triggered landslides on the HSR performance are the same: tunnels and bridges are not disrupted and cuts and embankments are fully disrupted, requiring reconstruction with a cost equal to the initial construction cost. Figure 5-52 summarizes the methodology adopted for the rainfall-triggered landslides HSR repair costs assessment.



\*Refers to disruptions on the HSR cross-section by landslide failure of the existing natural ground. Landslides on slopes of cuts and embankments designed for the HSR are not included in the analysis.

**Figure 5-52** Flowchart of the evaluation of repair costs due to rainfall-triggered landslides.

### 5.5.3 FLOOD

Flooding areas are assessed by the map in Figure 5-53 that shows these areas overlaid with the main rivers' map for a return period of 100 years, made available by the Portuguese National Information System on Hydrological Resources (SNIRH 2012). Information regarding the flooding level is not available.

The identification of the flooding areas depicted in Figure 5-53 is the combined result of susceptibility and triggering conditions for the return period of 100 years defined for the intense rainfall scenario.

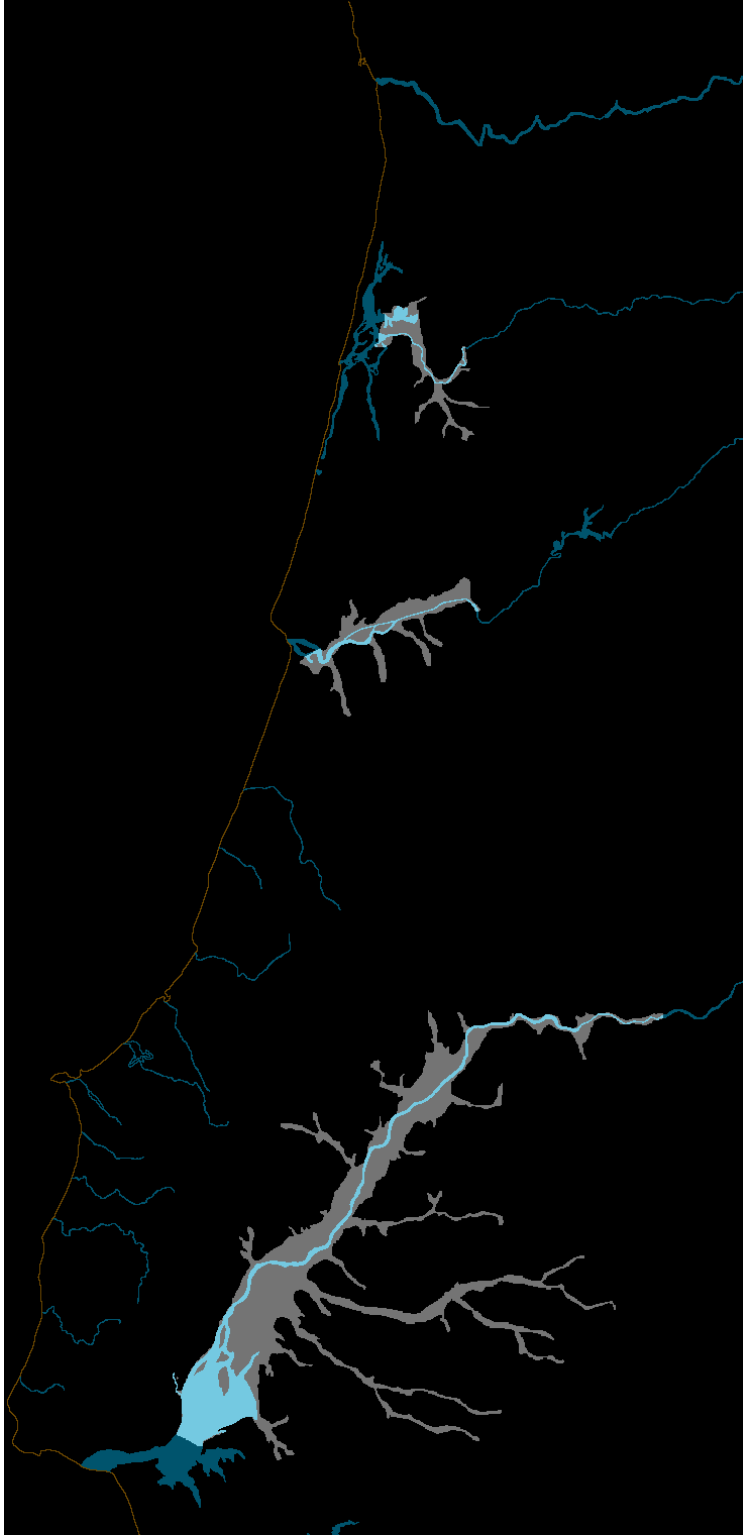


**Figure 5-53** Flood map for 100 years return period: main rivers in blue (darker shade) and flooding areas in gray (lighter shade).

5.5.3.1 *DAMAGES COST EVALUATION*

The performance of the HSR crossing flooded areas is assessed separately for the tunnels, bridges, cuts and embankments composing the infrastructure.

It is assumed that tunnels are not disrupted by floods. This is an assumption that may not be true for every flood event and dependent on the tunnel design, but the damage analysis requires detailed information not available at this planning stage.

Bridges are also considered as not being disrupted by floods. It is assumed that a minimum clearance is observed, even in the extreme case of a flood. Detailed analyses are to be performed in project design.

Cuts and embankments, however, are considered to be fully disrupted if crossing a flooded area. It is assumed that the damage requires the reconstruction of both cross-section types and the costs of reconstruction are considered to be equal to the construction costs.

In reality, the flood level varies and in some cases, especially close to the flooded area limits or in case of floodplains, as opposed to deep valleys, floods may be shallow and flow along the embankment without causing damages requiring full reconstruction. In these cases the cost of repair may be overestimated. On the other hand, HSR operation severely restricts the track displacements and thus minor damages may require track realignment and pose safety threats to high-speed circulating trains.

Figure 5-54 summarizes the methodology adopted for the assessment of the flood-induced HSR repair costs.

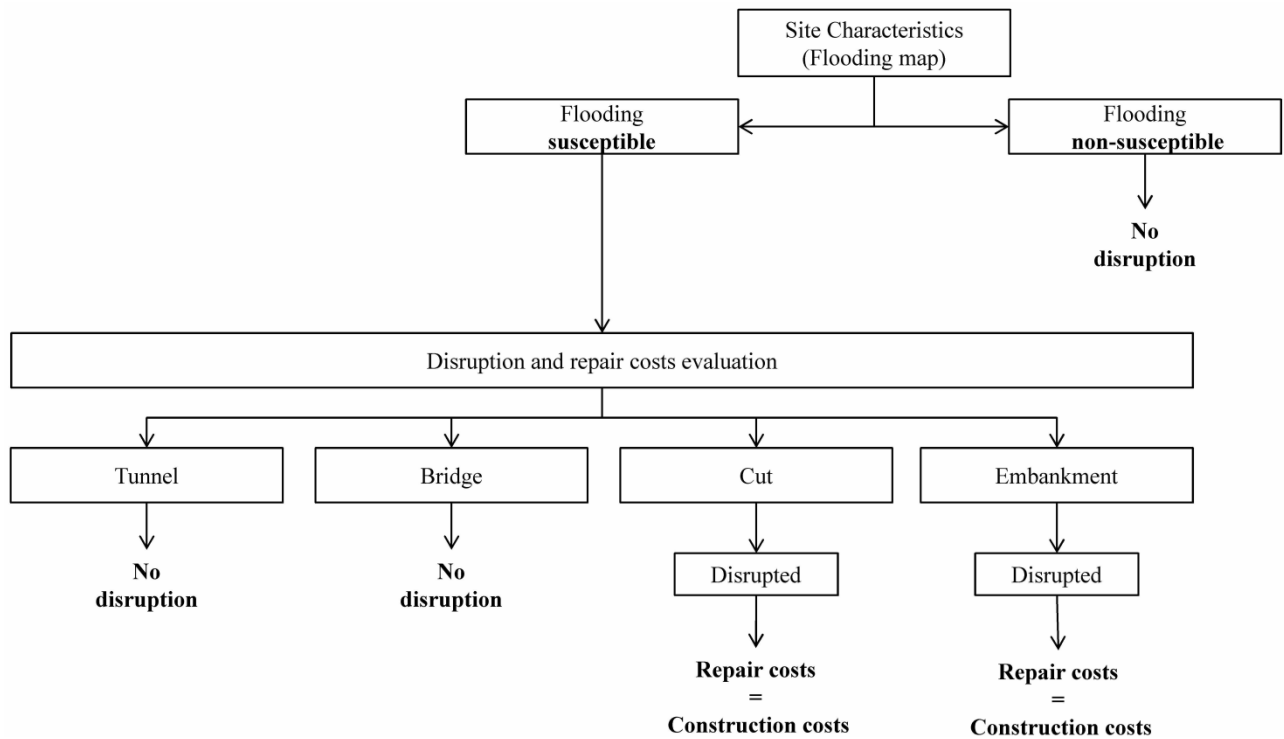


**Figure 5-54** Flowchart of the evaluation of repair costs due to floods.

## 5.6 SUMMARY REMARKS ON THE FORMULATION OF SCENARIOS

Table 5-10 summarizes the factors considered for the susceptibility assessment and the triggering criteria for earthquake- and rainfall-triggered landslides and earthquake- triggered liquefaction.

The areas exposed to floods are the combined result of susceptibility and triggering conditions for the return period of 100 years defined by the flood map (Figure 5-53).

**Table 5-10** Susceptibility and triggering conditions for earthquake- and rainfall-triggered landslides and earthquake- triggered liquefaction.

|  | Susceptibility   |   |  | Triggering Threshold   |  | Additional Comments   |
|--|--|---|--|--|--|---|
|  | Factor   | Criteria                                    | Comments   | Factor   | Criteria / Comments  |   |
| <b>Earthquake Triggered Landslides</b> | <b>Lithology</b>   | Recent lithology, up to the Tertiary period | Includes lithology units 1, 2, 3, 4, 6, 7, 8, 9, 10, 12. Criteria based on the literature. Case-studies were not found for Portugal.                           | Maximum epicentral distance based on earthquake moment magnitude | An earthquake is capable of triggering landslide susceptible deposits in the area within a circle centered at the earthquake epicenter and of radius equal to the maximum epicentral distance. | <ul style="list-style-type: none"> <li>- Rock falls are not considered: lack of data on jointing, bedding planes and fractures of rock masses and steeper slopes not captured properly from the coarse DEM.</li> <li>- Database of past earthquake-triggered landslides is not available.</li> <li>- Landslides are only assessed for the slopes of the existing natural ground; landslides of cuts and embankments built for the HSR infrastructure are not analyzed.</li> </ul> |
|  | <b>Slope</b>   | 20° to 40°                                  | Rockfalls are not considered. Coarse DEM does not capture slopes steeper than 40°. Criteria based on the literature. Case-studies were not found for Portugal. |  |  |   |
|  | <b>Four DEM derived maps: slope aspect, terrain roughness, slope roughness</b> | Not considered                              | Coarse DEM does not capture these factors properly and for the case-study area these are not as relevant as slope.   |  |  |   |
|  | <b>Saturation / pore water pressure</b>  | Not considered                              | Data are not available for the scale and area of the analysis.   |  |  |   |
|  | <b>Fault Proximity</b>   | Not considered                              |  |  |  |   |
|  | <b>Vegetation and land-use</b>   | Not considered                              |  |  |  |   |
|  | <b>Presence of old landslides</b>  | Not considered                              |  |  |  |   |

**Table 5-10** Susceptibility and triggering conditions for earthquake- and rainfall-triggered landslides and earthquake- triggered liquefaction. (Continued).

| Susceptibility                       |  |                                  | Triggering Threshold   |                              | Additional Comments  |   |
|--------------------------------------|--|----------------------------------|--|------------------------------|--|---|
| Factor                               | Criteria   | Comments                         | Factor   | Criteria / Comments          |  |   |
| <b>Rainfall Triggered Landslides</b> | <b>Lithology</b>   | Cohesionless lithology           | Includes lithology units 1, 2, 3, 4, 7, 8, 271 and 280. Based on lithological descriptions and considering 271 and 280 are weathered for a significant depth and behave as cohesionless soils. Literature states 271 and 280 have suffered landslides in the past. | Intensity-duration threshold | Rainfall equal or larger than 125 mm in a 24 hours period is able to trigger landslides. | - a return period of 100 is considered for the rainfall data  |
|                                      | <b>Slope</b>   | Slopes equal or steeper than 17° | 17° is the mean angle of landslides due to bank erosion observed in literature for the area north of Lisbon; it is considered that lower angle slopes have already been eroded and deposited. Rockfalls are not considered.  |                              |  | - Rock falls are not considered: lack of data on jointing, bedding planes and fractures of rock masses and steeper slopes not captured properly from the coarse DEM.  |
|                                      | <b>Four DEM derived maps: slope aspect, terrain roughness, slope roughness</b> | Not considered                   | Coarse DEM does not capture factors properly and for the case-study area these are not as relevant as slope.   |                              |  | - Landslides are only assessed for the slopes of the existing natural ground; landslides of cuts and embankments built for the HSR infrastructure are not analyzed.   |
|                                      | <b>Vegetation and land-use</b>   | Not considered                   |  |                              |  | - The susceptibility assessment is based on slides due to bank erosion: different landslide mechanisms were observed to be related with different triggering rainfall characteristics but triggering data are only available for short and intense rainfall episodes. |
|                                      | <b>Presence of old landslides</b>  | Considered                       | Available data for rainfall-triggered landslides in the north of Lisbon area.  |                              |  |   |

**Table 5-10** Susceptibility and triggering conditions for earthquake- and rainfall-triggered landslides and earthquake- triggered liquefaction. (Continued).

| Susceptibility      |                                |   | Triggering Threshold  |  | Additional Comments  |
|---------------------|--------------------------------|---|---|--|--|
| Factor              | Criteria                       | Comments  | Factor  | Criteria / Comments  |  |
| <b>Liquefaction</b> | <b>Lithology</b>               | Cohesionless soil units   | Includes lithology units 1, 2, 3 and 4. Criteria based on literature. Units 7 and 8 since they are formed by cohesionless materials mixed with sedimentary rocks and clays. |  |  |
|                     | <b>Soil saturation</b>         | River proximity   | River proximity is not a conclusive criterion but, lacking further information at this scale, provides support on the saturated condition of the deposits.                  | Maximum epicentral distance based on earthquake moment magnitude | An earthquake is capable of inducing liquefaction of susceptible deposits in the area within a circle centered at the earthquake epicenter and of radius equal to the maximum epicentral distance. |
|                     | <b>Historical Liquefaction</b> | Liquefaction tends to reoccur in sites where it has occurred for past earthquakes |   |  |  |



## Chapter 6.

# Solving the Lisbon-Oporto HSR Planning Problem: Standard Planning Conditions (SPC)

In this section, the proposed Standard Planning Conditions (SPC) model (section 4.1) is applied to the Lisbon-Oporto case-study (section 5) and solved with the implementation of the Simulated Annealing Algorithm (SAA).

Aiming at developing a robust approach for considering natural hazards and taking into account layout constraints for the HSR planning optimization problem, a progressive development methodology was considered. A deterministic model for the SPC, concerned with construction costs and problem constraints, was proposed in section 4.1. The implementation of the SAA is then used to solve the model according to the principles discussed in section 4.2. A user-friendly tool has been developed that can consider the model input location data, the HSR 3D geometry restrictions and is able to implement the SAA. The software testing was performed with the application to an intentionally simple and synthetic case-study and an analysis is presented for the estimation as to which combination of the SAA parameters works best (section 4.3).

Following the sound results obtained for the synthetic case-study, data were assembled for the Lisbon-Oporto case (section 5). These allowed one to observe that the software capabilities needed to be extended, as presented in section 4.4, to address the additional complexities of a real-world problem. This present chapter 6 discusses the assumptions and capabilities of the model and the tool for addressing the HSR planning problem for the SPC.

## 6.1 APPLICATION OF THE SPC MODEL TO THE LISBON-OPORTO HSR

The Lisbon-Oporto HSR case-study was presented in chapter 5 with the definition of the input spatial data (section 5.1), the HSR configuration geometry layout (section 5.2) and the cross-sections and construction costs (section 5.3). A summary of these input data, along with the definition of the problem constraints and of the penalty and benefit terms of the objective function (4.1) of the model for the SPC, is presented. In addition to the input presented in sections 5.1, 5.2 and 5.3, the penalty- and benefit- coefficients considered by the objective function (4.1) need to be defined.

It has been discussed in section 4.1.1 that the penalty and benefit coefficients  $\gamma_\eta$ ,  $\gamma_\beta$ ,  $\gamma_{\lambda_s}$  and  $\gamma_{v_i}$ , used in the definition of the penalty and benefit objective function terms are user-specified and are to be defined through expert judgment after consulting stakeholder panels and taking into consideration the problem specifics. Formal procedures exist to accomplish these tasks (section 4.1.1).

The model and the solving technique implemented consider a fully integrated 3D approach to the optimization problem. However, given the difficulties of graphically representing the 3D layout of the configuration, the discussion of the resulting solutions is supported by plan views and longitudinal profiles that, while being 2D graphics, fully characterize the 3D layout of the HSR configurations.

### 6.1.1 GEOMETRY PENALTIES: HORIZONTAL ANGLE AND GRADIENT

The geometry penalties are defined by expression (4.8) for gradient and by expression (4.9) for the horizontal angle. The geometry penalties establish trade-offs between the use of the more restrictive recommended gradient and horizontal angles, often at larger construction costs, with an improved performance during operation. These require the definition of the geometry normal values,  $\eta_{normal}$  and  $\beta_{normal}$ , the geometry limit values,  $\eta_{limit}$  and  $\beta_{limit}$ , and the penalty coefficients  $\gamma_\eta$  and  $\gamma_\beta$ .

The values adopted in the case-study are presented in Table 6-1. The gradient and horizontal angle normal and limit values are defined according to the studies in section 5.2. For application purposes, illustrating the possible effects of such trade-offs, the coefficients are considered indexed to the construction cost of the HSR.

**Table 6-1** Geometry parameters for the SPC application.

| Geometry parameter | Limit value               | Normal value               | Penalty cost coefficient                            |
|--------------------|---------------------------|----------------------------|---|
| Horizontal angle   | $\beta_{limit}=120^\circ$ | $\beta_{normal}=140^\circ$ | $\gamma_\beta=5\% \sum_{(i,j) \in \Omega_N} C_{ij}$ |
| Gradient           | $\eta_{limit}=35\%$       | $\eta_{normal}=20\%$       | $\gamma_\eta=5\% \sum_{(i,j) \in \Omega_N} C_{ij}$  |

### 6.1.2 LAND-USE PENALTY

The case-study does not include land-use restricted areas. Thus, the land-use penalty coefficient  $\gamma_{\lambda_s}$  is null for any space property elements  $s \in \Omega_E$ . This implies that the land-use penalty term of expression (4.1) is null for any section composing the HSR.

### 6.1.3 LOCATION BENEFIT

The case-study includes two cities, Aveiro and Leiria, for which a location benefit term is subtracted in the objective function (4.1) if connected by the HSR. Location coefficients aim at representing trade-offs between the effects of connecting intermediate locations, including increased accessibility but also larger connection times and political decisions, and the additional construction costs. Only the plan view location needs to be connected by the HSR for the consideration of the benefitting term. The elevation at which Aveiro and Leiria are connected may vary as elevated or underground stations are eligible.

The application considers Aveiro and Leiria defined by nodes contained in the problem discretization set  $\Omega_N$ . However, in reality the cities do occupy an area within the search space and HSR stations may be considered at different locations within the city but with different effects, namely in capturing demand (Brons et al. 2009; Givoni and Rietveld 2007). Illustrating the influence of such circumstances, the application considers benefit coefficients  $\gamma_v^{Aveiro}$  and  $\gamma_v^{Leiria}$  if the node representing the respective city is connected by the HSR and half of the coefficients value if the plan view of adjacent nodes is connected.

Table 6-2 identifies the location and the location benefit coefficients for both cities. For application purposes, illustrating the possible effects of such trade-offs, the coefficients are considered indexed to the construction cost of the HSR.

**Table 6-2** Location and location benefit coefficients for Aveiro and Leiria.

| City   | Location (x;y;z)<br>(km;km;m) | Location benefit<br>coefficient                             |
|--------|-------------------------------|---|
| Aveiro | (76;72;14.268)                | $\gamma_v^{Aveiro} = 30\% \sum_{(i,j) \in \Omega_N} C_{ij}$ |
| Leiria | (60;170;61.236)               | $\gamma_v^{Leiria} = 30\% \sum_{(i,j) \in \Omega_N} C_{ij}$ |

#### 6.1.4 LOCATION CONSTRAINTS

Table 6-3 defines the location of Oporto, Coimbra and Lisbon that constitute the set of all mandatory nodes  $\Omega_{MN}$  to be connected by the HSR configuration according to the coordinate system of Figure 5-3.

**Table 6-3** Definition of the location constraints for the SPC application.

| City    | Location (x;y;z)<br>(km;km;m) |
|---------|-------------------------------|
| Oporto  | (80;16;108.152)               |
| Coimbra | (92;118;13.106)               |
| Lisbon  | (34;280;32.348)               |

#### 6.1.5 GEOMETRY CONSTRAINTS

The geometry constraints impose the limit values (section 4.1.2.2) for the gradient and horizontal angles at intermediate nodes. The values are defined in section 5.2 and ensure that:

- the gradient of any linear section  $\eta_{(i,j)}$  composing the HSR configuration, either rising or falling, is smaller than  $\eta_{limit} = 35\%$ ;
- the horizontal angle at any intermediate node of the HSR configuration  $\beta_{(i,j,k)}$ , the smaller angle between the linear sections and ranging from  $0^\circ$  to  $180^\circ$ , is larger than the limit value  $\beta_{limit} = 120^\circ$ .

#### 6.1.6 LAND-USE CONSTRAINT

The land-use constraint ensures that the protected areas identified in Figure 5-5 are not overlaid by the HSR linear sections. The construction of the HSR network is forbidden within

all the protected areas, corresponding to all the space property elements with indices 9 through 38 of Table 5-2, which constitute the set  $\Omega_{FE}$  of the forbidden land-use elements.

## 6.2 IMPLEMENTATION OF THE SIMULATED ANNEALING ALGORITHM

Sound results were obtained in solving the SPC model (section 4.1) applied to a simple and synthetic case-study (section 4.3). The principles of implementing the SAA to solve the HSR planning optimization problem were discussed in section 4.2. The following definitions are required:

- an initial feasible HSR configuration;
- the procedures for generating candidate HSR configurations;
- the cooling schedule;

The initial HSR configuration, the generation of candidate configurations and the cooling schedule are discussed below.

### 6.2.1 INITIAL HSR CONFIGURATION

Existing literature discusses different possible methodologies for defining an initial system configuration (section 4.2) including an arbitrarily random or best guess configuration (Bertsimas and Nohadani 2010; Johnson et al. 1989; de Weck and Willcox 2010). The SAA implementation presented herein considers an arbitrarily defined initial configuration.

The initial configuration is described in Table 6-4 for its geometry, with indication of the 3D coordinates of the nodes that constitute the HSR, the cities connected, the gradient  $\eta$  (‰) of each linear section and the horizontal angle  $\beta$  (°) at each intermediate node. 15 linear sections are considered, sequentially linking the nodes 1 through 16.

Table 6-4 shows the configuration complies with the location constraint, by linking Oporto, Coimbra and Lisbon and complies with the geometry constraints by having all horizontal angles larger than  $\beta_{limit} = 120^\circ$  and all gradients smaller than  $\eta_{limit} = 35\text{‰}$ .

**Table 6-4** Geometry of the initial HSR configuration for the SPC application.

| Node | (x;y;z)<br>(km; km; m) |         | $\eta$<br>(%) | $\beta$<br>(°) |
|------|------------------------|---------|---------------|----------------|
| 1    | (80; 16; 108.152)      | Oporto  | -2            |                |
| 2    | (126; 24; 30)          |         | 5             | 121.7          |
| 3    | (134; 44; 140)         |         | -6            | 129.1          |
| 4    | (124; 62; 20)          |         | 6             | 164.1          |
| 5    | (88; 98; 310)          |         | -15           | 123.7          |
| 6    | (92; 118; 13.106)      | Coimbra | 18            | 157.6          |
| 7    | (100; 130; 280)        |         | -3            | 170.3          |
| 8    | (108; 148; 210)        |         | 1             | 163.2          |
| 9    | (112; 180; 230)        |         | -3            | 134.2          |
| 10   | (96; 200; 150)         |         | 2             | 133.7          |
| 11   | (100; 230; 200)        |         | 29            | 127.4          |
| 12   | (96; 234; 360)         |         | -6            | 148            |
| 13   | (70; 240; 210)         |         | -4            | 160.3          |
| 14   | (42; 258; 70)          |         | 5             | 162.5          |
| 15   | (32; 270; 150)         |         | -11           | 128.9          |
| 16   | (34; 280; 32.348)      | Lisbon  |               |                |

The initial HSR configuration is presented in Figure 6-1 overlaid on the protected land-use layer that defines the land-use constraint. Figure 6-1 shows the HSR configuration does not overlay any of the forbidden land-use areas and thus complies with the land-use constraint.

In addition to feasibility, Figure 6-1 shows the configuration does not connect Aveiro or Leiria and Table 6-4 shows that one linear section has a larger gradient than  $\eta_{normal}=20\%$  and that 7 horizontal angles are smaller than  $\beta_{normal}=140^\circ$ . The resulting cost breakdown is presented in Table 6-5.

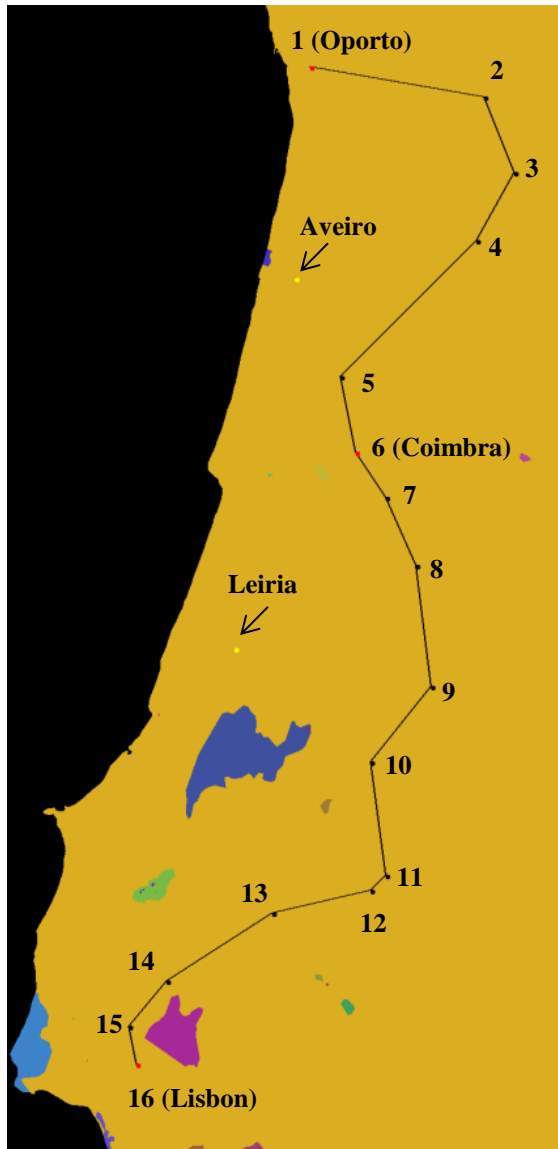


**Figure 6-1** Plan view of the initial HSR configuration overlaying the forbidden land-use layer. Aveiro and Leiria represented by yellow nodes and Oporto, Coimbra and Lisbon represented by red nodes. Numbers 1 through 16 correspond to the node numbering of Table 6-4.

**Table 6-5** Cost breakdown of the initial HSR configuration.

|  | Cost (Million €) |
|--|------------------|
| SPC Objective Function Value (1 + 2 + 3 - 4) | 113,788.19       |
| 1. CONSTRUCTION COST (1.1+1.2+1.3+1.4+1.5)   | 92,445.77        |
| 1.1 Expropriation                            | 24.93            |
| 1.2 Earthworks                               | 99.88            |
| 1.3 All Bridges                              | 86,351.28        |
| 1.4 All Tunnels                              | 5,536.04         |
| 1.5. Linear- dependent Costs                 | 433.63           |
| 2. GEOMETRY PENALTY                          | 21,342.42        |
| 3. LAND-USE PENALTY                          | 0.00             |
| 4. LOCATION BENEFIT                          | 0.00             |

### 6.2.2 GENERATION OF CANDIDATE HSR CONFIGURATIONS

The generation of candidate HSR configurations follows the guidelines presented in section 4.2.1, including the formulation which allows overcoming the “islands” of forbidden land-use constituting the land-use constraint of the Lisbon-Oporto case-study (Figure 5-5).

Two randomly chosen nodes of the HSR configuration are randomly perturbed in the neighborhood (Figure 4-11 and Figure 4-12). Perturbations of any kind are disallowed for the mandatory nodes representing Oporto, Coimbra and Lisbon.

A minimum length of 4,000 m has to be observed for each linear section (section 5.2.2). This considers the discussion in section 4.4.2 documenting the formation of node clusters without this specification and the requirements for the radii of the horizontal circular curves that can be inserted between linear sections of the HSR (section 5.2.1).

### 6.2.3 COOLING SCHEDULE

An adaptive geometric cooling schedule (section 4.2.2) is considered for the SAA implementation to solve the SPC Lisbon-Oporto HSR planning problem. The adaptive cooling schedule allows the SAA to spend more time at the intermediate temperature stages (between very high and very low temperatures) which is discussed by Johnson et al. (1989) to improve the quality of the solutions.

This implementation builds on the SAA implementation of section 4.3 to solve the synthetic case-study. In comparison, the Lisbon-Oporto case-study presents several additional difficulties for the solving technique. These include: (i) a larger search space area, 13 times larger in terms of space property elements but already excluding those corresponding to the Atlantic Ocean; (ii) the forbidden land-use areas of irregular shape and varying sizes scattered within the search space; (iii) the connection of three mandatory cities, instead of two, distances of 102 km (Oporto-Coimbra) and 172 km (Coimbra-Lisbon) instead of the circa 70 km of the synthetic case study; (iv) 2 locations for which the connection leads to potential benefits subtracted in the objective function; (v) a larger variation of the terrain elevation and (vi) the consideration of rivers to be crossed by either bridges or tunnels with their respective minimum clearances.



Given the increased complexity introduced by the simultaneous consideration of the above mentioned factors, a study for the estimation of the SAA cooling schedule parameters is considered for the following values:

- the elasticity of acceptance  $a = 0.9$ , subject to confirmation that this allows an 80% or higher rate of accepted HSR configurations at the initial temperature step, as suggested by Kirkpatrick (1984) and Van Laarhoven and Aarts (1987);
- the minimum number of accepted configurations at each temperature  $n_1 = 5,000$ , and  $n_1 = 10,000$ ;
- the temperature decrease rates  $r = 0.7$  and  $r = 0.8$ ;
- the stopping criterion  $n_2 = 10$ ;

The runs performed in section 4.3.2, for the simpler and smaller synthetic case-study, showed that a minimum number of accepted configurations at each temperature step smaller than 5000 did not result in consistent results even for the less complex synthetic case-study ( $n_1 = 1,000$ ;  $n_1 = 1,500$  and  $n_1 = 2,000$  were tested). Based on this observation, the SPC applications here described implement the SAA for  $n_1 = 5,000$  and  $n_1 = 10,000$ .

Similarly, the synthetic case-study (section 4.3.2) results were inconsistent for a temperature decrease rates smaller than  $r = 0.7$ . Considering the increased complexity, values lower than 0.7 are also not likely to produce consistent results for the Lisbon-Oporto case-study. Smaller values of  $r$  correspond to shorter annealing runs and, conversely, the quality of the solutions tends to improve for longer runs (Johnson et al. 1989). However, the larger the values of  $r$ , the larger the computation time, which increases exponentially with the problem size (Johnson et al. 1989). Given that solving the HSR planning optimization of the Lisbon-Oporto case study is burdensome time-wise, temperature decrease rates  $r = 0.7$  and  $r = 0.8$  are tested in a compromise between the quality of the solutions and the time the algorithm takes to run.

The stopping criterion  $n_2 = 10$ , defining the number of consecutive temperature decreases without improvements of either the current optimum or the average cost, is also adopted given its capability in the synthetic case study implementation (section 4.3.2). If improvements were to be observed, either to the optimum or the average cost, after 9 consecutive temperature decreases without improvements, a new stopping criterion would be tested. Such a situation

could resemble that of the synthetic case-study, in which  $n_2 = 5$  was too small and led to a premature termination of the algorithm, resulting in sub-optimal solutions.

It has been discussed in section 3.2.2 that by mathematically modeling the SAA using Markov chains, for certain conditions, asymptotic convergence to the global optimum can be proven to have probability 1. However, finite-time implementation trades off optimality for computation time and the convergence to the global optimum cannot be proven. In this context, it cannot be proven that the best configuration found by the SAA is, in fact, the global optimum solution of the Lisbon-Oporto case-study. Thus, the performance of the different cooling schedule parameter sets is analyzed by comparing the quality of the solutions produced.

The sets of SAA cooling schedule parameters analyzed are:

- $(a = 0.9; r = 0.7; n_1 = 5,000; n_2 = 10)$
- $(a = 0.9; r = 0.7; n_1 = 10,000; n_2 = 10)$
- $(a = 0.9; r = 0.8; n_1 = 5,000; n_2 = 10)$
- $(a = 0.9; r = 0.8; n_1 = 10,000; n_2 = 10)$

The results allowed one to verify that an elasticity of acceptance  $a = 0.9$  corresponds to an average 96% of accepted HSR configurations at the initial temperature step. The elasticity of acceptance thus conforms to the literature suggestions for implementing an initial temperature that allows at least 80% of the tested system configurations to be accepted at that temperature (section 3.2.2).

The SAA run for the set  $(a = 0.9; r = 0.8; n_1 = 10,000; n_2 = 10)$ , however, led to the establishment of an additional termination criterion: a maximum computation time. After 20 days running the SAA for this parameter set, the application had not reached the initial termination criterion: 10 consecutive temperature decreases without improvement of both the optimum and the averaged objective function value. The run was terminated, despite the solution being significantly costlier than the solutions obtained with the remaining parameter sets. The set  $(a = 0.9; r = 0.8; n_1 = 10,000; n_2 = 10)$  was thus discarded from further considerations. The present analysis discusses the quality of a solution by optimality. However, the computation time has to be limited to ensure the applicability of the SAA

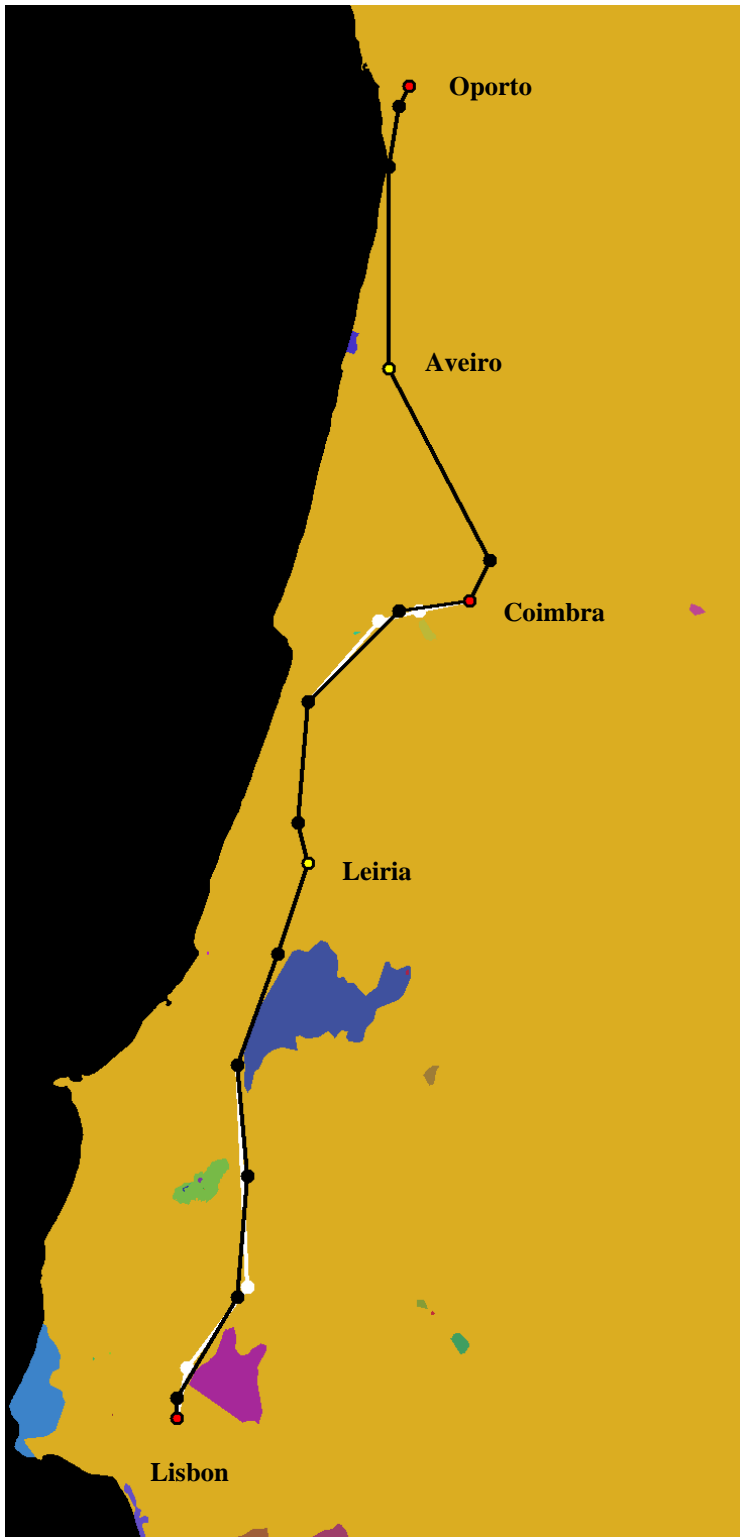
implementation and the additional termination criterion is defined by a maximum computation time of 20 days. The runs for the other 3 cooling schedule parameter sets did terminate with  $n_2 = 10$ , before reaching the 20 days of computation time. Larger values of  $r$  and  $n_1$ , in principle, both increase the computation time, and the remaining parameter sets have either smaller  $r$  or  $n_1$ , or both.

Table 6-6 summarizes the cost of the solutions found for the sets in which the SAA termination occurred within the maximum computation time criterion. One observes that the solution found for SPC with the set ( $a = 0.9$ ;  $r = 0.8$ ;  $n_1 = 5000$ ;  $n_2 = 10$ ) has an objective function value of €786.96 million, and the solutions found with ( $a = 0.9$ ;  $r = 0.7$ ;  $n_1 = 5000$ ;  $n_2 = 10$ ) and ( $a = 0.9$ ;  $r = 0.7$ ;  $n_1 = 10,000$ ;  $n_2 = 10$ ) correspond to objective function values, respectively, 43% and 4% larger.

**Table 6-6** SPC objective function value of the solutions for 3 sets of SAA cooling schedule parameters.

| SAA Parameter Set  | HSR SPC Objective Function Value<br>(Million €) |
|--|---|
| ( $a = 0.9$ ; $r = 0.7$ ; $n_1 = 5000$ ; $n_2 = 10$ )    | 1,124.52  |
| ( $a = 0.9$ ; $r = 0.7$ ; $n_1 = 10\,000$ ; $n_2 = 10$ ) | 819.95  |
| ( $a = 0.9$ ; $r = 0.8$ ; $n_1 = 5000$ ; $n_2 = 10$ )    | 786.96  |

While the HSR configuration corresponding to the €1,124.52 million is fairly sub-optimal, the value of the best HSR configurations found for the 2 remaining SAA parameter sets is similar. The objective function value analysis, however, does not allow one to identify how different the best HSR configurations actually are. To assess this, the plan view overlay in Figure 6-2 and the longitudinal profile in Figure 6-3 are determined. One observes that the configurations are rather similar and that the differences are located mainly close to Lisbon, in a 75 km extension. Additionally, small differences exist in the plan view southbound immediately after Coimbra and in the longitudinal profile Between Coimbra and Leiria. The comparison highlights how small changes to the HSR layout and its location may result in a 4% variation of the objective function value.



**Figure 6-2** Plan view of the best HSR configurations found with  $(a = 0.9; r = 0.7; n_1 = 10,000; n_2 = 10)$  in white and with  $(a = 0.9; r = 0.8; n_1 = 5,000; n_2 = 10)$  in black, overlaying the land-use layer.

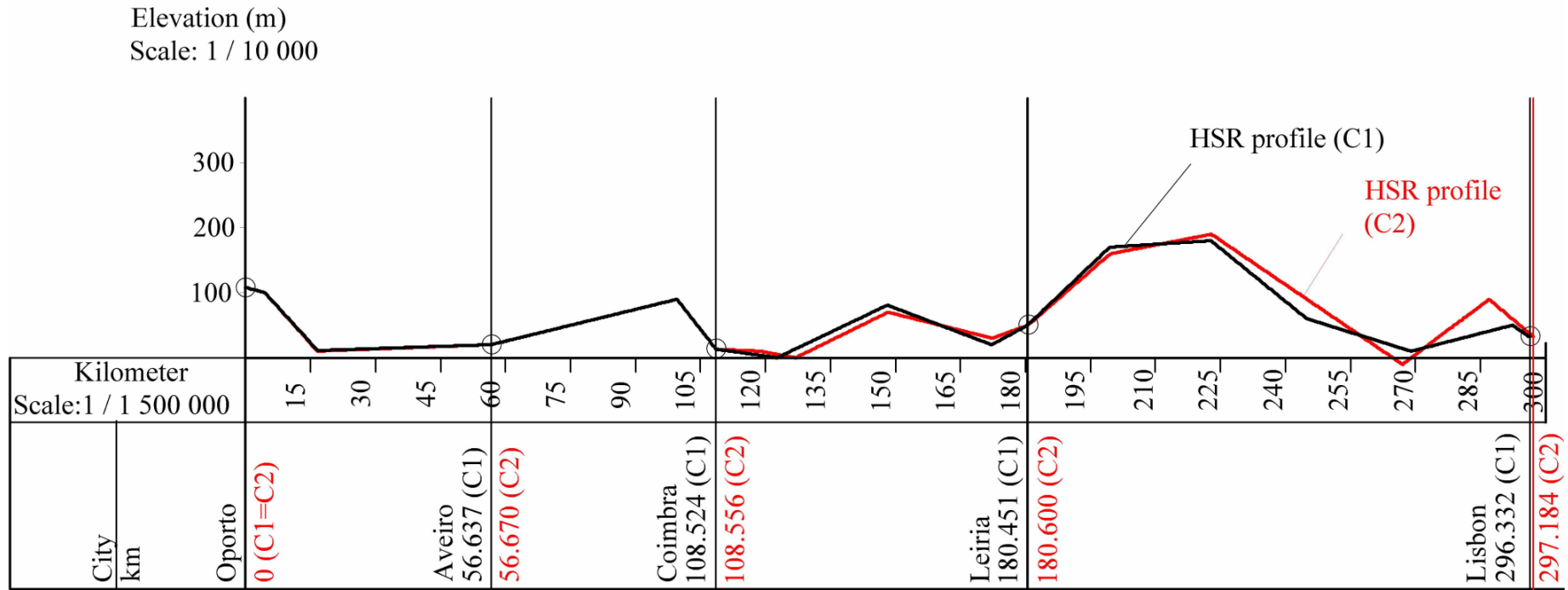
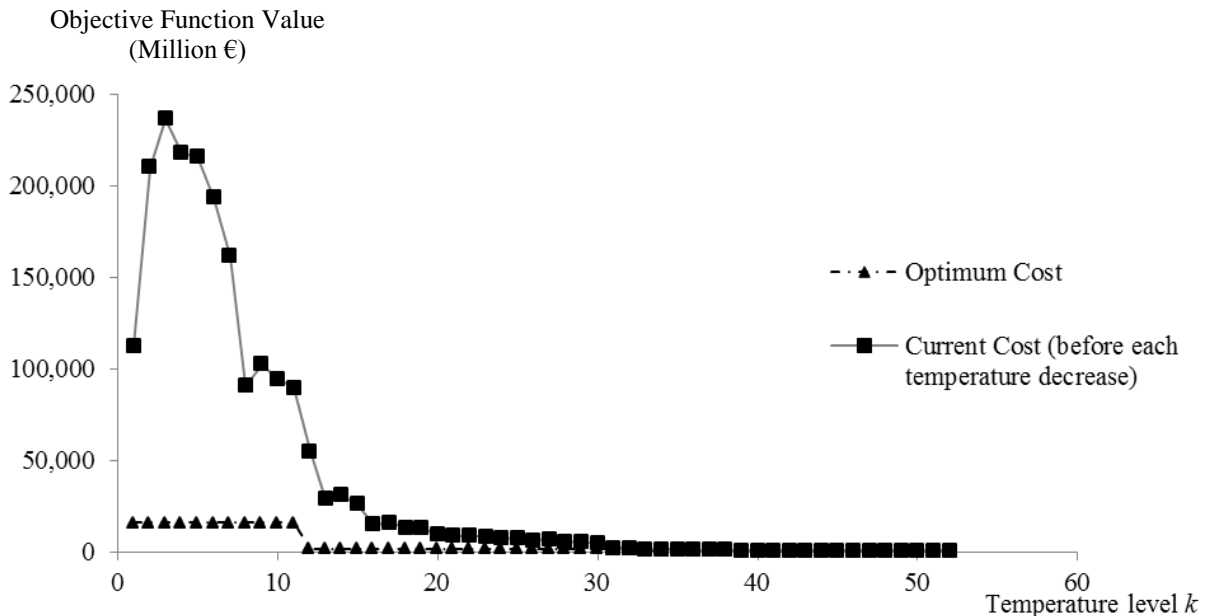


**Figure 6-3** Comparison of the longitudinal profiles of the best HSR configurations: C1 found for ( $a = 0.9$ ;  $r = 0.8$ ;  $n_1 = 5,000$ ;  $n_2 = 10$ ) in black and C2 found for ( $a = 0.9$ ;  $r = 0.7$ ;  $n_1 = 10,000$ ;  $n_2 = 10$ ) in red.

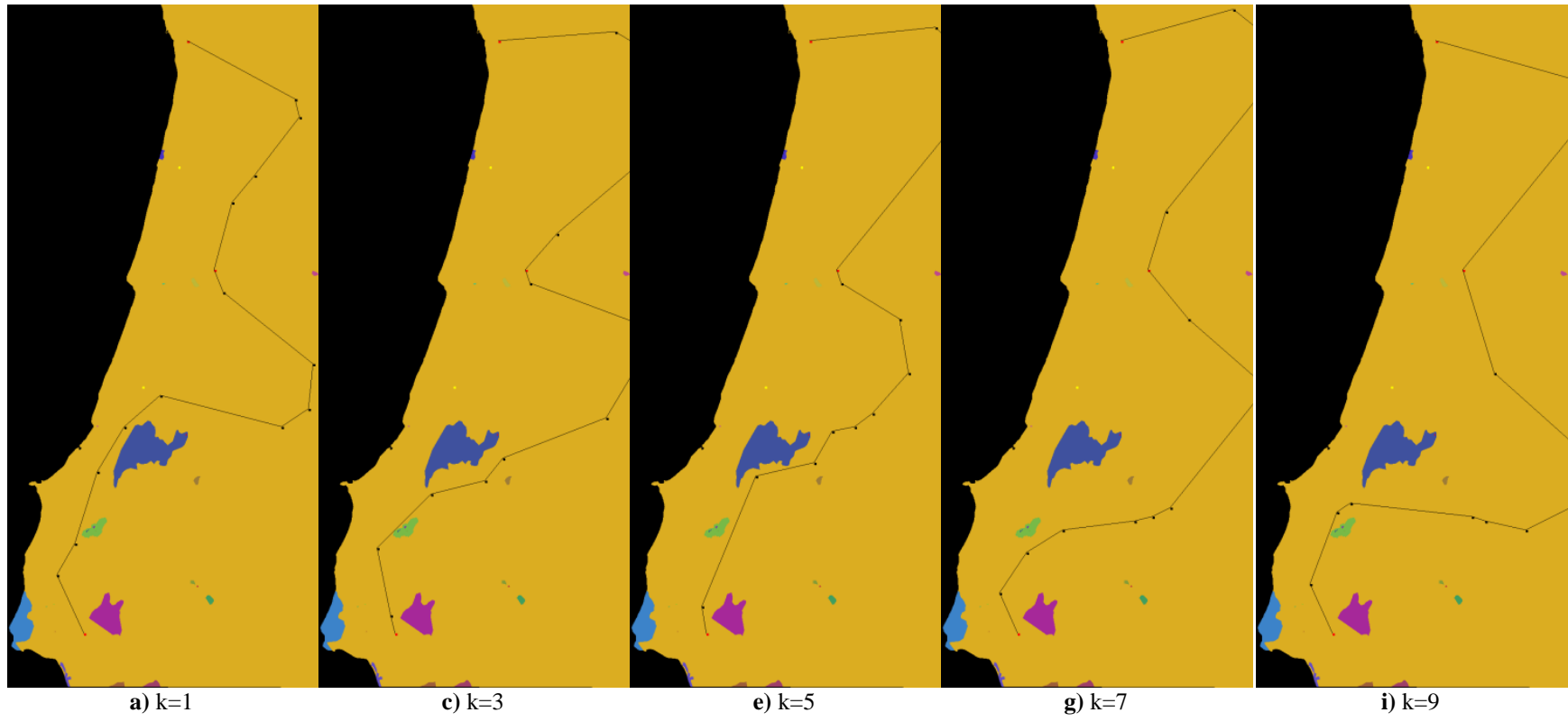
Given the quality of the results obtained for the cooling schedule governed by the parameter set ( $a = 0.9$ ;  $r = 0.8$ ;  $n_1 = 5,000$ ;  $n_2 = 10$ ), an additional analysis is performed to assess the convergence history and the ability to canvass the search space.

Figure 6-4 shows the convergence history for the HSR solution found with ( $a = 0.9$ ;  $r = 0.8$ ;  $n_1 = 5,000$ ;  $n_2 = 10$ ). Initially, at the early temperature steps, HSR configurations with large objective function values are accepted. As the algorithm progresses, the acceptance of worsening configurations decreases and the value of the accepted configurations converges to the optimum value found by the SAA. This ability to accept configurations with large objective function values at the beginning of the SAA run allows the algorithm to comprehensively canvassing the feasible search space of the problem.

Figure 6-5 shows the evolution of the accepted configurations (current cost) immediately before temperature decreases. For the indicated temperature steps  $k$ , Figure 6-5 shows the plan view of the HSR configuration overlaying the land-use layer.



**Figure 6-4** Convergence history for  $a = 0.9$ ,  $r = 0.8$ ,  $n_1 = 5,000$  and  $n_2 = 10$ : evolution of the last accepted configuration before a temperature decrease and of the current optimum at the time of each temperature decrease.



**Figure 6-5** Current HSR configuration at the end of the temperature step  $k$ , overlaying the land-use layer.

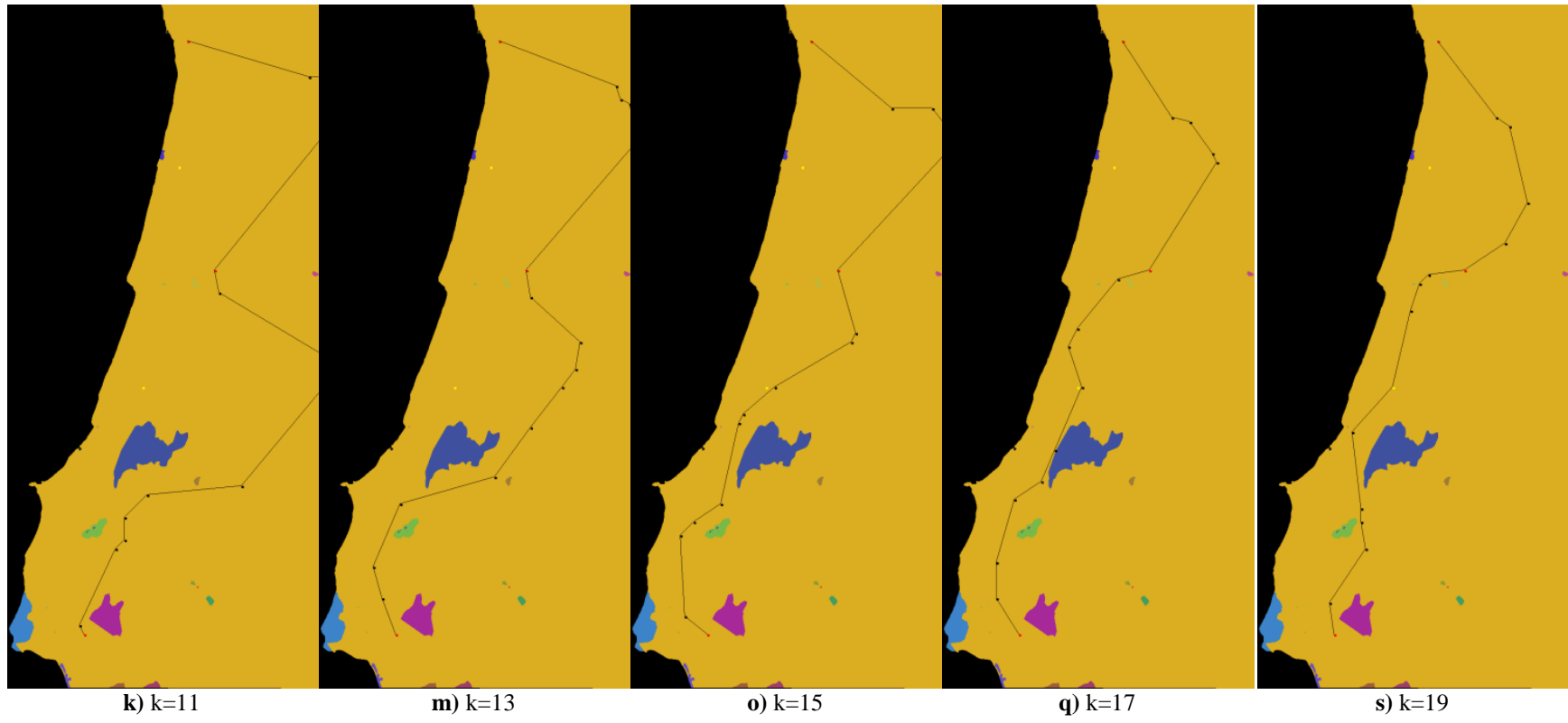


**Figure 6-5** Current HSR configuration at the end of the temperature step  $k$ , overlaying the land-use layer. (Continued).



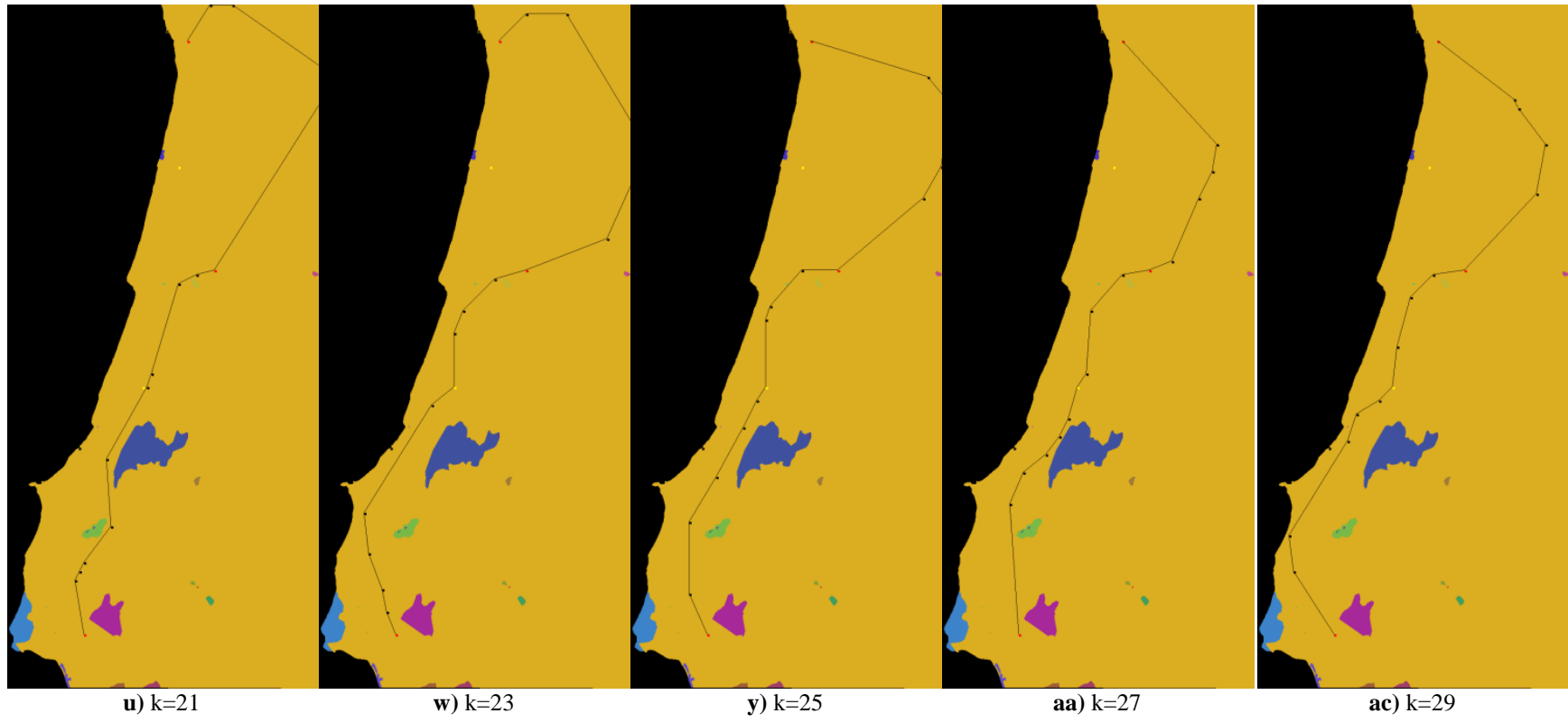


**Figure 6-5** Current HSR configuration at the end of the temperature step  $k$ , overlaying the land-use layer. (Continued).

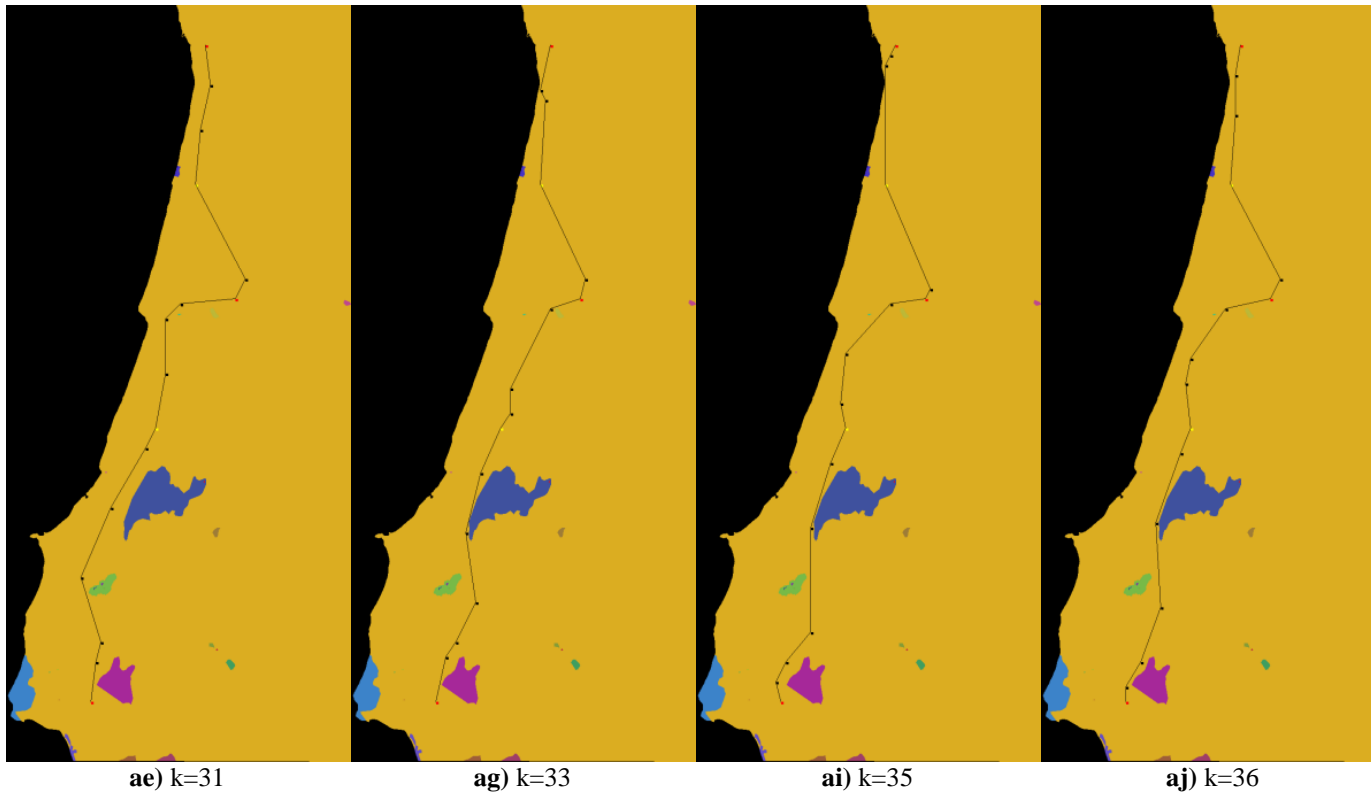


**Figure 6-5** Current HSR configuration at the end of the temperature step  $k$ , overlaying the land-use layer. (Continued).

Although the search space and the HSR configurations are three-dimensionally defined, Figure 6-5 gives evidence of the spread of candidate solutions across the plan view feasible space and the ability to leap over the forbidden land-use areas. The exploration of the feasible space enables the algorithm to consider radically different configurations and is central to the effectiveness in finding optimal or near-optimal solutions.

The SAA cooling schedule parameter set ( $a = 0.9$ ;  $r = 0.8$ ;  $n_1 = 5,000$ ;  $n_2 = 10$ ) is considered for further calculations in solving the SPC Lisbon-Oporto planning optimization problem (sections 6.3 and 6.4) based on the quality of the solutions produced and a convergence trajectory giving evidence of the ability to perform a general canvass of the search space.

## 6.3 SPC APPLICATION RESULTS

### 6.3.1 CHARACTERIZATION OF THE SOLUTION

The solution obtained with the implementation of the SAA (Section 6.2) to solve the model application described in section 6.1 is herein presented: Table 6-7 details the HSR configuration geometry, Figure 6-6 shows the plan view of the configuration overlaying the lithological-, land-use-, expropriation cost-, elevation- and river maps in a 1:1,800,000 scale, Figure 6-7, Figure 6-8 and Figure 6-9 show the respective longitudinal profiles in different scales and Table 6-8 details the cost breakdown.

Table 6-7 shows that the configuration complies with the geometry constraints defined for the case-study:  $\eta_{limit} = 35\%$  and  $\beta_{limit} = 120^\circ$ . The gradient of all linear sections is smaller than the normal gradient  $\eta_{normal} = 20\%$ , hence the null gradient penalty in Table 6-8. Two intermediate horizontal angles, however, at nodes 5 and 6 (Coimbra), are smaller than the normal value  $\beta_{normal} = 140^\circ$ . The location of these intermediate nodes is highlighted in Figure 6-6 b) by a discontinuous gray circle.

**Table 6-7** Best found HSR configuration geometry for SPC.

| Node | (x; y; z)<br>(km; km; m) | City    | $\eta$<br>(‰) | $\beta$<br>(°) |
|------|--------------------------|---------|---------------|----------------|
| 1    | (80;16;108.152)          | Oporto  | -2            |                |
| 2    | (78;20;100)              |         | -7            | 163            |
| 3    | (76;32;10)               |         | 0             | 171            |
| 4    | (76;72;20)               | Aveiro  | 2             | 152            |
| 5    | (96;110;90)              |         | -9            | 126            |
| 6    | (92;118;13.106)          | Coimbra | -1            | 125            |
| 7    | (78;120;0)               |         | 3             | 143            |
| 8    | (60;138;80)              |         | -3            | 140            |
| 9    | (58;162;20)              |         | 4             | 161            |
| 10   | (60;170;50)              | Leiria  | 6             | 148            |
| 11   | (54;188;170)             |         | 0             | 179            |
| 12   | (46;210;180)             |         | -5            | 155            |
| 13   | (48;232;60)              |         | -2            | 170            |
| 14   | (46;256;10)              |         | 2             | 154            |
| 15   | (34;276;50)              |         | -4            | 149            |
| 16   | (34;280;32.348)          | Lisbon  |               |                |

The HSR configuration also complies with the location constraint, connecting Lisbon, Coimbra and Oporto (Table 6-4), and with the land-use constraint since it does not cross forbidden land-use elements (Figure 6-6 b).

Besides the mandatory locations, the HSR configuration also links Aveiro and Leiria (Table 6-7).

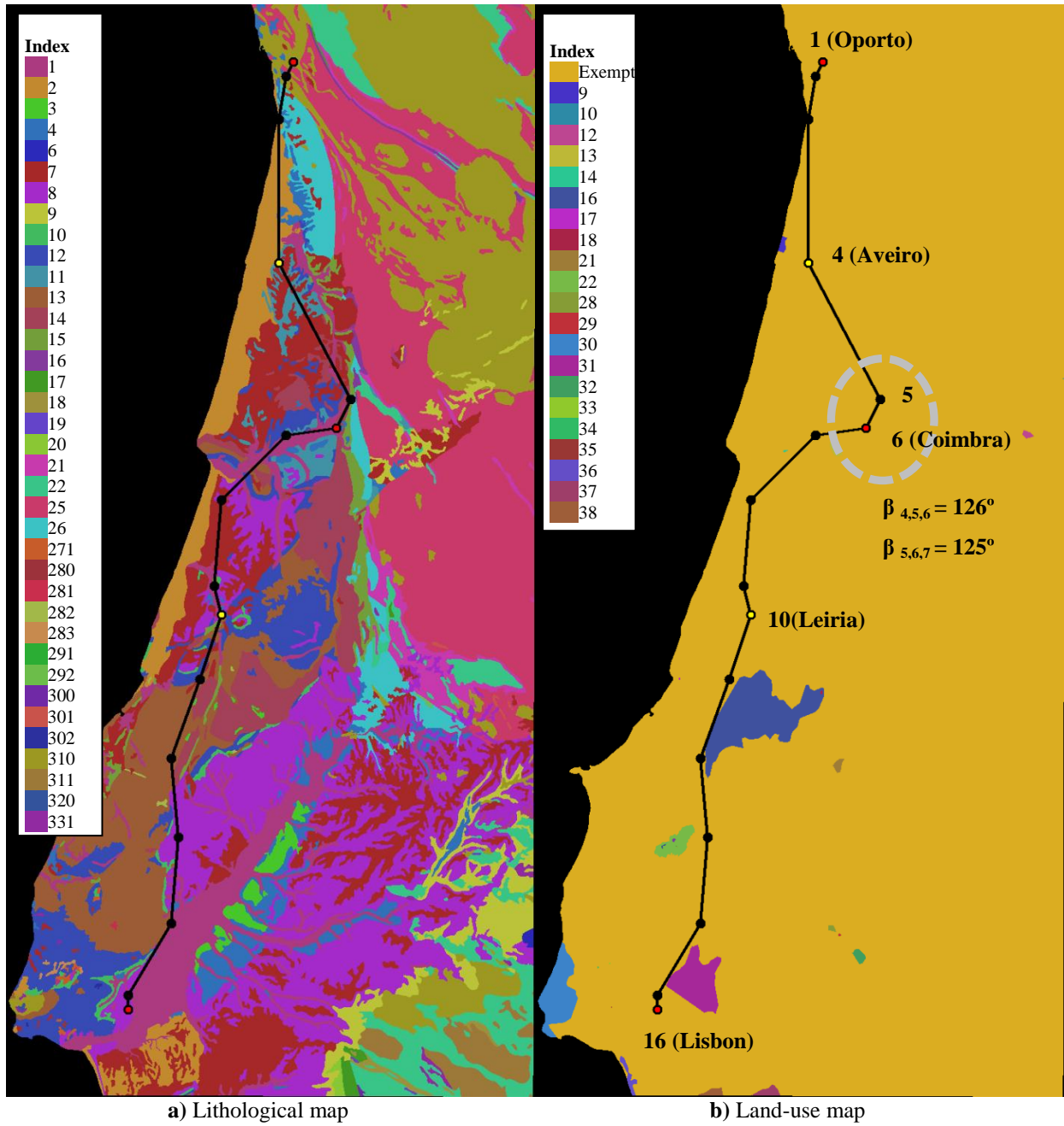


**Figure 6-6** Plan view overlay of the best HSR configuration found for the Lisbon-Oporto SPC case-study: a) lithological map, b) land-use map, c) expropriation cost map, d) elevation map and e) main rivers map.

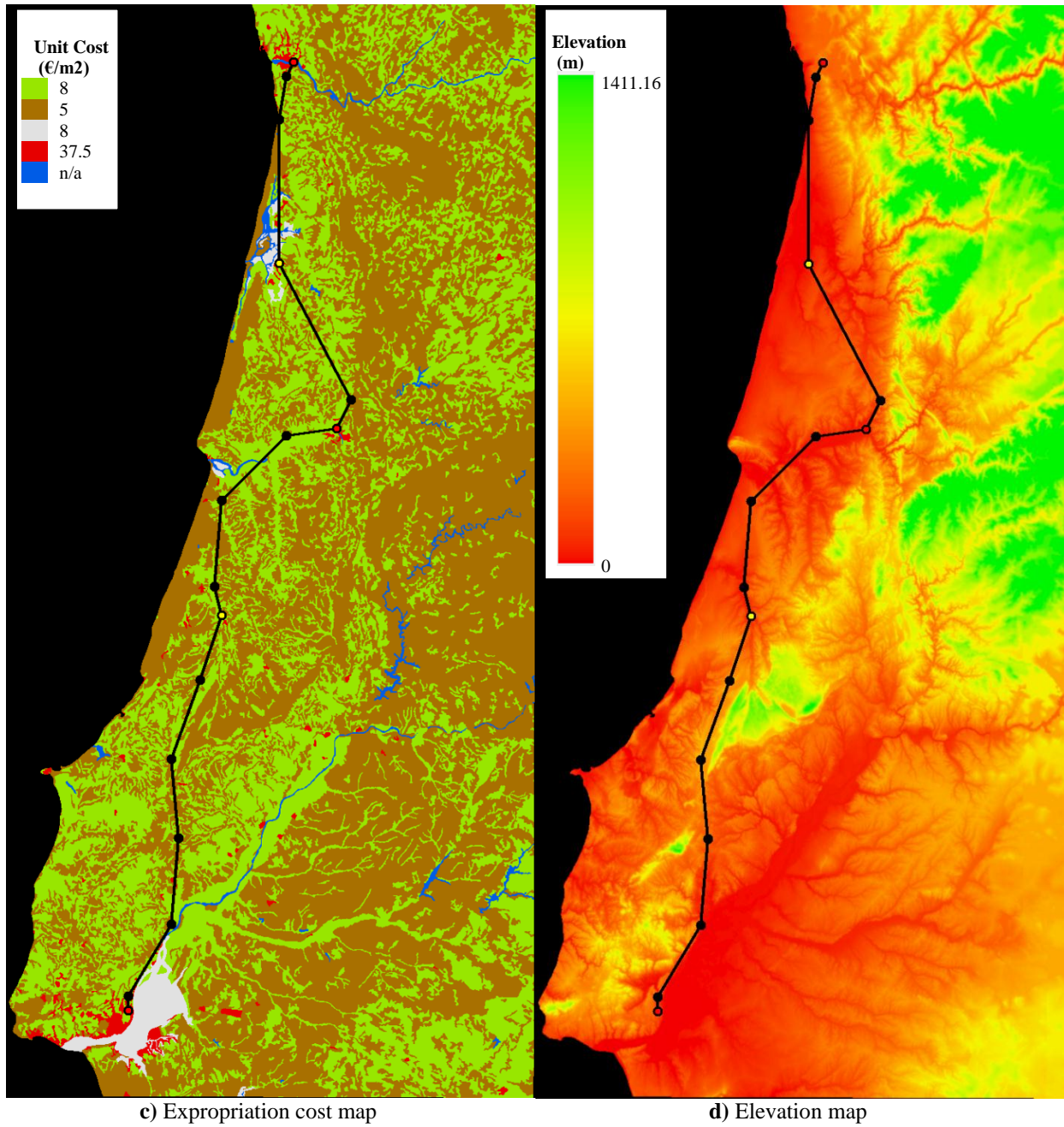
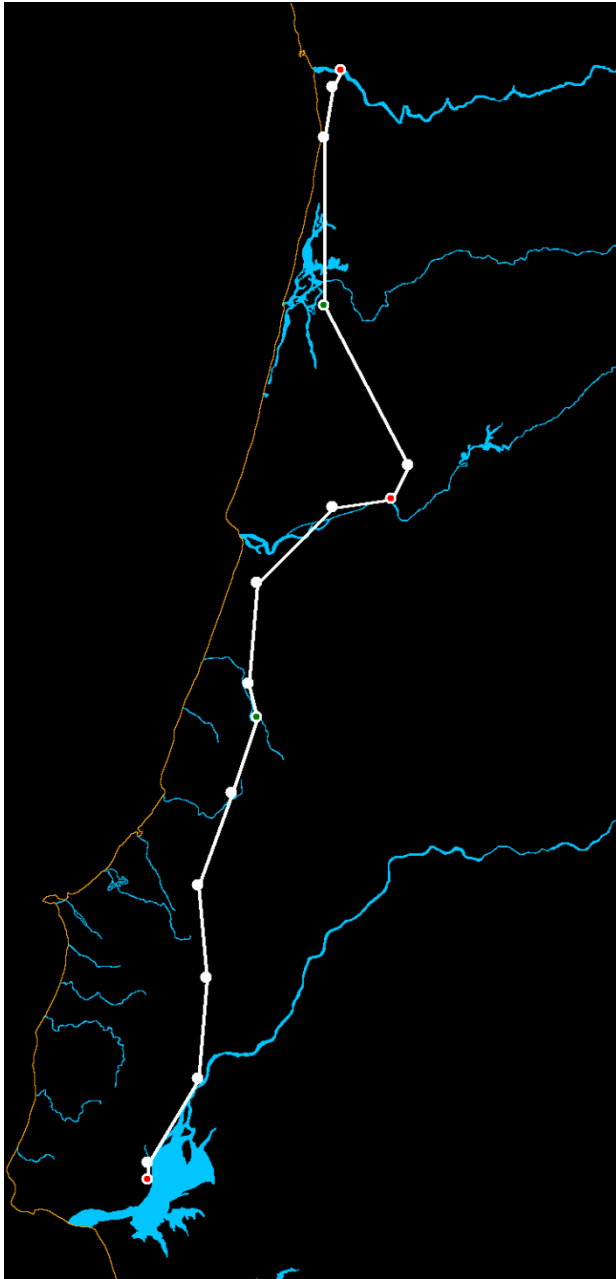


**Figure 6-6** Plan view overlay of the best HSR configuration found for the Lisbon-Oporto SPC case-study: a) lithological map, b) land-use map, c) expropriation cost map, d) elevation map and e) main rivers map. (Continued).



e) Main rivers map

**Figure 6-6** Plan view overlay of the best HSR configuration found for the Lisbon-Oporto SPC case-study: a) lithological map, b) land-use map, c) expropriation cost map, d) elevation map and e) main rivers map. (Continued).

Table 6-8 shows that the minimum clearance of 5 m is complied with for all bridges crossing rivers (by case-study definition all such bridges require launching systems for the construction process). The HSR configuration does not cross the Tagus River (Figure 6-6 e) and thus its navigability is not affected.

Table 6-8 specifies a horizontal angle penalty of €123.56 million, according to equation (4.9), derived from the small angles verified in nodes 5 and 6 (Coimbra), smaller than the recommended 140°. The connection of both Aveiro and Leiria corresponds to a benefit of €995.10 million (Table 6-8).

**Table 6-8** Cost breakdown of the best HSR configuration found for the Lisbon-Oporto SPC case-study.

|   | Quantity                                   | Units          | Bridge<br>Maximum<br>Height (m) | Bridge<br>Clearance<br>(m) | Cost<br>(Million €) |
|---|--|----------------|---------------------------------|----------------------------|---------------------|
| <b>Objective Function Value (1 + 2 + 3 - 4)</b> |  |                |                                 |                            | 778.72              |
| 1.  | CONSTRUCTION COST<br>(1.1+1.2+1.3+1.4+1.5) |                |                                 |                            | 1,658.50            |
| 1.1   | Expropriation                              |                |                                 |                            | 154.94              |
| 1.2   | Earthworks                                 |                |                                 |                            | 454.52              |
| 1.2.1   | 1,091,867                                  | m <sup>3</sup> |                                 |                            | 12.51               |
| 1.2.2   | 44,586,417                                 | m <sup>3</sup> |                                 |                            | 123.95              |
| 1.2.3   | 55,239,290                                 | m <sup>3</sup> |                                 |                            | 172.35              |
| 1.2.4   | 7,694,476                                  | m <sup>3</sup> |                                 |                            | 56.09               |
| 1.2.5   | 1,739,793                                  | m <sup>3</sup> |                                 |                            | 22.18               |
| 1.2.6   | 15,431,010                                 | m <sup>3</sup> |                                 |                            | 67.43               |
| 1.3   | ALL BRIDGES                                |                |                                 |                            | 429.98              |
| 1.3.1   | <u>1,109</u>                               | m              | <u>9.2</u>                      | <u>8.0</u>                 | 16.64               |
| 1.3.2   | 212  | m              | 21.3                            | 21.3                       | 2.09                |
| 1.3.3   | 395  | m              | 26.4                            | 24.7                       | 4.15                |
| 1.3.4   | <u>200</u>                                 | m              | <u>12.9</u>                     | <u>12.9</u>                | 3.17                |
| 1.3.5   | <u>1,600</u>                               | m              | <u>15.8</u>                     | <u>14.3</u>                | 23.91               |
| 1.3.6   | <u>600</u>                                 | m              | <u>18.0</u>                     | <u>14.8</u>                | 9.10                |
| 1.3.7   | <u>600</u>                                 | m              | <u>18.4</u>                     | <u>17.0</u>                | 9.10                |
| 1.3.8   | 447  | m              | 27.4                            | 20.7                       | 4.77                |
| 1.3.9   | 671  | m              | 31.6                            | 20.5                       | 7.63                |
| 1.3.10  | 671  | m              | 28.8                            | 20.5                       | 7.25                |
| 1.3.11  | 1,611                                      | m              | 27.9                            | 22.0                       | 16.94               |
| 1.3.12  | 2,953                                      | m              | 30.5                            | 21.3                       | 32.42               |
| 1.3.13  | 224  | m              | 23.3                            | 23.3                       | 2.28                |
| 1.3.14  | 447  | m              | 34.0                            | 28.8                       | 5.37                |
| 1.3.15  | 223  | m              | 32.3                            | 32.3                       | 2.68                |
| 1.3.16  | 224  | m              | 20.1                            | 20.1                       | 2.15                |
| <u>1.3.17</u>                                   | <u>283</u>                                 | <u>m</u>       | <u>13.0</u>                     | <u>13.0</u>                | 4.40                |
| <u>1.3.18</u>                                   | <u>1,414</u>                               | <u>m</u>       | <u>19.9</u>                     | <u>18.0</u>                | 21.15               |
| 1.3.19  | 1,980                                      | m              | 26.5                            | 20.4                       | 20.26               |
| <u>1.3.20</u>                                   | <u>849</u>                                 | <u>m</u>       | <u>28.6</u>                     | <u>27.9</u>                | 15.19               |
| 1.3.21  | 566  | m              | 33.0                            | 29.3                       | 6.62                |
| 1.3.22  | 283  | m              | 36.6                            | 36.6                       | 3.63                |
| 1.3.23  | 283  | m              | 21.7                            | 21.7                       | 2.76                |
| 1.3.24  | 2,263                                      | m              | 55.1                            | 40.1                       | 38.96               |
| <u>1.3.25</u>                                   | <u>631</u>                                 | <u>m</u>       | <u>31.2</u>                     | <u>15.0</u>                | 11.91               |
| 1.3.26  | 632  | m              | 34.3                            | 32.1                       | 7.57                |
| 1.3.27  | 222  | m              | 26.1                            | 26.1                       | 2.38                |
| 1.3.28  | 1,043                                      | m              | 37.2                            | 20.4                       | 13.06               |
| 1.3.29  | 190  | m              | 23.1                            | 23.1                       | 1.95                |



**Table 6-8** Cost breakdown of the best HSR configuration found for the Lisbon-Oporto SPC case-study.  
(Continued).

|               |                                   | Quantity   | Units    | Bridge<br>Maximum<br>Height (m) | Bridge<br>Clearance<br>(m) | Cost<br>(Million €) |
|---------------|-----------------------------------|------------|----------|---------------------------------|----------------------------|---------------------|
| 1.3.30        | Bridge Fixed Scaffolding_30       | 221        | m        | 20.5                            | 20.5                       | 2.15                |
| 1.3.31        | Bridge Fixed Scaffolding_31       | 221        | m        | 29.4                            | 29.4                       | 2.52                |
| 1.3.32        | Bridge Fixed Scaffolding_32       | 221        | m        | 28.3                            | 28.3                       | 2.47                |
| <u>1.3.33</u> | <u>Bridge Launching System_33</u> | <u>820</u> | <u>m</u> | <u>18.1</u>                     | <u>13.2</u>                | 12.36               |
| 1.3.34        | Bridge Fixed Scaffolding_34       | 2,118      | m        | 43.1                            | 21.5                       | 29.31               |
| 1.3.35        | Bridge Fixed Scaffolding_35       | 444        | m        | 22.2                            | 21.4                       | 4.31                |
| 1.3.36        | Bridge Fixed Scaffolding_36       | 410        | m        | 23.8                            | 20.9                       | 4.10                |
| 1.3.37        | Bridge Fixed Scaffolding_37       | 410        | m        | 32.8                            | 23.4                       | 4.83                |
| 1.3.38        | Bridge Fixed Scaffolding_38       | 199        | m        | 22.8                            | 22.8                       | 2.03                |
| 1.3.39        | Bridge Fixed Scaffolding_39       | 208        | m        | 20.7                            | 20.7                       | 2.03                |
| 1.3.40        | Bridge Fixed Scaffolding_40       | 199        | m        | 24.3                            | 24.3                       | 2.08                |
| 1.3.41        | Bridge Fixed Scaffolding_41       | 408        | m        | 25.1                            | 22.3                       | 4.18                |
| 1.3.42        | Bridge Fixed Scaffolding_42       | 199        | m        | 24.2                            | 24.2                       | 2.08                |
| 1.3.43        | Bridge Fixed Scaffolding_43       | 199        | m        | 22.1                            | 22.1                       | 2.00                |
| 1.3.44        | Bridge Fixed Scaffolding_44       | 199        | m        | 20.2                            | 20.2                       | 1.93                |
| 1.3.45        | Bridge Fixed Scaffolding_45       | 207        | m        | 23.4                            | 23.4                       | 2.13                |
| 1.3.46        | Bridge Fixed Scaffolding_46       | 199        | m        | 24.9                            | 24.9                       | 2.10                |
| 1.3.47        | Bridge Fixed Scaffolding_47       | 497        | m        | 29.2                            | 25.8                       | 5.45                |
| 1.3.48        | Bridge Fixed Scaffolding_48       | 943        | m        | 36.2                            | 24.9                       | 11.61               |
| 1.3.49        | Bridge Fixed Scaffolding_49       | 223        | m        | 21.4                            | 21.4                       | 2.19                |
| 1.3.50        | Bridge Fixed Scaffolding_50       | 223        | m        | 30.3                            | 30.3                       | 2.58                |
| 1.3.51        | Bridge Fixed Scaffolding_51       | 223        | m        | 26.7                            | 26.7                       | 2.42                |
| <u>1.3.52</u> | <u>Bridge Launching System_52</u> | <u>446</u> | <u>m</u> | <u>48.8</u>                     | <u>45.7</u>                | 11.69               |
| 1.3.53        | Bridge Fixed Scaffolding_53       | 637        | m        | 48.5                            | 39.1                       | 9.88                |
| 1.3.54        | Bridge Fixed Scaffolding_54       | 200        | m        | 24.2                            | 24.2                       | 2.08                |
| 1.4           | ALL TUNNELS                       |            |          |                                 |                            | 275.31              |
| 1.4.1         | Tunnel_1                          | 670        | m        |                                 |                            | 23.45               |
| 1.4.2         | Tunnel_2                          | 1,118      | m        |                                 |                            | 39.13               |
| 1.4.3         | Tunnel_3                          | 141        | m        |                                 |                            | 4.95                |
| 1.4.4         | Tunnel_4                          | 95         | m        |                                 |                            | 3.31                |
| 1.4.5         | Tunnel_5                          | 126        | m        |                                 |                            | 4.43                |
| 1.4.6         | Tunnel_6                          | 96         | m        |                                 |                            | 3.36                |
| 1.4.7         | Tunnel_7                          | 632        | m        |                                 |                            | 22.12               |
| 1.4.8         | Tunnel_8                          | 100        | m        |                                 |                            | 3.49                |
| 1.4.9         | Tunnel_9                          | 1,389      | m        |                                 |                            | 48.62               |
| 1.4.10        | Tunnel_10                         | 2,555      | m        |                                 |                            | 89.44               |
| 1.4.11        | Tunnel_11                         | 943        | m        |                                 |                            | 33.02               |
| 1.5.          | LINEAR- DEPENDENT COSTS           |            |          |                                 |                            | 343.75              |
| 1.5.1         | Track and Ballast                 | 296,332    | m        |                                 |                            | 232.62              |
| 1.5.2         | Catenary                          | 296,332    | m        |                                 |                            | 111.12              |
| 2.            | GEOMETRY PENALTY                  |            |          |                                 |                            | 123.56              |
| 2.1           | Horizontal Angle Penalty          |            |          |                                 |                            | 123.56              |
| 2.2           | Gradient Penalty                  |            |          |                                 |                            | 0                   |
| 3.            | LAND-USE PENALTY                  |            |          |                                 |                            | 0                   |
| 4.            | LOCATION BENEFIT                  |            |          |                                 |                            | 995.10              |
| 4.1           | Aveiro                            |            |          |                                 |                            | 497.55              |
| 4.2           | Leiria                            |            |          |                                 |                            | 497.55              |

The longitudinal profiles of the HSR configuration and of the ground elevation are presented in a 1/10,000 vertical scale and a 1/1,500,000 longitudinal scale in Figure 6-7. These are also represented in more detail in Figure 6-8 and Figure 6-9 in a 1/2,000 vertical scale and a 1/750,000 longitudinal scale. Figure 6-8 and Figure 6-9 include the identification of bridges and tunnels along the HSR solution with bars representing the length of each cross-section. The height of the bars is equal for all tunnels and bridges and does not relate to the actual height or depth. Given the available space for the representation (sheet size) the profiles appear distorted, with large gradients; it is again noted that all HSR section gradients are smaller than 20‰.

Figure 6-7 shows that unrealistically high bridges, as those discussed in section 5.3.3 are not part of the HSR configuration. The HSR elevation varies between 0 m and 180 m and the ground elevation, along the profile, varies between 0 m and 214.470 m. This produces an overall bridge cost of €429.98 million and a tunnel overall cost of €275.31 million corresponding to, respectively, 54 bridges and 11 tunnels (Table 6-8). Of the 54 bridges, 11 require the use of launching systems for the construction process (underlined in the Table 6-8). The largest maximum bridge height is 55.1 m, for bridge 24. However, Table 6-8 shows that earthworks are the largest cost item. The earthworks total €454.52 million, accounting for sub-ballast, embankment, cut with mechanical means, cut by blasting, form layer and ground improvement.

The longitudinal profile in Figure 6-7 also shows that the HSR configuration is 296.332 km long, corresponding to (Table 6-8): €232.62 million in track and ballast and €111.12 million in catenary. The cost of the land expropriation required for the deployment of the HSR is €154.94 million (Table 6-8).

The overall construction cost of the solution, accounting for expropriation, earthworks, bridges, tunnels and linear- dependent costs, totals €1,658.50 million (Table 6-8). The SPC objective function value is €786.96 million, smaller than the construction cost due to the location benefitting terms for the connection of both Aveiro and Leiria.

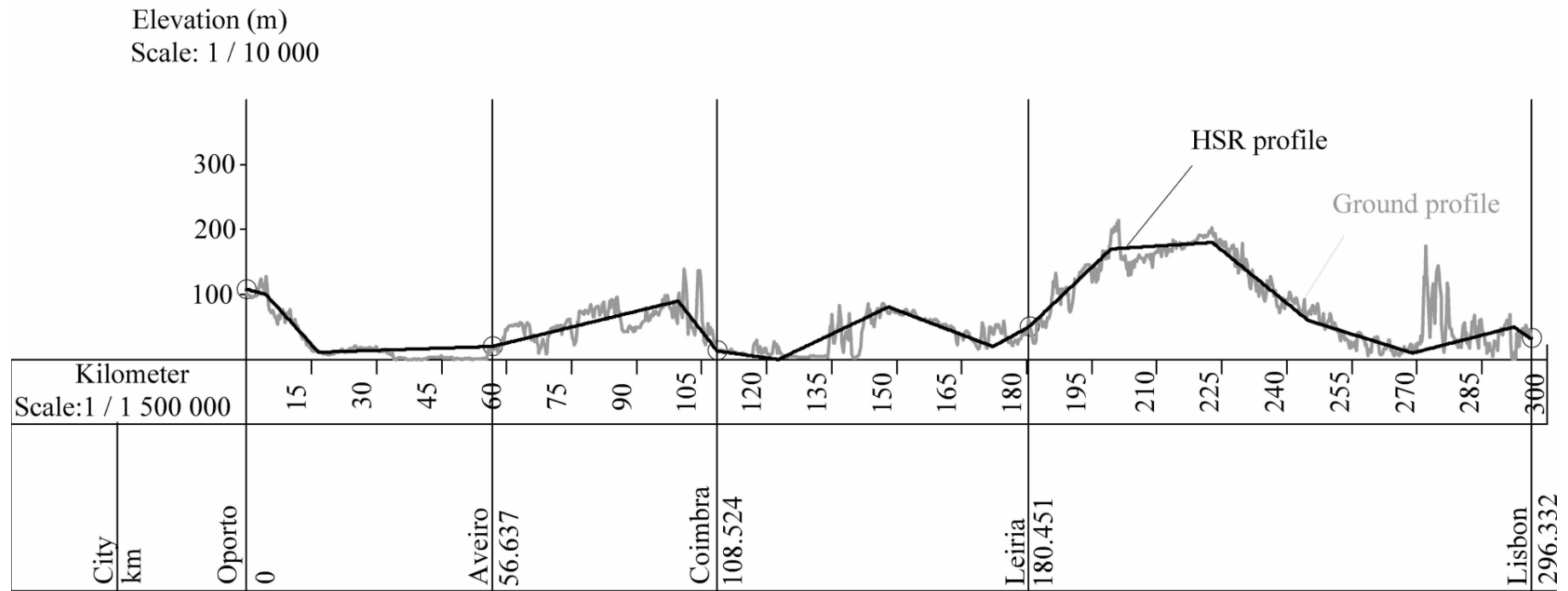


**Figure 6-7** Longitudinal profile of the best HSR configuration found for the Lisbon-Oporto SPC case-study. Vertical scale 1/10,000 and longitudinal scale 1/1,500,000.

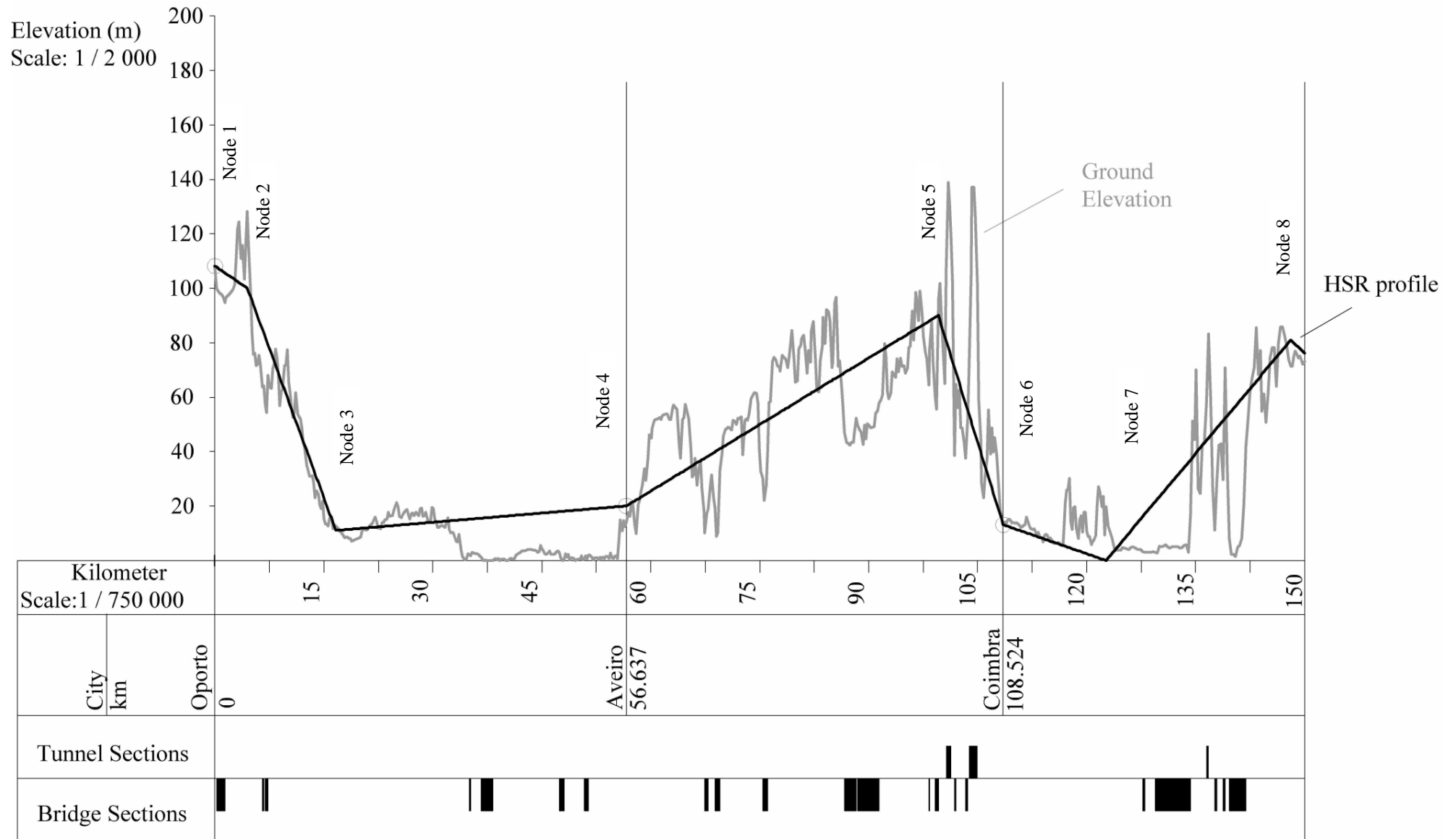


**Figure 6-8** Longitudinal profile of the HSR solution found for the Lisbon-Oporto SPC case-study from km 0 (Oporto) to km 150. Vertical scale 1/2,000 and longitudinal scale 1/750,000.

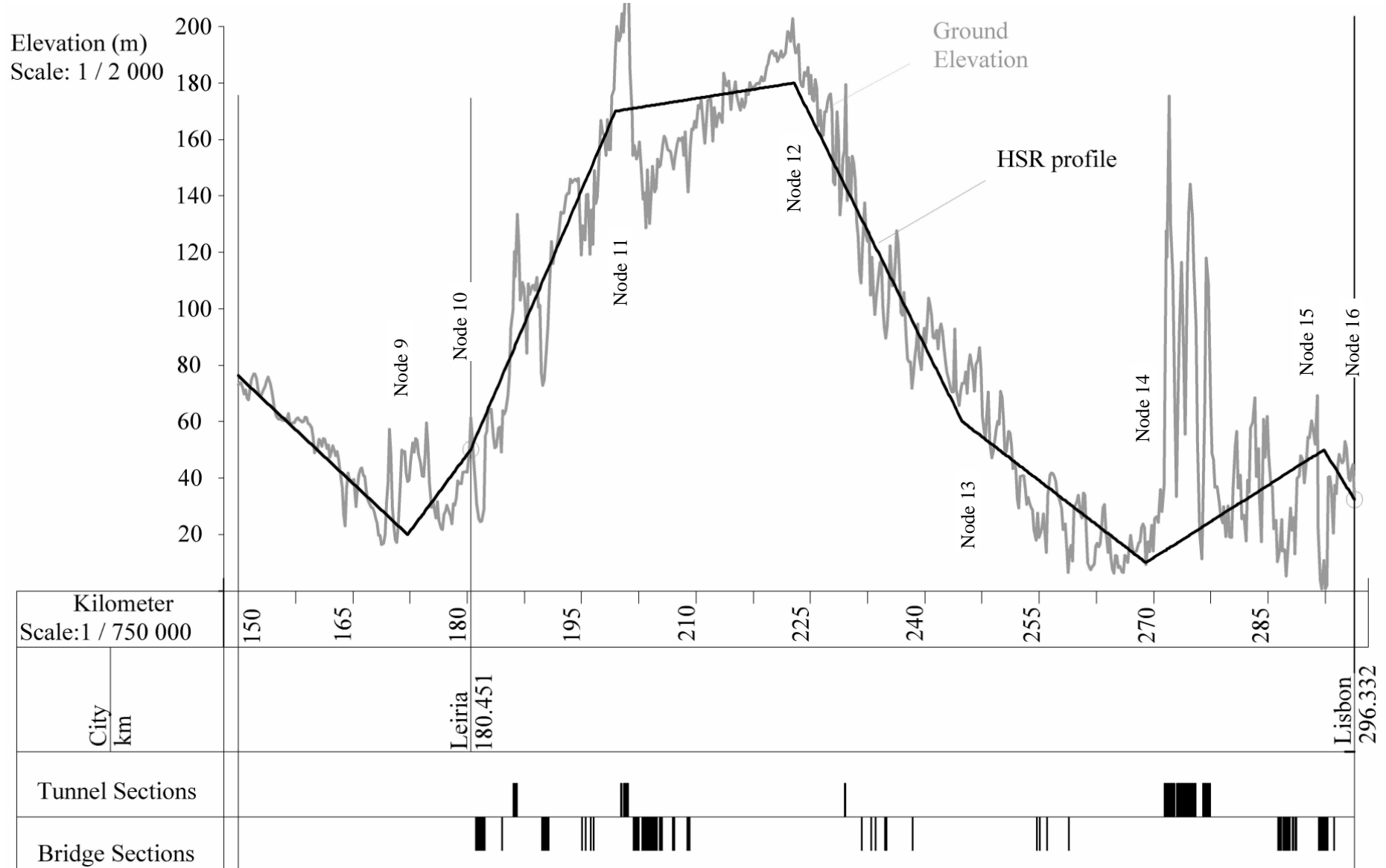


**Figure 6-9** Longitudinal profile of the HSR solution found for the Lisbon-Oporto SPC case-study from km 150 to km 296.332 (Lisbon). Vertical scale 1/2,000 and longitudinal scale 1/750,000.

Between Oporto (mandatory location) and Aveiro (benefitting location) the HSR configuration is aligned in an almost North-South direction. The first 15 km starting at Oporto, corresponding to the linear sections linking nodes 1, 2 and 3, require the crossing of the Douro River (Figure 6-6 e). The ground elevation is circa 110 m at the start and decreases to circa 20 m (Figure 6-8) at node 3, crossing mainly lithological units (26) schists, amphibolites, mica-schists, graywackes, quartzites, carbonate rocks and gneisses and (310) granites and derivations shown in Figure 6-6 a). Node 3 is located very near the coastline and the linear section linking it to Aveiro crosses almost exclusively (2) sand dunes and aeolian sands, as shown in Figure 6-6 a). The terrain is relatively flat presenting only small variations of elevation (Figure 6-8). Bridges are not required by elevation but to cross the existing bodies of water. Elevation is a major factor influencing the HSR configuration by increasing and varying significantly to the east, while the configuration deployment is limited in the west by the Atlantic Ocean (Figure 6-6 d).

Differing from the North-South alignment, two pronounced curves constitute the HSR around Coimbra. This increases the HSR configuration length by deviating from a more direct straight path and immediately increases the construction costs that depend directly infrastructure length (track, ballast and catenary). This sinuosity, however, is associated with trade-offs between other cost factors constituting the total construction costs and the objective function value. A more detailed analysis of the HSR configuration between Aveiro and Leiria, passing through Coimbra, is presented.

Figure 6-10 shows the HSR solution overlaying the expropriation cost map and zooms-in on Coimbra. One observes that the HSR avoids major construction in urban areas, with the larger expropriation cost (37.5 €/m<sup>2</sup>). The horizontal angle constraint makes an absolute avoidance of urban areas difficult by imposing a minimum angle of 120°.

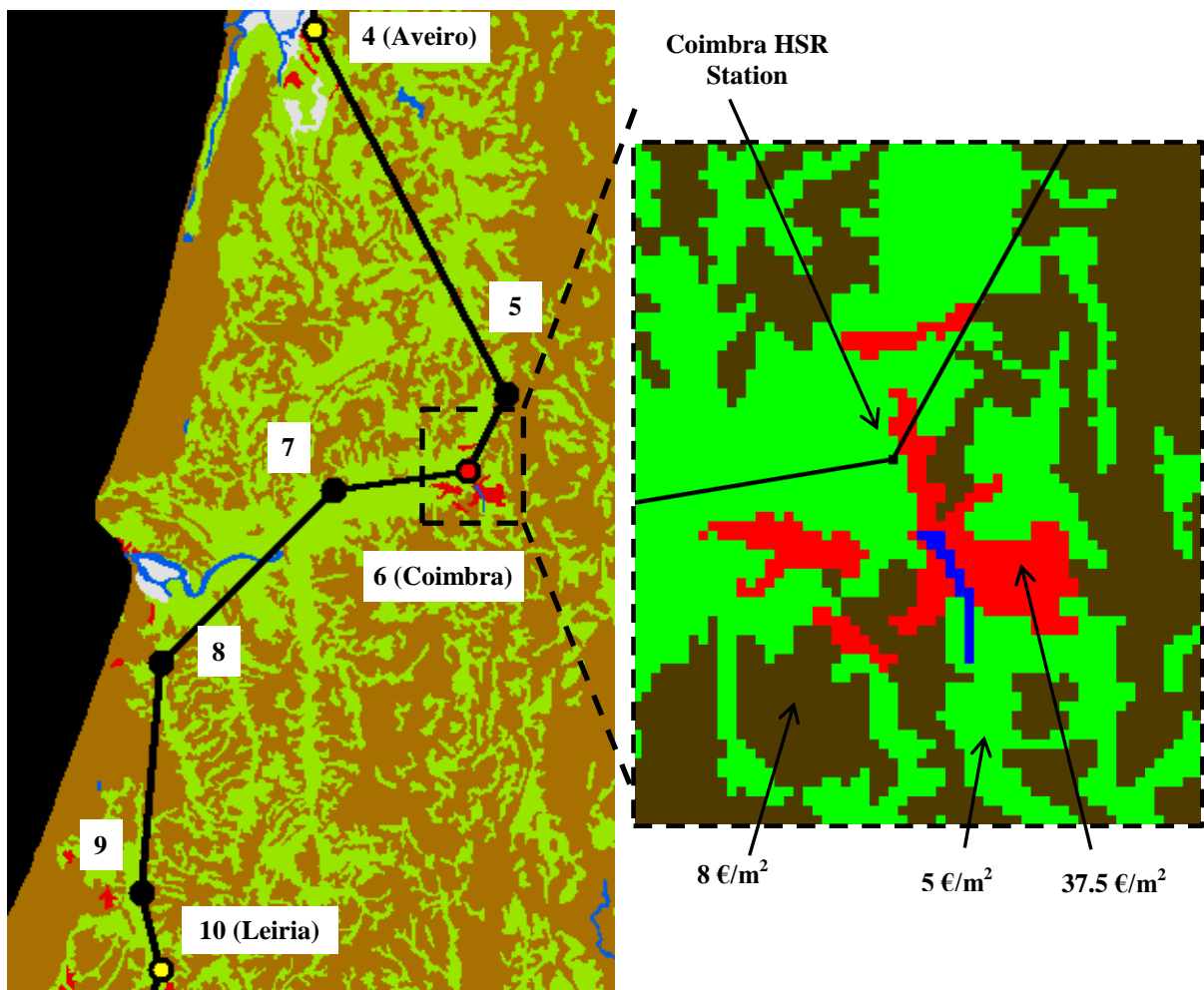
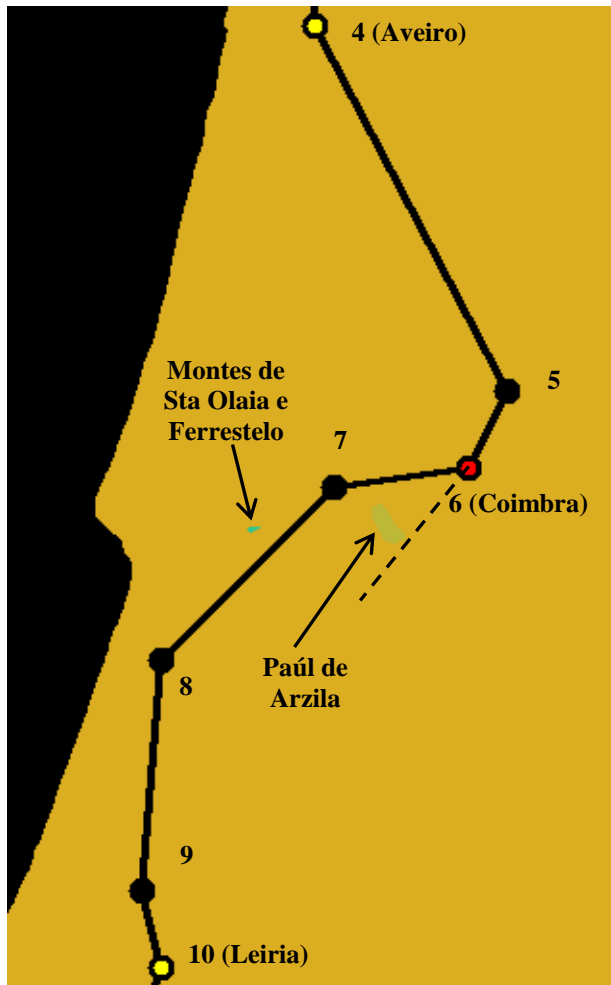


**Figure 6-10** Detail of the HSR plan view overlaying the expropriation cost map in Coimbra.

The angle at Coimbra station is  $125^\circ$  (Table 6-7), which is less than the normal angle  $\beta_{normal} = 140^\circ$  and thus a geometry penalty is added in the objective function. Besides Coimbra, the horizontal angle at node 5 also results in a penalty given its  $126^\circ$  value (Table 6-7), smaller than  $\beta_{normal} = 140^\circ$ . Considering the direction of the linear section linking Coimbra and node 7 (Figure 6-11), given the location constraint requiring the connection of Coimbra and a minimum angle of  $120^\circ$  between linear sections, a feasible HSR configuration has to develop a sinuosity if linking both Coimbra and Aveiro. Thus, node 5 is located northeast of Coimbra instead of northwest, the direction of Aveiro relative to Coimbra.

In relation to feasibility, land-use also limits the HSR configuration south of Coimbra (Figure 6-11). Two forbidden land-use areas, the Montes de Sta Olaia e Ferrestelo Classified Site

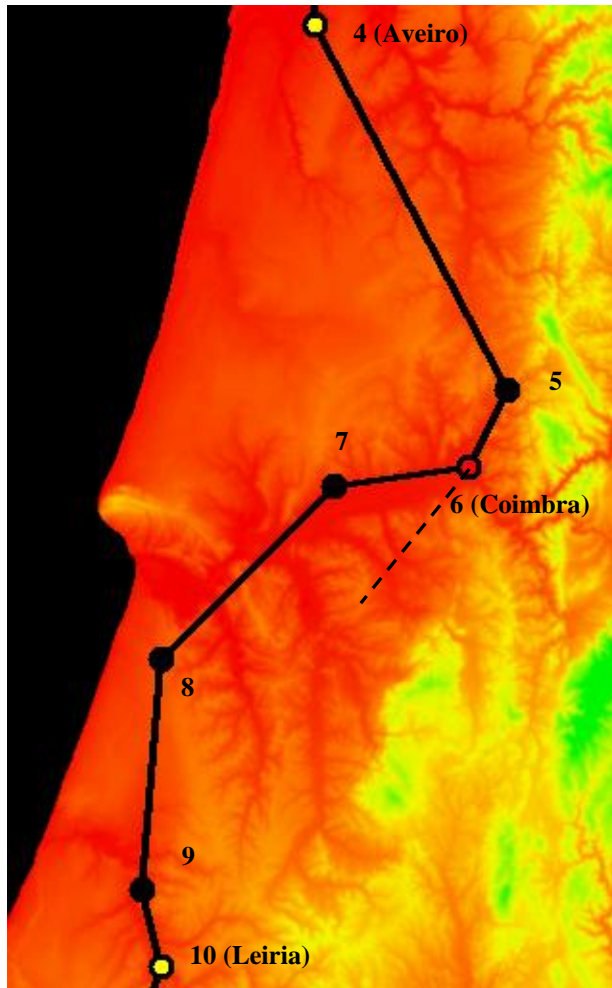
(land-use index 14) and the Paúl de Arzila Natural Reservation (land-use index 13) define space property elements where HSR construction is forbidden (Table 5-2). Thus, from Coimbra southwards, the HSR linear section has 3 feasible options: to cross between the two areas, as the problem solution does, or to cross westward of Montes de Sta Olaia e Ferrestelo or to cross eastward of the Paúl de Arzila Natural Reservation.



**Figure 6-11** Detail of the HSR plan view overlaying the land-use map between Aveiro and Leiria.

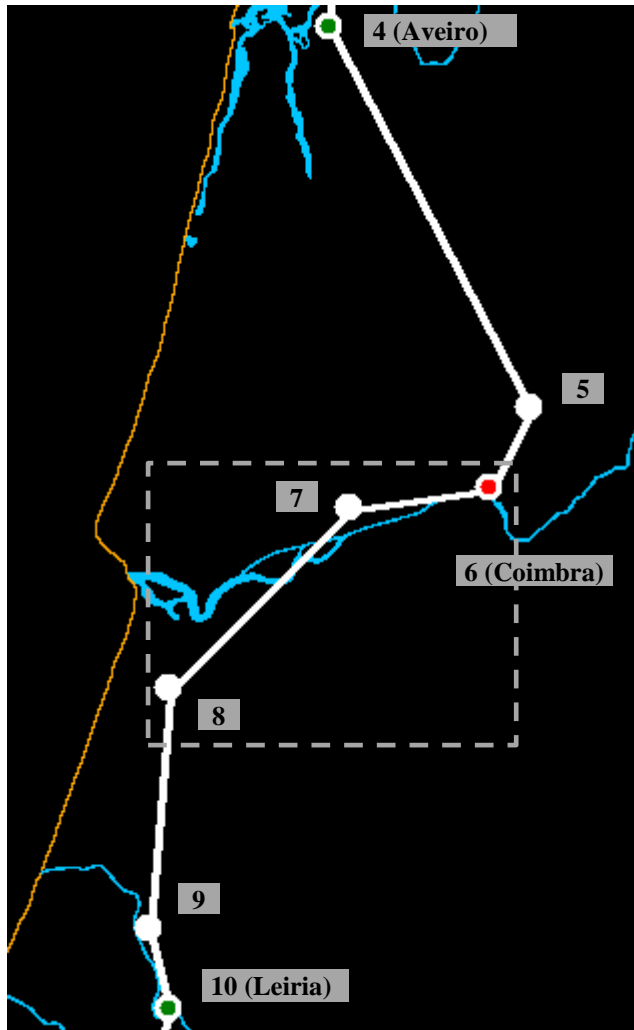
If the HSR crossed westward of Montes de Sta Olaia e Ferrestelo the horizontal angle at Coimbra would decrease and the solution's  $125^\circ$  is already very close to the feasibility limit. The other option is to cross eastward of the Paúl de Arzila Natural Reservation. This latter option is limited (the westernmost allowable position) by the dashed line in Figure 6-11. One can analyze the effects that crossing east of the dashed line may have in terms of ground elevation in Figure 6-12 and compare it with the solution's configuration.





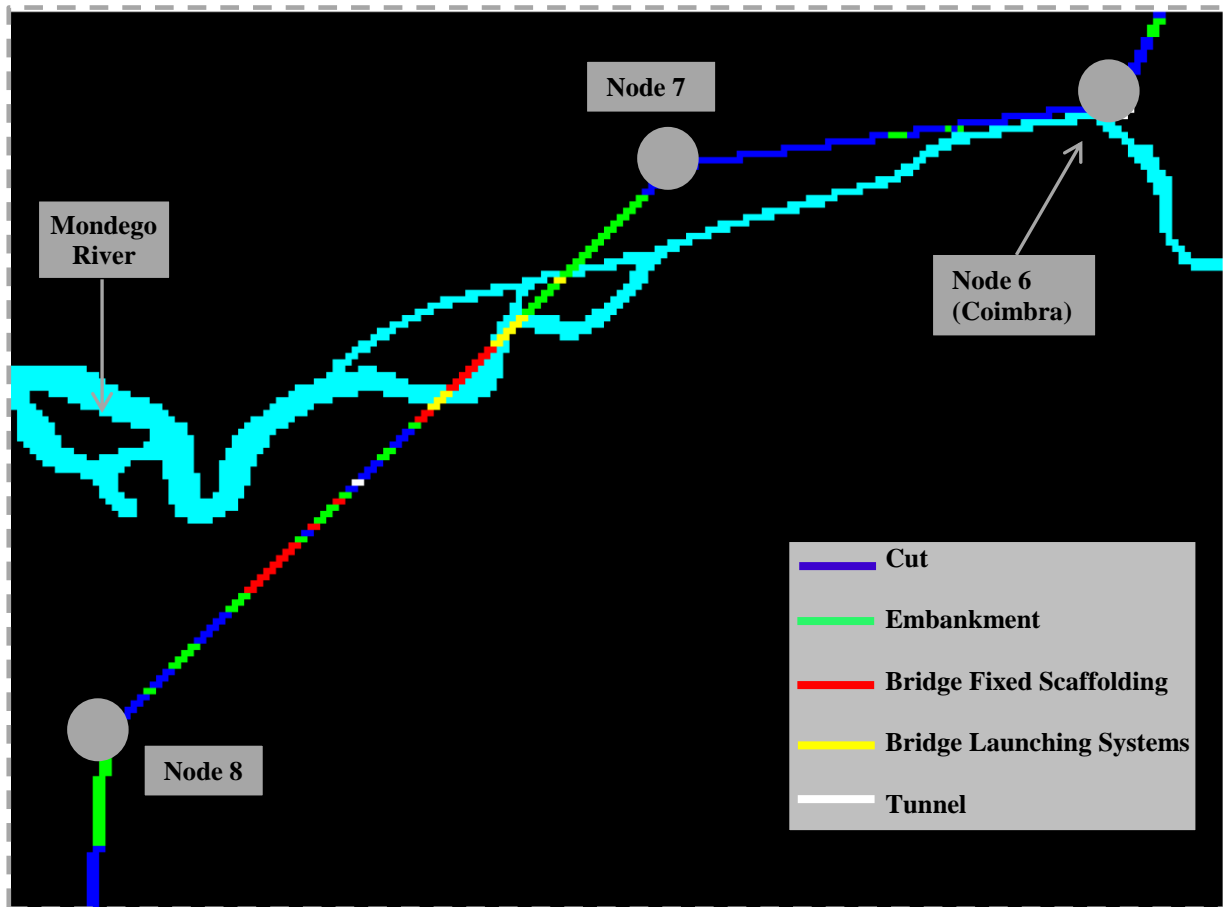
**Figure 6-12** Detail of the HSR plan view overlaying the ground elevation map between Aveiro and Leiria.

Figure 6-12 shows that crossing eastward of the dashed line implies larger variations of the ground profile that, given the gradient constraint of the HSR, would result in higher embankments, deeper cuts and possibly the need for bridges and/or tunnels. Such an alignment in larger construction costs when compared to the flatter ground profile along the problem solution. In fact, the longitudinal profile of Figure 6-8 shows that neither bridges nor tunnels are constructed between Coimbra and node 7. The following linear section, linking nodes 7 and 8 does include one tunnel due to elevation and bridges (Figure 6-8) due to both elevation and river crossing requirements (Figure 6-13).



**Figure 6-13** Detail of the HSR plan view overlaying the main rivers map between Aveiro and Leiria.

A zoom-in of the dashed box of Figure 6-13 is presented in Figure 6-14. The HSR is plotted with different colors for different cross-sections. Figure 6-14 shows that, in fact, the section linking Coimbra and node 7 is built with cuts and embankments only. Conversely, the linear section linking nodes 7 and 8 also includes bridges and one tunnel. Bridges using launching systems are, by case-study definition, required to cross bodies of water and the yellow segments of the HSR line in Figure 6-14 are built over the Mondego River. The distortions in the overlay are due to the graphics representation.



**Figure 6-14** Detail of the HSR plan view overlaying the main rivers map between Coimbra and Node 8: zoom-in of the dashed box of Figure 6-13. Cross-sections are represented by different colors: cuts in blue, embankments in green, bridge with fixed scaffolding in red, bridges requiring launching systems in yellow and tunnels in light gray.

By running almost parallel to the Mondego River between Coimbra and node 7, the cuts and embankments forming this HSR linear section are built on (1) Alluvium, as shown in the lithological map overlay of Figure 6-15. According to Table 5-6, both cuts and embankments built on alluvium have 1/2 lateral slopes, the smallest vertical/horizontal slope ratio. The smaller the slope ratio is, the larger the excavation and embankment volumes and the larger the footprints (and expropriation areas) for the same height or depth. Alluvium also requires a 5 meter depth of ground improvement by removal and replacement of that depth of the existing natural soil. North of Coimbra and South of node 7, between Aveiro and Leiria, the lithological units vary. The lithological map overlay of Figure 6-15 shows that mainly sandstones and limestones are crossed (in lithological units 7, 8, 11, 12, 13, 14 and 15).

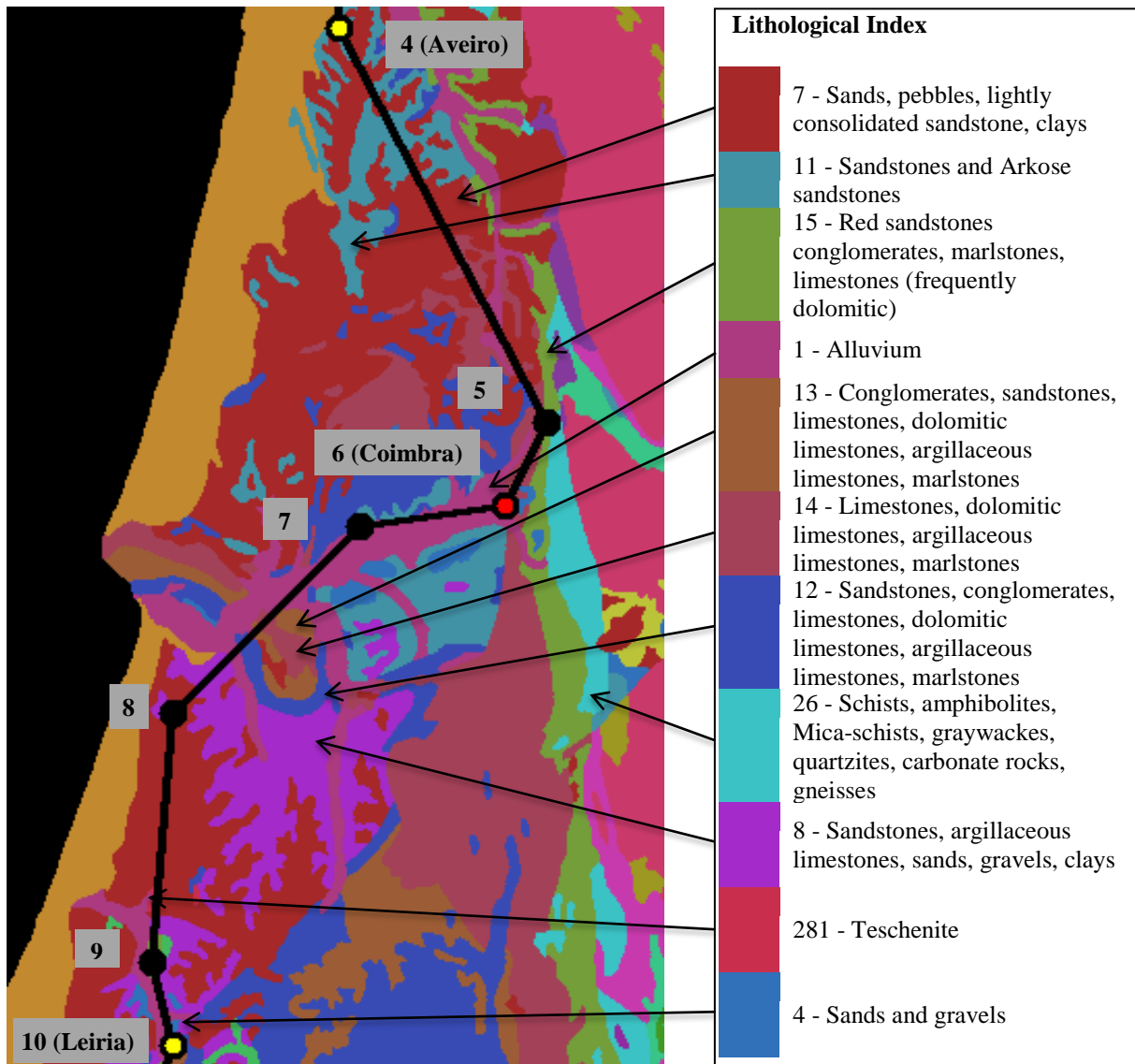


**Figure 6-15** Detail of the HSR plan view overlaying the lithological map between Aveiro and Leiria.

Between Leiria and Lisbon the HSR alignment returns to an almost North-South direction. The HSR configuration however, is again limited by the land-use constraint (Figure 6-16). The Serras de Aires e Candeeiros Natural Parks (land-use index 16), the Montejunto Mountain (land-use index 22) and the Estuário do Tejo Natural Reservation (land-use index 31) are the major forbidden land-use areas to account for (Figure 6-16). The first two areas represent mountain ranges and the third represents the Tagus River estuary.

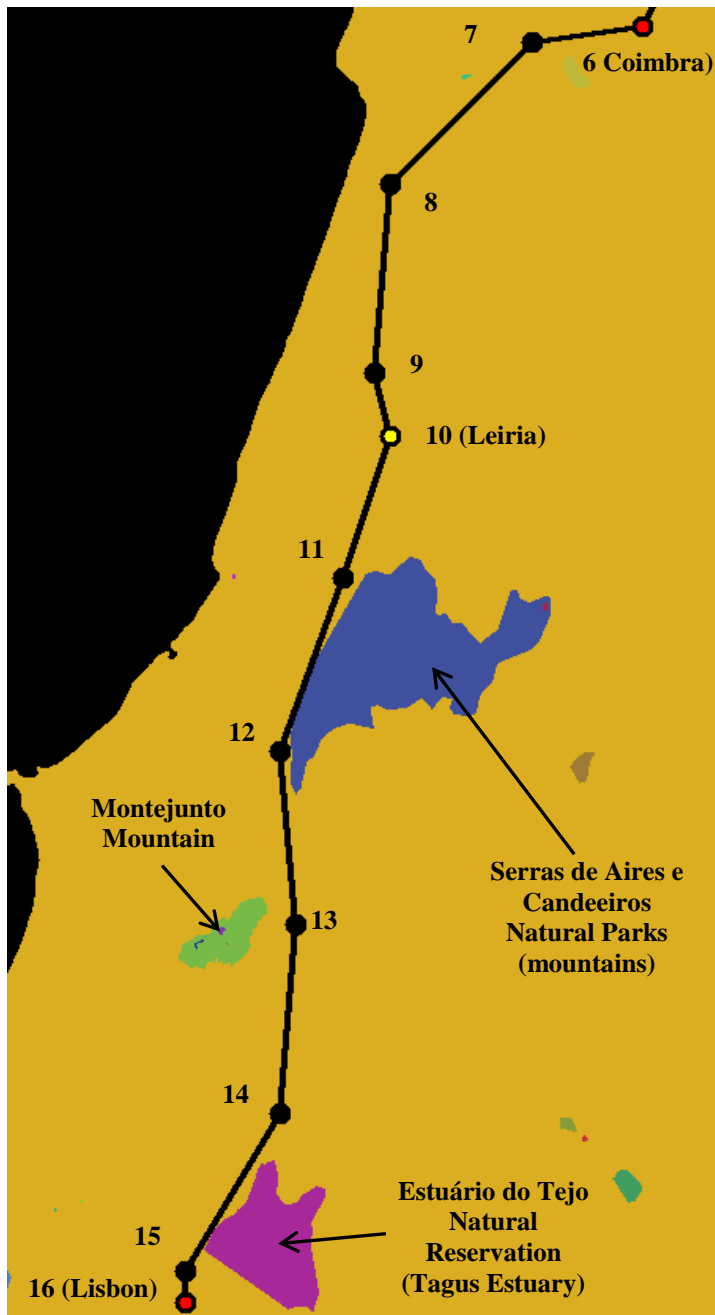


**Figure 6-16** Detail of the HSR plan view overlaying the land-use map between Coimbra and Lisbon.

The largest forbidden area is the Serras de Aires e Candeeiros Natural Parks (land-use index 16). The two feasible options are to cross either to the west, as does the solution, or to the east of this area. One can conclude that the benefit of linking Leiria has a significant influence on the HSR configuration. By linking Leiria, the western link is the shorter connection to Lisbon. Linear sections linking Leiria and nodes 11 and 12 run very close to this forbidden land-use

area, which avoids large variations of the ground elevation (Figure 6-6 d) and crossing additional bodies of water (Figure 6-6 e) existent in the western vicinity of the alignment. From km 210 (located between nodes 11 and 12) until km 270 (next to node 14) the HSR solution avoids major construction of bridges and tunnels, more expensive than earthworks (Figure 6-9). In the linear section linking nodes 14 and 15 tunnels are required (Figure 6-9), which cannot be avoided as the Estuário do Tejo Natural Reservation (land-use index 31) prevents the HSR from running more to the east and elevation increases to the west (Figure 6-6 d). Finally, bridges are required in the 10 km closest to Lisbon, from km 285 (Figure 6-9), both due to elevation (Figure 6-6 d) and for crossing a small tributary of the Tagus River (Figure 6-6 e).

By running adjacent to the Tagus River estuary, the HSR linear section linking nodes 14 and 15 is built, almost entirely, over (1) Alluvium. The remaining HSR linear sections linking Leiria and Lisbon are mainly built on (8) Sandstones, argillaceous limestones, sands, gravels, clays and (13) Conglomerates, sandstones, limestones, dolomitic limestones, argillaceous limestones, marlstones, as shown in Figure 6-6 a).

It is discussed that building the HSR over alluvium, the flatter areas constituting the floodplains of the Mondego and Tagus Rivers, allows one to obtain more inexpensive configurations. However, building embankments and cuts on the floodplains would bear some important concerns if one was to consider the time factor. One of the concerns is the construction time of embankments over the soft and compressible soils forming the floodplains. The construction method using pre-loading with drains, used for accelerating the consolidation of the soil and the construction of such embankments, takes longer than building an embankment without pre-loading requirements and thus has larger construction costs. Other solutions exist, such as building column-supported embankments, for accelerating the construction process, but also at larger construction costs (Dumas et al. 2003). Also, the creep behavior of soils, strain at constant stress, expected for alluvium leads, in the long-run, to concerns regarding secondary consolidation and the post-construction settlements (Coelho 2000). Given the strict displacement requirements of the HSR (section 2.2.1), the occurrence of these post-construction settlements can lead to significant operating costs (such as speed reduction) and maintenance costs (such as embankment rehabilitation and track re-alignment). In these cases, building the HSR with viaducts at larger construction

costs when crossing the floodplains may be desirable. These considerations are not included in the SPC model and thus, the Lisbon-Oporto solution does not take them into account.

In the preceding lines, comments were made on the HSR solution found by the SAA implementation to solve the SPC Lisbon-Oporto HSR planning problem. The geometry layout and the cost breakdown of the HSR configuration are presented. The HSR configuration was also discussed in the context of the problem constraints and the search space characteristics. The following sections discuss the results in the context of the construction costs of existing HSR lines in the world and the Portuguese conventional rail network.

### 6.3.2 CONSTRUCTION COSTS OF THE SOLUTION

From the characterization of the HSR solution of the SPC problem in section 6.3.1, one may derive an average construction cost per kilometer of €5.60 million. This cost includes most but not all the construction cost items that the actual construction of the proposed HSR would require. For instance, the case-study application does not include the interaction with the existing infrastructure such as roads, railways, electricity supply, gas supply, telecommunications, water supply or sewage. The fact that these existing infrastructures may need to be relocated and that bridges or tunnels may be required for, respectively, overpasses or underpasses can affect the construction cost of the HSR. These items are not included in the model construction costs and their future inclusion would require data on the location and elevation of such existing infrastructures.

This section analyzes how the solution costs compare with cost bounds of existing HSR projects. In section 2.3.1 average construction costs per kilometer of new and operating HSR lines around the world are discussed according to Mendoza et al. (2009). The average costs presented in Figure 2-5 exclude the expropriation costs but include two additional elements: signaling systems and communications and safety installations. Mendoza et al. (2009) indicate these two elements can represent, individually, an average 7.5% of the total costs. To establish the comparison, an analogous average value is estimated for the SPC solution. The average construction cost per kilometer of the solution (€5.60 million) is considered to represent 85% of the total cost ( $85\% + 2 \times 7.5\% = 100\%$ ), which is then discounted by the expropriation cost. This results in an average comparative cost per kilometer of €6.06 million that corresponds to a 2005 value of €5.61 million (Eurostat 2013b).

Comparing with the framework costs in Figure 2-5, one observes that the SPC solution's €5.61 million (2005) is larger than the lower cost bound of the French lines in service, €4.7 million (2005), and smaller but close to the lower bounds for Spanish HSR lines, €7.8 million (2005) for lines in service and €8.9 million (2005) for lines under construction.

Given that interaction with existing infrastructure is not accounted for and that costs are dependent of the project specifics and of the deployment site characteristics, a detailed comparative analysis is not appropriate. Instead, this comparison allows one to observe that the construction costs from the Lisbon-Oporto SPC solution are in line with the costs observed in real world HSR projects.

Having verified that the average construction cost of the HSR solution is within cost bounds of existing HSR lines, the construction cost breakdown analysis in Figure 6-17 is performed. The chart shows the accumulated costs along the HSR, from Oporto at km 0 to Lisbon at km 296.332, for expropriation, earthworks, bridges, tunnels and linear- dependent costs, separately, and the aggregate total construction cost.



Accumulated Partial Costs  
(Million €)

Accumulated Total  
Construction Cost  
(Million €)

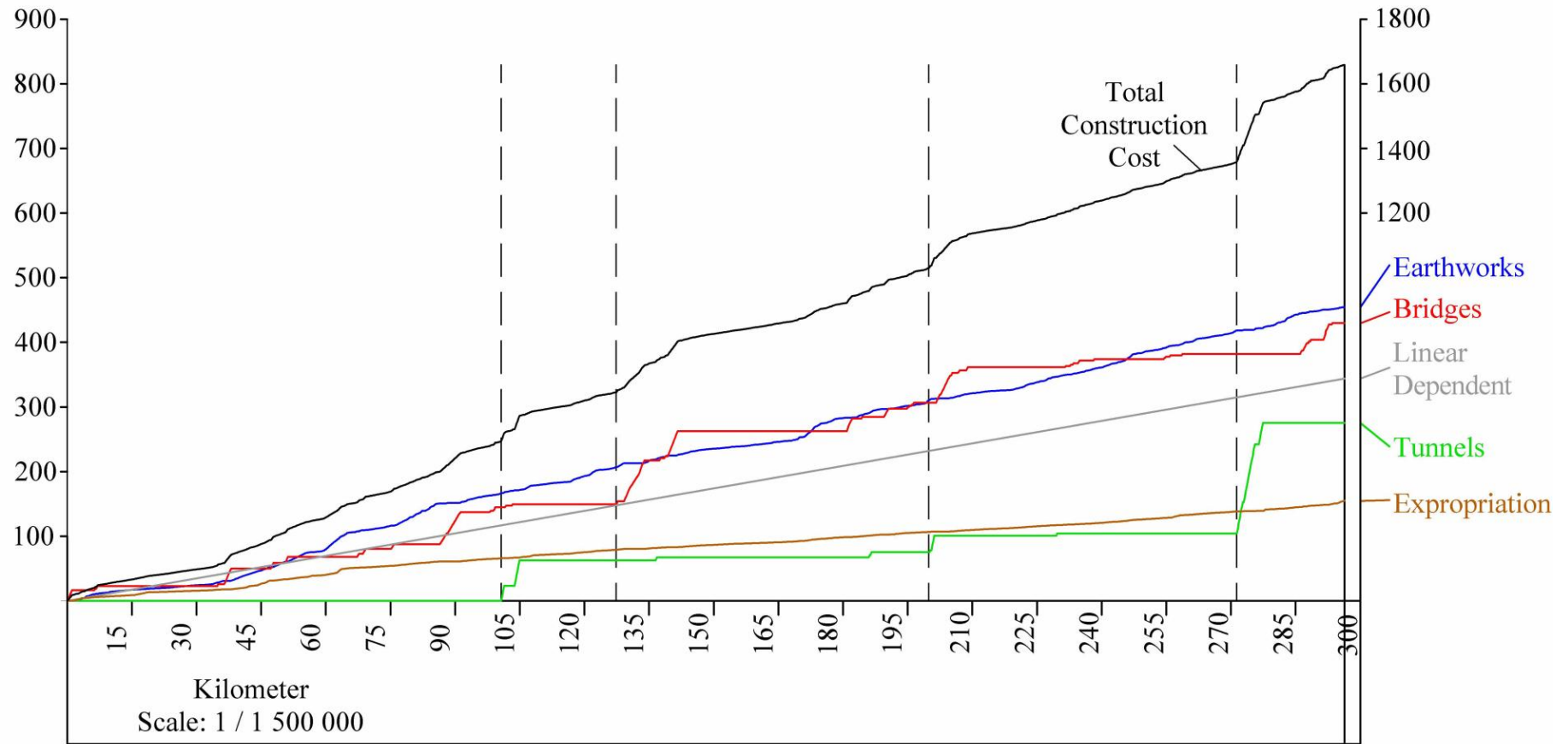


Figure 6-17 Accumulated costs along the longitudinal profile.

From Figure 6-17 one observes that, besides the obvious case of linear- dependent costs, the costs increase trend of earthworks and expropriation is almost linear. The opposite is the case of bridges and tunnels, which correspond to sharp and short (in HSR extension) cost increases, as expected. This influences the trend of the overall construction cost. Four of the most pronounced increases in the total construction costs are highlighted in Figure 6-17 with vertical dashed lines, at the beginning of the slope. One observes that one of the four slopes is originated by the bridges cost increase (between km 120 and km 135), two of the slopes are mostly due to the tunnels costs (between km 90 and km 105 and between km 270 and km 275) and the remaining slope is due to the construction of tunnels followed by bridges (between km 195 and km 210). This cost increase behavior is expected, given that the construction cost of tunnels averages €35 million per km and of bridges averages €13.0 million per km, compared with €1.8 million average earthworks construction cost per km. The order of the main contributors for the overall construction cost, however, is explained by the extent of earthworks of 255.3 km, much larger than that of bridges and tunnels of, respectively, 33.1 km and 7.8 km.

### 6.3.3 COMPARISON WITH THE PORTUGUESE CONVENTIONAL RAIL LINE

One additional comparison has been performed, to assess how the SPC solution relates with the existing conventional rail line linking Lisbon, Coimbra and Oporto. Figure 6-18 shows the plan view of the HSR configuration and the existing conventional rail line (named Line of the North) overlaying the land-use layer.

The conventional line intends to provide rail service to smaller cities and towns, in addition to major urban centers such as Oporto, Aveiro, Coimbra and Lisbon. Conversely, the HSR aims at offering a fast intercity connection. The lower speed of trains on the conventional line allow one to use smaller radii of horizontal curves that, along with detours for connecting locations in-between major centers, result in the sinuous plan view shown in Figure 6-18. One observes, as expected, that the HSR configuration eliminates the small radii curves present in the conventional rail.

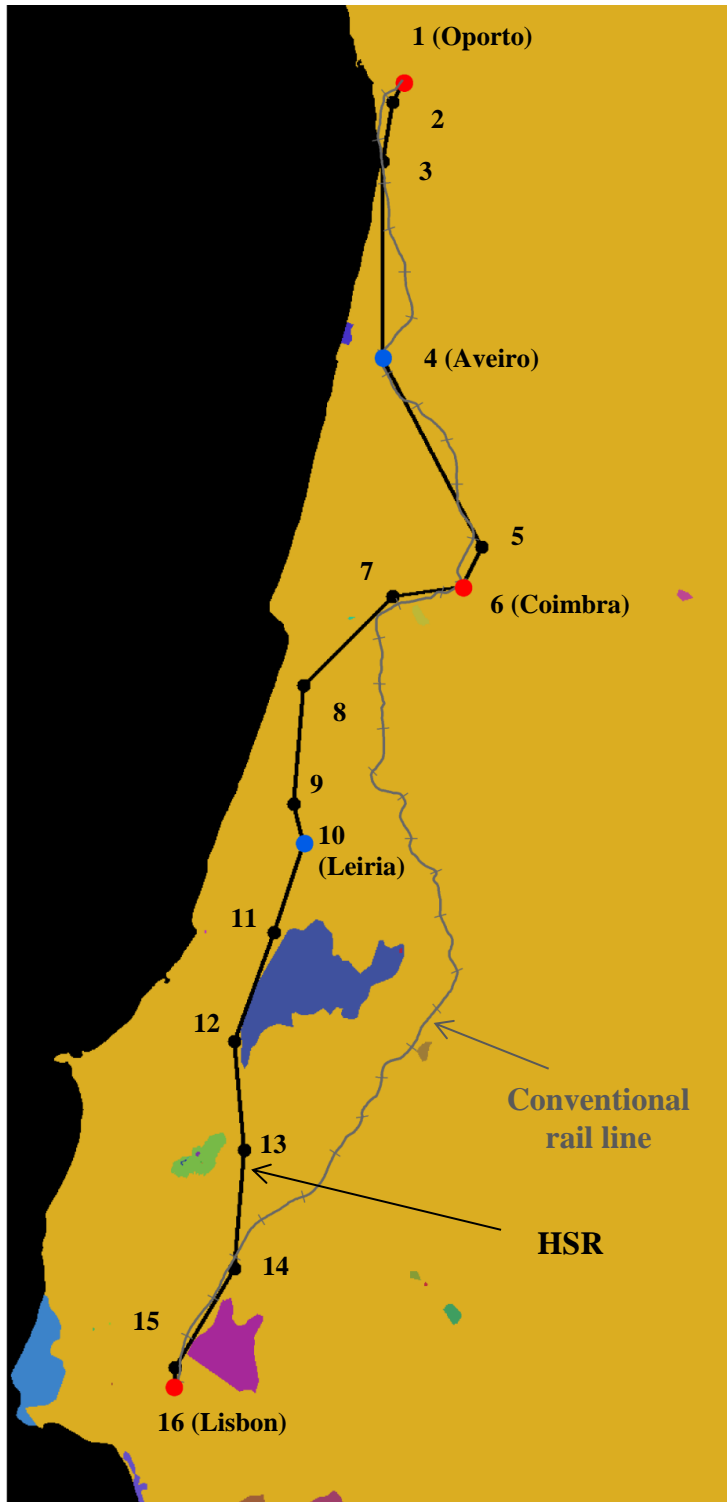


**Figure 6-18** Plan view of the best found HSR configuration and the existing conventional rail line overlaying the land-use layer.

Apart from the horizontal curvature and the connection of smaller towns, one observes that both the HSR SPC solution and the conventional rail share a common corridor between

Oporto and HSR node 7 and between node 14 and Lisbon. The deployment corridors, however, are substantially different between nodes 7 and 14.

The conventional rail does not connect Leiria and crosses to the east of Serras de Aires e Candeeiros Natural Parks (land-use index 16). Given that the connection of Leiria by the HSR leads to a benefit in the objective function, the connection of Leiria by the HSR may be the result of the benefit or, in fact, represent the most beneficial corridor for the SPC problem in terms of construction costs and geometry performance. Additional studies are performed to illustrate the possible effects of smaller benefits. These are discussed in section 6.4.

#### **6.4 THE EFFECT OF REDUCING THE LOCATION BENEFIT COEFFICIENTS**

The solution found for the SPC Lisbon-Oporto HSR planning problem crosses both Aveiro and Leiria. The two cities, if connected by the HSR, lead to an improvement of the objective function value equal to the sum of the location benefit coefficient of each city, and  $\gamma_v^{Aveiro}$  and  $\gamma_v^{Leiria}$ . Additional studies are performed considering a smaller value of the coefficients. This aims at assessing if a trade-off between smaller benefiting terms of crossing these cities and the smaller construction costs and geometry penalties can change the configuration of the HSR solution. A reduction of the coefficients to one-half of their initial value is considered.

SAA runs are performed to solve the Lisbon-Oporto HSR planning problem varying only the location benefit coefficients and maintaining all the remaining coefficients and specifics described in section 6.1. The solution found is described and compared to the initial application described in section 6.3.

For the sake of abbreviation, the solutions are herein referred to as HSR\_SPC (initial value of section 6.3) and HSR\_SPC\_1/2 (one-half reduction of the location benefit coefficient).

##### **6.4.1 CHARACTERIZATION OF THE SOLUTION**

Figure 6-19 shows the plan view comparison of both the HSR\_SPC and HSR\_SPC\_1/2.

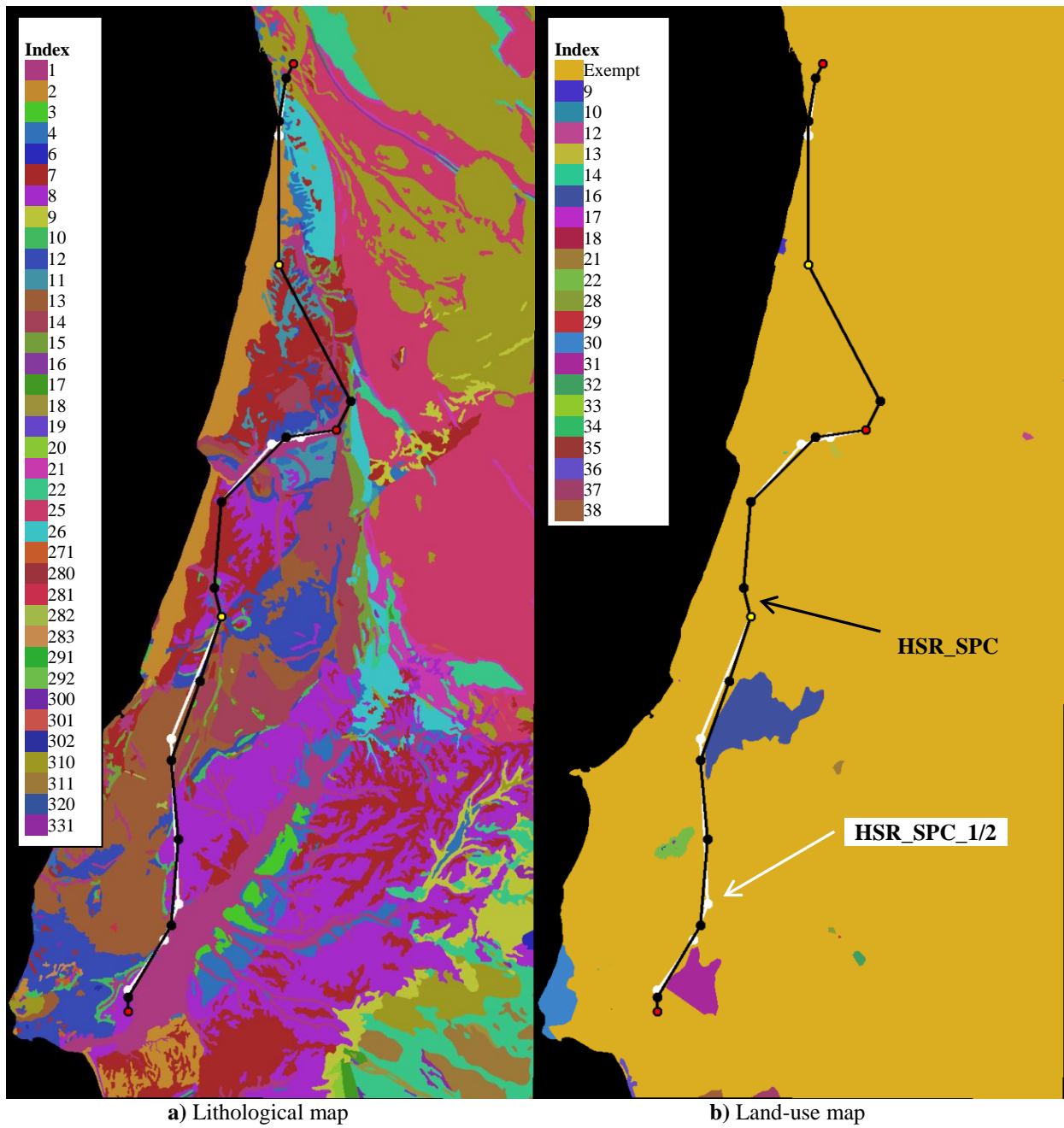


**Figure 6-19** Plan view overlay of HSR\_SPC (in black) and HSR\_SPC\_1/2 (in white): a) lithological map, b) land-use map, c) expropriation cost map, d) elevation map and e) main rivers map.

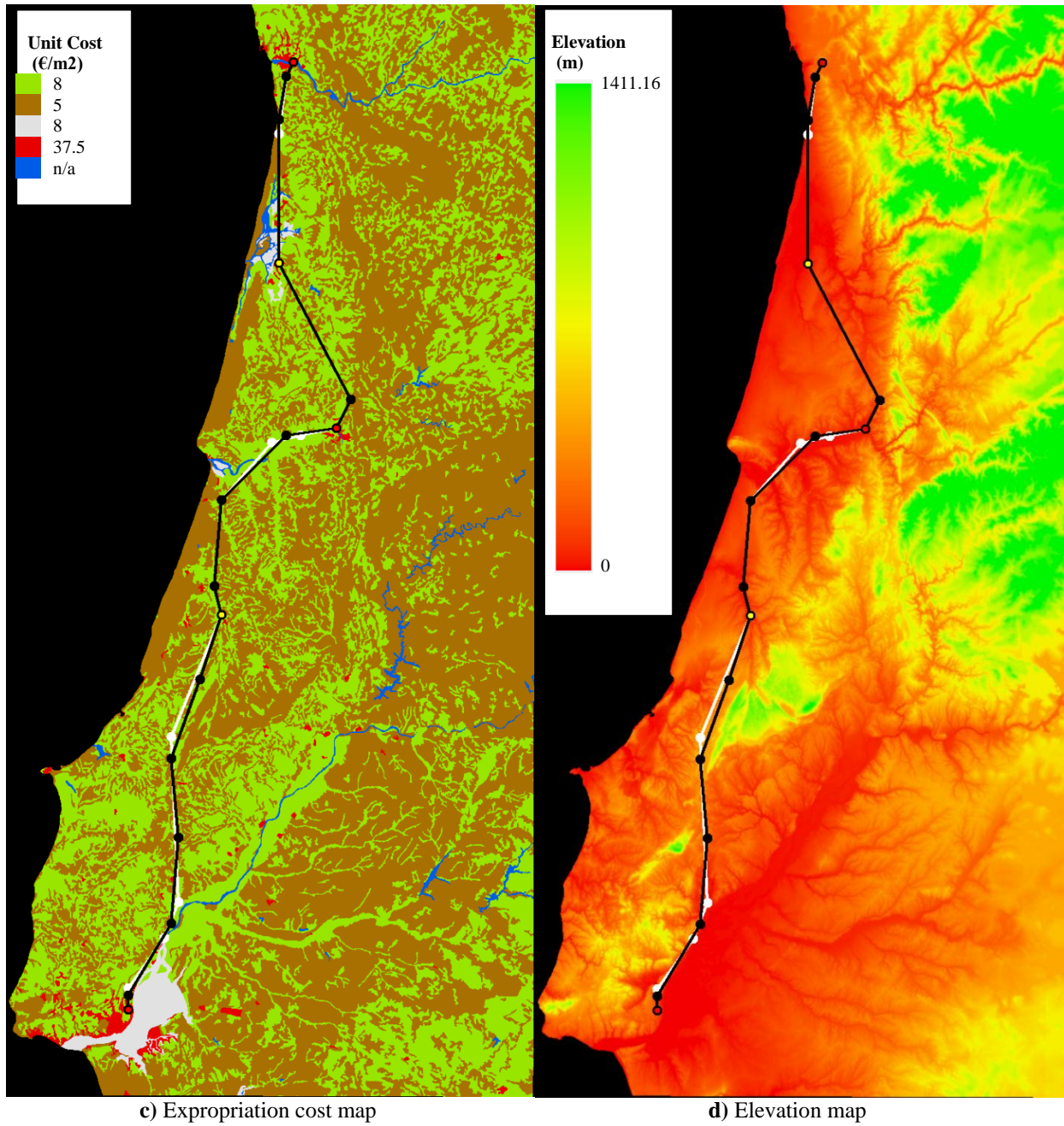
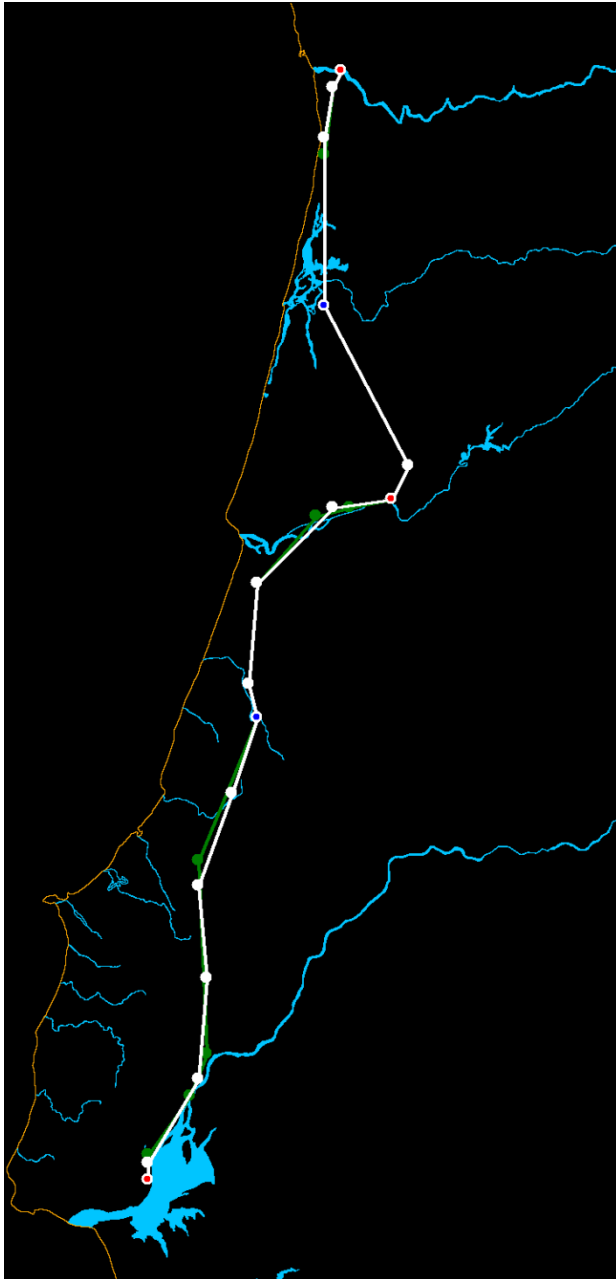


**Figure 6-19** Plan view overlay of HSR\_SPC (in black) and HSR\_SPC\_1/2 (in white): a) lithological map, b) land-use map, c) expropriation cost map, d) elevation map and e) main rivers map. (Continued).



e) Main rivers map

**Figure 6-19** Plan view overlay of HSR\_SPC (in black) and HSR\_SPC\_1/2 (in white): a) lithological map, b) land-use map, c) expropriation cost map, d) elevation map and e) main rivers map. (Continued).

From Figure 6-19 one observes that the alignment of both solutions runs in the same corridor and almost coincides between Oporto and Leiria and presents small differences between Leiria and Lisbon. The respective longitudinal profiles are presented in Figure 6-20.

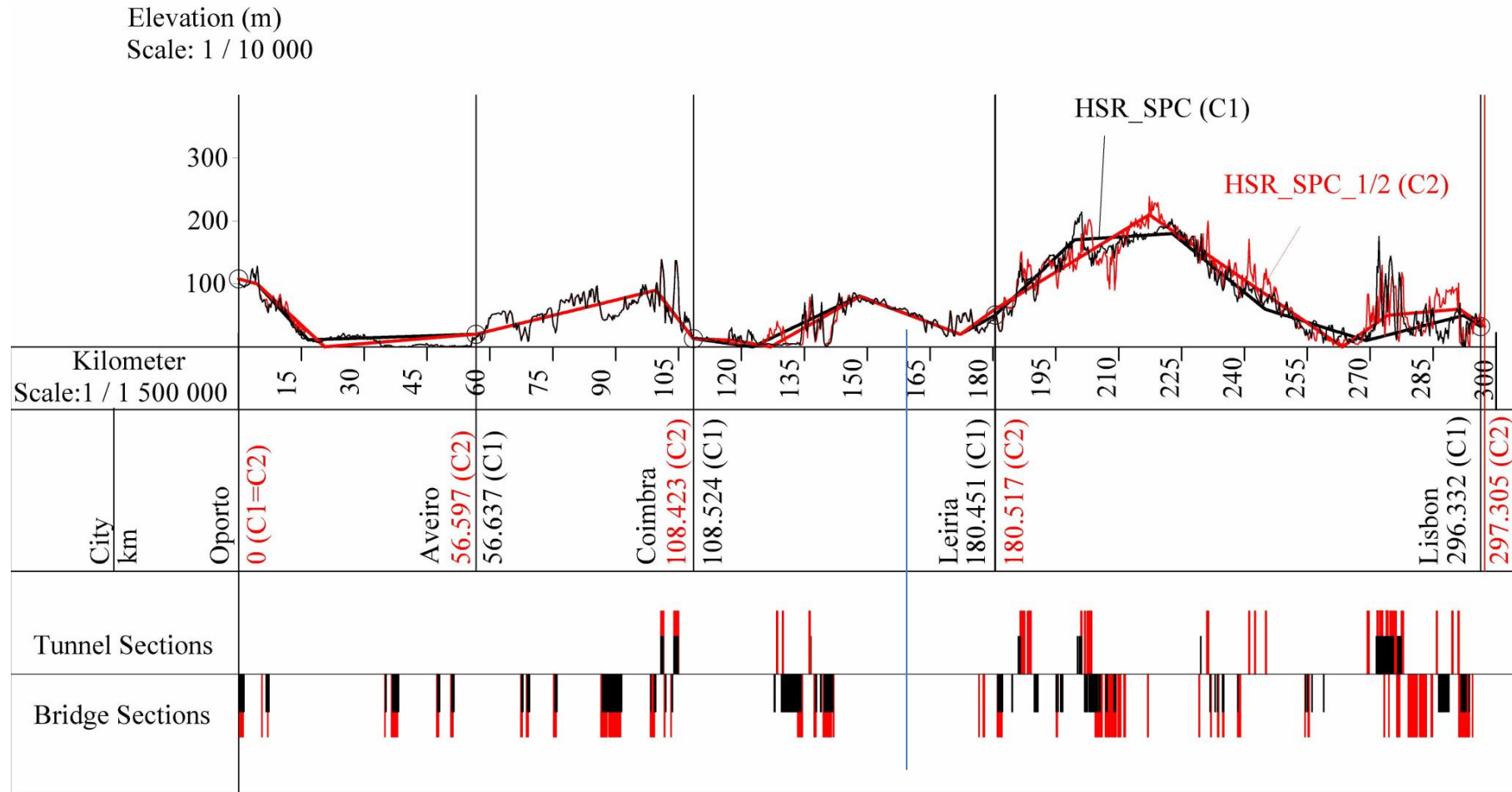


**Figure 6-20** Comparison of the longitudinal profiles of HSR\_SPC (in black) and HSR\_SPC\_1/2 (in red).



Figure 6-20 shows the longitudinal profiles almost coincide between Oporto and Coimbra. Also, the infrastructure extent built on bridges and tunnels between these two cities is almost identical in both solutions. Between Coimbra and Lisbon, however, differences exist in the longitudinal profile and the cross-sections it requires. The differences in the plan view (Figure 6-19), although small, lead to different ground elevations along the infrastructure. Thus, the longitudinal profile also changes for adjusting the elevation of the solutions and minimizing the construction of tunnels and bridges, costlier than cuts and embankments. This is achieved by decreasing the differences between the HSR and the ground elevation.

It is not expected that a random search algorithm such as the SAA can produce exactly the same HSR solutions. Its likelihood is very small as this would require the linear sections to be identical, meaning that the nodes would have to be positioned at exactly the same 3D coordinates in both solutions. When generating new candidate configurations, the nodes can be repositioned in any direction within the HSR neighborhood, as long as the configuration complies with the geometry constraints of the gradient and of the horizontal angle, the land-use constraint, the minimum clearance when crossing bodies of water and the minimum length of 4,000 m of each linear section. Furthermore, different HSR configurations can have similar objective function values, for which the convergence to the problem solution is measured. Thus, after more than 500,000 tested and randomly generated HSR configurations within the annealing runs, the likelihood that the configurations are exactly the same is small.

The attribution of a location benefit coefficient to the HSR linking Leiria plays an important role in the differences amongst the solutions. During the optimization search by the SAA the HSR configuration links Leiria within thousands of random perturbations of the HSR configurations. At the early stages of the algorithm implementation, worsening solutions are accepted with large probabilities. This allows the SAA to accept, from a current configuration that connects Leiria, a new HSR candidate configuration which does not connect Leiria, giving up the location benefit. However, as the SAA progresses and the temperature decreases, the probability of accepting worse solutions decreases. For low temperatures it is unlikely that the SAA accepts candidate configurations which do not connect Leiria from current HSR configurations which do. This means that, when low annealing temperatures are reached, it is unlikely that the HSR node positioned at Leiria, if any, changes.

One observes that the HSR\_SPC is formed by 4 linear sections between Coimbra and Leiria and by 6 linear sections between Leiria and Lisbon (Figure 6-19). Differently, the HSR\_SPC\_1/2 is formed by 5 linear sections between Coimbra and Leiria and by 5 linear sections between Leiria and Lisbon. In this sense, the HSR solutions do not have an equal plan view, resulting in different ground elevations that require different cross-section for the minimization of the construction cost, and which overlay terrain with different lithology and expropriation costs. As such, the construction costs for expropriation, earthworks, bridges and tunnels differ.

Discretizing the HSR configurations with a larger number of linear sections, and thus nodes, may compensate, at least partly, the differences amongst the HSR layout and costs. However, refining the discretization increases the degree of freedom of the problem and, as a consequence, increases the complexity to be addressed by the SAA implementation and the respective computational burden. Solving the SPC Lisbon-Oporto HSR planning problem is time consuming. The SAA running times for obtaining HSR\_SPC and HSR\_SPC\_1/2 are, respectively, 12 days and 18 days on a 3.40GHz Intel® Core™ i7-2600 CPU with 16GB RAM. Parallel programming has been implemented in the computational tool to reduce the computation time of the SAA runs. Improvements were observed but the computation is still time consuming given the sequential nature of the problem. On average, the generation of a new candidate HSR configuration and the evaluation of its objective function value take 1.71 s. However, when the mechanisms for transposing the “islands” of forbidden land-use are used (section 4.4.1), particularly for large areas such as the Serras de Aires e Candeeiros Natural Parks (land-use index 16 in Figure 6-19 b), the average time increases to 10.06 s.

The tenfold increase explains the 6 days discrepancy between the SAA running times for obtaining HSR\_SPC and HSR\_SPC\_1/2. Given the larger benefit given to the connection of Aveiro and Leiria in the application of section 6.3, the convergence is faster than for the reduced coefficient application. Given that the plan view of the solutions runs in the western vicinity of the Serras de Aires e Candeeiros Natural Parks, the slower convergence applications generates more HSR candidate configurations that employ the mechanisms for transposing the “islands” of forbidden land-use, extending the overall computation time.

In this context, a trade-off between accurateness by a refined HSR discretization and the acceptable computation time has to be considered.

The cost breakdown of both solutions is compared in Table 6-9. The construction cost is 10% larger for HSR\_SPC\_1/2, as the result of larger costs of earthworks, bridges and tunnels, smaller expropriations costs and approximately the same linear- dependent costs.

**Table 6-9** Cost breakdown of HSR\_SPC and HSR\_SPC\_1/2 and comparison of the partial costs and the objective function value of both HSR solutions.

| Solution  | Value (Million €) |               | HSR_SPC_1/2<br>/<br>HSR_SPC<br>(%) |
|---|-------------------|---------------|------------------------------------|
|   | HSR_SPC_1/2       | HSR_SPC       |                                    |
| <b>SPC Objective Function Value (1 + 2 + 3 - 4)</b> | <b>1,398.52</b>   | <b>786.96</b> | <b>178%</b>                        |
| 1. CONSTRUCTION COST<br>(1.1+1.2+1.3+1.4+1.5)       | 1,825.74          | 1,658.50      | <b>110%</b>                        |
| 1.1 Expropriation                                   | 151.17            | 154.94        | 98%                                |
| 1.2 Earthworks                                      | 492.35            | 454.52        | 108%                               |
| 1.3 ALL BRIDGES                                     | 517.25            | 429.98        | 120%                               |
| 1.4 ALL TUNNELS                                     | 320.11            | 275.31        | 116%                               |
| 1.5. LINEAR- DEPENDENT COSTS                        | 344.87            | 343.75        | 100%                               |
| 2. GEOMETRY PENALTY                                 | 120.50            | 123.56        | 98%                                |
| 3. LAND-USE PENALTY                                 | 0.00              | 0.00          |                                    |
| 4. LOCATION BENEFIT                                 | 547.72            | 995.10        | <b>55%</b>                         |

The geometry penalty of HSR\_SPC\_1/2 is also smaller as the solution improves the geometry layout to values closer to the normal ones. Table 6-10 shows that the 2 angles of HSR\_SPC\_1/2 smaller than  $\beta_{\text{normal}}=140^\circ$ , at nodes 5 and 6 (Coimbra), are larger than angles the observed for HSR\_SPC (Table 6-7). Given that the two HSR configurations both cross Aveiro and Leiria, the location benefit of HSR\_SPC\_1/2 is circa half of that benefitting the HSR\_SPC (Table 6-9), as expected. The 5% difference is explained by the indexation to the construction cost.

**Table 6-10** Geometry of the configuration HSR\_SPC\_1/2.

| <b>Node</b> | <b>(x;y;z)</b><br><b>(km;km;m)</b> | <b>City</b> | <b><math>\eta</math></b><br><b>(‰)</b> | <b><math>\beta</math></b><br><b>(°)</b> |
|-------------|------------------------------------|-------------|--|---|
| 1           | (80;16;108.152)                    | Oporto      | -2                                     |   |
| 2           | (78;20;100)                        |             | -6                                     | 161                                     |
| 3           | (76;36;0)                          |             | 1                                      | 173                                     |
| 4           | (76;72;20)                         | Aveiro      | 2                                      | 152                                     |
| 5           | (96;110;90)                        |             | -9                                     | 126                                     |
| 6           | (92;118;13.106)                    | Coimbra     | 0                                      | 128                                     |
| 7           | (82;120;10)                        |             | -1                                     | 177                                     |
| 8           | (74;122;0)                         |             | 4                                      | 145                                     |
| 9           | (60;138;80)                        |             | -2                                     | 144                                     |
| 10          | (58;162;20)                        |             | 5                                      | 161                                     |
| 11          | (60;170;60)                        | Leiria      | 4                                      | 144                                     |
| 12          | (46;204;210)                       |             | -5                                     | 155                                     |
| 13          | (48;250;0)                         |             | 5                                      | 156                                     |
| 14          | (44;260;50)                        |             | 1                                      | 166                                     |
| 15          | (34;274;60)                        |             | -5                                     | 145                                     |
| 16          | (34;280;32.348)                    | Lisbon      |  |   |

The cost breakdown of Table 6-9 compares the overall differences in the construction cost items. Figure 6-21 and Figure 6-22 analyze how the cost differences evolve along the longitudinal profile. Vertical dashed lines are positioned at four of the most pronounced increases in the total construction costs, for the same km as the vertical lines in Figure 6-17.

Accumulated Partial Costs  
(Million €)

Accumulated Total  
Construction Cost  
(Million €)

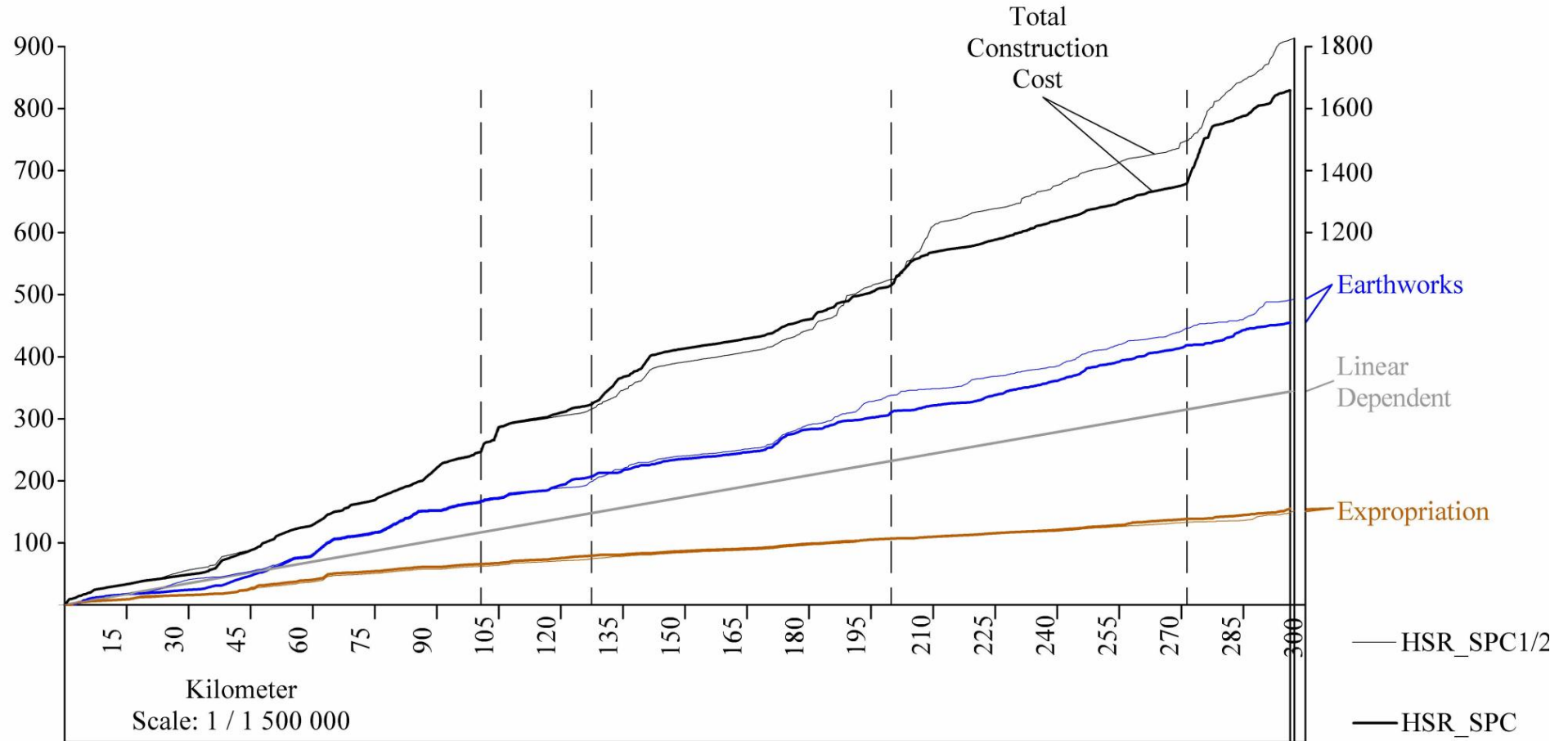


**Figure 6-21** Accumulated costs along the longitudinal profile: total construction costs, earthworks, linear- dependent and expropriation. Costs for HSR\_SPC represented in a thick line and for HSR\_SPC\_1/2 in a thin line.

Accumulated Partial Costs  
(Million €)

Accumulated Total  
Construction Cost  
(Million €)

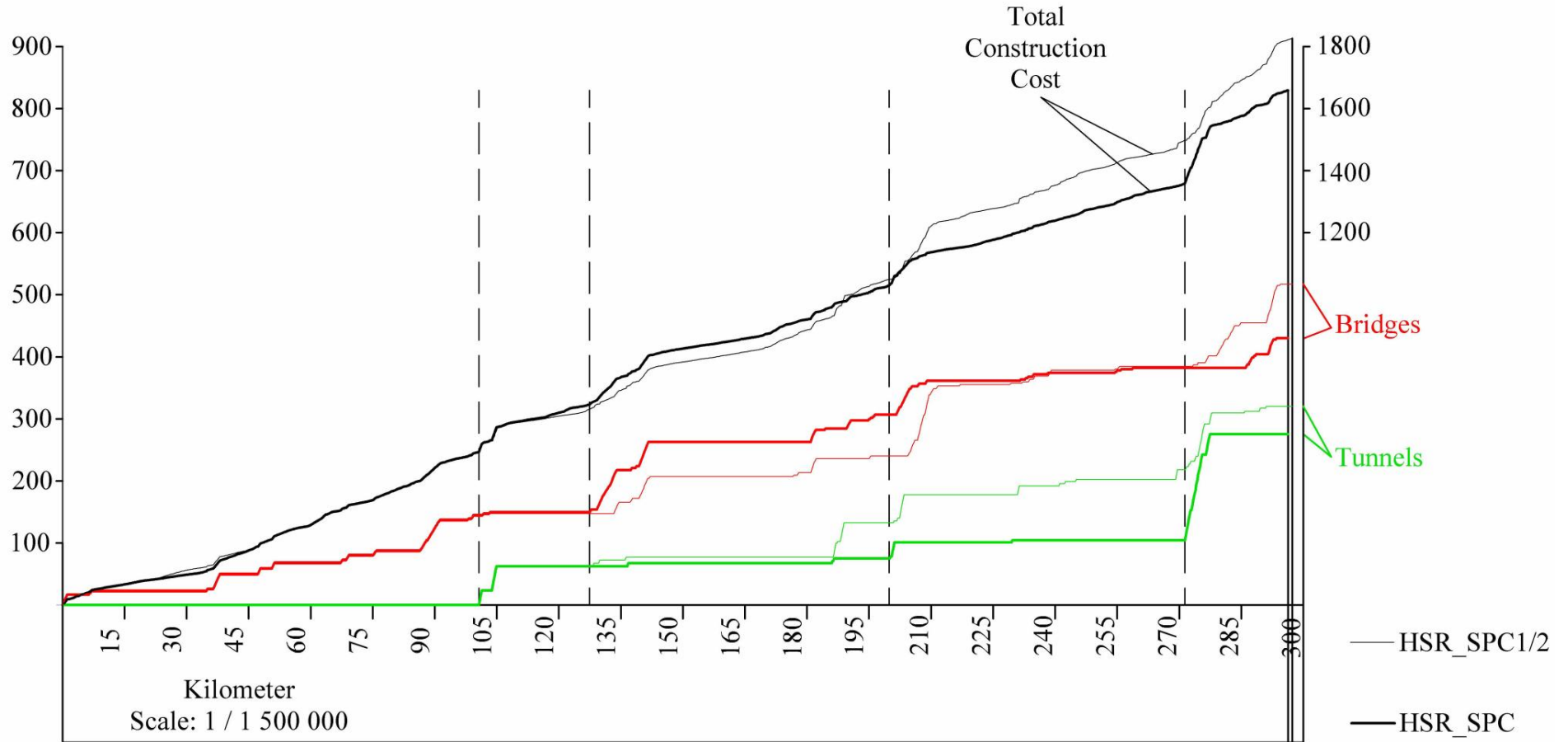


**Figure 6-22** Accumulated costs along the longitudinal profile: total construction costs, bridges and tunnels. Costs for HSR\_SPC represented in a thick line and for HSR\_SPC\_1/2 in a thin line.

Figure 6-21 shows the variation of the total construction costs and the evolution of expropriation, earthworks and linear-dependent costs of both solutions. One observes the total construction cost of both HSR configurations is identical from Oporto (km 0) to km 120, node 7 of the HSR\_SPC. As discussed, the plan view and longitudinal profiles are very similar resulting in almost identical HSR extent built on bridges, tunnels and earthworks. Between km 120 and km 190 the accumulated cost of HSR\_SPC is larger than that of HSR\_SPC\_1/2, mostly due to a larger extent of bridge construction (Figure 6-20, Figure 6-22). Between km 190 and km 200 the total accumulated construction costs equalize and from km 200 until Lisbon the HSR\_SPC\_1/2 has a larger cost increase that results in a larger overall construction cost. Figure 6-21 and Figure 6-22 show that the main construction cost items influencing the total cost differences are bridges, tunnels and earthworks.

Linear-dependent costs (Figure 6-21) differ only due to the different length of the solutions, as expected. Expropriation costs are also almost identical along the profile (Figure 6-21): the HSR\_SPC\_1/2 slightly improves this cost item around km 270. Of the cost items represented in Figure 6-21, earthworks have the largest variation among the solutions. The cost of earthworks is equivalent from Oporto until km 180 (Leiria). Between km 180 and km 200 the earthworks cost increase is larger in HSR\_SPC\_1/2 and the cost difference then continues until the end of the HSR: the lines representing the earthworks accumulated costs become again roughly parallel.

The costs of both bridges and tunnels (Figure 6-22) are identical in both HSR configurations from Oporto until km 130 (second dashed line). At this point in the longitudinal profile, the bridge cost increase is larger in HSR\_SPC, then equalized by a sharper increase in HSR\_SPC\_1/2 between km 190 and 210. The bridge cost remains identical until km 270 and, close to Lisbon, a larger increase of the bridge costs of HSR\_SPC\_1/2 results in a larger overall bridge cost. The tunnels cost is similar from Oporto until km 190 where HSR\_SPC\_1/2 has a larger cost increase. The difference is maintained until km 270. At this point, more tunnels are built in HSR\_SPC, reducing the difference but still resulting in a smaller overall tunnel cost than that of HSR\_SPC\_1/2.

One observes the main cost increase differences occur between km 130 (second dashed line) and km 145, between km 190 and km 210 and between km 270 and Lisbon. These sections correspond to the HSR\_SPC's linear sections linking nodes 7 and 8, Leiria and node 12 and

linking node 14 and Lisbon. Figure 6-19 shows these are the sections in which the horizontal alignment of the HSR solutions differ the most. As discussed in the analysis of Figure 6-20, the different ground elevation leads to a different longitudinal profile, affecting the elevation of the solutions to minimize the construction of tunnels and bridges, which also result in different overall costs. Figure 6-22 also shows how different combinations of the partial construction costs can result in the same accumulated cost, observed at km 200. Between Oporto and km 200, HSR\_SPC\_1/2 has a smaller cost of bridges, a larger cost of tunnels and earthworks and identical expropriation and linear- dependent costs, but results in an accumulated construction cost equal to its HSR\_SPC counterpart.

From a HSR planning point of view, both solutions suggest the same best corridor to be studied in the subsequent detailed stages of the project. The fact that a coarse discretization is sufficient for solving the initial planning problem implies that there is a broad range of options in terms of cross-sections that can fulfill the specified requirements. However, both solutions indicate that the most beneficial HSR configuration, according to the SPC model proposed in this research, crosses both Aveiro and Leiria.

## **6.5 REMARKS ON THE SPC APPLICATION**

The HSR planning optimization model proposed for SPC in section 4.1 has been applied to the Lisbon-Oporto case-study presented in section 5. The model application is discussed in section 6.1. The SAA was implemented for solving the Lisbon-Oporto HSR planning problem (section 6.2).

The capabilities of the model to represent the HSR network and of the SAA to solve the problem in a fully-integrated 3D optimization approach, including the design requirements and the best practice design parameters, are presented. The HSR solution HSR\_SPC found by the SAA (section 6.3.1) minimizes the geometry penalties by adopting gradients smaller than the normal gradient and horizontal angles larger than the normal one. Exceptions are made for the horizontal angles at Coimbra and node 7. At these locations, the solution trades off worse geometry for the benefit of connecting Aveiro and for smaller construction costs.

The results (section 6.3.1) also show the model ability to represent the location dependent factors such as lithology, elevation, expropriation costs, land-use and existent bodies of water



that condition the cross-sections of the HSR and influence the costs of the project. The 3D HSR configuration adjusts simultaneously the plan view, for crossing corridors with smoother ground elevation and expropriation costs, and the longitudinal profile, for minimizing bridges and tunnels.

The application reveals that the existent “islands” of forbidden land-use are successfully transposed by the procedures for generating new candidate HSR configurations (section 4.4.1). This allows the SAA to comprehensively canvass search space of the problem instead of performing a search confined to a partial area but significantly increases the running time of the SAA. Node clusters such as those discussed in section 4.4.2 are also successfully avoided by the implementation of the linear sections minimum length. Furthermore, these capabilities are demonstrated for real world data, showing the applicability to large and complex problems.

The output of the computational tool developed to implement the SAA and solve the HSR planning problem allows a comprehensive analysis of the HSR features in terms of plan view, longitudinal profiles and cost breakdown. It cannot be proven that the best HSR found by the SAA is the global optimum. This is a limitation of approximate optimization methods, such as the SAA, but required for solving NP-hard problems for which exact methods cannot provide a solution within a polynomial-bounded time (section 3.2). However, the characterization of the HSR solution and its analysis in terms of layout and costs show the SAA performs well in minimizing the objective function (4.1). A comparison (section 6.3.2) shows the construction cost of the solution is consistent with the lower bounds of French HSR lines in service and of Spanish HSR lines, both in service and under construction.

The comparison between the HSR solution and the existing conventional rail line (section 6.3.3) shows both rail lines run in the same corridor, except in the area of Leiria, connected by the HSR solution but not by the conventional rail Line of the North. Studies are performed in section 6.4 to evaluate the influence of the location benefit coefficient of Aveiro and Leiria in the HSR configuration.

Solving the SPC Lisbon-Oporto HSR planning problem with a one-half reduction of the location benefit coefficients (section 6.4.1) results in a HSR configuration, HSR\_SPC\_1/2, similar to the one obtained in section 6.3, HSR\_SPC. From a planning perspective, these solutions suggest the same layout for the subsequent detailed stages of the project. The

differences in the layout of both solutions are small. It is possible that a larger number of linear sections discretizing the HSR could reduce these differences. This, however, would increase the size of the problem to be solved by the SAA and the additional complexity increases the already large computation time. Trade-offs between the refinement of the HSR discretization and the computation effort can be made.

The sound results obtained for the SPC planning problem establish the basis for the consideration of natural hazards as the robust model builds on the SPC model considering a scenario-description of the effects of natural hazards.

## Chapter 7.

# Solving the Lisbon-Oporto HSR Planning Problem: Robust Approach

In this chapter, the HSR planning robust optimization model proposed in section 4.5 is applied to the Lisbon-Oporto case-study (section 5). The model is then solved with the implementation of the Simulated Annealing Algorithm (SAA), according to the principles presented in section 4.2, and the results are discussed.

The robust approach proposed in section 4.5 builds on the deterministic approach for SPC (section 4.1), which is extended with the incorporation of scenario descriptions of the uncertain natural hazards. Three scenarios have been proposed for the Lisbon-Oporto case-study area: a seismic scenario for a nearby intraplate earthquake (section 5.4), a seismic scenario for a distant interplate earthquake (section 5.4) and an intense rainfall scenario (section 5.5).

The aim of solving the robust approach applied to the Lisbon-Oporto HSR planning problem is to find HSR configurations that are not overly sensitive to the effects of the natural hazards. Earthquakes and severe rainfall have the capability to disrupt the HSR infrastructure (section 2.4.1) but decisions can be made at the planning stage that reduce the exposure, such as the corridors to cross, and that reduce the vulnerability, such as the cross-sections to adopt. Improving the HSR performance in case of a hazard can be made at a larger capital cost, but not necessarily so in all cases. The robust model (section 4.5) includes these tradeoffs between capital costs, the configuration layout and the performance for the natural hazards, according to the objective function formulation in expression (4.10).

This section solves the robust approach for the Lisbon-Oporto HSR planning problem for the same input data of the SPC application of section 6: the input spatial data in section 5.1, the HSR configuration geometry layout of section 5.2 and the cross-sections and construction costs of section 5.3. Except for the consideration of the natural hazards and the location benefit coefficients, all case-study definitions remain unchanged from the SPC application of section 6.

## 7.1 APPLICATION OF THE ROBUST MODEL TO THE LISBON-OPORTO HSR

The robust objective function in expression (4.10) corresponds to the sum of the HSR construction costs, the penalty terms for horizontal angle, gradient and land-use, the location benefit term and the HSR weighted performance for the scenarios set,  $\sum_{c \in \Omega_{sc}} \Psi_c \sum_{(i,j) \in \Omega_N} RC_{ij}^c$ , the latter multiplied by  $\omega$ . Analogously to the robust model of expressions (3.18) to (3.21) by Mulvey et al. (1995), the weight  $\omega$  is used to establish a spectrum of configurations that trade-off the HSR performance for natural hazards with the HSR performance in SPC. Large values of  $\omega$  increase the importance that the natural hazards performance has in the robust objective function, when compared with the SPC, and can be used to obtain solutions less affected by these extreme events. The larger the value of  $\omega$ , the less affected by the natural hazards the solutions are expected to be, always subject to the compliance with the problem constraints.

The model accounts for the direct market losses pertaining to the physical damage repair and/or replacement of damaged HSR sections in the performance and impact assessment for natural hazards. The weighted performance for the set of scenarios,  $\sum_{c \in \Omega_{sc}} \Psi_c \sum_{(i,j) \in \Omega_N} RC_{ij}^c$ , represents the weighted repair/reconstruction costs of the HSR infrastructure. This requires the definition of each weight  $\Psi_c$  attributed to each scenario  $c$  in  $\Omega_{sc}$ . The sum of the weights of all scenarios is equal to one, according to expression (4.11), establishing a relative importance amongst the effects of the scenarios. In fact, each combination of weights  $\Psi_c$  represents a particular relative importance given by the decision-maker to the HSR performance across the different scenarios. However, the decision-maker's risk aversion towards the effects of specific natural hazards includes subjective considerations. Thus, in addition to the input presented in sections 5.1, 5.2 and 5.3 and the penalty- and benefit-coefficients considered by the objective function in expression (4.10), combinations of

weights  $\Psi_c$  need to be defined for applying the robust approach to the Lisbon-Oporto HSR planning problem.

Three scenarios form the set of scenarios  $\Omega_{SC}$  considered: a seismic scenario for a nearby intraplate earthquake (section 5.4), a seismic scenario for a distant interplate earthquake (section 5.4) and an intense rainfall scenario (section 5.5). The three scenarios have distinct return periods: 100 years for the rainfall scenario, 68 years for the near intraplate earthquake and 1750 years for the distant interplate earthquake. In fact, the distant interplate earthquake has a larger return period, of a different order of magnitude, which translates to a much smaller probability of occurrence within the infrastructure lifetime but with a potential for extensive impacts. Given that planning for the worst-case scenario is not economically viable, compromises need to be made. The decision-maker's attitude towards the risks of each scenario can vary and, to reproduce this behavior, two combinations of weights  $\Psi_c$  are considered in the application. Combination #1 considers an equal importance amongst the effects of the scenarios, despite their differing probabilities of occurrence. Combination #2 considers an uneven attribution of the weights  $\Psi_c$ , qualitatively reflecting the different probabilities of occurrence.

Analogously to the SPC applications of Chapter 6, a fully integrated 3D approach to the optimization problem is considered. However, given the difficulties of graphically representing the 3D layout of the configuration, the discussion of the resulting solutions is supported by plan views and longitudinal profiles that fully characterize the 3D layout of the HSR configurations.

### 7.1.1 GEOMETRY PENALTIES: HORIZONTAL ANGLE AND GRADIENT

The geometry penalties are defined by expression (4.8) for the gradient and by expression (4.9) for the horizontal angle. These require the definition of the geometry normal values,  $\eta_{normal}$  and  $\beta_{normal}$ , the geometry limit values,  $\eta_{limit}$  and  $\beta_{limit}$ , and the penalty coefficients  $\gamma_\eta$  and  $\gamma_\beta$ . The values adopted in the robust approach (Table 7-1) remain unchanged from the SPC application.

**Table 7-1** Geometry parameters for the robust approach application.

| Geometry parameter | Limit value               | Normal value               | Penalty cost coefficient                        |
|--------------------|---------------------------|----------------------------|---|
| Horizontal angle   | $\beta_{limit}=120^\circ$ | $\beta_{normal}=140^\circ$ | $\gamma_\beta=5\%\sum_{(i,j)\in\Omega_N}C_{ij}$ |
| Gradient           | $\eta_{limit}=35\%$       | $\eta_{normal}=20\%$       | $\gamma_\eta=5\%\sum_{(i,j)\in\Omega_N}C_{ij}$  |

### 7.1.2 LAND-USE PENALTY

As discussed in section 6.1.2, the Lisbon-Oporto case-study does not include land-use restricted areas. Thus, the land-use penalty coefficient  $\gamma_{\lambda_s}$  is null for any space property element  $s \in \Omega_E$ , which results in a null land-use penalty term in expression (4.10), for any linear section composing the HSR.

### 7.1.3 LOCATION BENEFIT

Illustrating the potential effects of taking into account concerns such as accessibility, speed reductions or political considerations in connecting intermediate cities, the case-study defines location benefit coefficients for Aveiro and Leiria. If connected by the HSR, a benefit term is subtracted from the objective function in expression (4.10). Only the plan view location needs to be connected by the HSR for the benefitting term to be applied, as elevated or underground stations are eligible. Analogously to the SPC application, half of the coefficients value,  $\gamma_v^{Aveiro}$  and  $\gamma_v^{Leiria}$ , are considered if the plan views of adjacent nodes are connected, illustrating different possible station locations, within the city, with different overall value added to the HSR network (section 6.1.3). For application purposes, the location benefit coefficients are indexed to the construction cost (Table 7-2), as discussed in section 4.1.1. Two types of applications are considered in this chapter varying the location benefit coefficient ( $\gamma$  and  $\gamma/3$ ).

**Table 7-2** Location and location benefit coefficients for Aveiro and Leiria.

| City   | Location (x;y;z)<br>(km;km;m) | Application considering<br>$\gamma$                     | Application considering<br>$\gamma/3$                  |
|--------|-------------------------------|---|--|
| Aveiro | (76;72;14.268)                | $\gamma_v^{Aveiro} = 15\%\sum_{(i,j)\in\Omega_N}C_{ij}$ | $\gamma_v^{Aveiro} = 5\%\sum_{(i,j)\in\Omega_N}C_{ij}$ |
| Leiria | (60;170;61.236)               | $\gamma_v^{Leiria} = 15\%\sum_{(i,j)\in\Omega_N}C_{ij}$ | $\gamma_v^{Leiria} = 5\%\sum_{(i,j)\in\Omega_N}C_{ij}$ |

The SPC Lisbon-Oporto HSR applications of section 6.1.3, obtaining the HSR\_SPC solution, and of section 6.4, obtaining the HSR\_SPC\_1/2, both suggest linking Aveiro and Leiria and are considered equivalent from a planning perspective (section 6.4.1). Thus, in order to establish comparative analyses for assessing the effects of natural hazards in the planning process, the smallest objective function value configuration, HSR\_SPC, is considered. The analyses assess how the HSR\_SPC solution performs if the occurrence of natural hazards is taken into account. The repair/reconstruction costs of the physical damages that the HSR\_SPC would have for each scenario is computed, which allows one to assess the objective function value from a robust point of view. This is compared with the solutions obtained by solving the robust model in order to assess how the consideration of natural hazards influences the characteristics of the HSR configurations.

#### 7.1.4 LOCATION CONSTRAINTS

The location constraints of the robust approach are identical to those considered in the SPC application (section 6.1.4). Table 7-3 defines the location of Oporto, Coimbra and Lisbon that constitute the set of all mandatory nodes  $\Omega_{MN}$  to be connected by the HSR configuration according to the coordinate system of Figure 5-3.

**Table 7-3** Definition of the location constraints for the robust approach application.

| City    | Location (x;y;z)<br>(km;km;m) |
|---------|-------------------------------|
| Oporto  | (80;16;108.152)               |
| Coimbra | (92;118;13.106)               |
| Lisbon  | (34;280;32.348)               |

#### 7.1.5 GEOMETRY CONSTRAINTS

Both the geometry constraints for the gradient and for the horizontal angle are identical to those considered in the SPC application (section 6.1.5). These impose the limit values (section 4.1.2.2) for the gradient and horizontal angles at intermediate nodes. The values are defined in section 5.2 and ensure that:

- the gradient of any linear section  $\eta_{(i,j)}$  composing the HSR configuration, either rising or falling, is smaller than  $\eta_{limit}=35\%$ ;

- the horizontal angle at any intermediate node of the HSR configuration  $\beta_{(i,j,k)}$ , the smaller angle between the linear sections and ranging from  $0^\circ$  to  $180^\circ$ , is larger than the limit value  $\beta_{limit}=120^\circ$ .

#### 7.1.6 LAND-USE CONSTRAINT

The land-use constraint ensures that the protected areas identified in Figure 5-5 are not overlaid by the HSR linear sections. Identically to the SPC application (section 6.1.6), the construction of the HSR network is forbidden within all the protected areas, corresponding to all the space property elements of indices 9 through 38 of Table 5-2. These space property elements constitute the set  $\Omega_{FE}$  of the forbidden land-use elements.

#### 7.1.7 SCENARIO-WEIGHT ( $\Psi_c$ ) COMBINATIONS

To analyze the effects of the natural hazards in planning for the Lisbon-Oporto HSR, the objective function of the robust optimization model (section 4.5.1) includes a term assessing the HSR weighted scenario performance for the 3 scenarios forming the set  $\Omega_{SC}$  (sections 5.4 and 5.5).

Two combinations of weights  $\Psi_c$  are studied, reflecting two different attitudes towards the effects of the natural hazards. Combination #1 considers uniform weight values,  $\Psi_c = 1/3$ , for all 3 scenarios constituting the set  $\Omega_{SC}$ . This considers an equal importance amongst the effects of the natural hazards one aims at minimizing. Combination #2 considers different weights for all 3 scenarios, reflecting a larger aversion to the effects of natural hazards which have a larger probability of occurrence. Table 7-4 identifies the return periods of the scenarios and the two weight combinations considered in the analyses.

**Table 7-4** Return period and the scenario-weight  $\Psi_c$  combinations.

| Scenario                                  | Seismic Scenario 1-<br>Nearby Intraplate<br>Earthquake<br>(section 5.4) | Seismic Scenario 2- Distant<br>Interplate Earthquake<br>(section 5.4) | Intense Rainfall<br>Scenario<br>(section 5.5) |
|---|---|---|---|
| <b>Return Period</b>                      | 68 years  | 1750 years  | 100 years                                     |
| <b><math>\Psi_c</math> Combination #1</b> | 33.3(3) %   | 33.3(3) %   | 33.3(3) %                                     |
| <b><math>\Psi_c</math> Combination #2</b> | 50%   | 10%   | 40%   |



### 7.1.8 THE ROUBUST APPLICATIONS PERFORMED FOR COMPARATIVE ANALYSES

Comparative analyses are established by solving applications of the robust approach to the Lisbon-Oporto HSR planning problem varying: (i) the scenario-weight combination, (ii) the location benefit coefficients and (iii) the weight  $\omega$  multiplying, in the robust objective function of expression (4.10), the HSR weighted performance for the scenarios set,  $\sum_{c \in \Omega_{sc}} \Psi_c$   $\sum_{(i,j) \in \Omega_N} RC_{ij}^c$ .

Varying the scenario-weight combination aims at assessing the influence of different relative importance attributed to the effects of the natural hazards by the decision-maker. Considering different location benefit coefficients aims at analyzing the potential effects of varying the valuation attributed to the connection of the intermediate cities. Different weights  $\omega$  can be used to establish a spectrum of configurations that trade-off the HSR performance for natural hazards with the HSR performance in the SPC. Considering large values of  $\omega$  allow one to search for optimal or near-optimal HSR configurations that give preference to the natural hazards performance compared to the SPC performance (construction costs and configuration layout). The larger the value of  $\omega$ , the less affected by the natural hazards the solutions are expected to be, always subject to the compliance with the problem constraints (section 4.5.1).

To compare the isolated effects of each variation of the scenario-weight combination, location benefit coefficients and  $\omega$ , applications of the robust approach are performed according to Table 7-5. The larger value of  $\omega=30$  is academically defined for the purpose of illustrating the influence that a sufficiently large importance attributed to the overall natural hazards performance has on the robust solutions.

For each variation of the scenario-weight combination, location benefit coefficients and  $\omega$ , two applications can be identified in Table 7-5 that differ only by the respective parameter and consider all the remainder specifics equal. In section 7.3.2, an application for the location benefit  $\gamma/3$ , the scenario weight combination#1 and  $\omega = 1$  is performed. This solution is compared with the solution of 7.3.1 that considers the location benefit  $\gamma$  but equal scenario weight combination#1 and  $\omega = 1$ . Comparing both solutions allows one to assess the effects of reducing the location benefit coefficient. Analogously, the comparison of: (i) the solutions of sections 7.3.3 and 7.3.2 isolates the effects of increasing  $\omega$  and (ii) the solutions of sections 7.4.1 and 7.3.2 isolates the effects of varying the scenario-weight combination.

The solution obtained in section 7.3.1, considering the location benefit  $\gamma$ , the scenario weight combination #1 and  $\omega = 1$ , can also be compared with the HSR\_SPC solution as the location benefit is the same but the robust solution in 7.3.1 is optimized with the consideration of natural hazards. This highlights the result of taking into account the effects of natural hazards in the HSR planning compared to the solutions optimized for the SPC.

**Table 7-5** The robust applications performed for comparative analyses.

|   |            | $\Psi_c$ Combination #1 |               | $\Psi_c$ Combination #2 |
|---|------------|-------------------------|---------------|-------------------------|
|   |            | $\omega = 1$            | $\omega = 30$ | $\omega = 1$            |
| <b>Location Benefit</b>                   | $\gamma$   | section 7.3.1           |               |                         |
| <b>Coefficient</b>                        |            |                         |               |                         |
| $(\gamma_v^{Aveiro} = \gamma_v^{Leiria})$ | $\gamma/3$ | section 7.3.2           | section 7.3.3 | section 7.4.1           |

## 7.2 IMPLEMENTATION OF THE SIMULATED ANNEALING ALGORITHM

The SAA is implemented for solving the robust approach of the Lisbon-Oporto HSR planning problem, based on the implementation of section 6.2 to solve the SPC approach. It has been discussed (sections 4.2 and 6.2) that the SAA implementation requires the definition of:

- an initial feasible HSR configuration;
- the procedures for generating candidate HSR configurations;
- the cooling schedule;

Both the initial feasible HSR configuration and the procedures for generating new HSR candidate configurations remain unchanged from the SAA implementation of section 6.2. The problem constraints of both the robust and SPC approaches are the same. Thus, the initial HSR configuration remains feasible. Also, the procedures for generating new candidate HSR configurations produce sound results for the SPC application. These proved capable of transposing the “islands” of forbidden land-use, constituting the land-use constraint, and capable of comprehensively canvassing the problem search space. In addition, the results of chapter 6 show evidence of the capability of avoiding the formation of node clusters (section

4.4.2), as no such clusters are present in any of the HSR solutions obtained for the SPC approach.

Similarly to the SAA implementation for solving the SPC approach (section 6.2.3), an adaptive geometric cooling schedule (section 4.2.2) is also considered for solving the robust approach. The adaptive cooling schedule allows the SAA to spend more time at the intermediate temperature stages (between very high and very low temperatures) which is discussed by Johnson et al. (1989) to improve the quality of the solutions. However, given the additional consideration of the HSR performance for natural hazards, a larger complexity needs to be addressed by the SAA for solving the robust approach than for solving the SPC problem.

The adaptive cooling schedule implemented for solving the SPC planning problem, was initially implemented for solving the robust approach considered the following (section 6.2.3):

- the elasticity of acceptance  $a = 0.9$ ;
- the temperature decrease rate  $r = 0.8$ ;
- the minimum number of accepted configurations at each temperature  $n_1 = 5000$ ;
- the stopping criterion  $n_2 = 10$ ;

However, the initial SAA implementation with this cooling schedule parameter set for solving the robust approach resulted in sub-optimal solutions with a considerable variation of the solution's quality. Four SAA implementations were run, each with a different random seed number, considering the same location benefit coefficients of  $\gamma$  for both Aveiro and Leiria, the same  $\omega=1$  and the same combination #1 of the scenario-weighted performance. The results showed an average objective function value 5 times larger than the best HSR configuration found by the SAA. Thus, adjustments were made to the cooling schedule for improving the SAA performance in solving the robust approach.

In order to increase the time spent by the algorithm at the intermediate temperature stages, the minimum number of accepted configurations at each temperature was increased from  $n_1 = 5000$  for solving the SPC approach to  $n_1 = 6000$  for the robust approach. Two SAA runs were

performed for solving the robust approach. However, in both cases, it was observed that 10 consecutive temperature decreases without improvement of either the optimum or the average cost occurred within the first 12 temperature steps. This led to premature terminations of the algorithm, which resulted in sub-optimal configurations. Considering that a very high initial temperature may lead the SAA to perform similarly to a random walk (Aarts et. al 1997), the elasticity of acceptance  $a = 0.9$  (initially considered) was reduced to  $a = 0.8$ . Considering  $a = 0.8$  was subject to confirmation that at least 80% of the candidate HSR configurations were accepted at the initial temperature step, as suggested by Kirkpatrick (1984) and Van Laarhoven and Aarts (1987). The reduction from  $a = 0.9$  to  $a = 0.8$  aimed at decreasing the time length the SAA spends at the high temperatures, in which worsening HSR configurations are accepted with large probabilities. The verification of at least 80% of accepted candidate configurations at the initial temperature aimed at ensuring that the initial temperature was still high enough to allow for the comprehensive canvassing of the search space. Enabling such an exploration of the search space prevents the algorithm from being stuck in a confined area of the problem and is central to the effectiveness in finding optimal or near-optimal solutions. The reduction of the initial temperature thus represented a compromise between decreasing the possibility of a random walk behavior and still allowing a comprehensive search within the feasible space of the problem.

It is noted that the increase of the  $n_1$ , even with the reduction of  $a$ , may result in larger computation time than that required for solving the SPC planning problem. Thus, the additional stopping criterion defined in section 6.2.3 of a maximum of 20 days of computation time was extended for 31 days.

SAA runs were then performed to solve the same robust approach, with the  $\gamma$  benefit coefficients,  $\omega=1$  and scenario combination #1, considering the new  $n_1 = 6000$  and  $a = 0.8$  cooling schedule parameters and maintaining the temperature decrease rates  $r = 0.8$  and the stopping criterion  $n_2 = 10$ . The average objective function value of the solutions was reduced to being 7% larger than the best found HSR configuration. It was shown in section 6.4.1 how two HSR configurations suggesting the same corridor from a HSR planning perspective can differ 10% in construction costs. Thus, the adjusted SAA cooling schedule ( $a = 0.8$ ;  $r = 0.8$ ;  $n_1 = 6000$ ;  $n_2 = 10$ ) is deemed acceptable and considered for further calculations in solving the robust approach of the Lisbon-Oporto HSR planning problem.

### 7.3 SCENARIO-WEIGHT COMBINATION #1

The scenario-weight combination #1 considers uniform weights for the three scenarios:  $\Psi_{intraplate\ EQ} = \Psi_{interplate\ EQ} = \Psi_{rainfall} = 1/3$ . This combination aims at reproducing an equal importance given by the decision-maker to the performance of the HSR for different natural hazards, regardless of which their probabilities of occurrence may be.

Such an attitude towards the risks of the natural hazards is studied with the consideration of both  $\gamma$  and  $\gamma/3$  location benefit coefficients for Aveiro and Leiria. The robust application for the  $\gamma$  coefficient is comparable to the HSR\_SPC configuration found for SPC conditions and allows one to analyze the effects of considering the natural hazards in planning the HSR rail. The comparison between the solutions found for the location benefit coefficients  $\gamma$  and  $\gamma/3$  ( $\omega=1$  in both applications) analyze if the reduction of the benefits of connecting Aveiro and Leiria results in robust solutions connecting these cities.

In addition to the variation of the location benefit coefficient, one application is performed considering  $\gamma/3$  and  $\omega=30$ .  $\omega$  multiplies the weighted-scenario performance in the objective function value of expression (4.10). The value of  $\omega=30$  is academically defined for the purpose of illustrating that a significantly large  $\omega$  results in robust solutions governed by the natural hazards performance. Thus,  $\omega=30$  is used to obtain solutions less affected by natural hazards. By comparing the results with those obtained for the same location benefit  $\gamma/3$  and smaller  $\omega=1$ , an investigation is performed to assess if larger capital costs and worse layout performance (worse in SPC terms) can significantly improve the natural hazards performance.

#### 7.3.1 LOCATION BENEFIT COEFFICIENT $\gamma$ ( $\omega=1$ )

This section presents the best found solution of the robust approach for the scenario combination #1, the location benefit of  $\gamma$  and  $\omega=1$ , HSR\_Comb#1\_ $\gamma$ . By comparing HSR\_Comb#1\_ $\gamma$  with the solution for Standard Planning Conditions, HSR\_SPC, the influence of natural hazards during the planning process can be assessed.

The best HSR found by the SAA, which is termed HSR\_Comb#1\_ $\gamma$ , is described in Table 7-6 for its geometry, with indication of the 3D coordinates of the nodes that constitute the HSR, the cities connected, the gradient  $\eta$  (%) of each linear section and the horizontal angle  $\beta$  (°) at

each intermediate node. 15 linear sections compose the HSR\_Comb#1\_γ, sequentially linking the nodes 1 through 16.

One observes from Table 7-6 that HSR\_Comb#1\_γ complies with the location constraint, by linking Lisbon, Coimbra and Oporto and complies with the geometry constraints by having all gradients smaller than 35‰ and all horizontal angles larger than 120°. Furthermore, HSR\_Comb#1\_γ complies with the geometry normal values by having all gradients smaller than 20‰ and all horizontal angles larger than 140°.

**Table 7-6** Geometry of the configuration HSR\_Comb#1\_γ.

| <b>Node</b> | <b>(x;y;z)</b><br><b>(km;km;m)</b> | <b>City</b> | <b>η</b><br><b>(‰)</b> | <b>β</b><br><b>(°)</b> |
|-------------|------------------------------------|-------------|------------------------|------------------------|
| 1           | (80;16;108.152)                    | Oporto      | -2                     |                        |
| 2           | (78;20;100)                        |             | -7                     | 163                    |
| 3           | (76;32;10)                         |             | 0                      | 171                    |
| 4           | (76;72;10)                         | Aveiro      | 3                      | 163                    |
| 5           | (86;104;100)                       |             | -6                     | 174                    |
| 6           | (92;118;13.106)                    | Coimbra     | 15                     | 157                    |
| 7           | (92;126;130)                       |             | -2                     | 146                    |
| 8           | (76;150;70)                        |             | 12                     | 180                    |
| 9           | (72;156;160)                       |             | -3                     | 169                    |
| 10          | (64;164;130)                       |             | -12                    | 169                    |
| 11          | (60;170;40)                        | Leiria      | 7                      | 162                    |
| 12          | (54;192;200)                       |             | 0                      | 166                    |
| 13          | (46;206;200)                       |             | -5                     | 147                    |
| 14          | (48;244;20)                        |             | 3                      | 148                    |
| 15          | (38;262;80)                        |             | -3                     | 164                    |
| 16          | (34;280;32.348)                    | Lisbon      |                        |                        |

The compliance with the land-use constraint is observed in Figure 7-1b). Figure 7-1 shows the plan view of HSR\_Comb#1\_γ and HSR\_SPC overlaying the lithological-, land-use-, expropriation cost-, elevation-, main rivers-, intraplate landslide-, intraplate liquefaction-, interplate landslide-, interplate liquefaction-, rainfall landslide- and flood- maps in at a 1:1,800,000 scale.

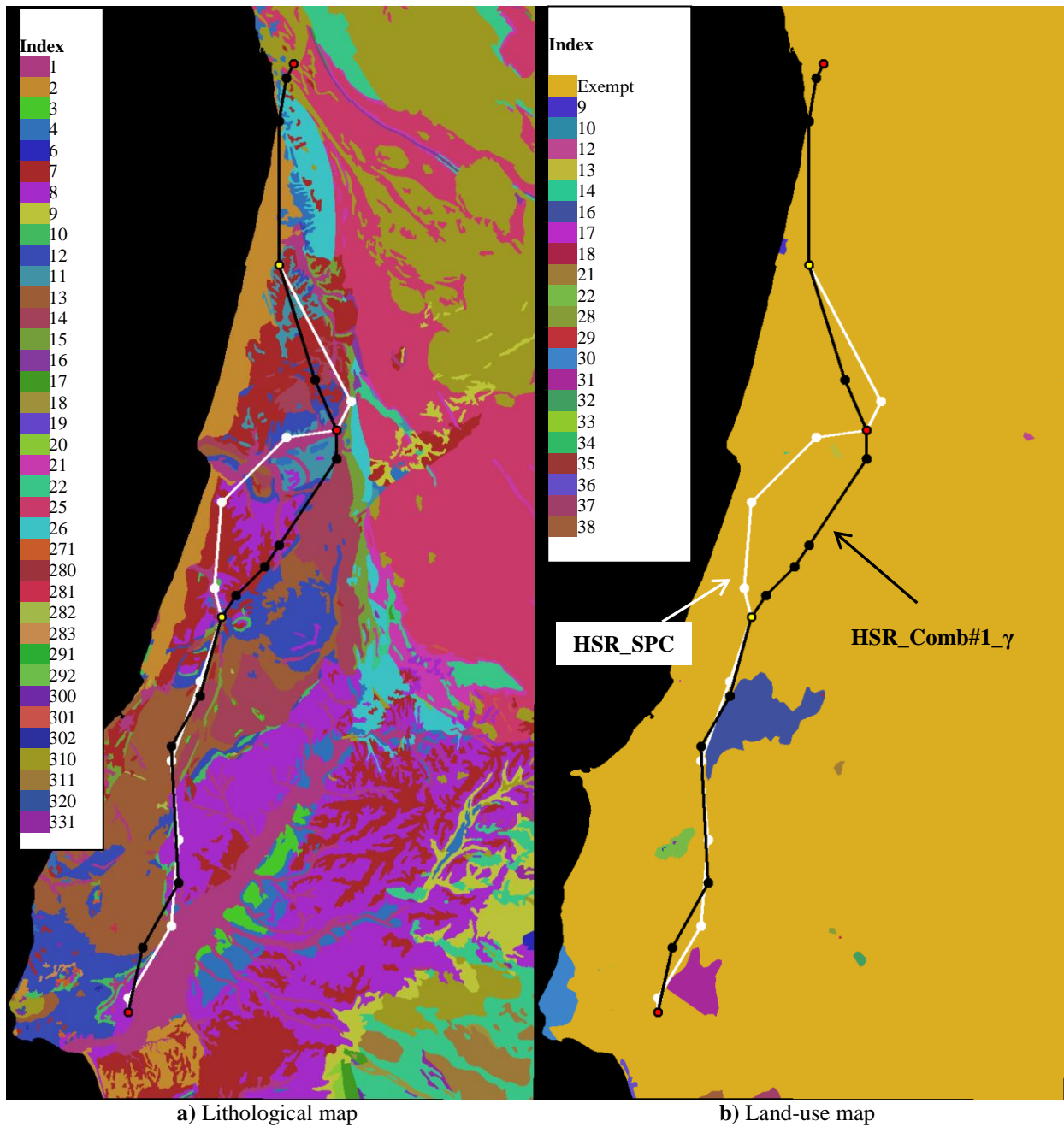


**Figure 7-1** Plan view overlay of configurations HSR\_Comb#1\_γ and HSR\_SPC: a) lithological map, b) land-use map, c) expropriation cost map, d) elevation map, e) main rivers map, f) intraplate landslide map, g) intraplate liquefaction map, h) interplate landslide map, i) interplate liquefaction map, j) rainfall landslide map and k) flood pap. HSR\_SPC white and HSR\_Comb#1\_γ in black in a), b), c), d) and e). HSR\_SPC in gray and HSR\_Comb#1\_γ in blue in f), g), h), i), j) and k). Aveiro and Leiria in yellow circles and Lisbon, Oporto and Coimbra in red circles.



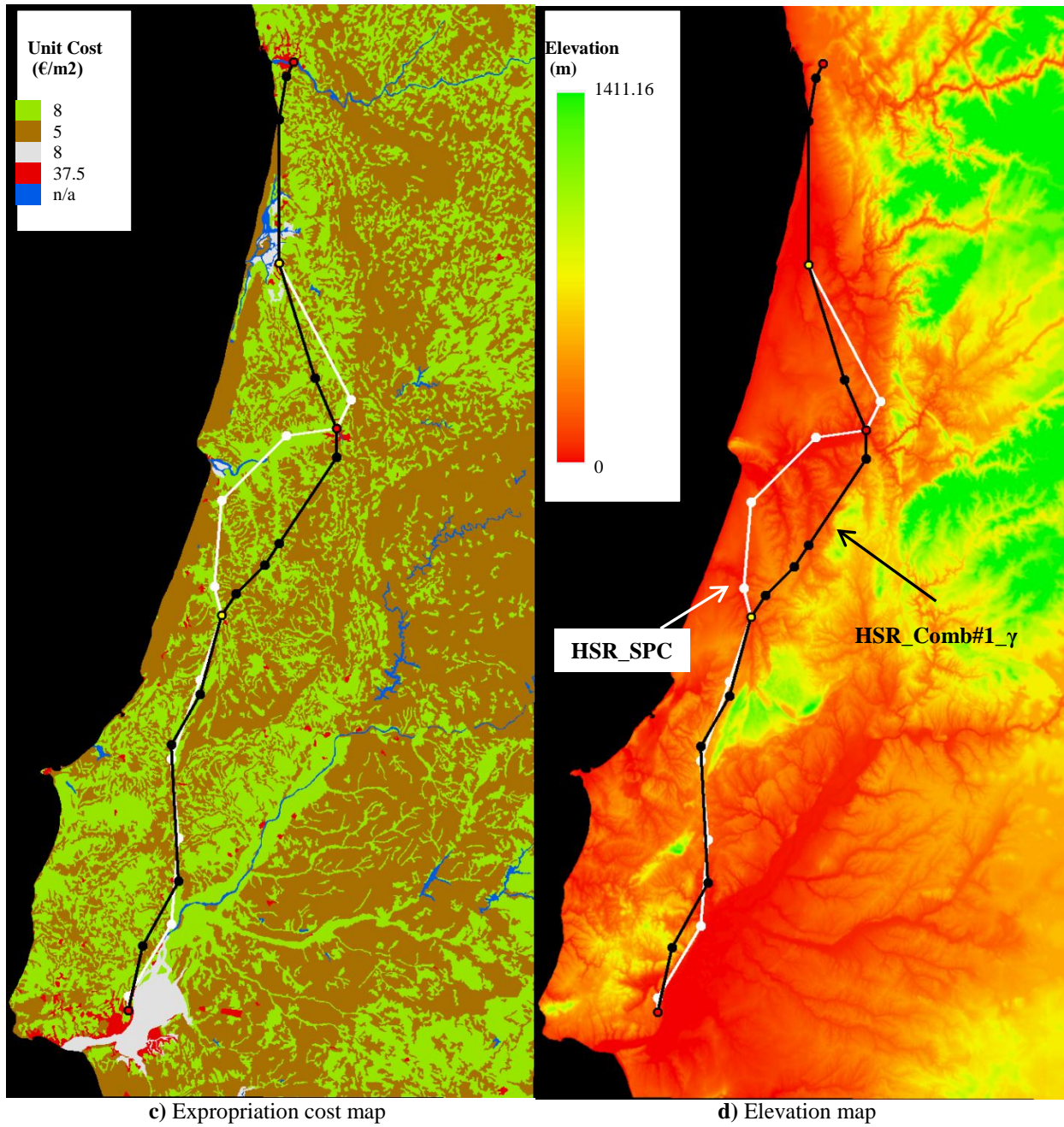


**Figure 7-1** Plan view overlay of configurations HSR\_Comb#1\_γ and HSR\_SPC: a) lithological map, b) land-use map, c) expropriation cost map, d) elevation map, e) main rivers map, f) intraplate landslide map, g) intraplate liquefaction map, h) interplate landslide map, i) interplate liquefaction map, j) rainfall landslide map and k) flood pap. HSR\_SPC white and HSR\_Comb#1\_γ in black in a), b), c), d) and e). HSR\_SPC in gray and HSR\_Comb#1\_γ in blue in f), g), h), i), j) and k). Aveiro and Leiria in yellow circles and Lisbon, Oporto and Coimbra in red circles. (Continued).

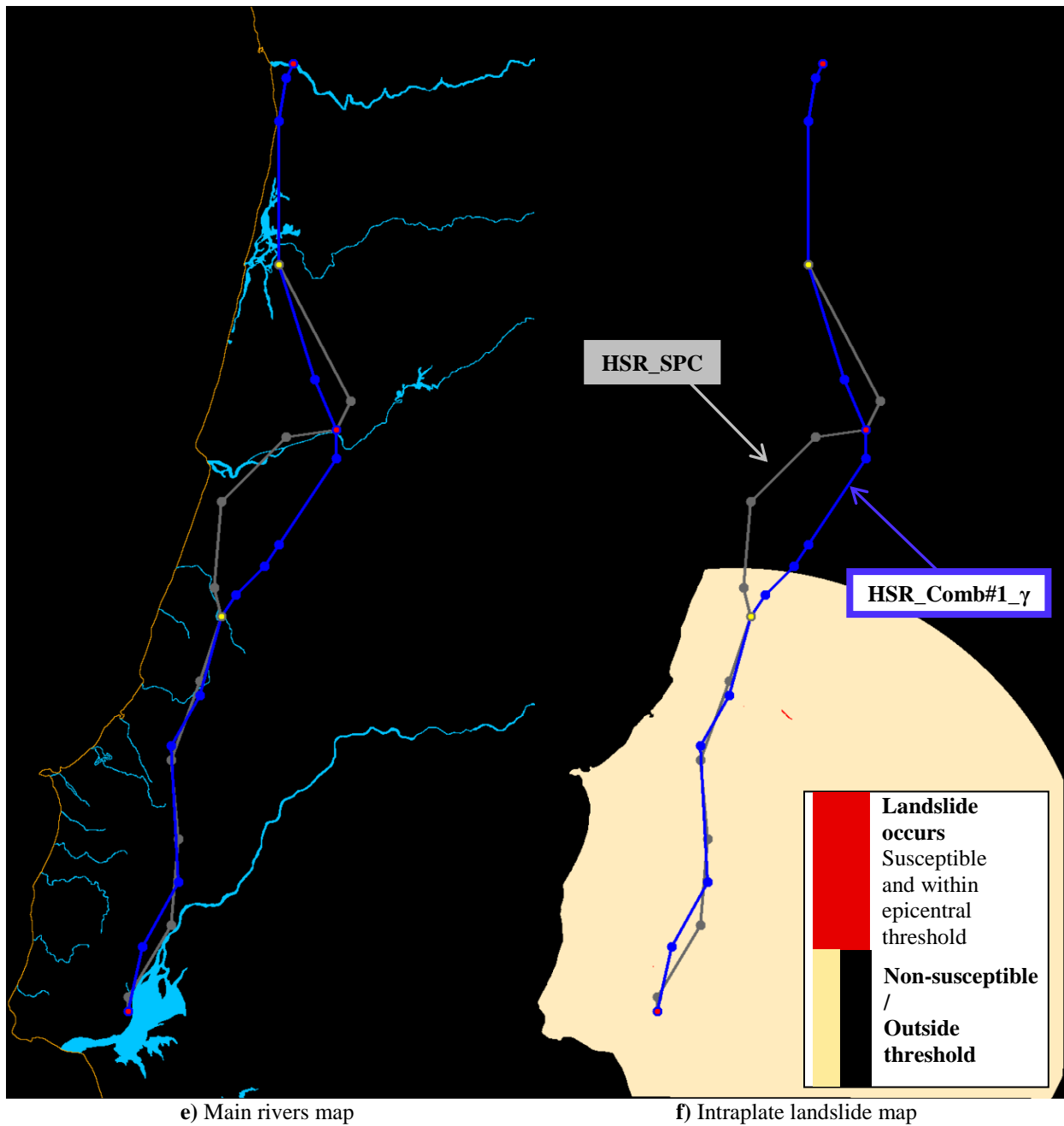


**Figure 7-1** Plan view overlay of configurations HSR\_Comb#1\_γ and HSR\_SPC: a) lithological map, b) land-use map, c) expropriation cost map, d) elevation map, e) main rivers map, f) intraplate landslide map, g) intraplate liquefaction map, h) interplate landslide map, i) interplate liquefaction map, j) rainfall landslide map and k) flood pap. HSR\_SPC white and HSR\_Comb#1\_γ in black in a), b), c), d) and e). HSR\_SPC in gray and HSR\_Comb#1\_γ in blue in f), g), h), i), j) and k). Aveiro and Leiria in yellow circles and Lisbon, Oporto and Coimbra in red circles. (Continued).

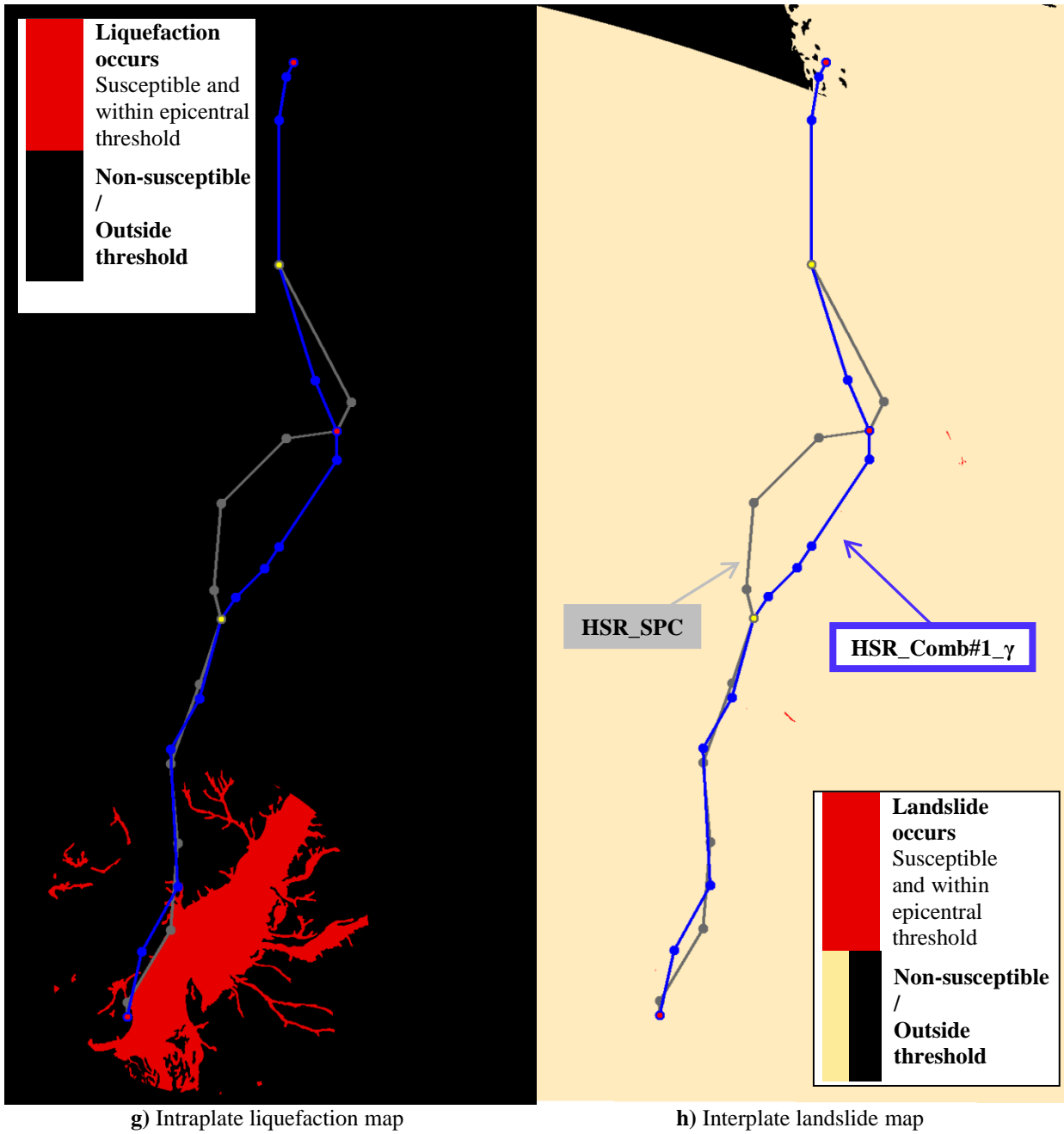


**Figure 7-1** Plan view overlay of configurations HSR\_Comb#1\_γ and HSR\_SPC: a) lithological map, b) land-use map, c) expropriation cost map, d) elevation map, e) main rivers map, f) intraplate landslide map, g) intraplate liquefaction map, h) interplate landslide map, i) interplate liquefaction map, j) rainfall landslide map and k) flood pap. HSR\_SPC white and HSR\_Comb#1\_γ in black in a), b), c), d) and e). HSR\_SPC in gray and HSR\_Comb#1\_γ in blue in f), g), h), i), j) and k). Aveiro and Leiria in yellow circles and Lisbon, Oporto and Coimbra in red circles. (Continued).

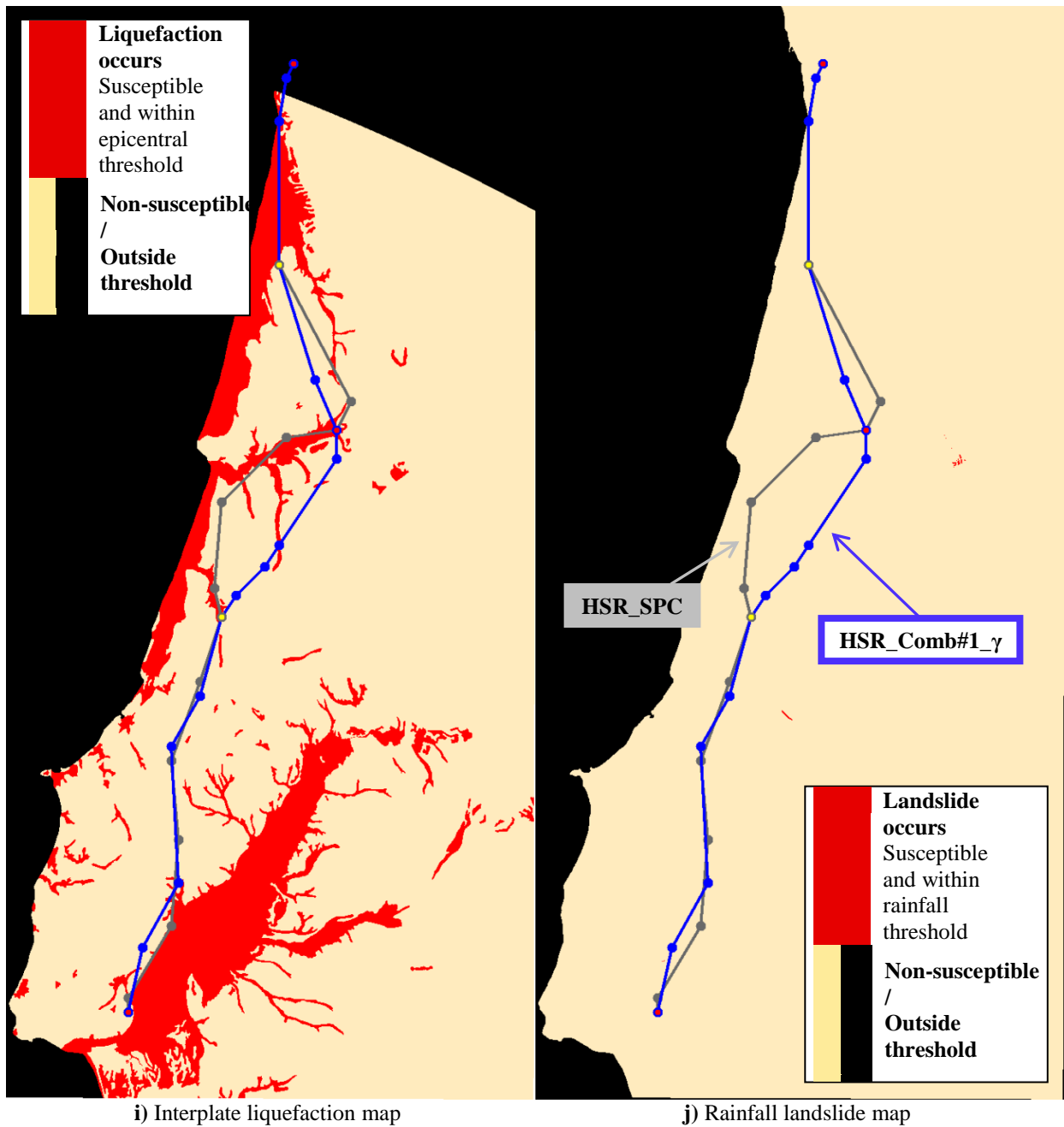


**Figure 7-1** Plan view overlay of configurations HSR\_Comb#1\_γ and HSR\_SPC: a) lithological map, b) land-use map, c) expropriation cost map, d) elevation map, e) main rivers map, f) intraplate landslide map, g) intraplate liquefaction map, h) interplate landslide map, i) interplate liquefaction map, j) rainfall landslide map and k) flood pap. HSR\_SPC white and HSR\_Comb#1\_γ in black in a), b), c), d) and e). HSR\_SPC in gray and HSR\_Comb#1\_γ in blue in f), g), h), i), j) and k). Aveiro and Leiria in yellow circles and Lisbon, Oporto and Coimbra in red circles. (Continued).

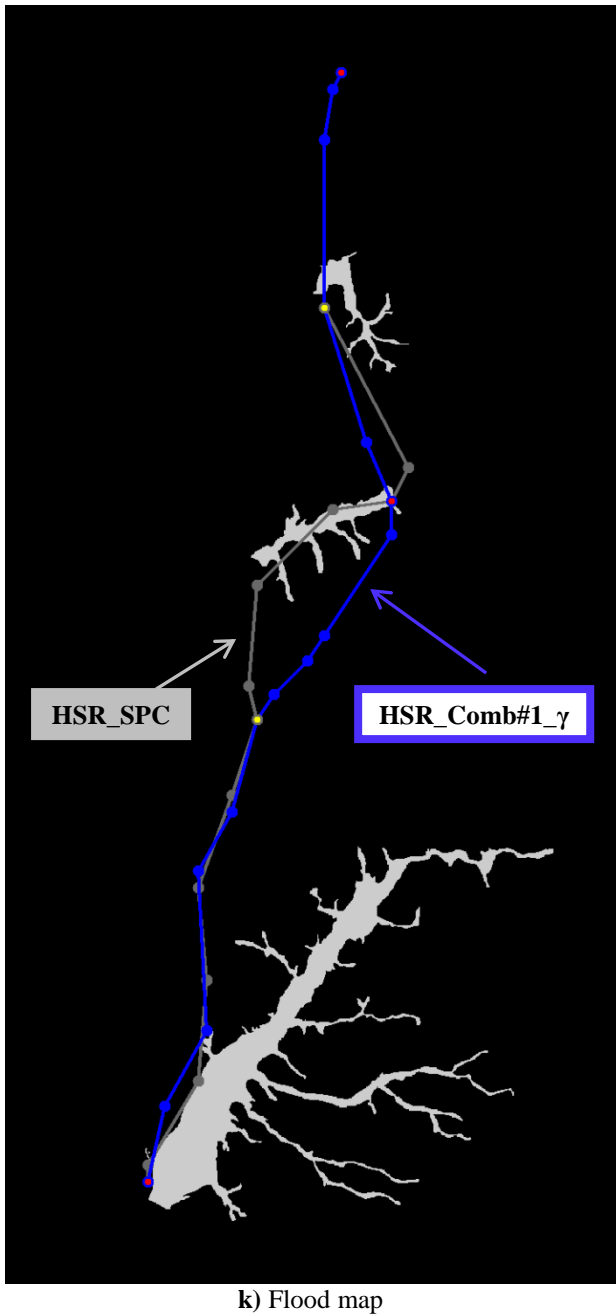


**Figure 7-1** Plan view overlay of configurations HSR\_Comb#1\_γ and HSR\_SPC: a) lithological map, b) land-use map, c) expropriation cost map, d) elevation map, e) main rivers map, f) intraplate landslide map, g) intraplate liquefaction map, h) interplate landslide map, i) interplate liquefaction map, j) rainfall landslide map and k) flood pap. HSR\_SPC white and HSR\_Comb#1\_γ in black in a), b), c), d) and e). HSR\_SPC in gray and HSR\_Comb#1\_γ in blue in f), g), h), i), j) and k). Aveiro and Leiria in yellow circles and Lisbon, Oporto and Coimbra in red circles. (Continued).

Figure 7-1 shows that the plan view of HSR\_Comb#1\_γ and HSR\_SPC differs mostly between Aveiro and Leiria and close to Lisbon, being almost coincident otherwise. In addition, Figure 7-2 shows that the longitudinal profile is similar between Oporto and Aveiro and differs significantly between Coimbra and Leiria. Between Leiria and Lisbon a displacement of the graphics (Figure 7-2) of circa 12 km needs to be considered for a comparison of the longitudinal profiles. The HSR\_Comb#1\_γ solution is 283.986 km long, 12.346 km shorter than HSR\_SPC, mainly due to the plan view differences between Coimbra and Leira. The distance between Oporto and Coimbra in both configurations differs circa 3kms, difference that increases to 12.451 kms by Leiria and then remains almost unchanged when connecting Lisbon (12.346 km). Analyzing the cross-sections, Figure 7-2 shows that between Leiria and Lisbon, HSR\_Comb#1\_γ requires significantly more bridges (between km 190 and km 210) and significantly more tunnels (between km 225 and km 275).

These different areas, between Aveiro and Leiria and next to Lisbon are analyzed in detail. However, it is first assessed how these differences affect the cost breakdown.

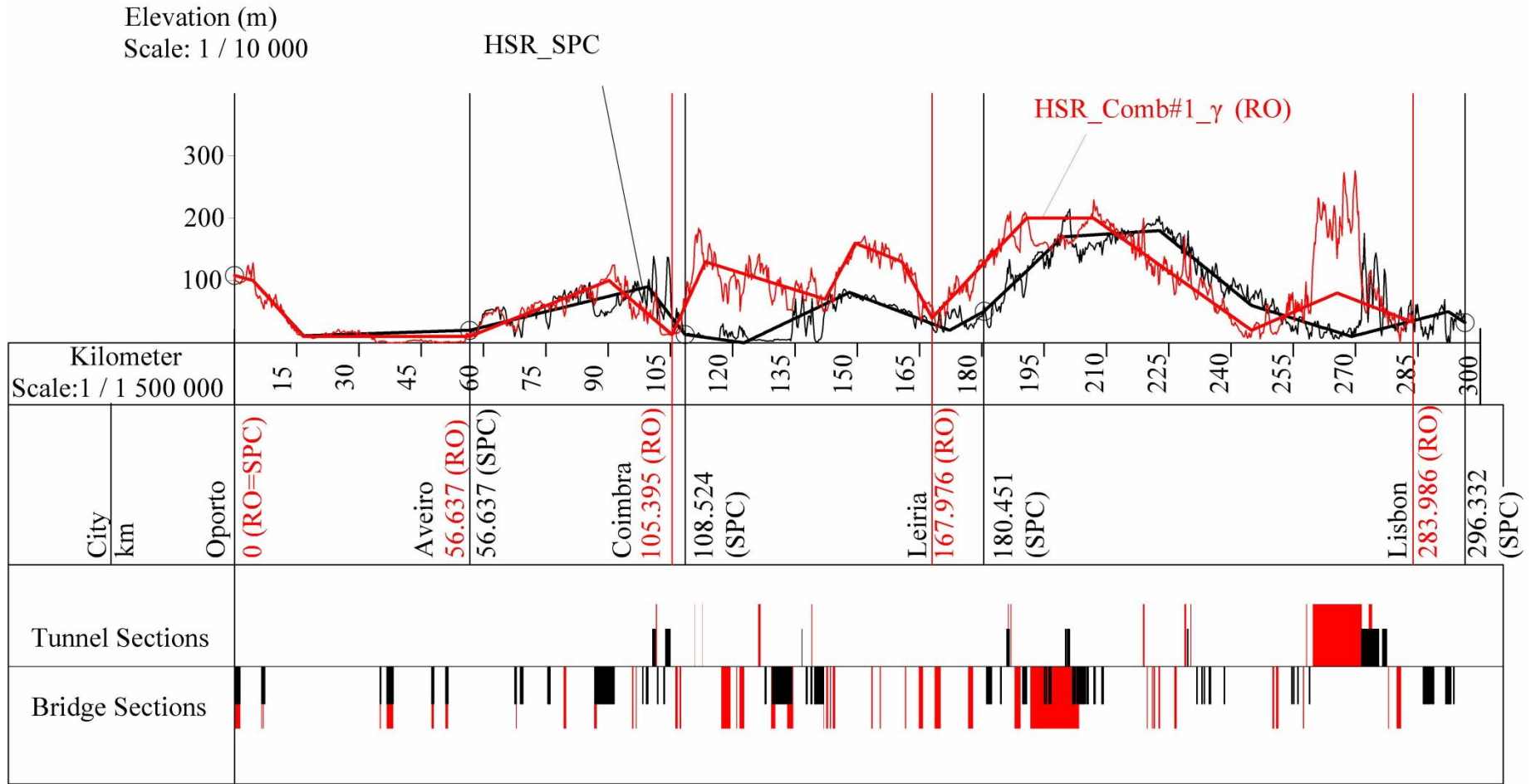


**Figure 7-2** Comparison of the longitudinal profiles of HSR\_Comb#1\_γ (in red) and HSR\_SPC (in black).

The HSR\_SPC was obtained for a different set of conditions than those used for obtaining the HSR\_Comb#1\_ $\gamma$ . The HSR\_SPC was obtained in chapter 6 by solving the SPC model and thus the effects of natural hazards were not taken into account. As such, neither the HSR weighted performance for the scenarios set,  $\sum_{c \in \Omega_{sc}} \Psi_c \sum_{(i,j) \in \Omega_N} RC_{ij}^c$ , nor the weight  $\omega$  multiplying the natural hazards performance in the robust objective function were defined to obtain HSR\_SPC. In order to compare both solutions, the value that HSR\_SPC would have if evaluated under the same conditions as HSR\_Comb#1\_ $\gamma$  is assessed. In this sense, Table 7-7 compares the value (in Million €) that both HSR\_Comb#1\_ $\gamma$  and HSR\_SPC have when one considers the effects of natural hazards for scenario combination#1, a location benefit of  $\gamma$  for both Aveiro and Leiria and  $\omega=1$ .

**Table 7-7** Value of both HSR\_Comb#1\_ $\gamma$  and HSR\_SPC considering the Combination#1, the location benefit coefficient of  $\gamma$  and  $\omega=1$ .

| HSR Configuration  | Value for Combination#1 and Location Benefit of $\gamma$ (Million €) |                 | HSR_Comb#1_ $\gamma$ / HSR_SPC (%) |
|--|--|-----------------|------------------------------------|
|  | HSR_Comb#1_ $\gamma$   | HSR_SPC         |                                    |
| <b>Objective Function Value</b>  | <b>1,455.08</b>  | <b>1,449.83</b> | 100%                               |
| <b>SPC (1 + 2 + 3 - 4)</b>   | 1,375.31   | 1,284.51        | 107%                               |
| 1. CONSTRUCTION COST<br>(1.1+1.2+1.3+1.4+1.5)                            | 1,964.73   | 1,658.50        | 118%                               |
| 1.1 Expropriation  | 128.11   | 154.94          | 83%                                |
| 1.2 Earthworks   | 410.23   | 454.52          | 90%                                |
| 1.3 ALL BRIDGES  | 521.29   | 429.98          | 121%                               |
| 1.4 ALL TUNNELS  | 575.68   | 275.31          | 209%                               |
| 1.5. LINEAR- DEPENDENT COSTS   | 329.42   | 343.75          | 96%                                |
| 2. GEOMETRY PENALTY  | 0  | 123.56          | -                                  |
| 3. LAND-USE PENALTY  | 0  | 0               | -                                  |
| 4. LOCATION BENEFIT  | 589.42   | 497.55          | 118%                               |
| 5. $\sum_{c \in \Omega_{sc}} \Psi_c \sum_{(i,j) \in \Omega_N} RC_{ij}^c$ | 79.77  | 165.32          | 48%                                |
| 5.1 $\sum_{(i,j) \in \Omega_N} RC_{ij}^{\text{Rainfall}}$                | 28.97  | 91.89           | 32%                                |
| 5.2 $\sum_{(i,j) \in \Omega_N} RC_{ij}^{\text{Intraplate}}$              | 29.09  | 89.72           | 32%                                |
| 5.3 $\sum_{(i,j) \in \Omega_N} RC_{ij}^{\text{Interplate}}$              | 181.39   | 314.58          | 58%                                |

Table 7-7 shows that the robust objective function value of both configurations under such conditions is equivalent but accomplished by a different value breakdown of cost components. At an 18% larger construction cost, the HSR\_Comb#1\_ $\gamma$  improves both the geometry layout and the performance for natural hazards. In fact, HSR\_Comb#1\_ $\gamma$  has a null geometry



penalty, improving from the HSR\_SPC performance whose 123.56 Million € penalty is caused by small horizontal angles close to Coimbra (section 6.3.1). In terms of the natural hazards performance, the reconstruction/repair costs in case each of the Rainfall, Intraplate Earthquake and Interplate Earthquake scenarios materializing is, respectively, 32%, 32% and 58% of that for HSR\_SPC.

This shows how the solution obtained for the SPC model, by optimizing only construction costs and the configuration layout without taking into consideration the effects of natural hazards, can perform poorly if such extreme events materialize. Assessing the natural hazards performance by  $\sum_{c \in \Omega_{sc}} \Psi_c \sum_{(i,j) \in \Omega_N} RC_{ij}^c$  with the  $\Psi_c$  combination #1 (Table 7-7), the SPC\_HSR cost impacts double those of HSR\_Comb#1\_γ (165.23€ / 79.77€ = 2.07). Or, in the opposite perspective, the HSR\_Comb#1\_γ optimized taking into account the effects of natural hazards, reduces by 48% the impacts that would be borne by HSR\_SPC.

Although improving the performance if natural hazards occur, the HSR\_Comb#1\_γ solution has a worse SPC value (Table 7-7). This is expected as the HSR\_SPC is the optimal or near-optimal solution found for the SPC model. Assuming a good functioning of the solving technique (SAA), solutions better than HSR\_SPC for the SPC should not be found.

Figure 7-3 and Figure 7-4 show the breakdown of the accumulated construction costs along the longitudinal profile. While earthworks, expropriation costs and linear-dependent costs of both HSR\_Comb#1\_γ and HSR\_SPC are similar in trend and overall value (Figure 7-3), the costs of bridges and tunnels differ, particularly from km 190 (next to Leiria) towards Lisbon (Figure 7-4).

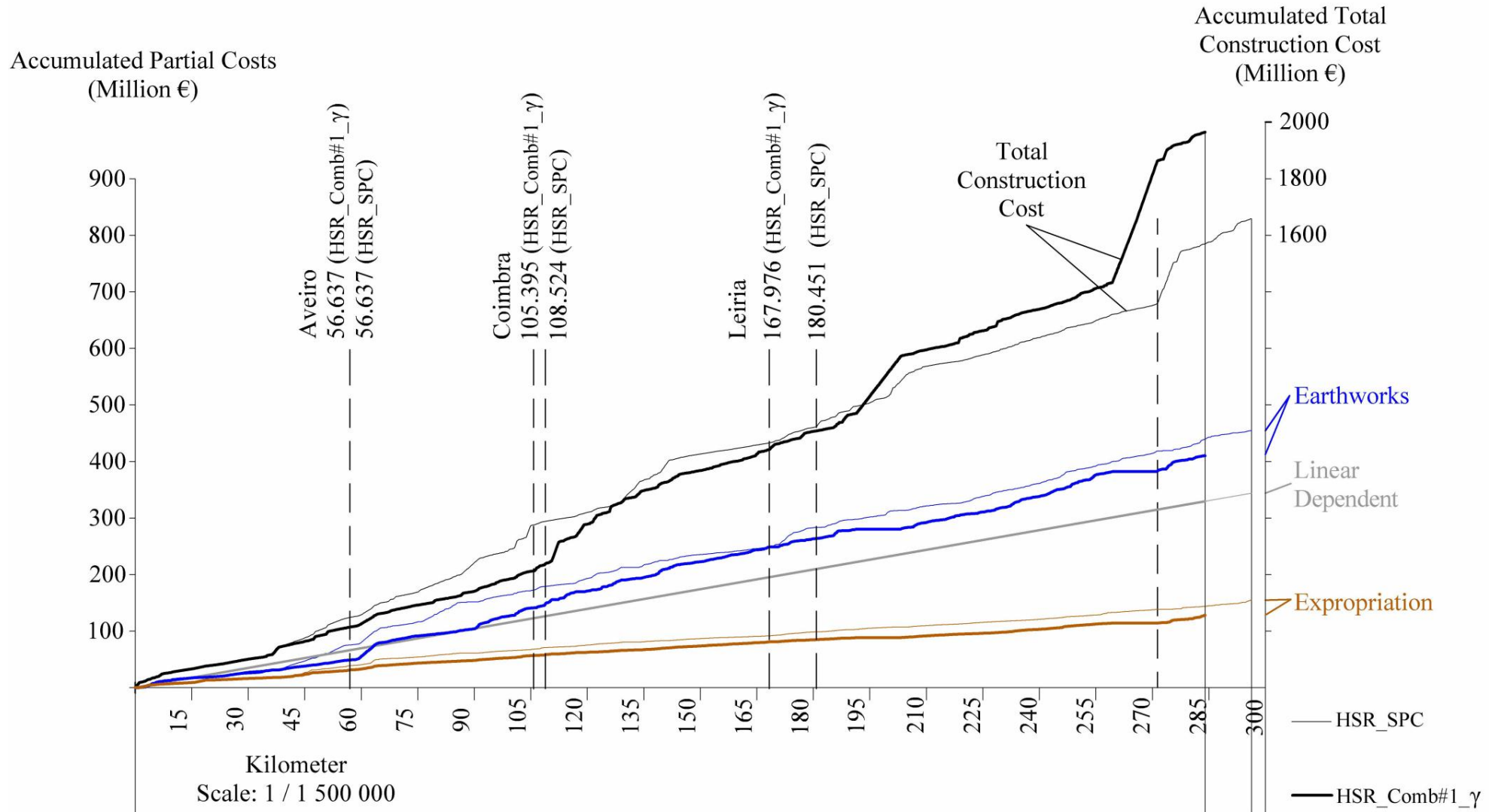


**Figure 7-3** Accumulated costs along the longitudinal profile: total construction costs, earthworks, linear- dependent and expropriation. Costs for HSR\_Comb#1\_γ represented in a thick line and for HSR\_SPC in a thin line.

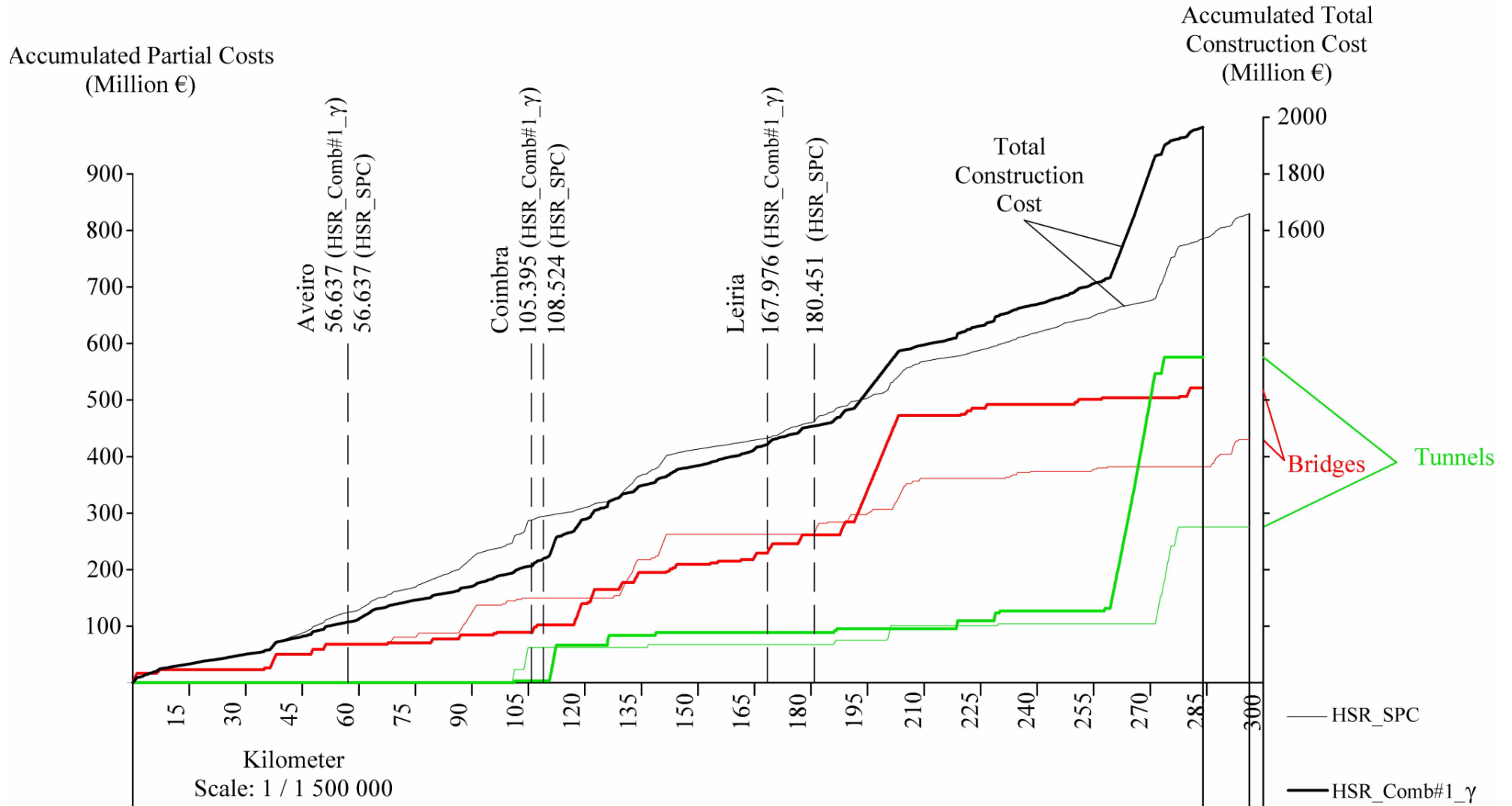


**Figure 7-4** Accumulated costs along the longitudinal profile: total construction costs, bridges and tunnels. Costs for HSR\_Comb#1\_γ represented in a thick line and for HSR\_SPC in a thin line.

To analyze in more detail the trade-offs between larger construction costs and an improved layout and natural hazards performance, the HSR configurations are discussed in detail for two sections: between Aveiro and Leiria and between Leiria and Lisbon. Given the analysis of Figure 7-3 showing the similarities of earthworks, expropriation costs and linear-dependent costs, both in terms trend and overall costs, the analyses presented focus mainly on the effects of the construction of bridges and tunnels, the HSR geometry and the performance for natural hazards.

7.3.1.1 DETAILED ANALYSIS OF THE AVEIRO-LEIRIA SECTION

Figure 7-5 shows the detail of HSR\_Comb#1\_γ and HSR\_SPC overlaying the land-use layer between Aveiro and Leiria.

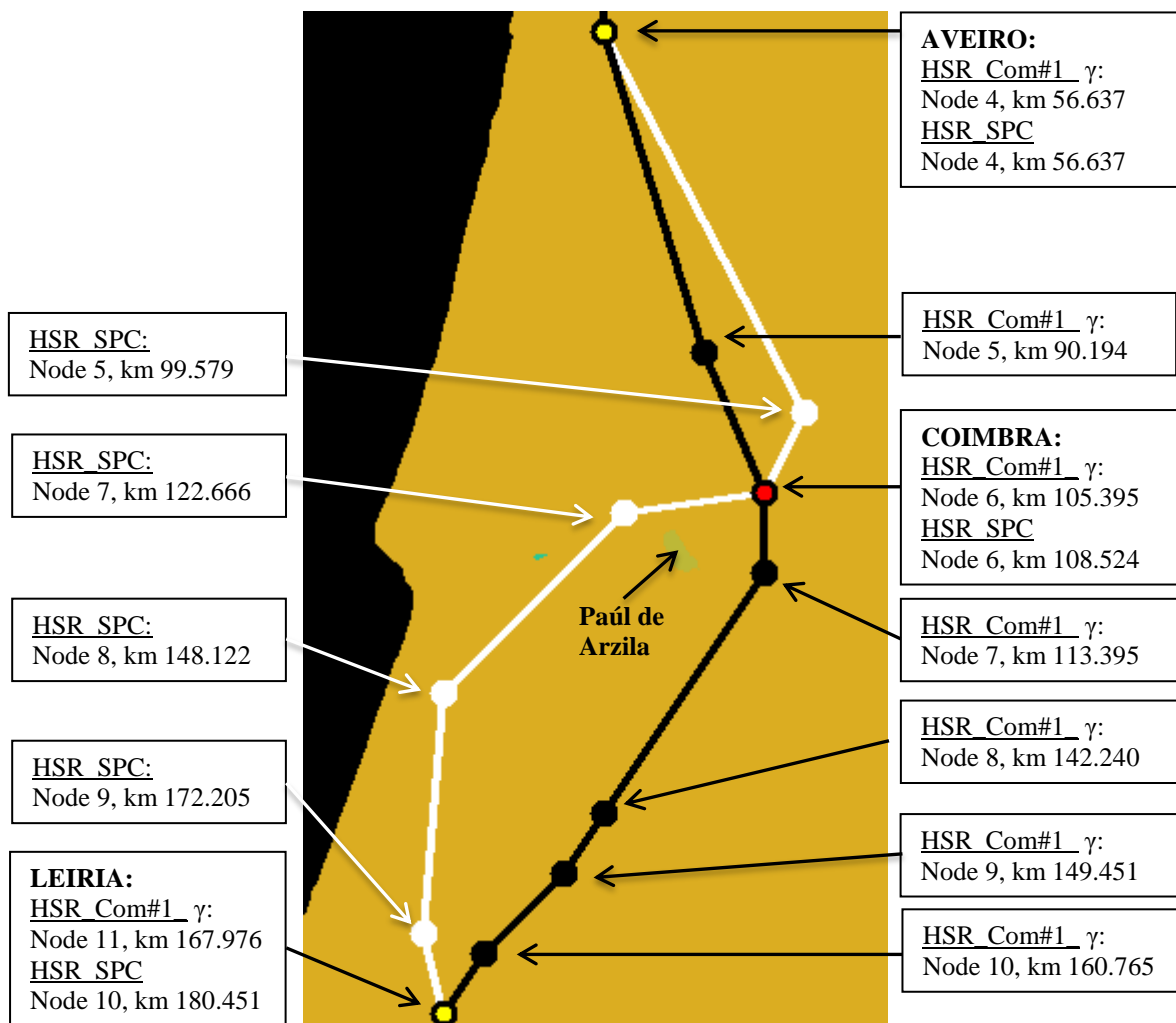
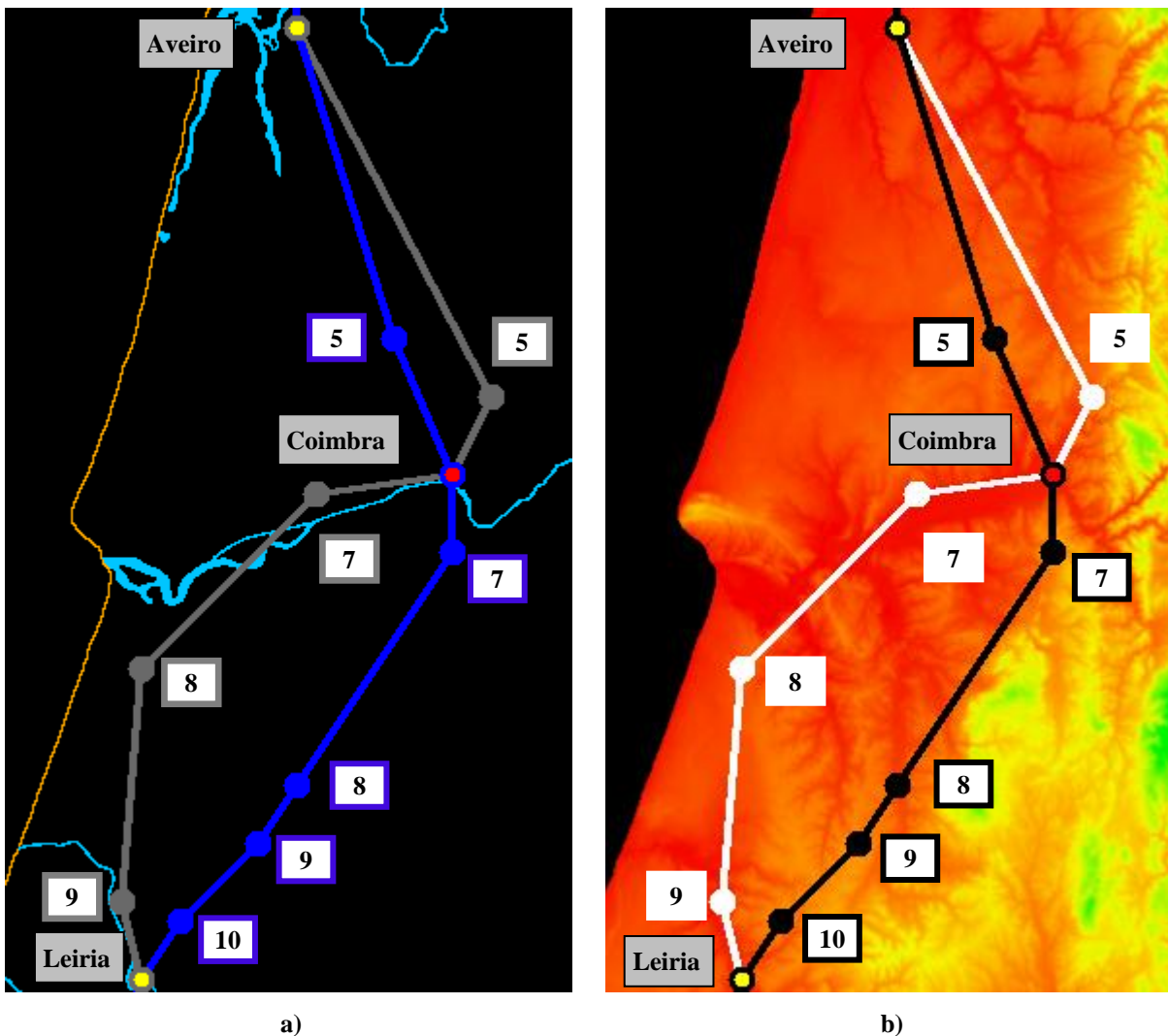


Figure 7-5 Detail of HSR\_Comb#1\_γ (in black) and HSR\_SPC (in white) plan view overlaying the land-use layer between Aveiro and Leiria.

Each node in Figure 7-5 is identified by its number, in accordance with Table 7-6 for HSR\_Comb#1\_ $\gamma$  and Table 6-7 for HSR\_SPC. The km reference of each node identifies the respective positions along the longitudinal profiles of Figure 7-2, Figure 7-3 and Figure 7-4.

Figure 7-5 shows how HSR\_Comb#1\_ $\gamma$  adopts larger intermediate horizontal angles than HSR\_SPC by running eastwards of the forbidden land-use area of Paúl de Arzila, thus avoiding geometry penalties. It has been discussed in section 6.3.1 that the SPC solution runs parallel to the Mondego River (Figure 7-6 a) where level ground (Figure 7-6 b) does not impose the need for building bridges and tunnels, costlier than earthworks.



**Figure 7-6** Detail of the HSR configurations plan view between Aveiro and Leiria overlaying: a) the main rivers map with HSR\_Comb#1\_ $\gamma$  in blue and HSR\_SPC in gray and b) the elevation map with HSR\_Comb#1\_ $\gamma$  in black and HSR\_SPC in white.

Conversely, the HSR\_Comb#1\_ $\gamma$  does not run parallel to the Mondego River (Figure 7-6 a) and has to deal with larger variations of the ground elevation south of Coimbra (Figure 7-6 b). Thus, a larger increase of the accumulated costs of bridges and tunnels is observed in HSR\_Comb#1\_ $\gamma$  between Coimbra and Leiria (Figure 7-4). However, by crossing the Mondego river in a North-South direction (between Coimbra and node 7), the HSR\_Comb#1\_ $\gamma$  is not required to have the node 5 positioned eastward of Coimbra, as does HSR\_SPC, to comply with the limit horizontal angle. As such, the HSR\_Comb#1\_ $\gamma$  avoids the construction of bridges immediately north of Coimbra which are required in HSR\_SPC between km 85 and km 95 (Figure 7-2 and Figure 7-4). It is also noted that, although both HSR configurations connect both Aveiro and Leiria, the elevation differs. Aveiro is connected at an elevation of 10 m by HSR\_Comb#1\_ $\gamma$  and at an elevation of 20m by HSR\_SPC. Leiria is connected at an elevation of 40 m by HSR\_Comb#1\_ $\gamma$  and at an elevation of 50 m by HSR\_SPC. These different elevations influence the cross-sections and construction costs northbound and southbound of both cities. Overall, the accumulated total construction cost increase between Aveiro and Leiria is similar (Figure 7-4).

In addition to improving the geometric performance by increasing all horizontal angles above the normal values, the HSR\_Comb#1\_ $\gamma$  also improves the natural hazards performance for scenario weight combination #1. Landslides (Figure 7-1 f)) and liquefaction (Figure 7-1 g)) triggered by the intraplate (near) earthquake, landslides triggered by the interplate (distant) earthquake (Figure 7-1 h)) and rainfall-triggered landslides (Figure 7-1 j)) are not considered by the scenarios to affect the area between Aveiro and Leiria under consideration. However, liquefaction triggered by the interplate (distant) earthquake (Figure 7-1 i)) and floods caused by the rainfall scenario (Figure 7-1 k)) affect this area. Figure 7-7 shows how HSR\_Comb#1\_ $\gamma$  reduces the overlaid extent of liquefaction hazard zones of the interplate earthquake (Figure 7-7a) and the flooded areas by the rainfall scenario (Figure 7-7b), in comparison to the HSR\_SPC.

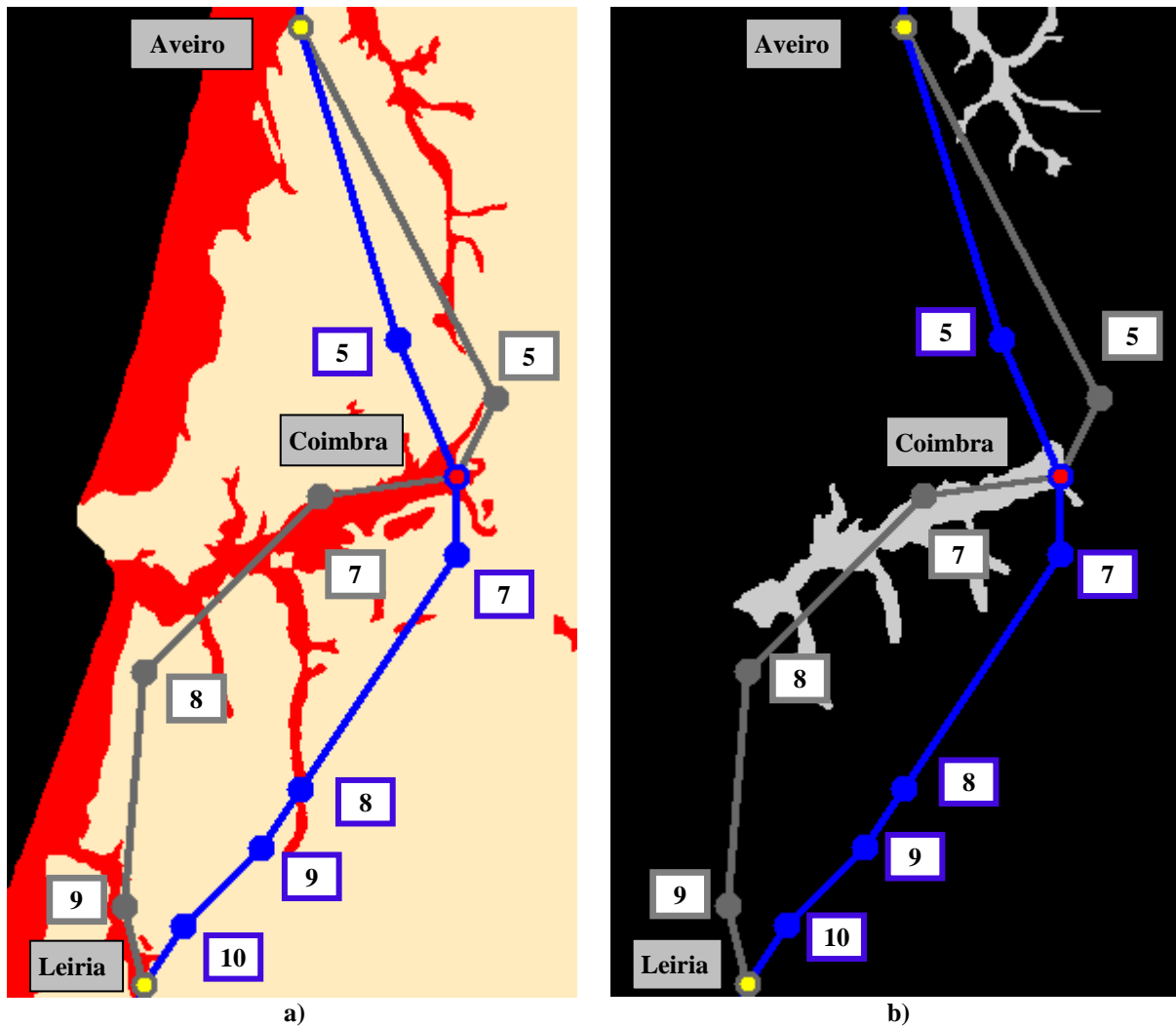


**Figure 7-7** Detail of HSR\_Comb#1\_γ (blue) and HSR\_SPC (gray) plan view between Aveiro and Leiria overlaying: a) the interplate liquefaction hazard map and b) the flood map.

The area around the Mondego River, flatter and that allows the HSR\_SPC to avoid bridges and tunnels due to elevation, is particularly affected by both floods and the interplate earthquake-triggered liquefaction (Figure 7-7). The HSR\_Comb#1\_γ reduces extent overlaid of these hazard zones along the Mondego and also the smaller zones, next to both Aveiro and Leiria, which are crossed by the HSR\_SPC.

It should be noted that not all cross-sections are specified by the scenarios as vulnerable to liquefaction or floods. In fact, floods are considered not to damage bridges and tunnels (section 5.5.3.1) and liquefaction is considered not to damage tunnels (section 5.4.3.3).

Figure 7-8 details the alignments of both HSR configurations overlaying the interplate earthquake liquefaction and flood maps between Aveiro and Coimbra. It shows that HSR\_SPC crosses liquefaction hazard zones with cuts, embankments and bridges (Figure 7-8a) and flood areas with embankments and cuts (Figure 7-8b).

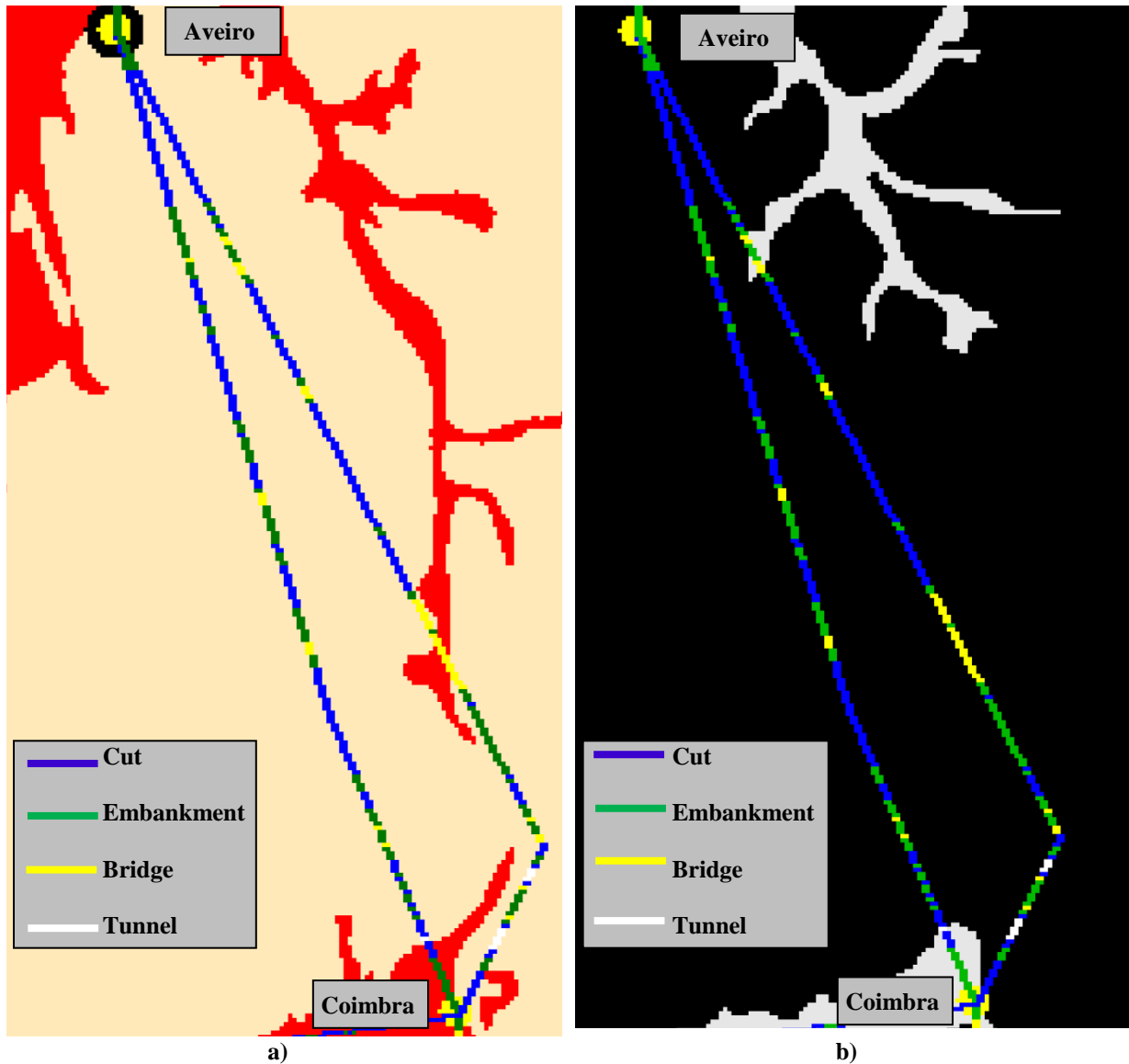


**Figure 7-8** Detail of HSR\_Comb#1\_γ and HSR\_SPC plan views between Aveiro and Coimbra overlaying: a) the interplate liquefaction hazard map and b) the flood map. Cross-sections are represented by different colors: cuts in blue, embankments in green, bridges in yellow and tunnels in light white.

Figure 7-9 details the alignments of both HSR configurations overlaying the interplate earthquake liquefaction map and Figure 7-10 overlays the configurations in the flood map, both between Coimbra and Leiria. The figures show how, in both cases, the HSR\_SPC has a



larger extent of hazard zones overlaid by the infrastructure with vulnerable cross-sections and thus a worse natural hazards performance than HSR\_Comb#1\_ $\gamma$ .

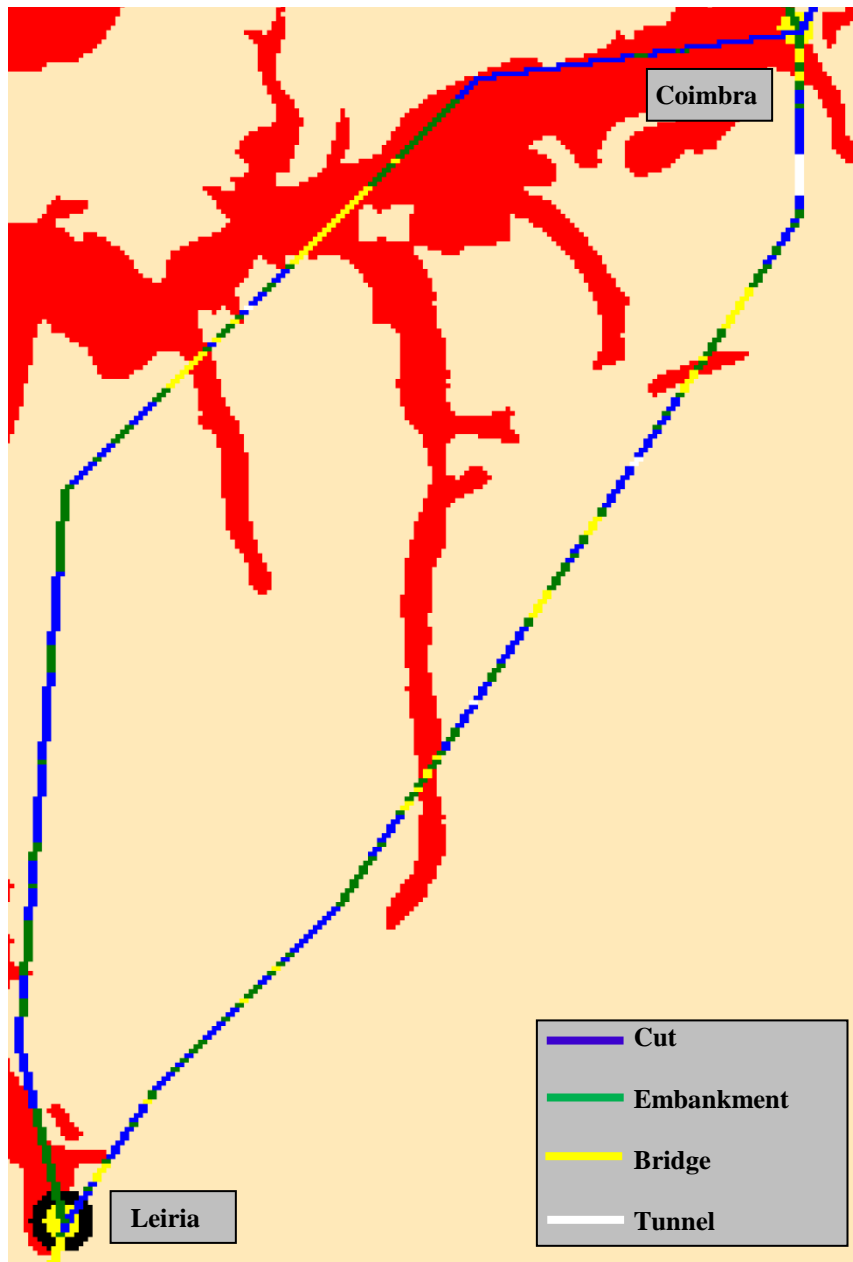


**Figure 7-9** Detail of HSR\_Comb#1\_ $\gamma$  and HSR\_SPC plan views between Coimbra and Leiria overlaying the interplate liquefaction hazard map. Cross-sections are represented by different colors: cuts in blue, embankments in green, bridges in yellow and tunnels in white.

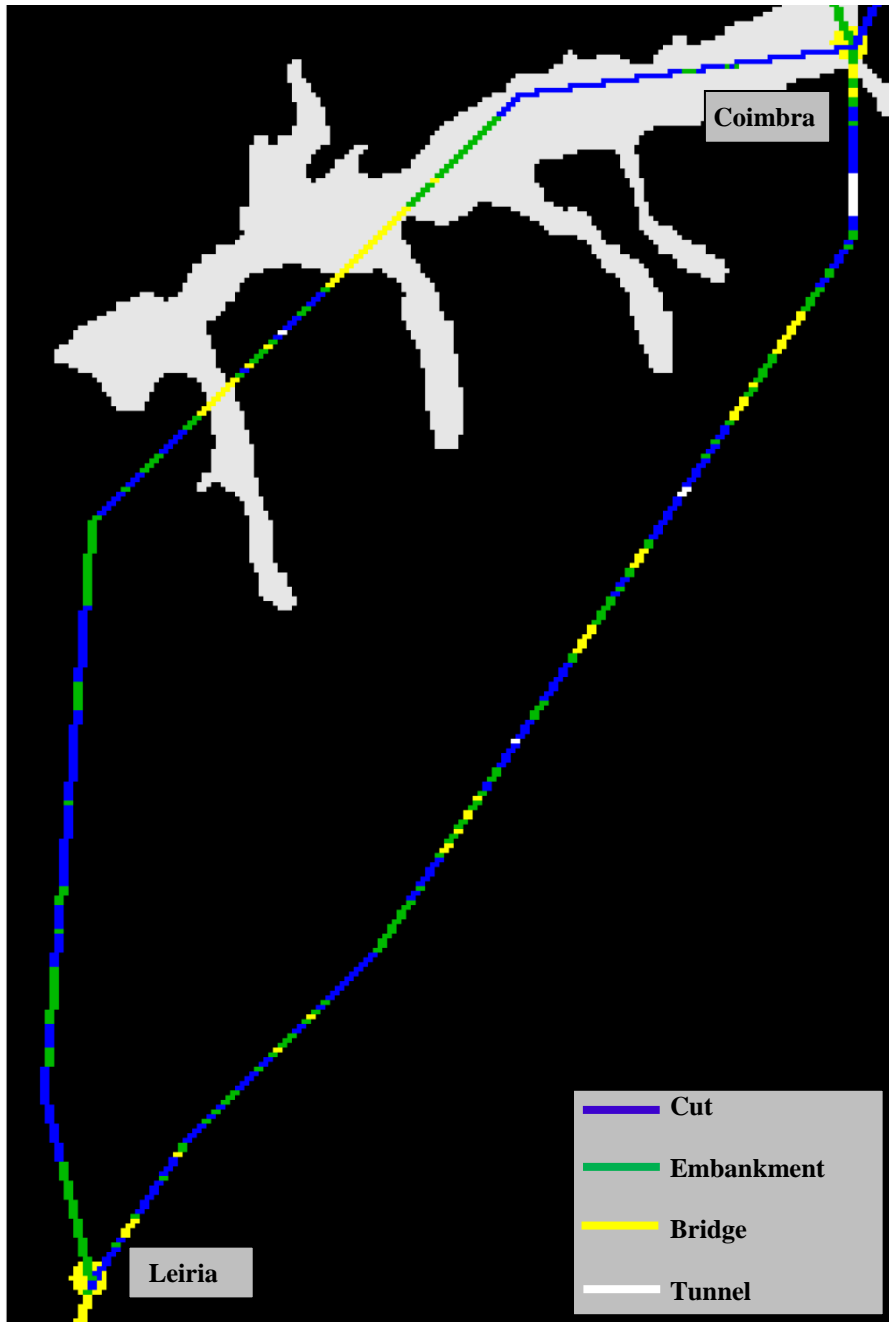
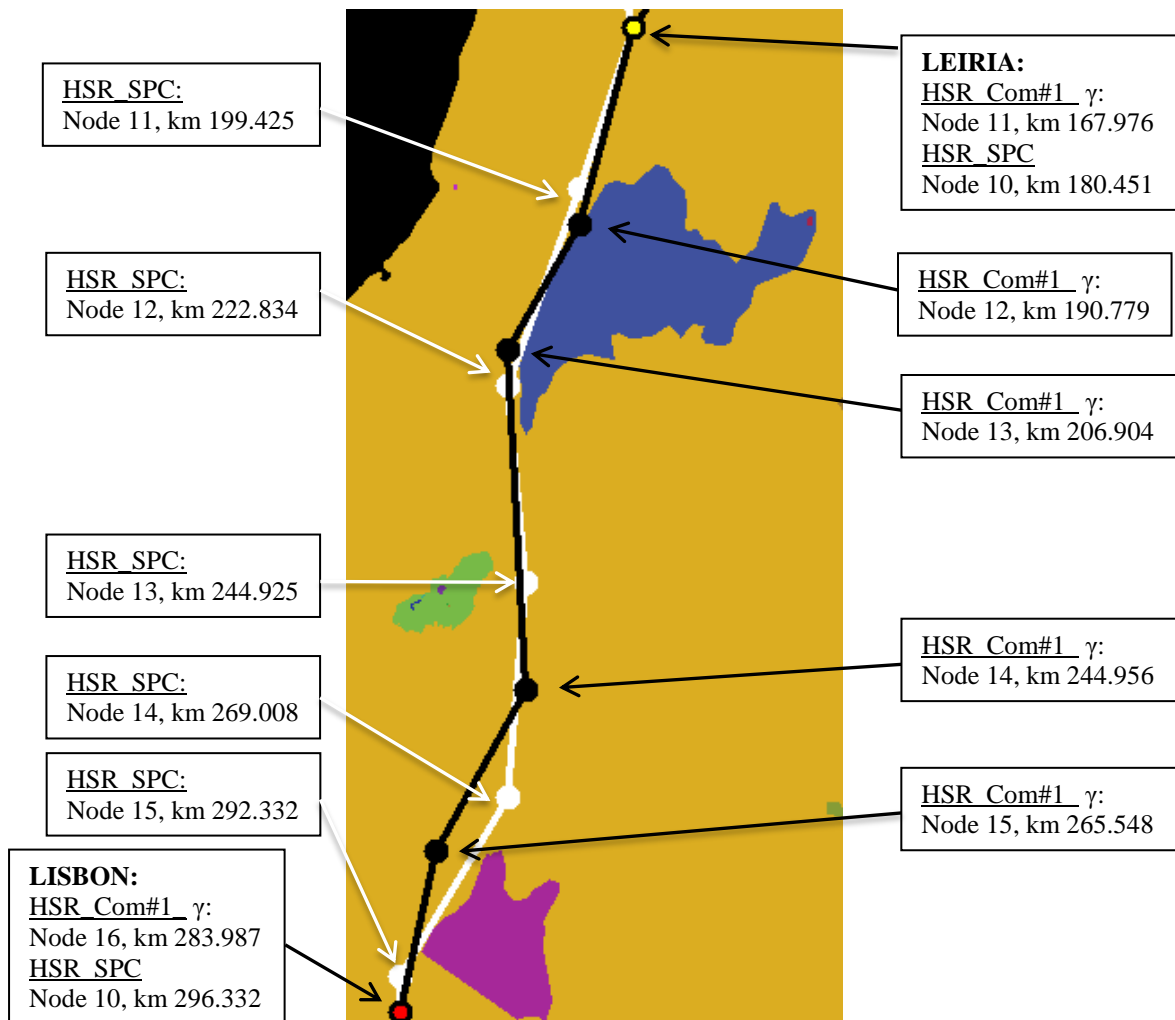


**Figure 7-10** Detail of HSR\_Comb#1\_γ and HSR\_SPC plan views between Coimbra and Leiria overlaying the flood map. Cross-sections are represented by different colors: cuts in blue, embankments in green, bridges in yellow and tunnels in white.

7.3.1.2 DETAILED ANALYSIS OF THE LEIRIA-LISBON SECTION

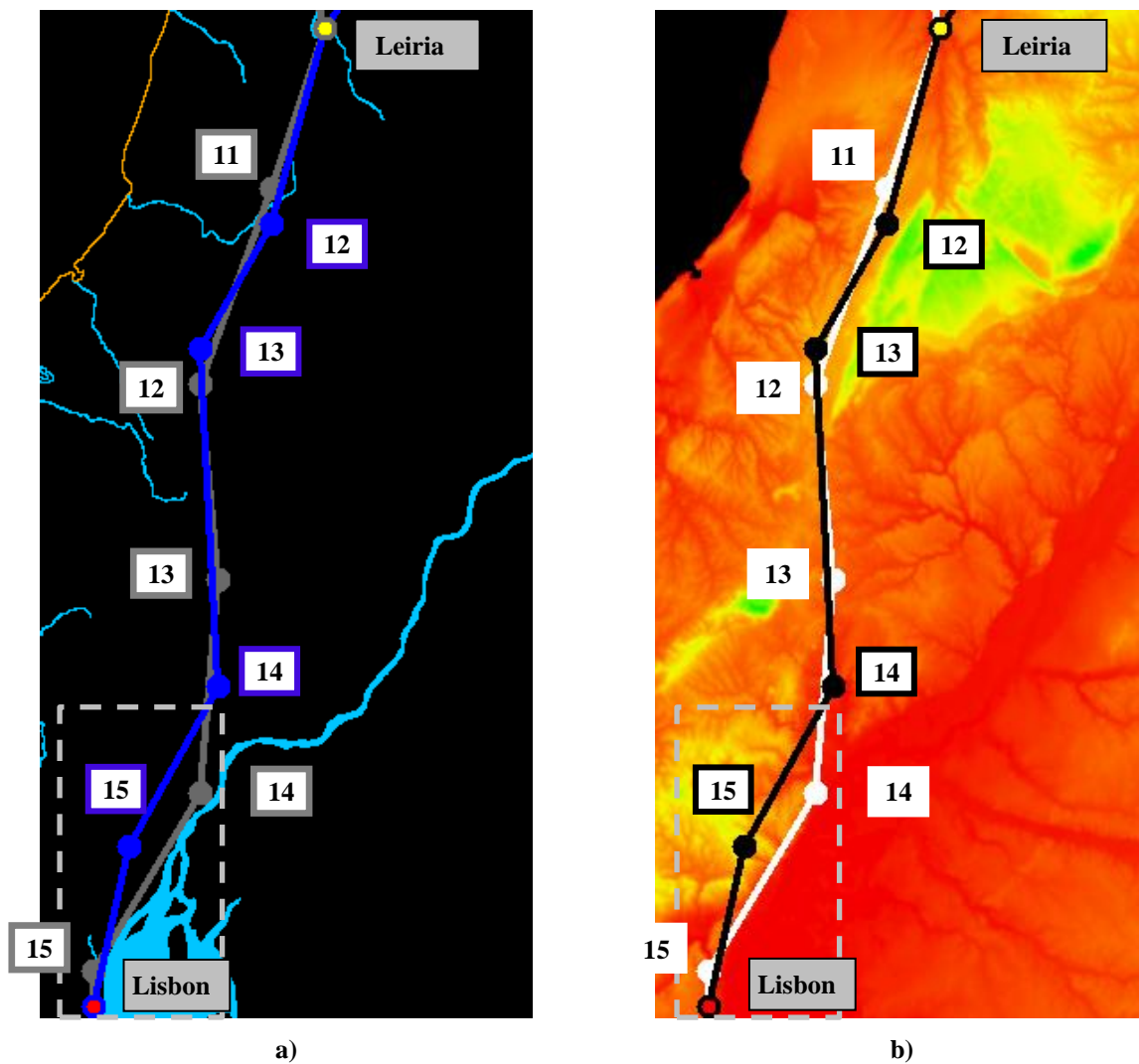
Figure 7-11 shows the detailed HSR\_Comb#1\_γ and HSR\_SPC overlaying the land-use layer between Leiria and Lisbon. Each node in Figure 7-11 is identified by its number, in accordance to Table 7-6 for HSR\_Comb#1\_γ and to Table 6-7 for HSR\_SPC. The km reference of each node identifies the respective positions along the longitudinal profiles of Figure 7-2, Figure 7-3 and Figure 7-4.

Figure 7-11 shows a similar plan view of both configurations between Leiria and node 14 of HSR\_Comb#1\_γ and shows HSR\_Comb#1\_γ running more westerly of HSR\_SPC from this point towards Lisbon.



**Figure 7-11** Detail of HSR\_Comb#1\_γ (in black) and HSR\_SPC (in white) plan view overlaying the land-use layer between Leiria and Lisbon.

Figure 7-2 shows that the longitudinal profile of both solutions is similar between Leiria and km 244.956 of HSR\_Comb#1\_γ (Node 14). A larger extent of bridges, however, is observed in HSR\_Comb#1\_γ between km 185 (immediately before HSR\_Comb#1\_γ's node 12) and km 205 (next to HSR\_Comb#1\_γ's node 13). Bridges or tunnels are required for crossing the existing river immediately before HSR\_Comb#1\_γ's node 12 (Figure 7-12 a). In addition, the plan view differences of both HSR configurations, between km 185 and km 205, occur in an area of large variations of the ground elevation (Figure 7-12 b) which, along with the different elevations when connecting Leiria, result in the larger extent of bridges.

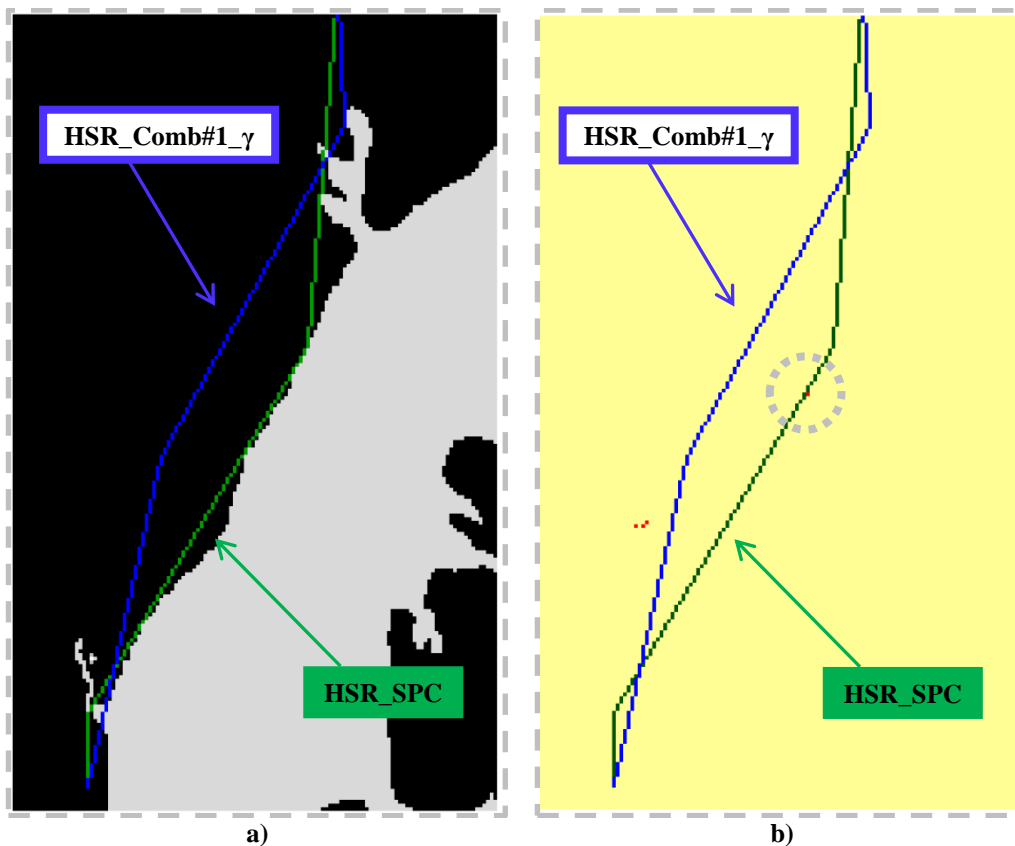


**Figure 7-12** Detail of the HSR configurations plan view between Leiria and Lisbon overlaying: a) the main rivers map with HSR\_Comb#1\_γ in dark blue and HSR\_SPC in gray and b) the elevation map with HSR\_Comb#1\_γ in black and HSR\_SPC in white.

Neither HSR configuration is significantly affected by the scenarios between Leiria and km 244.956 (Node 14) of HSR\_Comb#1\_ $\gamma$  (Figure 7-1). However, this changes from this point towards Lisbon and the performance within the dashed boxes of Figure 7-12 is discussed.

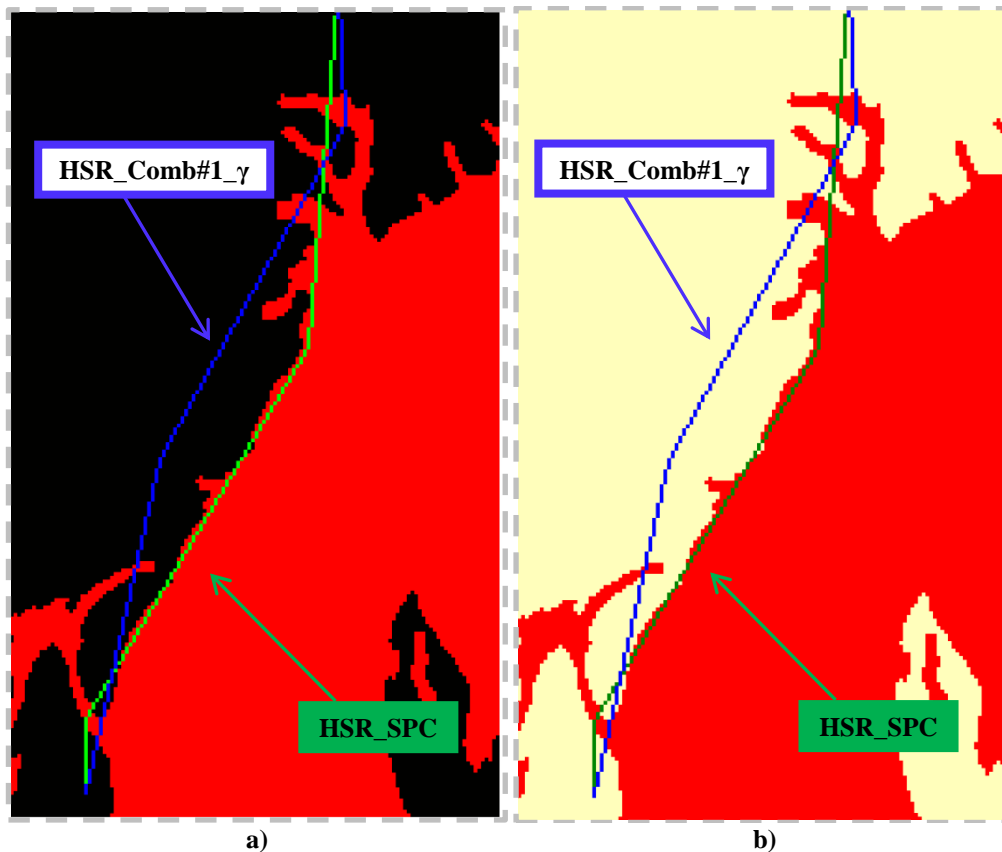
Both HSR configurations are shown overlaying the flood map (Figure 7-13a), the rainfall-triggered landslides map (Figure 7-13b), the intraplate liquefaction map (Figure 7-14a) and the interplate liquefaction map (Figure 7-14b). The intra- and interplate earthquake triggered landslides do not affect either HSR\_Comb#1\_ $\gamma$  or HSR\_SPC.

Figure 7-13a) shows that both configurations cross similar extents of flood zones. Despite running very close to the flood area of the Tagus River, the HSR\_SPC avoids it. In addition, Figure 7-13b) shows that HSR\_SPC also crosses a rainfall-triggered landslide zone (highlighted with a dashed circle). However, an even more detailed analysis allowed one to observe that the HSR\_SPC crosses this area with a tunnel, not vulnerable to the effects of the rainfall scenario's landslides.



**Figure 7-13** Detail of HSR\_Comb#1\_ $\gamma$  (blue) and HSR\_SPC (green) plan view for the dashed rectangles of Figure 7-12 overlaying: a) the flood map and b) the rainfall triggered landslides hazard map.

On the other hand, the HSR\_SPC performs poorly for earthquake-triggered liquefaction. Figure 7-14 a) and b) show how the HSR\_Comb#1\_ $\gamma$  significantly reduces the liquefaction hazard zones crossed by the HSR\_SPC. The figures show an identical effect of liquefaction induced by both the inter- and intra-plate earthquakes. This is expected as the zoomed area is within the maximum epicentral distance capable of inducing liquefaction for both seismic scenarios (section 5.4.3.2) and the liquefaction susceptibility map is identical (section 5.4.3.1).



**Figure 7-14** Detail of HSR\_Comb#1\_ $\gamma$  (blue) and HSR\_SPC (green) plan view for the dashed rectangles of Figure 7-12 overlaying: a) the intraplate liquefaction map and b) the interplate liquefaction map.

The liquefaction hazard zones are overlaid with vulnerable sections (all but tunnels) for HSR\_SPC (Figure 7-15), thus contributing to the poor earthquake-induced liquefaction performance. Conversely, Figure 7-15 shows that the HSR\_Comb#1\_ $\gamma$  avoids these areas by running westward of the liquefaction hazard zone. It can be observed that the layout avoiding the liquefaction hazards leads to a larger extent of tunnels (Figure 7-15), which explains the sharp increase of the HSR accumulated costs near Lisbon (Figure 7-4). In fact, the HSR\_SPC,

by disregarding the effects of natural hazards, optimizes the construction costs and runs in the flatter corridor next to the Tagus River. The HSR\_Comb#1\_ $\gamma$ , optimizing the robust objective function, trades off larger construction costs for an improved performance for natural hazards.

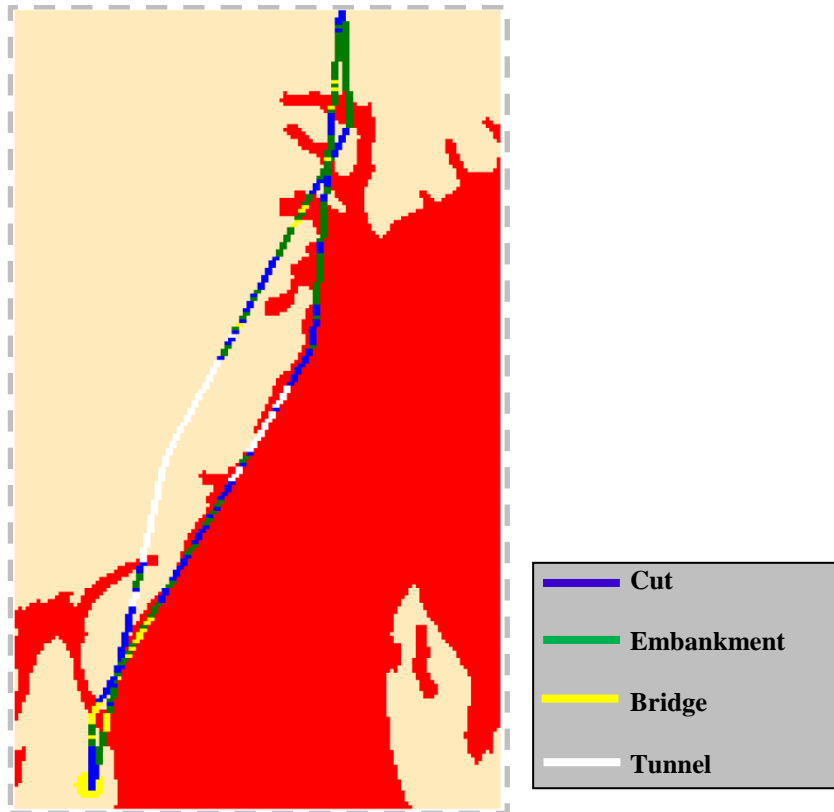


**Figure 7-15** Detail of HSR\_Comb#1\_ $\gamma$  and HSR\_SPC plan views for the dashed rectangles of Figure 7-12 overlaying the interplate liquefaction hazard map. Cross-sections are represented by different colors: cuts in blue, embankments in green, bridges in yellow and tunnels in white.

### 7.3.2 LOCATION BENEFIT COEFFICIENT $\gamma/3$ ( $\omega=1$ )

This section presents the best HSR configuration found by the SAA implementation considering the scenario combination #1 and a reduction of the location benefit coefficient, of both Aveiro and Leiria, to  $\gamma/3$ . This HSR configuration is herein termed HSR\_Comb#1\_ $\gamma/3$ . The results are compared with the best configuration found for combination #1 and location benefit coefficient  $\gamma$ , HSR\_Comb#1\_ $\gamma$ , discussed in section 7.3.1. This aims at assessing the effects of reducing the location benefit when considering the robust optimization model.

Table 7-8 presents the geometry of HSR\_Comb#1\_ $\gamma/3$  and shows the solution complies with the location, horizontal angle and gradient constraints. It links Lisbon, Coimbra and Oporto,

all horizontal angles are larger than  $120^\circ$  and all gradients are smaller than 35‰. Furthermore, HSR\_Comb#1\_γ/3 complies with the geometry normal values by having all gradients smaller than 20‰ and all horizontal angles larger than  $140^\circ$ .

The compliance with the land-use constraint is observed in Figure 7-16 b). Figure 7-16 shows the plan view of HSR\_Comb#1\_γ/3 and HSR\_Comb#1\_γ overlaying the lithological-, land-use-, expropriation cost-, elevation-, main rivers-, intraplate landslide-, intraplate liquefaction-, interplate landslide-, interplate liquefaction-, rainfall landslide- and flood- maps in a 1:1,800,000 scale..

**Table 7-8** Geometry of the configuration HSR\_Comb#1\_γ/3.

| Node | (x;y;z)<br>(km;km;m) | City    | η<br>(‰) | β<br>(°) |
|------|----------------------|---------|----------|----------|
| 1    | (80;16;108.152)      | Oporto  | -4       |          |
| 2    | (78;20;90)           |         | -3       | 153      |
| 3    | (78;48;10)           |         | 0        | 175      |
| 4    | (76;72;10)           | Aveiro  | 2        | 156      |
| 5    | (88;106;100)         |         | -7       | 179      |
| 6    | (92;118;13.106)      | Coimbra | 15       | 162      |
| 7    | (92;130;190)         |         | -3       | 180      |
| 8    | (92;140;160)         |         | 15       | 180      |
| 9    | (92;148;280)         |         | -8       | 174      |
| 10   | (90;168;120)         |         | 1        | 162      |
| 11   | (94;186;130)         |         | -5       | 149      |
| 12   | (88;204;40)          |         | 0        | 161      |
| 13   | (62;238;50)          |         | -1       | 172      |
| 14   | (50;250;30)          |         | 2        | 170      |
| 15   | (36;270;90)          |         | -6       | 156      |
| 16   | (34;280;32.348)      | Lisbon  |          |          |



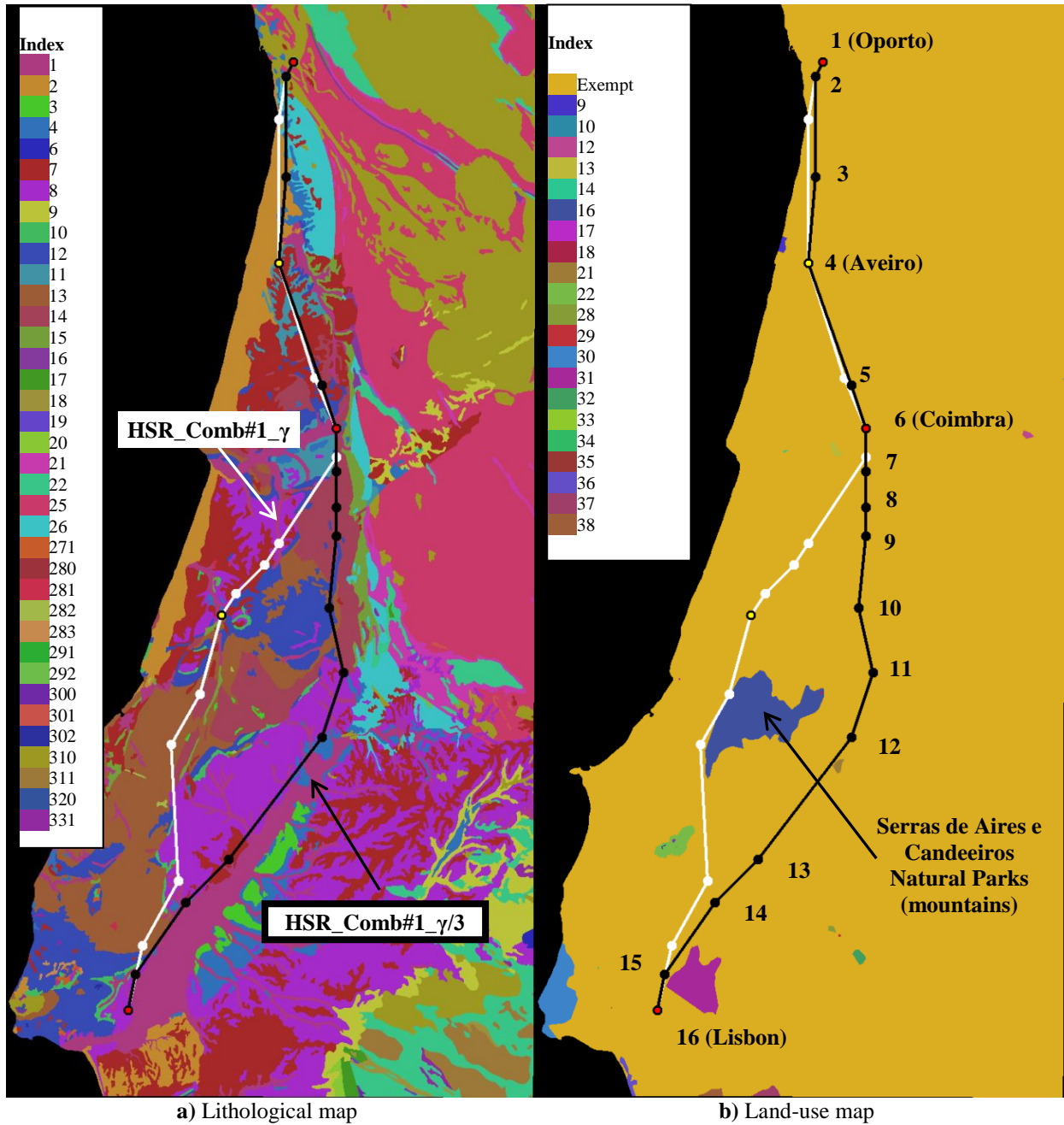


**Figure 7-16** Plan view overlay of configurations HSR\_Comb#1\_γ/3 and HSR\_Comb#1\_γ (section 7.3.1): a) lithological map, b) land-use map, c) expropriation cost map, d) elevation map, e) main rivers map, f) intraplate landslide map, g) intraplate liquefaction map, h) interplate landslide map, i) interplate liquefaction map, j) rainfall landslide map and k) flood map. HSR\_Comb#1\_γ in white and HSR\_Comb#1\_γ/3 in black in a), b), c), d) and e). HSR\_Comb#1\_γ in gray and HSR\_Comb#1\_γ/3 in blue in f), g), h), i), j) and k). Node numbers of HSR\_Comb#1\_γ/3 are identified in b). Zoom-ins of the dashed boxes of g), i) and k) are presented in Figures 20, 21 and 22.

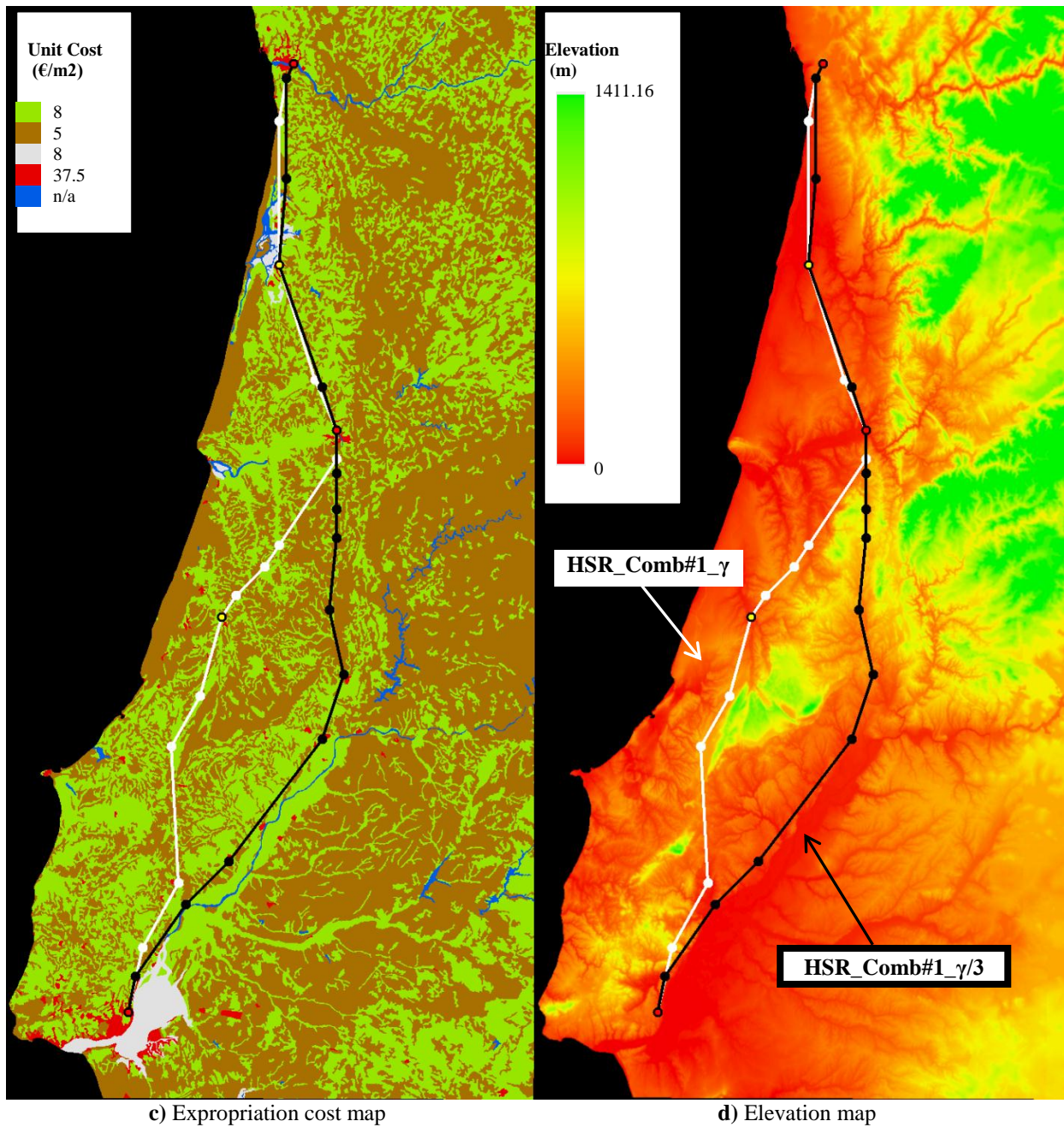


**Figure 7-16** Plan view overlay of configurations HSR\_Comb#1\_ $\gamma/3$  and HSR\_Comb#1\_ $\gamma$  (section 7.3.1): a) lithological map, b) land-use map, c) expropriation cost map, d) elevation map, e) main rivers map, f) intraplate landslide map, g) intraplate liquefaction map, h) interplate landslide map, i) interplate liquefaction map, j) rainfall landslide map and k) flood map. HSR\_Comb#1\_ $\gamma$  in white and HSR\_Comb#1\_ $\gamma/3$  in black in a), b), c), d) and e). HSR\_Comb#1\_ $\gamma$  in gray and HSR\_Comb#1\_ $\gamma/3$  in blue in f), g), h), i), j) and k). Node numbers of HSR\_Comb#1\_ $\gamma/3$  are identified in b). Zoom-ins of the dashed boxes of g), i) and k) are presented in Figures 20, 21 and 22. (Continued).

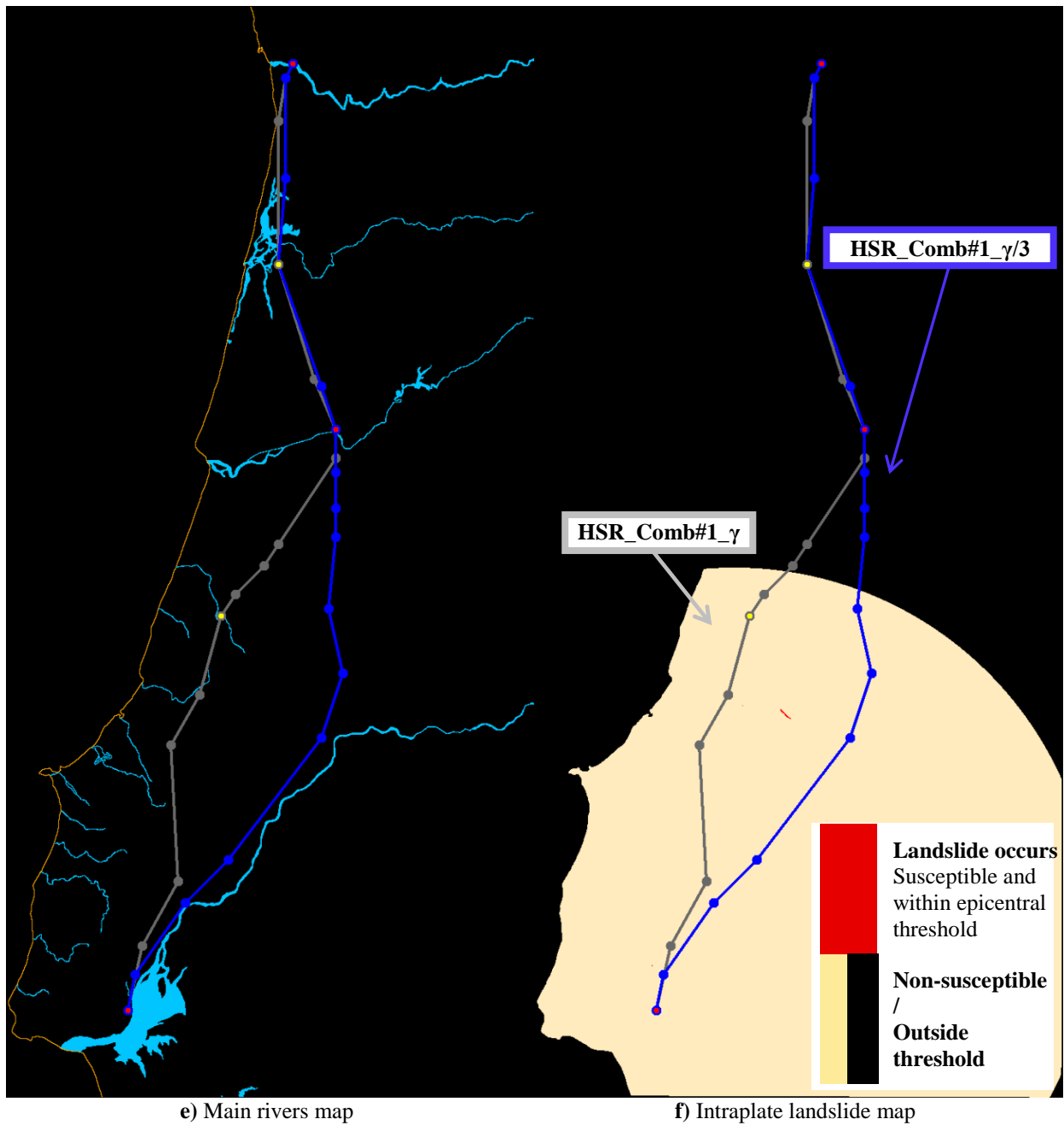


**Figure 7-16** Plan view overlay of configurations HSR\_Comb#1\_γ/3 and HSR\_Comb#1\_γ (section 7.3.1): a) lithological map, b) land-use map, c) expropriation cost map, d) elevation map, e) main rivers map, f) intraplate landslide map, g) intraplate liquefaction map, h) interplate landslide map, i) interplate liquefaction map, j) rainfall landslide map and k) flood map. HSR\_Comb#1\_γ in white and HSR\_Comb#1\_γ/3 in black in a), b), c), d) and e). HSR\_Comb#1\_γ in gray and HSR\_Comb#1\_γ/3 in blue in f), g), h), i), j) and k). Node numbers of HSR\_Comb#1\_γ/3 are identified in b). Zoom-ins of the dashed boxes of g), i) and k) are presented in Figures 20, 21 and 22. (Continued).

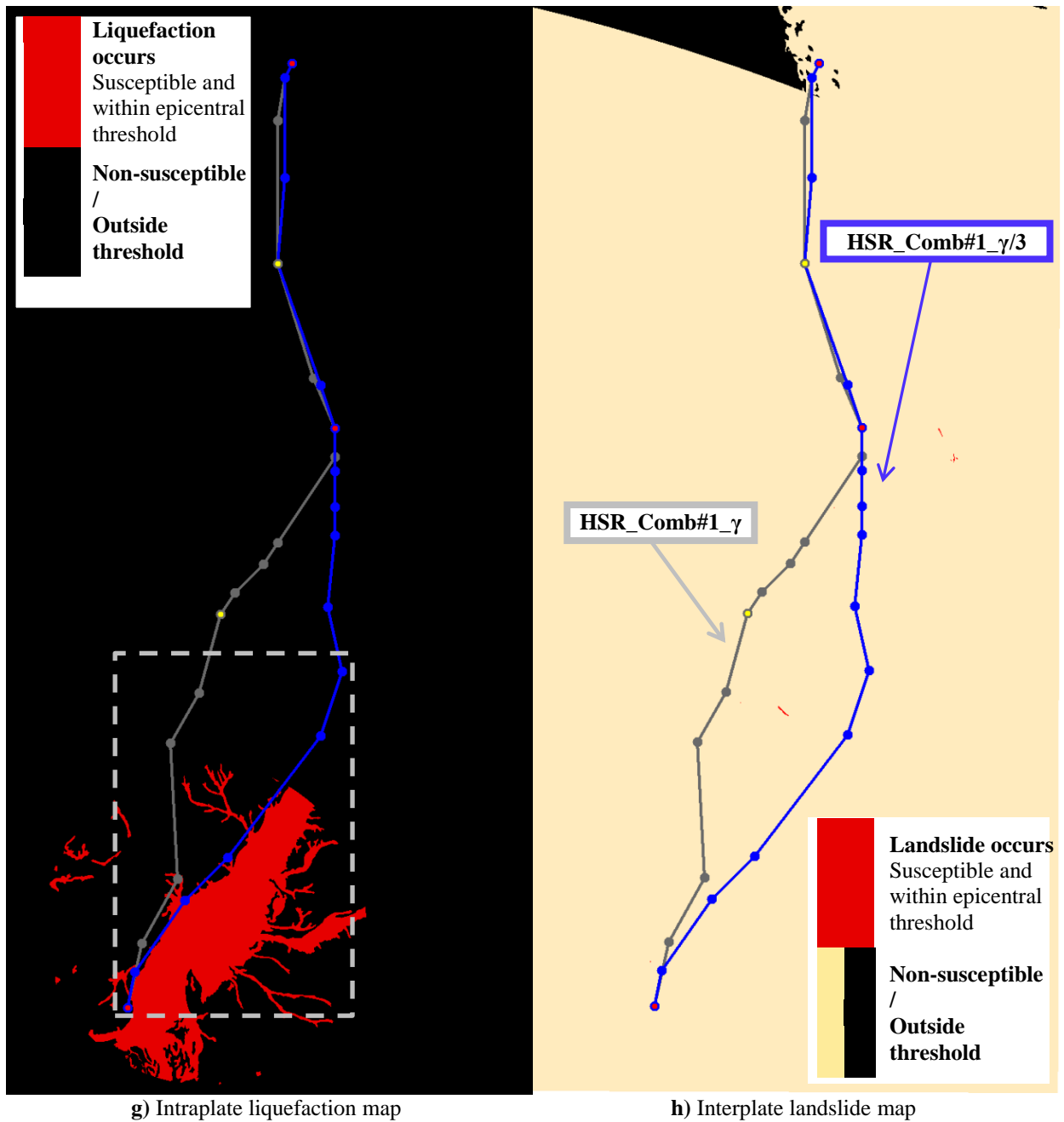


**Figure 7-16** Plan view overlay of configurations HSR\_Comb#1\_ $\gamma/3$  and HSR\_Comb#1\_ $\gamma$  (section 7.3.1): a) lithological map, b) land-use map, c) expropriation cost map, d) elevation map, e) main rivers map, f) intraplate landslide map, g) intraplate liquefaction map, h) interplate landslide map, i) interplate liquefaction map, j) rainfall landslide map and k) flood map. HSR\_Comb#1\_ $\gamma$  in white and HSR\_Comb#1\_ $\gamma/3$  in black in a), b), c), d) and e). HSR\_Comb#1\_ $\gamma$  in gray and HSR\_Comb#1\_ $\gamma/3$  in blue in f), g), h), i), j) and k). Node numbers of HSR\_Comb#1\_ $\gamma/3$  are identified in b). Zoom-ins of the dashed boxes of g), i) and k) are presented in Figures 20, 21 and 22. (Continued).

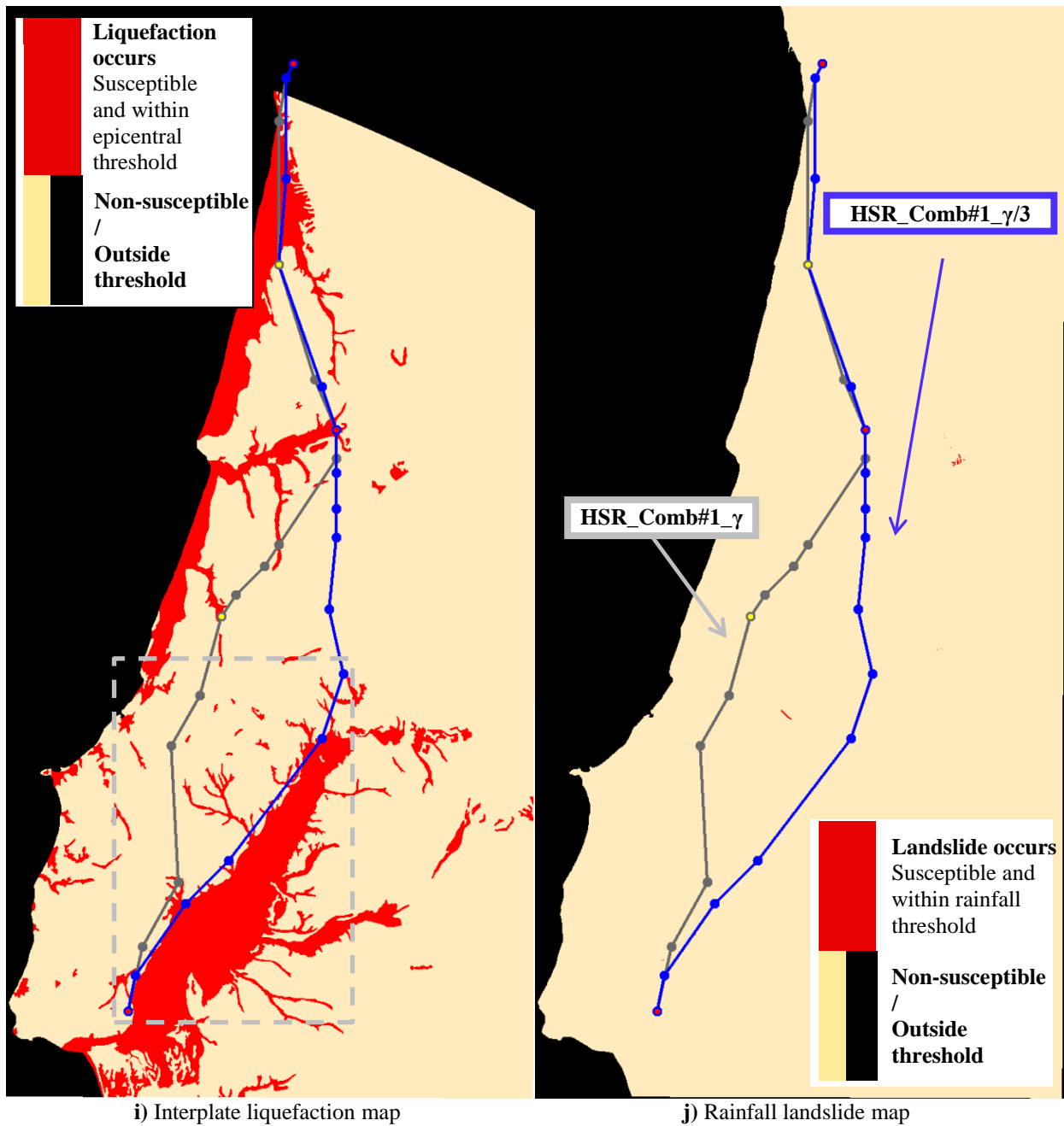
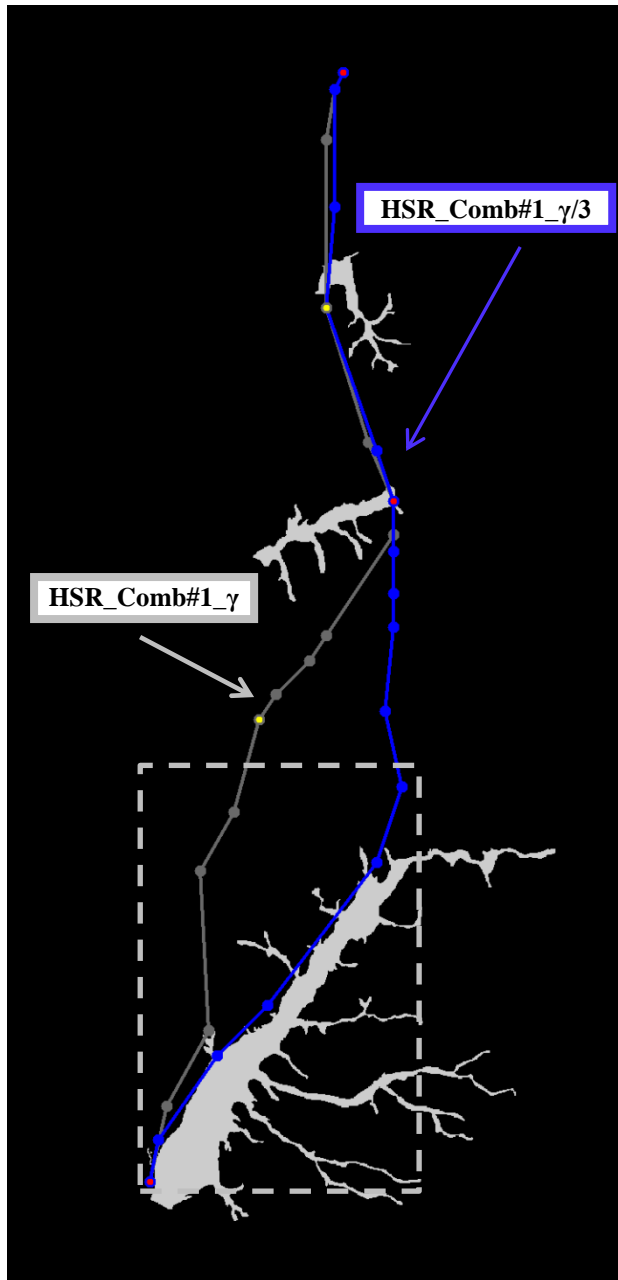


**Figure 7-16** Plan view overlay of configurations HSR\_Comb#1\_ $\gamma/3$  and HSR\_Comb#1\_ $\gamma$  (section 7.3.1): a) lithological map, b) land-use map, c) expropriation cost map, d) elevation map, e) main rivers map, f) intraplate landslide map, g) intraplate liquefaction map, h) interplate landslide map, i) interplate liquefaction map, j) rainfall landslide map and k) flood map. HSR\_Comb#1\_ $\gamma$  in white and HSR\_Comb#1\_ $\gamma/3$  in black in a), b), c), d) and e). HSR\_Comb#1\_ $\gamma$  in gray and HSR\_Comb#1\_ $\gamma/3$  in blue in f), g), h), i), j) and k). Node numbers of HSR\_Comb#1\_ $\gamma/3$  are identified in b). Zoom-ins of the dashed boxes of g), i) and k) are presented in Figures 20, 21 and 22. (Continued).



k) Flood map

**Figure 7-16** Plan view overlay of configurations HSR\_Comb#1\_ $\gamma/3$  and HSR\_Comb#1\_ $\gamma$  (section 7.3.1): a) lithological map, b) land-use map, c) expropriation cost map, d) elevation map, e) main rivers map, f) intraplate landslide map, g) intraplate liquefaction map, h) interplate landslide map, i) interplate liquefaction map, j) rainfall landslide map and k) flood map. HSR\_Comb#1\_ $\gamma$  in white and HSR\_Comb#1\_ $\gamma/3$  in black in a), b), c), d) and e). HSR\_Comb#1\_ $\gamma$  in gray and HSR\_Comb#1\_ $\gamma/3$  in blue in f), g), h), i), j) and k). Node numbers of HSR\_Comb#1\_ $\gamma/3$  are identified in b). Zoom-ins of the dashed boxes of g), i) and k) are presented in Figures 20, 21 and 22. (Continued).

Figure 7-16 shows that by reducing the location benefit from  $\gamma$  to  $\gamma/3$ , the best solution found by the SAA does not connect Leiria and, instead, runs eastward of the Serras de Aires e Candeeiros Natural Parks (Figure 7-16b). The plan views of both HSR\_Comb#1\_ $\gamma/3$  and HSR\_Comb#1\_ $\gamma$  are similar between Oporto and Coimbra, differing substantially between Coimbra and Lisbon.

The plan view differences also correspond to different ground and HSR longitudinal profiles and cross-sections (Figure 7-17). Between Oporto and km 30 the ground profiles differ but the elevation of HSR\_Comb#1\_ $\gamma/3$  adjusts to reduce the need of bridges and tunnels. The HSR\_Comb#1\_ $\gamma/3$ , similarly to HSR\_Comb#1\_ $\gamma$ , avoids the extensive overlay of interplate earthquake-induced liquefaction (Figure 7-16 i) and flood (Figure 7-16 k) hazard zones observed for HSR\_SPC (section 7.3.1), which runs parallel to the Mondego River (Figure 7-1 i) and k). Also similarly to HSR\_Comb#1\_ $\gamma$ , the HSR\_Comb#1\_ $\gamma/3$  improves the configuration layout from the HSR\_SPC by increasing all horizontal angles to values larger than 140°.

From Coimbra towards Lisbon, large differences are observed in both the ground elevation and the HSR longitudinal profile, as expected, given the differences observed in the plan view. The total length of the configurations, however, is similar: the HSR\_Comb#1\_ $\gamma/3$  is 287.156 km long, 3.170 km lengthier than HSR\_Comb#1\_ $\gamma$ .

By running eastward of the Serras de Aires e Candeeiros Natural Parks, the HSR\_Comb#1\_ $\gamma/3$  avoids crossing 2 rivers crossed by HSR\_Comb#1\_ $\gamma$  south of Leiria (Figure 7-16e). Figure 7-16d) shows that HSR\_Comb#1\_ $\gamma/3$  is also surrounded by larger elevation variations between Coimbra and node 11 (km 173.799) but manages to find a corridor which does not require an extensive construction of bridges or tunnels (Figure 7-17). The plan views approximate around node 14 of HSR\_Comb#1\_ $\gamma/3$  and from this point towards Lisbon, the HSR\_Comb#1\_ $\gamma/3$  is formed mainly by bridges and tunnels.

The objective function value of HSR\_Comb#1\_ $\gamma/3$  and its respective breakdown are analyzed and compared in Table 7-9 with the value (in Million €) of HSR\_Comb#1\_ $\gamma$  when one considers a location benefit of  $\gamma/3$  for both Aveiro and Leiria and  $\omega=1$ .

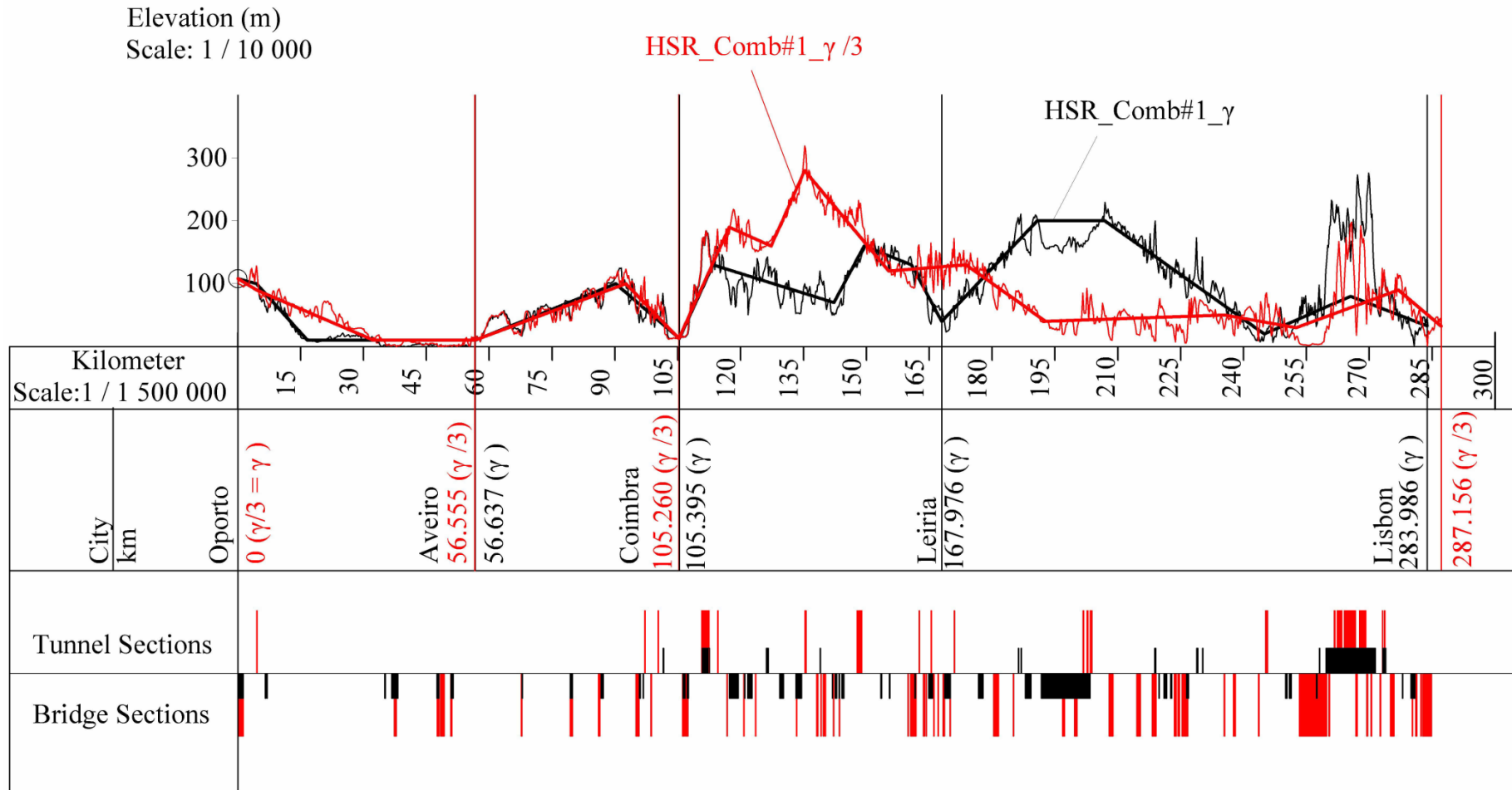


**Figure 7-17** Comparison of the longitudinal profiles of HSR\_Comb#1\_γ/3 (in red) and HSR\_Comb#1\_γ (in black).



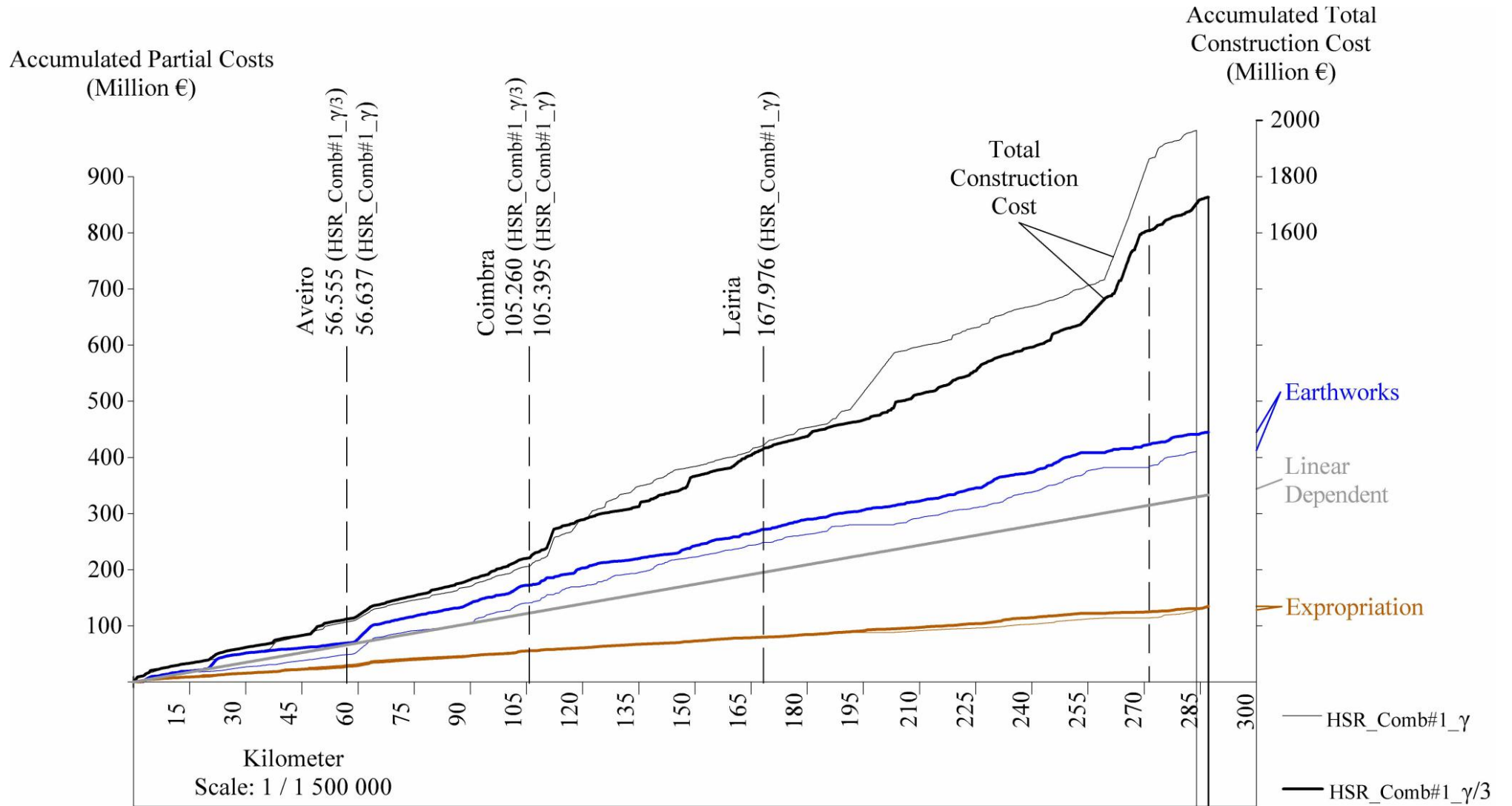
**Table 7-9** Value of both HSR\_Comb#1\_γ/3 and HSR\_Comb#1\_γ considering the Combination#1, the location benefit coefficient of γ/3 and ω=1.

| HSR Configuration  | Value for Combination#1 and Location Benefit of γ/3 (Million €) |                | HSR_Comb#1_γ/3 / HSR_Comb#1_γ (%) |
|--|---|----------------|-----------------------------------|
|  | HSR_Comb#1_γ/3  | HSR_Comb#1_γ   |                                   |
| <b>Objective Function Value</b>  | <b>1748.93</b>  | <b>1848.03</b> | 95%                               |
| <b>SPC (1 + 2 + 3 - 4)</b>   | 1640.80   | 1768.26        | 93%                               |
| 1. CONSTRUCTION COST<br>(1.1+1.2+1.3+1.4+1.5)                            | 1727.15   | 1964.73        | 88%                               |
| 1.1 Expropriation  | 134.80  | 128.11         | 105%                              |
| 1.2 Earthworks   | 444.90  | 410.23         | 108%                              |
| 1.3 ALL BRIDGES  | 426.02  | 521.29         | 82%                               |
| 1.4 ALL TUNNELS  | 388.33  | 575.68         | 67%                               |
| 1.5 LINEAR- DEPENDENT COSTS  | 333.10  | 329.42         | 101%                              |
| 2. GEOMETRY PENALTY  | 0.00  | 0.00           | -                                 |
| 3. LAND-USE PENALTY  | 0.00  | 0.00           | -                                 |
| 4. LOCATION BENEFIT  | 86.36   | 196.47         | 44%                               |
| 5. $\sum_{c \in \Omega_{sc}} \Psi_c \sum_{(i,j) \in \Omega_N} RC_{ij}^c$ | 108.13  | 79.77          | 136%                              |
| 5.1 $\sum_{(i,j) \in \Omega_N} RC_{ij}^{Rainfall}$                       | 46.88   | 28.97          | 162%                              |
| 5.2 $\sum_{(i,j) \in \Omega_N} RC_{ij}^{Intraplate}$                     | 71.44   | 29.09          | 246%                              |
| 5.3 $\sum_{(i,j) \in \Omega_N} RC_{ij}^{Interplate}$                     | 206.26  | 181.39         | 114%                              |

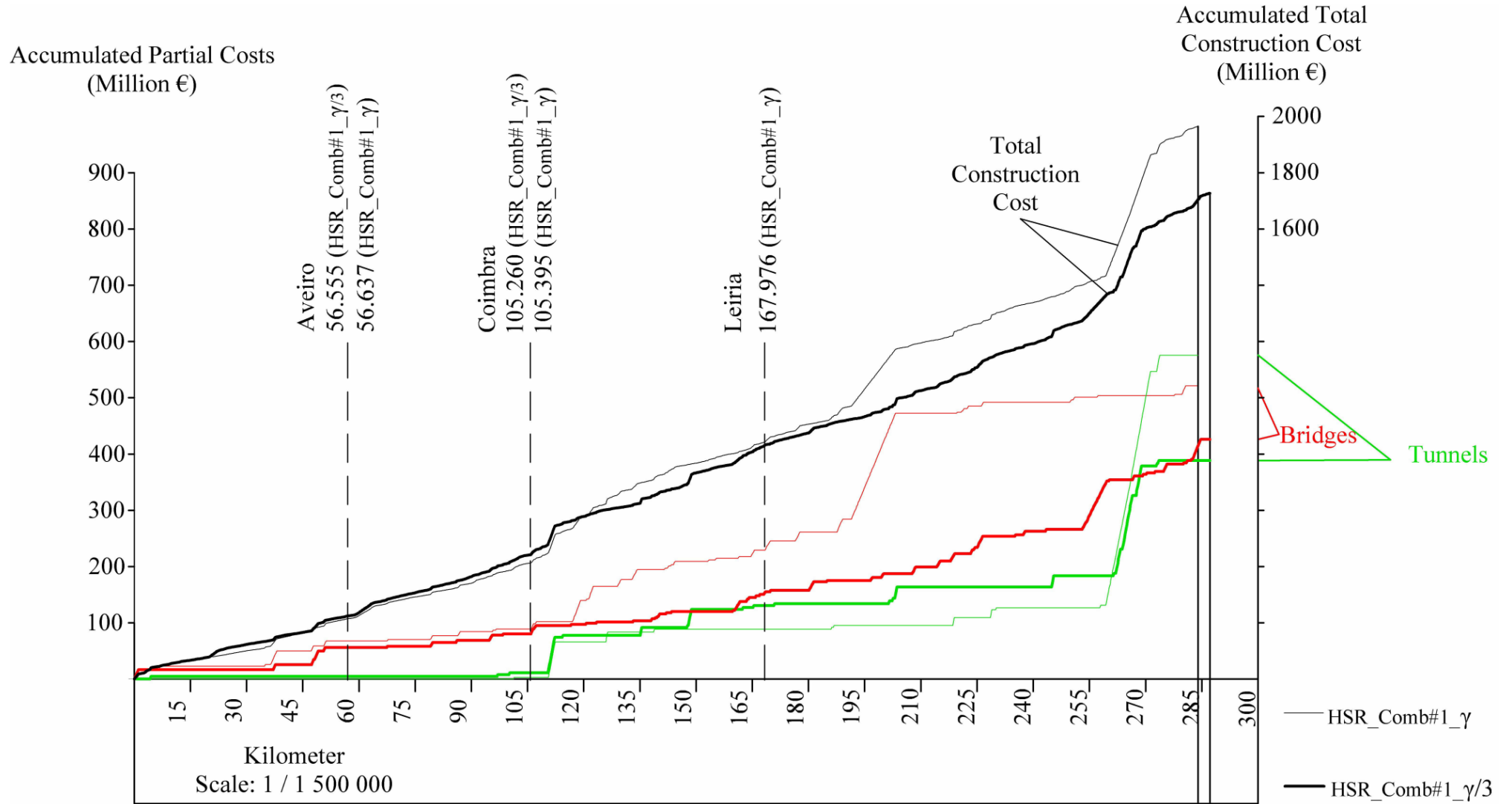
Table 7-9 shows that the objective function value of HSR\_Comb#1\_γ/3 is 5% smaller than that of HSR\_Comb#1\_γ, when scenario combination#1 and γ/3 location benefit coefficients are considered. This is obtained by a trade-off between the construction costs, the location benefit and the natural hazards performance (geometry and land-use penalties are both null).

HSR\_Comb#1\_γ/3 reduces the construction costs of HSR\_Comb#1\_γ by 12% with smaller costs for bridges and tunnels (respectively 82% and 67% of those of HSR\_Comb#1\_γ) but larger costs for expropriation, earthworks and linear-dependent costs. The smaller construction costs (237.58 Million € difference) are partly counteracted by the lower location benefit, by not linking Leiria, and a worst scenario combination performance. The weighted scenario cost of HSR\_Comb#1\_γ/3 is 136% of that of HSR\_Comb#1\_γ, mainly due to the worst intraplate earthquake and rainfall scenarios performance. However, the effects of the construction costs prevail and the HSR\_Comb#1\_γ/3 has a lower objective function value. This shows that as the location benefit is reduced, a more economical solution, in terms of

construction costs, can be achieved. Figure 7-18 and Figure 7-19 show the evolution of the accumulated construction costs along the longitudinal profile.



**Figure 7-18** Accumulated costs along the longitudinal profile: total construction costs, earthworks, linear- dependent and expropriation. Costs for HSR\_Comb#1\_γ/3 represented in a thick line and for HSR\_Comb#1\_γ in a thin line.



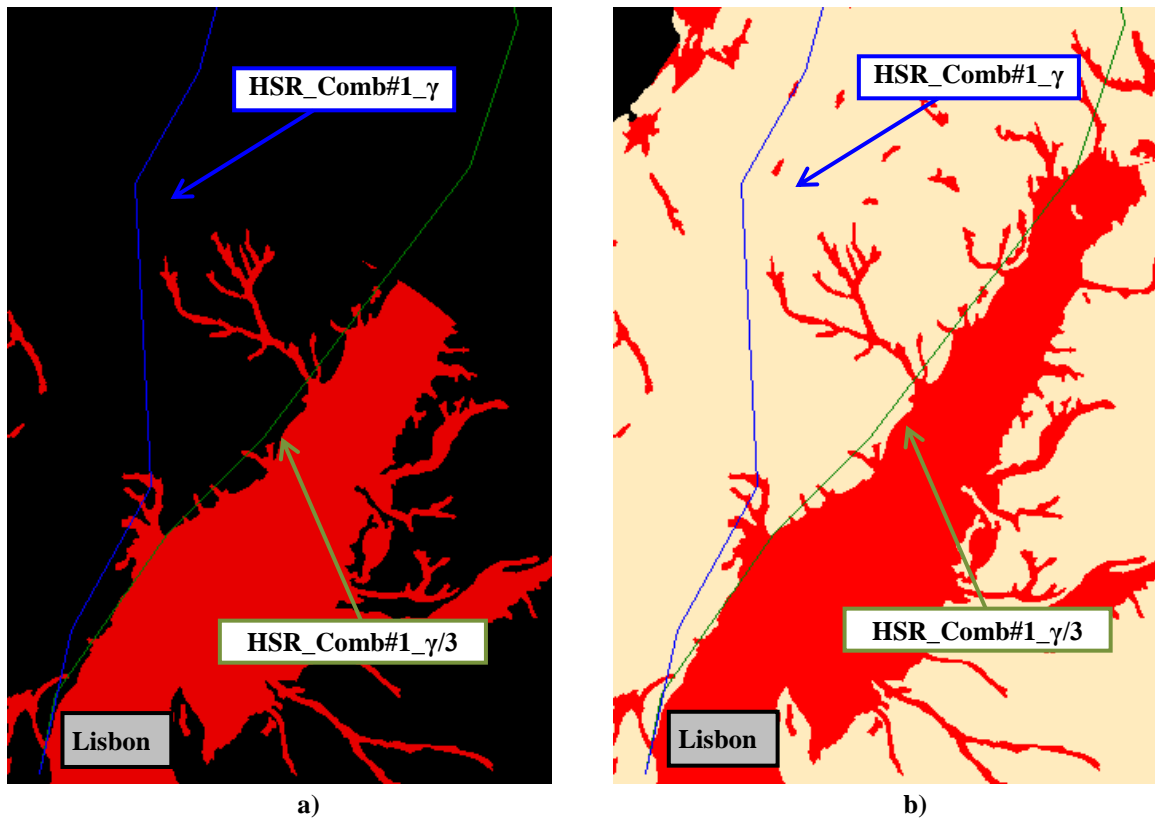
**Figure 7-19** Accumulated costs along the longitudinal profile: total construction costs, bridges and tunnels. Costs for HSR\_Comb#1\_γ/3 represented in a thick line and for HSR\_Comb#1\_γ in a thin line.

Figure 7-18 shows the larger costs of earthworks, expropriation and linear-dependent costs have a similar and rising trend. It also shows that the accumulated total construction costs of both HSR\_Comb#1\_ $\gamma/3$  and HSR\_Comb#1\_ $\gamma$  are similar from Oporto until circa km 190. However, from this point to Lisbon, the construction cost of HSR\_Comb#1\_ $\gamma/3$  increases less sharply, given the smaller extent built on bridges and tunnels (Figure 7-19). These cost differences correspond to the HSR crossing eastward (HSR\_Comb#1\_ $\gamma/3$ ) and westward (HSR\_Comb#1\_ $\gamma$ ) of Serras de Aires e Candeeiros Natural Parks. By running to the West the HSR\_Comb#1\_ $\gamma$  connects Leiria and, when the  $\gamma$  benefit is considered, improves the objective function value by compensating the larger construction costs. On the other hand, when the benefit coefficient is reduced to  $\gamma/3$ , the impact of connecting Leiria in the objective function value is smaller and does not compensate the larger construction costs.

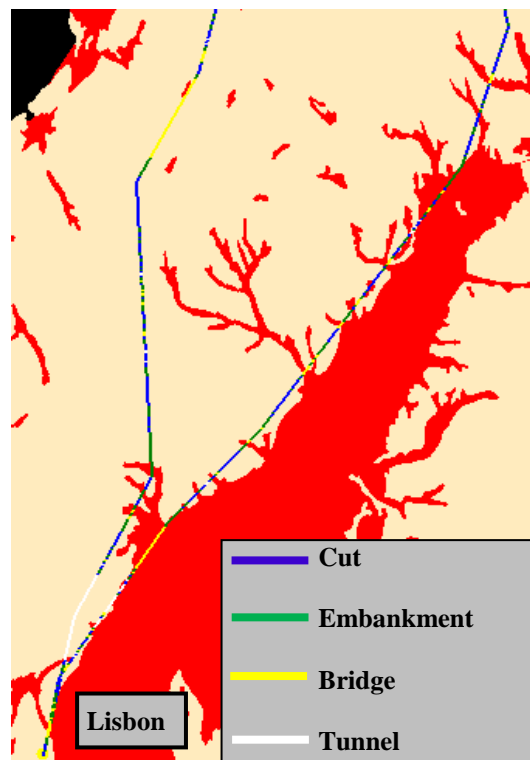
In addition to the effects of the construction costs and the location benefit, both solutions differ in the weighted natural hazards performance. Between Oporto and km 113, just south of Coimbra, both the plan views (Figure 7-16) and the cross-sections (Figure 7-17, Figure 7-18 and Figure 7-19) are similar, thus having similar exposure and vulnerability. South of this point, the plan views differ which results in a larger exposure of HSR\_Comb#1\_ $\gamma/3$ , particularly to the effects of floods and liquefaction. Landslide hazard zones, both earthquake- and rainfall-triggered, are not overlaid by the infrastructure (Figure 7-16 f), h) and j).

Figure 7-20 shows how HSR\_Comb#1\_ $\gamma/3$  overlays a larger extent of both the intraplate (Figure 7-20 a) and interplate (Figure 7-20 b) liquefaction hazard zones than HSR\_Comb#1\_ $\gamma$ . Furthermore, most of the HSR\_Comb#1\_ $\gamma/3$  overlaying the liquefaction hazard zones is built on cuts, embankments or bridges (Figure 7-21), subject to liquefaction damages (section 5.4.3.3).

The extent of flood hazard zones overlaid by HSR\_Comb#1\_ $\gamma/3$  is also larger than that of HSR\_Comb#1\_ $\gamma$  (Figure 7-22 a). However, a significant part of the configuration overlaying the flood areas is built on bridges (Figure 7-22 b), not vulnerable to the effects of the rainfall scenario floods (section 5.5.3.1). Thus, the cost of damages repair is larger for liquefaction than for rainfall (Table 7-9).



**Figure 7-20** Detail of HSR\_Comb#1\_γ (blue) and HSR\_Comb#1\_γ/3 (green) plan views for the dashed rectangles of Figure 7-16 overlaying: a) intraplate earthquake-induced liquefaction map b) interplate earthquake-induced liquefaction map.



**Figure 7-21** Detail of HSR\_Comb#1\_γ and HSR\_Comb#1\_γ/3 plan view for the dashed rectangle of Figure 7-16 overlaying the interplate earthquake-induced liquefaction hazard map. Cross-sections identified by different colors.

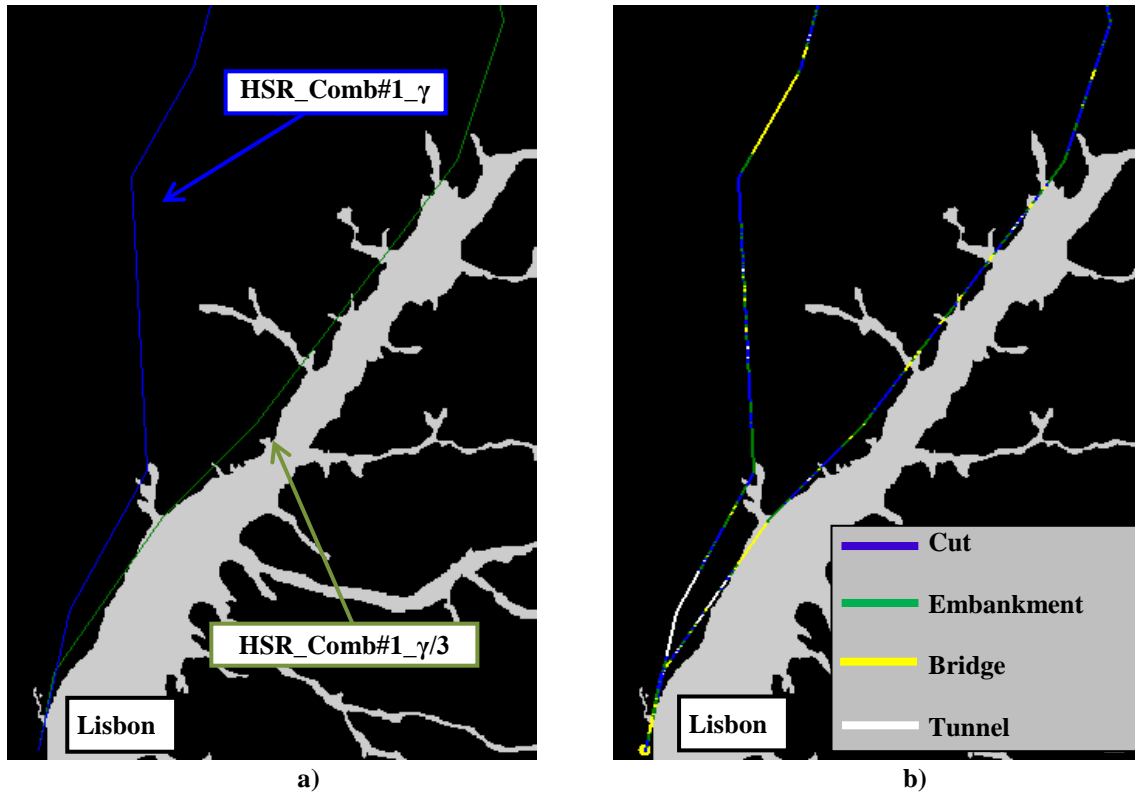


**Figure 7-22** Detail of HSR\_Comb#1\_γ and HSR\_Comb#1\_γ/3 plan views for the dashed rectangle of Figure 7-16 overlaying the flood hazard map: a) HSR\_Comb#1\_γ in blue and HSR\_Comb#1\_γ/3 in green and b) cross-sections of both configurations represented by different colors.

This section shows how reducing of the benefit of connecting each of Aveiro and Leiria to one-third and considering the scenario combination #1 results in a robust solution that connects only Aveiro but not Leiria. The improved objective function value for such conditions is obtained by smaller construction costs, albeit the smaller location benefit and larger costs for the weighted scenario performance.

### 7.3.3 LOCATION BENEFIT COEFFICIENT $\gamma/3$ ( $\omega=30$ )

This section analyses the influence of increasing the importance attributed by the decision-maker to the joint effects of natural hazards. This is illustrated by increasing  $\omega=1$  to  $\omega=30$ . The weight  $\omega$  multiplies the weighted-scenario performance,  $\sum_{c \in Q_{sc}} \Psi_c \sum_{(i,j) \in Q_N} RC_{ij}^c$ , in the robust objective function of expression (4.10).  $\omega$  is used to find optimal or near-optimal HSR configurations establishing different trade-offs between the HSR performance for natural hazards and the HSR performance in SPC. The previous application results of sections 7.3.1

and 7.3.2 consider  $\omega=1$ . The larger the value of  $\omega$ , the larger the influence of the natural hazards performance in the robust objective function and the less affected by natural hazards the robust solutions are expected to be.

SAA runs are performed to solve the application of the robust approach and the best solution found, termed HSR\_Comb#1\_ $\gamma/3$ \_ $\omega 30$ , is compared with HSR\_Comb#1\_ $\gamma/3$  (section 7.3.2). Both configurations are obtained for applications differing only by the value of  $\omega$ .

Table 7-10 presents the geometry of HSR\_Comb#1\_ $\gamma/3$ \_ $\omega 30$ . Table 7-10 shows the configuration complies with the location constraints, connecting Lisbon, Coimbra and Oporto, but does not connect either Aveiro or Leiria. Despite not connecting Leiria at the corresponding node located at  $(x; y; z) = (60 \text{ km}; 170 \text{ km}; 100 \text{ m})$ , the HSR\_Comb#1\_ $\gamma/3$ \_ $\omega 30$  configuration connects an adjacent node. This is the configuration's node number 10 (Table 7-10) located at  $(x; y; z) = (62 \text{ km}; 170 \text{ km}; 100 \text{ m})$ . It is defined in section 7.1.3 that half of the coefficients value,  $\gamma_v^{Aveiro}$  and  $\gamma_v^{Leiria}$ , is considered if the plan views of adjacent nodes are connected. This illustrates how different possible locations for the HSR station, within the city surroundings, can differ in overall value added to the HSR network by decreasing, for example, its accessibility. While solutions were found for the previous robust applications that link Leiria (HSR\_Comb#1\_ $\gamma$ ) and that did not link Leiria (HSR\_Comb#1\_ $\gamma/3$ ), both did connect Aveiro which HSR\_Comb#1\_ $\gamma/3$ \_ $\omega 30$  does not.

Table 7-10 also shows HSR\_Comb#1\_ $\gamma/3$ \_ $\omega 30$  complies with both the normal and limit geometry values, having all horizontal angles larger than  $140^\circ$  and all gradients smaller than 20%. The compliance with the land-use constraint is observed in Figure 7-23 b). Figure 7-23 shows the plan view of HSR\_Comb#1\_ $\gamma/3$ \_ $\omega 30$  and HSR\_Comb#1\_ $\gamma/3$  overlaying the lithological-, land-use-, expropriation cost-, elevation-, main rivers-, intraplate landslide-, intraplate liquefaction-, interplate landslide-, interplate liquefaction-, rainfall landslide- and flood- maps in a 1:1,800,000 scale.



**Table 7-10** Geometry of the configuration HSR\_Comb#1\_γ/3\_ω30

| <b>Node</b> | <b>(x;y;z)</b><br><b>(km;km;m)</b> | <b>City</b> | <b>η</b><br><b>(‰)</b> | <b>β</b><br><b>(°)</b> |
|-------------|------------------------------------|-------------|------------------------|------------------------|
| 1           | (80;16;108.152)                    | Oporto      | -4                     |                        |
| 2           | (78;20;110)                        |             | 0                      | 170                    |
| 3           | (88;68;100)                        |             | 3                      | 167                    |
| 4           | (96;84;50)                         |             | -7                     | 148                    |
| 5           | (96;100;120)                       |             | -4                     | 153                    |
| 6           | (92;118;13.106)                    | Coimbra     | 18                     | 143                    |
| 7           | (96;132;280)                       |             | 2                      | 154                    |
| 8           | (90;154;230)                       |             | 13                     | 173                    |
| 9           | (80;164;280)                       |             | -7                     | 174                    |
| 10          | (62;170;100)                       |             | 1                      | 162                    |
| 11          | (50;188;110)                       |             | -5                     | 149                    |
| 12          | (48;204;180)                       |             | 0                      | 161                    |
| 13          | (46;208;190)                       |             | -1                     | 172                    |
| 14          | (48;232;60)                        |             | 2                      | 170                    |
| 15          | (42;242;150)                       |             | -6                     | 156                    |
| 16          | (34;280;32.348)                    | Lisbon      |                        |                        |

Figure 7-23 shows that the consideration of  $\omega=30$  instead of  $\omega=1$ , has a significant impact on the plan view of the HSR layout. The horizontal projection of HSR\_Comb#1\_γ/3\_ω30 differs almost entirely from that of HSR\_Comb#1\_γ/3, exceptions made for the extension between Coimbra and node 8 of HSR\_Comb#1\_γ/3\_ω30 and in a small stretch that connects Lisbon.

Between Oporto and Coimbra, the HSR\_Comb#1\_γ/3\_ω30 configuration does not connect Aveiro and runs to the east of HSR\_Comb#1\_γ/3. Between Coimbra and Lisbon, HSR\_Comb#1\_γ/3\_ω30 crosses adjacent to Leiria and westward of the Serras de Aires e Candeeiros Natural Parks.

The differences in the layouts of the configurations are also observed in the longitudinal profile of Figure 7-24.

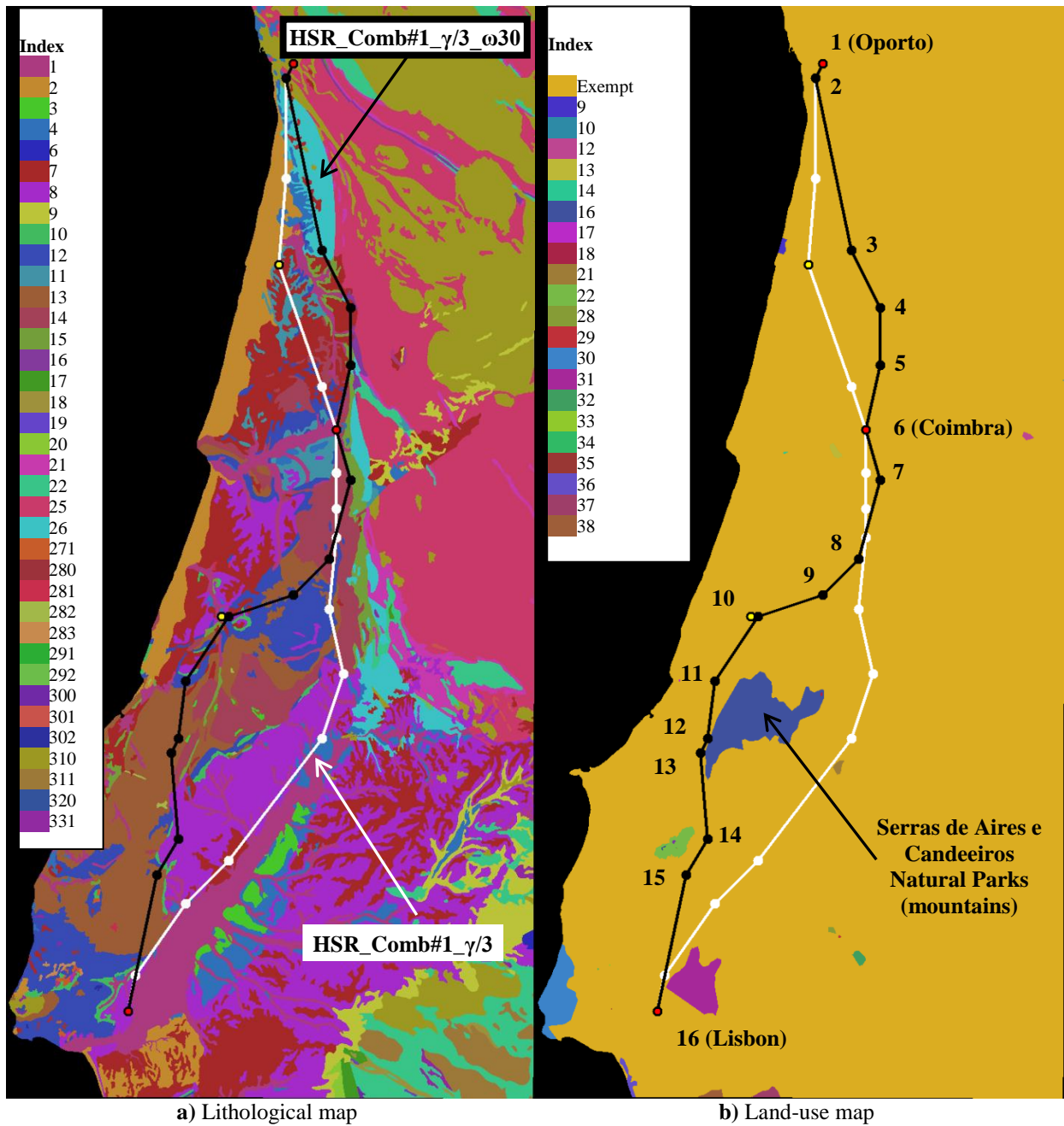


**Figure 7-23** Plan view overlay of configurations HSR\_Comb#1\_γ/3\_ω30 and HSR\_Comb#1\_γ/3: a) lithological map, b) land-use map, c) expropriation cost map, d) elevation map, e) main rivers map, f) intraplate landslide map, g) intraplate liquefaction map, h) interplate landslide map, i) interplate liquefaction map, j) rainfall landslide map and k) flood map. HSR\_Comb#1\_γ/3\_ω30 in black and HSR\_Comb#1\_γ/3 in white in a), b), c), d) and e). HSR\_Comb#1\_γ/3\_ω30 in blue and HSR\_Comb#1\_γ/3 in gray in f), g), h), i), j) and k). Node numbers of HSR\_Comb#1\_γ/3\_ω30 are identified in b).

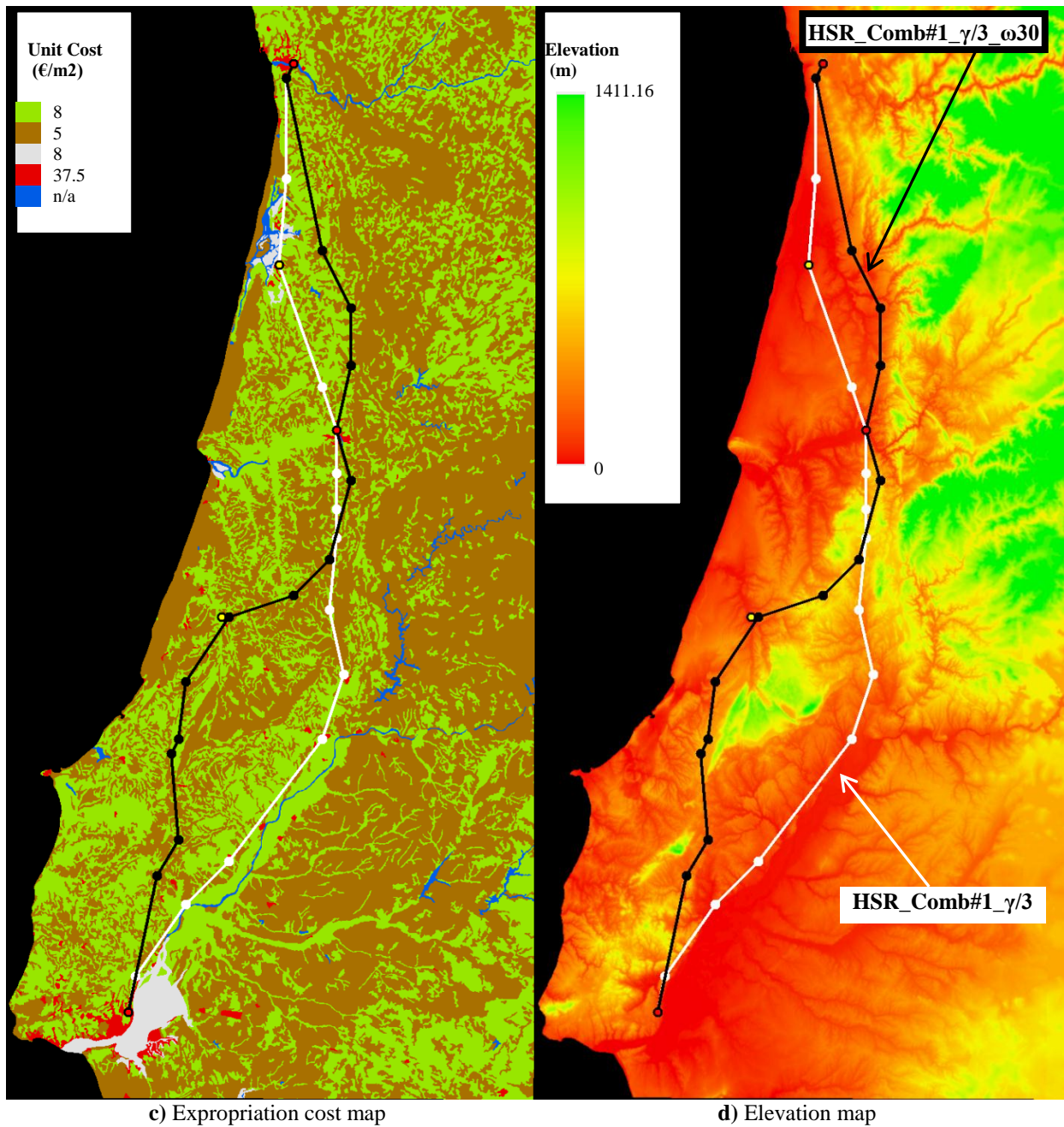


**Figure 7-23** Plan view overlay of configurations HSR\_Comb#1\_γ/3\_ω30 and HSR\_Comb#1\_γ/3: a) lithological map, b) land-use map, c) expropriation cost map, d) elevation map, e) main rivers map, f) intraplate landslide map, g) intraplate liquefaction map, h) interplate landslide map, i) interplate liquefaction map, j) rainfall landslide map and k) flood map. HSR\_Comb#1\_γ/3\_ω30 in black and HSR\_Comb#1\_γ/3 in white in a), b), c), d) and e). HSR\_Comb#1\_γ/3\_ω30 in blue and HSR\_Comb#1\_γ/3 in gray in f), g), h), i), j) and k). Node numbers of HSR\_Comb#1\_γ/3\_ω30 are identified in b). (Continued).

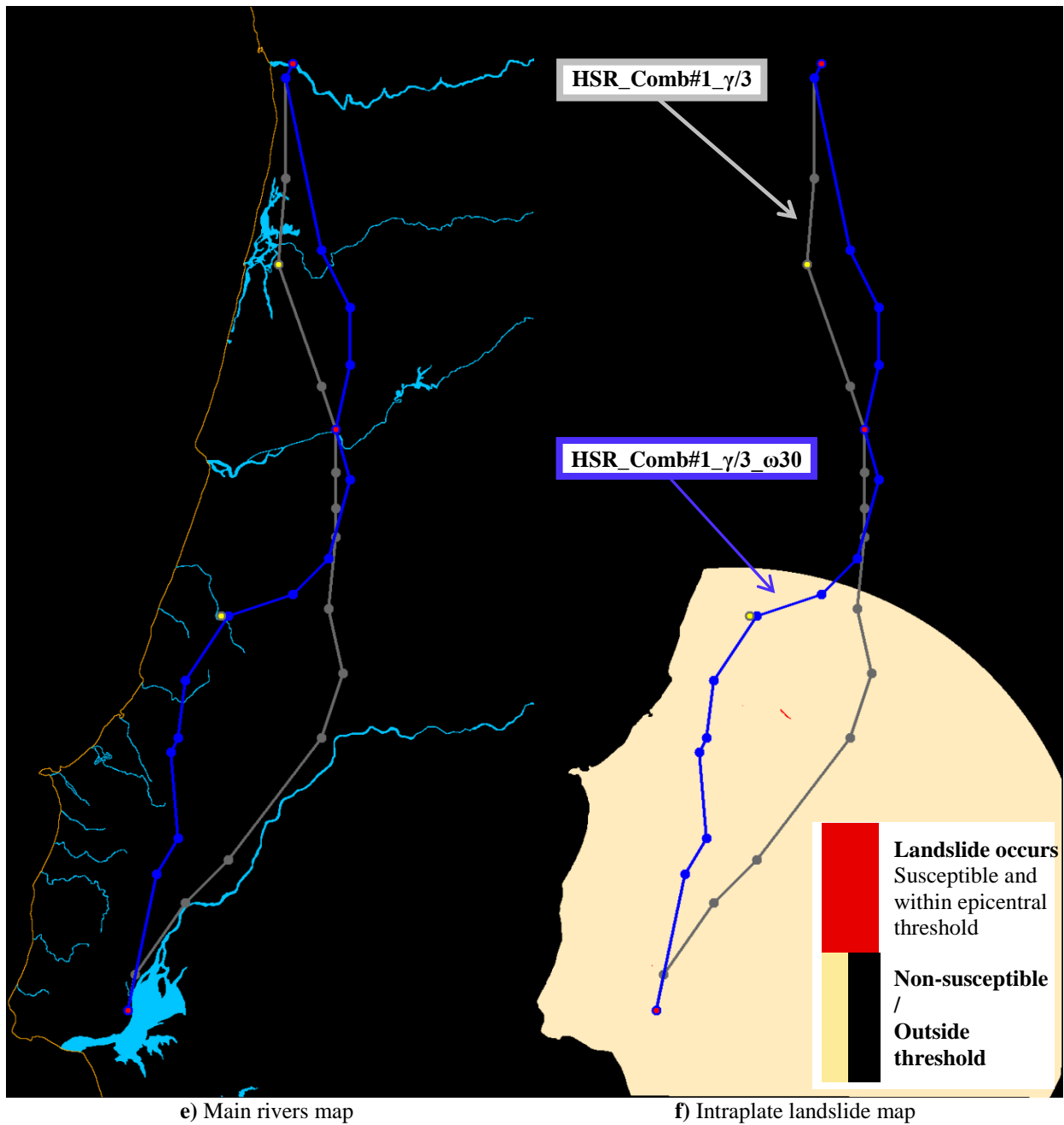


**Figure 7-23** Plan view overlay of configurations HSR\_Comb#1\_γ/3\_ω30 and HSR\_Comb#1\_γ/3: a) lithological map, b) land-use map, c) expropriation cost map, d) elevation map, e) main rivers map, f) intraplate landslide map, g) intraplate liquefaction map, h) interplate landslide map, i) interplate liquefaction map, j) rainfall landslide map and k) flood map. HSR\_Comb#1\_γ/3\_ω30 in black and HSR\_Comb#1\_γ/3 in white in a), b), c), d) and e). HSR\_Comb#1\_γ/3\_ω30 in blue and HSR\_Comb#1\_γ/3 in gray in f), g), h), i), j) and k). Node numbers of HSR\_Comb#1\_γ/3\_ω30 are identified in b). (Continued).

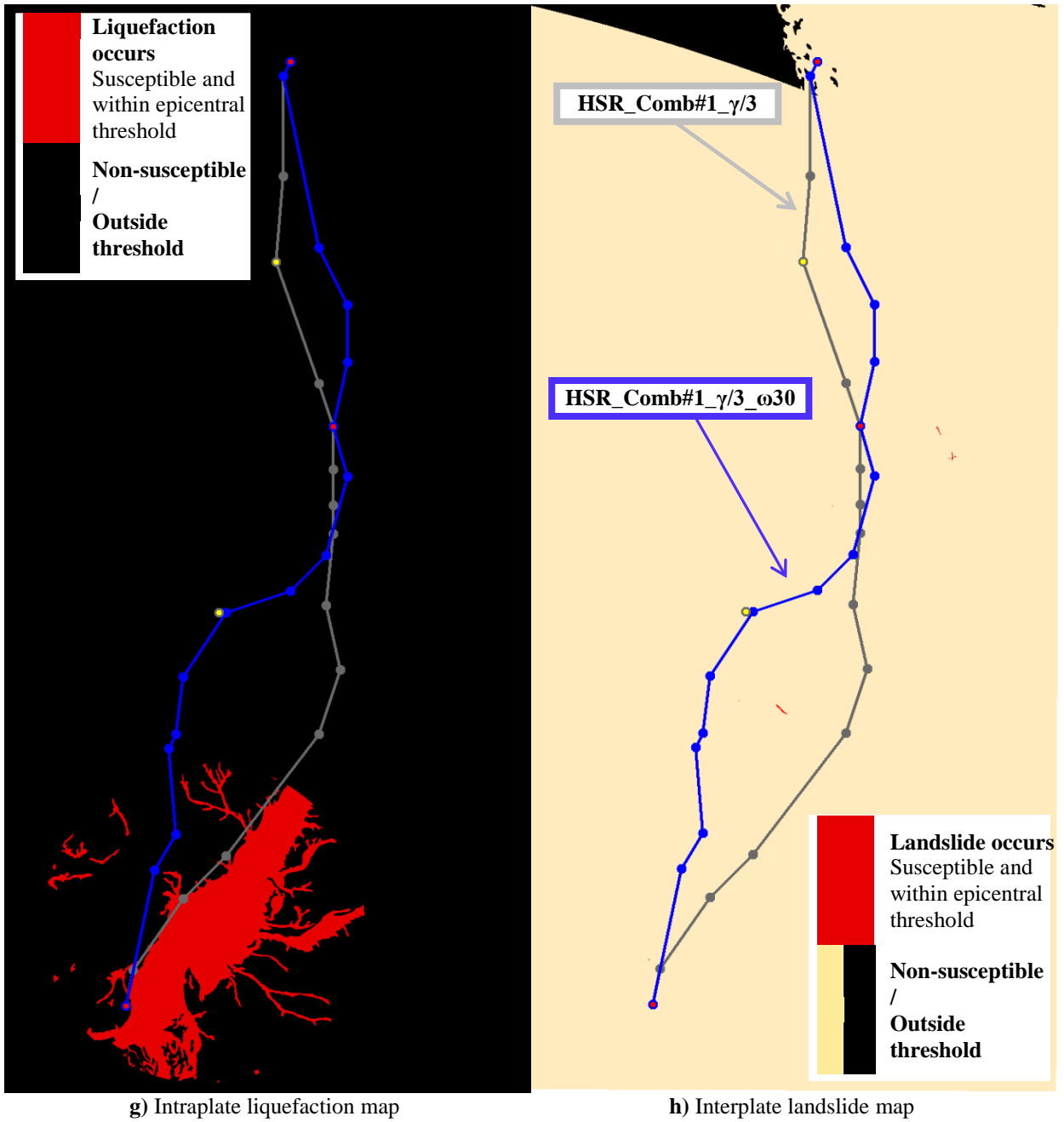


**Figure 7-23** Plan view overlay of configurations HSR\_Comb#1\_γ/3\_ω30 and HSR\_Comb#1\_γ/3: a) lithological map, b) land-use map, c) expropriation cost map, d) elevation map, e) main rivers map, f) intraplate landslide map, g) intraplate liquefaction map, h) interplate landslide map, i) interplate liquefaction map, j) rainfall landslide map and k) flood map. HSR\_Comb#1\_γ/3\_ω30 in black and HSR\_Comb#1\_γ/3 in white in a), b), c), d) and e). HSR\_Comb#1\_γ/3\_ω30 in blue and HSR\_Comb#1\_γ/3 in gray in f), g), h), i), j) and k). Node numbers of HSR\_Comb#1\_γ/3\_ω30 are identified in b). (Continued).

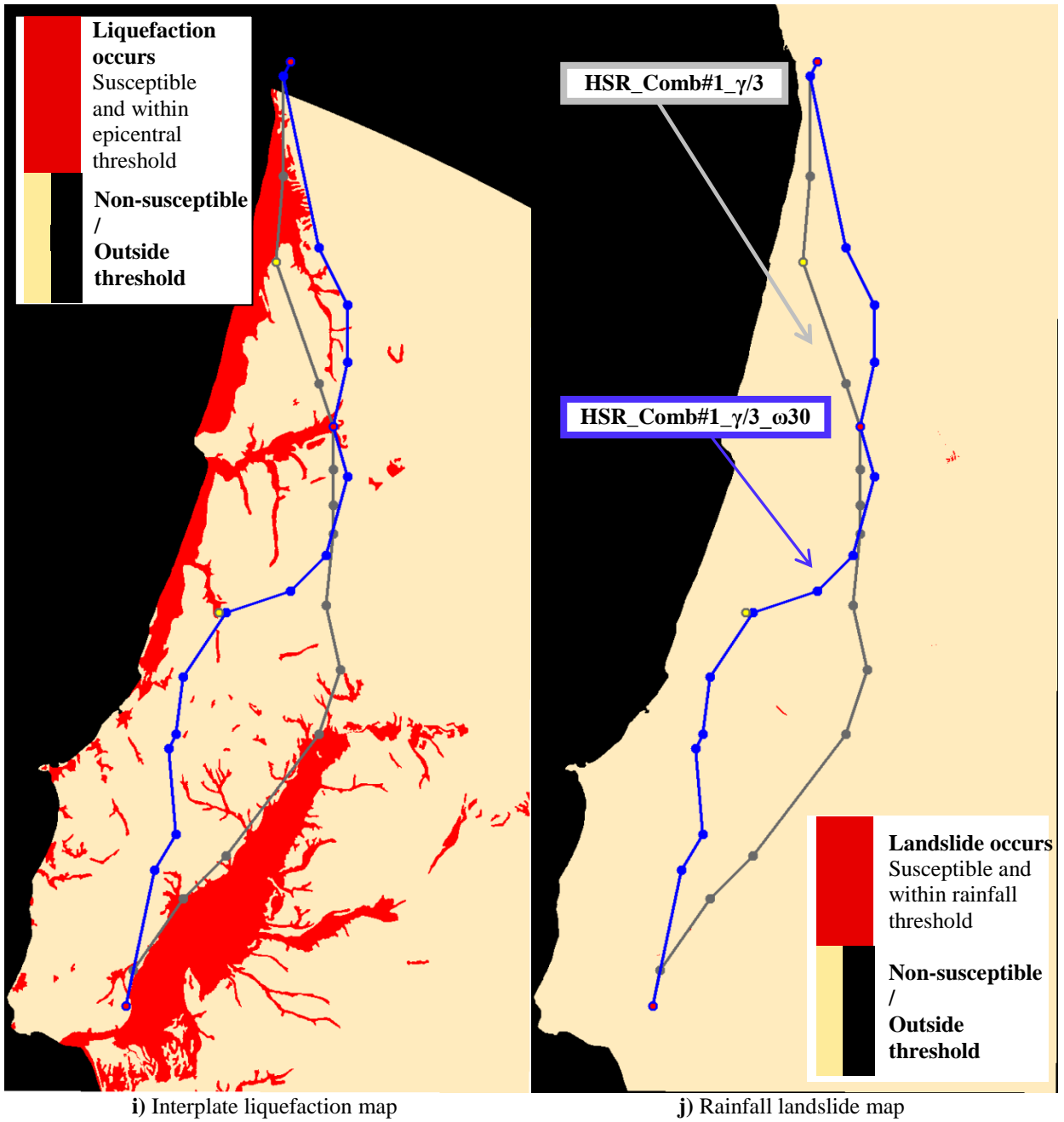
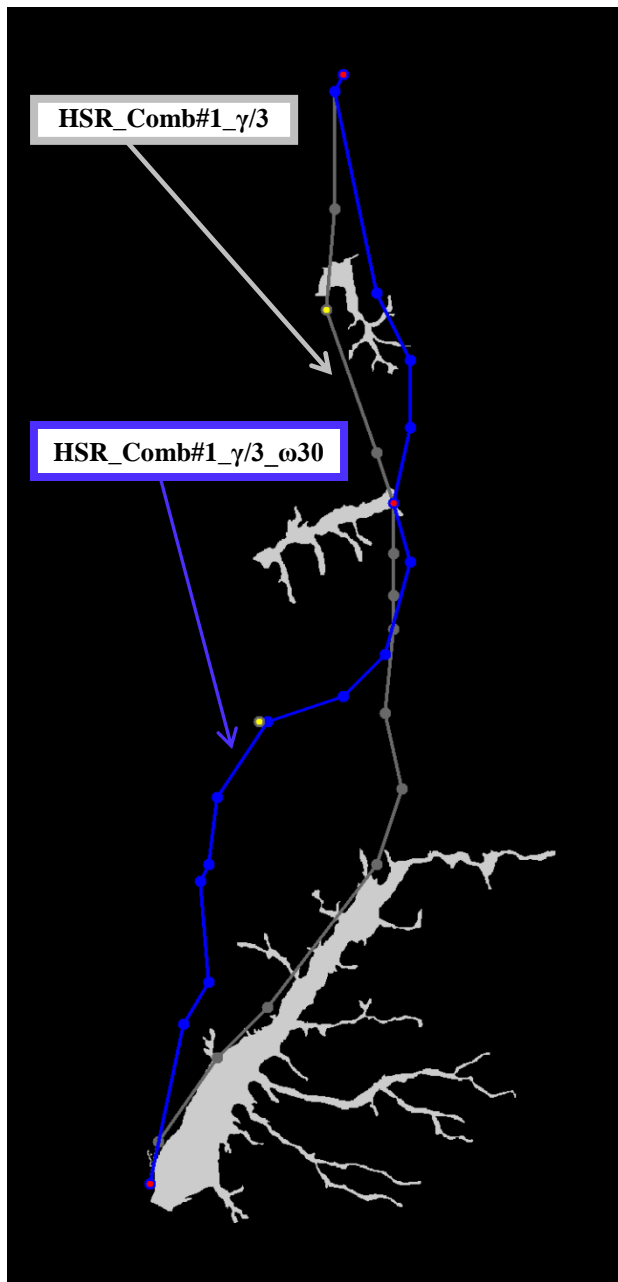


**Figure 7-23** Plan view overlay of configurations HSR\_Comb#1\_γ/3\_ω30 and HSR\_Comb#1\_γ/3: a) lithological map, b) land-use map, c) expropriation cost map, d) elevation map, e) main rivers map, f) intraplate landslide map, g) intraplate liquefaction map, h) interplate landslide map, i) interplate liquefaction map, j) rainfall landslide map and k) flood map. HSR\_Comb#1\_γ/3\_ω30 in black and HSR\_Comb#1\_γ/3 in white in a), b), c), d) and e). HSR\_Comb#1\_γ/3\_ω30 in blue and HSR\_Comb#1\_γ/3 in gray in f), g), h), i), j) and k). Node numbers of HSR\_Comb#1\_γ/3\_ω30 are identified in b). (Continued).



k) Flood map

**Figure 7-23** Plan view overlay of configurations  $HSR\_Comb\#1_{\gamma/3_{\omega30}}$  and  $HSR\_Comb\#1_{\gamma/3}$ : a) lithological map, b) land-use map, c) expropriation cost map, d) elevation map, e) main rivers map, f) intraplate landslide map, g) intraplate liquefaction map, h) interplate landslide map, i) interplate liquefaction map, j) rainfall landslide map and k) flood map.  $HSR\_Comb\#1_{\gamma/3_{\omega30}}$  in black and  $HSR\_Comb\#1_{\gamma/3}$  in white in a), b), c), d) and e).  $HSR\_Comb\#1_{\gamma/3_{\omega30}}$  in blue and  $HSR\_Comb\#1_{\gamma/3}$  in gray in f), g), h), i), j) and k). Node numbers of  $HSR\_Comb\#1_{\gamma/3_{\omega30}}$  are identified in b). (Continued).

By not connecting Aveiro and running more easterly, HSR\_Comb#1\_γ/3\_ω30 overlays different ground elevations (Figure 7-23 b). Figure 7-24 shows how the ground elevation along HSR\_Comb#1\_γ/3\_ω30 and between Oporto and km 60 is higher than that along HSR\_Comb#1\_γ/3. Most importantly, larger variations of the ground elevation are observed between Oporto and Coimbra, which impose a larger extension of bridges built for HSR\_Comb#1\_γ/3\_ω30. This pattern of higher and larger variations of the ground elevation is consistent along the entire HSR\_Comb#1\_γ/3\_ω30, leading to an overall larger extension of bridges and tunnels, the latter particularly observed between circa km 225 and Lisbon (Figure 7-24).

The plan views overlay also show that HSR\_Comb#1\_γ/3\_ω30 almost entirely avoid areas exposed to earthquake-induced liquefaction (Figure 7-23 g) and i)) and exposed to floods (Figure 7-23 k) while completely avoiding the exposure to landslides (Figure 7-23 f), h), and j)).

In relation to length, Figure 7-24 shows that HSR\_Comb#1\_γ/3\_ω30 is 5.962 km longer than HSR\_Comb#1\_γ/3.



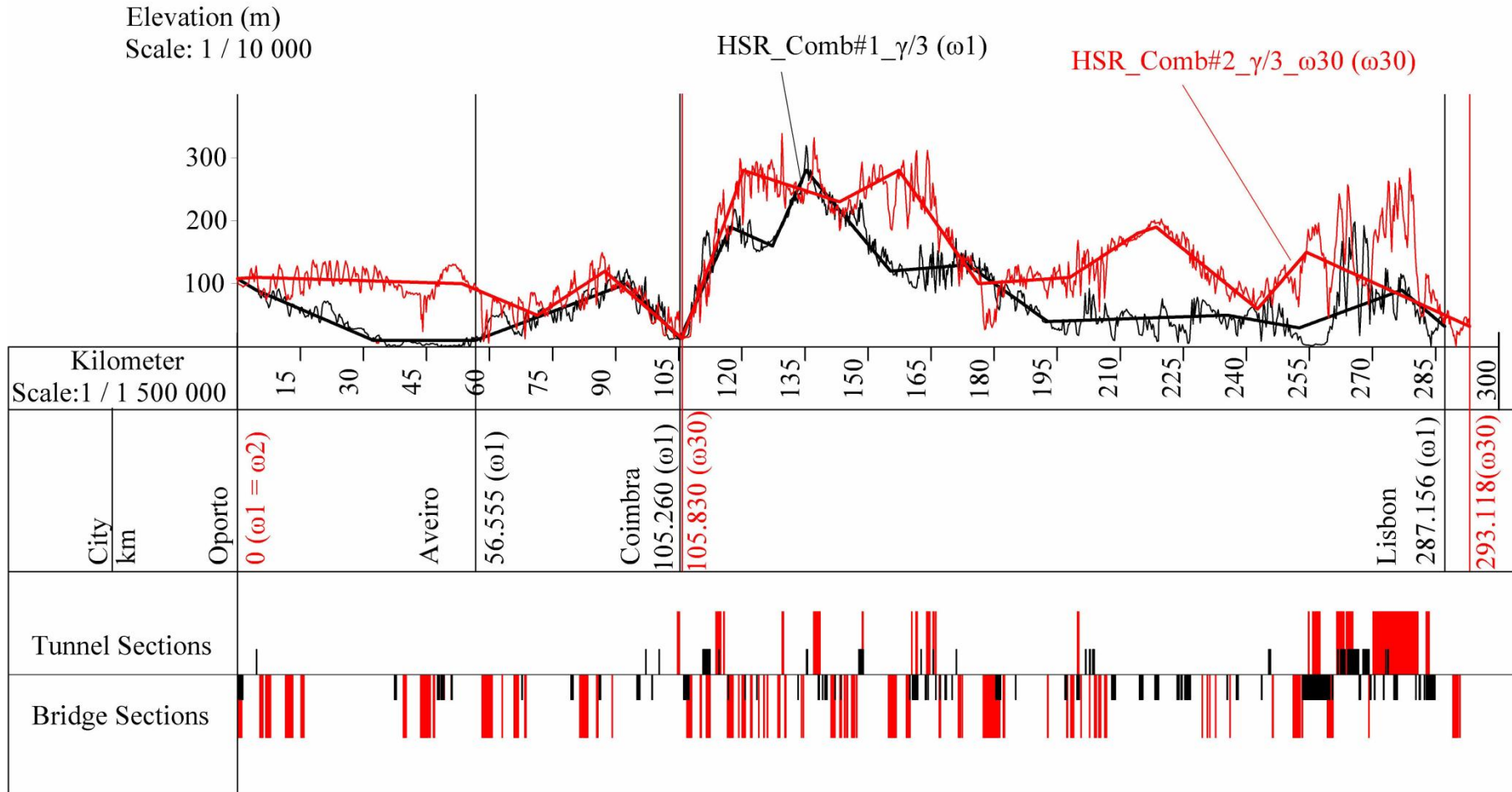


**Figure 7-24** Comparison of the longitudinal profiles of HSR\_Comb#1\_γ/3\_ω30 (in red) and HSR\_Comb#1\_γ/3 (in black).

The differences between HSR\_Comb#1\_γ/3\_ω30 and HSR\_Comb#1\_γ/3 are explained by their different performances for both SPC and the effects of natural hazards and by the different trade-off imposed by ω=30, which significantly increases the importance of the natural hazards performance. Table 7-11 compares the value of HSR\_Comb#1\_γ/3\_ω30 with the value that HSR\_Comb#1\_γ/3 would have if ω=30 is considered.

Table 7-11 shows that, for these circumstances, the objective function value of HSR\_Comb#1\_γ/3\_ω30 reduces the objective function value to 60% of that of HSR\_Comb#1\_γ/3. This is achieved by the improvement of the performance for natural hazards but with a worst SPC performance.

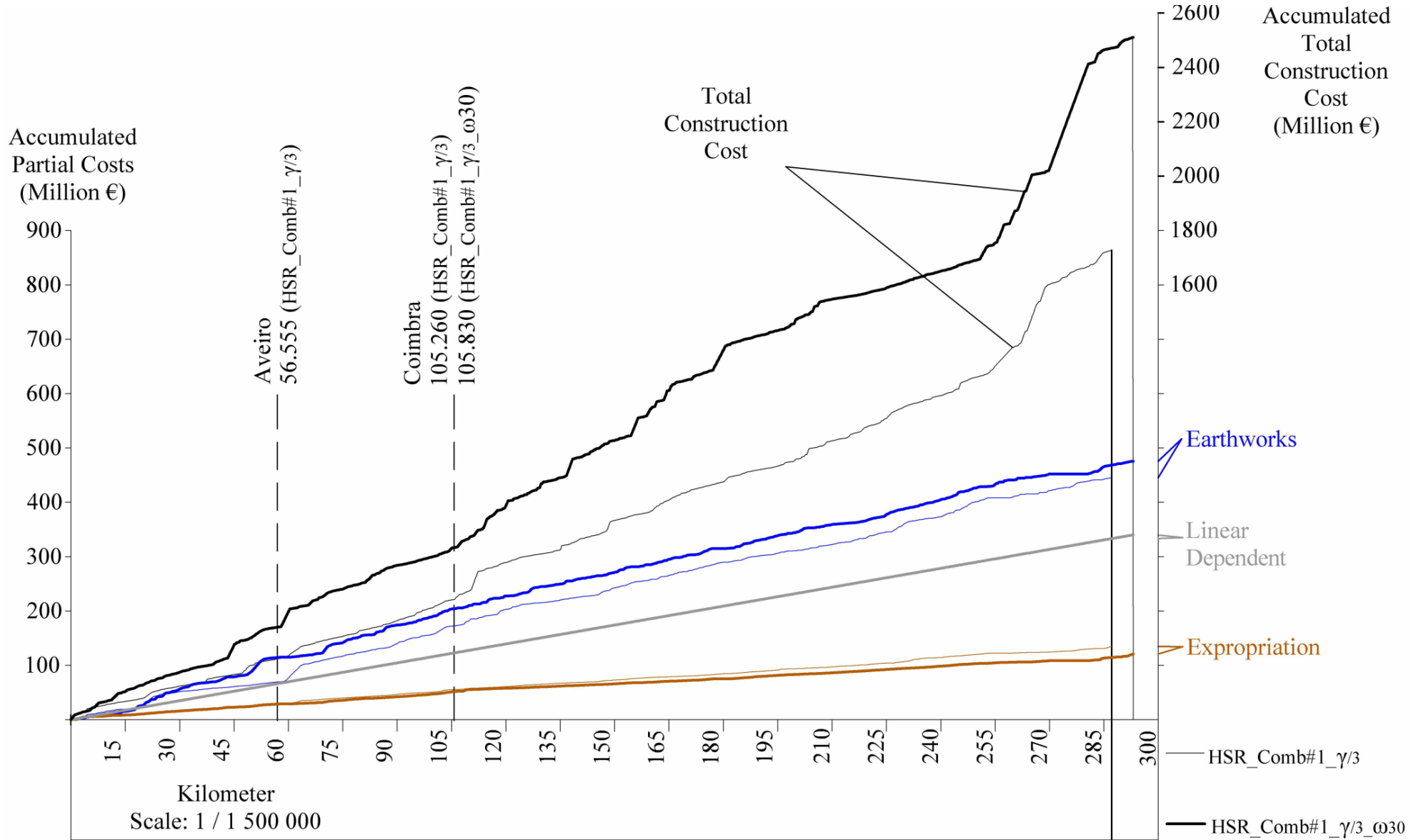
**Table 7-11** Value of both HSR\_Comb#1\_γ/3\_ω30 and HSR\_Comb#1\_γ/3 considering the Combination#1, the location benefit coefficient of γ/3 and ω=30.

| HSR Configuration  | Value for Combination#1 and Location Benefit of γ/3 (Million €) |                | HSR_Comb#1_γ/3_ω30 / HSR_Comb#1_γ/3 |
|--|---|----------------|-------------------------------------|
|  | HSR_Comb#1_γ/3_ω30  | HSR_Comb#1_γ/3 |                                     |
| <b>Objective Function Value</b>  | <b>2947.01</b>  | <b>4884.81</b> | 60%                                 |
| <b>SPC (1 + 2 + 3 - 4)</b>   | 2447.87   | 1640.80        | 149%                                |
| 1. CONSTRUCTION COST (1.1+1.2+1.3+1.4+1.5)                               | 2510.63   | 1727.15        | 145%                                |
| 1.1 Expropriation  | 120.60  | 134.80         | 89%                                 |
| 1.2 Earthworks   | 475.41  | 444.90         | 107%                                |
| 1.3 ALL BRIDGES  | 780.48  | 426.02         | 183%                                |
| 1.4 ALL TUNNELS  | 794.14  | 388.33         | 204%                                |
| 1.5 LINEAR-DEPENDENT COSTS   | 340.02  | 333.10         | 102%                                |
| 2. GEOMETRY PENALTY  | 0.00  | 0.00           | -                                   |
| 3. LAND-USE PENALTY  | 0.00  | 0.00           | -                                   |
| 4. LOCATION BENEFIT  | 62.77   | 86.36          | -                                   |
| 5. $\sum_{c \in \Omega_{sc}} \Psi_c \sum_{(i,j) \in \Omega_N} RC_{ij}^c$ | 16.64   | 108.13         | 15%                                 |
| 5.1 $\sum_{(i,j) \in \Omega_N} RC_{ij}^{Rainfall}$                       | 8.06  | 46.88          | 17%                                 |
| 5.2 $\sum_{(i,j) \in \Omega_N} RC_{ij}^{Intraplate}$                     | 9.39  | 71.44          | 13%                                 |
| 5.3 $\sum_{(i,j) \in \Omega_N} RC_{ij}^{Interplate}$                     | 32.49   | 206.26         | 16%                                 |

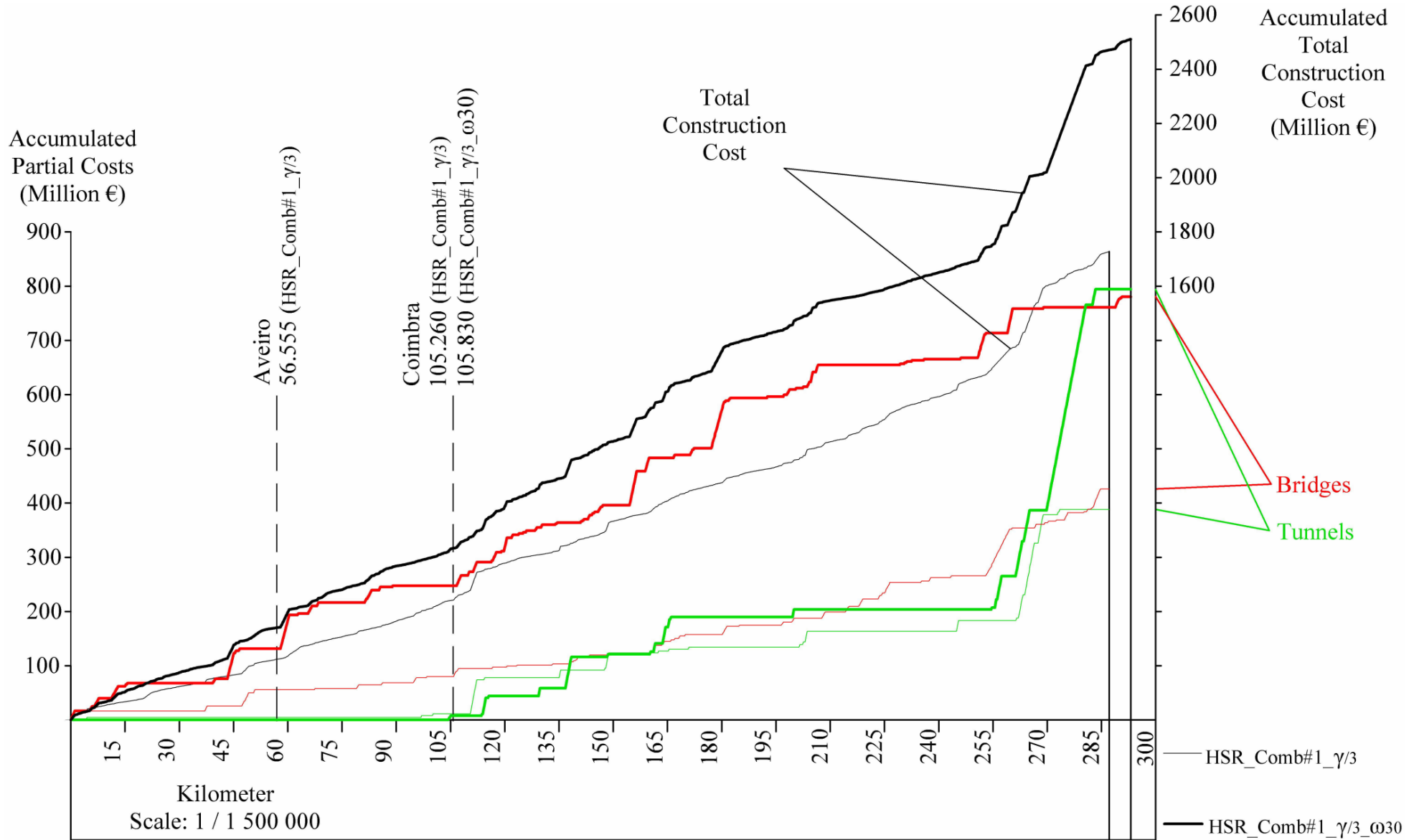
Since HSR\_Comb#1\_γ/3 connects Aveiro but not Leiria and that HSR\_Comb#1\_γ/3\_ω30 connects a node adjacent to Leiria, the location benefit of both configurations is similar. And, given that neither configuration has land-use and geometry penalties, the main factor influencing the SPC differences is the construction cost.

Table 7-11 shows the construction cost of HSR\_Comb#1\_γ/3\_ω30 is 145% larger, mainly due to the larger costs for building bridges (183%) and tunnels (204%). The cost of earthworks, expropriation and linear-dependent cost factors of both configurations is approximate, both in terms of overall value (Table 7-11) and in trend along the longitudinal profile (Figure 7-25).

Figure 7-26 presents the evolution of the total accumulated costs and the bridge and tunnel accumulated costs along the HSR longitudinal profiles. It shows bridges are built in a larger number for HSR\_Comb#1\_γ/3\_ω30 spread throughout the longitudinal profile, culminating in the respective 183% larger overall cost (Table 7-11). On the other hand, the cost of tunnels in both configurations is similar from Oporto to circa km 265 (Figure 7-26). At this point, a larger extent of tunnels is built in HSR\_Comb#1\_γ/3\_ω30 and a sharp cost increase is observed, leading to the more than double (204%) overall tunnel cost.



**Figure 7-25** Accumulated costs along the longitudinal profile: total construction costs, earthworks, linear- dependent and expropriation. Costs for HSR\_Comb#1\_γ/3\_ω30 represented in a thick line and for HSR\_Comb#1\_γ/3 in a thin line.



**Figure 7-26** Accumulated costs along the longitudinal profile: total construction costs, bridges and tunnels. Costs for HSR\_Comb#1\_γ/3\_ω30 represented in a thick line and for HSR\_Comb#1\_γ/3 in a thin line.

Figure 7-27 details how the HSR\_Comb#1\_γ/3\_ω30 avoids major exposure to interplate earthquake-induced liquefaction (Figure 7-27 a) and to floods (Figure 7-27 b) by deviating to the east and refraining from connecting Aveiro. This layout, however, corresponds to higher and larger variations of elevations requiring larger extents of bridges to be built (Figure 7-28).

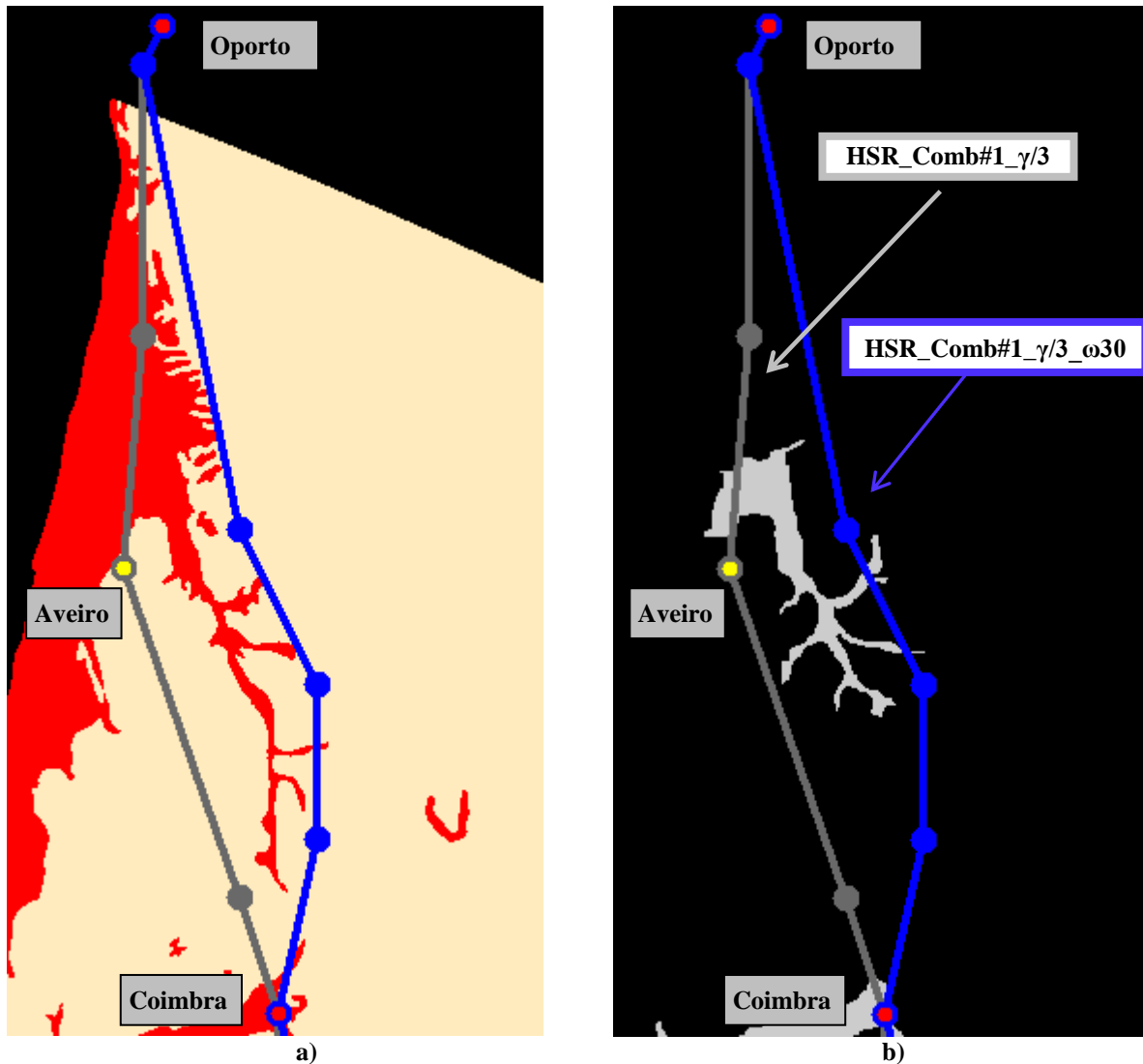


**Figure 7-27** Detail of HSR\_Comb#1\_γ/3\_ω30 (blue) and HSR\_Comb#1\_γ/3 (gray) plan view between Oporto and Coimbra overlaying: a) the interplate liquefaction map, b) the flood hazard map and c) elevation map.

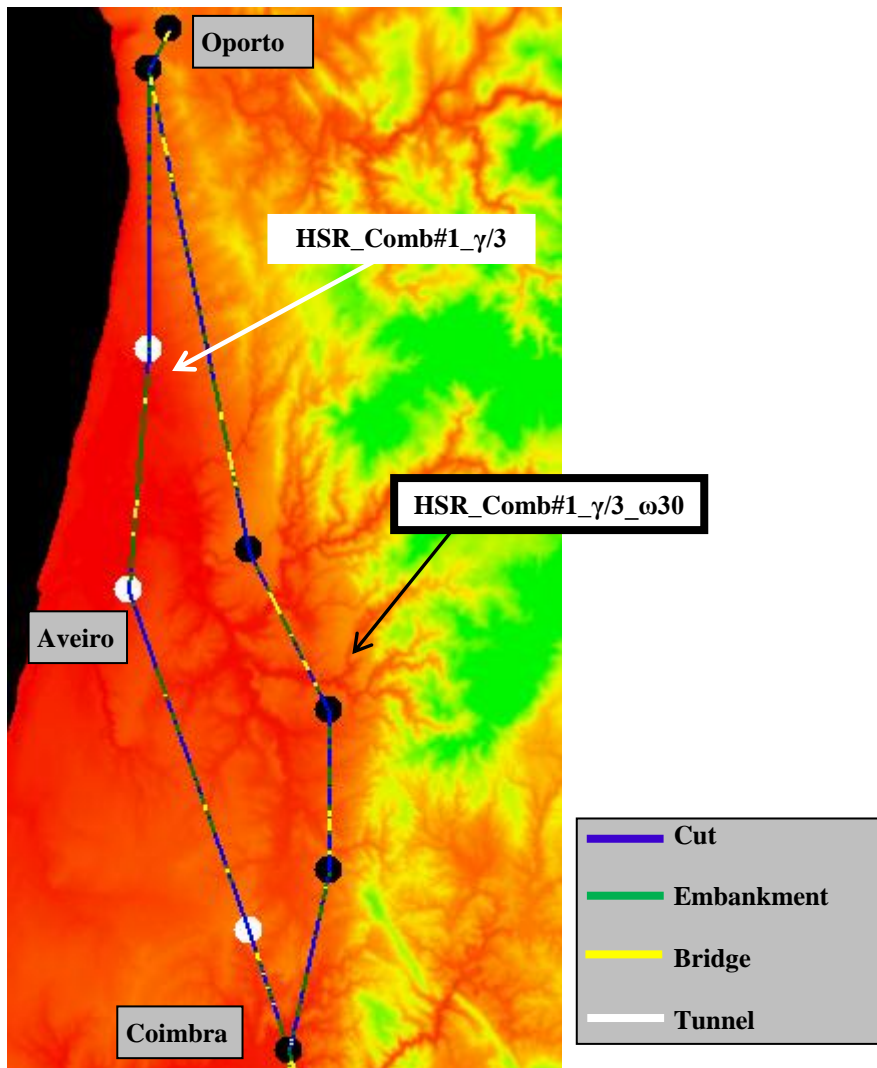


**Figure 7-28** Detail of HSR\_Comb#1\_γ/3\_ω30 and HSR\_Comb#1\_γ/3 plan view between Oporto and Coimbra overlaying the elevation map. The cross-sections of both configurations are represented by different colors.

Between Coimbra and Leiria the HSR\_Comb#1\_γ/3\_ω30 configuration has a similar layout to HSR\_Comb#1\_γ discussed in section 7.3.1.2. However, HSR\_Comb#1\_γ/3\_ω30 connects an adjacent node to Leiria. Figure 7-29 a) shows that the node corresponding to Leiria is located in an area subject to interplate earthquake-induced liquefaction. This is avoided by HSR\_Comb#1\_γ/3\_ω30 by connecting the adjacent node.

In section 7.3.1.2 it is also discussed that to avoid liquefaction- and flood-exposed areas near Lisbon, a HSR configuration is required to run westward of such areas as the forbidden land-use of the Tagus River estuary prevents crossing to the east. This however corresponds to larger elevations (Figure 7-23 b) that require the construction of tunnels, which explains the sharp increase of the HSR accumulated costs near Lisbon (Figure 7-26).

By increasing  $\omega$  to 30, the objective function trades-off larger construction costs by an improved HSR performance and HSR\_Comb#1\_ $\gamma/3$ \_ $\omega 30$  avoids almost entirely the hazard exposed areas next to Lisbon. This is shown in Figure 7-29 for the interplate earthquake-induced liquefaction and for floods. The intraplate earthquake-induced liquefaction also affects the area next to Lisbon but the areas exposed to such hazard (Figure 7-23 g)) are a subset of Figure 7-29 a).

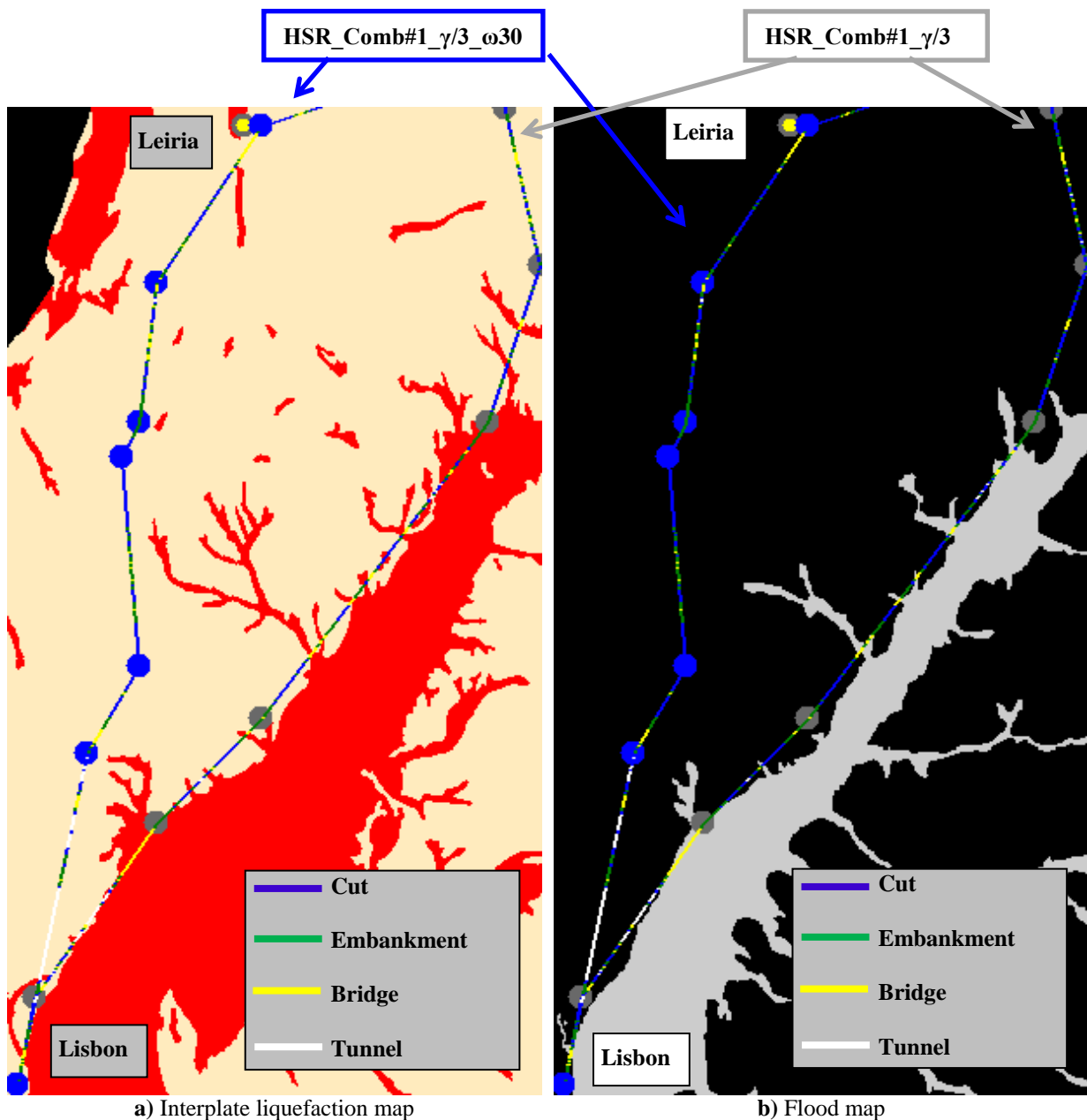


**Figure 7-29** Detail of HSR\_Comb#1\_ $\gamma/3$ \_ $\omega 30$  (blue nodes) and HSR\_Comb#1\_ $\gamma/3$  (grey nodes) plan view between Leiria and Lisbon overlaying: a) the interplate liquefaction map and b) the flood hazard map. The cross-sections of both configurations are represented by different colors.



The application performed illustrates how increasing the value of  $\omega$  results in optimal or near-optimal solutions that can significantly improve the performance for natural hazards, even if that implies much larger construction costs and trade-offs with the cities connected.

#### **7.4 SCENARIO-WEIGHT COMBINATION #2**

The scenario-weight combination #2 considers different weights for the three scenarios:  $\Psi_{intraplate\ EQ} = 0.50$ ,  $\Psi_{interplate\ EQ} = 0.10$  and  $\Psi_{rainfall} = 0.40$ . This combination aims at reproducing a variable importance given by the decision-maker to the performance of the HSR for different natural hazards, according to their probability of occurrence. Larger weights are attributed to the scenarios with smaller return periods, hence larger probability of occurrence.

Such an attitude towards the risks of the natural hazards is studied with the consideration of location benefit coefficients of  $\gamma/3$  for Aveiro and Leiria and  $\omega=1$ . SAA runs are performed to solve the application of the robust approach and the best solution found, termed HSR\_Comb#2\_ $\gamma/3$ , is compared with HSR\_Comb#1\_ $\gamma/3$  (section 7.3.2). Both configurations are obtained for applications differing only by the scenario-weight combination.

##### **7.4.1 LOCATION BENEFIT COEFFICIENT $\gamma/3$ ( $\omega=1$ )**

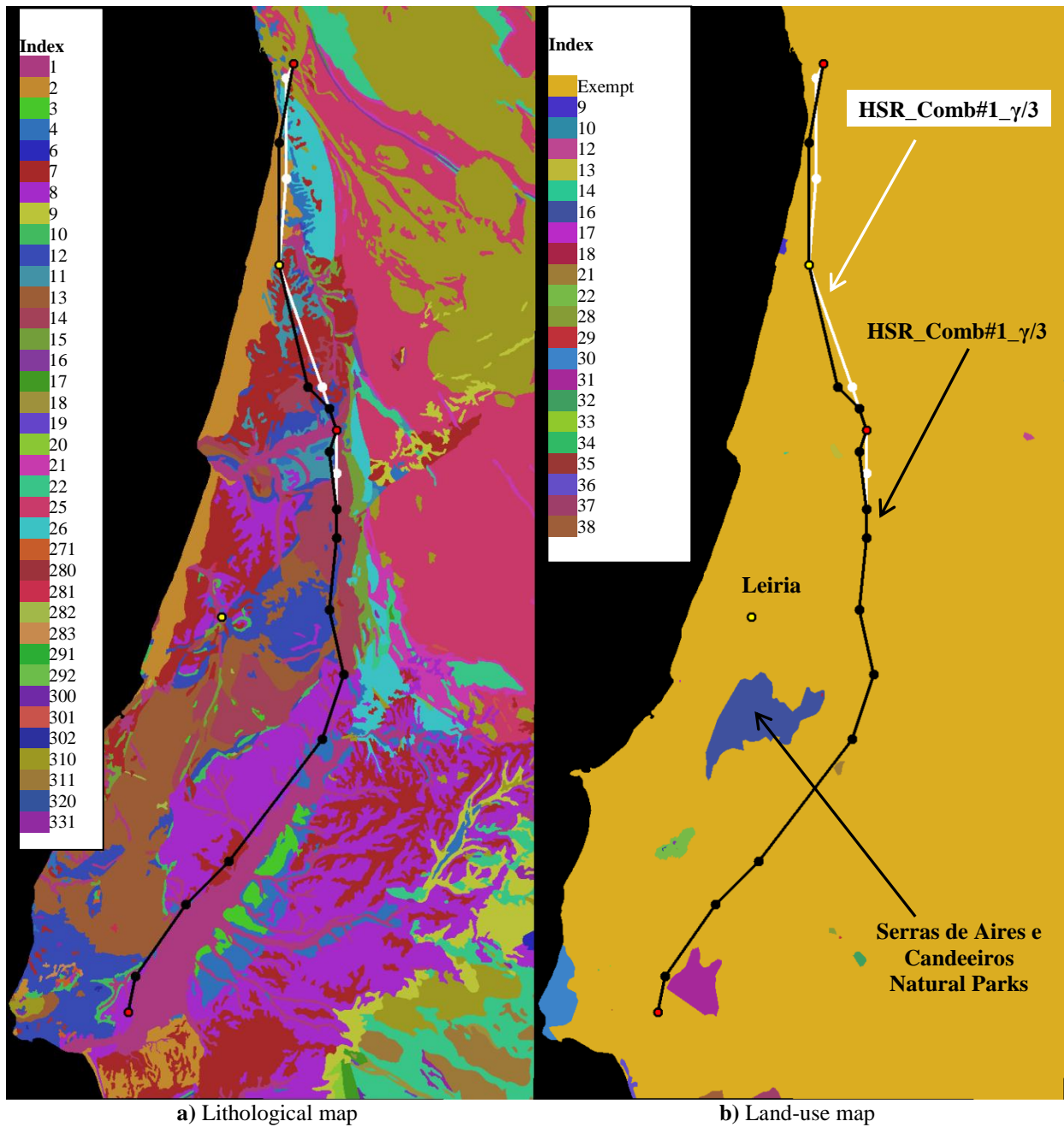
Table 7-12 presents the geometry of HSR\_Comb#2\_ $\gamma/3$ . Table 7-12 shows the HSR\_Comb#2\_ $\gamma/3$  complies with the location, horizontal angle and gradient constraints. It links Lisbon, Coimbra and Oporto, all horizontal angles are larger than  $120^\circ$  and all gradients are smaller than 35‰. Additionally, all gradients are smaller than  $\eta_{normal} = 20\text{‰}$  and all horizontal angles are larger than  $\beta_{normal} = 140^\circ$ . The HSR\_Comb#2\_ $\gamma/3$  solution also avoids the overlaying all forbidden land-use areas (indices 9 through 38 of Figure 7-30b)), thus complying with the land-use constraint.

**Table 7-12** Geometry of the configuration HSR\_Comb#2\_ $\gamma/3$ .

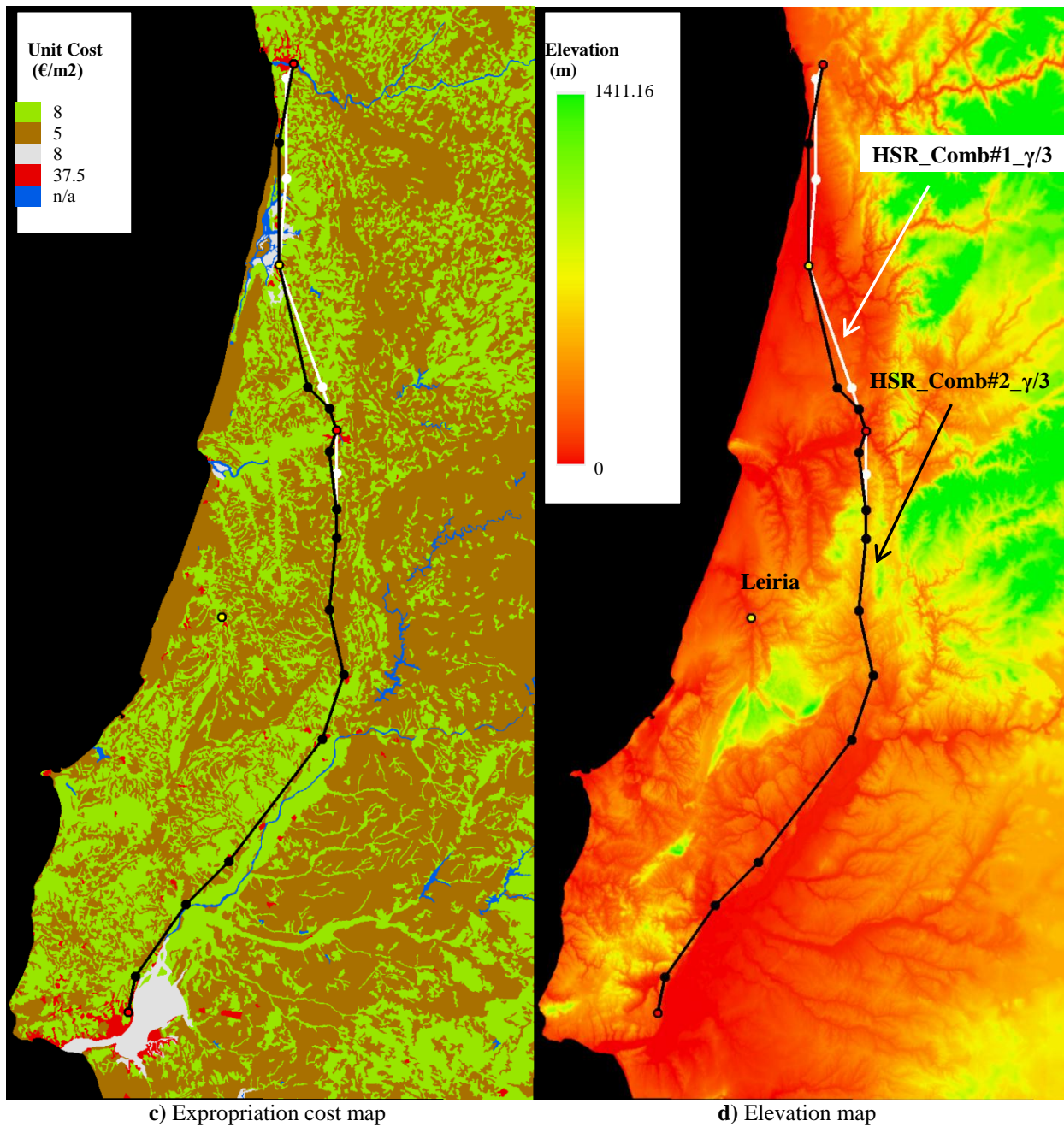
| Node | (x;y;z)<br>(km;km;m) | City    | $\eta$<br>(‰) | $\beta$<br>(°) |
|------|----------------------|---------|---------------|----------------|
| 1    | (80;16;108.152)      | Oporto  | -4            |                |
| 2    | (76;38;10)           |         | 0             | 170            |
| 3    | (76;72;10)           | Aveiro  | 3             | 167            |
| 4    | (84;106;100)         |         | -7            | 148            |
| 5    | (90;112;40)          |         | -4            | 153            |
| 6    | (92;118;13.106)      | Coimbra | 18            | 143            |
| 7    | (90;124;130)         |         | 2             | 154            |
| 8    | (92;140;170)         |         | 13            | 173            |
| 9    | (92;148;270)         |         | -7            | 174            |
| 10   | (90;168;120)         |         | 1             | 162            |
| 11   | (94;186;130)         |         | -5            | 149            |
| 12   | (88;204;40)          |         | 0             | 161            |
| 13   | (62;238;50)          |         | -1            | 172            |
| 14   | (50;250;30)          |         | 2             | 170            |
| 15   | (36;270;90)          |         | -6            | 156            |
| 16   | (34;280;32.348)      | Lisbon  |               |                |

Figure 7-30 shows the plan view of HSR\_Comb#1\_ $\gamma/3$  and HSR\_Comb#1\_ $\gamma$  overlaying the lithological-, land-use-, expropriation cost-, elevation-, main rivers-, intraplate landslide-, intraplate liquefaction-, interplate landslide-, interplate liquefaction-, rainfall landslide- and flood- maps in a 1:1,800,000 scale.

Figure 7-30 shows that considering the weighted-scenario combination#2, for the location benefit  $\gamma/3$  and  $\omega=1$ , results in a HSR configuration very similar to that obtained for combination #1 and equal remaining application specifics. In fact, HSR\_Comb#2\_ $\gamma/3$  overlaps HSR\_Comb#1\_ $\gamma/3$  almost entirely between Coimbra and Lisbon. Neither HSR\_Comb#2\_ $\gamma/3$  nor HSR\_Comb#1\_ $\gamma/3$  connect Leiria and, instead, both solutions run eastwards of the Serras de Aires e Candeeiros Natural Parks (mountain range). Figure 7-31 compares the longitudinal profiles of both configurations.



**Figure 7-30** Plan view overlay of configurations HSR\_Comb#2\_γ/3 and HSR\_Comb#1\_γ/3: a) lithological map, b) land-use map, c) expropriation cost map, d) elevation map, e) main rivers map, f) Intraplate landslide map, g) Intraplate liquefaction map, h) Interplate landslide map, i) Interplate liquefaction map, j) Rainfall landslide map and k) Flood map. HSR\_Comb#2\_γ/3 in black and HSR\_Comb#1\_γ/3 in white in a), b), c), d) and HSR\_Comb#2\_γ/3 in blue and HSR\_Comb#1\_γ/3 in gray e). in f), g), h), i), j) and k). Aveiro and Leiria are represented by yellow circles and Lisbon, Oporto and Coimbra by red circles.



**Figure 7-30** Plan view overlay of configurations HSR\_Comb#2\_ $\gamma/3$  and HSR\_Comb#1\_ $\gamma/3$ : a) lithological map, b) land-use map, c) expropriation cost map, d) elevation map, e) main rivers map, f) Intraplate landslide map, g) Intraplate liquefaction map, h) Interplate landslide map, i) Interplate liquefaction map, j) Rainfall landslide map and k) Flood map. HSR\_Comb#2\_ $\gamma/3$  in black and HSR\_Comb#1\_ $\gamma/3$  in white in a), b), c), d) and HSR\_Comb#2\_ $\gamma/3$  in blue and HSR\_Comb#1\_ $\gamma/3$  in gray e). in f), g), h), i), j) and k). Aveiro and Leiria are represented by yellow circles and Lisbon, Oporto and Coimbra by red circles. (Continued).

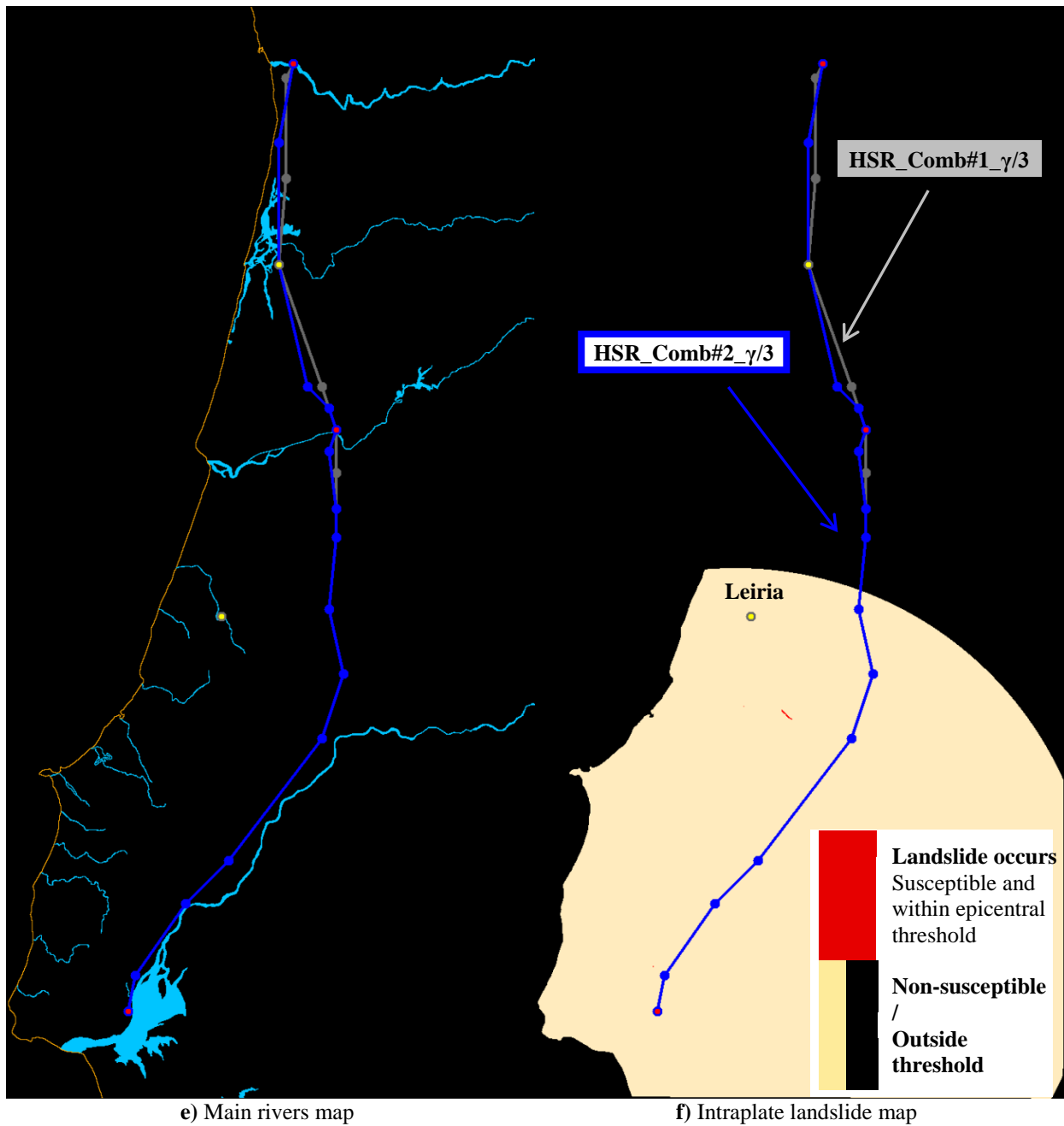


**Figure 7-30** Plan view overlay of configurations HSR\_Comb#2\_ $\gamma/3$  and HSR\_Comb#1\_ $\gamma/3$ : a) lithological map, b) land-use map, c) expropriation cost map, d) elevation map, e) main rivers map, f) Intraplate landslide map, g) Intraplate liquefaction map, h) Interplate landslide map, i) Interplate liquefaction map, j) Rainfall landslide map and k) Flood map. HSR\_Comb#2\_ $\gamma/3$  in black and HSR\_Comb#1\_ $\gamma/3$  in white in a), b), c), d) and HSR\_Comb#2\_ $\gamma/3$  in blue and HSR\_Comb#1\_ $\gamma/3$  in gray e). in f), g), h), i), j) and k). Aveiro and Leiria are represented by yellow circles and Lisbon, Oporto and Coimbra by red circles. (Continued).

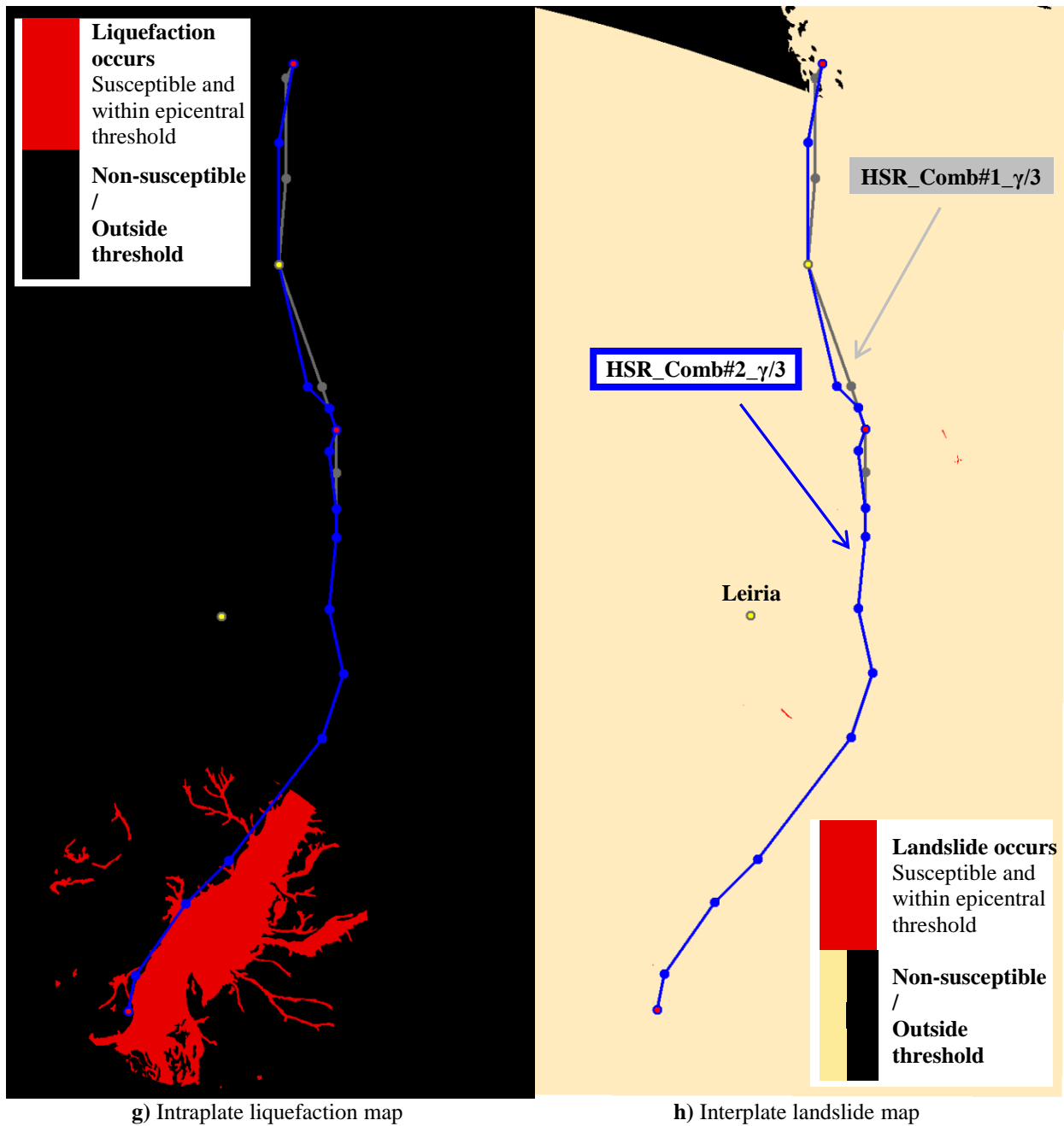


**Figure 7-30** Plan view overlay of configurations HSR\_Comb#2\_ $\gamma/3$  and HSR\_Comb#1\_ $\gamma/3$ : a) lithological map, b) land-use map, c) expropriation cost map, d) elevation map, e) main rivers map, f) Intraplate landslide map, g) Intraplate liquefaction map, h) Interplate landslide map, i) Interplate liquefaction map, j) Rainfall landslide map and k) Flood map. HSR\_Comb#2\_ $\gamma/3$  in black and HSR\_Comb#1\_ $\gamma/3$  in white in a), b), c), d) and HSR\_Comb#2\_ $\gamma/3$  in blue and HSR\_Comb#1\_ $\gamma/3$  in gray e). in f), g), h), i), j) and k). Aveiro and Leiria are represented by yellow circles and Lisbon, Oporto and Coimbra by red circles. (Continued).

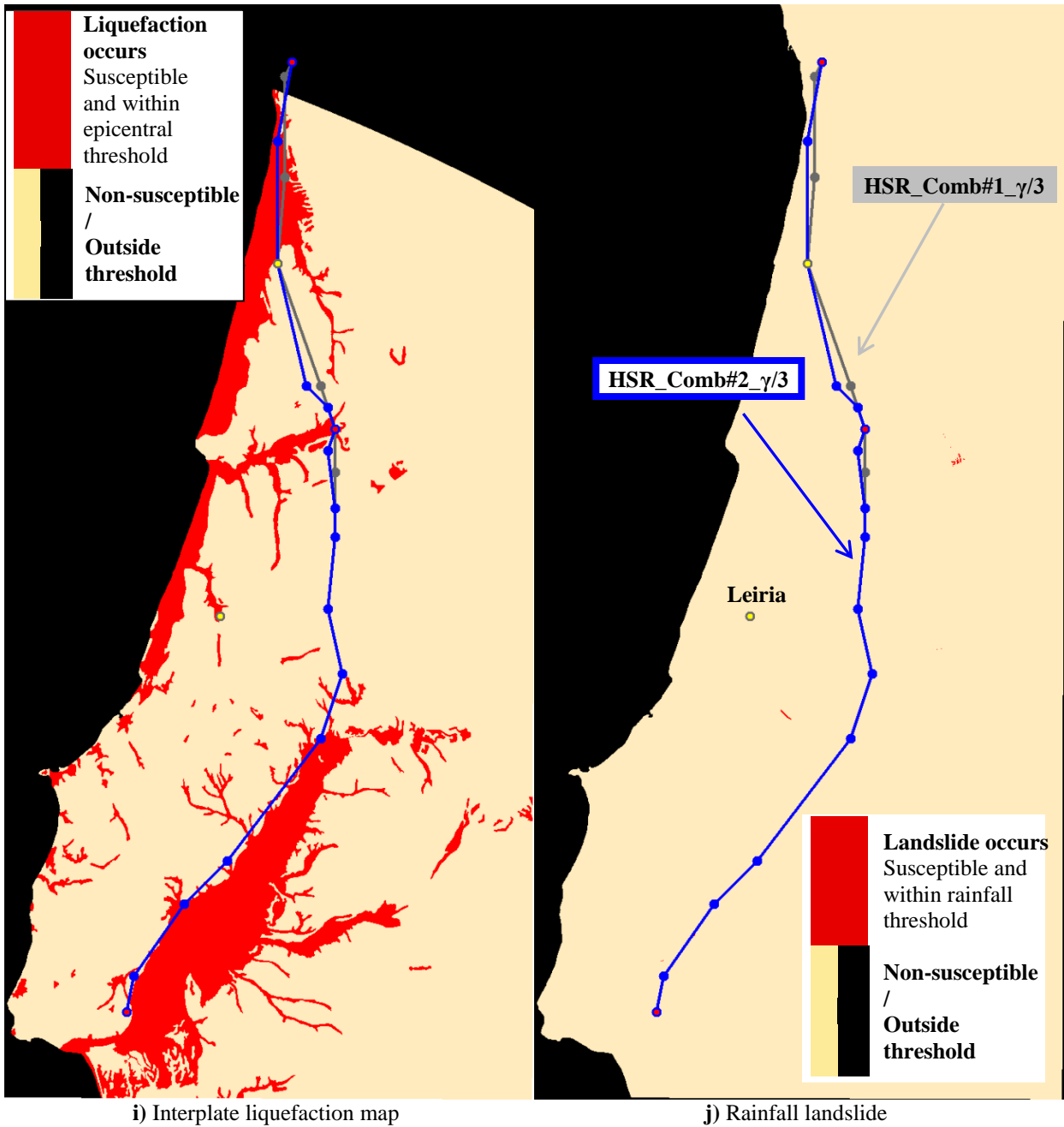
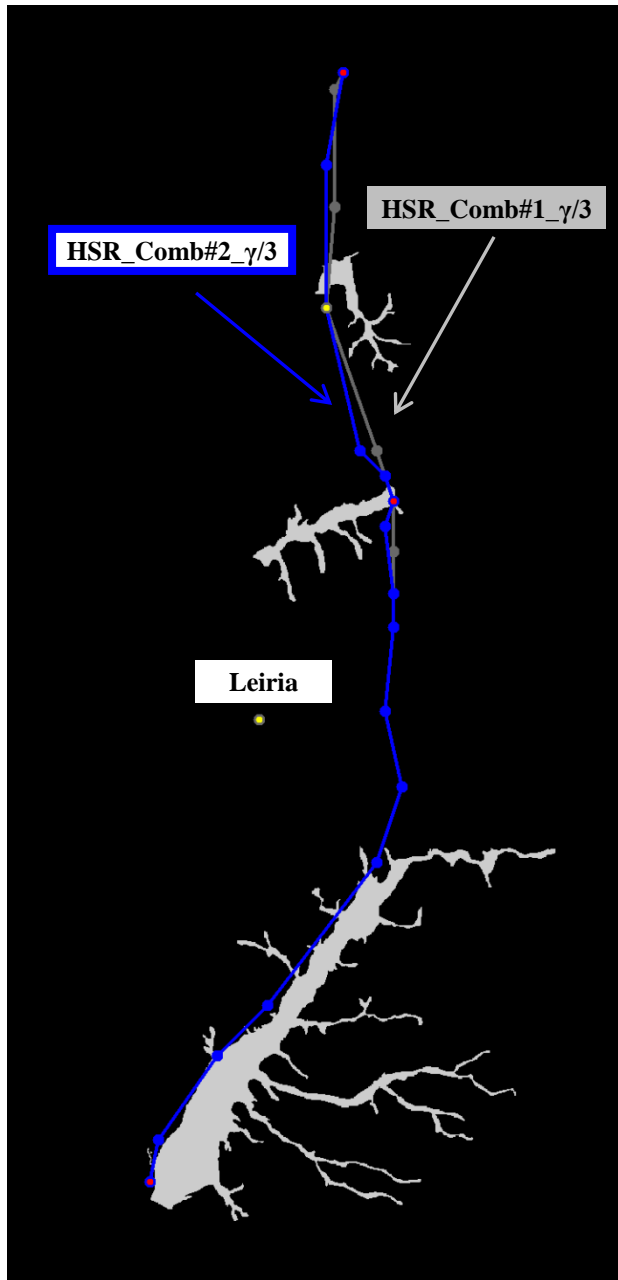


**Figure 7-30** Plan view overlay of configurations HSR\_Comb#2\_ $\gamma/3$  and HSR\_Comb#1\_ $\gamma/3$ : a) lithological map, b) land-use map, c) expropriation cost map, d) elevation map, e) main rivers map, f) Intraplate landslide map, g) Intraplate liquefaction map, h) Interplate landslide map, i) Interplate liquefaction map, j) Rainfall landslide map and k) Flood map. HSR\_Comb#2\_ $\gamma/3$  in black and HSR\_Comb#1\_ $\gamma/3$  in white in a), b), c), d) and HSR\_Comb#2\_ $\gamma/3$  in blue and HSR\_Comb#1\_ $\gamma/3$  in gray e). in f), g), h), i), j) and k). Aveiro and Leiria are represented by yellow circles and Lisbon, Oporto and Coimbra by red circles. (Continued).



k) Flood Map

**Figure 7-30** Plan view overlay of configurations HSR\_Comb#2\_ $\gamma/3$  and HSR\_Comb#1\_ $\gamma/3$ : a) lithological map, b) land-use map, c) expropriation cost map, d) elevation map, e) main rivers map, f) Intraplate landslide map, g) Intraplate liquefaction map, h) Interplate landslide map, i) Interplate liquefaction map, j) Rainfall landslide map and k) Flood map. HSR\_Comb#2\_ $\gamma/3$  in black and HSR\_Comb#1\_ $\gamma/3$  in white in a), b), c), d) and HSR\_Comb#2\_ $\gamma/3$  in blue and HSR\_Comb#1\_ $\gamma/3$  in gray e). in f), g), h), i), j) and k). Aveiro and Leiria are represented by yellow circles and Lisbon, Oporto and Coimbra by red circles. (Continued).



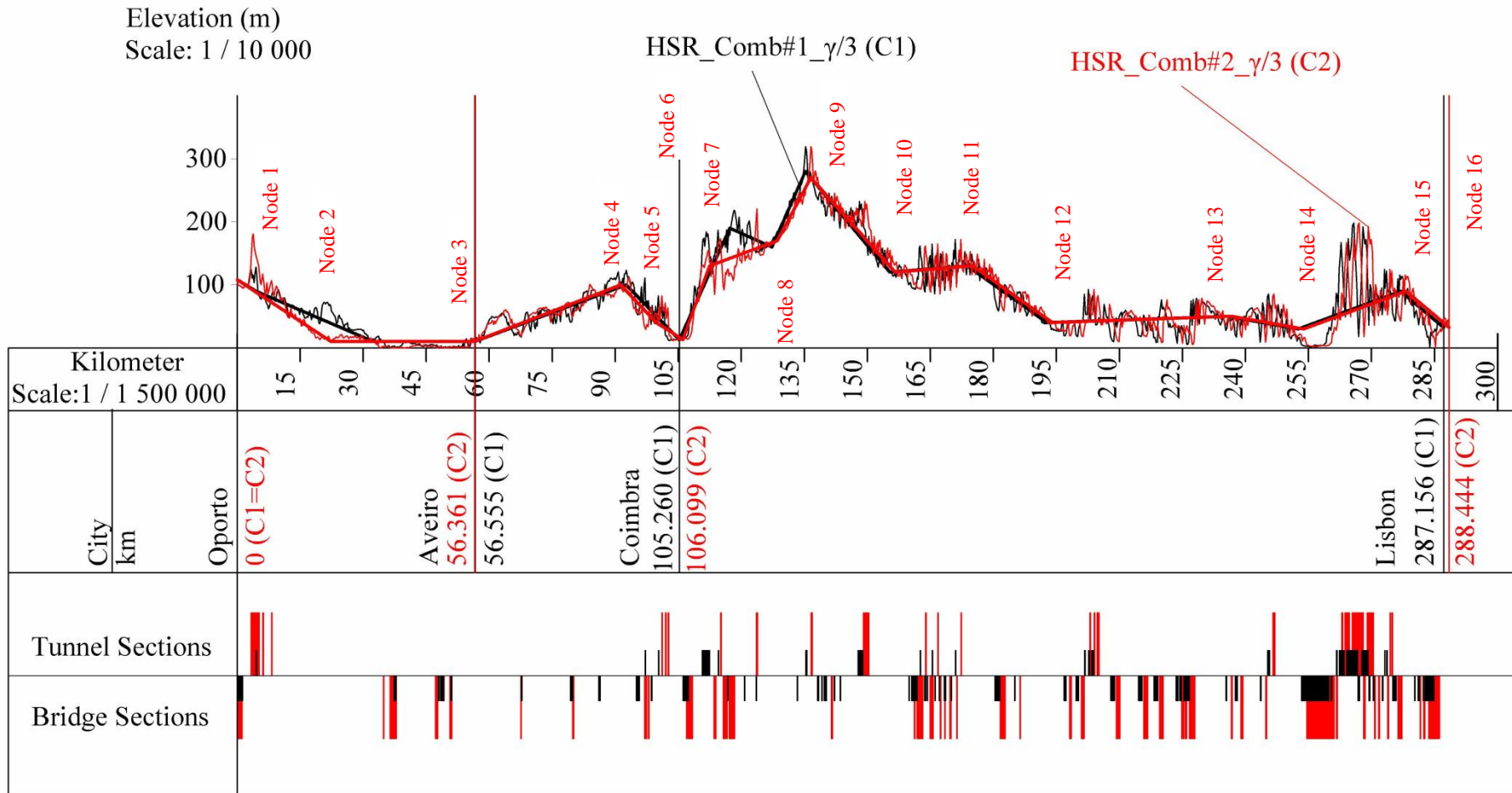


**Figure 7-31** Comparison of the longitudinal profiles of HSR\_Comb#2\_γ/3 (in red) and HSR\_Comb#1\_γ/3 (in black). Identification of HSR\_Comb#2\_γ/3 node numbers.

Figure 7-31 shows that the differences in the plan view between Oporto and Aveiro and between Coimbra and km 130 result in different ground profiles on which the HSR configurations are built. In these sections, the HSR longitudinal profile and the cross-sections of the configurations also differ. HSR\_Comb#2\_γ/3 requires a larger extent of tunnels in the first 15 km starting at Oporto than HSR\_Comb#1\_γ/3. Around Coimbra, between km 90 and km 120, HSR\_Comb#2\_γ/3 has a smaller extent of tunnels but a larger extent of bridges. Nodes 8 and 9 have the same plan view in both configurations but differ in elevation (Table 7-8 and Table 7-12). Thus, the cross-sections also differ and between km 120 and km 150 and HSR\_Comb#2\_γ/3 has a smaller extent of bridges. From this point towards Lisbon, both configurations are the same, given the equal plan views and longitudinal profiles.

The resulting differences in the objective function value and the cost breakdown of both HSR\_Comb#2\_γ/3 and HSR\_Comb#1\_γ/3 are compared in Table 7-13, assessed for the same conditions: scenario-weight combination #2, the location benefit coefficient of γ/3 and ω=1.

**Table 7-13** Value of both HSR\_Comb#2\_γ/3 and HSR\_Comb#1\_γ/3 considering the Combination#2, the location benefit coefficient of γ/3 and ω=1.

| HSR Configuration  | Value for Combination#2 and Location Benefit of Coefficient of γ/3 (Million €) |                 | HSR_Comb#2_γ/3 / HSR_Comb#1_γ/3 |
|--|--|-----------------|---------------------------------|
|  | HSR_Comb#2_γ/3   | HSR_Comb#1_γ/3  |                                 |
| <b>Objective Function Value</b>  | 1,756.49   | <b>1,715.90</b> | 102%                            |
| <b>SPC (1 + 2 + 3 - 4)</b>   | 1,682.40   | 1640.80         | 103%                            |
| 1. CONSTRUCTION COST<br>(1.1+1.2+1.3+1.4+1.5)                            | 1,770.95   | 1,727.15        | 103%                            |
| 1.1 Expropriation  | 134.82   | 134.80          | 100%                            |
| 1.2 Earthworks   | 440.46   | 444.90          | 99%                             |
| 1.3 ALL BRIDGES  | 437.56   | 426.02          | 103%                            |
| 1.4 ALL TUNNELS  | 423.51   | 388.33          | 109%                            |
| 1.5 LINEAR- DEPENDENT COSTS  | 334.60   | 333.10          | 100%                            |
| 2. GEOMETRY PENALTY  | 0.00   | 0.00            | -                               |
| 3. LAND-USE PENALTY  | 0.00   | 0.00            | -                               |
| 4. LOCATION BENEFIT  | 88.55  | 86.36           |                                 |
| 5. $\sum_{c \in \Omega_{sc}} \Psi_c \sum_{(i,j) \in \Omega_N} RC_{ij}^c$ | 74.09  | 75.10           | 99%                             |
| 5.1 $\sum_{(i,j) \in \Omega_N} RC_{ij}^{Rainfall}$                       | 42.70  | 46.88           | 91%                             |
| 5.2 $\sum_{(i,j) \in \Omega_N} RC_{ij}^{Intraplate}$                     | 71.44  | 71.44           | 100%                            |
| 5.3 $\sum_{(i,j) \in \Omega_N} RC_{ij}^{Interplate}$                     | 212.88   | 206.26          | 103%                            |

Table 7-13 shows that the objective function value of HSR\_Comb#2\_γ/3 is very close, albeit 2% larger, to that of HSR\_Comb#1\_γ/3 when one assesses the weighted-scenario performance with combination #2.

It was discussed in section 6.4.1 that the likelihood of a random search algorithm such as the SAA to produce exactly the same HSR solutions for the HSR planning problem is low. Three main factors contribute for this: (i) the problem is very large and complex, (ii) a large number of randomly generated HSR configurations are tested within the annealing runs, in the order of 500,000 and (iii) the influence of attributing location benefit coefficients to Leiria and Aveiro. Although both configurations connect Aveiro, the number of linear sections between Oporto, Aveiro and Coimbra differs (Figure 7-30). HSR\_Comb#2\_γ/3 is formed by 2 linear sections between Oporto and Aveiro and by 3 linear sections between Aveiro and Coimbra. HSR\_Comb#1\_γ/3 is formed by 3 linear sections between Oporto and Aveiro and by 2 linear sections between Aveiro and Coimbra. This fact, based on the discussion of section 6.4.1 for the small likelihood of changing the HSR node located in a benefitting position at low temperatures of the SAA, explains the differences between the configurations. The HSR solutions do not have an equal plan view, which results in different ground elevations that require different cross-section for the minimization of the construction cost, and which overlay terrain with different characteristics including the exposure to natural hazards.

In fact, the construction costs differ and are larger in HSR\_Comb#2\_γ/3 (103%), mainly due to larger costs of bridges (3%) and tunnels (9%), which then results in an also larger SPC value (103%) of the HSR\_Comb#2\_γ/3 (Table 7-13). Conversely, the performance for natural hazards slightly improves in HSR\_Comb#2\_γ/3 from HSR\_Comb#1\_γ/3. The weighted-scenario performance of HSR\_Comb#2\_γ/3 is 99% of that of HSR\_Comb#1\_γ/3. Although the differences are small, it is interesting to observe that HSR\_Comb#2\_γ/3 aggravates the reconstruction costs of the distant interplate earthquake, with a smaller impact in combination#2 than in combination#1 and decreases the rainfall scenario reconstruction costs, which has a larger objective function impact for combination#2.

By attributing a small weight of 0.1 to the effects of the distant interplate earthquake, an event with low probability of occurrence, combination #2 creates the possibility of obtaining a HSR configuration that may be more sensitive to the occurrence of such an event than HSR\_Comb#1\_γ/3. This means that having large reconstruction/repair costs for the interplate

(distant) earthquake scenario has a larger negative impact in the robust objective function value if Combination#1 is considered. Assuming the earthquake-induced liquefaction (Figure 7-30 i) as the main factor influencing the HSR performance for the scenario, based on a larger affected area than for landslides (Figure 7-30 h)), this means the possibility of overlapping liquefaction hazard zones with vulnerable cross-sections. Two of the main areas subject to liquefaction are located next to the Tagus valley and along the Mondego floodplain. However, the Tagus Valley region is also subject to the effects of the intraplate-earthquake-induced liquefaction (Figure 7-30 g)) and floods (Figure 7-30 k)), the latter also affecting the Mondego floodplain. In these areas, worsening the performance for the distant interplate earthquake scenario also implies worsening the performance for the nearby intraplate scenario and the rainfall scenario, which is avoided. In light of these observations, the solutions found for both combinations soundly suggest, from a planning perspective, the same HSR configuration to be further studied in detailed stages of the problem.

The evolution of the accumulated construction costs, partial and total, along the longitudinal profile of both configurations is shown in Figure 7-32 and Figure 7-33.

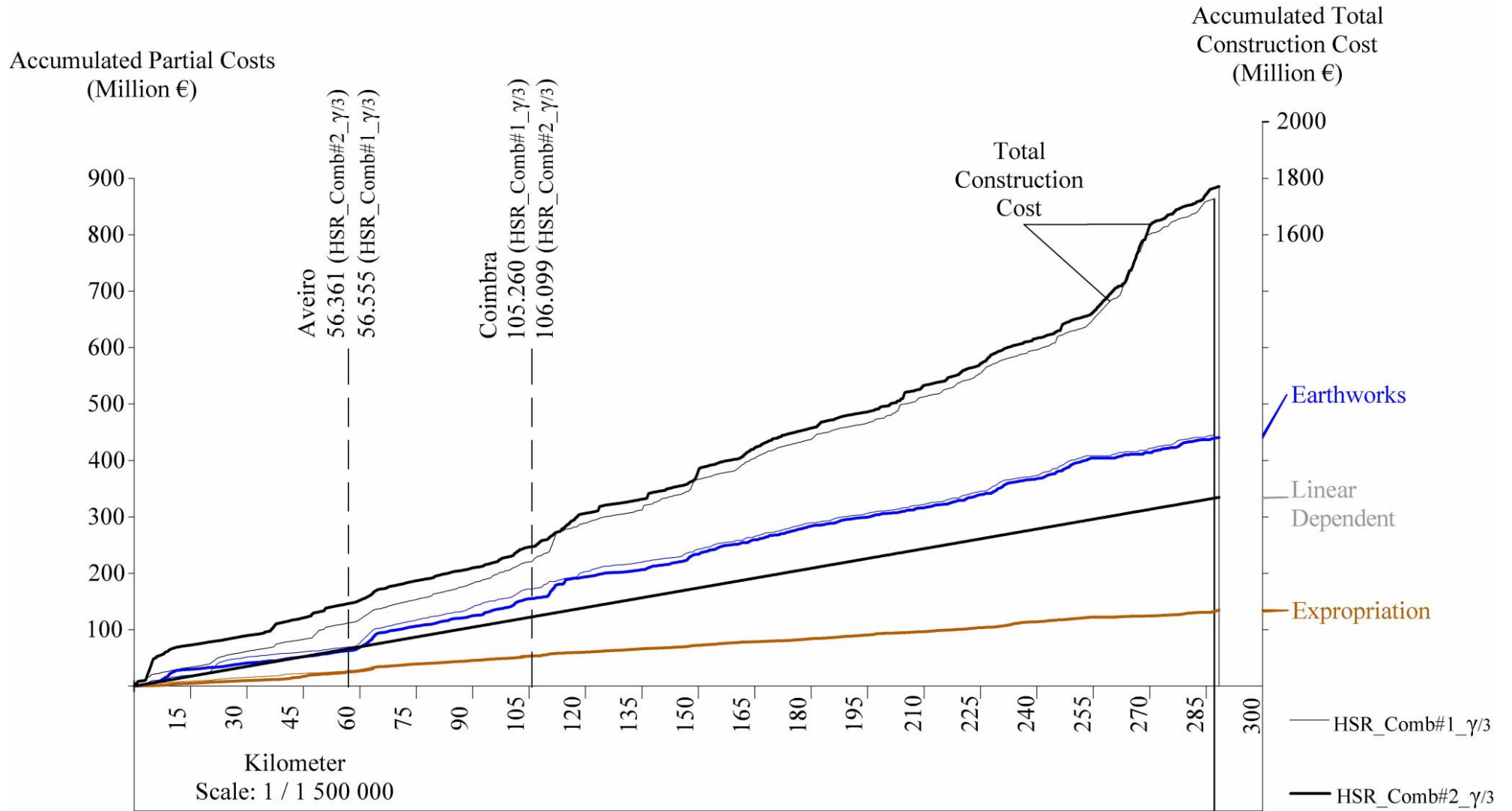


**Figure 7-32** Accumulated costs along the longitudinal profile: total construction costs, earthworks, linear- dependent and expropriation. Costs for HSR\_Comb#2\_γ/3 represented in a thick line and for HSR\_Comb#1\_γ/3 in a thin line.

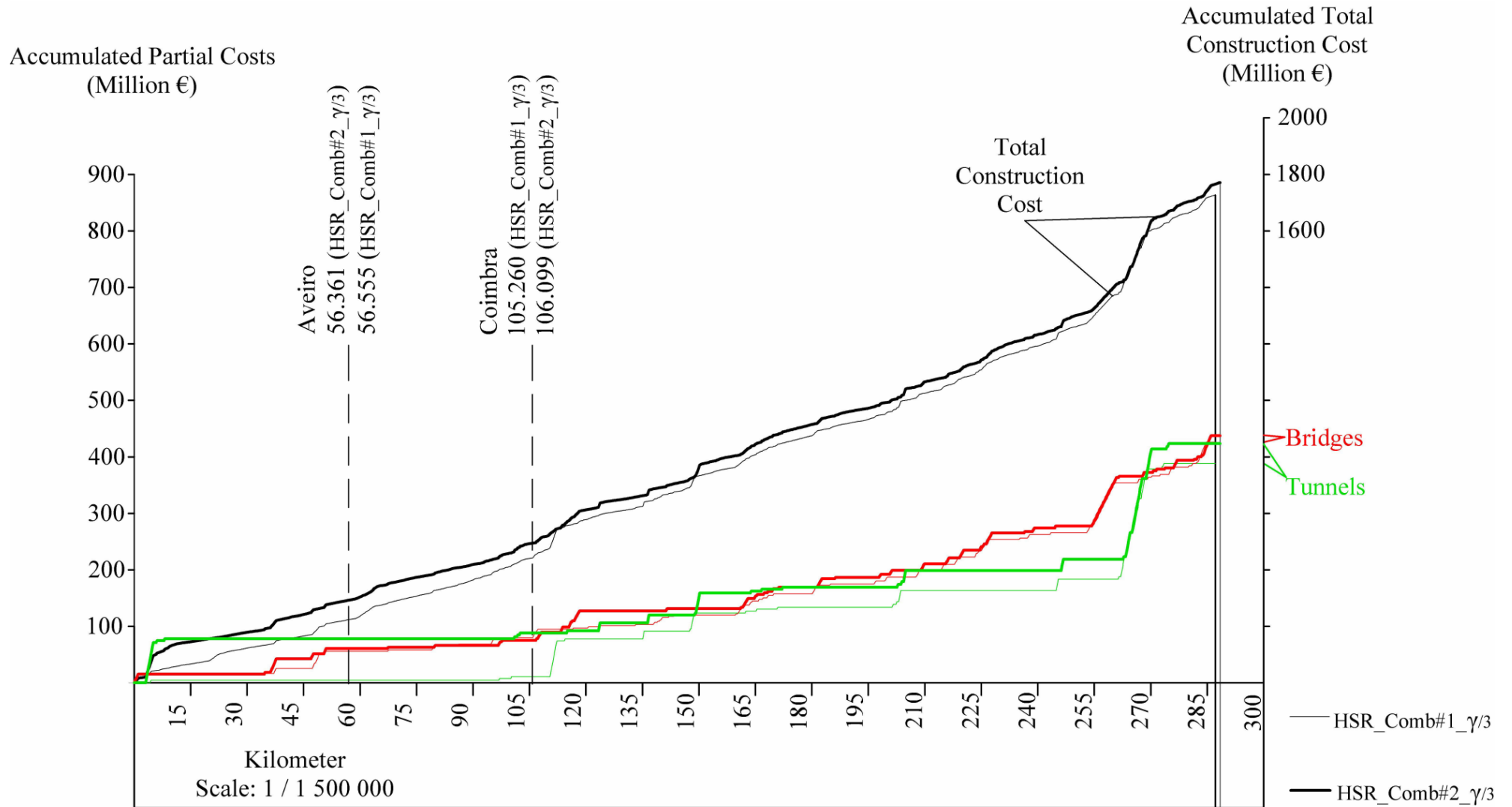


**Figure 7-33** Accumulated costs along the longitudinal profile: total construction costs, bridges and tunnels. Costs for HSR\_Comb#2\_γ/3 represented in a thick line and for HSR\_Comb#1\_γ/3 in a thin line.

Figure 7-32 shows that the main differences in the accumulated total construction cost occur within the first 15 km, equalizing between Coimbra and km 120, after which a small difference occurs and is maintained until Lisbon. While the total accumulated construction cost of HSR\_Comb#2\_γ/3 is always larger or equal to that of HSR\_Comb#1\_γ/3, the costs of earthworks, expropriation and linear- dependent track and catenary have an identical trend along the longitudinal profiles of both HSR configurations. Exception is made for the trend of the earthwork costs between Aveiro and km 150. In this HSR section, the costs of earthworks are larger for HSR\_Comb#1\_γ/3, given the different plan views and longitudinal profiles, resulting in different cross-sections. Figure 7-33 shows how the costs of bridges, but mainly tunnels, influence the trend of the total costs. In fact, the tunnels built in the first 15 km of HSR\_Comb#2\_γ/3 dictate the larger total cost of HSR\_Comb#2\_γ/3, for which part of the cost difference is progressively attenuated until km 150 and resulting in an overall 9% difference between the two HSR configurations (Table 7-13).

## 7.5 REMARKS ON THE ROBUST APPROACH APPLICATIONS

The robust model proposed in section 4.5 for the HSR planning problem is applied to the Lisbon-Oporto case-study. Comparative analyses are performed to illustrate the influence of varying: (i) the scenario-weight combination, (ii) the location benefit coefficients and (iii) the weight  $\omega$  multiplying in the objective function the HSR weighted performance for the scenarios set,  $\sum_{c \in \Omega_{sc}} \Psi c_{\Sigma(i,j) \in \Omega_N} RC_{ij}^c$ . All other application specifics remain unchanged from the SPC applications discussed in chapter 6.

The results show that all HSR solutions found for the robust applications performed (Table 7-5) have larger construction costs than that of HSR\_SPC. However, all HSR configurations improve the geometry layout by having all gradients smaller than  $\eta_{normal} = 20\%$  and all horizontal angles smaller than  $\beta_{normal} = 120^\circ$ . The HSR\_SPC solution has two angles smaller than  $\beta_{normal} = 120^\circ$  next to Coimbra, which allow the connection of Aveiro, Coimbra and Leiria while running parallel to the Mondego River floodplain where low construction costs can be achieved (section 6.3.1). This area however is exposed to flooding by the rainfall scenario (Figure 7-1 k)) and liquefaction induced by the distant interplate earthquake (Figure 7-1 i)). The robust solutions found trade-off larger construction costs for avoiding these areas

exposed to the effects of natural hazards and also for a geometry layout with comparative operational advantages by complying in all circumstances with the geometry normal values.

The results also show that the optimized 3D HSR configurations adjust the combined cross-sections, longitudinal profiles and plan views so that different construction costs but of the same order of magnitude are obtained. These are found for significantly different HSR configurations that correspond to varying ground characteristics including ground elevation and the exposure to natural hazards, with major impacts on the objective function value. The analysis of the construction costs, in terms of breakdown and accumulated costs along the longitudinal profile, shows that the differences are mainly due to differing extents of bridges and particularly tunnels. Earthworks, expropriation and linear-dependent costs correspond, in general, to a similar trend and overall value. The length of the HSR configurations is also similar, bounded between the 283.986 km of HSR\_Comb#1\_ $\gamma$  and 296.332 km of HSR\_SPC.

When comparing the HSR configurations obtained for scenario-weight combinations #1 (section 7.3.2) and #2 (section 7.4.1), considering the location benefit coefficient  $\gamma/3$  and  $\omega=1$ , one obtains the same HSR configurations. The optimized configurations for the one-third reduction of the location benefit results in HSR\_Comb#1\_ $\gamma/3$  and HSR\_Comb#2\_ $\gamma/3$ , neither of which connects Leiria and instead both run eastwards of the Serra de Aires e Candeeiros Natural Parks. Both HSR configurations, when compared to HSR\_Comb#1\_ $\gamma$ , have lower construction costs but larger repair/reconstruction costs for each of the scenarios. These results show how a reduction of the location benefit coefficient trades-off the connection of Leiria by configurations with smaller construction costs that are not overly sensitive to the effects of natural hazards, such as the HSR\_SPC, despite not being the best natural-hazards performing HSR configuration. A compromise between the factors influencing the objective function is achieved by trading off the construction costs, the HSR layout and the natural hazards performance.

When  $\omega=30$  is considered, however, the weight of the natural hazards performance in the objective function value increases. The configuration found in section 7.3.3, HSR\_Comb#1\_ $\gamma/3_{\omega 30}$ , for  $\omega=30$ , scenario-weight combination #1 and location benefit coefficient of  $\gamma/3$  does not connect Aveiro. Instead, the connection of Oporto to Coimbra runs eastward of the areas surrounding Aveiro subject to liquefaction and flood hazards. Between Coimbra and Lisbon, the HSR\_Comb#1\_ $\gamma/3_{\omega 30}$  solution is similar to HSR\_Comb#1\_ $\gamma$ ,



which is the best natural hazards performing configuration within the set of solutions obtained for  $\omega=1$ .



# Chapter 8.

## Conclusions and Future Research

Within the global perspective of HSR planning one can consider significantly different configurations for assessing the performance of the infrastructure. This performance includes the investments made for building and operating the infrastructure but also the capacity to avoid and/or withstand the effects of natural hazards. The strict safety requirements of the infrastructure and the disruptive capabilities of natural hazards attest the need for taking these extreme events into account, especially in a context of large public investments and a society urging for reliable public services (Chapter 2).

Recognizing the need for a fully-integrated 3D approach addressing the planning stage and considering the effects of natural hazards (Chapter 3), the research presented in this thesis formulates a robust approach for the HSR planning problem with scenario-descriptions of the uncertain natural hazards. An optimization model for Standard Planning Conditions (SPC), addressing construction costs, HSR layout and land-use concerns is proposed and subsequently extended to incorporate the effects of natural hazards. A computational tool is developed for implementing the optimization models and applications with real-world data and representing different possible decision-maker views perspectives are presented for planning a new HSR line. This Chapter 8 presents the fundamental findings of the research and suggestions for future developments.

## 8.1 CONCLUSIONS

### 8.1.1 MODELLING THE HSR PLANNING PROBLEM

A Standard Planning Conditions (SPC) model is formulated for the HSR planning problem, which establishes the basis for the robust model considering natural hazards ultimately proposed (Chapter 4). The SPC model (section 4.1) establishes trade-offs between minimizing construction costs and adopting the use of the more restrictive recommended geometry parameters (horizontal angle and gradient), discouraging the crossing of land-use sensitive areas and considering linking additional cities besides the mandatory ones. To establish such trade-offs, the model represents the following problem aspects:

- Mapped data for the characterization of the HSR planning problem.
- 3D layout of the HSR configuration (plan view and longitudinal profile) and its interaction with the mapped properties. Considering the mapped properties that the HSR overlays and the comparison between the HSR and ground elevation is required for assessing the feasibility of the configurations and assessing the objective function value.
- Cross-sections varying with the height and depth of the HSR and the ground behaviour units the HSR is built on. These establish the technical solutions to adopt and define the construction costs.

The fully-integrated 3D optimization overcomes the limitations of 2D analyses: the plan view optimization does not allow assessing the cross-sections and technical solutions required and the respective construction costs; the optimization of the longitudinal profile is limited to a given horizontal alignment. The 3D optimization, however, significantly increases the size and complexity of the problem. For implementing the 3D optimization and cover large areas, as required in planning a HSR infrastructure, the HSR configuration is represented by linear sections only, a simplification of the linear sections, circular curves and transition curves that in reality compose the HSR. This model representation proved a reasonable approach to the HSR planning problem.

While overcoming these difficulties of the HSR planning problem, limitations to the SPC model are recognized. The cross-sections to implement (bridges, tunnels, embankments and cuts) are established by height and depth thresholds. In some cases, building bridges and tunnels below these thresholds or embankments and cuts beyond the thresholds may be appropriate, especially in cases of embankments built on soft and compressible soils. Retaining walls and other similar technical solutions are also effective options. Interaction with the built environment may also increase the construction costs of the infrastructure, with additional requirements such as over- and underpasses and/or reestablishment of existing infrastructure. The time factor is not included in the proposed model and can affect the value of the HSR configuration in terms of construction, operation and maintenance. Acknowledging these limitations, the SPC model is formulated so that it can be extended for the additional incorporation of these complexities in the future.

The SPC model forms the basis of the robust approach to the HSR planning problem. The robust approach is based on the recognition of the capabilities of the uncertain natural hazards to damage the HSR lines. These, in general, cross regions subject to multiple natural hazards and planning for the worst case scenario is economically unrealistic (Chapter 2). The robust model (section 4.5) establishes a trade-off between the SPC performance and the weighted performance for scenarios representing the natural hazards, aiming at finding optimal or near-optimal configurations which are not overly sensitive to any of the scenarios. Each weighted-scenario performance combination represents a particular relative importance given by the decision-maker to the HSR performance across the different scenarios. The performance for each scenario is assessed by the direct market losses pertaining to the physical damage repair and/or replacement of sections damaged by the scenario's natural hazard. A weight  $\omega$  multiplies, in the robust objective function of expression (4.10), the weighted-scenario performance. Considering large values of  $\omega$  allow one to search for optimal or near-optimal HSR configurations that give preference to the natural hazards performance compared to the SPC performance (construction costs and configuration layout). The larger the value of  $\omega$ , the less affected by the natural hazards the solutions are expected to be, always subject to the compliance with the problem constraints (section 4.5.1).

The fundamental achievement of the robust approach is the integrated optimization of the HSR performance for distinct natural hazards and for SPC. This allows for the concurrent analysis of investment levels for ordinary conditions and extreme conditions of performance.

Such integrated approach at the planning scale establishes macro-decisions that set boundaries for the detailed project design and allows the performance assessment of significantly different HSR solutions.

The merits of the robust approach proposed are not without limitations. The HSR disruptions can cause damages beyond the direct market losses of the repair/reconstruction costs, including other direct and indirect losses, both market and non-market. Their consideration requires overcoming difficulties presented by the planning and optimization contexts of the approach and incorporating the time factor in the analysis. Also, other sources of uncertainty can affect the HSR performance, such as geological and geotechnical variability. In addition to these, the limitations presented for the SPC model naturally apply to the robust approach.

#### **8.1.2 COMPUTATIONAL TOOL AND SOLVING TECHNIQUE**

A computational tool is developed to implement both the SPC and robust models and solve these applied to HSR planning problems by implementing the SAA.

This thesis shows how the tool is capable of addressing the feasibility concerns established by both models. For any given configuration, feasibility is assessed by establishing the interrelation between the HSR 3D layout, the deployment site characteristics represented in a raster format and the compliance with thresholds based on applicable standards or on project definitions.

These capabilities are required as the problem constraints can be spatially defined, as in case of land-use, threshold defined, as is the case of geometry, or a combination of both, as in the case of crossing bodies of water. Feasibility concerning the clearance of tunnels and bridges for crossing bodies of water is addressed by incorporating a layer that defines the required clearance threshold along each body of water mapped.

Analogously to feasibility, the construction cost of any feasible HSR configuration is determined by the interrelation between the HSR 3D layout, the deployment site characteristics and the project threshold and unit cost definitions. The different cross-sections are defined by height and depth thresholds that require the comparison of the HSR and ground elevations. Furthermore, depending on the cross-section and the ground behaviour, the HSR

has a varying footprint and this in turn influences cost components such as the expropriation cost.

In fact, apart from track and catenary, which are assumed to vary only with length, all other construction cost items depend on such interrelation of factors. This is also true for the remaining SPC and robust models' objective function terms.

The capabilities in dealing with large input datasets are shown for the Lisbon-Oporto HSR planning problem. In this case, geo-referenced data obtained from Geographic Information Systems (GIS) and corresponding to 44,868.56 square kilometres are stored for 11 layers characterizing the search space. Data storage and management is possible with the use of Microsoft SQL Server 2008 R2, which successfully allowed dealing with varying information for the 1,121,714 space property elements of the problem. Input data can be adjusted within the SQL Server datasets or within a user-friendly interface designed in Microsoft Visual Studio 2010 for a facilitated process.

Solving the Lisbon-Oporto HSR planning problem with the implementation of the Simulated Annealing Algorithm (SAA) for both the SPC and robust models shows the algorithm's and the tool's capabilities for real-world sized problems.

The algorithm implementation is capable of transposing isolated areas of forbidden land-use scattered in the search space by the procedures for generating new candidate HSR configurations. This allows the SAA to comprehensively canvass search space of the problem for finding optimal or near-optimal configurations instead of performing a search confined to a partial area but increases the running time of the SAA. Node clusters such as those discussed in section 4.4.2 are also successfully avoided by the implementation of the linear sections minimum length. The generation of a new candidate HSR configuration and the evaluation of its objective function value take an average 1.71 s. However, the mechanisms for transposing the forbidden land-use areas, particularly for large such areas, are shown to increase this average time to 10.06 s.

If intermediate locations for a benefitting objective function term are considered in the problem, HSR configurations suggesting the same corridor from a planning perspective to be further studied in detail in subsequent stages may be very similar, although not identical. This is due to the random nature of the algorithm coupled with the coarseness of the configuration

discretization (section 6.4.1). However, SAA running times for the SPC model in chapter 6 (varying between 12 days and 18 days on a 3.40GHz Intel® Core™ i7-2600 CPU with 16GB RAM) show that a compromise between the level of discretization and the quality of the solutions produced need to be established for practical applicability. Increasing the level of detail increases the degree of freedom of the problem, which in turn increases the complexity to be addressed by the algorithm and thus the computation running time.

The SAA cooling schedule parameters require an adjustment when solving either the SPC (section 6.2) or the robust model (section 7.2), showing that the quality of the results produced by the SAA implementation is influenced by both the model and problem specifics. In fact, this thesis shows the SAA is capable of solving the HSR planning problem but requires a judicious study on the algorithm implementation and in particular the cooling schedule parameters.

### 8.1.3 THE LISBON-OPORTO HSR PLANNING PROBLEM

The results obtained for the SPC model (chapter 6) and for the robust model (chapter 7) applications show how both models and the tool can address real world problems. Moreover, the comparison of the results highlights that the HSR performance for natural hazards can be improved at moderately larger construction costs that vary with the SPC and hazard performance trade-off. The fundamental findings are discussed.

The analysis of the results obtained for the SPC (chapter 6) show the ability of the SAA to find sound solutions for the SPC planning problem. The solution found for the SPC model connects both Leiria and Aveiro, but performs poorly when evaluated considering the effects of natural hazards (section 7.3.1). This configuration was particularly exposed and vulnerable to floods and earthquake-induced liquefaction around the Mondego and Tagus rivers. The robust optimization model was applied and solved for the same conditions, except for the consideration of natural hazards (section 7.3.1). The results show the robust solution reduces the vulnerability and particularly the exposure to the effects of natural hazards, at 18% larger construction costs. The robust configuration also improves the geometry by having all horizontal angles larger than the normal values. This shows how the combined effects of the construction costs and the intermediate cities prevail in the objective function value of the SPC solution.



The improvement of the HSR natural hazards performance is observed for the robust model when reproducing two possible attitudes of the decision-maker towards natural hazards: a uniform importance given to the effects all three hazards (scenario weight combination #1) and a varying importance depending on the scenario's probability of occurrence (scenario weight combination #2). Applications varying only the scenario combination suggest the same HSR configuration to be further detailed in subsequent stages of the project. This observation shows how different decision-maker attitudes towards the risks of natural hazards can result in the same HSR solution when the overlay of natural hazards affected areas coincides, even if partially.

The effect of the value associated with the connection of Aveiro and Leiria is also studied for a one third benefit reduction in section 7.3.2. The results show that the benefit reduction leads to a robust solution that does not cross Leiria and instead runs eastwards of the forbidden land-use area Serras de Aires e Candeeiros Natural Parks. This observation shows that the valuation of crossing intermediate cities has an important impact on the HSR solution. It illustrates that a thorough evaluation of such location value should be conducted. Namely, in accounting for the negative impacts of linking the intermediate cities, such as speed reductions and the impacts of longer connecting times that may affect the quality of the service and the demand captured.

An additional trade-off between the SPC performance and the HSR performance for natural hazards is studied. By considering  $\omega=30$ , the weighted scenario performance increases its influence in the robust objective function value. The solution found (section 7.3.3) does not connect Aveiro to avoid natural hazards affected areas, being the only solution to do so within all the applications performed. This illustrates how sufficiently large values of  $\omega$  can be used to increase the importance attributed to the extreme scenario robustness that results in solutions less affected by natural hazards. In fact, varying the value of  $\omega$  can be used to adjust to the decision-maker perspective or to derive a set of solutions adopting different levels of robustness for extreme events and support an informed decision-making.

Overall, it is observed that increasing the HSR performance for natural hazards increases, as expected, the construction cost of the optimized solution. The lowest construction cost is achieved for the SPC solution, the most affected by hazards, followed by the construction cost of the robust solutions found for  $\omega=1$ . The costliest solution is obtained with  $\omega=30$ , roughly

150% more expensive than those obtained for  $\omega=1$ . Solutions with similar construction costs but crossing notably different corridors are found for SPC and  $\omega=1$ , giving evidence of the capabilities of the approach in optimizing the HSR configuration for different circumstances. Furthermore, the construction cost of the HSR configurations is within cost bounds of existing HSR projects around the world, particularly closer to the lower bounds.

The applications performed for the Lisbon-Oporto HSR planning problem shows the model and tool capabilities in solving large and complex problems. These can be applied to other HSR problems as neither the model nor the tool (including the SAA) is case-specific. The ability to consider spatially distributed data with GIS derived formats is central for the characterization of the HSR planning problem as GIS is commonly used for storing and managing such information. Also, the feasibility and other project requirements can be adjusted by the user to accommodate varying particularities of the problem.

## **8.2 FUTURE DEVELOPMENTS**

Multiple factors affect the decision-making in HSR planning. To comprehensively consider them and the interrelations established amongst them increases the odds for the success of the HSR project and supports a conscious allocation of resources. Based on the conclusions discussed and the limitations identified in this thesis, subjects for future research are identified.

Based on the sound results obtained, integrated approaches should be reproduced in modelling the HSR planning problem and should continue to establish the intricate relations between the spatially distributed characteristics of the implementation area, the HSR configuration, the project specifics and applicable standards. These should also fully-integrate the three-dimensionality of the problem within the optimization process, as considered in this thesis, the only approach that allows for the global consideration of the problem and refrains from being restrained to the partial perspective of 2D analyses. Considering these recommendations, directions for further developments are proposed.

It is suggested that a more comprehensive formulation for the construction cost is developed. Building bridges and tunnels beyond the height thresholds may be an option in certain circumstances. Other technical solutions can also be implemented such as retaining walls that

may constitute effective options in cuts where the footprint of the HSR is limited by external factors. The HSR interaction with existing infrastructure (roads, railways, electricity supply, telecommunications, etc.) should also be included. The same principles used for crossing bodies of water with bridges or tunnels, with the identification of clearance thresholds, apply to grade-separated crossings and can be extended for the consideration of infrastructure interaction.

Future developments should incorporate operating costs in the optimization of the HSR layout. Both the alignment geometry and the existence of intermediate stops along the HSR alignment may require speed reductions during operation. These speed reductions affect the travel time, which can affect demand and thus operations costs. An integrated approach considering the optimization models proposed in this thesis combined with existing models for the optimization of the HSR station number and station locations is also suggested. This should judiciously account for the operational positive and negative impacts of HSR intermediate stops. In addition, maintenance of the infrastructure is also required and varies, amongst other factors, with the interrelation between the cross-section and local ground characteristics.

The methodology for assessing the HSR vulnerability to the effects of natural hazards should also be refined. Degrees of vulnerability should be considered in light of the threat and the HSR characteristics. Based on a refined HSR vulnerability assessment, a methodology for including social and economic factors when assessing the impacts of HSR disruptions due to natural hazards should be developed. Such an approach addresses the fact that HSR service disruptions, ranging from short delays to the complete lack of service, produce additional impacts and losses that add to the costs of the physical damages. Accounting for the social and economic impacts should complement the losses due to the physical damage of the infrastructure.

The preceding suggestions aim at extending the capabilities in modelling the HSR planning problem. For practical applicability, the additional complexities of the approach have to be addressed by both the computational tool and the solving algorithm. The algorithm implementation should require additional studies based on the new complexities added to the problem. Moreover, the computational tool capabilities have to address the extended requirements. Besides the possibility of machines with faster processing capabilities, parallel

programming, which is already implemented in this thesis, is suggested to tackle the additional complexity.

# Literature References

- Aarts, E. H. L., and Vanlaarhoven, P. J. M. (1985). "Statistical cooling: a general approach to combinatorial optimization problems." *Philips Journal of Research*, 40(4), 193–226.
- Aarts, E., Korst, J., and Van Laarhoven, P. J. M. (1997). "Simulated Annealing." *Local Search in Combinatorial Optimization*, E. Aarts and J. K. Lenstra, eds., John Wiley & Sons, Inc., New York, NY, USA, 91–120.
- Aarts, E., and Lenstra, J. K. (1997). "Introduction." *Local Search in Combinatorial Optimization*, E. Aarts and J. K. Lenstra, eds., John Wiley & Sons, Inc., New York, NY, USA, 1–16.
- Ahlfeldt, G. M., and Feddersen, A. (2010). "From Periphery to Core: Economic Adjustments to High Speed Rail." London School of Economics & University of Hamburg. (Unpublished), <<http://eprints.lse.ac.uk/29430/>>.
- Ambraseys, N. N. (1988). "Engineering seismology." *Earthquake Engineering & Structural Dynamics, Special Issue: The 1987 Mallet-Milne Lecture*, 17(1), 1–50.
- Angulo, E., Castillo, E., Garcia-Rodenas, R., and Sanchez-Vizcaino, J. (2012). "Determining highway corridors." *Journal of Transportation Engineering*, 138(5), 557–570.
- APA. (2012). "Environmental Atlas." *Portuguese Environmental Agency*, <<http://sniamb.apambiente.pt/webatlas/>> (Mar. 14, 2012).
- Arias, A. (1970). "A measure of earthquake intensity." *Seismic Design for Nuclear Power Plants*, R. J. Hansen, ed., M.I.T. Press, Cambridge, MA, 438 – 483.
- Ashford, S. A., and Kawamata, Y. (2006). "Performance of transportation systems during the 2004 Niigata Ken Chuetsu, Japan, earthquake." *Earthquake Spectra*, 22(1), S111–S132.
- Azevedo, J., Guerreiro, L., Bento, R., Lopes, M., and Proença, J. (2009). "Seismic vulnerability of lifelines in the greater Lisbon area." *Bulletin of Earthquake Engineering*, 8(1), 157–180.
- Bai, D. W., Carpenter, T., and Mulvey, J. (1997). "Making a case for robust optimization models." *Management Science*, 43(7), 895–907.
- BBC News. (2010). "Landslide in Jiangxi China derails train killing 19." <<http://www.bbc.co.uk/news/10143258>>.
- BBC News. (2012). "Sellafield train derails as floods hit Cumbria." <<http://www.bbc.co.uk/news/uk-england-cumbria-19420159>>.

- Bertsimas, D., Brown, D. B., and Caramanis, C. (2011). "Theory and Applications of Robust Optimization." *SIAM Review*, 53(3), 464–501.
- Bertsimas, D., and Nohadani, O. (2010). "Robust optimization with simulated annealing." *Journal of Global Optimization*, 48(2), 323–334.
- Betâmio de Almeida, A. (2009). "The 1755 Lisbon Earthquake and the genesis of the risk management concept." *Geotechnical, Geological and Earthquake Engineering, Volume 7 - The 1755 Lisbon Earthquake: Revisited*, A. Mendes-Victor, L.; Sousa Oliveira, C.; Azevedo, J.; Ribeiro, ed., Springer Netherlands, 147–155.
- Betâmio de Almeida, A. (2011). *Gestão da Água - Incerteza e Riscos. Conceptualização Operacional*. (Esfera do Caos, ed.), Lisbon, Portugal, 237.
- Blanchard, B. (2012). "Rare Beijing protest takes aim at high speed rail project." *Reuters*, <<http://in.reuters.com/article/2012/12/09/china-protest-beijing-rail-idINDEE8B803N20121209>> (Feb. 27, 2013).
- Blum, C., and Roli, A. (2003). "Metaheuristics in combinatorial optimization: Overview and conceptual comparison." *Acm Computing Surveys*, 35(3), 268–308.
- Brandão, C., Rodrigues, R., and Costa, J. (2001). *Analysis of Extreme Phenomena of Intense Rainfall in Mainland Portugal*. Lisbon, Portugal.
- Brandão, C., Rodrigues, R., and Costa, J. (2004). *The floods in Portugal - Public Sensibilization Session*. (MAOT, ed.), Lisbon, Portugal.
- Brons, M., Givoni, M., and Rietveld, P. (2009). "Access to railway stations and its potential in increasing rail use." *Transportation Research Part A: Policy and Practice*, 43(2), 136–149.
- Byers, W. G. (2008). "The Shake Out Scenario Supplemental Study - Railway Network." U.S. Geological Survey Open File Report 2008-1150, United States Geological Survey and California Geological Survey.
- Cabral, J., Moniz, C., Batlló, J., Figueiredo, P., Carvalho, J., Matias, L., Teves-Costa, P., Dias, R., and Simão, N. (2011). "The 1909 Benavente (Portugal) earthquake: search for the source." *Natural Hazards*, Springer Netherlands, (Publishe online DOI:10.1007/s11069-011-0062-8), 1–17.
- Campos Costa, A. (2008). "Fundamentals of probabilistic risk analysis – Methods and applications." *Advanced Course on Risk Management in Civil Engineering*, LNEC, Lisbon.
- Campos Costa, A., and Sousa, M. (2008). "Seismic zonation for Portuguese National Annex of Eurocode 8." *14 th World Conference on Earthquake Engineering*, Beijing, China, 8–15.
- Campos, J., and de Rus, G. (2009). "Some stylized facts about high-speed rail: A review of HSR experiences around the world." *Transport Policy*, 16(1), 19–28.
- Castellanos Abella, E. A., and Van Westen, C. J. (2008). "Qualitative landslide susceptibility assessment by multicriteria analysis: A case study from San Antonio del sur, Guantanamo, Cuba." *Geomorphology*, 94(3-4), 453–466.

- CEN. (2002). "Railway application - Track alignment design parameters - Track gauges 1435 mm and wider - Part 1: Plain Line." *ENV 13803-1, CEN - European Committee for Standardization*.
- Cerny, V. (1985). "Thermodynamical approach to the Traveling Salesman problem - an efficient simulation algorithm." *Journal of Optimization Theory and Applications*, 45(1), 41–51.
- Chang, S. E. (2003). "Transportation planning for disasters: an accessibility approach." *Environment and Planning*, 35(6), 1051–1072.
- Chang, S. E., and Nojima, N. (2001). "Measuring post-disaster transportation system performance: the 1995 Kobe earthquake in comparative perspective." *Transportation Research Part A: Policy and Practice*, 35(6), 475–494.
- Chang, S., and Nojima, N. (1997). "Highway system performance measures and economic impact." *Proceedings of the 7th U.S.-Japan Workshop on Earthquake Disaster Prevention for Lifeline Systems*, Seattle, Washington, USA.
- Chang, Y.-H., Yeh, C.-H., and Shen, C.-C. (2000). "A multiobjective model for passenger train services planning: application to Taiwan's high-speed rail line." *Transportation Research Part B: Methodological*, 34(2), 91–106.
- Cheng, J. F., and Lee, Y. S. (2006). "Model for three-dimensional highway alignment." *Journal of Transportation Engineering*, 132(12), 913–920.
- Chester, D. K. (2008). "The effects of the 1755 Lisbon earthquake and tsunami on the Algarve region, southern Portugal." *Geography*, 93(Part 2), 78–90.
- China Daily. (2011). "Landslides strand 5,000 on 4 trains." <[http://www.china.org.cn/china/2011-06/18/content\\_22811102.htm](http://www.china.org.cn/china/2011-06/18/content_22811102.htm)>.
- Cho, S., Gordon, P., Moore II, J. E., Richardson, H. W., Shinozuka, M., and Chang, S. (2001). "Integrating Transportation Network and Regional Economic Models to Estimate the Costs of a Large Urban Earthquake." *Journal of Regional Science*, 41(1), 39–65.
- Christian, J. T. (2004). "Geotechnical engineering reliability: How well do we know what we are doing?" *Journal of Geotechnical and Geoenvironmental Engineering*, 130(10), 985–1003.
- Cimellaro, G. P., Reinhorn, A. M., and Bruneau, M. (2010). "Framework for analytical quantification of disaster resilience." *Engineering structures*, 32(11), 3639–3649.
- Coelho, P. A. L. F. (2000). "Geotechnical Characterization of Soft Soils - Study of the Quinta da Foja (Lower Mondego) Experimental Site." Master Thesis. Department of Civil Engineering, Faculty of Sciences and Technology, University of Coimbra.
- Coelho, P., and Costa, A. (2009). "Identification and characterization of liquefaction risks for high-speed railways in Portugal." *Geotechnical Safety and Risk: Proceedings of the 2nd International Symposium on Geotechnical Safety and Risk*, Y. Honjo, T. Hara, M. Suzuki, and F. Zhang, eds., CRC Press-Taylor & Francis Group, Gifu.
- Coelho, P., Haigh, S., and Madabhushi, S. (2006). "Effects of successive earthquakes on saturated deposits of sand." *Physical Modelling in Geotechnics Proceedings of the Sixth International*

- Conference on Physical Modelling in Geotechnics*, C. W. W. Ng, Y. H. Wang, and L. M. Zhang, eds., Taylor & Francis, Hong-Kong.
- Cohanim, B. E., Hewitt, J. N., and de Weck, O. (2004). "The Design of Radio Telescope Array Configurations using Multiobjective Optimization: Imaging Performance versus Cable Length." *The Astrophysical Journal Supplement Series*, 154(2), 705–719.
- Costa, A. L., Cunha, C., Coelho, P. A. L. F., and Einstein, H. H. (2013). "Solving High-Speed Rail Planning with the Simulated Annealing Algorithm." *Journal of Transportation Engineering*, 139(6), 635–642.
- Cunha, M. C. (1999). "On solving aquifer management problems with simulated annealing algorithms." *Water Resources Management*, 13(3), 153–169.
- Cunha, M. C., and Sousa, J. J. O. (2001). "Hydraulic infrastructures design using simulated annealing." *Journal of Infrastructure Systems*, 7(1), 32–39.
- Cunha, M. C., and Sousa, J. J. O. (2009). "Robust design of water distribution networks: A comparison of two different approaches." *Integrating Water Systems: Proceedings of Computer and Control in the Water Industry*, C. Boxall, J and Maksimovic, ed., CRC Press-Taylor & Francis Group, Sheffield, UK, 181–187.
- Cunha, M. C., and Sousa, J. J. O. (2010). "Robust Design of Water Distribution Networks for a Proactive Risk Management." *Journal of Water Resources Planning and Management*, 136(2), 227–236.
- Daskin, M. S., Hesse, S. M., and Revelle, C. S. (1997). " $\alpha$ -Reliable p-minimax regret: A new model for strategic facility location modeling." *Location Science*, 5(4), 227–246.
- Dekkers, A., and Aarts, E. (1991). "Global optimization and simulated annealing." *Mathematical Programming*, 50(1), 367–393.
- De Weck, O., and Willcox, K. (2010). "Lecture 10: Simulated Annealing - A Basic Introduction." ESD.77 Multidisciplinary System Design Optimization, Spring 2010. (Massachusetts Institute of Technology: MIT OpenCourseWare), <http://ocw.mit.edu> (Accessed 08 Apr, 2013). License: Creative Commons BY-NC-SAMassachusetts Institute of Technology, Cambridge.
- Dickenson, S. E., McCullough, N. J., Barkau, M. G., and Wavra, B. J. (2002). "Assessment and Mitigation of Liquefaction Hazards to Bridge Approach Embankments in Oregon." Report No. FHWA-OR-RD-03-04, Oregon Department of Transportation Research Group, Salem, Oregon and Federal Highway Administration, Washington, D.C.
- Dorren, L. K. ., and Seijmonsbergen, A. C. (2003). "Comparison of three GIS-based models for predicting rockfall runout zones at a regional scale." *Geomorphology*, 56(1-2), 49–64.
- Dorren, L. K. a. (2003). "A review of rockfall mechanics and modelling approaches." *Progress in Physical Geography*, 27(1), 69–87.
- Dumas, C., Mansukhani, S., Porbaha, A., Short, R. D., Cannon, R. R., McLain, K. W., Putcha, S., Macnab, A., Lwin, M., Pelnik III, T. W., Brown, D. A., and Christopher, B. R. (2003). *Innovative Technology for Accelerated Construction of Bridge and Embankment Foundations In Europe - Report No. FHWA-PL-03-014*. Washington, DC 20590, 1–90.



- EC. (2008). "Commission Decision of 20 December 2007 concerning a technical specification for interoperability relating to the infrastructure sub-system of the trans-European high-speed rail system." *Official Journal of the European Union*, <<http://eur-lex.europa.eu/>> (Nov. 30, 2011).
- EC. (2010). "Risk Assessment and Mapping Guidelines for Disaster Management." *Commission Staff Working Paper SEC(2010) 1626 final*, European Commission, Brussels, 1–43.
- EC. (2013). "Code of Good Practice For Consultation of Stakeholders." *Directorate-General Health and Consumers, European Commission*, <[http://ec.europa.eu/dgs/health\\_consumer/dgs\\_consultations/docs/code\\_good\\_practices\\_consultation\\_en.pdf](http://ec.europa.eu/dgs/health_consumer/dgs_consultations/docs/code_good_practices_consultation_en.pdf)>.
- EEA. (2010). "Mapping the impacts of natural hazards and technological accidents in Europe: An overview of the last decade." *Mapping the impacts of natural hazards and technological accidents in Europe: An overview of the last decade*, Technical report No 13/2010, European Environment Agency, Copenhagen.
- Einstein, H. H., Sousa, R. L., Karam, K., Manzella, I., and Kveldsvik, V. (2010). "Rock slopes from mechanics to decision making." *Rock Mechanics in Civil and Environmental Engineering*, J. Zhao, J and Labiouse, V and Dudt, JP and Mathier, ed., CRC Press-Taylor & Francis Group, 3–13.
- EQE. (1994). *The January 17, 1994 Northridge, California Earthquake, An EQE Summary Report*. San Francisco, 1–66.
- EQE. (1995). *The January 17, 1995 Kobe Earthquake - An EQE Summary Report*. *Earthquake*, San Francisco, 1–106.
- EQECAT. (2002). *Central European Flooding, August 2002, An EQECAT Technical Report*. Oakland, CA 94612, 1–21.
- Ermini, L., Catani, F., and Casagli, N. (2005). "Artificial Neural Networks applied to landslide susceptibility assessment." *Geomorphology*, 66(1-4), 327–343.
- Eurostat. (2013a). "Euro/ECU exchange rates - annual data." *European Commission*, <[http://epp.eurostat.ec.europa.eu/portal/page/portal/exchange\\_rates/data/database](http://epp.eurostat.ec.europa.eu/portal/page/portal/exchange_rates/data/database)> (Jul. 21, 2013).
- Eurostat. (2013b). "HICP - Inflation Rate." *European Commission*, <<http://epp.eurostat.ec.europa.eu/tgm/table.do?tab=table&plugin=1&language=en&pcode=tec00118>> (Jun. 27, 3013).
- Evans, W. A., and Morrison, A. D. (1997). "Incorporating Accident Risk and Disruption in Economic Models of Public Transport." *Journal of Transport Economics and Policy*, 31(2), 117–146.
- Faber, M. H., and Stewart, M. G. (2003). "Risk assessment for civil engineering facilities: critical overview and discussion." *Reliability Engineering & System Safety*, 80(2), 173–184.
- FEMA. (2001). "Port-to-Port Transportation Corridor Earthquake Vulnerability Study." *Project Impact - A Partnership between King and Pierce Counties, "Creating Disaster Resistant Communities"*, Washington, D.C., <<http://www.fema.gov/library/viewRecord.do?id=4306>>.

- Fortunato, E. M. C. (2005). "Renewal of Railway Platforms - Studies about Bearing Capacity." PhD dissertation, Faculty of Engineering of the University of Porto.
- Fukao, Y. (1973). "Thrust Faulting at a Lithospheric Plate Boundary Portugal Earthquake of 1969." *Earth and Planetary Science Letters*, 18(2), 205–216.
- Fwa, T. F., Chan, W. T., and Sim, Y. P. (2002). "Optimal vertical alignment analysis for highway design." *Journal of Transportation Engineering*, 128(5), 395–402.
- Gipps, P. G., Gu, K. Q., Held, A., and Barnett, G. (2001). "New technologies for transport route selection." *Transportation Research Part C: Emerging Technologies*, 9(2), 135–154.
- Givoni, M., and Rietveld, P. (2007). "The access journey to the railway station and its role in passengers' satisfaction with rail travel." *Transport Policy*, 14(5), 357–365.
- Gordon, P., Richardson, H. W., and Davis, B. (1998). "Transport-related impacts of the Northridge Earthquake." *Journal of Transportation and Statistics*, 1(2), 21–36.
- Greager, B., Werle, B., Krogman, J., and Erker, M. (2005). "Evaluation of Quantm Software Final Report, Report No. CDOT-DTD-E-2006-1." Colorado Department of Transportation - Research Branch, Denver, CO.
- Günneç, D., and Salman, F. S. (2011). "Assessing the reliability and the expected performance of a network under disaster risk." *OR Spectrum*, 33(3, SI), 499–523.
- Gutscher, M. A. (2006). "The great Lisbon earthquake and tsunamis of 1755: lessons from the recent Sumatra earthquakes and possible link to Plato's Atlantis." *European Review*, (14), pp 181–191.
- Hallegatte, S., and Przulski, V. (2010). "The Economics of Natural Disasters: Concepts and Methods." *The World Bank*, The World Bank.
- Hansen, W. G. (1959). "How Accessibility shapes land-use." *Journal of the American Institute of Planners*, 25(2), 73–76.
- Hintz, C., and Vonderohe, A. P. (2011). "Comparison of Earthwork Computation Methods." *Transportation Research Record*, 2215, 100–104.
- Ingber, L. (1993). "Simulated annealing: Practice versus theory." *Mathematical and Computer Modelling*, 18(11), 29–57.
- Ip, W. H., and Wang, D. (2011). "Resilience and Friability of Transportation Networks: Evaluation, Analysis and Optimization." *IEEE Systems Journal*, 5(2), 189–198.
- IPCC. (2012). *Managing the Risks of Extreme Events and Disasters to Advance Climate Change Adaptation*. Cambridge University Press, Cambridge, UK, and New York; NY, USA, 582 pp.
- Ishihara, K. (1993). "Liquefaction and flow failure during earthquakes." *Géotechnique*, 43(3), 351–451.
- ISSMGE. (2004). "Glossary of Risk Assessment Terms - Version 1." *TC32 - Technical Committee on Risk Assessment and Management*.

- Jenelius, E., and Mattsson, L.-G. (2012). "Road network vulnerability analysis of area-covering disruptions: A grid-based approach with case study." *Transportation Research Part A: Policy and Practice*, 46(5), 746–760.
- Jha, M. K. (2003). "Criteria-based decision support system for selecting highway alignments." *Journal of Transportation Engineering*, 129(1), 33–41.
- Jha, M. K., and Schonfeld, P. (2000). "Integrating genetic algorithms and geographic information system to optimize highway alignments." *Transportation Research Record: Journal of the Transportation Research Board*, Washington, D.C., 1719, 233–240.
- Jha, M. K., and Schonfeld, P. (2004). "A highway alignment optimization model using geographic information systems." *Transportation Research Part a-Policy and Practice*, 38(6), 455–481.
- Jha, M. K., Schonfeld, P., and Samanta, S. (2007). "Optimizing rail transit routes with genetic algorithms and geographic information system." *Journal of Urban Planning and Development*, 133(3), 161–171.
- Jilla, C. D., and Miller, D. W. (2001). "Assessing the performance of a heuristic simulated annealing algorithm for the design of distributed satellite systems." *Acta Astronautica*, 48(5-12), 529–543.
- Johnson, D. S. (2012). "A Brief History of NP-Completeness , 1954 – 2012." *Documenta Mathematica*, (Extra Volume: Optimization Stories), 359–376.
- Johnson, D. S., Aragon, C. R., McGeoch, L. A., and Schevon, C. (1989). "Optimization by Simulated Annealing - An Experimental Evaluation . Part 1. Graph Partitioning." *Operations Research*, 37(6), 865–892.
- Johnson, D. S., and McGeoch, L. A. (1997). "The traveling salesman problem: a case-study." *Local Search in Combinatorial Optimization*, E. Aarts and J. K. Lenstra, eds., John Wiley & Sons Ltd, New York, NY, USA, 215–310.
- Jong, J. C. (1998). "Optimizing highway alignments with genetic algorithms." *PhD dissertation, Department of Civil and Environmental Engineering, University of Maryland, College Park, Md.*
- Jong, J. C., Jha, M. K., and Schonfeld, P. (2000). "Preliminary highway design with genetic algorithms and geographic information systems." *Computer-Aided Civil and Infrastructure Engineering*, 15(4), 261–271.
- Jong, J. C., and Schonfeld, P. (1999). "Cost Functions for Optimizing Highway Alignments ." *Transportation Research Record: Journal of the Transportation Research Board*, 1959(Volume 1659 / 1999), 58–67.
- Jorge, C. (1993). "Zoning of liquefaction potential. Application attempt to the Portuguese territory." *MSc dissertation, New University of Lisbon, Lisboa.*
- Jorge, C., and Vieira, A. M. (1997). "Liquefaction potential assessment - Application to the Portuguese territory and to the town of Setubal." *Special Technical Session on Earthquake Geotechnical Engineering at the 14th International Conference on Soil Mechanics and Foundation Engineering*, P. S. SecoePinto, ed., A a Balkema Publishers, Hamburg, Germany, 33–43.

- JRC. (2003). *Lessons Learnt from Landslide Disasters in Europe, EUR 20558 EN*. (J. Hervás, ed.), Joint Research Centre, European Commission, Ispra, Italy, 91.
- Kang, M. W., Jha, M. K., and Schonfeld, P. (2012). “Applicability of highway alignment optimization models.” *Transportation Research Part C: Emerging Technologies*, 21(1), 257–286.
- Kang, M. W., Schonfeld, P., and Jong, J.-C. (2007). “Highway alignment optimization through feasible gates.” *Journal of Advanced Transportation*, 41(2), 115–144.
- Keefer, D. K. (1984). “Landslides caused by earthquakes.” *Geological Society of America Bulletin*, 95(4), 406–421.
- Kim, E., Jha, M. K., and Schonfeld, P. (2004). “Intersection construction cost functions for alignment optimization.” *Journal of Transportation Engineering*, 130(2), 194–203.
- Kim, E., Jha, M. K., Schonfeld, P., and Kim, H. S. (2007). “Highway alignment optimization incorporating bridges and tunnels.” *Journal of Transportation Engineering*, 133(2), 71–81.
- Kircher, C. a., Whitman, R. V., and Holmes, W. T. (2006). “HAZUS Earthquake Loss Estimation Methods.” *Natural Hazards Review*, 7(2), 45–59.
- Kirkpatrick, S. (1984). “Optimization by simulated annealing: quantitative studies.” *Journal of Statistical Physics*, 34(5-6), 975–986.
- Kirkpatrick, S., Gelatt, C. D., and Vecchi, M. P. (1983). “Optimization by simulated annealing.” *Science*, 220(4598), 671–680.
- Koenig, J. G. (1980). “Indicators of urban accessibility - Theory and application.” *Transportation*, 9(2), 145–172.
- Van Laarhoven, P. J. M., and Aarts, E. H. L. (1987). *Simulated annealing: theory and applications*. Kluwer Academic Publishers Group, Dordrecht, The Netherlands.
- Laguna, M. (1998). “Applying robust optimization to capacity expansion of one location in telecommunications with demand uncertainty.” *Management Science*, 44(11, Part 2), S101–S110.
- Lee, C. T., Huang, C. C., Lee, J. F., Pan, K. L., Lin, M. L., and Dong, J. J. (2008). “Statistical approach to earthquake-induced landslide susceptibility.” *Engineering Geology*, 100, 43–58.
- Lee, Y., Tsou, Y. R., and Liu, H. L. (2009). “Optimization method for highway horizontal alignment design.” *Journal of Transportation Engineering*, 135(4), 217–224.
- Lempert, R. J., Groves, D. G., Popper, S. W., and Bankes, S. C. (2006). “A general, analytic method for generating robust strategies and narrative scenarios.” *Management Science*, 52(4), 514–528.
- Levinson, D., Mathieu, J. M., and Gillen, D. (1997). “The full cost of high-speed rail: an engineering approach.” *The Annals of Regional Science*, 31, 189–215.
- Lindahl, M. (2001). *Track geometry for high-speed railways - A literature survey and simulation of dynamic vehicle response TRITA-FKT Report 2001:54*. Department of Vehicle Engineering, Royal Institute of Technology, Stockholm, 1–148.

- Link, L. E. (2010). "The anatomy of a disaster, an overview of Hurricane Katrina and New Orleans." *Ocean Engineering*, 37(1), 4–12.
- List, G. F., Wood, B., Nozick, L. K., Turnquist, M. A., Jones, D. A., Kjeldgaard, E. A., and Lawton, C. R. (2003). "Robust optimization for fleet planning under uncertainty." *Transportation Research Part E-Logistics and Transportation Review*, 39(3), 209–227.
- Lu, Q.-C., and Peng, Z.-R. (2011). "Vulnerability Analysis of Transportation Network Under Scenarios of Sea Level Rise." *Transportation Research Record*, (2263), 174–181.
- Luna, R., Hoffman, D., and Lawrence, W. T. (2008). "Estimation of Earthquake Loss due to Bridge Damage in the St. Louis Metropolitan Area. I: Direct Losses." *Natural Hazards Review*, 9(1), 1–11.
- Mackie, K. R., Wong, J.-M., and Stojadinović, B. (2010). "Post-earthquake bridge repair cost and repair time estimation methodology." *Earthquake Engineering & Structural Dynamics*, 39, 281–301.
- Malcolm, S. A., and Zenios, S. A. (1994). "Robust Optimization for Power-Systems Capacity Expansion under Uncertainty." *Journal of the Operational Research Society*, 45(9), 1040–1049.
- Markowitz, H. (1991). "Foundations of Portfolio Theory." *Journal of Finance*, 46(2), 469–477.
- Martins, I., and Mendes-Victor, L. A. (1993). "A actividade sísmica na região Oeste da Península Ibérica. Energética e períodos de retorno, Publ. IGIDL, Vol. 20," *Publ. IGIDL*, Lisbon University, 20.
- Mendoza, G. de R., Mendez, F. J. C., Gagnepain, P., Nash, C., Segui, A. U., Vickerman, R., and Angoití, I. M. B. (2009). *Economic Analysis of High Speed Rail in Europe*. (G. De Rus, ed.), Fundación BBVA, 1–140.
- Merlot, L., and Gipps, P. (2008). "Improving the Method of Seed Generation for a Route Optimization Software Package - Abstract." *SIAM Conference on Optimization*, Society for Industrial and Applied Mathematics, Boston, Massachusetts, May 10-13.
- Metropolis, N., Rosenbluth, A. W., Rosenbluth, M. N., Teller, A. H., and Teller, E. (1953). "Equation of State Calculations by Fast Computing Machines." *Journal of Chemical Physics*, 21(6), 1087–1092.
- Mileti, D. (1999). "Chapter 3 Losses, Costs, and Impacts." *Disasters by Design: A Reassessment of Natural Hazards in the United States*, Joseph Henry Press, Washington, DC, 65–104.
- Moran, A. P., Thieken, A. H., Schöbel, A., and Rachoy, C. (2010). "Documentation of Flood Damage on Railway Infrastructure." *Data and Mobility, Transforming Information into Intelligent Traffic and Transportation Services, Proceedings of the Lakeside Conference 2010*, J. Düh, H. Hufnagl, E. Juritsch, R. Pfliegl, H.-K. Schimany, and H. Schönegger, eds., Springer Berlin Heidelberg, 61–70.
- Moret, Y. (2011). "Modeling cost and Time Uncertainty in Rail Line Construction." PhD Thesis, Department of Civil and Environmental Engineering, Massachusetts Institute of Technology, Cambridge, MA.

- Mudchanatongsuk, S., Ordonez, F., and Liu, J. (2008). "Robust solutions for network design under transportation cost and demand uncertainty." *Journal of the Operational Research Society*, 59(5), 652–662.
- Mulvey, J. M., Vanderbei, R. J., and Zenios, S. A. (1995). "Robust Optimization of Large-Scale Systems." *Operations Research*, 43(2), 264–281.
- Munoz, D. (2011). "Australia floods causing long-term damage." *REUTERS*, Gladstone, Australia, <<http://www.reuters.com/article/2011/01/07/us-australia-floods-idUSTRE6BU09620110107>>.
- Von Neumann, J., and Morgenstern, O. (1953). *Theory of Games and Economic Behavior*. Princeton University Press, Princeton, New Jersey, 1–635.
- Ogura, M. (2006). "The Niigata Chuetsu Earthquake —Railway Response and Reconstruction." *Japan Railway & Transport Review*, 43/44(March), 46–63.
- Oliveira, C. S. (2008). "Lisbon earthquake scenarios: A review on uncertainties, from earthquake source to vulnerability modelling." *Soil Dynamics and Earthquake Engineering*, 28(10-11), 890–913.
- Osman, I. H., and Laporte, G. (1996). "Metaheuristics: A bibliography." *Annals of Operations Research*, 63, 513–623.
- Pantha, B. R., Yatabe, R., and Bhandary, N. P. (2009). "Optimal Preliminary Highway Alignment, with Slope Disaster Risk Management, in Himalayan Regions." *Transportation Research Record*, (2120), 93–100.
- Pardalos, P. M., Romeijn, H. E., and Tuy, H. (2000). "Recent developments and trends in global optimization." *Journal of Computational and Applied Mathematics*, 124(1-2), 209–228.
- Parsons Brinckerhoff. (2009). *California High-Speed Train Project - Technical Memorandum: Earthwork and Track Bed Design Guidelines TM 2.6.7*. USA, 1–46.
- Parsons Brinckerhoff. (2010). *California High-Speed Train Project - Technical Memorandum: Hydraulics and Hydrology Design Guidelines TM 2.6.5*. 1–24.
- Perry, C. A. (2000). "Significant Floods in the United States During the 20th Century - USGS Measures a Century of Floods." *USGS Fact Sheet 024-00*, <<http://ks.water.usgs.gov/pubs/fact-sheets/fs.024-00.html>>.
- Profillidis, V. A. (2006). *Railway management and engineering*. Ashgate Publishing Co., 1–469.
- Puchinger, J., and Raidl, G. R. (2005). "Combining metaheuristics and exact algorithms in combinatorial optimization: A survey and classification." *Artificial Intelligence and Knowledge Engineering Applications: A Bioinspired Approach, First International Work-Conference on the Interplay Between Natural and Artificial Computation, IWINAC 2005, Las Palmas, Canary Islands, Spain, June 15-18, 2005, Proc*, 3562, 41–53.
- Ranf, R. T., Eberhard, M. O., and Berry, M. P. (2001). *Damage to Bridges during the 2001 Nisqually Earthquake, PEER Report 2001/15*. 1–46.

- RAVE. (2005). "2004 Annual Report." Rede Ferroviária de Alta Velocidade, s.a., <<http://www.refer.pt/MenuPrincipal/TransporteFerroviario/AltaVelocidade/Relatorios.aspx>>.
- RAVE. (2008). "High-Speed Rail Connection between Lisbon and Oporto." *Preliminary Project Design*, Lisbon, Portugal.
- REFER. (2012). "High speed." <<http://www.refer.pt/MenuPrincipal/TransporteFerroviario/AltaVelocidade/Enquadramento.aspx>> (Mar. 18, 2013).
- Repolho, H. M., Antunes, A. P., and Church, R. L. (2013). "Optimal Location of Railway Stations: The Lisbon-Porto High-Speed Rail Line." *Transportation Science*, 47(3), 330–343.
- Rodríguez, C. ., Bommer, J. ., and Chandler, R. . (1999). "Earthquake-induced landslides: 1980–1997." *Soil Dynamics and Earthquake Engineering*, 18(5), 325–346.
- Rose, A. (2004). "Economic Principles, Issues, and Research Priorities in Hazard Loss Estimation." *Modeling Spatial and Economic Impacts of Disasters*, Y. Okuyama and S. Chang, eds., Springer, Berlin, 14–36.
- RTRI. (2007a). "Design Standards for Railway Structures - Displacement Limits." Railway Research Technical Institute, Japan.
- RTRI. (2007b). "Design Standards for Railway Structures - Seismic Design." Railway Technical Research Institute, Japan.
- Saldivar-Sali, A., and Einstein, H. H. (2007). "A landslide risk rating system for Baguio, Philippines." *Engineering Geology*, 91(2-4), 85–99.
- Samanta, S., and Jha, M. K. (2011). "Modeling a rail transit alignment considering different objectives." *Transportation Research Part A: Policy and Practice*, 45(1), 31–45.
- SNIRH. (2012). "Atlas da Água." *Sistema Nacional de Informação de Recursos Hídricos*, <<http://geo.snirh.pt/AtlasAgua/>> (Apr. 21, 2012).
- Soares da Silva, A. (1983). "Environmental Atlas - Explanatory Note I.13, Lithological Map." Lisbon, Portugal.
- Sohn, J. (2006). "Evaluating the significance of highway network links under the flood damage: An accessibility approach." *Transportation Research Part A: Policy and Practice*, 40(6), 491–506.
- Sousa, M. L., and Oliveira, C. S. (1996). "Hazard mapping based on macroseismic data considering the influence of geological conditions." *Natural Hazards*, 14(2), 207–225.
- Steer Davies Gleave. (2011). "Evaluation of Regulation 881 /2004 - Final Report." Directorate General for Mobility and Transport, European Commission, <[http://ec.europa.eu/transport/facts-fundings/evaluations/doc/2011\\_era-evaluation-881-2004.pdf](http://ec.europa.eu/transport/facts-fundings/evaluations/doc/2011_era-evaluation-881-2004.pdf)>.
- Tatano, H., and Tsuchiya, S. (2008). "A framework for economic loss estimation due to seismic transportation network disruption: a spatial computable general equilibrium approach." *Natural Hazards*, 44(2), 253–265.

- Teixeira, P. F., López Pita, A., and Ferreira, P. A. (2010). "New possibilities to reduce track costs on high-speed lines using a bituminous sub-ballast layer." *International Journal of Pavement Engineering*, 11(4), 301–307.
- TEN-T EA. (2012). "Studies supporting the PPP programme for high speed rail implementation in Portugal." *The Trans-European Transport Network Executive Agency*, <[http://tentea.ec.europa.eu/en/ten-t\\_projects/ten-t\\_projects\\_by\\_country/portugal/2010-pt-93306-s.htm](http://tentea.ec.europa.eu/en/ten-t_projects/ten-t_projects_by_country/portugal/2010-pt-93306-s.htm)> (Mar. 18, 2012).
- Teves-Costa, P., Borges, J. F., Rio, I., Ribeiro, R., and Marreiros, C. (1999). "Source Parameters of Old Earthquakes: Semi-Automatic Digitization of Analog Records and Seismic Moment Assessment." *Natural Hazards*, 19(2), 205–220.
- Törnquist, J., and Persson, J. A. (2007). "N-tracked railway traffic re-scheduling during disturbances." *Transportation Research Part B: Methodological*, 41(3), 342–362.
- Trimble. (2013). "The Application of Quantm for High-Speed Rail." <<http://www.trimble.com/alignment/>> (May. 22, 2013).
- U.S. DOT. (2002). *Effects of Catastrophic Events on Transportation System Management and Operations, Northridge Earthquake–January 17, 1994*. Washington, DC, 1–59.
- Ueda, T., and Koike, A. (2000). "Economic Damage Assessment of Catastrophe in High Speed Rail Network." *Proceedings of 1st workshop for Comparative Study on Urban Earthquake Disaster Management*, US-Japan Cooperative Research for Urban Earthquake Disaster Mitigation, Kobe, Japan.
- UIC. (1994). "Ouvrages en terre et couches d'assise ferroviaires." Code UIC 719R 2<sup>ème</sup> édition.
- UIC. (2001). "Design of New Lines for Speeds of 300-350 Km/h, State of the Art." <[http://www.uic.org/IMG/pdf/2-09\\_Repor350\\_en.pdf](http://www.uic.org/IMG/pdf/2-09_Repor350_en.pdf)> (Dec.19, 2011).
- UIC. (2010). "High speed rail: Fast track to sustainable mobility." <[http://www.uic.org/IMG/pdf/20101124\\_uic\\_brochure\\_high\\_speed.pdf](http://www.uic.org/IMG/pdf/20101124_uic_brochure_high_speed.pdf)> (Mar. 19, 2013).
- UIC. (2011). "High Speed Lines in the World." <<http://www.uic.org/spip.php?article573>> ( Dec.15, 2011).
- Ukkusuri, S. V, Mathew, T. V, and Waller, S. T. (2007). "Robust transportation network design under demand uncertainty." *Computer-Aided Civil and Infrastructure Engineering*, 22(1), 6–18.
- UNESCO. (2013). "Convention Concerning the Protection of the World Cultural and Natural Heritage." *World Heritage Convention*, <<http://whc.unesco.org/>> (Aug. 21, 2013).
- UNISDR. (2005). "World Conference on Disaster Reduction." *Proceedings of the Conference Building the Resilience of Nations and Communities to Disasters*, UN, Geneva, 18-22 January 2005, Kobe, Hyogo, Japan,.
- UNISDR. (2009). "2009 UNISDR Terminology on Disaster Risk Reduction." United Nations International Strategy for Disaster Reduction, Geneva, Switzerland, <<http://www.unisdr.org/we/inform/terminology>>.



- Urquhart, W. (2011). "Italy high-speed rail protest turns violent." *BBC News*, <<http://www.bbc.co.uk/news/world-europe-14007565>> (Feb. 27, 2013).
- USGS. (1994). "The Loma Prieta , California , Earthquake of October 17 , 1989-Loss Estimation and Procedures." *U.S. Geological Survey Professional Paper 1553: Societal Response*, S. K. Tubbesing, ed., U.S. Geological Survey, Denver, CO.
- USGS. (1998a). "The Loma Prieta, California, Earthquake of October 17, 1989—Lifelines." *U.S. Geological Survey Professional Paper 1552: Performance of the Built Environment*, A. J. Schiff, ed., U.S. Geological Survey, Denver, CO.
- USGS. (1998b). "The Loma Prieta , California , Earthquake of October 17 , 1989-Highway Systems." *U.S. Geological Survey Professional Paper 1552: Performance of the Built Environment*, M. Yashinsky, ed., U.S. Geological Survey, Denver, CO.
- USGS. (1998c). "The Loma Prieta, California, Earthquake of October 17, 1989-Recovery, Mitigation, and Reconstruction." *U.S. Geological Survey Professional Paper 1553: Societal Response*, J. M. Nigg, ed., U.S. Geological Survey, Denver, CO.
- USGS. (1998d). "The Lorna Prieta , California , Earthquake of October 17 , 1989-Liquefaction." *U.S. Geological Survey Professional Paper 1551B: Strong Motion and Ground Failure*, T. L. Holzer, ed., U.S. Geological Survey, Denver, CO.
- USGS. (1998e). "The Lorna Prieta , California , Earthquake of October 17 , 1989-Landslides." *U.S. Geological Survey Professional Paper 1551 B: Strong Motion and Ground Failure*, D. K. Keefer, ed., U.S. Geological Survey, Denver, CO.
- USGS. (1998f). "Loma Prieta, California, Earthquake October 17, 1989. Oakland. Support column failure and collapsed upper deck on the Cypress viaduct of Interstate 880." *U.S. Geological Survey Professional Paper 1552 B: The Loma Prieta, California, Earthquake of October 17, 1989—Highway Systems*, <[http://libraryphoto.cr.usgs.gov/cgi-bin/show\\_picture.cgi?ID=ID.3ct;SIZE=medium](http://libraryphoto.cr.usgs.gov/cgi-bin/show_picture.cgi?ID=ID.3ct;SIZE=medium)> (Jan. 2, 2012).
- USGS. (2012a). "Glossary of Terms on EQ Maps." <<http://earthquake.usgs.gov/earthquakes/glossary.php>> (May. 11, 2012).
- USGS. (2012b). "Earthquake Glossary - magnitude." <<http://earthquake.usgs.gov/learn/glossary/?term=magnitude>> (May. 11, 2012).
- USGS. (2012c). "Historic Earthquakes." <[http://earthquake.usgs.gov/earthquakes/world/events/1755\\_11\\_01.php](http://earthquake.usgs.gov/earthquakes/world/events/1755_11_01.php)> (May. 11, 2012).
- Van Westen, C. J., Rengers, N., and Soeters, R. (2003). "Use of geomorphological information in indirect landslide susceptibility assessment." *Natural Hazards*, 30(3), 399–419.
- Varnes, D. J. (1978). "Slope movement types and processes." *Landslides: Analysis and Control*, R. L. Schuster and J. Krizek, Raymond, eds., National Academy of Sciences, Transportation Research Board Special Report 176, Washington, D.C., 11–33.
- Vilanova, S., and Fonseca, J. (2004). "Seismic hazard impact of the Lower Tagus Valley Fault Zone (SW Iberia)." *Journal of Seismology*, 8(3), 331–345.

- Wang, C., Peng, Y., and Liu, Y. (2009). "Crossing The Limits." *Civil Engineering*, 79(1), 64–80.
- Wang, H. B., Sassa, K., and Xu, W. Y. (2007). "Analysis of a spatial distribution of landslides triggered by the 2004 Chuetsu earthquakes of Niigata Prefecture, Japan." *Natural Hazards*, 41(1), 43–60.
- Wang, M., Qiao, J. P., and He, S. M. (2010). "GIS-based earthquake-triggered landslide hazard zoning using contributing weight model." *Journal of Mountain Science*, 7(4), 339–352.
- Wang, Z., and Lee, G. (2009). "A comparative study of bridge damage due to the Wenchuan, Northridge, Loma Prieta and San Fernando earthquakes." *Earthquake Engineering and Engineering Vibration*, 8(2), 251–261.
- Wardman, M. (2004). "Public transport values of time." *Transport Policy*, 11(4), 363–377.
- Watkins, D. W., and McKinney, D. C. (1997). "Finding robust solutions to water resources problems." *Journal of Water Resources Planning and Management*, 123(1), 49–58.
- Wilson, J. C. (2003). "Repair of New Long-Span Bridges Damaged by the 1995 Kobe Earthquake." *Journal of Performance of Constructed Facilities*, 17(4), 196–205.
- Wilson, J. P., and Gallant, J. C. (2000). *Terrain Analysis: Principles and Applications*. John Wiley & Sons, Inc., 56–58.
- World Bank, and United Nations. (2010). *Natural Hazards, UnNatural Disasters: The Economics of Effective Prevention*. The International Bank for Reconstruction and Development / The World Bank, Washington, DC.
- Yamazaki, F. (2004). "Report on The 2004 Mid Niigata Earthquake." Chiba University, Chiba, Japan.
- Youd, T. (1984). "Recurrence of liquefaction at the same site." *Proceedings of the Eighth World Conference on Earthquake Engineering*, Earthquake Engineering Research Institute, San Francisco, CA, 231–238.
- Zeferino, J. A., Cunha, M. C., and Antunes, A. P. (2012). "Robust optimization approach to regional wastewater system planning." *Journal of Environmental Management*, 109, 113–122.
- Zêzere, J. L., Ferreira, A. B., and Rodrigues, M. L. (1999). "Landslides in the North of Lisbon Region (Portugal): Conditioning and triggering factors." *Physics and Chemistry of the Earth, Part A: Solid Earth and Geodesy*, 24(10), 925–934.
- Zêzere, J. L., Trigo, R. M., Fragoso, M., Oliveira, S. C., and Garcia, R. A. C. (2008). "Rainfall-triggered landslides in the Lisbon region over 2006 and relationships with the North Atlantic Oscillation." *Natural Hazards and Earth System Science*, 8(3), 483–499.
- Zêzere, J., and Rodrigues, M. (2002). "Rainfall Thresholds for Landsliding in Lisbon Area (Portugal)." *Landslides: Proceedings of the First European Conference on Landslides, Prague, Czech Republic, June 24-26, 2002*, J. Rybar, J. Stemberk, and P. Wagner, eds., A.A. Balkema, 333–338.
- Zitellini, N., Gracia, E., Matias, L., Terrinha, P., Abreu, M. A., DeAlteriis, G., Henriët, J. P., Danobeitia, J. J., Masson, D. G., Mulder, T., Ramella, R., Somoza, L., and Diez, S. (2009). "The

quest for the Africa-Eurasia plate boundary west of the Strait of Gibraltar.” *Earth and Planetary Science Letters*, 280(1-4), 13–50.